A. I. Ch. E. JOURNAL

EMICAL ENGINEERING RESEARCH AND DEVELOPMENT / DECEMBER 1959

CONTENTS

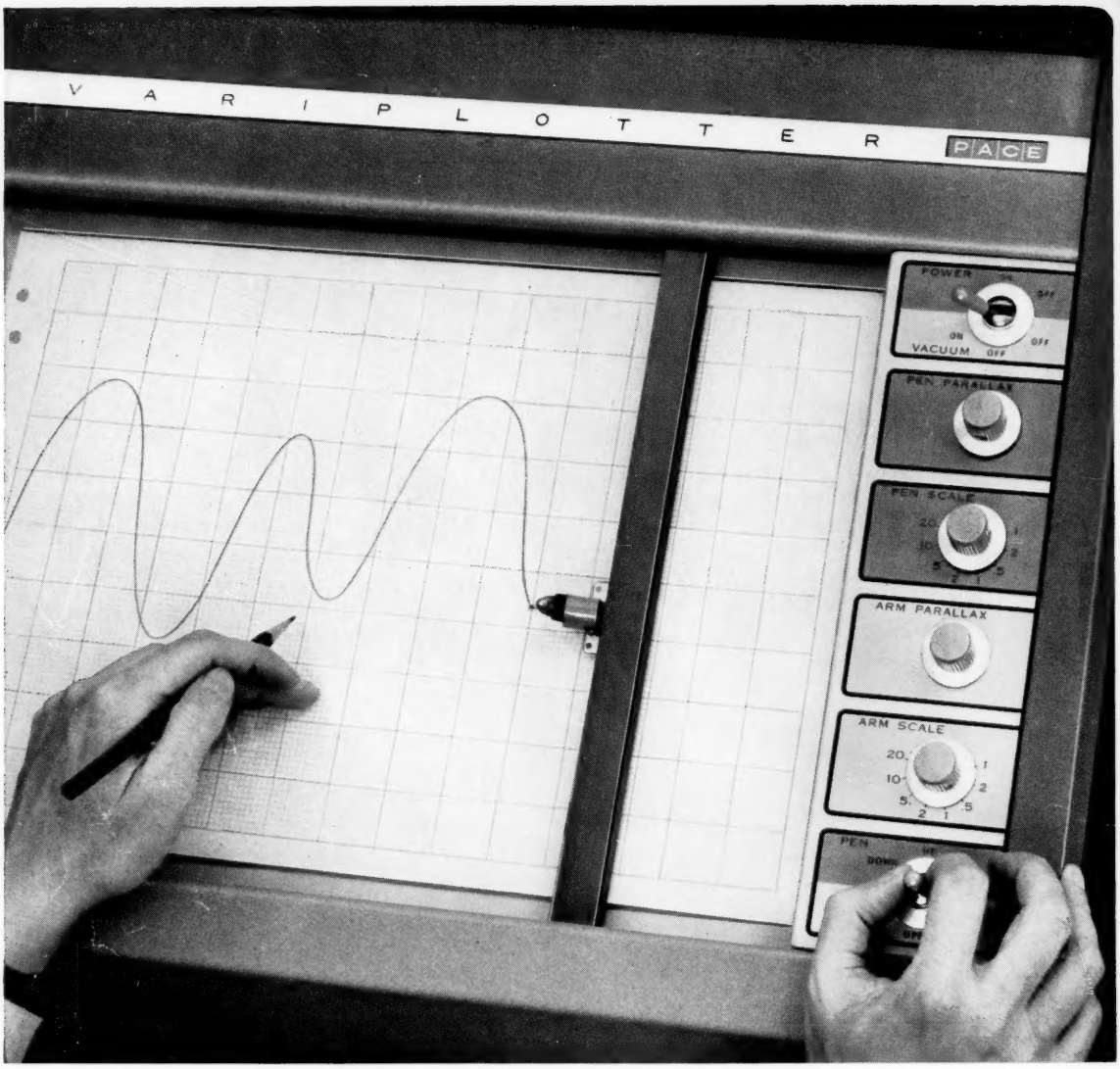

with **EAI** *portable X-Y plotter—*

you can convert data to graphic form quickly...accurately...reliably

With Electronic Associates' new Variplotter Model 1100E, data can be converted immediately to graphic form for quick, easy interpretation and understanding. Graphic display adds life to performance data—makes X and Y relationships instantly, unmistakably clear . . . provides permanent picture-like records of performance.

With the addition of accessories, versatile Variplotter will operate as a function generator, or will plot digital information from a keyboard. Its small size (23" L by 17½" W by 9½" H) and light weight (43 lbs.) make it a convenient laboratory tool.

The Variplotter combines high dynamic and static accuracy with a wide range of input sensitivities. Its rugged construction assures dependable, low-maintenance performance.

For name of our nearest representative write Dept. S

VARIPLOTTER MODEL 1100E FEATURES:

- Portable table top size
- Vacuum hold down
- Wide range of input sensitivities
- High dynamic and static accuracy
- Rugged construction
- Ease of maintenance
- Differential inputs

For complete specifications write for Booklet AP-810 P

EAI ELECTRONIC ASSOCIATES, INC. *Long Branch, New Jersey*

A.I.Ch.E. JOURNAL

DECEMBER, 1959 ● VOL. 5, NO. 4

The A.I.Ch.E. Journal, an official publication of the American Institute of Chemical Engineers, is devoted in the main to theoretical developments and research in chemical engineering and allied branches of engineering and science. Manuscripts should be submitted to the New York office.

Publication Office, 1407 Sherwood Avenue, Richmond 22, Virginia. Published quarterly in March, June, September, and December by the American Institute of Chemical Engineers, 25 West 45 Street, New York 36, New York. Manuscripts and other communications should be sent to the New York office. Correspondence with the editor may be addressed to him at Yale University, 225 Prospect Street, New Haven 11, Connecticut. Statements and opinions in the *A.I.Ch.E. Journal* are those of the contributors, and the American Institute of Chemical Engineers assumes no responsibility for them. Subscriptions: one year, member $6.00, nonmember $12.00; additional yearly postage, Canada 50 cents, Pan American Union $1.50, other foreign $2.00 (foreign subscriptions payable in advance). Single copies: $4.00. Second-class mail. Postage paid at Richmond, Virginia. Copyright 1959 by the American Institute of Chemical Engineers. National headquarters of A.I.Ch.E. is concerned about nondelivery of copies of the *A.I.Ch.E. Journal* and urgently requests subscribers to give prompt notification of any change of address. Sixty days must be allowed for changes to be made in the records.

A.I.Ch.E. JOURNAL

Conservation and Engineering

II. Utilization of Land

The continental United States has about two and a quarter billion acres of land, which is utilized approximately as follows: 47 per cent cropland and pasture for food production (vastly more pasture); 6 per cent cropland and pasture for fiber production and other industrial products (also vastly more pasture); 30 per cent forest; 5 per cent cities, towns, roads, national parks, etc.; and 12 per cent unused and presumably unusable desert and mountains. This is the land we have. It isn't going to grow, and it isn't going to improve through use. Indeed, in many cases the land is deteriorating through use. It may seem utterly foreign to us with our history of abundance, but this land is going to be subjected to enormous stresses if we are to feed the population which is predicted. That the food we must grow may be a principal limiting factor in the days to come seems almost impossible to those of us who fret about the present farm programs, based as they are on too much food, but nonetheless our capacity to grow food will be a very serious matter.

Cropland for food production must be effectively increased, and there are essentially only two ways to do it: we must divert to this purpose some land otherwise used, and we must increase our production of food per acre.

The diversion to food production of land now otherwise used is not going to be easy, but there is one category of land use which is capable of such diversion. That is the land now used for growth of fibers and other materials for industrial use. The principal items here are cotton and the pasturing of sheep for wool. The former is moderately destructive to the soil; the latter extremely so. The present governmental practice of subsidizing the wool grower for the difference between the market price and an artificial price of 62 cents a pound has been called by William Vogt simply a subsidy of soil erosion. In any case the land now used for cotton and wool production is wastefully used, badly used, and unnecessarily used. The average production of cotton is about 470 pounds per acre per year, that of wool is about 2 pounds per acre per year. But, through research and invention, wholly synthetic fibers may be made in factories at a current rate of about 300,000 pounds per acre per year. The area on which these figures were based includes everything connected with the factories—intermediates manufacture, storage tanks, offices, even parking lots. It should be noted that these fibers are the wholly synthetic ones, such as nylon, which do not require any raw materials grown on land.

Thus by turning to the manufacture of fibers instead of the growth of them we shall be able to produce the required amount of fibers in about 1/1,000 of the area now used for fiber production. For all practical purposes this will permit us to have for food production essentially all of the 6 per cent of our land now used for fibers. However this is only a 28 per cent increase in our land for food production, which is a step in the right direction, but only a step.

Two facts about this conversion should be noted moreover. (1) Cotton and sheep-grazing land is not usually very good land. Its productivity for food will have to be carefully studied and improved through research. (2) This enormous development of synthetic fibers was not begun as a conservation measure. These fibers were discovered and developed as a natural part of orderly research programs, which are devoted to a constant search for better and cheaper materials—and for new profits. The aid to conservation here is a kind of by-product of this research—free enterprise at its best.

Returning to the tabulation of main land uses, can any other diversions be expected? The only other big item is the forests, and one might think that we could get land for food production by cutting them down. One would be thinking in historical perspective because this is exactly what man has done for thousands of years.

Further cutting of our forests, however, must not be done. We simply cannot count at all on possible diversion of woodlands for food production. Our woodlands are enormously important to us for several reasons. First, the wood products such as lumber and pulpwood are essential to our lives. We are only now approaching the successful application of the sustained-yield concept, which ensures that these wood products are taken out only as fast as they are grown. Second, forests play a great part in the hydrologic cycle, and any further destruction of them may yield grievous deterioration in our climate. Third, forests represent the only remaining places for recreation in natural surroundings. This use of woodlands will become more and more important as our cities and suburban areas continue to grow. Furthermore, forests are constantly threatened with destruction through fire, insects, disease, and depredators of all types. Incidentally, we must credit technology with the very existence of our forests; they would have been gone long since had it not been for the discovery and perfection of the use of coke in steel manufacture, which made obsolete the use of charcoal.

There are two prospects through which science and engineering may help us to protect our forests. The first is that the greatest loss of our forests is due to insects and disease. It is certainly to be expected that through research progress will be made in reducing these losses. The second is that we may change the uses to which our wood cut is put. The distribution is approximately as follows: 52 per cent lumber; 22 per cent pulpwood; 16 per cent fuel; 10 per cent veneers, plywood, and others. Since a growing population will require more of these items (particularly lumber), how can we accommodate such need without a serious drain on the forests? One thing to do is to try to reduce and ultimately to eliminate the 22 per cent used as pulpwood. Such pulpwood is grown primarily for the manufacture of paper, paperboard, and rayon. Rayon is gradually being replaced by the wholly synthetic fibers, and this will be more and more the case. Paper and paperboard are next on the list; there is no scientific reason why these products cannot be made wholly synthetically from other raw materials, thus relieving this great drain on our forests.

It thus appears that diversion of certain land now used for the growth of fibers to the growth of food will be helpful but only to a moderate degree. Forestland offers no promise for the supply of food.

Increased productivity of the land will be considered in a later issue.

H.B.

BOOKS

Plant Design and Economics for Chemical Engineers, Max S. Peters, McGraw-Hill Book Company, Inc., New York (1958). 511 pages. $11.00.

Consideration of the complete chemical plant rather than the individual unit operations and processes marks one of the objectives of chemical engineering education. This book, which is directed toward the attainment of that objective, effectively combines the engineering principles of plant design with the essentials of economic analysis.

Emphasizing the interdependence of the cost and engineering aspects of the design the author introduces the economic viewpoint by detailing the costs involved in the construction and operation of the chemical plant. Later chapters discuss investment costs, interest, depreciation, replacement costs, and the evaluation of alternative investments. Taxes and insurance are discussed in a brief chapter which will be of considerable value to the novice. Cost-estimation methods used in evaluating ehemical plant construction and operation are presented in detail. A chapter on cost and asset accounting surveys the methods and terminology used in this field. These sections are especially pertinent because the effects of present tax and depreciation policies are included.

Half the book is devoted to equipment—design methods and cost data. The development of more detailed methods is preceded by a chapter devoted to a general discussion of scale up, methods of fabrication, safety, corrosion problems, and materials of construction. Optimum design concepts are developed and applied in examples. Design methods and recent cost data are presented for piping, pumps, heat transfer equipment, mass transfer equipment, and filters. Prefacing certain of the design sections are rather complete outlines of applicable, fundamental unit-operations theory. Cost information is also given for other types of equipment.

The presentation of topics which represent combinations of the economic and technical points of view is, in the opinion of this reviewer, of primary importance, since these are not readily available in the proper form. Under the heading of general design considerations the author presents brief discussions of plant layout, location, and safety, structural design, instrumentation, and patent law. Perhaps the treatment of these topics could have been expanded at the expense of the more fundamental portions of the equipment-design sections. Additionally waste treatment and disposal and design report writing occupy a chapter each. Sections of the material on report writing might have been ommitted in favor of other topics.

Illustrative examples are included and are used, where applicable, to clarify the various topics. Unsolved problems are given at the end of most chapters, and longer design problems are included in the appendix. Adequate bibliographies are included for most topics, and the listing of cost references is recent and usefully organized.

(*Continued on page 563.*)

Evaporation Rates of Liquids to Flowing Gas Streams

D. E. SEVERSON, A. J. MADDEN, and EDGAR L. PIRET

University of Minnesota, Minneapolis, Minnesota

The influence of high concentration gradients and high evaporative velocities on rates of mass transfer was studied by evaporating liquids into low-speed inert gas streams at pressures approaching the vapor pressure of the liquids.

Inert gas concentration in some experiments changed nearly fivefold across the boundary layer. The velocity normal to the surface (owing to evaporation), usually neglected in comparison with main-stream velocity, varied from 0.038 to 19 times the main-stream velocity.

The data for air-water, air–carbon tetrachloride, air-chlorobenzene, and helium-chlorobenzene systems were represented within experimental error over the Graetz number range of 0.1 to 1,800 by the flat-duct equations of Butler and Plewes (*2*) and also by the usual dimensionless plots.

The influence of high concentration gradients on the rates of mass transfer from evaporating liquids is of considerable interest to chemical engineering practice and has been much speculated upon (*12*). Presented herein are experimental data on the evaporation rates of several liquids into low-velocity gas streams over such a wide range of absolute pressures and flow rates, that the partial pressure of the nondiffusing component varied as much as fivefold within the boundary layer. By using subatmospheric pressures only slightly above the vapor pressures of the vaporizing liquids one could obtain high diffusivities and high evaporation velocities normal to the surface as compared to the main-stream velocities. Also, for example, the Schmidt number varied by a factor as high as 35 between surface and bulk-gas properties.

The data were computed in terms of several available equations; among these the equation of Butler and Plewes (*2*) was found to correlate the data within experimental accuracy over a range of Graetz numbers from 0.1 to 1,800 for diverse systems. Correlations were also obtained by plotting the Sherwood, Schmidt, and Reynolds number groups.

The importance to the rate of evaporation of the flow of heat through the liquid to its surface is underscored by the examination of a temperature profile for a particular run (Figure 1). In this case a temperature gradient of about 3.9°C./mm. of depth in the liquid was obtained. A 0.3-mm.–diameter thermistor was used to measure the temperature of the evaporating surface in all runs.

Data on the effect of concentration levels on mass transfer rates in the high Reynolds number range of 600 to 15,000 have been presented by Westkaemper and White (*13*) and Cairns and Roper (*3*).

EVAPORATION-RATE MEASUREMENTS

Scope

The liquid was evaporated from the open end of a 13-mm. O.D., 10.5-mm. I.D. vertical glass tube projecting into a 26.4-mm. I.D. horizontal round glass tube through which the inert gas was caused to flow at various rates and total pressures. The evaporation rate was determined by keeping the liquid surface level with the top of the vertical tube and measuring at various times the volume of liquid remaining in the supply tubing.

The systems studied were air-water, air–carbon tetrachloride, air-chlorobenzene, and helium-chlorobenzene. In addition, a few points were determined for helium-water and air-bromobenzene. Four measurements of the rates of evaporation of water into air from a 1.37- by 1.37-cm.–square surface, set flush with the bottom of a 2.54-by 2.54-cm.–square duct are also reported.

Total pressures ranging from 15 to 700 mm. Hg and average inert-gas flow velocities of 0.013 to 58 cm./sec. were used. Since all determinations were made at room temperature and all entering gas streams contained pure inert gas, variations in relative vapor concentration were attained by varying the total pressure and by studying several systems.

In most cases operation was adiabatic; that is, the room temperature was controlled at a constant value and the liquid surface, initially at room temperature, was allowed to approach a steady state temperature resulting from the evaporation regime. The surface temperature of the evaporating liquid was determined with a calibrated thermistor, 0.3 mm. in diameter, located just under and practically in contact with the under side of the evaporating surface.

The experimental arrangement of a cylinder projecting into a circular tube is perhaps not the simplest case for fluid-dynamics analysis. It was arrived at, after several other designs had been attempted, as convenient for this investigation, the objective of which was to investigate primarily from an experimental viewpoint the effect of high ratios of vapor to inert gas and the effect of high gradients on mass transfer rates.

Rate-Measuring System

A flow diagram of the experimental apparatus is shown in Figure 2. The evaporation section, consisting of a vertical tube the open end of which projected into a larger horizontal tube serving as the gas duct, may be seen in Figures 3 and 4.

D. E. Severson is at the University of North Dakota, Grand Forks, North Dakota, and Edgar L. Piret is at the American Embassy, Paris, France.

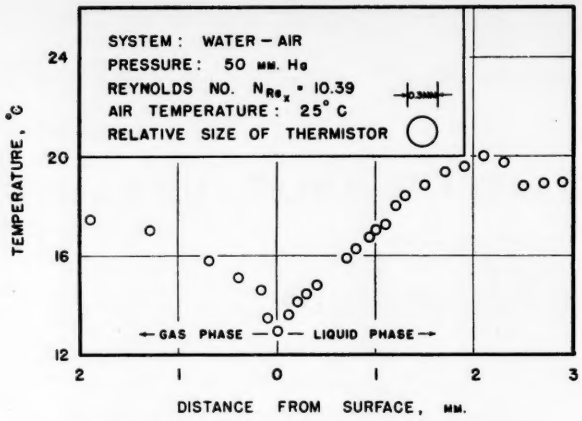

Fig. 1. Gas- and liquid-temperature profiles for an air-water run showing high gradients encountered.

These are photographs of evaporation in progress of titanium tetrachloride liquid into moist air. The evaporation section was built of Pyrex glass to facilitate cleaning and to permit observation of the progress of the evaporation. The square-duct experiments were made in a similar apparatus.

Evaporation rates were determined by measuring the time rate of change in the volume of the liquid supply contained in a U tube. The liquid was held in position by a column of mercury open on its other side to the atmosphere. The positions of the mercury-evaporating liquid meniscus and thus of the evaporating surface were adjusted first by the addition of mercury to the open end of the U tube and during a run by raising or lowering a glass rod. This rod extended into the mercury on the atmospheric side of the U tube and was moved by means of a screw-gear mechanism. During runs adjustments were made at frequent intervals to maintain the evaporating surface flat across the opening of the vertical tube. Timed observations of the position of the mercury-evaporating liquid meniscus with a cathetometer gave the evaporation-rate data.

It was found in a series of experiments that a change of 0.3 mm. in the position of the meniscus either above or below the flat surface of the glass tube changed the evaporation rate 2 or 3%.

The inert-gas flow rate was measured with a wet-test gas meter and the system operating pressure determined with a Zimmerli gauge or with a mercury manometer open to the atmosphere.

On the high-pressure side of the system (Figure 2) the gas train consisted of a wet-test meter, a capillary flow meter equipped with a water manometer, followed by desiccants silica gel, drierite, and calcium chloride, and a cotton-filled tube for removal of entrained dust. Reduction to operating pressure was made by a needle valve. A horizontal, round Pyrex tube of 2.64-cm. I.D. formed a calming section 70 cm. long preceding the evaporating surface, that is the flat, open end of a vertical Pyrex tube of 1.05-cm. I.D. and 1.30-cm. O.D. A needle-valve control was located following a 24-cm. length of the same-diameter tubing and a shorter constricted length. This in turn was followed by a 4-ft. vertical section of 2-in. standard pipe serving as a surge volume and finally by a vacuum pump. A bleeder-valve opening to the atmosphere was attached to the upper end of the 2-in. pipe to permit independent adjustment of flow rate and system pressure. The vertical evaporator tube projected into the horizontal tube at about 0.4 cm. below the center line (Figures 3 and 4).

Rate-Determination Procedure

Mercury was placed in the U tube (Figure 2), and the system was evacuated to a pressure below that at which the run was to be made. The liquid to be evaporated, having first been purged of dissolved air by boiling, was drawn into the system above the mercury through the sidearm filling tube. Final adjustments of the flow rate and system pressure to desired run conditions were made, and the liquid level was brought up to the level of the flat surface by the addition of more mercury to the U tube. A precise setting of the liquid level at the flat surface was made by adjustment of the glass rod. The time was recorded and the position of the mercury-evaporating liquid meniscus read with a cathetometer.

Evaporation was then allowed to proceed for a time interval which depended upon the rate for the particular run and varied from 30 sec. to 10 min. The level was then adjusted precisely to the original position by again lowering the glass rod by means of the screw mechanism. The new position of the mercury-liquid meniscus was noted. The volume of liquid evaporated during the time interval was equal to the tube volume displaced. This procedure was continued until enough observations had been made to establish the evaporation rate, the necessary run time being from 15 min. up to about 4 hr.

Following each cathetometer reading the evaporation surface temperature was measured with the calibrated 0.3-mm.-diameter spheroidal glass-coated bead thermistor, with a temperature coefficient of resistance of about 3.4%/°C. Since the thermistor reading depended upon the current flow, all readings were made with a potentiometer at a standard thermistor current of 10 μa. The thermistor was placed so that the bead tangentially just touched the under surface of the liquid when the liquid surface was flat across the opening.

During each run intermittent readings were taken of the wet-test meter, capillary flow manometer, meter thermometer, room thermometer, barometer, and system pressure gauge.

One of the major experimental difficulties encountered was in the release of dissolved gases by the evaporating liquid during the course of the measurement. To avoid this liquid was boiled several minutes to remove dissolved gases and taken up into a 50-cc. hypodermic syringe. The syringe needle was thrust into a cork and the liquid cooled in the syringe under the pressure of the weight of the plunger, thus preventing dissolution of air before introduction into the system under vacuum. The sidearm was first filled with gas-free liquid, the cork inserted into the flanged opening, and the liquid admitted slowly through the needle and stopcock.

Because of the tendency for organic compounds to accumulate at the surface of an immiscible liquid and markedly to affect evaporation rates, it was also essential to use great care to minimize contact between the stopcock lubricants and the liquid to be evaporated, especially in the runs with water.

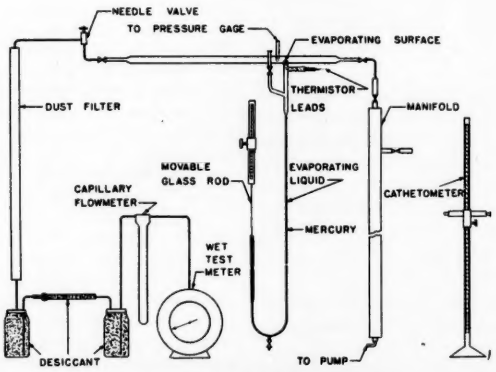

Fig. 2. Flow diagram of apparatus.

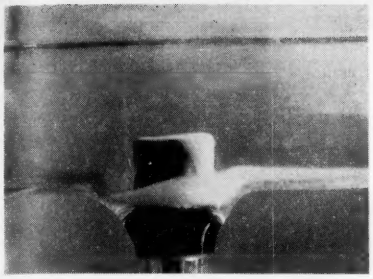

Fig. 3. Evaporation pattern of titanium tetrachloride into a stream of moist air; scale 4:3; data: p_T = 686 mm. Hg, N_{Re_s} = 66.8, $1/\psi$ = 958, v_n/u_0 (estimated) = 0.070.

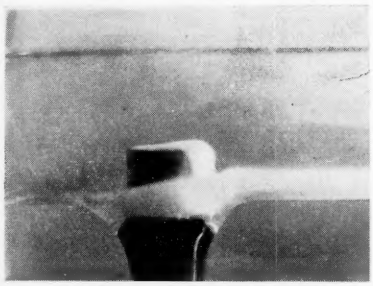

Fig. 4. Evaporation pattern of titanium tetrachloride into a stream of moist air; scale 4:3; data: p_T = 508 mm. Hg, N_{Re_s} = 58.7, $1/\psi$ = 840, v_n/u_0 (estimated) = 0.075.

High-vacuum silicone grease was found to be sufficiently insoluble for stopcock sealing purposes during runs.

Surface Temperature Important

The over-all mass transfer rate is highly dependent on the liquid surface temperature, since this determines the vapor pressure of the liquid at the interface and hence the driving force for evaporation. The surface temperature in turn depends on the evaporation rate and also upon the heat flow to the surface from the gas and liquid phases.

The magnitude of the temperature gradient near the evaporating surface is illustrated by the data of Figure 1. In this experiment the rigid thermistor connections were removed and the leads brought into the system through a flexible rubber tube. This permitted positioning the thermistor at various distances from the evaporating surface. The evaporation rate could not be measured simultaneously with the temperature profile in this experiment because the system volume was no longer rigid enough with the rubber connections to permit accurate measurement of the liquid volume change.

The temperature profile of Figure 1 was determined with evaporation proceeding under the conditions of run 88 (air-water at 50 mm. Hg). The very high temperature gradients through both gas and liquid films are to be noted, the liquid film gradient being 3.9°C./mm. of depth. By far the greater portion of the heat of vaporization in this run was transferred through the liquid film.

This extremely large temperature gradient in the liquid phase showed the necessity of very careful measurement of the surface temperature in evaporative runs to determine accurately the vapor pressure of the liquid at the surface where the evaporation occurs. Hence in evaporative-rate determinations the thermistor was placed as close to the surface as possible without its actually distorting the surface. This was accomplished by bringing the surface level to a point where the thermistor touched its reflection in the under surface of the liquid at each level adjustment. The thermistor was so placed in the system that the meniscus was flat across the opening after this adjustment had been made.

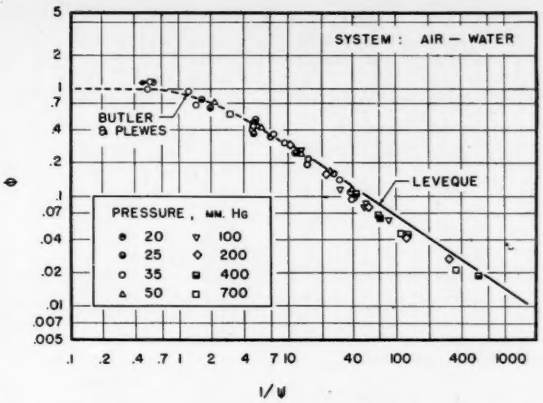

Fig. 6. Experimental mass transfer data for system air-water.

Practical utilization of any mass transfer correlation demands an accurate knowledge of the heat transfer situation as well as the flow situation. As a further illustration of the importance of this point, the results of runs 119 and 120 may be considered; both were made with air-water at 35 mm. total pressure, flow rates differing by less than 3%, and ambient air temperature 25°C. Run 119 was made in the usual manner, the surface being allowed to approach a steady state temperature which as measured with the thermistor averaged 14.7°C. Run 120 differed from 119 only in that additional heat was supplied to the surface by radiation from a hot chromel resistance wire suspended above the evaporating surface by means of a conical reflector. In this run the steady state temperature was 20.3°C. The

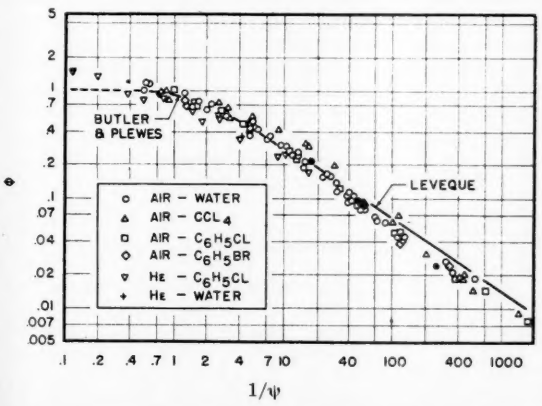

Fig. 5. Experimental mass transfer data for all systems studied; fractional saturation plotted vs. the Graetz number, curves calculated from Butler and Plewes's equations.

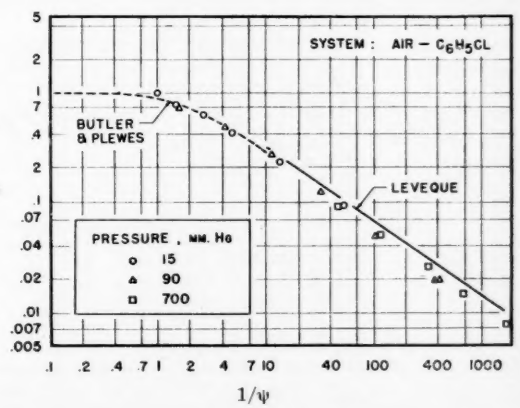

Fig. 7. Experimental mass transfer data for system air-chlorobenzene.

TABLE 1. SUMMARY OF EXPERIMENTAL DATA

Run number	System pressure p_T, mm. Hg	Temperature, gas t_o °C.	Temperature, surface t_s °C.	Vapor pressure P^*, mm. at surf.	Dry-gas rate, S.T.P. cu. ft./hr.	Evaporation rate, lb./ sq. ft./hr.	ϕ	$1/\psi$	v_n/u_o	$\frac{p_{Bo}}{p_{Bs}}$
System: Air-water.										
120	35.1	25.1	22.4	20.3	0.0136	1.55	1.17	0.543	17.8	2.37
119	35.0	25.1	17.1	14.7	0.0140	0.686	1.14	0.561	10.7	1.72
114	35.1	25.0	12.3	10.7	0.960	1.94	0.118	39.2	0.590	1.42
88	50.0	25.0	15.2	13.0	0.959	1.64	0.119	38.5	0.603	1.351
64	197.0	21.8	18.4	15.8	0.254	0.336	0.298	10.2	1.49	1.087
94	198.0	25.1	17.1	14.6	7.66	0.840	0.0276	307.	0.137	1.080
92	699.3	25.0	24.7	23.3	0.0748	0.0804	0.586	2.97	2.86	1.034
93	702.6	25.0	23.1	21.2	8.80	0.304	0.0213	350.	0.104	1.031
*SD5	187.	25.1	19.4	16.9	2.08	0.458	0.0971	50.1	0.339	1.10
*SD4	330.	25.0	20.9	18.5	0.765	0.218	0.201	18.5	0.703	1.06
*SD3	331.	25.0	20.5	18.1	11.7	0.407	0.0255	284.	0.0877	1.06
System: Air-chlorobenzene.										
153	15.0	25.0	21.4	9.48	0.00503	2.74	0.980	0.697	12.6	2.72
125	15.0	25.0	14.5	6.38	0.378	5.34	0.0947	52.9	0.487	1.74
141	90.0	25.1	23.4	10.6	0.236	1.15	0.121	32.6	0.608	1.13
145	700.	25.1	25.1	11.7	0.350	0.179	0.0903	48.5	0.447	1.017
143	700.	25.0	24.0	11.0	13.2	0.550	0.00787	1813.	0.0388	1.016
System: Air-carbon tetrachloride.										
166	120.	25.1	21.1	95.8	0.00639	5.45	0.816	0.885	11.4	4.96
157	118.	24.9	15.5	73.6	4.08	16.8	0.0142	571.	0.0707	2.66
123	200.	25.0	15.3	72.8	0.113	7.10	0.330	15.8	1.85	1.57
165	700.	25.0	24.6	113.	0.00602	0.505	0.960	0.829	5.57	1.19
159	700.	25.1	22.3	101.	10.4	6.19	0.00898	1440.	0.0442	1.17
System: Helium-chlorobenzene.										
186	15.0	25.0	18.6	8.09	0.0114	3.65	0.903	0.359	8.65	2.17
181	15.4	25.0	11.6	5.36	0.276	8.70	0.247	8.73	1.33	1.53
174	90.0	25.0	24.3	11.2	0.00373	0.283	1.48	0.116	8.91	1.14
175	696.	25.0	24.1	11.1	0.529	0.479	0.169	16.5	0.840	1.016
176	699.	25.1	23.9	11.0	1.71	0.680	0.0754	53.2	0.371	1.016
System: Air-bromobenzene.										
133	15.0	25.0	21.8	3.48	0.342	3.46	0.0911	50.4	0.461	1.30
136	35.0	25.0	24.1	4.01	0.00856	0.399	0.788	1.25	4.27	1.13
132	99.2	25.1	23.7	3.90	2.24	0.978	0.0236	329.	1.17	1.041
System: Helium-water.										
90	35.1	25.0	11.6	10.2	0.359	2.23	0.354	4.15	1.96	1.49

*Square duct runs

measured evaporation rate was 2.25 times as large in run 120 as in run 119, but the value of ϕ obtained was only 1.025 times as large showing that within experimental error the correlation of Figure 5 was equally valid for both runs.

Flow-Pattern Photographs

Because of the geometry used it was desirable to observe experimentally whether or not the evaporation pattern appeared undisturbed over the entire length of the cylinder. For this purpose liquid titanium tetrachloride was evaporated into moist air. The vapor pressure is comparable to that of chlorobenzene, and vapor densities are of the order of some of the systems studied. At the boundary layer a dense smoke was produced by the interaction of titanium tetrachloride and water, and the over-all shape of the boundary layer could be seen.

The photographs of Figures 3 and 4 show the visible boundary layer for the evaporation of titanium tetrachloride into streams of moist air at near-atmospheric pressure and at two air-flow rates near the high end of the range covered in the rate measurement runs. Even at these higher velocities, where separation or disturbance in the flow pattern might occur, the shape of the boundary layer appeared to be smooth and unbroken over the entire length of the evaporating surface. The calculated Reynolds numbers for all runs in the investigation are of course very low.

Visual observations of the titanium tetrachloride evaporation at lower flow rates, where the smoke was not dense enough to be photographed, also showed no evidence of tripping into turbulence along the evaporating surface.

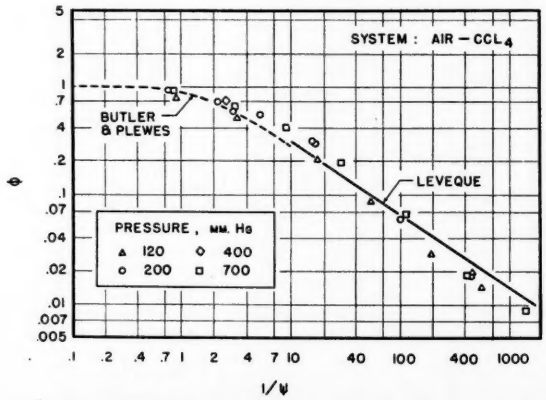

Fig. 8. Experimental mass transfer data for system air-carbon tetrachloride.

EXPERIMENTAL RESULTS

Representative data are summarized in Table 1*. Among the dimensionless groups calculated are the fractional saturation of the gas stream leaving the

*Tabular material has been deposited as document No. 5975 with the American Documentation Institute, Photoduplication Service, Library of Congress, Washington 25, D. C., and may be obtained for $2.50 for photoprints or $1.75 for 35-mm. microfilm

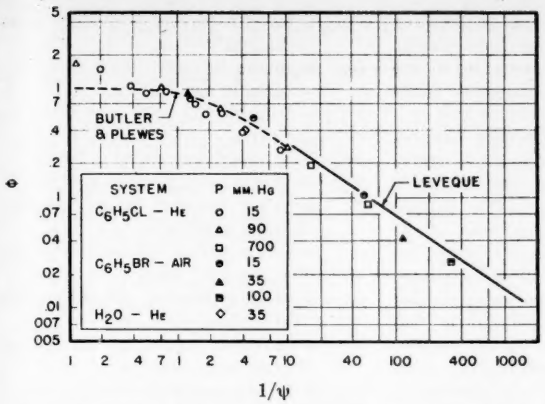

Fig. 9. Experimental mass transfer data for systems helium-chlorobenzene, air-bromobenzene, and helium-water.

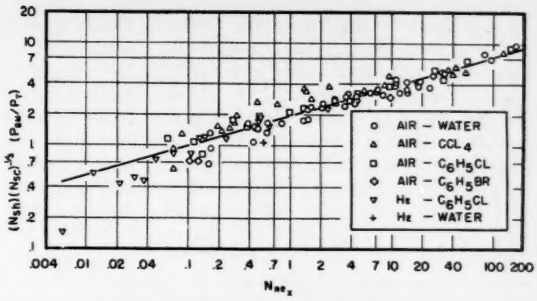

Fig. 10. Sherwood-Schmidt-Reynolds number plot of experimental data for all systems studied.

apparatus and the Graetz number for mass transfer.

It is important to note that in the calculation of the Graetz number the weight rate of flow was taken as the weight rate of flow of incoming dry gas and does not include the weight of vapor present after evaporation. Also, since the evaporation surface was a circle of diameter 1.05 cm., the integrated average length of path presented to the gas passing over the surface, $\pi D/4$, or 0.825 cm., was used in all calculations.

In the calculation of the ϕ the vapor pressure of the liquid was taken at the liquid surface temperature, and consequently a calculated value of ϕ equal to unity corresponds to saturation in the exit gas at the surface temperature of the liquid and not at the exit gas temperature.

The ranges of variables covered are summarized in Table 2. The ratio p_{B0}/p_{Bs} is the ratio of the partial pressure of inert component above the boundary layer to that at the surface, with the evaporating liquid assumed to exert its full vapor pressure in the surface layer. The horizontal approach velocity is calculated by dividing the volumetric rate of flow of inert gas through the system by the open cross section of the duct at the evaporating surface, that is the cross area of the tube minus the cross area of the projecting evaporator tube. The vapor velocity normal to the liquid surface was computed from the measured evaporation rate, the vapor density being evaluated at the surface temperature and vapor pressure.

Physical Properties

The diffusivity values used are from experimental literature tabulated by Wilke and Lee (*14*) or calculated from the equation of Hirschfelder, Bird, and Spotz (*4*). Corrections were made as needed for operating temperature and pressure.

System	D, sq. cm./sec. at 25°C., 1 atm.	Source
Air-water	0.260	Experimental
Air–carbon tetrachloride	0.0740	Calculated
Air-bromobenzene	0.0703	Calculated
Air-chlorobenzene	0.0747	Calculated
Helium-water	0.908	Experimental
Helium-chlorobenzene	0.329	Calculated

Viscosities for air, helium, and water vapor were taken from the literature (*6*); those for bromobenzene, chlorobenzene, carbon tetrachloride, and mixtures were calculated according to Bromley and Wilke (*1*). Vapor pressures for water, carbon tetrachloride, chlorobenzene, and bromobenzene are from the literature (*5, 8*).

Data Correlation

The data were calculated in terms of the analytical treatment of Butler and Plewes (*2*) for evaporation from one of two infinite parallel surfaces into a laminar air stream. The results for all systems studied are shown in Figure 5 and for individual systems in Figure 6 through 9. It is seen that the data of the present investigation are well correlated by the functional relation developed by Butler and Plewes; that is

$$\phi = 1 - 0.896e^{-2.43\psi} - 0.0609e^{-23.5\psi} - \cdots \qquad (1)$$
$$(0 < 1/\psi < 10)$$

and

$$\phi = 1.47(1/\psi)^{-\frac{1}{2}} \qquad (1/\psi > 10) \quad (2)$$

where

$$\phi = \frac{y_s p_T}{p^*}$$

and

$$1/\psi = \frac{w}{\rho D_v x}$$

Equation (1) was derived on the assumption of a laminar velocity distribution between the two plates and is an infinite series converging only for $1/\psi$ less than 10. Butler and Plewes obtained Equation (2), applicable to higher values of $1/\psi$, by using a solution of Leveque (*7*) which is based on the assumption of a linear velocity gradient through a boundary layer in laminar flow between parallel plates. Both equations are two-dimensional solutions which neglect the effect of property differences

TABLE 2. RANGES OF VARIABLES COVERED

System	System pressure p_T, mm. Hg	Vapor pressure p^* mm. Hg	Dry-gas velocity u_0, cm./sec.	Diffusivity (operating condition) D_{12}, sq. cm./sec.	Reynolds number, N_{Re_x}	Graetz number, $1/\psi$	Schmidt number (surface)	Schmidt number (bulk)	v_n/u_0	p_{B0}/p_{Bs}
Air-H_2O	20–700	9.9–23.3	0.161–58.2	0.280–9.50	0.155–153.	0.51–570	0.544–0.596	0.592–0.596	0.0877–17.8	1.03–2.37
Air-C_6H_5Cl	15–700	6.3–11.7	0.191–48.8	0.0810–3.77	0.072–134.	0.70–1,800	0.366–1.90	2.07–2.07	0.0388–12.6	1.01–2.75
Air-CCl_4	120–700	72.–112.	0.0129–52.1	0.0808–0.471	0.082–112.	0.76–1,440	0.272–1.08	2.07–2.07	0.0442–11.4	1.17–4.96
He-C_6H_5Cl	15–700	5.4–11.2	0.0625–27.0	0.356–16.3	0.006–2.4	0.12–52	0.105–2.45	3.74–3.74	0.370–19.4	1.02–2.17
Air-C_6H_5Br	15–100	3.5–4.0	0.369–12.2	0.537–3.54	0.098–24.	1.2–330	0.640–1.74	2.20–2.20	0.461–4.45	1.04–1.34
He-H_2O	35	10.2	15.4	19.0	0.5	4	0.483	1.35	1.96	1.49
All Systems	15–700	3.5–112.	0.0129–58.2	0.0808–19.0	0.006–153.	0.12–1,800	0.105–2.45	0.592–3.74	0.0388–19.4	1.01–4.96

in the direction normal to the evaporating surface. Schenck (*11*) obtained an equation practically identical with (1) for heat transfer from one of two infinite parallel plates to a gas in laminar flow.

Plewes, Butler, and Marshall (*9*) tested their theory with data on evapotion of solids from the bottom of a rectangular duct with data covering only the range of Equation (2), that is $1/\psi$ greater than 10. They found the slope of a log-log plot of ϕ vs. $1/\psi$ to be minus $\frac{2}{3}$, as predicted by Equation (2), but separate lines were obtained for each system studied.

In Figures 5 to 9 the dashed curves are calculated from Equation (1) and the solid lines (labeled Leveque) from Equation (2). The correlation of the present data is quite good, covering the wide range of evaporation rates, diffusivities, and other physical properties of the systems studied and the high ratio of partial pressures across the boundary layer. The diffusivities are often high in the present work because of the low pressures used.

It was not expected that the analysis of Butler and Plewes would apply to the data of this work, since their derivation was for the case of very dilute gas mixtures and for a constant stream velocity. A substantial part of the present data is for rich gas mixtures, and furthermore the evaporation increased the stream velocity severalfold in some cases. The agreement of the data with the Butler-Plewes and Leveque equations would appear to be fortuitous, and the very good correlation obtained must be considered to be empirical until shown otherwise.

In the Butler-Plewes treatment the evaporating surface is one of two parallel plates, whereas in the present work it is the flat open end of a vertical tube extending into a cylindrical horizontal glass duct. In this connection, however, it may be noted that the four points of the present investigation for evapotion of water from a nonprojecting surface into a stream of air in a square duct were also correlated in Figure 5 (shown as solid circles). It is surprising that the data for these dissimilar geometries follow the same correlation.

The data were also plotted with the conventional functions $N_{Sh} = F(N_{Re_x}, N_{Sc}, p_{Bm}/p_T)$ used. By analogy to the classical equation of Pohlhausen on heat transfer from a gas stream to a flat plate (*10*), the Sherwood number was assumed to be proportional to the one-third power of the Schmidt number. Correlation was improved somewhat by multiplying the Sherwood number by the first power of p_{Bm}/p_T (Figure 10).

For many of the experimental runs there was a very large difference between the Schmidt number at the upper edge of the boundary layer, calculated from the properties of the pure inert gas, and the Schmidt number at the evaporating surface, calculated for the properties at the composition and temperature of the surface layer. These differences result from high density gradients and appreciable viscosity differences through the boundary layer. In an extreme instance (run 186) the bulk Schmidt number was 3.74 and the surface Schmidt number 0.106, a ratio of 35 to 1. In such cases the use of an arithmetic average amounts to using practically one-half the larger number, and thus any effect of the surface conditions nearly drops out. In the absence of adequate theory there is little basis for a rational choice of the method of averaging to be used. In Figure 10 the geometric mean was arbitrarily chosen for the correlation in order to give weight to each end condition. Other methods of averaging, as well as other exponents such as 0.44 for the Schmidt number and 0.83 for the p_{Bm}/p_T ratio, could also be used with little effect on the scatter (*13*).

The data for the air-water and air-chlorobenzene systems (Figures 6 and 7) were quite good; for the air–carbon tetrachloride and helium-chlorobenzene systems (Figures 8 and 9) more scattering was in evidence. The reasons for this difference are, at least in part, experimental. In the helium runs flow control from the high-pressure tank was less steady. In the runs for air–carbon tetrachloride and helium-chlorobenzene the evaporation rates were much higher than for the other systems. This necessitated shorter time intervals between readings, leaving less time for careful measurements. There was a more rapid change in the position of the evaporating surface between readings, rendering measurement of surface temperature less accurate. Because the surface temperature fixes the vapor pressure and thus the driving force, the largest contribution of error to the experimental data is due to the temperature measurement rather than to the rate of evaporation measurement.

ACKNOWLEDGMENT

This investigation was carried out with financial support of the National Science Foundation. The University of North Dakota provided space, facilities, and equipment.

Dewey Wahl made the photographs of, and James Braus built the apparatus for, and obtained the data on, the square duct as senior thesis projects at the University of North Dakota.

NOTATION

D_s = diffusion coefficient for system carrier gas-evaporating substance, sq. ft./hr.

G = mass velocity of inert gas stream, lb./(hr.)(sq. ft.) of duct cross section.

K_g = mass transfer coefficient, lb. mole/hr. sq. ft. atm.

N_{Re_x} = length Reynolds number = $(xG)/\mu$

N_{Sc} = Schmidt number = $\mu/(\rho D_s)$

N_{Sh} = Sherwood number = $(K_g RTx)/D_s$

p^* = vapor pressure of evaporating liquid at T_s, atm.

p_{Bm} = mean partial pressure between p_{B0} and p_{Bs}, atm.

p_{B0} = partial pressure of carrier gas at leading edge, atm., = p_T.

p_{Bs} = partial pressure of carrier gas at surface, atm., = $p_T - p^*$

p_T = total pressure in system, atm.

R = gas constant, 0.729 (cu. ft.)(atm.)/(lb. mole)(°R.)

T = temperature, °R.

T_0 = bulk gas temperature, °R.

T_s = surface temperature, °R.

u_0 = average velocity of carrier gas approaching surface, ft./hr.

v_n = average normal velocity of vapor at surface, ft./hr.

w = carrier gas flow rate, lb./hr.

x = average length of evaporation surface, ft.

y_s = mole fraction of vapor in exit gas.

Greek Letters

μ = viscosity, lb./ft. hr.

ρ = density of gas, lb./cu. ft.

ϕ = $(y_s p_T)/p^*$ = fractional saturation of exit gas.

$1/\psi$ = $w/(\rho D_s x)$ = Graetz number for mass transfer.

LITERATURE CITED

1. Bromley, L. A., and C. R. Wilke, *Ind. Eng. Chem.*, **43**, 1641 (1951).
2. Butler, R. M., and A. C. Plewes, *Chem. Eng. Progr. Symposium Ser. No. 10*, **50**, 121 (1954).
3. Cairns, R. C., and G. H. Roper, *Chem. Eng. Sci.*, **3**, 97 (1954); **4**, 221 (1955).
4. Hirschfelder, J. O., R. B. Bird, and E. L. Spotz, *Chem. Revs.*, **44**, 205 (1949).
5. Lange, N. A., "Handbook of Chemistry," 5 ed., pp. 1422, 1443, Handbook Publishers, Sandusky, Ohio (1944).
6. *Ibid.*, p. 1588.
7. Leveque, J., *Ann. mines* (*12*), **13**, 201, 305, 381 (1928).
8. Perry, J. H., ed., "Chemical Engineers' Handbook," 3 ed., p. 154, McGraw-Hill, New York (1950).
9. Plewes, A. C., R. M. Butler, and H. E. Marshall, *Chem. Eng. Progr.*, **50**, 77 (1954).
10. Pohlhausen, E., *Zeit. angew. Math. u. Mech.*, **1** (2), 115 (1921).
11. Schenck, J., *Appl. Sci. Research*, **A5**, 241 (1955).
12. Sherwood, T. K., and R. L. Pigford, "Absorption and Extraction," 2 ed., p. 67, McGraw-Hill, New York (1952).
13. Westkaemper, L. E., and R. R. White, *A. I. Ch.E. Journal*, **3**, 69 (1957).
14. Wilke, C. R., and C. Y. Lee, *Ind. Eng. Chem.*, **47**, 1253 (1955).

Manuscript received August 14, 1958; revision received November 24, 1958; paper accepted January 21, 1959.

Solid-catalyzed Reaction in a Fluidized Bed

W. K. LEWIS, E. R. GILLILAND, and WERNER GLASS

Massachusetts Institute of Technology, Cambridge, Massachusetts

Results are presented for the solid-catalyzed hydrogenation of ethylene in fixed and fluidized beds. The effect of gas velocity, bed height, catalyst activity, particle size, and internal baffles on fluidized reactor efficiency are given, and Equations derived from a simplified mathematical model correlate the data.

The success of the fluidized solid technique for the catalytic cracking of petroleum fractions led to its consideration for and application to many solid-vapor reactions encountered in the chemical and petroleum industries. The results of laboratory studies and of the use of large-scale equipment indicated that while the units had the advantages of uniformity of temperature and the ability to circulate the solid rapidly and thereby to maintain an enthalpy balance or catalyst activity, they had certain deficiencies from the viewpoint of gas-solid contacting. The relatively uniform temperature obtained is a result of the rapid solid circulation within the reactor, which results in some back mixing of the vapor. A sizable fraction of the vapor flows through the bed in gas pockets or bubbles, resulting in poor contact between the solid and gas. These factors all tend to lower the over-all reaction rate per unit of solid present that can be obtained in a fluidized bed. The interaction of these and other phenomena makes the quantitative design of fluidized reactors difficult. This study was undertaken to gain further insights into fluid-bed behavior.

Various investigators have attempted to isolate the factors affecting fluid-bed behavior for individual study. Bart (*2*), Girouard (*8*), Reman (*16*), Singer *et al.* (*20*), and others have reported on solid-mixing studies. Both eddy diffusivity and directed flow-pattern concepts were used to interpret the data. Askins *et al.* (*1*), Danckwerts *et al.* (*5*), Gilliland and Mason (*6*), Handlos *et al.* (*10*), and Reman (*16*), studying gas mixing in fluidized beds, concluded that gas back mixing is present but, at least in laboratory-sized reactors, is not very extensive. Gilliland, Mason, and Oliver (*7*) found that gas bypassing was more of a problem than gas back mixing. Such gas-solid heat or mass transfer experiments as, for example, those of Chu *et al.* (*4*), Hsu and Molstad (*12*), and Heertjes (*11*) showed that physical equilibrium between gas and solid was very readily obtained.

Fluid bed behavior can also be studied in another manner: (a) use a fluidized bed to carry out a solid-catalyzed reaction that has a known rate equation. (*b*) determine the over-all conversion when the reaction proceeds under various conditions, and (*c*) synthesize a "model" that could account for the observed results. This is the method used in this work to determine the efficiency of fluidized beds as chemical reactors.

A solid-catalized reaction that has a first-order rate equation was carried out in a 2.05-in. I.D. fluidized bed. To determine the catalyst activity (that is, the constant in the rate equation), the reaction was also carried out over a sample of the particular catalyst in question in a catalyst tester. This tester was an approximately isothermal fixed-bed reactor where piston flow of the gas and zero horizontal concentration gradients were assumed. Shen and Johnstone (*19*) and Mathis and Watson (*14*) have reported on similar studies. Their results are discussed later.

EXPERIMENTAL PROGRAM

Details of the program are given in reference *9*.

Reaction Used

The reaction used for this study was the hydrogenation of ethylene catalyzed by a nickel-coated cracking catalyst:

$$C_2H_4 + H_2 \xrightarrow{Ni} C_2H_6$$

Reaction occurred with a large excess of ethylene present. This facilitated near-isothermal operation and permitted smooth fluidization with only very small gas shrinkage in the bed. Inlet stream composition to the fluidized reactor averaged about 10% hydrogen, 90% ethylene. Feed to the fixed-bed catalyst tester averaged 5% hydrogen, 95% ethylene. Temperature and pressure averaged 235°F., 77 cm. Hg abs. Auxiliary batch experiments, detailed below, showed that under these conditions the reaction was first order in hydrogen, as predicted by several equations in the literature (*3*, *17*, etc.). Moreover, at these conditions the reverse reaction is negligible and the apparent energy of activation is very low, being given as 0 to 4 kcal./g. mole (*13*, *17*, etc.).

Determination of Reaction Order

A sample of the ethylene-hydrogen reaction mixture was repeatedly passed from one analytical gas burette, over a differential bed of catalyst maintained at reaction temperature, into another gas burette. The differential bed contained less than 50-mg. catalyst. The entire experiment was performed at nearly constant pressure. For each pass the duration and the volume of gas remaining was recorded. In due course no more shrinkage occurred. For such an experiment it can readily be shown (*9*) that if the reaction is first order in hydrogen,

$$V_c \ln (V_{h0}/V_h) + (V_{h0} - V_h) = K'mR'T'\theta$$

and if second order,

$$V_c^2\left(\frac{1}{V_h} - \frac{1}{V_{h0}}\right) + 2V_c \ln \frac{V_{h0}}{V_h} + (V_{h0} - V_h) = K''PmR'T'\theta$$

Werner Glass is with Esso Research and Engineering Company, Linden, New Jersey.

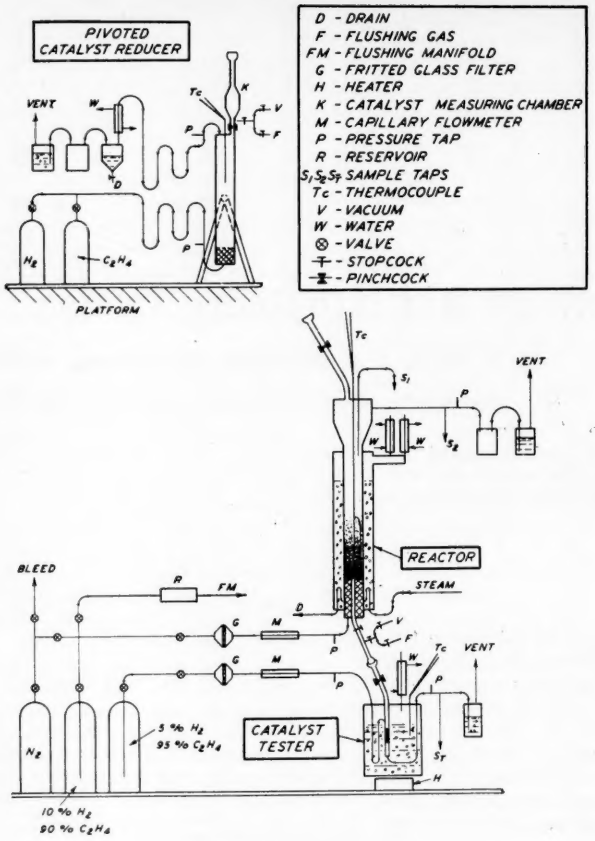

Fig. 1. Apparatus, schematic.

Table 1 lists values of K' and K'' calculated for a typical run. K' is seen to be constant enough to show that a first-order rate equation was acceptable.

Solids Used

The solid fluidized consisted primarily of the −100- + 140-mesh fraction (average particle diameter D_p:122 μ) of microspheroidal Aerocat (MS-A) cracking catalyst, which was treated to carry 2.5 or 4 wt. % either of nickel or of catalytically inactive additional alumina. Table 2 lists some properties of this solid. Some work was also done with the −65- + 80-mesh (average D_p:188 μ) and −170- + 200-mesh (average D_p:80 μ) fractions of similarly impregnated alumina.

Equipment

A flow sheet for the experimental equipment is shown in Figure 1. The equipment train consisted of three main parts.

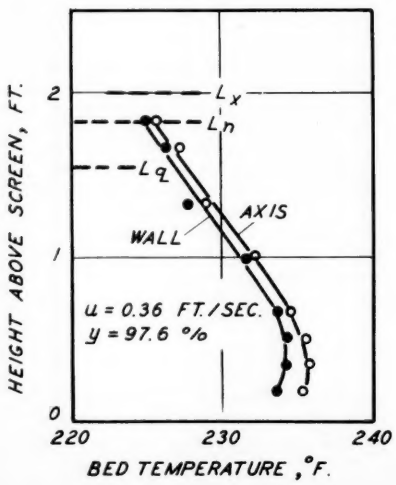

Fig. 2. Temperature profile.

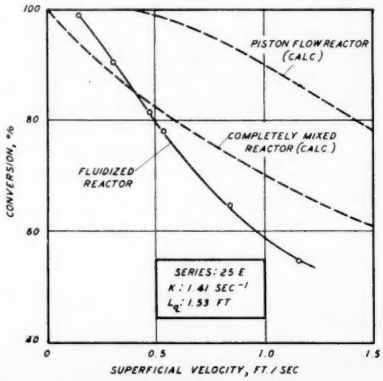

Fig. 3. Conversion vs. velocity.

Table 1. Determination of Reaction Order

Reaction time, sec.	First-order, K', × 10^6	Second order, K'', × 10^6
136	3.22	0.45
173	2.90	0.53
258	3.19	0.72
306	3.17	0.80
434	3.15	1.07
513	3.18	1.33
616	3.13	1.71
717	3.11	2.25
880	3.17	3.87
1,142	3.33	11.5

Pivoted Catalyst Reducer

This served to prepare catalytically active solid (MS-A carrying nickel) from a charge of MS-A carrying nickel oxide. Reduction took place by fluidizing with hydrogen at about 750°F. After reduction the charge was cooled to about 235°F., was fluidized with ethylene, and then, by pivoting of the catalyst reducer, was allowed to drop into the reactor.

Fluidized Reactor

This consisted of a 4-ft. length of 2.05-in. I.D. Pyrex tubing. A boiling-water jacket helped to maintain the desired reaction temperature. A solids disengaging section and a packed gas-inlet section were also provided.

A 325-mesh on 40-mesh stainless steel screen sandwich supported the fluidized bed. A plug normally sitting on a ¼-in. hole in these screens could be raised to permit a catalyst sample to fall into the catalyst tester below. A probe carrying a pair of thermocouples, one at the axis and one at the wall, could be inserted in the bed.

Some runs were made with a multiple baffle temporarily inserted in the bed. This baffle consisted of twelve horizontal 2-in. circles of 6-mesh stainless steel screen soldered at 2-in. intervals onto an axially located supporting tube.

Catalyst Tester

Samples of the solid being fluidized were withdrawn from the fluidized bed into a fixed-bed catalyst tester. The section of the tester in which the fixed bed was located consisted of a flattened 3-in. length

Table 2. Properties of −100- + 140-Mesh Solid

Average particle diameter, (for equal surface/volume ratio)	122 μ
Quiescent bed density,	32 lb./cu. ft.
Quiescent gas velocity,	0.024 ft./sec.
Bed expansion factors	
Maximum, $\frac{L_x - L_q}{L_q(u - u_q)}$	1.1 sec./ft.
Minimum, $\frac{L_n - L_q}{L_q(u - u_q)}$	0.5 sec./ft.
Packed-bed thermal conductivity (in ethylene)	0.05 B.t.u./(hr.)(sq. ft.)(°F./ft.)

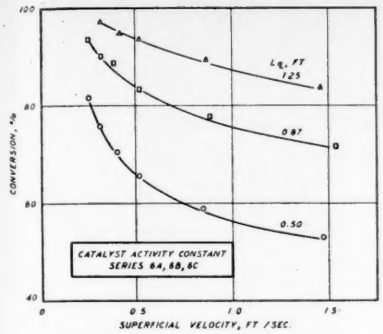

Fig. 4. Conversion vs. velocity.

of ¼-in. stainless steel tubing. The internal cross-sectional axes of this test section measured 0.11 by 0.30 in.

Procedure

A series of runs at several gas-flow rates was taken for each charge of solid in the fluidized reactor. After some series an appreciable fraction of the solid charge present was withdrawn and the next series taken on a lesser amount of the same catalyst.

Samples of catalyst were withdrawn from the fluidized reactor and the activity determined in the fixed-bed catalyst tester. The average temperature within the test section was adjusted to the average fluid-bed temperature by adjusting the calcium chloride content of the boiling liquid surrounding the tester. Several runs were made at different gas-flow rates for each sample of catalyst.

Gas samples were taken from the inlet and outlet streams of the fluidized reactor and catalyst tester. They were analyzed volumetrically for hydrogen content by being repeatedly passed over a hydrogenation catalyst until all the remaining hydrogen was used up.

RESULTS AND DISCUSSION

The results of this investigation are summarized.* Some of the data are plotted in Figures 2 to 4.

*Tabular material has been deposited as document No. 5977 with the American Documentation Institute, Photoduplication Service, Library of Congress, Washington 25, D. C., and may be obtained for $1.25 for photoprints or 35-mm. microfilm.

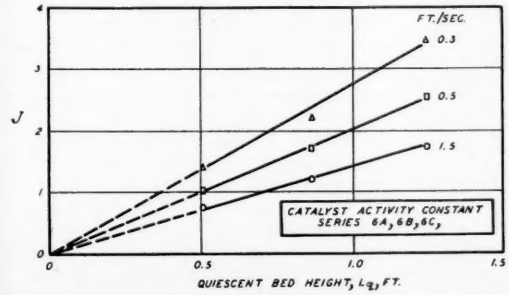

Fig. 5. J vs. catalyst quantity.

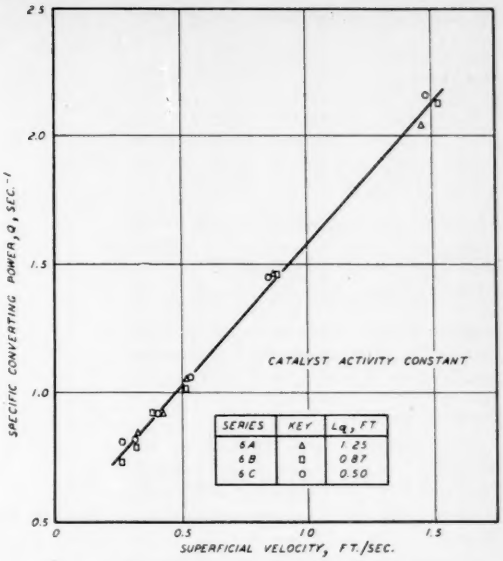

Fig. 6. Specific converting power vs. velocity.

The measurements employed in the derivations and figures are

gas-flow-rate, superficial velocity

catalyst quantity, bed height at quiescence

catalyst activity, defined by Equation (1), applicable at a given temperature and pressure:

$$-\frac{d(Auz)}{d(AL_q)} = Kz \qquad (1)$$

conversion, the fraction of hydrogen reacted

alternate measure of conversion, J, dimensionless. Equation (1) is readily integrated for an idealized piston-flow reactor without horizontal concentration gradients. Allowing for shrinkage, one gets

$$\frac{u}{L_q}\left[(1 - z_0)\ln(1/1 - y) + z_0 y\right] = K \qquad (2)$$

For brevity the bracketed term is defined as J. For zero shrinkage, hydrogenation with $z_0 \to 0$, J is the familiar $\ln(1/1 - y)$.

specific converting power, $Q = uJ/L_q$, sec.$^{-1}$. Q is a measure of what the reactor accomplished per unit of solid present. For an idealized piston-flow reactor $Q = uJ/L_q = K$; that is Q is independent of conversion, flow rate, or catalyst

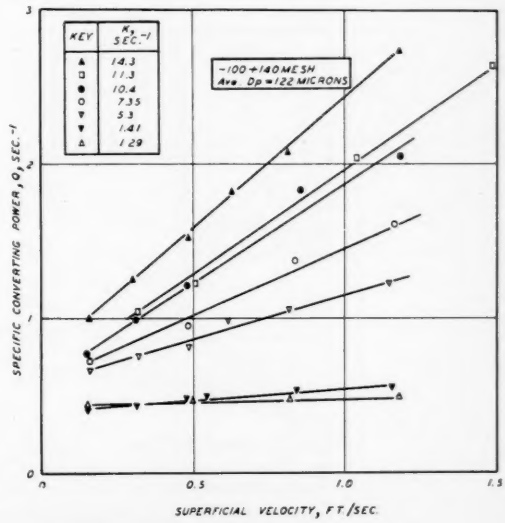

Fig. 7. Specific converting power vs. velocity.

TABLE 3. FIXED-BED RUNS—SAMPLE 25E

Run	L_q, ft.	u, ft./sec.	Conversion, %	K, sec.$^{-1}$
1	0.156	0.468	36.5	1.35
2	0.156	0.226	65.0	1.49
3	0.156	0.372	43.8	1.36
4	0.156	0.149	78.7	1.44

quantity and numerically equal to the catalyst activity. Other types of reactors will usually not make so efficient use of the catalyst and will have $Q < K$.

reactor efficiency (relative to piston flow), $E = Q/K$. For an idealized piston-flow reactor $Q = K$, and thus $E = 1$.

Range of Variables

The variables were studied in the following ranges: superficial velocity, 0.15 to 1.5 ft./sec.; quiescent bed height, 0.35 to 1.75 ft.; measured catalyst activity: 1.1 to 14.3 sec.$^{-1}$. The entire range of any one variable was not always investigated for all values of the other variables. The fluidized-bed conversions ranged from 15 to 99+%.

Fixed-Bed Runs

The conversions obtained in the fixed-bed runs for each catalyst sample were used with Equation (2) to determine the catalyst activity. Table 3 presents the data for one such sample.

Many experimental difficulties beset the determination of K, and K values were obtained for only nineteen of the sixty-three successful series of fluidized runs taken.

Fluidized-Bed Runs

The solids fluidized relatively smoothly in the 2.05-in. I.D. column used. Thermocouple traverses indicated that the temperature varied from 2° to 15°F. between the top and bottom of the bed.

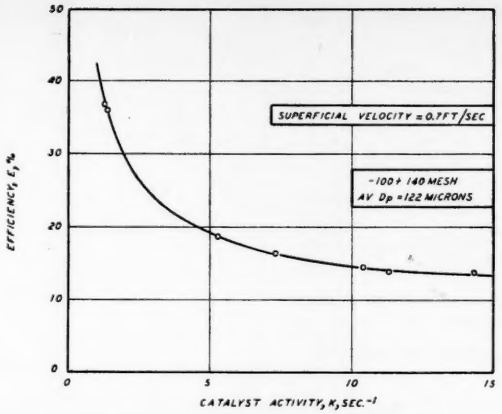

Fig. 9. Reactor efficiency vs. catalyst activity.

Radial temperature differences were small. Figure 2 shows typical profiles.

Each of the sixty-three different solid charges in the reactor resulted in a conversion vs. velocity curve. The percentage conversion always decreased with increasing velocity. In general these curves were primarily concave upward. Figure 3 shows a typical curve. Also included are the curves calculated for idealized piston flow and completely mixed reactors operating with the same quantity of the same activity catalyst as the actual fluidized bed. In all the nineteen series where K values were available for such a comparison, the fluidized-reactor conversions were less than those calculated for the corresponding piston-flow reactors. Under some reaction conditions fluidized-bed conversions were higher, and under others they were lower than those calculated for the corresponding completely mixed reactors. Thus gas back mixing alone cannot account for the lowering of conversions below those of a piston-flow reactor.

Figure 4 shows the conversion-velocity plots obtained for a set of three series taken with varying quantities (L_q) of the same catalyst. (The actual catalyst activity was not determined for these series.) A cross plot of these data is shown in Figure 5. Instead of the conversion the quantity J (defined above) is plotted vs. L_q at various constant values of gas velocity; at any given velocity J is proportional to L_q.

A plot of specific converting power vs. velocity for this same set of three series is shown in Figure 6. At any given gas velocity the specific converting power of the fluidized reactor was independent of catalyst quantity. Six other similar sets of two or three series also showed Q independent of L_q for a given catalyst. Thus the top of a deep bed must have had the same specific converting power as the bottom.

Plots of Q vs. velocity for those series made with −100- +140-mesh solid for which K values were determined are presented in Figure 7. A general fan-shaped pattern may be observed; that is for high-K catalyst the Q vs. u line is quite steep, and for low-K catalyst Q does not vary greatly with velocity. For an idealized piston-flow reactor $Q = K$; that is Q is independent of velocity for a given catalyst. All the Q values obtained were considerably below the K value of the catalyst concerned.

Figure 8 presents a cross plot made from the data for the −100- +140-mesh solid, where Q is plotted vs. K at various constant values of velocity. Also included is the line $Q = K$ pertaining to an idealized piston-flow reactor at all velocities. The specific converting power of a fluidized bed is seen to increase continuously with increasing catalyst activity. Thus for a sufficiently active catalyst the specific converting power will be high enough to give effectively 100% conversion. (For any specified

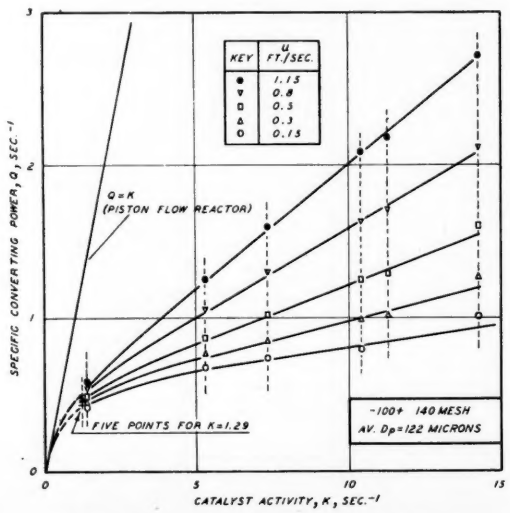

Fig. 8. Specific converting power vs. velocity.

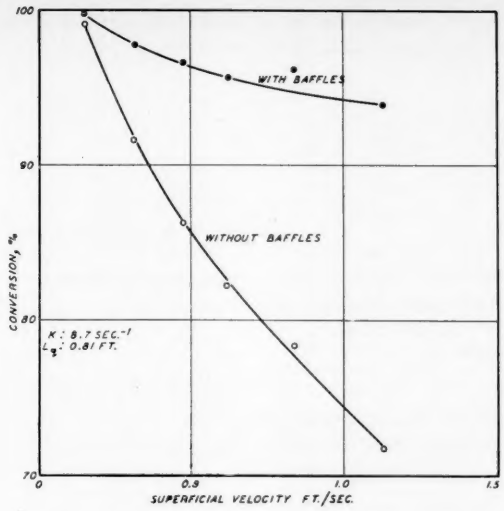

Fig. 10. Effect of baffles, conversion vs. velocity.

high-conversion level, however, far less catalyst would be needed in an idealized piston-flow reactor.) The fact that essentially complete conversion is possible shows that all the gas contacts some catalyst. This is borne out by those investigators who studied physical reactions in fluidized beds.

Figure 9 shows a cross plot of reactor efficiency $E(= Q/K)$ vs. K at a constant velocity of 0.7 ft./sec. At high enough activities the efficiency approaches a nonzero asymptotic value. The fluidized-bed efficiencies represented by the data of Figure 7 run from about 7% (at $K =$ 14.3 sec.$^{-1}$, $u = 0.15$ ft./sec.) to about 39% ($K = 1.29$, $u = 1.18$).

Inserting the multiple 6-mesh screen baffle in the bed resulted in markedly increased conversions. Alternate runs were made with the same solid charge and at the same velocity with the screens either out of or in the bed. Typical results are shown in Figure 10. However operation was never truly satisfactory. The reduced solid circulation and possibly the build-up of a stagnant layer of the low-conductivity solid at the inside wall of the reactor caused very poor temperature control. The data for baffled runs were obtained while the temperature was rising continually, averaging up to 15°F. or so higher than for the unbaffled runs.

FLUID-REACTOR MODEL

Several investigators [for example, Mathis and Watson (*14*), May (*15*), and Shen and Johnstone (*19*)] have set up simplified models of flow patterns in a fluidized reactor. Appropriate integrations then predict the amount of chemical reaction that will occur in the postulated bed. In most of the proposed models the bed consists of two phases; gas flows up through one or both phases; catalyst is present in one or both phases; gas back mixing within each phase is either zero, finite, or infinite; there is interphase transfer of either the gas present or of the reacting component; and catalyst activity is independent of time and location in the bed.

A simplified model of this type for the gas flow through a fluidized bed was set up, and two extreme modifications were examined mathematically; both fitted the data equally well, with an average deviation of about 3% between actual and calculated specific converting powers. The proposed model assumes that

1. A fluidized bed consists of two phases, a gas pocket phase and an emulsion phase.

2. The gas composition at any given horizontal level is uniform within each phase but may be different in the two phases.

3. All the gas flowing up through the bed does so in the gas-pocket phase with zero back mixing.

4. The fraction a of the catalyst causes reaction to occur at a rate determined at each level of the bed by the composition of the gas in the gas-pocket phase. This a is not a function of bed level or catalyst activity.

5. The fraction $(1 - a)$ of the catalyst causes reaction to occur at a rate determined at each level of the bed by the composition of the gas in the emulsion phase.

6. Gas in the gas-pocket phase and gas in the emulsion phase undergo interchange at the rate of F cu. ft. gas/sec./cu. ft. quiescent emulsion. F is not a function of bed level or of catalyst activity.

7a. In the vertically unmixed emulsion (VUE) modification the gas in the emulsion phase is mixed in the horizontal direction only.

7b. In the completely mixed emulsion (CME) modification the emulsion-phase gas is uniform throughout the reactor.

Mathematical Description

A first-order reaction occurring without shrinkage will be considered. This would correspond to hydrogenation with $z_0 \to 0$.

The amount of catalyst in the whole bed is L_q. A horizontal slice of the bed contains dh catalyst, of which $(1 - a)dh$ catalyst sees emulsion-phase gas and adh catalyst sees gas-pocket-phase gas (Figure 11).

Reactant balances can be written for the gas in both phases.

VUE Modification

For the gas-pocket phase gas

Input	from gas stream	xu
	from emulsion	$x_eF(1 - a)dh$
Output:	to gas stream	$(x + dx)u$
	to emulsion	$xF(1 - a)dh$
	to chemical reaction	$x\,Kadh$

Equating input to output and rearranging, one gets

$$\frac{dx}{dh} + \frac{F(1 - a)(x - x_e)}{u} + \frac{aKx}{u} = 0 \qquad (3)$$

For the emulsion phase gas

Input:	from gas stream	$xF(1 - a)dh$
Output:	to gas stream	$x_eF(1 - a)dh$
	to chemical reaction	$x_eK(1 - a)dh$

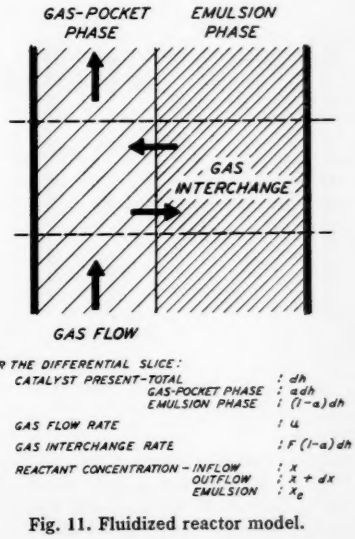

Fig. 11. Fluidized reactor model.

When one rearranges,

$$F(x - x_e) = Kx_e \qquad (4)$$

The concentration in the emulsion can be eliminated between these two equations and the resulting equation integrated by use of the boundary conditions

$$x = x_1 \quad \text{at} \quad h = 0$$

$$x = x_2 \quad \text{at} \quad h = L_q$$

and noting $y = (x_1 - x_2)/x_1$. The solution can be written

$$\ln (1/1 - y) = \frac{L_q}{u}\left[aK + \frac{1 - a}{1/K + 1/F}\right]$$

A derivation taking shrinkage into account would be unduly cumbersome. In the present study complete conversion would give only 10% shrinkage, and so the actual effect is probably small.

This VUE model corresponds to a special case (zero upflow through the emulsion) of the model proposed by Mathis and Watson (*14*)

CME Modification

Again a first-order reaction without shrinkage is considered. Here the emulsion-phase gas is uniform throughout the reactor with a reactor concentration x_e.

For a horizontal slice of the bed a reactant balance for the gas-pocket phase gas is the same as for the VUE.

$$\frac{dx}{dh} + \frac{F(1 - a)(x - x_e)}{u} + \frac{aKx}{u} = 0 \qquad (3)$$

When all the emulsion phase gas in the bed is considered,

Input: from gas stream $\int_0^{L_q} xF(1 - a)\, dh$

Output: to gas stream $x_eF(1 - a)L_q$

to chemical reaction $x_eK(1 - a)L_q$

When one rearranges,

$$\int_0^{L_q} xF(1 - a)\, dh = x_e(1 - a)L_q(K + F) \qquad (7)$$

Eliminating x_e and solving with the same boundary conditions as before results in

$$\frac{1}{y} = \frac{1}{1 - \exp\left[-\left(\frac{KL_q}{u}\right)\left(a + \frac{1 - a}{K/F}\right)\right]} + \frac{1}{\left(\frac{KL_q}{u}\right)\left(1 + a\frac{K}{F}\right)\left(1 + \frac{a}{1 - a}\frac{K}{F}\right)} \qquad (8)$$

Comparison with the Data

The vertically unmixed emulsion modification (VUE) leads to Equation (5), which has Q independent of L_q. The CME solution does not lead to a Q mathematically independent of L_q. Thus at first sight the VUE appears more likely to fit the data, as experimentally Q did not vary with L_q for a given catalyst at constant velocity.

VUE Modfication

The fit of Equation (5) for the VUE to the data can be readily checked by transformation to

$$\frac{KQ}{K - Q} = \frac{aK^2}{K - Q} + F \qquad (9)$$

A plot of $KQ/(K - Q)$ vs. $K^2/(K - Q)$ at constant gas velocity for a given particle size should give a straight line of slope a and intercept F. Figure 12 presents such plots for the −100- + 140-mesh solid at velocities of 0.3 and 0.8 ft./sec. Good straight lines are obtained. Thus at a given velocity single values of a and F will allow Equation (9) to fit the data for the seven series run with different catalyst activities.

Values of a and F obtained from the data are plotted against gas velocity in Figures 13 and 14. For any one solid a increases appreciably with velocity, and F decreases slightly. The nature of a and F will be further discussed later.

In accordance with the VUE model, the efficiency is given by

$$E = \frac{Q}{K} = a + \frac{1 - a}{1 + K/F} \qquad (6a)$$

Thus at high values of K, or with very little gas interchange, the efficiency ap-

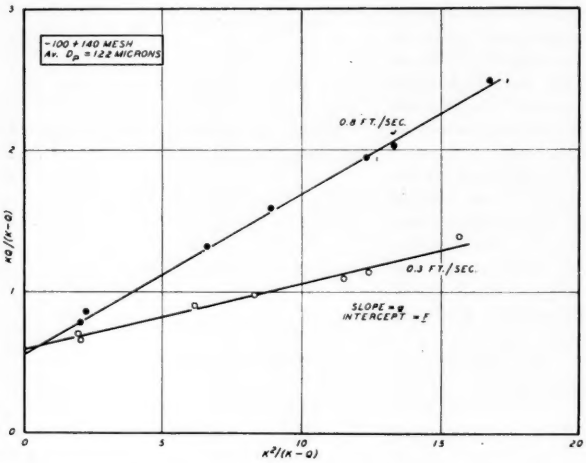

Fig. 12. Applicability of Equation (6).

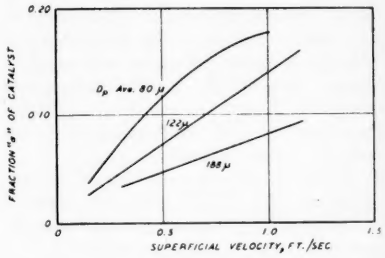

Fig. 13. Values of a.

Table 4. Comparison With Data of Shen (*18*)

Temperature, °F.	Fixed beds: Data K, sec.$^{-1}$ Range	Fixed beds: Data K, sec.$^{-1}$ Avg.	Fluidized beds: Data Q, sec.$^{-1}$ Range	Fluidized beds: Data Q, sec.$^{-1}$ Avg.	Fluidized beds: Model Q, sec.$^{-1}$ for avg. K
700	0.00590–0.00636	0.00613	0.00555–0.00602	0.00578	0.00605
750	0.0114–0.0122	0.0118	0.0107–0.0121	0.0114	0.0115
800	0.0198–0.0212	0.0205	0.0169–0.0190	0.179	0.0194

proaches a. At very low activities or high gas-interchange rates the efficiency would approach 1, that is that of an idealized piston-flow reactor.

CME Modification

Equation (8) gives the solution for the CME model; no ready way to obtain a and F explicitly could be found.

The differences between the VUE and CME models will be considered. The VUE assumes that emulsion-phase gas is not vertically mixed and the CME assumes that it is. The VUE predicts that the reactant concentration x_e in the emulsion at any level in the bed is given by Equation (4). When one rearranges and substitutes conversions,

$$y_{e,h} = \frac{y_h + K/F}{1 + K/F}$$

Thus if K/F is large or if y is small, the emulsion-phase gas of a VUE reactor is going to be very uniform, and the conversion will be the same as in a CME reactor. This was the case in the ranges of K/F and conversions covered in the present study. The values of a and F obtained by fitting the VUE model to the data, when used in Equation (8) along with the experimental values of K, L_q, and u, predicted conversions negligibly different from those predicted by Equation (5). These experiments were thus not able to pin down the amount of gas back mixing in the emulsion phase. The effect of any such back mixing would become important for deeper beds of less active catalyst and at high gas-interchange rates.

The Catalyst Fraction a

The model assumes that the fraction a of the solid differs from the rest. It alone sees the flowing gas-pocket phase gas. Slow-motion movies showed that differences between fractions of the solid exist.

Some nickeled (black) microspheres were added to a batch of normal (white) microspheres and the mixture was fluidized in a rectangular cross-section column having one plate-glass face. The entire column was tilted backward a few degrees from the vertical so that the solid flow patterns made visible by frontal illumination would be more representative of conditions within a fluidized bed.

The movie showed that the microspheres were aggregated in two distinct forms. The main part made up the emulsion proper. This emulsion phase moved around quite showly with little apparent motion of the particles relative to their immediate neighbors. A different type of solid phase existed (1) directly underneath most of the gas pockets, (2) inside the gas pockets, (3) above some of the gas pockets, and (4) between some pairs of gas pockets where one was more or less vertically above the other. In these zones the microspheres appeared to be moving rapidly, and no individual particles could be recognized. This solid may well correspond to the fraction a which the model specifies as seeing gas-pocket phase gas.

No quantitative estimate of the amount of solid present in this second phase could be made. However more solid was involved at high gas velocities than at low ones.

The Gas-Interchange Rate F

Gas interchange between gas pocket and emulsion can be assumed to occur in two main ways: (1) gas flowing from one phase to the other through the surface of the gas pockets and (2) gas being transferred along with the bulk transfer of solid from one phase to the other. At low gas rates the limited bed expansion shows that the volume of the gas-pocket phase is small. The velocity across the gas-pocket surface is probably less than at higher gas rates. The calculated gas interchange rate is however no less than at higher throughputs. If flow across the surface were the only means of interchange, extremely small gas pockets would be needed to provide enough of this surface. Postulating direct interchange of gas from one phase to the other, in conjunction with the transfer of solid, can help to account for the calculated values of F.

Effect of the Multiple Baffle

Values of a and F were obtained for runs where the multiple coarse-screen baffle was present in the fluid bed. Figures 15 and 16 show these values compared to those obtained without the screens; there was no great difference in a. Values of F, interpreted as gas interchange between gas-pocket and emulsion phases, were appreciably higher for the runs with screens in the bed; the increase ranged from about 50% at low velocities to about 600% at high velocities.

It seems plausible that the numerous coarse screens continuously break up the emulsion and thus help the transfer of gas from one phase to the other. This breakup of the emulsion can be relatively slight at lower gas velocities, where the gas pockets are small and the motion of the emulsion phase engendered by them quite gentle. At higher velocities, though, the emulsion is subjected to more violent forces and the screens will be far more restrictive; that is they will obstruct the free motion of the emulsion more. They will then cause far greater breakup of the emulsion and thus bring about greater gas interchange with the gas-pocket phase.

Comparison With Data of Shen (18)

Shen carried out fixed- and fluid-bed decomposition of nitrous oxide in a 4½ in.-diameter column. Air or nitrogen was used as the carrier gas. His results for −165- + 200-mesh catalyst with air as a carrier are shown in Table 4. To make comparison easier, the results are expressed in the units used here.

Shen's catalysts had very low values of K (<0.021 sec.$^{-1}$). The VUE model

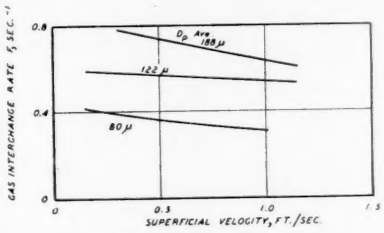

Fig. 14. Values of F.

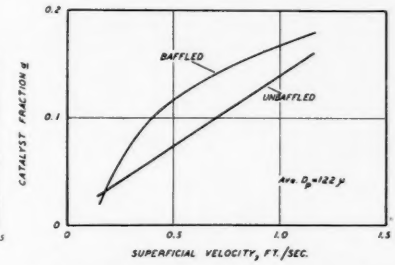

Fig. 15. Effect of baffles, values of a.

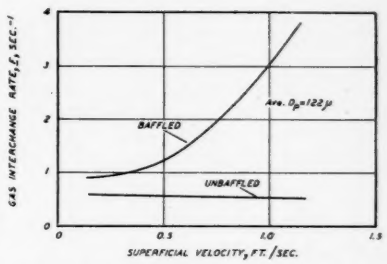

Fig. 16. Effect of baffles, values of F.

predicts that for such low K's the efficiency should be > 95%, that is that there should be little difference between fixed and fluidized beds. That this was so is evident from his data.

Also included in Table 4 are values of Q predicted from the VUE model for the average values of K. To make the predictions, values of F and a were obtained from the present data for −170- + 200-mesh catalyst. For the low velocities at which Shen's fluidized runs were made (0.025 to 0.19 ft./sec.) a was taken as 0.02 and F as 0.4 sec.$^{-1}$. Reasonably good agreement between measured and predicted Q's was obtained. However any other model that asymptotes to fixed-bed efficiency at very low conversions would fit as well.

Comparison With Data of Mathis and Watson (14)

Mathis and Watson dealkylated cumene in fixed and fluidized beds 2, 3, and 4 in. in diameter. Their results differed from those of this study in two major points:

1. Reactor efficiency reached a maximum at gas velocities of about 0.4 ft./sec. (Conversion vs. velocity curves slightly concavely downward.) This maximum was most pronounced for rather shallow beds 1 to 6 in. deep.

2. Reactor efficiency decreased as bed height increased from 1 to 12 in.

All their runs were made with the same catalyst activity. From their fixed-bed data a pseudo first-order activity of $K = 1$ sec.$^{-1}$ can be assigned as an approximation. For such a catalyst the VUE model would predict efficiencies of around 40% on the basis of F and a values obtained in the present work. The reported efficiencies ranged from about 15 to 100%. If the shallow beds of 6 in. or less are not considered, the range of efficiencies for the deeper beds decreases to 25 to 55%, with eight out of eleven runs between 35 and 45%. Thus the VUE model would be quite satisfactory for beds of about the same depth as those used in the present work.

CONCLUSIONS

1. Gas back mixing alone could not explain the difference between the conversions obtained in a fluid bed and those calculated for the corresponding idealized piston-flow reactor.

2. The efficiency of a fluid bed as a reactor for carrying out a first-order, solid-catalyzed reaction was independent of bed height. The top and bottom of a bed were equally effective.

3. The reactor efficiency increased appreciably with gas velocity for fluid beds of very active catalyst and was almost independent of velocity for beds of less active catalyst.

4. For a given particle size the reactor efficiency could be correlated by

$$E = \frac{F + aK}{F + K}$$

where F and a are functions of velocity only, with a roughly proportional to velocity and F decreasing slightly with increasing velocity. Increasing particle size raised F and lowered a.

5. The data were correlated by a simplified two-phase model where F is the gas interchange rate between emulsion and gas-pocket phases, a is the fraction of catalyst causing reaction to occur in the up-flowing gas-pocket phase gas, and $(1 - a)$ is the fraction of catalyst causing reaction to occur in the emulsion phase gas. No conclusions regarding the degree of back mixing in the emulsion could be drawn.

6. Inspection of slow motion movies qualitatively supported the division of the solid into two different fractions.

7. Gas interchange occurred as gas flow between the two phases or as bodily transfer of one phase (including the solid therein) into the other. Several coarse horizontal screens placed in the bed markedly increased this gas interchange. The effect was most pronounced at high gas rates.

8. The correlations developed agreed quite well with Mathis and Watson's data (*14*) for beds deeper than 6 in. and with the data of Shen (*18*).

ACKNOWLEDGMENT

This work was carried out as part of a research project sponsored by the Esso Research and Engineering Company. The American Cyanamid Company donated over 600 lb. of MS-A cracking catalyst. H. H. Carter prepared the drawings.

NOTATION

A = reactor cross section, sq. ft.
a = catalyst fraction causing reaction in gas-pocket phase gas
CME = completely mixed emulsion model
D_p = average particle diameter, μ
E = reactor efficiency = Q/K
F = gas-interchange rate, (cu. ft. gas/sec.)/(cu. ft. quiescent emulsion) or sec.$^{-1}$
h = variable for L_q, ft.
J = measure of conversion = $(1 - z_0) \ln (1/1 - y) + z_0 y$
K = catalyst activity, sec.$^{-1}$
K' = activity, (g. mole/sec.)/(g. cat.)(cm. Hg)
K'' = activity, (g. mole/sec.)/(g. cat.)(cm. Hg)^2
L_n = minimum bed height, ft.
L_q = quiescent bed height, ft., measure of catalyst quantity
L_x = maximum bed height, ft.
m = weight of catalyst, g.
P = pressure, cm. Hg
Q = specific converting power = uJ/L_q, sec.$^{-1}$
R' = gas constant, cc. − cm. Hg/g. mole °K.
T' = temperature of gas in measuring burette, °K.
u = superficial gas velocity, ft./sec.
u_q = quiescent velocity, ft./sec.
VUE = vertically unmixed emulsion model
V_c = residual volume, cc.
V_h = volume hydrogen at time θ, cc.
V_{h0} = volume hydrogen at zero time, cc.
x = mole-fraction reactant in gas-pocket phase gas
x_e = mole-fraction reactant in emulsion phase gas, reactor concentration
y = conversion
$y_{e,h}$ = emulsion phase-gas conversion at any level in the bed
y_h = gas-pocket phase-gas conversion at that level
z = mole fraction hydrogen
z_0 = mole fraction hydrogen in the inlet stream
θ = reaction time, sec.

LITERATURE CITED

1. Askins, J. W., G. P. Hinds, Jr., and F. Kunreuther, *Chem. Eng. Progr.*, **47**, 401 (1951).
2. Bart, Roger, thesis, Mass. Inst. Technol., Cambridge, Massachusetts (1950).
3. Beeck, Otto, *Rev. Mod. Phys.*, **17**, 61 (1945).
4. Chu, J. C., James Kalil, and W. A. Wetteroth, *Chem. Eng. Progr.*, **49**, 141 (1953).
5. Danckwerts, P. V., J. W. Jenkins, and G. Place, *Chem. Eng. Sci.*, **3**, 26 (1954).
6. Gilliland, E. R., and E. A. Mason, *Ind. Eng. Chem.*, **41**, 1191 (1949).
7. ———, and R. C. Oliver, *ibid.*, **45**, 1177 (1953).
8. Girouard, H. D., thesis, Mass. Inst. Technol., Cambridge, Massachusetts (1954).
9. Glass, Werner, thesis, Mass. Inst. Technol., Cambridge (1956).
10. Handlos, A. E., R. W. Kunstman, and D. O. Schissler, *Ind. Eng. Chem.*, **49**, 11 (1957).
11. Heertjes, P. M., H. G. J. de Boer, and A. H. de H. van Dorsser, *Chem. Eng. Sci.*, **2**, 97 (1953).
12. Hsu, C. T., and M. C. Molstad, *Ind. Eng. Chem.*, **47**, 1550 (1955).
13. Klar, Richard, *Z. physik. Chem.*, **A168**, 215 (1934).
14 Mathis, J. F., and C. C. Watson, *A.I.Ch.E. Journal*, **2**, 518 (1956).
15. May, W. G., personal communication (1954).
16. Reman, G. H., *Chem. & Ind. (London)*, Jan. 15, 46 (1955).
17. Schuster, Curt, *Z. physik. Chem.*, **B14**, 249 (1931).
18. Shen, C. Y., Ph.D. thesis, *Univ. Illinois*, Urbana, Illinois (1954).
19. Shen, C. Y., and H. F. Johnstone, *A.I.Ch.E. Journal*, **1**, 349 (1955).
20. Singer, E., D. B. Todd, and V. P. Guinn, *Ind. Eng. Chem.*, **49**, 11 (1957).

Manuscript received March 3, 1958; revision received December 31, 1958; paper accepted January 8, 1959. Paper presented at A.I.Ch.E. Chicago meeting.

Void Fractions in Two-Phase Flow

H. S. ISBIN, H. A. RODRIGUEZ, H. C. LARSON, and B. D. PATTIE

University of Minnesota, Minneapolis, Minnesota

Void fractions (fraction of the flow cross-sectional area occupied by the gas phase) have been measured for steam-water flows in an adiabatic, horizontal test section of 0.484 in. I.D. at 400, 600, 800, and 1,000 lb./sq. in. gauge. A comprehensive survey of void data for two-phase concurrent flow is included in the paper, and the data, including the Martinelli and homogeneous flow model predictions, are compared. System characteristics, involving one- and two-component flows in horizontal and vertical test sections with and without heat transfer over a range of flow ratios, total flow rates, and pressure, are too complex, and the data available are neither extensive nor precise enough to warrant the generation of over-all correlations. Use of the void data in correlating two-phase frictional pressure drops is discussed. A model has been presented for the prediction of critical flows based upon the void data, and calculations have been made for steam-water critical flows over a range of critical pressures from 15 to 2,000 lb./sq. in. abs.

A significant property of two-phase gas-liquid flow is the fraction of the cross-sectional flow area that is occupied by the gas. This fraction is known as the *void*, or *gas, fraction*. Methods of measurement have been reviewed (*7, 18, 23,* and *26*), and additional methods noted (*10, 20,* and *25*). It is recognized that such measurements yield averaged values and that very little can be said about the detailed distribution of the liquid phase in the flow channel.

Void fractions are used to determine the mixture flow density. The density term is required for the evaluation of the hydrostatic head term and is a required parameter in determining reactivity in water-cooled reactors. Use is made of the void fraction to calculate the ratio of the gas and liquid velocities. Again, in the use of this ratio, called the *slip ratio,* it is recognized that the mean velocity, calculated for each phase based upon the known volumetric flow rate and the flow areas available for each phase, is not necessarily the correct velocity to be used in the momentum and kinetic energy terms. Nevertheless the slip ratio is a very useful parameter for the evaluation of specific designs (*11, 22*).

This paper is concerned with the presentation of void-fraction measurements for adiabatic, horizontal flow of steam-water mixtures at 400, 600, 800, and 1,000 lb./sq. in. gauge and comparisons with other measurements and correlations. Further, a note is included regarding the use of the void fractions to predict critical steam-water flows.

EXPERIMENTAL

The void-fraction equipment used at the University of Minnesota has been described (*18*). The description of the high-pressure steam-water flow test stand is given in reference *16*. The measurements reported in this paper were made with a collimated beam of gamma rays (approximately 1/32 in. in diameter) produced from a 20-curie (November, 1956) thulium-170 source. A horizontal test section consisting of a ¾-in. seamless mechanical tubing with an inside diameter of 0.484 in. was used for the steam-water flows. The two-phase flows were generated by the mixing of separate sources of high-pressure steam and water flows. The test section was 8 ft. long, and the void measurements were made at an L/D ratio of about 110. Gamma ray traverses were made across the tube starting from the top to the bottom and from the bottom to the top. The readings were taken at 1/16-in. intervals except near the extreme top and bottom positions where 1/32-in. intervals were used.

The length of water in any chord position was obtained from

$$l_w = \frac{1}{\beta_w - \beta_s} \ln \frac{I_s}{I_{TP}} \qquad (1)$$

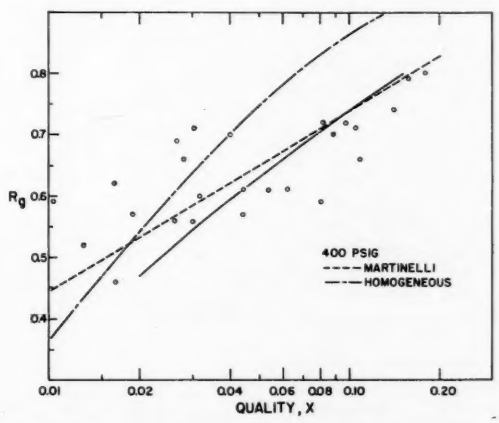

Fig. 1. Void fractions in steam-water flows at 400 lb./sq. in. gauge.

H. A. Rodriguez is with Loza Fina S. A., Guadalajara, Jalisco, Mexico, and H. C. Larson and B. D. Pattie are with Union Carbide Chemicals Company, South Charleston, West Virginia.

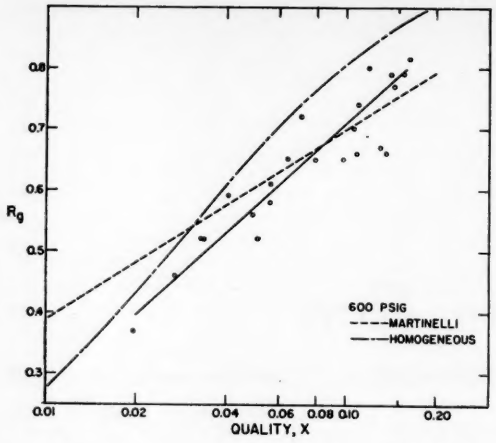

Fig. 2. Void fractions in steam-water flows at 600 lb./sq. in. gauge.

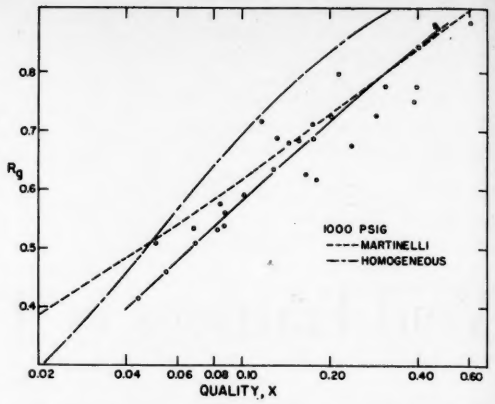

Fig. 4. Void fractions in steam-water flows at 1,000 lb./sq. in. gauge.

The absorption coefficient $(\beta_w - \beta_s)$ was experimentally determined by measuring the counting rates for the pipe filled with liquid and the pipe filled with steam. For the experimental conditions used and for a range of water temperatures from 392° to 567°F

$$(\beta_w - \beta_s) = 0.00557\rho_w \text{ in.}^{-1} \qquad (2)$$

The chordal lengths were integrated graphically over the pipe traverse to obtain the pipe cross-sectional area occupied by the liquid phase. Illustrations of the method are given in reference *18*.

Measurements were made at 400 lb./sq. in. gauge for a quality (x) range of 2 to 17.8%, total flow (W_m) range of 2,400 to 4,200 lb./hr.; 600 lb./sq. in. gauge, x from about 2 to 16.5%, W_m from 2,000 to 3,910; 800 lb./sq. in. gauge, x from 2 to 17%, W_m from 2,170 to 3,450; and at 1,000 lb./sq. in. gauge, x from 4 to 60%, and W_m from 1,330 to 2,540.

RESULTS

The experimental values for the void fractions are given in Figures 1, 2, 3, and 4, covering the measurements made at 400, 600, 800, and 1000 lb./sq. in. gauge. Included on the figures are the void fractions that would be obtained from the Martinelli curves (*24, 15*) and from the homogeneous model (*15*). In the homogeneous model

$$R_g = \frac{xv_g}{xv_g + (1 - x)v_l}$$

where x is the quality. The extrapolation of the Martinelli curves leads to the crossing of the homogeneous curves, and modified curves have been suggested (*29*) to keep the Martinelli curves below the homogeneous curves.

The 1,000, 800, and 600 lb./sq. in. gauge curves, as shown in Figures 2, 3, and 4, were used to estimate a curve for the 400 lb./sq. in. gauge data. Further, the curve, as represented in Figure 1, was not permitted to cross the homogeneous curve. The scatter of the experimental data is believed to be mainly due to errors in maintaining constant quality during a run and in the precision of determining the low values of quality from the heat balances. It was not possible to distinguish an effect of total flow rate upon the void fraction.

The slip ratios, calculated as

$$\frac{u_g}{u_l} = \left(\frac{x}{1 - x}\right)\left(\frac{v_g}{v_l}\right)\left(\frac{1 - R_g}{R_g}\right) \qquad (4)$$

are presented in Figure 5 and are based upon the solid curves of Figures 1 to 4. The experimental points given in Figures 1 to 4 lying above the solid curves have lower slip ratios, approach 1 as the points approach the homogeneous curve, and fall below 1 for points lying above the homogeneous curve.

COMPARISONS OF VOID-FRACTION DATA AND CORRELATIONS

The curves representing the University of Minnesota void data (Rodriguez and Larson's) and Popper's summary of the Argonne National Laboratory data are presented in Figure 6. Again the Martinelli curves are shown and in every case are above the Minnesota curves at the low qualities and cross them at the higher qualities. The Argonne curves are below the Minnesota curves. The Argonne data were determined for upward flow in rectangular channels with boiling heat transfer. The 1,200 lb./sq. in.

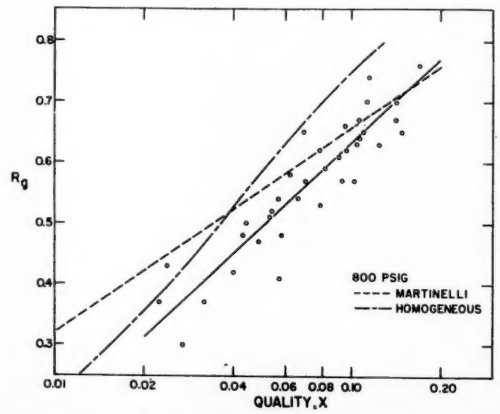

Fig. 3. Void fractions in steam-water flows at 800 lb./sq. in. gauge.

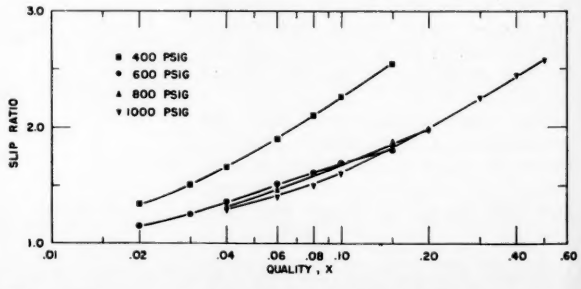

Fig. 5. Slip ratios at 400, 600, 800, and 1,000 lb./sq. in. gauge.

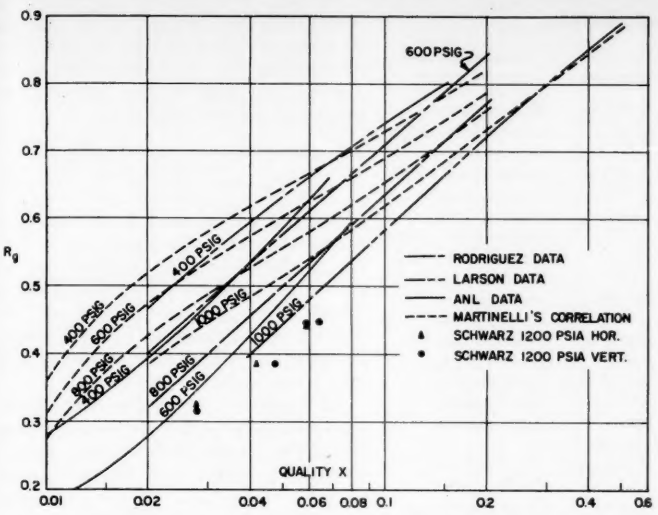

Fig. 6. Comparison of void-fraction measurements and correlations at high pressures.

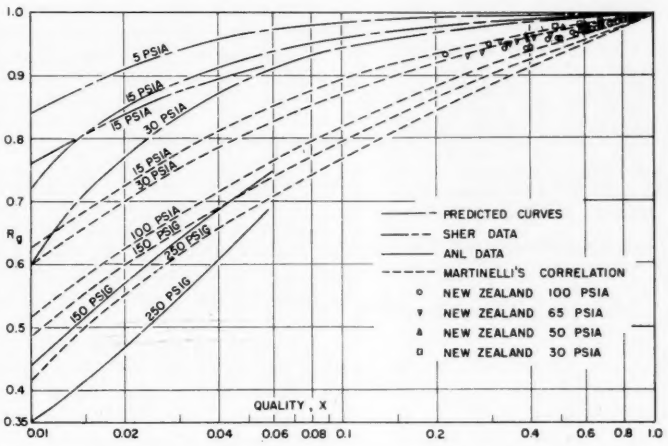

Fig. 7. Comparison of void-fraction measurements and correlations at low pressure.

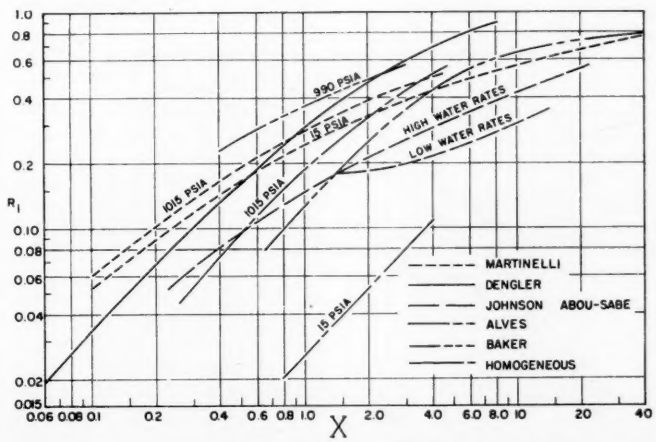

Fig. 8. R_l vs. X curves.

abs. horizontal and vertical flow data of Schwarz (*28*) are consistent with the Minnesota data.

Figure 7 presents the low-pressure void-fraction data. The New Zealand void-fraction data (*30*), determined in 4- and 6-in. horizontal pipes at 30 to 100 lb./sq. in. abs. range from 0.93 to 1 and appear to be in close agreement with the Martinelli correlation. The Argonne data fall below the Martinelli correlation, and the Minnesota data and predictions are above the Martinelli correlation. The predictions given in Figure 7 are based upon a critical flow model. (See section on critical flow.)

Liquid-fraction correlations are compared in Figure 8 as a function of the Martinelli parameter, which is the ratio of the single-phase frictional pressure drops of the liquid to the gas flow in the entire channel. Baker's curve represents data at 990 lb./sq. in. abs. (*5*), Alves's at 100 lb./sq. in. abs. (*1*), Dengler's at 7.2 to 29 lb./sq. in. abs. (*8*), and Johnson and Abou-Sabe's at 1 to 50 lb./sq. in. abs. (*19*). Curves for the homogeneous and Martinelli correlations are shown for comparison. The characteristics of the systems used by the different investigators are summarized in Table 1. Two component systems, such as gas-water and gas-oil, were employed by Alves, Martinelli, Johnson and Abou-Sabe, and Baker. (See also Note 2.) In all other systems reported, one component systems, steam-water, were used.

Armand (*2*) developed an empirical correlation for air-water mixtures in horizontal pipes, and interestingly enough a good prediction of the Minnesota data can be made over a short range of quality. (See Figure 9.) The Armand equation, for void fractions up to 0.75, is

$$R_g = 0.833 \frac{V}{V + L} \qquad (5)$$

Yagi's correlation (*34, 35*) for upward, vertical flow of air-water and air-oil mixtures (near atmospheric pressure) is

$$\frac{R_l}{R_g} = 700 \left(\frac{u_l'}{u_g'} \right)^{0.88} w_l \mu_l^{0.3} \qquad (6)$$

The Yagi correlation is not suitable for the high-pressure steam-water data but did appear adequate for the prediction of the New Zealand data for high void fraction at 30 and 100 lb./sq. in. abs.

A simplified model has been suggested by Untermeyer (*31*) as a qualitative correlation. Specific application to the 165 lb./sq. in. abs. Argonne National Laboratory data indicated that the predicted values are much higher than the experimental ones.

The Zmola-Bailey correlation (*3*) when applied to steam-water flow is limited to low qualities at low pressures. At higher pressures the predicted values were lower than the Argonne National Laboratory data at 165 and 615 lb./sq. in. abs.,

Table 1. Survey of Void-Fraction Investigations

Reference	X range*	Pressure, lb./sq. in. abs.	Conditions	Geometry	Method of void measurement
(*1*)	0.65–100	100	FC NHT	HP 1 in.	Isolate test section and weigh
(*24*)	0.10–50	near atm.	FC NHT	HP ½ and 1 in.	Isolate test section and weigh
(*8*)	0.05–10	7.2 to 29	FC WHT	VT 1 in.	Radioisotope in fluid mixture
(*19*)	0.2–15	1-50	FC NHT	HT 1 in.	Isolate test section and weigh
(*5*)	0.4–3 Quality	990	FC NHT	HP 8 and 10 in.	Separate phases and weigh
(*22*)	0.012–0.079	165, 265 415, 615	NC WHT	VC ½ and 1 in.	Tm^{170} γ attn. Cross section
(*32*)	0.01–0.074	165, 265 215, 615	NC WHT	VC ¼ and 2 in.	Tm^{170} γ attn. Cross section
(*23*)	0.019–0.082	115, 274 314, 414 514, 614	NC WHT	VC Four 7/16 and 3 11/16 in.	Tm^{170} γ attn. Cross section
(*7*)	0.012–0.140	614	NC WHT	VC Four 7/16 and 3 11/16 in.	Tm^{170} γ attn. Cross section
(*9*)	0–0.04	2000	FC WHT	VC 1 by 0.103 in.	Tm^{170} γ attn. Cross section
Rodriguez	0.02–0.20	415, 615 815	FC NHT	HP 0.484 in.	Tm^{170} γ attn. Chordal lengths
Larson	0.04–0.40	1,015	FC NHT	HP 0.484 in.	Tm^{170} γ attn. Chordal lengths
Eddy	0.012–0.048	25	FC NHT	HP 1.049 in.	Se^{75} γ attn. Chordal lengths
Sher	0.004–0.042	15	NC NHT	VT 0.872 in.	Se^{75} γ attn. Chordal lengths
(*30*)	0.21–1.0	100, 65 50, 30	FC NHT	HP 4 and 6 in.	Dye injection and sound
(*28*)	0.028–0.064	1,200	HC NHT	HT and VT 60 mm.	Ir^{192} γ attn. Chordal lengths

Note 1. The following symbols were used in this table: V—vertical, H—horizontal, P—pipe, T—tube, C—rectangular channels, FC—forced circulation, NC—natural circulation, WHT—with heat transfer, NHT—no heat transfer.

2. See Armand (*1*), Zmola-Bailey (*3*), Yagi (*34, 35*), Untermeyer (*31*), Bergelin and Gazley (*4*), and Govier et al. (*12*).

*X = Martinelli's parameter.

and lower than the Minnesota data at 815 lb./sq. in. abs.

The effect of flow rate cannot be distinguished in the Minnesota data; however, Lottes and Flinn (*22*) have suggested that although the slip-ratio dependence upon power density, voids, quality, recirculation flow, pressure, and geometry is not fully understood, a useful empirical relation may be used showing the slip ratio dependence upon total mass velocity and system pressure. Marchaterre (*23*) found that in his heated test sections, with inlet fluid at saturation temperature, the assumption of constant slip along a channel length was reasonable. The initial rise of the slip ratio with length of heated section is extended if the liquid is subcooled and if the vaporizing flow is at low pressure with higher void fractions. Cook, in his studies at 614.7 lb./sq. in. abs. (*7*), found that there is an increase in the slip ratio with length of the heated channel and that the change is related to the rate of vaporization. At the initiation of vaporization the slip ratio was approximately 1.5 and appeared to be independent of inlet velocity. Steam-void fractions up to 10% were found at positions in the channel where a heat balance would indicate zero quality. The presence of steam was believed to be indicative of stratification. (See also reference *9*.) Petrick (*26*) suggests the following approximation for the slip ratio:

$$\frac{u_g}{u_l} = K u_{lo}'^{N} \qquad (7)$$

where N is an exponent that varies with pressure (about 0.31 at 150 lb./sq. in abs., 0.2 at 1,500 lb./sq. in. abs., and zero at the critical pressure for steam-water flows). The approximation was used to develop a relationship between static pressure and void fractions before and after a contraction or expansion.

An analytical model has been developed for two-phase flow by Westmoreland (*33*). The model differs from Levy's model (see reference *15* for comparison of models) in that at the liquid-gas interface it is assumed that the phase velocities and the shearing stresses are equal. Although the equations for predicting the two-phase frictional drops will not show a dependency on total flow (other than flow types), the predictions for the slip ratio, for example for steam-water at 615 lb./sq. in. abs., are good.

CRITICAL-FLOW PREDICTIONS

Measured and predicted critical flows of steam-water mixtures at low pressures are given in reference *17*. The approximations used in developing the model are noted, and in the examples given use was made of the Martinelli void correlations. At low qualities (less than 10%) the deviations between the predicted critical flows and the observed values were significant. It was found that slight changes in the void-fraction correlation could improve the correlation. For example, the difference between measured critical flows and predicted flows could be made less than 3% for the entire quality range if the void fraction curves were changed as noted

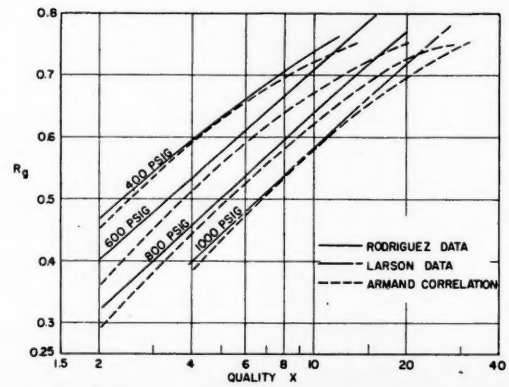

Fig. 9. Comparison of University of Minnesota void data with Armand correlation.

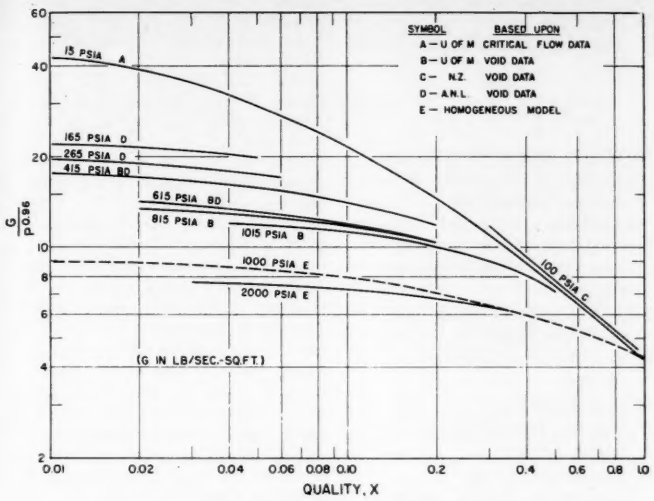

Fig. 10. Critical-flow predictions.

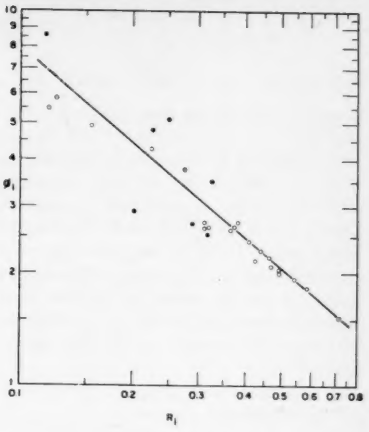

Fig. 11. ϕ_l vs. R_l for 1,000 lb./sq. in. gauge data. (Solid points lying above the curve represent the lowest flow rates and those below, the highest flow rate.)

in Figure 7, under Predicted Curves.*

Figure 10 is a presentation of predicted, critical steam-water mass-flow rates as a function of quality and with the critical pressure a parameter. The form of the plot with $G/P^{0.96}$ used was adapted from the previous correlations at low pressure (*17*). The Minnesota, Argonne, and New Zealand void data were used to predict critical flows over the range of data available. Critical flows based upon the 415 and 615 lb./sq. in. abs. Argonne and Minnesota data could be grouped into single curves at each pressure. The 2,000 lb./sq. in. abs. curve is based on the homogeneous model, which investigators at Battelle (*9*) used to correlate their void-fraction data at 2,000 lb./sq. in. abs. above a quality of 0.03. For comparison at lower pressure the 1,000 lb./sq. in. abs. curve, based upon the homogeneous model, lies about 40% below the predicted curve. Data are not yet available to check critical-flow predictions at pressures above 45 lb./sq. in abs., and thus the usefulness of the model has not been established.

PRESSURE-DROP–VOID-FRACTION RELATIONSHIPS

Several modifications of the friction-factor method have been suggested for correlating two-phase frictional pressure drops. Mosher (*36*) started with the Linning model (*21*), which noted that the frictional forces are exhibited at the wall only and that with annular flow the correct velocity to use in the Fanning equation is the mean velocity of the liquid. Liquid density and liquid viscosity are to be used as well as the pipe diameter. Some comparisons of the predicted to measured steam-water pressure drops were made, based upon the Martinelli void-fraction correlation; however, the predictions were not much better than the homogeneous model.

An independent analysis was made by Flinn and Lottes (*22*) in which they, too, assumed that the frictional effect of the two-phase flow is due primarily to the drag of the water phase along the wall. For small qualities

$$\phi_{lo}^2 = \frac{(\Delta P_{TPF}/\Delta L)}{(\Delta P_{lo}/\Delta L)} \simeq \frac{1}{(1 - R_g)^2} \quad (8)$$

The two-phase frictional pressure drop gradient is taken as

$$\frac{dP_{TPF}}{dL} = \frac{f_l \rho_l u_l^2}{2gD} \quad (9)$$

where u_l equals the superficial velocity divided by the liquid fraction, $(1 - R_g)$. If the Reynolds number defining the friction factor is based upon the total liquid flow and pipe diameter, then the friction factor for the two-phase flow model is the same as that used in calculating ΔP_{lo}. With this restriction and the inclusion of the quality

$$\phi_{lo}^2 = \left(\frac{1 - x}{1 - R_g}\right)^2 \quad (10)$$

Petrick's experiments (*26*) (air-water upward flow at atmosphere pressure) indicated that this model was not satisfactory, particularly over wide ranges of flow rate.

If it is assumed that $f_l \propto 1/u_l^m$ and if the two-phase frictional pressure drop is compared with the pressure drop due to just the liquid flow, then

$$\phi_l^2 = \left(\frac{\Delta P_{TPF}/\Delta L}{\Delta P_l/\Delta L}\right) = \left(\frac{1}{1 - R_g}\right)^{2-m} \quad (11)$$

Chisholm and Laird (*6*) found that the majority of their data (horizontal air-water flows in 1-in. bore) for smooth and galvanized tubes lie within ±20% of the equations

$$\phi_l^2 = \frac{0.8}{(1 - R_g)^{1.75}}$$

for smooth tubes (12)

and

$$\phi_l^2 = \frac{0.8}{(1 - R_g)^{1.875}}$$

for galvanized tubes (13)

Hoopes (*14*) considered the relationship

$$\phi_{lo}^2 = \frac{f_{TPF} r_{HTP}}{f_l r_{Hl}} \left(\frac{1 - x}{1 - R_g}\right)^2 \quad (14)$$

The plot of ϕ_{lo}^2 vs. $[(1 - x/(1 - R_g)]^2$ exhibits considerable scatter owing in part to the difficulty in accurately determining the frictional two-phase pressure drops and the quality.

Other references on the use of

$$\phi_l^a R_l^b = C \quad (15)$$

are given by Moen (*37*) and Sher (*18*).

Figure 11 is a plot of the ϕ_l vs. R_l Minnesota steam-water data at 1,000 lb./sq. in. gauge. A very definite flow-rate effect is noted. The solid points lying above the curve represent the lowest flow rates, and those below the curve represent the highest. The flow-rate effect is due to the influence of the total flow on the frictional two-phase pressure drop, and a limited correlation is presented in reference *16*. Petrick (*26*) also noted a flow-rate effect in his air-water data.

An empirical correlation was found by Petrick (*26*) to be satisfactory in correlating air-water data at atmospheric pressure and boiling steam water at 2,000 lb./sq. in.

*The 15 lb./sq. in. abs. curve approximates Sher's data (*18*).

$$\phi_{l0}^2 = \frac{KR_g^n}{\left(\frac{G}{10^6}\right)^{0.76}} \qquad (16)$$

where G is the mass flow rate in lb./(hr.)(sq. ft.); $K = 9.6$ and $n = 1.25$ for air-water; $K = 8.5$ and $n = 1.4$ for steam-water at 2,000 lb./sq. in.; n is a function of G for range of variables beyond R_g from 0.3 to 0.7, and G from 0.3 to 2×10^6. The Larson 1,000 lb./sq. in. data were approximated by Equation (16) with n about 1.4 and K about 14. Further work is being done to check the correlation over a wider pressure range for steam-water flows.

ACKNOWLEDGMENT

The investigations reported were made possible through Atomic Energy Commission contracts AT-(11-1)-210, 211, and 433 with the Chemical Engineering Department, University of Minnesota.

NOTATION

Pressure Drops and Pressure-Drop Ratios

$\Delta P_{TPF}/\Delta L$ = frictional two-phase pressure drop per unit length

$\Delta P_{l0}/\Delta L$ = frictional pressure drop per unit length calculated for the total flow as liquid flow in the entire channel

$\Delta P_l/\Delta L$ = frictional pressure drop per unit length calculated for just the liquid flow in the entire channel

$\Delta P_g/\Delta L$ = frictional pressure drop per unit length calculated for just the liquid flow in the entire channel

ϕ_{l0}^2 = $(\Delta P_{TPF}/\Delta L)/(\Delta P_{l0}/\Delta L)$, ratio of two-phase frictional pressure drop per unit length to the frictional pressure gradient calculated for the total flow as liquid

ϕ_l^2 = $(\Delta P_{TPF}/\Delta L)/(\Delta P_l/\Delta L)$

X = Martinelli parameter, $(\Delta P_l/\Delta L)/(\Delta P_g/\Delta L)$

Flow Quantities

w_g and w_l = mass flow of gas and liquid, respectively ($W_m = w_l + w_g$), kg./(sq. meter)(sec.) in Equation (6)

V and L = volumetric flow rate of gas and liquid, respectively

u_g' and u_l' = superficial velocities of the gas phase and liquid phase, respectively, meter/sec. in Equation (6)

u_g and u_l = velocity of gas phase and liquid phase, respectively, based upon cross-sectional area available for flow of phase

G = mass flow rate, lb./(hr.)(sq. ft.)

u_g/u_l = slip ratio

u_{l0} = superficial entering velocity

Others

β_w and β_s = linear gamma-absorption coefficient for water and steam, respectively

μ_l and μ_g = viscosity of liquid and gas phase, respectively, kg./(meter)(sec.) in Equation (6)

ρ_l or ρ_w and ρ_g = density of liquid and gas, respectively, lb./cu. ft.

A = cross-sectional area of pipe for flow

D = pipe diameter

f = Fanning friction factor

f_l = friction factor

g = conversion factor

K, m, n, N = constants (given in defining equations)

l_w = chordal length of water in tube

I_{TP}, I_s, I_w = radiation intensity transmitted through two-phase flow, steam flow, and water flow respectively

P = pressure at critical flow

p = pressure

r = hydraulic radius for the flows

r_{HTP}, r_{Hl} = hydraulic radius for two-phase flow and liquid flow, respectively

R_g = void fraction, fraction of cross-sectional flow area occupied by gas phase

R_l = liquid fraction = $1 - R_g$, fraction of cross-sectional flow area occupied by liquid phase

v_l and v_g = specific volume of liquid and gas phase, respectively

x = quality

LITERATURE CITED

1. Alves, G. E., *Chem. Eng. Progr.*, **50**, 449 (1954).
2. Armand, A. A. [As given by Gresham (*13*)], *Vsesoiuzniyi Teplotekhnichesku Izvestia*, No. 1, 16 (1946).
3. Bailey, R. V., P. C. Zmola, F. M. Taylor, and R. J. Planchet, *U. S. Atom Energy Comm. CF-55-12-118* (Dec. 1955); Zmola, P. C., and R. V. Bailey, *Trans. Am. Soc. Mech. Engrs.*, **78**, 881 (1956).
4. Bergelin, O. P., and C. Gazley, Heat Transfer and Fluid Mechanics Inst.; Am. Soc. Mech. Engrs. (1949).
5. Baker, O., *Oil Gas J.*, **53**, No. 12, 185 (1954).
6. Chisholm, D., and A. D. K. Laird, *Trans. Am. Soc. Mech. Engrs.*, **80**, 276 (1958).
7. Cook, W. H., *Argonne Natl. Lab. Rept.*, ANL-5621 (Nov., 1956).
8. Dengler, C. E., Ph.D. thesis, Mass. Inst. Technol., Cambridge (1952).
9. Egen, R. Å., D. A. Dingee, and J. W. Chastain, Battelle Memorial Inst.-1163 (Feb., 1957).
10. English, D., P. T. Blacker, and W. E. Simmons, Atomic Energy Research Establishment ED/M 20, Harwell, Berks., Great Britain (1955).
11. Flinn, W. S., and Michael Petrick, *Argonne Natl. Lab. Rept.*, ANL-5720 (Oct., 1957).
12. Govier, G. W., B. A. Radford, and J. S. C. Dunn, *Can. J. Chem. Eng.*, **35**, 58 (Aug., 1957).
13. Gresham, W. A., P. A. Foster, and R. J. Kyle, Interim Report No. 1 Project No. A-186, *Eng. Expt. Sta., Georgia Inst. Technol.*, Atlanta (June, 1955).
14. Hoopes, John W., Jr., *A.I.Ch.E. Journal*, **3**, 268 (1957).
15. Isbin, H. S., R. H. Moen, and D. R. Mosher, AECU-2994 (Nov., 1954).
16. Isbin, H. S., R. H. Moen, R. O. Wickey, D. R. Mosher, and H. C. Larson, *Chem. Eng. Progr. Symposium Ser. No. 23*, **55** (1959).
17. Isbin, H. S., J. E. Moy, and A. J. R. Cruz, *A.I.Ch.E. Journal*, **3**, 361 (1957).
18. ———, N. C. Sher, and K. C. Eddy, *ibid.*, 136 (1957).
19. Johnson, H. A., and A. H. Abou-Sabe, *Trans. Am. Soc. Mech. Engrs.*, **74**, 977 (1952).
20. Katarzhis, A. K., S. I. Kosterin, and B. I. Sheinen, Atomic Energy Research Establishment Lib/Trans. 590 [from *Izvest. Akad. Nauk S.S.S.R., Otdel. Tekh. Nauk*, No. 2, 132 (1955)].
21. Linning, D. L., *Proc. Inst. Mech. Engrs. (London)*, **1B**, No. 2 (1952).
22. Lottes, P. A., and W. S. Flinn, *Nuclear Sci. and Eng.*, 1, 461 (1956).
23. Marchaterre, J. F., *Argonne Natl. Lab. Rept.*, ANL-5522 (Feb., 1956).
24. Martinelli, R. C., and D. B. Nelson, *Trans. Am. Soc. Mech. Engrs.*, **70**, 695 (1948).
25. McManus, H. N., Jr., Am. Soc. Mech. Engrs., Paper No. 57-A-144.
26. Petrick, Michael, *Argonne Natl. Lab. Tech. Memo. 14; Argonne Natl. Lab. Rept.*, ANL-5787 (March, 1958).
27. Popper, G. F., Argonne Natl. Lab. Memo. to W. S. Flinn (Nov., 1956).
28. Schwarz, K., *Z. Ver. deut. Ingre. Forschungsheft 445*, **20** (1954).
29. Sher, Neil C., personal communication (1956).
30. Smith, G. M., and Y. L. Hoe, C. E. 174, Report No. DL 118/6, Dominion Lab., Dept. Scientific and Industrial Research, New Zealand (Sept., 1956).
31. Untermeyer, S., Am. Soc. Mech. Engrs., 57-Nuclear Engineering and Science Congress-80 (March, 1957).
32. Weatherhead, R. J., Argonne Natl. Lab. Memo. to P. A. Lottes (Feb., 1957).
33. Westmoreland, J. C., *Nuclear Sci. and Eng.*, **2**, 533 (1957); Am. Soc. Mech. Engrs., Paper 57A-50; Knolls Atomic Power Lab.-1792 (Feb., 1957).
34. Yagi, Sakae, and T. Sasaki, *Chem. Eng. (Japan)*, **17**, 216 (1953).
35. ———, and Y. Kato, *ibid.*, **18**, 2 (1954).
36. Mosher, D. R., M. S. thesis, Univ. Minn., Minneapolis, Minnesota (September, 1954).
37. Moen, R. H., Ph. D. thesis, Univ. Minn., Minneapolis, Minnesota (August, 1956).

Manuscript received August 20, 1958; revision received March 23, 1959; paper accepted April 16, 1959.

Transistion from Laminar to Turbulent Flow in Pipes

N. W. RYAN and M. M. JOHNSON

University of Utah, Salt Lake City, Utah

In pipeline design, for which one needs a means of ascertaining whether the flow will be laminar or turbulent, the Reynolds number is the criterion for Newtonian fluids. The principal purpose of this study was to formulate a more general criterion to characterize the flow regime and to test this form in application to non-Newtonian fluids.

Intuitive physical arguments suggested the use of a local stability parameter which is a function of the ratio of input energy to energy dissipation for an element of fluid. If the parameter is applied to a Newtonian fluid in laminar pipe flow, one finds that it has a maximum value of 0.385 times the critical Reynolds number, or 808. As the criterion is presumed to be general, it is inferred that the value of 808 defines the boundary between stable laminar and stable turbulent pipe flow for all fluids. The inference has been varified for several pseudoplastic fluids.

Osborne Reynolds (*1*) and those who followed his lead established that the dimensionless group subsequently named after Reynolds

$$N_{Re} = (DV\rho/\mu)$$

is for Newtonian fluids flowing isothermally in straight, smooth, circular ducts, a criterion of type of flow, laminar or turbulent. When the Reynolds number is less than a critical value of about 2,100, laminar flow exists; transient flow disturbances are damped out. When the value of the Reynolds number is greater than critical, turbulent flow is usually encountered. Although under special conditions laminar flow can be produced at supercritical Reynolds numbers, it is metastable. A transient disturbance can induce turbulent flow, which will not revert to laminar flow unless the Reynolds number is reduced below 2,100.

The Reynolds number applies only to Newtonian fluids whose rheological character is described by the coefficient of viscosity. As distinct regimes of laminar and turbulent flow are also observed for other kinds of fluids, it is to be inferred that the Reynolds number is a special form of a more general criterion.

DEVELOPMENT OF CRITERION

The search for the flow criterion starts along the classical approach to the theoretical study of laminar flow stability, in which small perturbation theory is applied to the Navier-Stokes and continuity equations (for example reference 2). Concerned only with Newtonian fluids, this approach as usually followed has not produced the flow criterion sought. It does however, as developed below, suggest the forms of perturbation energy supply and dissipation terms.

The equations of motion (precursors of the Navier-Stokes equations, surface stresses not expressed in terms of shear rates) can be written as

$$\left.\begin{aligned} \rho \frac{Du}{Dt} &= \frac{\partial \sigma_{xx}}{\partial x} + \frac{\partial \sigma_{yx}}{\partial y} \\ \rho \frac{Dv}{Dt} &= \frac{\partial \sigma_{xy}}{\partial x} + \frac{\partial \sigma_{yy}}{\partial y} \end{aligned}\right\} \qquad (1)$$

The equations are written in two dimensions for a fluid on which no body forces act. The x and u direction is parallel to the axis. As small regions are to be considered, Cartesian coordinates are used in place of the less convenient cylindrical coordinates. The first subscript on the stress symbol indicates the face of a cubical element on which the stress acts; the second subscript indicates the direction of action. It is evident that σ_{xx} and σ_{yy} are normal stresses; σ_{xy} and σ_{yx} which are equal are shear stresses.

When no disturbance is present, steady state values are to be used:

$$u = U, \qquad v = 0, \qquad \sigma_{ij} = \tau_{ij}$$

When a small disturbance is present,

$$u = U + u'$$
$$v = v'$$
$$\sigma_{ij} = \tau_{ij} + \tau_{ij}'$$

The energy equation is produced by taking the scalar product of the vector velocity and the equations of motion in vector form. The energy equation for the steady state is subtracted from that for the disturbed state leaving significant first-order perturbation terms:

$$\rho \frac{D}{Dt}(Uu') - \left\{U \frac{\partial \tau_{xx}'}{\partial x} + u' \frac{\partial \tau_{xx}}{\partial x}\right\} = -\rho v' U \frac{\partial U}{\partial y} + \left\{U \frac{\partial \tau_{yx}'}{\partial y} + u' \frac{\partial \tau_{yx}}{\partial y}\right\} \qquad (2)$$

The terms on the left side of the equation represent the time rate of increase, unit-volume basis, of surplus energy in the disturbed region. The first term on the right represents the rate at which energy is supplied; the remaining terms represent the rate at which it is dissipated.

To carry this analysis further one would need to relate shear stress to shear rate, that is to specify the rheological nature of the fluid and thus lose generality. Also one would need to define the form of the perturbation stream function, which is not known for the kinds of disturbances of interest. Carried this far, however, the analysis does suggest that the energy-dissipation term takes the form of a perturbation in the quantity

$$-u \frac{\partial \sigma_{yx}}{\partial y} \qquad (3)$$

The energy-supply term can be arrived at in another way if the radial transport of axial momentum across a unit surface normal to the y direction is considered. There results a tangential force on the unit surface $-\rho v'u$ which, when multiplied by the velocity gradient, gives the rate of perturbation energy supply from the base flow. In first-order perturbation form the term is

$$-\rho v' U \frac{\partial U}{\partial y} \qquad (4)$$

The fluid transported radially moves from a position where the dissipation rate is given by Equation (3) to a position where the rate is greater by the amount

$$\frac{\partial}{\partial y}\left(-u \frac{\partial \sigma_{yx}}{\partial y}\right) \delta y$$

In first-order perturbation form the term is

$$\frac{\partial}{\partial y}\left(-U \frac{\partial \tau_{yx}}{\partial y}\right) \delta y \qquad (5)$$

The ratio of Equations (4) and (5) is proposed as the stability index. Elimination of the remaining perturbation factors δy and v' is necessary. It is noted that their ratio is a time interval, and it is postulated that for effective disturances this time must be related to a characteristic time of the undisturbed flow, which is taken as the reciprocal of the velocity gradient. The substitution of $\partial U/\partial y$ is therefore made for $-v'/\delta y$. Finally it is noted that

$$\frac{\partial \tau_{yx}}{\partial y} = -\frac{\tau_w}{r_w}$$

The stability parameter is, with these changes

$$Z = \frac{r_w \rho U}{\tau_w} \frac{\partial U}{\partial y} \qquad (6)$$

Inspection shows that Z is zero at both the pipe wall and the center line and has a maximum value at an intermediate position. The maximum value can be obtained if the steady state velocity is known as a function of radial position. For a Newtonian fluid

$$Z_{max} = \sqrt{\frac{4}{27}} \frac{DV\rho}{\mu}, \quad \text{at} \quad \frac{r}{r_w} = \frac{1}{\sqrt{3}}$$

Thus the maximized stability function meets the necessary condition that the Reynolds number be a special form of it.

As the critical value for the Reynolds number is 2,100, it is assumed that the critical value of Z_{max} above which turbu-

M. M. Johnson is with the Phillips Petroleum Company, Bartlesville, Oklahoma.

lent flow is to be expected is, for all nonthixotropic, true fluids

$$Z_c = 2{,}100\sqrt{\frac{4}{27}} = 808$$

A stability parameter similar to Z was proposed by Rouse (*10*), who, from dimensional analysis and the recognition that the parameter should have zero value at both the axis and the pipe wall, suggested the stability parameter

$$\frac{y^2\rho}{\mu}\frac{\partial U}{\partial y}$$

This parameter, meaningful only for Newtonian fluids, maximizes at r/r_w of 1/3, the maximum value being 8/27 of the Reynolds number.

Clearly the maximized form of Rouse's parameter is equivalent to the Reynolds number. Its validity as a general parameter has been tested in two ways. In the first the coefficient of viscosity was interpreted, for non-Newtonian fluids, as the ratio of shear stress to rate of shear, and the parameter was tested in the same manner as Z in the next section. It did not successfully predict the onset of turbulence in pseudoplastic fluids.

A second test consists in the prediction of where, in the cross section of the stream, laminar flow of a Newtonian fluid is least stable. Rouse predicts the critical r/r_w as 0.333; the authors predict it as 0.577. Gibson (*11*), who observed dye filaments in water, reported that the critical ratio is 0.58 for large pipes, increasing somewhat as pipe diameter decreases below about 2 in. From his data one would estimate a ratio of 0.64 for standard ½-in. pipe. A similar conclusion is inferred from the work of Leite and Kuethe (*12*), who produced air flow at supercritical Reynolds numbers, introduced a disturbance, and made hot-wire anemometer measurements downstream from the source of the disturbance. At a short distance downstream, where the parabolic profile was still well approximated, they observed maximum fluctuations in the anemometer signal at r/r_w of 0.6.

It should be mentioned that Leite and Kuethe and others have observed that a stream at supercritical Reynolds number sometimes will not become turbulent when a finite disturbance is introduced. Their observations appear to be at variance with an essential premise of the derivation outlined above, namely that a very small disturbance can grow and produce turbulence. There is no contradiction if only certain kinds of small disturbances are effective; then one might speculate further that effective kinds are probably always present in the complex vibrations to which industrial piping is subjected.

TEST OF CRITERION

An attempt has been made to verify the criterion for pseudoplastic fluids. It is assumed that the behavior of these fluids is described by the power law

$$\tau_{yx} = K\left(\frac{\partial U}{\partial y}\right)^n \qquad (7)$$

The expression for Z_{max} becomes

$$Z_{max} = \frac{r_w^2\rho\Gamma^2}{\tau_w}\phi(n),$$

at

$$\frac{r}{r_w} = \left(\frac{1}{n+2}\right)^{n/n+1}$$

where

$$\phi(n) = \frac{(3n+1)^2}{n}\left(\frac{1}{n+2}\right)^{n+2/n+1} \qquad (8)$$

Here use is made of the flow function, which proves to be a convenient variable in the analysis of many problems of rheology. If the critical value of 808 is used

$$\tau_{wc} = \frac{r_w^2\rho\Gamma_c^2}{808}\phi(n) \qquad (9)$$

Equation (9) can be solved together with the analogue of the Hagen-Poiseuille Law

$$\tau_w = K\left(\frac{3n+1}{n}\right)^n\Gamma^n \qquad (10)$$

which applies to laminar flow, to yield the maximum flow rate (as Γ) at which laminar flow is stable.

If this method of verification is to be employed, Γ, τ_w pipe-flow data are needed.

Pipe-flow data were obtained in a horizontal pipe system differing only slightly from that described by Christiansen, Ryan, and Stevens (*3*). Clean steel pipes of ½-, ¾-, and 1-in. nomial diameter were employed. The pressure drop was measured over a 10-ft. length following an 8-ft. calming section. Flow rate and pressure drop were measured, and Γ was computed from the former and τ_w from the latter as

$$\tau_w = \frac{r_w}{2}\left(-\frac{\Delta p}{\Delta x}\right)$$

Some flow data were also taken in ¾-in. Pyrex pipe. Viscometer data were obtained in the rotating viscometer described by Stevens (*4*), a rotating-shell instrument with a shell radius of 3.808 cm., a clearance of 0.155 cm., and a shearing surface height of 16.2 cm.

The fluids used in the experimental work were carboxy-methyl cellulose (CMC) in water. Additional pipe-flow data were obtained from the literature: on 52% rock solids in water from Wilhelm, Wroughton, and Loeffel (*5*); on 23% yellow clay in water from Caldwell and Babbitt (*6*); on Carbopol in water and Attasol clay in water from Dodge (*7*).

Plots on logarithmic paper of experimental values of τ_w and Γ are shown on Figures 1 through 6. From the portion of these plots in the laminar-flow range n was determined as the slope and $\phi(n)$ computed for use in Equation (10) with experimental values of τ_w to determine the τ_{wc} vs. Γ_c lines (dashed lines) on Figures 1 through 6. Each slope value (n) was measured from the best straight line through all data for laminar flow. This measurement is not critical because, as shown in the table of f_c values, $\phi(n)$ is a very weak function of n.

The test of the criterion is in how precisely the transition to turbulence, as

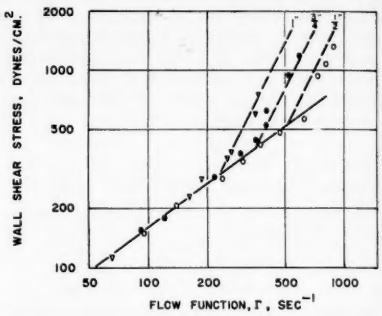

Fig. 1. Wall stress vs. flow rate for 1.0% carboxy methyl cellulose in water (*9*).

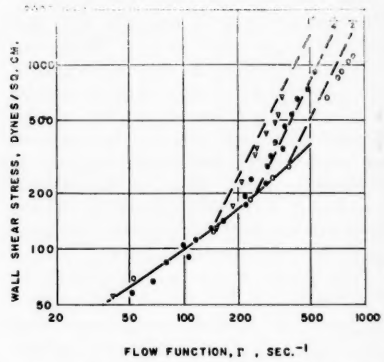

Fig. 2. Wall stress vs. flow rate for 0.75 and 0.78% carboxy methyl cellulose in water (*9*).

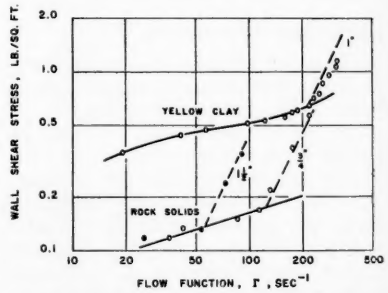

Fig. 3. Wall stress vs. flow rate for 23% yellow clay in water (*6*) and for 52% rock solids in water (*5*).

indicated by the experimental data, is predicted by the intersection of the appropriate calculated $\tau_{wc} - \Gamma_c$ (dashed) lines with the laminar flow line [equivalent to solving Equations (9) and (10) simultaneously]. It is seen that the predicted transition conditions agree reasonably well with the observed conditions. This test of the criterion is not however

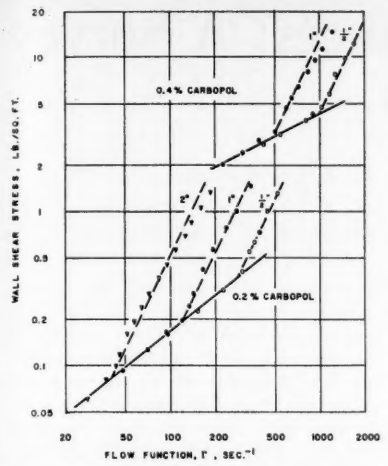

Fig. 4. Wall stress vs. flow rate for Carbopol in water (7).

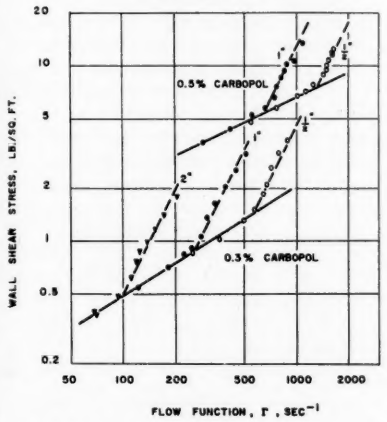

Fig. 5. Wall stress vs. flow rate for Carbopol in water (7).

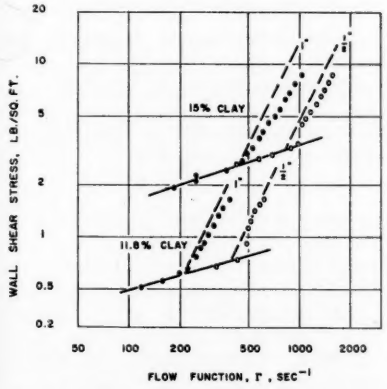

Fig. 6. Wall stress vs. flow rate for Attasol clay in water (7).

conclusive, partly because the pipe-flow data lack the desired precision and partly because the assumption that the fluids conform to the power law, Equation (7), is only approximate. The dashed lines are not intended to represent the data for turbulent flow; for most pseudoplastic fluids they do not do so over a large range of flow rates.

An interesting observation can be made relative to the suggestion of Metzner and Reed (8) that the value of the friction factor may be the same for all fluids at the critical condition. By definition the friction factor is given by the expression

$$f = \frac{2\tau_w}{r_w^2 \rho \Gamma^2} \qquad (11)$$

For fluids obeying the power law, Equation (7), one may combine Equations (8) and (11), setting $Z_{max} = 808$ to obtain

$$f_c = \frac{\phi(n)}{404}$$

Values of f_c calculated from this equation are

n	$f_c = \frac{\phi(n)}{404}$
1.0	0.0076
0.8	0.0072
0.6	0.0068
0.4	0.0066
0.2	0.0075

It is seen that $\phi(n)$ is rather insensitive for the useful range $0.2 < n < 1$. If the criterion proposed here is correct, the suggestion of Metzner and Reed is an approximation suitable for most engineering work.

SUMMARY

From largely intuitive arguments, guided by the theory of laminar-flow stability, a criterion of flow type in straight tubes of circular cross section has been developed:

$$Z = \frac{r_w \rho U}{\tau_w} \frac{\partial U}{\partial y}, \quad \text{at} \quad \frac{dZ}{dy} = 0$$

Application requires knowledge of the laminar velocity profile, which can be derived from the rheological law for the fluid of interest. The value of this criterion at laminar-turbulent transition is 808, laminar flow being predicted for values less than, and turbulent flow for values greater than, 808.

The criterion has been verified analytical for Newtonian fluids and experimentally by means of pipe-flow data for several pseudoplastic liquids, the rehological behavior of these liquids being approximated by the power law.

ACKNOWLEDGMENT

This work was carried on under a grant from the National Science Foundation after preliminary phases supported by a fellowship from the Phillips Petroleum Company. Valuable assistance in analyzing data and preparing the manuscript was rendered by Professor D. L. Salt and R. W. Hanks of the University of Utah.

NOTATION

Force (F), length (L), time (T) dimensions given

D = tube diameter, L
f = friction factor, dimensionless
K = contant in power law, Equation (7)
n = constant in power law, Equation (7)
N_{Re} = Reynolds number, dimensionless
p = pressure, FL^{-2}
Q = volumetic flow rate, L^3T^{-1}
r = radial distance from tube axis, L
t = time
u = local axial velocity, LT^{-1}
U = local axial velocity, undisturbed flow, LT^{-1}
v = local radial velocity, positive when toward axis, LT^{-1}
V = mean velocity, LT^{-1}
x = distance in axial direction, L
y = distance from wall, normal to axis, L
Z = stability parameter, dimensionless

Greek Letters

Γ = flow function $Q/\pi r_w^3$, T^{-1}
ρ = density, FT^2L^{-4}
σ = stress, FL^{-2}
τ = stress, FL^{-2}
τ_w = sheaf stress
μ = coefficient of viscosity, FTL^{-2}

Subscripts

c = value at critical condition
w = value at tube wall
x, y = direction indexes
$'$ = perturbation quantities

LITERATURE CITED

1. Reynolds, Osborne, *Phil. Trans. Royal Soc. London*, **174**, 935 (1883).
2. Lin, C. C., "Hydrodynamic Stability," Cambridge University Press, Cambridge, England (1955).
3. Christiansen, E. B., N. W. Ryan, and W. E. Stevens, *A.I.Ch.E. Journal*, **1**, 544 (1955).
4. Stevens, W. E., Ph.D. thesis, University of Utah, Salt Lake City, Utah (1953).
5. Wilhelm, R. H., D. M. Wroughton, and W. F. Loeffel, *Ind. Eng. Chem.*, **31**, 622 (1939).
6. Caldwell, D. H., and H. E. Babbitt, *Trans. Am. Inst Chem. Engrs.*, **37**, 237 (1941).
7. Dodge, D. W., Ph.D. thesis, University of Delaware, Newark, Delaware (1958).
8. Metzner, A. B., and J. C. Reed, *A.I.Ch.E. Journal*, **1**, 434 (1955).
9. Johnson, M. M., Ph.D. thesis, University of Utah, Salt Lake City, Utah (1958).
10. Rouse, Hunter, "Elementary Mechanics of Fluids," p. 171, Wiley, New York (1946).
11. Gibson, A. H., *Phil. Mag.*, Series 7, **15**, 637 (1933).
12. Leite, R. J., and A. M. Kuethe, *J. Aeronaut. Sci.*, **23**, 444 (1956).

Manuscript received October 27, 1958; revision received January 5, 1959; paper accepted January 8, 1959. Paper presented at A.I.Ch.E. Salt Lake City meeting.

Some Properties of Polar Substances: A Survey

R. BYRON BIRD and JAMES R. BROCK Technische Hogeschool, Delft, Holland, and University of Wisconsin, Madison, Wisconsin

The current understanding of the macroscopic (bulk) properties of polar substances in terms of molecular theory, or the correlation of them in terms of corresponding-states principles is summarized.

Some electrical properties of molecules are defined, and the way in which they contribute to the intermolecular force field is indicated. Then the calculation of the bulk properties for various molecular models is summarized, and finally some of the recent proposals for corresponding-states correlations are discussed, with particular emphasis on the polar compounds.

Polar substances are those consisting of molecules which possess a permanent dipole moment. It should be noted, however, that many polar molecules are rather complex and that consequently their physical properties are dependent on a number of molecular properties: (*a*) the dipole moment, (*b*) the quadrupole and higher multipole moments, (*c*) the polarizability, (*d*) the shape, and (*e*) the tendency to form hydrogen bonds. Hence methods of prediction and correlation of physical properties of polar molecules which involve only the dipole moment must be regarded from the very outset as oversimplifications.

SOME ELECTRICAL PROPERTIES OF MOLECULES

A continuous distribution of electronic charge such as that shown in Figure 1 is considered. The charge density is given by $\rho(\mathbf{R})$. The first three multipole moments are

$$C = \int \rho \, d\mathbf{R} \tag{1}$$

= electric charge (a scalar)

$$\boldsymbol{\mu} = \int \rho \mathbf{R} \, d\mathbf{R} \tag{2}$$

= electric dipole moment (a vector with components μ_x, μ_y, μ_z).

$$\boldsymbol{\Theta} = \int \rho \mathbf{R}\mathbf{R} \, d\mathbf{R} \tag{3}^*$$

= electric quadrupole moment (a second-order tensor with nine components

$$\Theta_{xx}, \Theta_{yy}, \Theta_{zz}, \Theta_{xy} = \Theta_{yx}, \text{ etc.})$$

in which the integrals are all taken over the entire charge distribution. According to Equation (1) the total charge is just the integral over the charge density. The dipole moment is the first moment of the charge distribution; the strength of the dipole of the distribution is given by the scalar value $\mu = \sqrt{\mu_x^2 + \mu_y^2 + \mu_z^2}$. For the quadrupole moment a second definition is frequently used:

$$\mathbf{Q} = \int \rho(3\mathbf{R}\mathbf{R} - R^2\mathbf{U}) \, d\mathbf{R} = 3\boldsymbol{\Theta} - (\Theta_{xx} + \Theta_{yy} + \Theta_{zz})\mathbf{U} \tag{4}$$

Hence this traceless quadrupole moment bears a simple relation to the quadrupole moment defined in Equation (3). For a linear charge distribution along the z axis or for a charge distribution symmetric about the z axis $Q_{xz} = Q_{yz} = Q_{xz} = 0$, and $Q_{xx} = Q_{yy} = -Q_{zz}/2$. The scalar quantity $Q_{zz} \equiv Q$ is then referred to as the strength of the quadrupole. Other definitions of the quadrupole moment are also used (*13*).

The multipole moments arise in the calculation of the electrostatic potential at a point r resulting from a continuous charge distribution. The contribution to the electrostatic potential dV_e, because of the interaction of a unit test charge at $\mathbf{r}$ with an infinitesimal element $\rho \, d\mathbf{R}$ of the distribution, is, according to Coulomb's law,

$$dV_e = \frac{\rho \, d\mathbf{R}}{|\mathbf{r} - \mathbf{R}|} = \frac{\rho(X, Y, Z) \, dX \, dY \, dZ}{\sqrt{(x - X)^2 + (y - Y)^2 + (z - Z)^2}} \tag{5}$$

The square-root expression can be expanded in a Maclaurin series about the origin ($\mathbf{R} = 0$) to give

$$dV_e = \rho \, d\mathbf{R}\left[\frac{1}{\mathbf{r}} - (\mathbf{R}\cdot\nabla\frac{1}{r}) + \tfrac{1}{2}\left(\mathbf{R}\mathbf{R}:\nabla\nabla\frac{1}{r}\right) - \cdots\right] \tag{6}$$

Integration over the entire charge distribution gives the potential resulting from the distribution

$$V_e = \left(\int \rho \, d\mathbf{R}\cdot\frac{1}{r}\right) - \left(\int \rho\mathbf{R} \, d\mathbf{R}\cdot\nabla\frac{1}{r}\right) + \tfrac{1}{2}\left(\int \rho\mathbf{R}\mathbf{R} \, d\mathbf{R}:\nabla\nabla\frac{1}{r}\right) - \cdots \tag{7}$$

The integrals which arise are then just the multipole moments, so that Equation (7) can be written in one of two forms:

$$V_e = C\cdot\frac{1}{r} - \left(\boldsymbol{\mu}\cdot\nabla\frac{1}{r}\right) + \tfrac{1}{2}\left(\boldsymbol{\Theta}:\nabla\nabla\frac{1}{r}\right) - \cdots \tag{8}$$

$$V_e = \frac{C}{r} + \frac{(\boldsymbol{\mu}\cdot\mathbf{r})}{r^3} + \tfrac{1}{2}\frac{(\mathbf{Q}:\mathbf{r}\mathbf{r})}{r^5} + \cdots \tag{9}$$

The general expressions for the electric potential at points within and without charge distributions (both continuous and discrete) and the general expressions for the interaction energy between two arbitrary charge distributions (both overlapping and nonoverlapping) are given elsewhere (*13*). The electric field associated with V_e is then given by $\mathbf{E} = -\nabla V_e$.

The physical significance of Equation (9) is that the potential due to a charge distribution is given by a superposition of (a) potential due to a point charge + (b) the potential due to a point dipole + (c) the potential due to a point quadrupole + etc., each of these point multipoles being located at the origin. For a neutral molecule, then, the dipole moment gives the first approximation to the electrostatic field surrounding the molecule. Until recently little has been done in connection with the examination of the role of the quadrupole in intermolecular force fields and bulk properties.

The polarizability of a molecule is a second-order tensor describing the extent to which the electron cloud becomes distorted in an electric field. If the molecule is placed in an electric field of strength $\mathbf{E}$, then an induced dipole moment is produced:

$$\boldsymbol{\mu}^{(ind)} = (\boldsymbol{\alpha}\cdot\mathbf{E}) \tag{10}$$

In many calculations it is assumed that the molecule is isotropic, so that the polarizability may be regarded as a scalar. In such instances the scalar value of the polarizability is usually defined as the arithmetic average of the three principal components of the polarizability: $\alpha = (\alpha_{xx} + \alpha_{yy} + \alpha_{zz})/3$.

Extensive tables of dipole moments (*19, 30*) and polarizabilities (*19*) are available. Very little information is available about molecular quadrupole moments; what little is known has been obtained from molecular orbital calculations (*8*), broadening of microwave spectra (*10, 11*), and second virial-coefficient calculations (*27*). It is possible that pressure-induced absorption measurements may be another source of information (*29*).

R. Byron Bird is at present at the University of Wisconsin, Madison, Wisconsin. James R. Brock is currently at the University of Texas, Austin, Texas.

*For example

$$\Theta_{xy} = \iiint_{\substack{\text{volume of} \\ \text{charge dist.}}} \rho(X, Y, Z)XY \cdot dX \, dY \, dZ \tag{4}$$

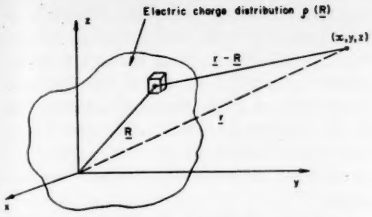

Fig. 1. Calculation of electrostatic potential V_e at position r. It is assumed in the text that $|r| > |R|_{max}$.

FORCES BETWEEN POLAR MOLECULES

Extensive discussions of intermolecular forces are given elsewhere (*13a*). Here the important contributions to the interaction energy between two neutral polar molecules which are chemically alike are briefly summarized. It is assumed that the electronic distribution is symmetrical about the z axis, so that the quadrupole can be described by the single scalar Q, and that the molecules are isotropic, so that the polarizability is given by the single scalar α.

It is convenient (but also artificial) to subdivide the contributions to the intermolecular potential energy into the following types:

Short-Range Forces

When molecules are very close, they generally repel one another quite strongly. The detailed dependence of this energy on intermolecular distance and orientation is complex, and the details have been calculated for only very simple systems. Generally the interaction energy is approximated by a simple exponention or inverse power function just because further details are lacking:

$$\phi^{(s.r.)} \approx b \exp(-ar) \text{ or } \approx d/r^n \quad (11)$$

with n usually between 9 and 15.

Long-Range Forces

The electrostatic contributions to the energy of interaction are the interactions of the various permanent multipoles (See Figure 2 for the definition of angles):

$$\phi^{(\mu,\mu)} = -(\mu^2/r^3)(2c_1c_2 - s_1s_2c) \quad (12)$$

$$\phi^{(\mu,Q)} = -(3/4)(\mu Q/r^4) \cdot (c_1 - c_2)(2s_1s_2c - 3c_1c_2 - 1) \quad (13)$$

$$\phi^{(Q,Q)} = +(3/16)(Q^2/r^5) \cdot [1 - 5c_1^2 - 5c_2^2 - 15c_1^2c_2^2 + 2(s_1s_2c - 4c_1c_2)^2] \quad (14)$$

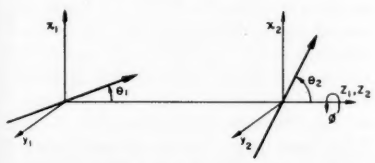

Fig. 2. Angles used to described mutual orientation of two dipoles or two symmetry axes. In the text the following abbreviations are used: $c_1 = \cos\theta_1$, $s_1 = \sin\theta_1$, $c = \cos(\phi_2 - \phi_1)$.

Equation (12) represents the interaction energy of two ideal dipoles; deviations because of the finite size of a dipole are discussed elsewhere (13). Equation (13) represents the electrostatic interaction between two charge distributions each having a permanent dipole and a permanent quadrupole.

The induction contributions arise because the permanent multipoles in one molecule induce multipole moments in the other molecule, and then these interact with one another:

$$\phi^{(\mu,ind\mu)} = -(1/2)(\mu^2\alpha/r^6)(3c_1^2 + 3c_2^2 + 2) \quad (15)$$

$$\phi^{(\mu Q,ind\mu)} = -6(\mu Q\alpha/r^7)(c_1^3 + c_2^3) \quad (16)$$

$$\phi^{(Q,ind\mu)} = -(9/32)(Q^2\alpha/r^8) \cdot (s_1^4 + s_2^4 + 4c_1^4 + 4c_2^4) \quad (17)$$

Equation (15) represents the interaction energy of two molecules with permanent rigid dipole moments which produce an instantaneous induced dipole moment with which they interact; if the distortion of the permanent dipoles is accounted for, then an additional term proportional to $\mu^2\alpha^2/r^9$ must be introduced (*3, 9*). Equations (16) and (17) are contributions to the intermolecular potential energy when permanent quadrupoles participate in the induction effects.

The dispersion contributions, which may be explained quantum mechanically, are attractive forces arising because of instantaneous mutually induced moments. These contributions have the following form for simple molecules:

$$\phi^{(ind\mu,ind\mu)} = -c'/r^6 \quad (18)$$

$$\phi^{(ind\mu,indQ)} = -c''/r^8 \quad (19)$$

$$\phi^{(indQ,indQ)} = -c'''/r^{10} \quad (20)$$

These forces occur between molecules which have no permanent multipole moments. The forms given here are for spherical molecules [for nonspherical molecules see (*13*)].

On the basis of the various contributions summarized above a number of molecular models, listed in Table 1. have been proposed. These models can be divided into two general classifications: rigid molecules to which multipoles are added and Lennard-Jones (6–12) molecules to which multipole interactions are added.

MOLECULAR CALCULATIONS OF PHYSICAL PROPERTIES

The theory of the equation of state of moderately dense gases has been worked out in detail for molecules with angular dependent potential functions (*13b*). Hence formulas are available for the calculation of the virial coefficients, but these involve manifold integrals which require considerable effort to evaluate. The second virial coefficient has been evaluated for all the models listed in Table 1, the details being given in the publications referred to there. The third virial coefficient has been calculated only for the Stockmayer potential (*26*). The second virial coefficients for all the rigid models listed in Table 1 may be written in the form

$$B = \tfrac{2}{3}\pi N\sigma_0^3 \cdot \sum_{h=0}^{\infty}\sum_{i=0}^{\infty}\sum_{j=0}^{\infty}\sum_{k=0}^{\infty} B_{hijk} \cdot \left(\frac{\mu^2}{\sigma_0^3 kT}\right)^h \left(\frac{Q^2}{\sigma_0^5 kT}\right)^i \left(\frac{\alpha}{\sigma_0^3}\right)^j (x)^k \quad (21)$$

TABLE 1. MOLECULAR MODELS FOR POLAR-POLAR INTERACTIONS

Electrical characteristics	Rigid molecules	Lennard-Jones (6–12) molecules
Embedded point dipoles (nonpolarizable)	Keesom I (*15*) Rigid spheres of diameter σ_0 with $\phi = \phi^{(\mu,\mu)}$ for $r > \sigma_0$	Stockmayer (*28*) $\phi = \phi^{(L.J.)} + \phi^{(\mu,\mu)}$
Embedded point dipoles (polarizable)	Falkenhagen (*9*) Rigid spheres of diameter σ_0 with $\phi = \phi^{(\mu,\mu)} + \phi^{(\mu,ind\mu)} + (\mu^2\alpha^2/r^9)(-8c_1c_2 + s_1s_2c)$	Buckingham and Pople I (*3*) $\phi = \phi^{(L.J.)} + \phi^{(\mu,\mu)} + \phi^{(\mu,ind\mu)} + (\mu^2\alpha^2/r^9)(-8c_1c_2 + s_1s_2c)$
Embedded point linear quadrupoles (nonpolarizable)	Keesom and Van Leeuwen (*16, 17*) Rigid spheres of diameter σ_0 with $\phi = \phi^{(Q,Q)}$ for $r > \sigma_0$	
Embedded point linear quadrupoles (polarizable)	Keesom II (*18*) Rigid spheres of diameter σ_0 with $\phi = \phi^{(Q,Q)} + \phi^{(Q,ind\mu)}$ for $r > \sigma_0$	
Embedded point dipoles and quadrupoles (nonpolarizable)		Rowlinson (*27*) $\phi = \phi^{(L.J.)} + \phi^{(\mu,\mu)} + \phi^{(\mu,Q)}$ Buckingham and Pople II (*3*) $\phi = \phi^{(L.J.)} + \phi^{(\mu,\mu)} + \phi^{(\mu,Q)} + \phi^{(Q,Q)}$
Embedded point dipoles in nonspherical molecules (nonpolarizable)	Muckenfuss, Curtiss, and Bird (*22*) Rigid ellipsoids of revolution with symmetry axis σ_0, and other axes σ_1; eccentricity $x = [1 - (\sigma_1/\sigma_0)^2]^{\frac{1}{2}}$ Interact according to $\phi = \phi^{(\mu,\mu)}$.	Buckingham and Pople III (*3*) $\phi = \phi^{(L.J.)} + \phi^{(\mu,\mu)} + 4D\epsilon(\sigma/r)^{12}(3c_1^2 + 3c_2^2 - 2)$ in which D is a dimensionless parameter

Table 2. Tabulation of Expansion Coefficients B_{hijk} for Calculation of the Virial Coefficients for Various Rigid Models

B_{h0j0}—Coefficients for Keesom I and Falkenhagen models

h \ j	0	1	2	3	4
0	1	0	0	0	0
1	0	−4	0	0	0
2	−1/3	0	−3.27	0	0
3	0	−0.533	0	−4.93	0
4	−1/75	0	−0.920	0	−9.47

B_{h00k}—Coefficients for Keesom I and Muckenfuss-Curtiss-Bird models

h \ k	0	2	4
0	1	−1	1/15
2	−1/3	−4/15	−26/105
4	−1/75	−17/525	−151/3675

B_{0ij0}—Coefficients for Keesom-Van Leeuwen and Keesom II models

i \ j	0	1
0	1	0
1	0	−9/20
2	−3/80	0
3	+9/7840	−27/1600
4	−639/1066240	...

the values of the coefficients B_{hijk} being given in Table 2. This table can be used for estimating the order of magnitude of the various effects considered. The extensive tables needed for calculating B for the modified Lennard-Jones models can be found in the original references; the same dimensionless groups appear as in Equation (21). Although quite a bit of work has been done on second virial coefficients, no calculations at all have been made for the equation of state of polar liquids.

A usable theory of transport porperties of dilute and dense gases has been worked out only for molecules with spherically symmetrical potential functions. Hence it is not at present possible to make any rigorous calculations of the transport properties. The only calculations which have been made are for the Krieger potential (*13c*), which is $\phi = \phi^{(L.J.)} - 2(\mu^2/r^3)$; this is a spherically symmetric potential function, in which the angle-dependent dipole-dipole interaction is approximated by the maximum value of the function, that is the value corresponding to perfect alignment of the dipoles. This potential is however so unrealistic that the integral for the second virial coefficient does not converge; hence there is no possibility of interrelating transport coefficients and equation of state in terms of the parameters of the Krieger potential. The only moderately successful molecular calculation method involving polar gases is one for the calculation of the coefficient of binary diffusion for a polar-nonpolar binary mixture (*13d*). Nothing seems to have been done along the line of developing even a rough theory for the transport coefficients of polar liquids.

In addition to the above-mentioned properties there are also molecular theories for some electrical and optical properties, and ultimately these theories coupled with experimental measurements should lead to information about intermolecular forces. Of interest are recent publications on the second dielectrical virial coefficient (*2*), the second refractivity virial coefficient (*5*), and a virial development of the pressure-induced absorption in homopolar diatomic gases (*29*).

CORRESPONDING-STATES CORRELATIONS

From the previous section it is clear that only for the second virial coefficient have practical results been obtained. And at the present the amount of accurate equation-of-state data for polar molecules is so small that it is not possible to make meaningful deductions in terms of the various molecular models proposed.

Hence one is led to explore the possibility of correlating physical properties by means of dimensional analysis or corresponding-states methods. First the equation of state of a substance which is made up of molecules which interact according to a potential function which contains a length parameter σ, an energy parameter ϵ, the electrical properties α, μ, and Q, and some shape factor will be considered. Then the pressure will depend on two state variables, all the molecular parameters, the molecular mass, and also on Planck's constant:

$$p = p(V,RT,\sigma,\epsilon,\mu,Q,\alpha,x,m,h) \qquad (22)$$

According to the Buckingham Pi-Theorem of dimensional analysis a possible functional relationship between these various quantities is the dimensionless relationship

$$pV/RT = Z(V/\sigma^3,\ RT/\epsilon,\ \mu^2/\epsilon\sigma^3,\ Q^2/\epsilon\sigma^5,\ \alpha/\sigma^3,\ h/\sigma\sqrt{m\epsilon},\ x) \qquad (23)$$

It is not at present possible to use this relation as a basis for correlation of experimental data for polar molecules because of lack of information about the molecular parameters and the electrical properties. For simple molecules (with negligible effect of μ, Q, α, and x) this relation reduces to the quantum mechanical principle of corresponding states which enabled de Boer and his collaborators to predict many of the physical properties of He^3; the group containing h is important only for correlating quantum deviations at very low temperatures (*7*) and is not further discussed here.

Because of the lack of information about molecular force parameters, another possibility is to use the macroscopic quantities V_c and RT_c as units of volume and energy (instead of σ^3 and ϵ). In that case a similar dimensional analysis leads to

$$pV/RT = Z(V/V_c,\ T/T_c,\ \mu^2/V_cRT_c,\ Q^2/V_c^{5/3}RT_c,\ \alpha/V_c,\ x) \qquad (24)$$

A correlation more or less of this form was used by Hall and Ibele (*12*), who presented a graph including the effect of the reduced dipole moment (but neglecting the explicit dependence on Q, α, and x, which are, however, included implicitly in the critical constants). These forms of the principle of corresponding states have been fully discussed by Nelson and Obert (*23*).

Corresponding-states correlations based on Equation (24) have not been pushed very var because very little is known about the quadrupole and higher moments and extensive accurate experimental data are needed to sort out the dependence on the various groups. Hence in recent years there has been a flurry of activity in connection with modified principles of corresponding states in which a single characterizing parameter is used in addition to the reduced-state variables; that is, for the equation of state the two most widely proposed principles are

$$pV/RT = Z(p/p_c,\ T/T_c,\ Z_c) \qquad (25)$$

in which

$$Z_c = p_cV_c/RT_c$$

$$pV/RT = Z(p/p_c,\ T/T_c,\ Y_c) \qquad (26)$$

in which

$$Y_c = \left(\frac{d\ \ln\ p_{vap}}{d\ \ln\ T}\right)_{T=T_c}$$

The first of these was suggested by Meissner and Seferian (*21*) and was used to prepare extensive tables by Lydersen, Greenkorn, and Hougen (*20*). The second has been used extensively by Riedel (*25*) and is very similar to correlating procedures suggested by Pitzer and colleagues (*6, 24*). Because the parameters Z_c and Y_c do not seem to be simply related (*20a*) a method employing both of these parameters has recently been developed by Hirschfelder, Buehler, McGee, and Sutton (*14*). Equation (25) states that one needs a separate compressibility-

factor chart with Z as a function of p/p_c and T/T_c for each value of Z_c (the latter quantity varies from about 0.21 to 0.30 for various substances). When the available equation-of-state data are presented in this way, the resulting charts enable one to predict compressibility data for a wide variety of polar and nonpolar substances to within about 5%. Equation (26) leads to similar satisfying results.

Clearly these types of corresponding-states correlations may be applied to various other physical properties. The authors (*1*) have shown that the surface-tension data for a large number of polar and nonpolar substances are summarized by the equations

$$\frac{\gamma}{p_c^{\frac{2}{3}}T_c^{\frac{1}{3}}} = \left(-0.951 + \frac{0.432}{Z_c}\right) \cdot\left(1 - \frac{T}{T_c}\right)^{11/9} \tag{27}$$

$$\frac{\gamma}{p_c^{\frac{2}{3}}T_c^{\frac{1}{3}}} = (-0.281 + 0.133\,Y_c) \cdot\left(1 - \frac{T}{T_c}\right)^{11/9} \tag{28}$$

For eighty-four chemical compounds studied, the average error of Equation (27) is about 6% and that of Equation (28) about 3%. Similar expressions (with different choices of the reduced variables) have been proposed by Riedel (*25*) and by Curl and Pitzer (*6*).

For thermal conductivity of liquids at atmospheric pressure (where presumably the dependence on p/p_c is negligible) Riedel (*25*) has arrived at

$$\frac{\lambda}{p_c^{\frac{2}{3}}/V_0^{\frac{1}{3}}M^{\frac{1}{2}}} = (-0.128 + 0.028\,Y_c) \cdot\left[1 + 6.7\left(1 - \frac{T}{T_c}\right)^{\frac{2}{3}}\right] \tag{29}$$

which shows the use of the correlating parameter. No similar relations seem to have been proposed for viscosity or diffusion.

These various correlation schemes with Z_c and Y_c used apply rather well to substances which are not extremely polar and which do not exhibit hydrogen bonding. Furthermore they enable one, by summarizing the experimental data in dimensionless form, to indicate to the experimentalist in what ranges of reduced variables further measurements are most urgently needed. The usefulness of these correlations in engineering design cannot be denied, but it should be noted that they give no new information regarding the physical or chemical processes involved. Certainly increased attention to the molecular theories of polar substances should be encouraged.

ACKNOWLEDGMENT

James R. Brock wishes to acknowledge the support of the Wisconsin Alumni Research Foundation. R. Byron Bird was the holder of a Fulbright Lectureship and a Guggenheim Research Grant during the course of this work.

NOTATION

B	= second virial coefficient
B_{hijk}	= expansion coefficients in Equation (21)
C	= total charge
c, c_1, c_2	= cosines of angles in Figure 2
$\mathbf{E}$	= electric field strength
h	= Planck's constant
k	= Boltzmann's constant
m	= molecular mass
M	= molecular weight
N	= Avogadro's number
p, p_c	= pressure, critical pressure
Q	= quadrupole moment
R	= gas constant
$\mathbf{R}$	= position vector for element of charge
s_1, s_2	= sines of angles in Figure 2
T, T_c	= temperature, critical temperature
V, V_c	= volume, critical volume, per mole
V_e	= electrostatic potential
V_0	= molar volume at absolute zero
x	= eccentricity of ellipsoid
Y_c	= Riedel's parameter
Z	= compressibility factor
Z_c	= critical compressibility factor

Greek Letters

α	= polarizability
γ	= surface tension
ϵ, σ	= parameters in potential function
$\boldsymbol{\Theta}$	= quadrupole tensor
λ	= thermal conductivity
μ	= permanent dipole moment
$\mu^{(ind)}$	= induced dipole moment
ρ	= electric charge distribution
σ_0	= diameter of rigid sphere
ϕ	= potential function
$\phi^{(L.J.)}$	= $4\epsilon[(\sigma/r)^{12} - (\sigma/r)^6]$ = Lennard-Jones (6–12) potential

Vector and Tensor Notation

$\mathbf{r}$	= position vector with components x, y, z and length $r = \sqrt{x^2 + y^2 + z^2}$
$\mathbf{R}$	= position vector with components X, Y, Z, and length $R = \sqrt{X^2 + Y^2 + Z^2}$
$(\boldsymbol{\mu}\cdot\mathbf{r})$	= $\mu_x x + \mu_y y + \mu_z z$
$(\mathbf{Q} : \mathbf{rr})$	= $Q_{xx}x^2 + Q_{yy}y^2 + Q_{zz}z^2 + 2Q_{xy}xy + 2Q_{zx}xz + 2Q_{yz}yz$ (for symmetrical $\mathbf{Q}$)
$(\boldsymbol{\alpha}\cdot\mathbf{E})_x$	= $\alpha_{xx}E_x + \alpha_{xy}E_y + \alpha_{xz}E_z$
$\mathbf{U}$	= unit tensor ($U_{xx} = U_{yy} = U_{zz} = 1$, all other components are zero)

LITERATURE CITED

1. Brock, J. R., and R. B. Bird, *A.I.Ch.E. Journal*, **1**, 174 (1955).
2. Buckingham, A. D., and J. A. Pople, *Trans. Faraday Soc.*, **51**, 1029 (1955).
3. *Ibid.*, 1173 (1955).
4. *Ibid.*, 1179 (1955).
5. Buckingham, A. D., *ibid.*, **52**, 747 (1956).
6. Curl, R. F., Jr., and K. S. Pitzer, *Ind. Eng. Chem.*, **50**, 265 (1958).
7. de Boer, H. G. J., *Physica*, **14**, 139 (1948); de Boer, H. G. J., and B. S. Blaisse, *ibid.*, 149; de Boer, H. G. J., and R. L. Lunbeck, *ibid.*, 520.
8. Duncan, A. B. F., and J. A. Pople, *Trans. Faraday Soc.*, **49**, 217 (1953).
9. Falkenhagen, H., *Phys. Zeits.*, **23**, 87 (1922).
10. Feeny, Harold, Walter Madigowsky, and B. Winters, *J. Chem. Phys.*, **27**, 898 (1957).
11. Gordy, Walter, W. V. Smith, and Ralph Trambarulo, "Microwave Spectroscopy," John Wiley, New York (1957).
12. Hall, N. A., and W. Ibele, *Trans. Am. Soc. Mech. Engrs.*, **27**, 1003 (1955).
13. Hirschfelder, J. O., C. F. Curtiss, and R. B. Bird, "Molecular Theory of Gases and Liquids," John Wiley, New York (1954); *a*, pp. 916–1035; *b*, pp. 151–155; *c*, pp. 597–600; *d*, 600–604.
14. Hirschfelder, J. O., R. J. Buehler, H. A. McGee, Jr., and J. R. Sutton, *Ind. Eng. Chem.*, **50**, 355 (1958).
15. Keesom, W. H., *Comm. Phys. Lab. Univ. Leiden*, Suppl. 24b, Sec. 6 (1912).
16. ———, *Koninkl. Akad. Wetenschap. Amsterdam*, **14**, 614 (1915).
17. ———, and C. van Leeuwen, *ibid.*, **14**, 1699 (1916).
18. Keesom, W. H., *Phys. Zeits.*, **22**, 129 (1921).
19. Landolt-Börnstein, "Physikochemische Tabellen," vol. 1, part 3, Springer, Berlin, Germany (1951).
20. Lydersen, A. L., R. A. Greenkorn, and O. A. Hougen, *Univ. Wisconsin Eng. Expt. St. Rep. No. 4* (1955).

20a. *Ibid.*, p. 7.

21. Meissner, H. P., and R. Seferian, *Chem. Eng. Progr.*, **47**, 579 (1951).
22. Muckenfuss, Charles, C. F. Curtiss, and R. B. Bird, *J. Chem. Phys.*, **23**, 1542 (1955); *Univ. Wisconsin Naval Res. Lab. Rep., WIS-NSF-2*, Series 10 (1955).
23. Nelson, L. G., and E. F. Obert, *A.I.Ch.E. Journal*, **1**, 74 (1955).
24. Pitzer, K. S., D. Z. Lippmann, R. F. Curl, Jr., C. M. Huggins, and D. E. Petersen, *J. Am. Chem. Soc.*, **77**, 3427 (1955).
25. Riedel, L., *Chem. Ingr. Tech.*, **26**, 83, 259, 679 (1954); **27**, 209, 475 (1955); **28**, 557 (1956).
26. Rowlinson, J. S., *J. Chem. Phys.*, **19**, 827 (1951).
27. ———, *Trans. Faraday Soc.*, **47**, 120 (1951).
28. Stockmayer, W. H., *J. Chem. Phys.*, **9**, 398 (1941).
29. van Kranendonk, J., *Physica*, **24**, 347 (1958).
30. Wesson, L. G., "Table of Electric Dipole Moments," Mass. Inst. Technol. Press, Cambridge, Massachusetts (1948).

Manuscript received October 1, 1958; revision received November 24, 1958; paper accepted November 24, 1958. Paper presented at A.I.Ch.E. Salt Lake City meeting.

Expansion and Contraction of an Air-Water Mixture in Vertical Flow

MICHAEL PETRICK and BERNET S. SWANSON

Argonne National Laboratory, Lemont, Illinois

An experimental two-phase flow study was made on an air-water system at atmospheric pressure to obtain information on the effect of expansion and contraction of flow area on the relative velocity of the two phases. The data show that the relative velocity and hence the mean void fraction of the air-water mixture changed following either an expansion or contraction; however the magnitude of the change was not great and could be predicted by a semitheoretical equation. The air-water data are also compared with data taken from a steam-water system at 150 to 600 lb./sq. in. In addition, a photographic study was made of the transition zone, and phase distributions were obtained by the use of a radiation attenuation traversing technique.

Prediction of the density of an adiabatic two-phase fluid in motion is difficult because of inadequate information concerning the relative velocity between the gas and liquid phases. The gas-volume fraction is interrelated with the velocity of the two phases and the gas-weight fraction through the continuity equation. At the present time all the factors that affect the relative velocity, or "slippage," between phases are not well established. There is meager experimental evidence which indicates that the relative velocity of the two phases is a function of the liquid flow rate, the gas-weight fraction, pressure, and possibly the geometry of the flow path.

Behringer (*1*) in a series of experiments on a static steam-water system showed that the relative velocity of the two phases decreases with increasing pressure. Marchaterre (*2*) observed a similar effect over a pressure range of 25 to 600 lb./sq. in. with a natural circulation system. He also noted an effect of liquid flow rate on the relative velocity of the two phases. Schurig (*3*) reported a marked influence of the circulation rate on the relative velocity. The recent data of Lottes *et al.* (*4*) for a natural- and a forced-circulation boiling system shows both a flow rate and a quality effect on the slippage between the two phases. They obtained local two-phase density measurements by gamma-ray attenuation methods and readily converted the data to a slip ratio V_g/V_w. Cook (*5*), on the basis of an extensive two-phase density study of steam water in multisection rectangular channels, found that an increase of V_g/V_w occurs with length along the heated channel, the increase is a function of the rate of vaporization, and with no vaporization V_g/V_w is merely a function of geometry and the volume flow of the two phases. Dengler (*6*), using a radioactive-tracer technique, measured liquid holdups in a 1-in.-diameter pipe and correlated them as a function of the mixture quality. Eddy (*7*) obtained local density values at atmospheric pressure for steam-water mixtures in a horizontal tube and showed the distribution of each phase in the tube. Sher (*8*) performed similar tests in a vertical tube. His vapor volume fraction-quality data were approximately 10% higher than the data of Martinelli, *et al.*

Zmola *et al.* (*9*) measured two-phase densities of an air-water system over a wide geometrical range of flow paths. These results checked with the data of Behringer in the high-volume fraction range. A radial parabolic distribution of the vapor-volume fraction was observed in the various geometries. Schwarz (*10*) investigated the density and relative velocities of the water and steam phases in vertical and horizontal boiler tubes (2.36 I.D.). He also showed a radial parabolic distribution of the vapor-volume fraction.

Up to the present no data have been published showing the liquid holdup variation due to a sudden change in the flow area resulting from either an expansion or contraction. Utilizing presently available information on the two-phase flow, one could not make a firm prediction as to whether a change in relative velocities of the two-phase mixture will occur with a change of flow area, let alone estimate the magnitude of the change. Therefore an experimental investigation was undertaken to explore further the factors which affect the relative velocity of the two phases and to attempt to provide adequate information on the effect of changes of flow area on the liquid holdup.

THEORY

The density of a two-phase mixture is given by

$$\rho_m = (1 - \alpha)\rho_w + \alpha\rho_g \qquad (1)$$

The relationship of the gas-volume fraction with the relative velocity of the two phases and the gas-weight fraction can be shown through the continuity equation and is

$$\frac{V_g}{V_w} = \frac{X}{1 - X}\,\frac{1 - \alpha}{\alpha}\,\frac{\rho_w}{\rho_g} \qquad (2)$$

As mentioned previously, experimental evidence indicates that the relative velocity of the two phases is a function of both circulation rate and the quality. For the case of an adiabatic system, where it can be assumed that the quality is a constant, the liquid holdup will vary only if the slip ratio changes. Further, the liquid holdup should change owing to an expansion or contraction only if the slip ratio is a function of the velocity, when one assumes that the geometry effect is negligible.

A change of flow area between two points as depicted below is considered.

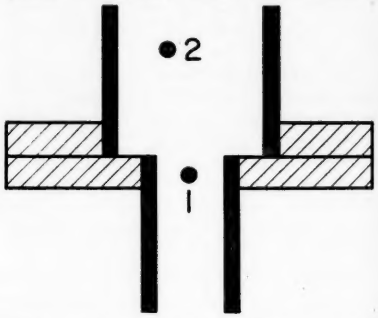

The gas-volume fraction can be expressed at each point by

$$\left(\frac{V_g}{V_w}\right)_1 = \left(\frac{X_1}{1 - X_1}\right) \cdot \left(\frac{1 - \alpha_1}{\alpha_1}\right)\left(\frac{\rho_w}{\rho_g}\right)_1 \qquad (3)$$

$$\left(\frac{V_g}{V_w}\right)_2 = \left(\frac{X_2}{1 - X_2}\right) \cdot \left(\frac{1 - \alpha_2}{\alpha_2}\right)\left(\frac{\rho_w}{\rho_g}\right)_2 \qquad (4)$$

Dividing Equation (3) by Equation (4) and rearranging, one gets

$$\frac{(\alpha_1)/(1 - \alpha_1)}{(\alpha_2)/(1 - \alpha_2)} = \frac{\dfrac{(X_1/1 - X_1)(\rho_w/\rho_g)_1}{(V_g/V_w)_1}}{\dfrac{(X_2/1 - X_2)(\rho_w/\rho_g)_2}{(V_g/V_w)_2}} \qquad (5)$$

For an adiabatic system where it can be shown that

Bernet S. Swanson is at Illinois Institute of Technology, Chicago, Illinois.

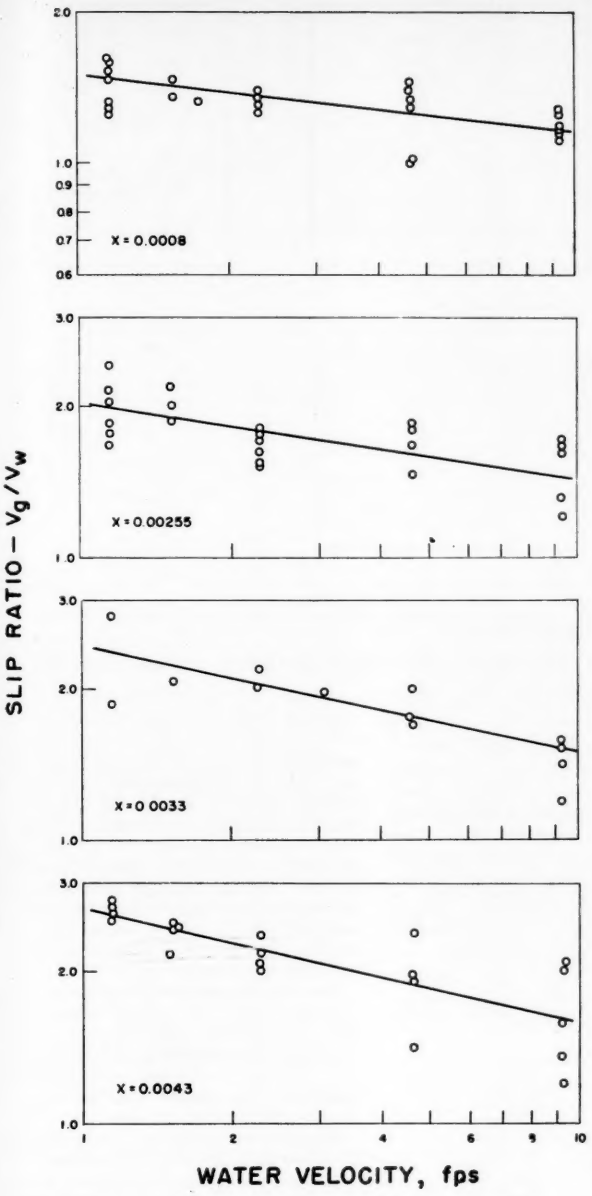

Fig. 1. Variation of slip ratio with water velocity and quality.

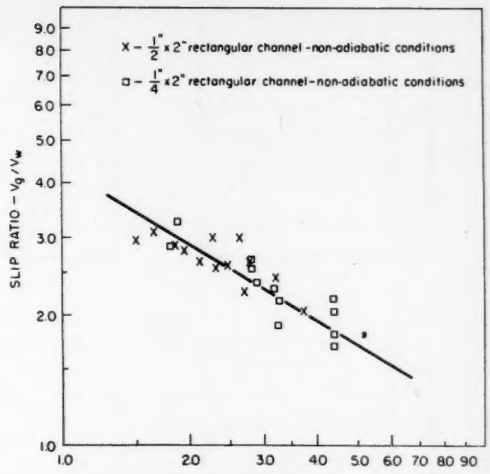

Fig. 2. Superficial water velocity V_{wo}, ft./sec.

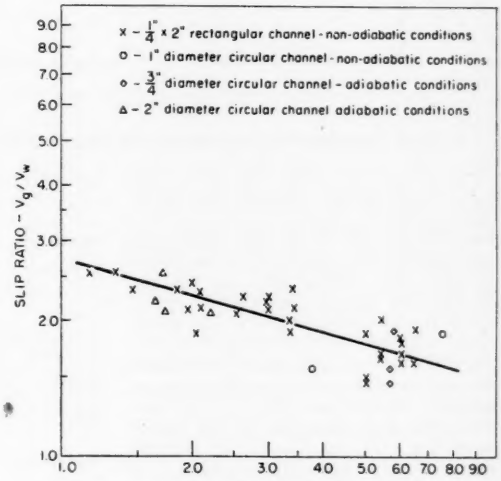

Fig. 3. Superficial water velocity V_{wo}, ft./sec.

$$X_1 = X_2$$

and

$$(\rho_w)_1 = (\rho_w)_2$$

Equation (5) becomes

$$\frac{\frac{\alpha_1}{1-\alpha_1}}{\frac{\alpha_2}{1-\alpha_2}} = \frac{\left(\frac{V_g}{V_w}\right)_2 (\rho_g)_2}{\left(\frac{V_g}{V_w}\right)_1 (\rho_g)_1} \tag{6}$$

It may be assumed that

$$\frac{V_g}{V_w} = K V_{w_o}{}^N \tag{7}$$

Since

$$W = V_{w_o} A \rho \tag{8}$$

then

$$V_{w_o} = \frac{W}{A\rho} = \frac{K'''}{A} \tag{9}$$

for the constant total flow.

Substituting Equation (9) into Equation (7) one obtains

$$\frac{V_g}{V_w} = \frac{K''}{(A)^N} \tag{10}$$

also where

$$\frac{1}{\rho_g} = \frac{RT}{PM} \tag{11}$$

so that

$$\rho_g = K'P \tag{12}$$

When one substitutes Equations (10) and (12) into Equation (6) and rearranges

$$\alpha_2 = \frac{1}{\{(P_2/P_1)[(1/\alpha_1) - 1]/(A_1/A_2)^N\} + 1} \tag{13}$$

The static pressure ratio P_2/P_1 must be included because of the large changes in the specific volumes of the gaseous phase at the lower pressures. In addition to the change of the gas-volume fraction due to the velocity effect, the gas-volume fraction will also change owing to the static pressure difference between positions. The latter effect will become negligible as the system pressure is increased ($P > 25$ lb./sq. in. abs.). The exponent N is obtained empirically.

EXPERIMENTAL APPARATUS

The experimental apparatus basically consisted of a water and air-injection system, the mixing section, the test sections, and an air-water separator. The

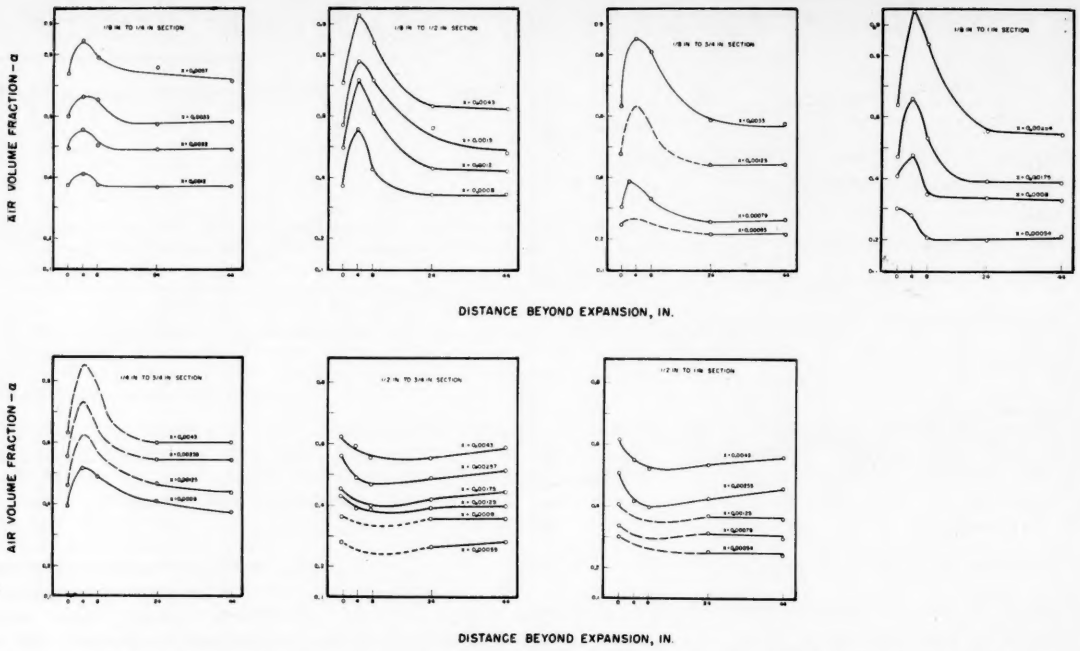

Fig. 4. Variation of air-volume fraction with length following an expansion in flow area; dashed curves represent estimated variation.

metered streams of air and water were injected into the mixer. The two-phase mixture then flowed through the test sections and into the overhead separator, where the air was liberated to the atmosphere and the water was diverted back to the make-up tank. The ranges of variables selected for study were flow-area changes, minimum 1.25:1 and a maximum of 8:1; the void-volume fractions, α, 0.2 to 0.8; mass flow rate, G, 250,000 to 2,000,000 lb./(hr.)(sq. ft.); and water velocity 1 to 10 ft./sec.

Test Section

Five test sections, each 4 ft. long and 2 in. wide, with channel spacings of ⅛, ¼, ½, ¾, and 1 in., respectively, were constructed from Lucite. Lucite was used to allow visual observation and photographic studies. The sections could be interchanged to obtain the desired geometrical combinations.

Density Measurement

The equipment used for measuring the density of the two-phase mixture consisted of a 0.085-mev. thulium source, a DuMont photomultiplier tube with a sodium iodide thallium-activated scintillation crystal, a linear current amplifier, and a Brown recorder (0 to 10 mv.). The gamma rays were directed through the test section to the photomultiplier tube, where the unattenuated portion of the beam produced a signal, which was amplified and transmitted to the recorder.

The source and photomultiplier tube were mounted on a carriage which could move in either a horizontal or vertical direction. The movement of the carriage was controlled by two constant-speed motors in conjunction with a series of relays and a switch box.

The gamma beam was collimated at the photomultiplier tube by a lead window, 1 in. thick. Cooling coils were placed around the photomultiplier tube to maintain a constant temperature, since both the sodium iodide crystal and the tube are sensitive to temperature changes.

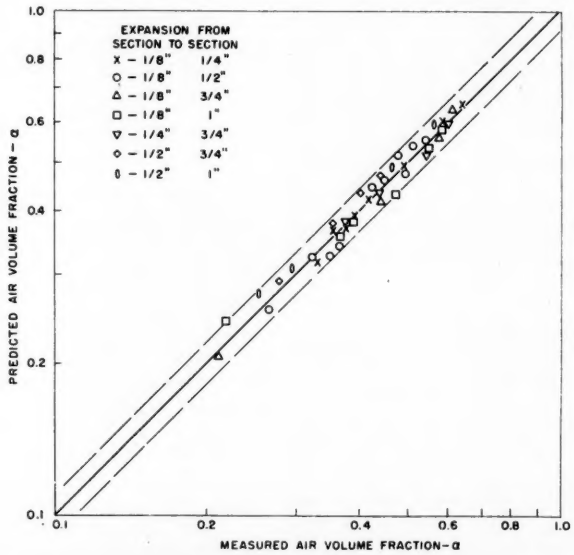

Fig. 5. Comparison of the predicted and measured air-volume fraction for a series of expansions.

Data Procurement

A series of expansion and contraction tests was made with various section combinations. Data on expansions were obtained with the following section combinations: ⅛ to ¼ in., ⅛ to ½ in., ⅛ to ¾ in., ⅛ to 1 in., ¼ to ¾ in., ½ to ¾ in., and ½ to 1 in. The section combinations used for obtaining data on contractions were 1 to ¾ in., 1 to ½ in., 1 to ¼ in., 1 to ⅛ in., ¾ to ¼ in., ½ to ¼ in., and ½ to ⅛ in. It was felt that the various geometric combinations investigated gave an adequate cross section of the expansion and contraction geometries possible. (All future reference to the sections will be with respect to spacing.)

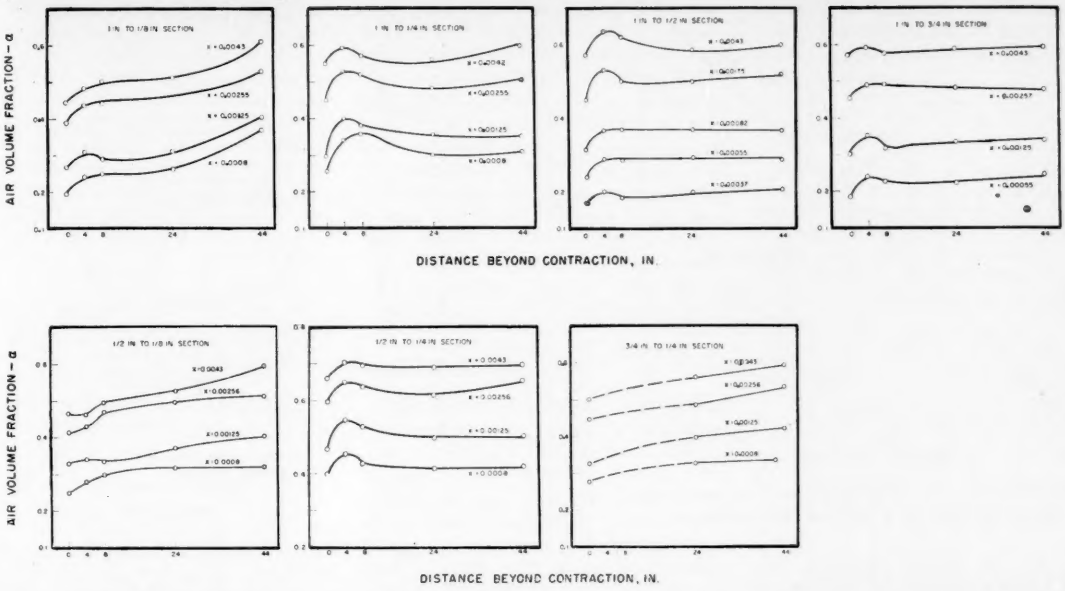

Fig. 6. Variation in air-volume fraction with length following a contraction in flow area; dashed curves represent estimated variation.

A series of runs with varying air-volume fractions was made for each geometry combination. The air-volume fraction was varied from $\alpha = 0.2$ to $\alpha = 0.75$, primarily by adjusting the flow rate of air. Owing to the relationship between specific volumes of the two phases, the quality range corresponding to the air-volume fraction range studied was very low ($X = 0.00055$ to $X = 0.0045$).

Measurements of the air-volume fraction were taken at the exit of the lower section and at positions 4, 8, 24, and 44 in. in the upper section. These positions were selected so that the transition zone could be studied (with positions at 4 and 8 in.) and the actual over-all change in the liquid holdups could be determined (with positions at 24 and 44 in.).

The air-volume fraction was measured and the data were reduced by the methods described by Petrick (*11*) and Hooker and Popper (*12*).

RELATIVE VELOCITY OF THE GASEOUS AND LIQUID PHASES

The relative velocity of the two phases was calculated for a number of data points from the measured air-volume fraction and quality and was plotted in terms of slip ratio (V_g/V_w) vs. the water velocity (based on section flow area) for constant quality parameters (Figure 1). The data show that the slip ratio is a function of both the water velocity and quality. As the velocity increases, the slip ratio decreases. Also, as the quality increases, the slip ratio increases and the velocity effect becomes more pronounced.

An interesting comparison is obtained between the air-water data of this investigation and the data obtained from boiling-water studies. The experimental loops used in these studies are described by Lottes and Petrick *et al.* (*13*). The data for steam-water mixtures in vertical channels at pressures of 150 and 600 lb./sq. in. were reduced to slip ratios in a manner analogous to that described above and are plotted as V_g/V_w vs. the superficial water velocity in Figures 2 and 3. The data shown are local values of the velocity ratio for a constant mixture quality of $X = 0.03 \pm 0.005$. The data were obtained from both adiabatic and nonadiabatic systems of widely differing geometries, which are indicated on the figures. Although there is a basic difference between the air-water and steam-water systems, there is good agreement between the two sets of data.

It can been seen that the slip ratio shows the same dependency on the superficial water velocity noted for the air-water mixtures at atmospheric pressure. As the superficial velocity increases, the slip ratio decreases. It is interesting to note that the velocity effect is greater at 150 lb./sq. in. than observed at atmospheric pressure. The fact that the effect is greater at atmospheric pressure could be due to the difference in the quality

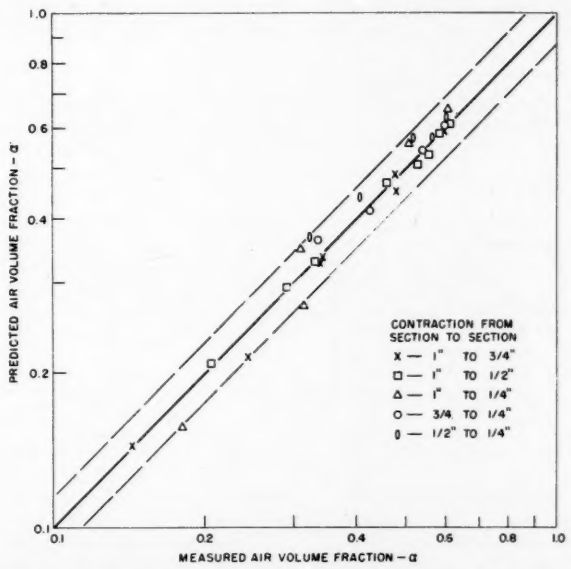

Fig. 7. Comparison of the predicted and measured air-volume fraction for a series of contractions.

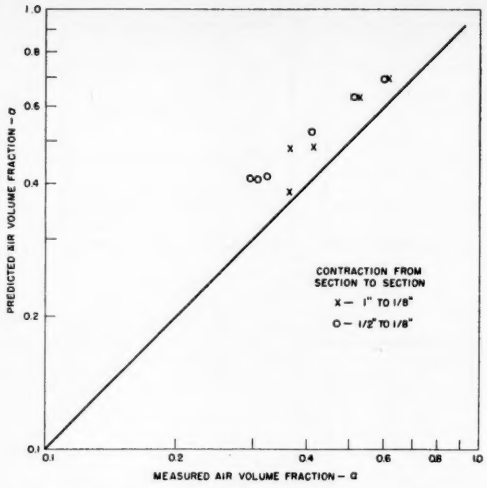

Fig. 8. Comparison of the predicted and measured air-volume fraction for a series of contractions.

range. As the quality increases, the velocity effect becomes more pronounced (Figure 1). Extrapolation of the quality range of air-water data to coincide with the quality range of the steam-water data would place the values of slip ratio above the 150 lb./sq. in. data.

The decrease of the velocity effect with pressure as shown in the figures may be anticipated if the buoyancy force is acknowledged as a major factor which influences the relative velocity of the two phases. The density difference between the two phases, which is a measure of the buoyancy force, decreases with pressure and becomes zero at the critical pressure. At that point, by definition, the slip ratio must be 1, and the slip ratio therefore would be expected to decrease with pressure. As the liquid velocity tends toward zero, the buoyancy force is the dominant factor affecting the relative velocity of the two phases, when one assumes that the geometry effects are negligible. As the mass velocity of the phases increases however, the interaction between the phases increases and as a result the relative effect of the buoyancy forces on the relative velocity should diminish. Therefore the pressure effect should be more pronounced in the lower mass velocity range. Such variations would cause the velocity effect on the slip ratio to diminish as the pressure increases.

Since the slip ratio changes with the fluid velocity, the liquid holdup and hence the mean void fraction must also change following an expansion or contraction as pointed out previously.

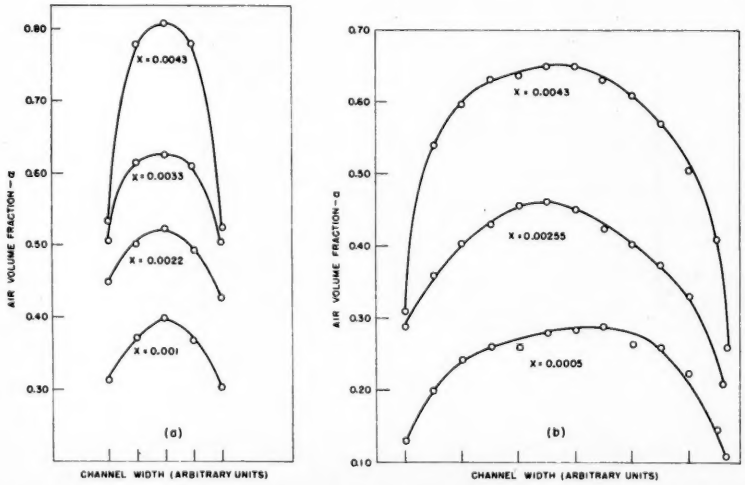

Fig. 9. Distribution of air in water in a 1/8-in. section (*a*) and in a 1-in. section (*b*) for various qualities.

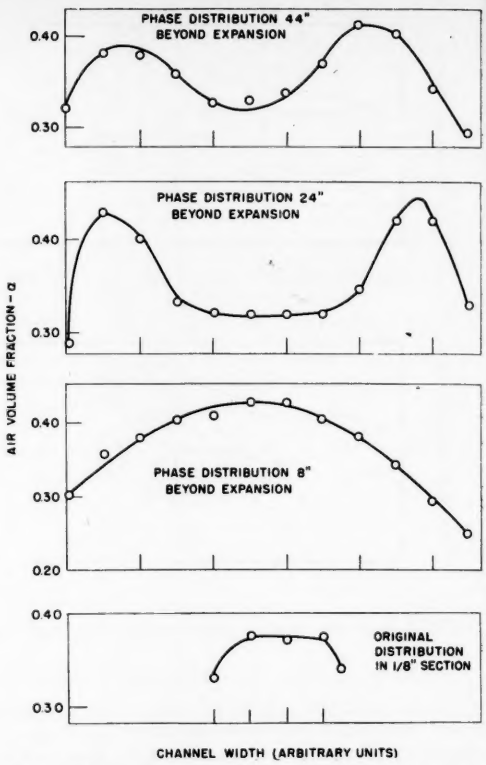

Fig. 10. Flow patterns in a $\frac{1}{2}$-in. section following an expansion from a 1/8-in. section.

AIR-VOLUME FRACTION CHANGES: EXPANSION OF FLOW AREA

The air-volume fractions are plotted as a function of the test-section length in Figure 4 for a series of expansions. It is interesting to note the variation of the void-volume fraction in the transition zone immediately following the expansion. The erratic behavior of the void-volume fraction in the transition zone is a function of the fluid velocity, mixture quality, and enlargement of the flow area. The sharp increase in void fraction shown in Figure 4 for certain conditions is due to the formation of a jet over the first few inches past the expansion and creation of air pockets. The jet dissipates into a very turbulent transition-flow region, after which the regular flow pattern is established. The severity of the jet action increases with increasing mixture quality, fluid velocity, and area enlargement.

Such severe transition zones were not found for expansions of small area enlargement with low fluid velocities and mixture quality. Under such conditions

the void-volume fraction dropped immediately past the expansion and did not rise.

The data for the over-all change in the mean void fraction were correlated by Equation (13), and the exponent N was taken to be 0.2. In the correlation of the data the variation of the velocity effect with quality was neglected, since the quality range studied was not very wide and the change in the slope of the quality parameter in the plot of V_g/V_w vs. V_{w_0} was not great. Over different parameter ranges such an omission might not be tolerable. A comparison between the experimental data and the empirical fit is shown in Figure 5. The maximum deviation is $\pm$ 10%, and the average deviation 5%.

AIR-VOLUME FRACTION CHANGES: CONTRACTION IN FLOW AREA

The variation of air-volume fraction with test-section length, for the series of contractions studied, is plotted in Figure 6. In general the transition zone appears to be very short and less well defined than in the case of expansion of flow area. The air-volume fraction increases to a final value in the first few inches past the contraction.

The apparent instability of the air-volume fraction in the riser section for contractions of 1 to $\frac{1}{8}$ in. and $\frac{1}{2}$ to $\frac{1}{8}$ in., as shown in Figure 6, was due to the large static-pressure changes in the $\frac{1}{8}$-in. section which resulted from the excessive two-phase pressure drops. As the static pressure dropped along the riser length, the specific volume of the air changed markedly which, in turn, affected the air-volume fraction. Under some conditions the static pressure dropped from 30 to 15 lb./sq. in. abs. across the $\frac{1}{8}$-in. section. Such a drop would approximately double the air-volume fraction if a change in the relative velocities of the two phases did not occur. For the other series of contractions the static-pressure change across the riser section was not severe, and therefore the air-volume fraction stabilized fairly rapidly.

The change in the air-volume fraction was again calculated with Equation (13) by the use of the same value of 0.2 for N as for the expansions. The results are compared with the data in Figure 7. Again, as for the expansions, the data

$$\alpha_2 = \frac{1}{\{(P_2/P_1)[(1/\alpha_1) - 1]/(A_1/A_2)^{0.2}\} + 1}$$

is adequately represented by Equation (13), with a maximum deviation of $\pm$15% and an average of 7%.

The maximum deviation occurred for contractions of from 1 to $\frac{1}{8}$ in. and from $\frac{1}{2}$ to $\frac{1}{8}$ in., as shown in Figure 8. This can be attributed to the large static-pressure changes in the $\frac{1}{8}$-in. section. Error in the predicted value of the air-volume fraction was introduced from inaccurate static-pressure readings obtained from the gauges. The flow pattern in the $\frac{1}{8}$-in. riser section was a collapsing annular type, which resulted in very severe static-pressure fluctuations. Since the magnitude of the fluctuations was, in most cases, beyond the range of the gauges, it was very difficult to obtain a mean static-pressure reading; this in turn was reflected in the predicted air-volume fraction change through the static-pressure ratio P_2/P_1. [See Equation (13).]

PHASE DISTRIBUTIONS

The extensive air-volume fraction data (obtained with the traversing technique) shows a parabolic type of distribution of the air in the liquid. Generally, the average to maximum ratio of the air-volume fraction ($\alpha_{ave}/\alpha_{max}$) which characterizes the distribution varied with the quality of the mixture and the channel spacing. Figure 9 shows typical air-liquid distributions in $\frac{1}{2}$- and 1-in. sections at various qualities. In general the distributions are symmetrical with respect to the vertical axis.

Some interesting air-volume fraction-distribution-pattern changes for expansion occurred in the riser section. A typical example is shown in Figure 10. A distribution pattern of the double annular type was formed at the midpoint of the riser. This phenomenon was observed in all riser sections at low qualities or low air-volume fractions ($\alpha > 0.4$). Except for rare instances, this type of flow pattern was not observed in sections with normal flow and no expansion of flow area. The exceptions may be due to the jet flow pattern which was shown to occur at the expansion.

CONCLUSIONS

The void-volume fraction, and hence slip ratio, of an air-water mixture changes following an expansion or contraction of flow area. The change is due to the variation of the relative velocity of the air and water phase with the fluid velocity. The relative velocity of the two phases is also a function of the mixture quality. The magnitude of the change at atmospheric pressure can be estimated by the following semitheoretical equation:

The length of the transition zone following an expansion or contraction is a function of the mixture quality, mass flow rate, and the flow area change. The transition zone following a contraction is not so pronounced as for an expansion. The distribution of the air phase in the water phase was parabolic in nature, but the ratio of maximum void-volume fraction to the average void-volume fraction, which characterizes the distribution, varied at random.

ACKNOWLEDGMENT

The authors wish to express their appreciation to Elmer R. Gunchin and Glenn Popper, who constructed and operated the experimental apparatus; to Sanford E. Cohen and Gerald T. Peterson, who assisted greatly in the reduction of the data; and to Jean Radcliff for typing the original manuscript.

NOTATION

α	=	void-volume fraction (air, vapor, gas, etc.)
A	=	cross-sectional flow area
G	=	mass flow rate, lb./(hr.) (sq. ft.)
V	=	fluid velocity, ft./sec.
ρ	=	fluid density, lb./cu. ft.
W	=	flow rate, lb./hr.
X	=	mixture quality, ratio of mass flow of gas to total mass flow rate of both phases
N	=	exponent in Equation (13)
P	=	pressure, lb./sq. in. abs.
T	=	absolute temperature, °R.
M	=	molecular weight
L	=	length, ft.

Subscripts

w	=	liquid phase
g	=	gaseous phase
w_0	=	liquid phase flowing alone in conduit
m	=	two-phase mixture
1, 2	=	position

LITERATURE CITED

1. Behringer, Philipp, *Z. Ver. deut. Ingre.*, **365B**, 4 (1934).
2. Marchaterre, J. F., *Argonne Natl. Lab. Rept.*, 5522 (February 1956).
3. Schurig, W., *Z. Ver. duet. Ingre.*, **365B**, 13 (1934).
4. Lottes, P. A., W. S. Flinn, R. J. Weatherhead, and Michael Petrick, *Argonne Natl. Lab. Rept.*, 5735, to be published.
5. Cook, W. H., *ibid.*, 5621 (November, 1956).
6. Dengler, C. E., Sc.D. thesis, Mass. Inst. Technol., Cambridge (1952).
7. Eddy, K. D., M.S. thesis, Univ. Minn., Minneapolis (1954).
8. Sher, N. C., *ibid.* (1954).
9. Zmola, P. C., and R. V. Bailey, paper presented at Am. Soc. Mech. Engrs. Meeting, Boston, Massachusetts (1955).
10. Schwarz, K., *Z. Ver. deut. Ingre.*, **445B**, 1 (1954).
11. Petrick, Michael, *Argonne Natl. Lab. Rept., 5787* (March 1958).
12. Hooker, H. H., and G. F. Popper, *ibid. 5766*, to be published.
13. Lottes, P. A., Michael Petrick, *et al.*, Geneva Conference Paper P/1983 (1958).

Manuscript received October 10, 1958; revision received April 2, 1959; paper accepted April 15, 1959.

Performance of a Reciprocating-Plate Extraction Column

ANDREW E. KARR

Hoffmann-La Roche, Inc., Nutley, New Jersey

An open type of reciprocating-plate extraction column was developed, and it is proposed that the scaling up of such a column should be straightforward; that is, the height of an equivalent theoretical stage (H.E.T.S.) and the throughput per unit area should be independent of the diameter of the column.

Plates having 5/8-in.-diameter holes and 62.8% free space were selected to minimize the resistance to countercurrent flow in the column. With this design low H.E.T.S. values were achieved at throughputs much higher than those reported for other columns. Thus for two systems the present column was shown to require the lowest volume of column to accomplish a given extraction job. Data were obtained in a 3-in.-diameter column on two systems, methyl isobutyl ketone–acetic acid–water and *o*-xylene–acetic acid–water. Throughputs studied on the first system ranged from 547 to 1,837 gal./hr./sq. ft., and the corresponding minimum H.E.T.S. values achieved were 4.3 and 7.5 in. respectively. For the second system minimum H.E.T.S. values of 7.7 and 9.1 in. were attained at throughputs of 424 and 804 gal./hr./sq. ft. respectively.

Extraction column design procedures are discussed. The fabrication of the reciprocating-plate column is relatively simple, and this should encourage its use first in pilot-scale sizes and ultimately in large-scale columns.

The ideal extraction column is one which has a high capacity and a high efficiency. It should also be easy to construct and capable of being scaled up from small test sizes to commercial columns in a simple, reliable manner. The purpose of the present work was to attempt to develop an extraction column which approaches these ideal requirements. In a recent review of liquid extraction (*1*) it was emphasized that the "major difficulty in the design of extraction equipment continues to be the lack of well-correlated mass transfer rate data and reliable scale-up procedures when such data are gathered in pilot plants." It is hoped that the present work will be a significant step toward the reliable scaling up of a high-efficiency, high-capacity extraction column.

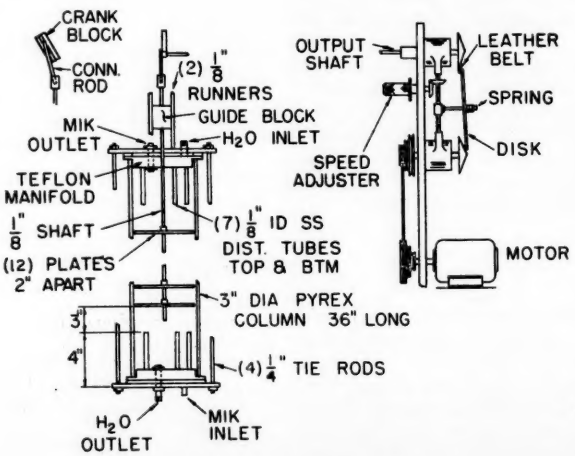

Fig. 1. Extraction-column details.

It is generally recognized today that efficient extraction columns require the application of some form of mechanical energy other than that due to the difference in the specific gravity of the countercurrent streams. Two principal classes of extraction columns utilizing added mechanical energy are now employed in the process industries:

a. Columns employing a series of rotating impellers of various designs in conjunction with different arrangements of baffles, packing, and calming zones (*2* to *8*).

b. Pulse columns in which the entire contents of the column is given a reciprocating motion by means of a pulsing mechanism located near the bottom of the columns (*9* to *16*).

Columns having rotating impellers are inherently difficult to scale up accurately, because there is as yet no sound theoretical basis for doing so. As shown by Rushton (*17*), if two fluid property forces are operative, as for example interfacial tension and viscosity, then it is not possible to obtain dynamic similarity with liquids having the same physical properties. This is true even if geometric similarity is maintained; if geometric similarity is not maintained, then dynamic similarity is impossible, by definition.

Of course empirical correlations can be obtained (*3*, *5*, *18*), but their ranges

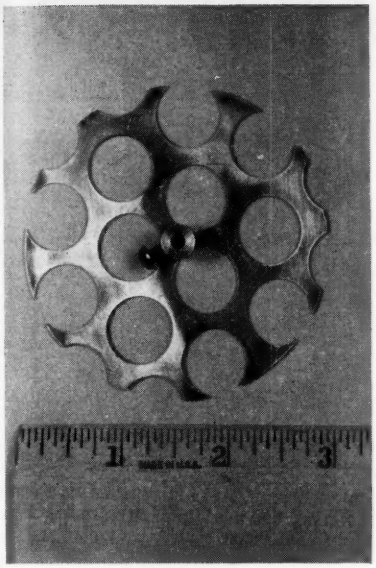

Fig. 2. Reciprocating plate.

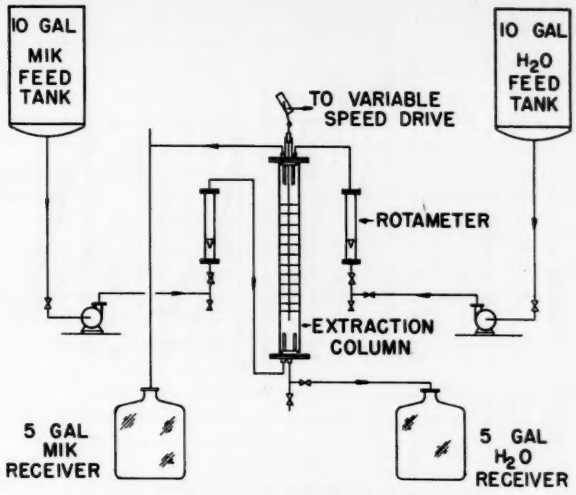

Fig. 3. Flow sheet of liquid extraction unit.

of application and extrapolation are necessarily limited.

Some data on pulsed sieve-plate extraction columns indicated that it should be possible to scale up such columns with no increase in the height of the column (*15, 19*). In other words H.E.T.S. and throughput were presumed to be independent of column diameter. However, Woodfield and Sege (*16*) showed that, as the column diameter increases, "the countercurrently flowing liquid phases display an increasing tendency to channel in some portion of the column cross section rather than to distribute evenly across it. This increasing channeling tendency brings with it increasing over-all transfer unit heights." These authors developed a redistributor which minimized the channeling effect, but throughput was thereby reduced, depending on the design of the redistributor.

DESCRIPTION OF COLUMN

The reciprocating-plate column shown in Figure 1 was employed in the present work. The column consisted of a series of plates mounted on a central shaft which was recripocated by a simple drive mechanism at the top of the column. The amplitude could be varied between 0 and about 2 in. by simply adjusting the length of a crank arm.

The variable-speed drive shown in Figure 1 made it possible to operate over a range of speeds of 100 to 3,000 strokes/min.

The plates were made from 0.04-in. stainless steel sheet which was drilled with $\frac{5}{8}$-in.-diameter holes on $\frac{3}{4}$-in. triangular centers. This arrangement has a free area of 62.8%. After a large section of the sheet had been drilled, the individual plates were cut out. A typical plate is shown in Figure 2. The diameter of the plates was 2 29/32 in. A 5/16-in.-diameter hub was attached to the center of the plate, and the plates were attached to the $\frac{1}{8}$-in.-diameter shaft with set screws.

The column was made from a 36-in. section of nominal 3-in.-diameter Pyrex pipe. The plates were distributed over a height of approximately 22 to 24 in. at varying plate spacings, which left about 6 to 8 in. above and below the plates for disengaging space. An attempt was made to distribute the feed streams uniformly by means of seven $\frac{1}{8}$-in. I.D. inlet tubes manifolded at the top and bottom of the column and extending 4 in. into the column at either end.

Pyrex pipe is not uniform in diameter, variations of $\frac{1}{4}$ in. or more in inside diameter being possible, and the clearance between the plates and pipe wall was estimated to have varied from substantially 0 to $\frac{1}{8}$ in.

The relatively large openings and high free area in the plates were deliberately selected for this work for the following reasons:

1. It was thought that a relatively open type of plate would offer the minimum resistance to flow of the countercurrent streams and that therefore the capacity of the column would be maximized.

2. Providing a high free area of large openings would eliminate the need for close clearance between the plates and the column wall. Thus Van Dijck (*20*) described a reciprocating-plate column with relatively small perforations which required very careful sealing against the shell to prevent excessive bypassing around the perimeter of each plate. In the present work the dispersed droplets could flow freely by gravity through the large openings and did not require the upward or downward motion of the plates to force them through. Thus there is no tendency for the drops preferentially to flow toward the wall of the column, and therefore there is no need to have a tight fit between the plates and the column; it is necessary only that the plate cover substantially the entire cross section of the column, and a moderate clearance is not detrimental.

The plates employed in this work are looked upon simply as reciprocating agitators which impart energy to the counterflowing streams as they flow through the column. The higher the speed of reciprocation, the greater the energy imparted and the finer the dispersion produced. Very fine dispersions can be produced in a reciprocating-plate column.

It was pointed out above that the flow of the dispersed phase in such a column should be essentially uniform throughout the cross section of the column. There is no preferential tendency for the drops to pass around the perimeter of the plates, as long as the clearance between the column and the plates is not excessive. Even if there is a preferential tendency for the dispersed phase to wet the wall, the effect of the agitation of each plate ensures a uniform dispersion over the entire cross section of the column. At design operating speeds, the close proximity of the reciprocating plates to the wall is sufficient to ensure against a preferential wetting effect along the wall.

If it is accepted that in the reciprocating-plate column described a uniform dispersion is bound to exist throughout the cross section of the column, then the scale up of such a column should be straightforward. Large-scale columns of this design have not been built yet; therefore final proof of the proposed hypothesis of scale up is still required. It is hoped that this information will soon be forthcoming.

SYSTEMS INVESTIGATED

Data were obtained on the following two systems:

System 1. Methyl isobutyl ketone (M.I.K.)–acetic acid–water.

System 2. *o*-xylene–acetic acid–water. These systems were used, because various investigators have employed them in obtaining performance data on other columns (*4, 6, 7, 9, 10, 18*). Thus the relative effectiveness of the present column employed could be evaluated.

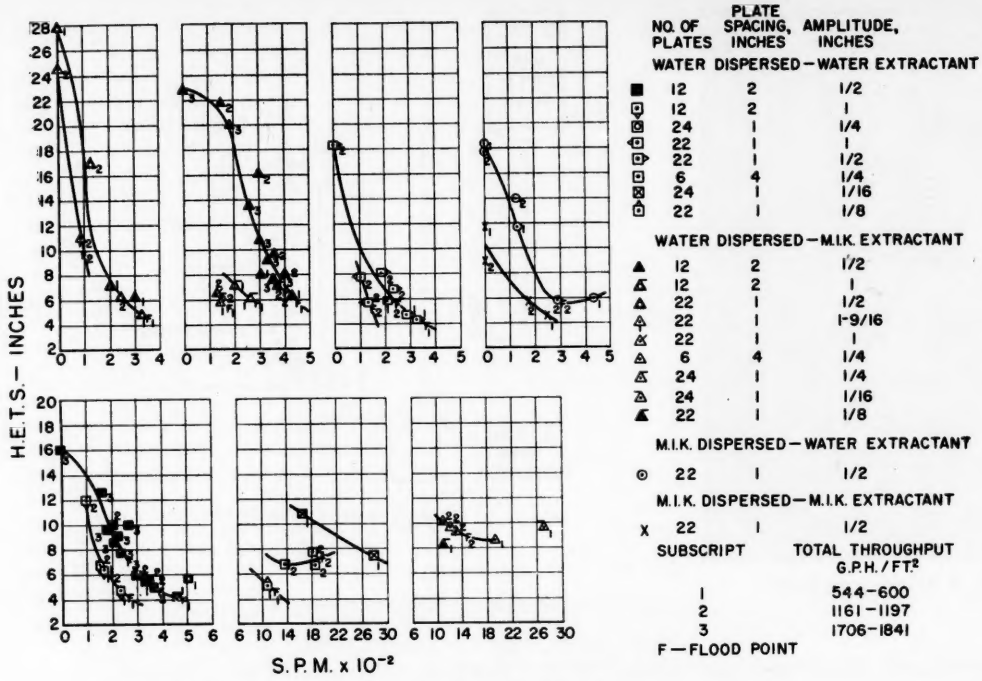

Fig. 4. Effect of reciprocating speed on H.E.T.S., M.I.K.–acetic acid–water system.

DISTRIBUTION DATA

The distribution data employed were the same as those previously reported (*3*).

OPERATING PROCEDURE

With system 1 the solute was first extracted from the aqueous solution by the M.I.K. phase. In the following run the solute was extracted from the organic phase by the aqueous phase. Four types of runs were made as follows:

1. Water dispersed–M.I.K. extractant
2. Water dispersed–water extractant
3. M.I.K. dispersed–water extractant
4. M.I.K. dispersed–M.I.K. extractant

With system 2 only one type of operation was studied, namely water dispersed–water extractant, since the H/L ratios employed for this system were of the order of 1/20.

The solvent ratios employed for both systems were mainly such that the operating line was approximately parallel to the equilibrium curve. The solvent ratios employed are given in the tables of data. The concentration of acid in the feed solutions was purposely not varied greatly in order to minimize the

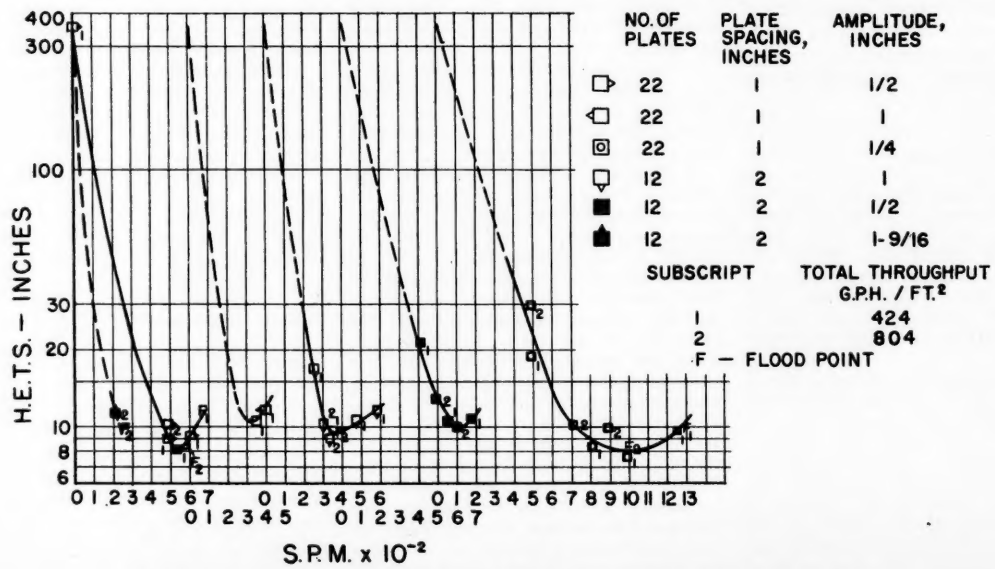

Fig. 5. Effect of reciprocating speed on H.E.T.S., o-xylene–acetic acid–water system.

effect of solute concentration on the results.

Figure 3 is a flow sheet of the liquid-extraction unit employed. The feed solutions were maintained at 25°C. and were mutually saturated in the 10-gal. stainless steel storage tanks. In the case of system 2 the aqueous feed was stored in a 1-gal. feed tank. The aqueous and organic feed streams were metered into the column by means of small centrifugal pumps via calibrated rotameters and needle valves. All lines were made of stainless steel, and care was taken to avoid contamination of the solvents by pipe dope, gaskets, and packings.

The plates were not reciprocated until the interface at either the top or bottom of the column was established. Then the flow rates were adjusted, and the desired reciprocating speed was set by means of the adjusting screw of the variable-speed drive. The interface was maintained in as constant a position as possible by setting the bottoms draw-off valve. The interface was usually maintained at about 2 in. from the top or bottom of the column, depending on which phase was dispersed.

The column came to steady conditions by the time the contents of the column had been replaced two or three times. Usually considerably more than three times the volume of the column was fed before samples of the exit streams were taken for analysis.

RESULTS

The data obtained* are shown in Table 1*a*, *b*, and *c* for the M.I.K.–acetic acid–water system and Table 2 for the *o*-xylene–acetic acid–water system. In Tables 1*a*, *b*, and *c* the quantity $(H/L)_{Rot.}/(H/L)_{M.S.C.}$ is a severe test of the material balance. It is the H/L ratio, as it measures by the calibrated rotameters divided by the H/L ratio for the feed streams determined by the mix point of feed and product streams on the ternary mutual solubility diagram. A value of $(H/L)_{Rot.}/(H/L)_{M.S.C.}$ of unity would correspond to a perfect material balance. In Table 2 the material balance was calculated from the rotameter readings and analyses of the feed and product streams, neglecting the mutual solubility of the phases.

As shown in Tables 1*a*, *b*, and *c* and 2 the ranges of variables studied for the two systems were as follows:

	System 1	System 2
Number of plates	6 to 24	12 to 22
Plate spacing, in.	1 to 4	1 to 2
Amplitude, in.	1/16 to 1 9/16	¼ to 1 9/16
Agitator speed, strokes/min.	0 to 2,800	0 to 1,250
Total throughput, gal./(hr.)(sq. ft.)	544 to 1,841	424 to 804

*Tabular material has been deposited as document 6052 with the American Documentation Institute, Photoduplication Service, Library of Congress, Washington 25, D. C., and may be obtained for $2.50 for photoprints or $1.75 for 35-m.m microfilm.

Effect of Reciprocating Speed, Strokes Per Minute (S.P.M.)

Figure 4 shows all the data for the M.I.K.–acetic acid–water system plotted as strokes per minute vs. H.E.T.S. Separate curves are shown for the different combinations of amplitude and plate spacing. Figure 5 shows similar data for the *o*-xylene–acetic acid–water system. In the figures the letter *F* designates the estimated strokes per minute at which flooding first occurs. The subscripts 1, 2, and 3 correspond to the different indicated throughputs. Generally no minima in the H.E.T.S. values were detected for the M.I.K. system. However definite minima were observed for the xylene system at the low throughput of 424 gal./(hr.)/(sq. ft.) but not at the higher throughput of 804 gal./(hr.)/(sq. ft.). As shown in Figure 4 H.E.T.S. values as low as 4.3 in. were achieved, and the minimum H.E.T.S. varies with the throughput as well as the combination of plate spacing and amplitude. This is discussed further below.

Effect of Throughput

Most of the data shown in Figures 4 and 5 indicate that up to the flood points H.E.T.S. is substantially independent of throughput and depends only on strokes per minute. Some of the data indicate that at low values of strokes per minute H.E.T.S. is not quite independent of throughput, but low values of strokes per minute are not of particular practical interest. In Figure 4 it is seen that the strokes per minute at which flooding occurs decrease with increased throughput. This is also shown for one case in Figure 6. Since H.E.T.S. decreases continuously with increased strokes per minute, it follows that the minimum H.E.T.S. attainable increases with increasing throughput. This is shown in Figure 7, where the minimum H.E.T.S. attained is plotted against throughput. Thus for the case water dispersed–water extractant shown in Figure 7 the following minimum H.E.T.S. values were attained:

Throughput, gal./(hr.)(sq. ft.)	Min. H.E.T.S., in.
547	4.3
1,172	5.0
1,707	7.75

Only a twofold range of throughput was studied for the xylene system, and no definite increase in the minimum H.E.T.S. attained is observed with increasing throughput (Figure 5). The probable reason for this is that for this system the H.E.T.S.–Strokes-per-minute curve passes through a minimum, and the minimum H.E.T.S. is the same for both throughputs.

Effect of Amplitude

In this paper the amplitude is defined as the distance between the lowest and highest position of the plates, expressed in inches. Before the data were obtained it was felt that small amplitudes would be the best for obtaining minimum H.E.T.S. values. It was expected that by reciprocating the plates at high speed and small amplitude there would be a minimum of back mixing between adjacent plates. Indeed, inspection of Figures 4 and 5 shows that at the highest amplitude of 1 9/16 in. the minimum H.E.T.S. values obtained were the highest. However for amplitudes up to 1 in. no superiority of the smaller amplitudes is apparent. From a practical point of view it appears that amplitudes of ¼ to 1 in. are optimum. At smaller amplitudes excessively high agitator speeds are required.

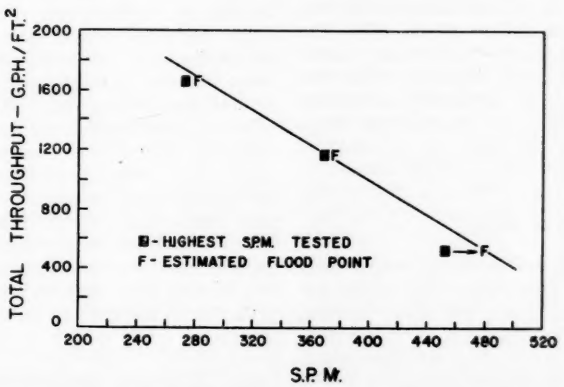

Fig. 6. Effect of strokes per minute on maximum throughput; M.I.K. system; water dispersed–water extractant; twelve plates, 2-in. plate spacing, ½-in. amplitude.

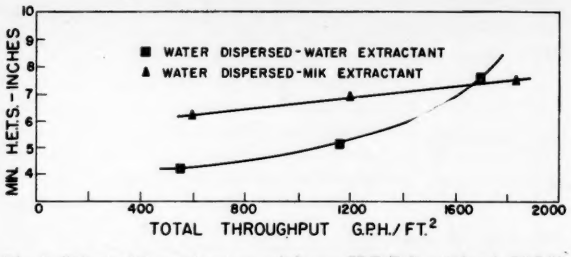

Fig. 7. Effect of throughput on minimum H.E.T.S. attained; M.I.K. system; twelve plates, 2-in. plate spacing, ½-in. amplitude.

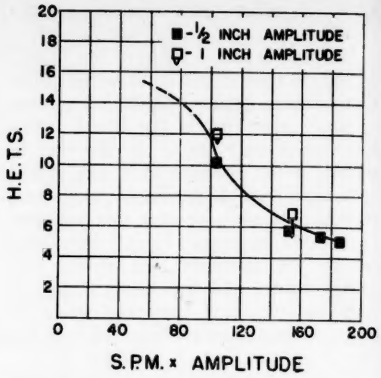

Fig. 8. Example of correlation of H.E.T.S. with product of strokes per minute × amplitude; M.I.K. system; water dispersed-water extractant; throughput 1,167–1,185 gal./(hr.) (sq. ft.), twelve plates, 2-in. plate spacing.

Effect of Plate Spacing

From Figure 4 and Tables 1*a*, *b*, and *c* no significant effect of plate spacing on the minimum H.E.T.S. attained was apparent for plate spacings of 1 and 2 in. However at a 4-in. plate spacing, although plate efficiences as high as 60% were obtained, the minimum H.E.T.S. value obtained was 6.7 in. This compares with minimum H.E.T.S. values of 4.3 in. obtained with 1- and 2-in. plate spacing on the same type of operation, namely water dispersed–water extractant. Thus it can be concluded that in order to obtain the greatest number of stages in a given height of column the plates should be spaced not more than 2 in. apart. Although this conclusion applies to the M.I.K.–acetic acid–water system, it can probably also be applied to the xylene–acetic acid–water system as inspection of Figure 5 will indicate.

Actually, for optimum performance of an extraction column the plate spacing should not be constant throughout the column. This is discussed further in a subsequent section.

Effect of Physical Properties

A comparison of Figures 4 and 5 shows that the M.I.K. system requires lower agitator speeds and gives lower H.E.T.S. values than the xylene system. This has also been observed in previous work on these systems (*3*, 7). The ratio of density difference to interfacial tension ($\Delta\rho/\sigma$) for the M.I.K. system is about 5.5 times that for the xylene system (*3*). The author has used this function as a useful guide in selecting values of strokes per minute and in predicting minimum H.E.T.S. values for other systems. However insufficient data are available to present a quantitative correlation.

CORRELATION OF DATA

It is apparent that there is an infinite number of combinations of strokes per minute, amplitude, and plate spacing which will result in the same H.E.T.S. An attempt was made at an approximate correlation of these variables.

On the bases of the available data it was found that for a given throughput and plate spacing H.E.T.S. was a fairly consistent function of the product of strokes per minute times amplitude. Figure 8 is an example of the several plots of this type which were made. Strokes per minute times amplitude represents the average linear velocity of the plates. To introduce plate spacing, a plot was made of H.E.T.S. vs. (strokes per minute times amplitude)/plate spacing. This ratio can be considered to represent the average total linear rate of motion of the plates in a given height of column. Figure 9 shows the data for the M.I.K. system for the case water dispersed–M.I.K. extractant. The subscripts 1, 2, and 3 correspond to three different total flow rates ranging from 598 to 1,841 gal./(hr.) (sq. ft.). The different flow rates were included in the plot, since it had been previously shown that H.E.T.S. was not significantly affected by flow rate. The range of amplitudes represented in Figure 9 is $\frac{1}{8}$ to 1 in., and the range of plate spacing is 1 to 4 in. The range of the ratio amplitude/plate spacing is $\frac{1}{16}$ to 1. It is seen that for the range of variables covered the correlation is significant. A similar plot for the case water-dispersed–water extractant was not quite so consistent as Figure 9 but was fairly good considering the 16 to 1 variation in amplitude/plate spacing. The xylene data could also be correlated satisfactorily by the method shown in Figure 9.

The correlation shown in Figure 9 should be used with caution, since it is strictly empirical and probably not valid over wider ranges than indicated. It applies to a particular system and to a particular dispersed phase–extractant combination. Furthermore it does not take into consideration the flooding data shown in Figure 4. If Figure 9 is used to select an operating amplitude, strokes per minute, and plate spacing, it is necessary first to check whether this condition is below the flood point. Flooding is a complicated function of amplitude, strokes per minute, plate spacing, and throughput, and no satisfactory correlation was found.

COMPARISON WITH OTHER COLUMNS

The data presented show that the reciprocating-plate column employed in this work has a high capacity as well as a high efficiency. Table 3 compares the present capacity and efficiency data with those of other types of extraction columns reported in the literature within the past decade. The minimum H.E.T.S. and maximum throughput for any system depends to some degree on which phase is dispersed as well as which phase is the extractant. In Table 3 most of the data are for the case water dispersed, but some data for the case M.I.K. dispersed are also included because the particular investigator did not operate with water as the dispersed phase.

The fact that the diameters of the various columns listed in Table 3 are different complicates a comparison of the relative merits of the different columns; nevertheless, if it is accepted that the present reciprocating-plate column can be scaled up with no increase in H.E.T.S., then the following statements can be made:

1. The reciprocating-plate column has a considerably higher throughput than that reported for the other columns listed in Table 3.

2. At comparable throughputs the minimum H.E.T.S. values achieved are equal to or lower than those obtained with most of the other columns. Scheibel (*18*) reported somewhat lower H.E.T.S. values than those obtained in the present work at relatively low throughputs. However as seen in Table 3 the capacity-efficiency relationship of the reciprocating-plate column is such that the lowest volume of column is required to do a given extraction job. This is shown in the last column of Table 3. The throughput per volume per stage which has the net units reciprocal hour was suggested by Treybal (*21*) as a measure of the effectiveness of a given column. The greater this number is, the smaller is the volume of column required to do a given extraction job.

TABLE 3. PERFORMANCE DATA REPORTED IN THE LITERATURE

Reference	Type of column	Diameter of column, in.	Max. total throughput reported, gal./(hr.)(sq. ft.)	Dispersed phase	Minimum corresponding H.E.T.S., in.	Throughput/volume /stage, cu. ft./(hr.) (cu. ft.)
	System: M.I.K.—acetic acid—water					
(6)	Rotating disk, R.D.C.	8	980	Water	4.3*	366
		8	1,030		6.3†	262
(9)	Pulsed—spray	1.5	920	M.I.K.	HTU_{OO} = 0.26 ft. HTU_{OA} = 1.55 ft.	
(18)	Turbine agitator—horizontal baffles	11.5	458	Water	3.0	245
(7)	Alternate agitated and packed sections	11.5	595	Water	9.2	104
(4)	Turbine agitators in vertically baffled compartments	6	286	M.I.K.	3.7	124
			500	M.I.K.	5.5	146
(10)	Pulsed—packed	1.57	149	M.I.K.	5.1	47
	Pulsed—sieve tray	1.57	267		10.1	42
Present work	Reciprocating plate	3	547	Water	4.3	204
			1,172		5.0	376
			(Water extractant) 1,707	Water	7.75	353
			(M.I.K. extractant) 1,837	Water	7.5	393
	System: O-Xylene-acetic acid—water					
(18)	Turbine agitator—horizontal baffles	11.5	385	Water	6.0	103
(7)	Alternate agitated and packed sections	11.5	330	Water	13.3	40
Present work	Reciprocating plate	3	424	Water	7.7	88
			804		9.1	142

*Rotor diameter = 3.1 in.; stator opening = 4.9 in.
†Rotor diameter = 4.7 in.; stator opening = 6.3 in.

DESIGN OF AN EXTRACTION COLUMN

As mentioned previously, the present reciprocating column was developed because it was felt that such a column has the ideal characteristic of H.E.T.S. and throughput per unit area being independent of the diameter of the column. To date no actual data are available to substantiate this, but it is hoped that such data will soon be available.

Until more basic mass transfer information is available, an extraction column must be designed from performance data obtained on a pilot-scale column. In the case of the reciprocating plate column it is only necessary to increase the column diameter. The plate spacing, strokes per minute, and amplitude will remain the same as the optimum values determined in the pilot-scale column. The plate spacing in an extraction column requiring many theoretical stages is of paramount importance. Normally the plate spacing will not be uniform throughout the column because of the differences in concentration in different parts of the column. In a simple countercurrent extraction column one end of the column is usually high and the other end low in solute concentration. Consequently if the plate spacing were uniform throughout the column, the mixing obtained would be good in the rich portion of the column but worse in the lean portion. To overcome this effect the plates are placed closer together in the lean portion of the column. This is necessary if the maximum number of stages in a given height of column is desired.

The effect of solute concentration on the intensity of agitation required for a given H.E.T.S. is related to the physical properties of the two phases in the different sections of the column. It was previously shown (3) that the single most important physical property is interfacial tension. Thus, as the solute concentration increases, the interfacial tension of most liquid-liquid systems decreases rapidly, and the mixing energy required to obtain a good dispersion decreases. In the case of the reciprocating plate column this would necessitate placing the plates further apart in the rich section of the column, if premature flooding of the column is to be avoided. In a fractional liquid extraction column the solute concentrations are usually greatest near the feed stage, and thus the plates would be placed further apart at the feed stage than at the ends of the column.

The above analysis is of course only qualitative. Although the writer has been able to correlate extraction efficiency with the function $(\Delta\rho/\sigma)^{1.5}$ (3), usually insufficient data are available to permit an accurate prediction of optimum plate spacing required in different portions of the column. Therefore it is recommended that an experimental approach be employed, tempered by the foregoing discussion. Usually only one change in plate spacing is necessary after visual observation of the first design of the pilot scale column. The reciprocating plate column is so simple in design and so easy to take apart and put together again that this procedure is very convenient.

Extraction columns with rotating agitators must also take into account the differences in agitation required in different portions of the column for optimum performance. Because of the complicated internals of such columns the above optimizing procedure is much more difficult with these columns. Furthermore, as previously discussed, the scale up of such columns must be done empirically.

Figure 10 shows a section of a 3-in.–diameter pilot plant fractional liquid extraction column 22 ft. high. For optimum performance it was necessary to vary the plate spacing from 4 in. near the center feed stage to 1 in. at one end of the column and 2 in. at the other end. The plates used in this column were made of commercially available flattened expanded stainless steel. A photograph of a single plate is shown in Figure 11. The mesh width is 0.46 in., and the mesh length is 1.26 in. The strand width is 0.085 in.

Several 1-in.–diameter laboratory columns with reciprocating plates have been built. The plates were punched out of Teflon sheet. Figure 12 is a photograph of the plate employed. A 6-in.–diameter by 20 ft. all–Teflon-and-glass reciprocating-plate column is now being employed for a pharmaceutical application

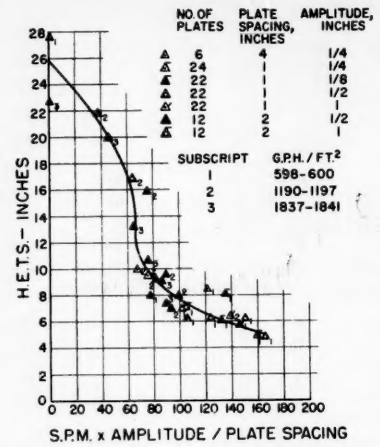

Fig. 9. Correlation of H.E.T.S. with strokes per minute × amplitude/plate spacing; M.I.K. system; water dispersed–M.I.K. extractant.

in which no metals can be tolerated. The Teflon plates are 3/16 in. thick and are drilled with 9/16-in. holes on 0.64-in. triangular centers.

SUMMARY

A reciprocating-plate extraction column was developed because it is believed that such a column can be scaled up in diameter with no increase in H.E.T.S.

For the M.I.K. system H.E.T.S. was found to decrease continuously with strokes per minute until flooding occurs. This performance is unlike that in other columns reported in the literature (*4, 6, 7, 18*), in which H.E.T.S. goes through a minimum value. The xylene system did exhibit a minimum H.E.T.S. for the lower throughput studied (424 gal./(hr.)/(sq. ft.), but at the higher throughput of 804 gal./(hr.)/(sq. ft.) no minimum was observed.

H.E.T.S. was found to be substantially independent of throughput, especially at values of strokes per minute approaching the flood point. The capacity of the reciprocating plate column was shown to be higher than other columns reported in the literature (Table 3). Furthermore, the reciprocating-plate column required the smallest volume of column to do a given extraction job.

The H.E.T.S. data were satisfactorily correlated by the function strokes per minute times amplitude/plate spacing. The limitations of the correlation were pointed out.

Extraction-column design procedures are discussed.

ACKNOWLEDGMENT

Grateful thanks are extended to Hoffmann-La Roche, Inc., for generously supplying the space, equipment, and materials used in this work and for permission to publish this paper. Thanks are due Mr. Kenneth Wilson for the fabrication of the various columns and to Mr. Teh-Cheng Lo for assistance in the calculations.

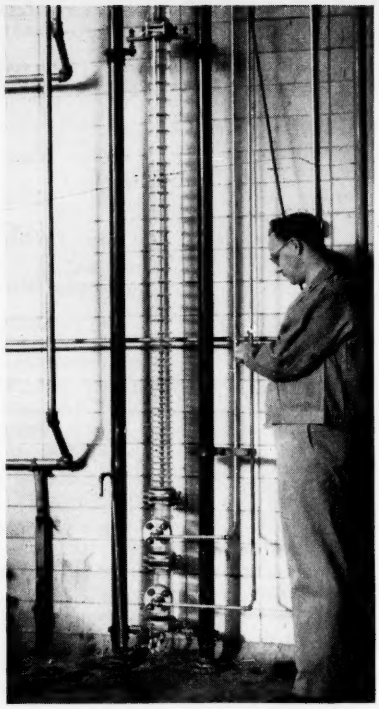

Fig. 10. Section of 3-in. pilot plant extraction column.

NOTATION

F	=	flooding point
H	=	flow rate of heavy phase, lb./(hr.) (sq. ft.)
L	=	flow rate of light phase, lb./(hr.)(sq. ft.)
$\Delta\rho$	=	density difference, g./ml.
σ	=	interfacial tension, dynes/cm.
S.P.M.	=	strokes/min.

Subscripts

Rot.	=	rotameter
M.S.C.	=	mutual solubility curve

LITERATURE CITED

1. Treybal, R. E., *Ind. Eng. Chem.*, **50**, 463 (1958).
2. Dykstra, J., B. H. Thompson, and R. J. Clouse, *ibid.*, 161 (1958).
3. Karr, A. E., and E. G. Scheibel, *Chem. Eng. Progr., Symposium Ser. No. 10*, **50**, 73 (1954).
4. Oldshue, J. Y., and J. H. Rushton, *Chem. Eng. Progr.*, **49**, 297 (1953).
5. Reman, G. H., *Petrol. Refiner*, **36**, 269 (1957).
6. ———, and R. B. Olney, Solvent Extraction Symposium, Annual Meeting American Institute of Chemical Engineers (Dec., 1954).
7. Scheibel, E. G., and A. E. Karr, *Ind. Eng. Chem.*, **42**, 1048 (1950).
8. Rometsch, R., *Helv. Chim. Acta*, **33**, 184 (1950).
9. Billerbeck, C. J., *et al.*, *Ind. Eng. Chem.*, **48**, 182 (1956).

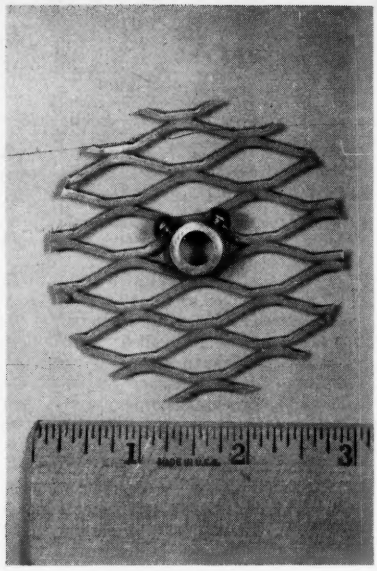

Fig. 11. Reciprocating plate made of expanded metal.

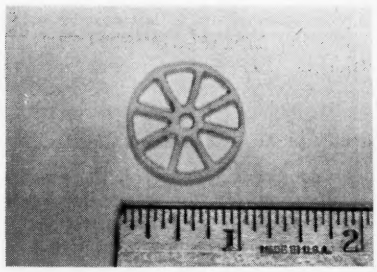

Fig. 12. One-inch reciprocating plate made of Teflon sheet.

10. Chantry, W. A., R. L. Von Berg, and A. F. Wiegandt, *Ind. Eng. Chem.*, **47**, 1153 (1955).
11. Edwards, R. B., and G. H. Beyer, *A.I.Ch.E. Journal*, **2**, 148 (1956).
12. Jealous, A. C., and E. Lieberman, *Chem. Eng. Progr.*, **52**, 366 (1956).
13. ———, and H. F. Johnson, *Ind. Eng. Chem.*, **47**, 1159 (1955).
14. Sege, G., and F. W. Woodfield, *Chem. Eng. Progr.*, **50**, 396 (1954).
15. Wiegandt, H. F., and R. L. Von Berg, *Chem. Eng.*, **61** (July, 1954).
16. Woodfield, F. W., and G. Sege, *Chem. Eng. Progr. Symposium Ser. No. 13*, **50**, 14 (1954).
17. Rushton, J. H., Symposium on Relationship between Pilot-Scale and Commercial Chemical Engineering Equipment, Am. Inst. Chem. Engrs., White Sulfur Springs (March, 1951).
18. Scheibel, E. G., *A.I.Ch.E. Journal*, **2**, 74 (1956).
19. Thornton, J. D., *Chem. Eng. Progr., Symposium Ser. No. 13*, **50**, 39 (1954).
20. Van Dijck, W. J., U.S. Patent 2,011,186 (Aug. 13, 1935).
21. Treybal, R. E., personal communication.

Manuscript received December 1, 1958; revision received April 2, 1959; paper accepted April 4, 1959. Paper presented at A.I.Ch.E. Atlantic City meeting.

Kinetics of the Hydrogenation of Ethylene

(On a Nickel Catalyst)

A. C. PAULS, E. W. COMINGS, and J. M. SMITH

Purdue University, Lafayette, Indiana

A differential type of flow reactor, 0.25-in. I.D., was used to study the kinetics of the hydrogenation of ethylene on an alumina-supported nickel catalyst. This is apparently the first investigation made above atmospheric pressures. Data were obtained from 14.7 to 70 lb./sq. in. abs. and feed compositions from 40 to 90 mole % hydrogen. Measurements at temperatures from 30° to 80°C. indicated an apparent activation energy of 11,600 cal./g.-mole.

It was found that the activity of the catalytic surface was reduced by exposure to ethylene, or mixtures containing an excess of ethylene, owing to the formation of acetylene residues. Pretreatment of the catalyst at temperatures of 170°C. with mixtures of ethylene and hydrogen stabilized the catalyst so that reliable rate data could be obtained.

The rate measurements at 70°C. were correlated by an equation. While the mechanism of the reaction cannot be determined from the data, the rate expression and other kinetic studies suggest a process in which hydrogen is adsorbed on the small fraction of the surface not occupied by acetylenic residues and the reaction takes place between this adsorbed hydrogen and ethylene in the gas phase.

The hydrogenation of ethylene has served as a basis for numerous kinetic studies and as a reaction medium for studying surface catalysis [for example, the work of Beeck and coworkers (*1, 2*)]. Most of the investigations were made by following the decrease in pressure with time in a static system. Wynkoop and Wilhelm (*16*) employed a tubular flow reactor and carried out rate measurements on a copper-chromium oxide catalyst. Their data were taken at atmospheric pressure restricting the possible conclusions concerning the kinetics of the reaction. The objective of the present study was to make a kinetic study of the nickel catalyzed reaction, using a commerical type of catalyst, that is one with porous material as a carrier; (⅛-in., cylindrical alumina pellets were employed for this purpose). To strengthen the kinetic interpretation, data were obtained up to 5 atm.

Table 1 summarizes the previous kinetic studies with a nickel catalyst. Most measurements were made with pure, unsupported nickel in a static system, and all the results were obtained at pressures less than atmospheric. The works of Rideal (*7, 15*), Twigg (*13*), and their colleagues provided the most extensive measurements. Their efforts, along with those of Beeck (*1*), established the existence of acetylenic residues on the nickel surface. This concept appears to be the most likely explanation for the adverse effect of ethylene on the rate. The ethylene is considered to be adsorbed by a dissociative mechanism, so that there remains an acetylenic complex occupying four adjacent active sites on the catalyst.

The previous studies demonstrated that ethane had no effect on the reaction other than that of an inert diluent. Hence in the present work no data were obtained with ethane added to the feed. As indicated in Table 1, many of the data were consistent with a first-order (with respect to hydrogen) rate equation. This result was not found in the present study, as brought out later in the development. Measurements over a range of partial pressures of each reactant show that ethylene has a significant effect on the rate. The quantitative evaluation of ethylene's part in the reaction is complicated by the side effects that occur, particularly the acetylenic complex formation on the catalyst surface.

A. C. Pauls is with Monsanto Chemical Company, Dayton, Ohio, and J. M. Smith is at Northwestern University, Evanston, Illinois.

EXPERIMENTAL WORK

The apparatus, as shown schematically in Figure 1, consisted of a reactants-purifying section, a gas-metering section, a packed-bed flow reactor, and a gas-analyzing section.

Reactor

The reactor was made of 0.25-in. I.D. stainless steel tubing packed with catalyst pellets and jacketed with a 1-in. brass pipe for a length of 24 in. As depicted in Figure 2, temperatures were measured in a 0.065-in. thermocouple well (stainless steel) extending the length of the reactor. Two copper-constantan thermocouples, prepared from 30-gauge wire, were employed, one inserted through each end of the well.

Gas-Purification System

The hydrogen was first purified (of oxygen) by being passed through an electrically heated converter consisting of a 3-ft. section of ¼-in. galvanized pipe. It was packed with 6-20-mesh copper–magnesium oxide catalyst. After leaving the converter, the gas was cooled in a ¼-in. copper tube jacketed for a length of 35-in. with ½-in. copper tubing. Water passed through the jacketed section. Finally the gas was dried by flowing through ¼-in. black iron pipe packed with 6-16-mesh silica gel for a length of 3 ft. To ensure proper operation of the equipment temperatures were continuously recorded at the exit of the converter and the entrance to the dryer.

Oxygen was removed from the ethylene stream by passing through a ¼ in., 3 ft. long, galvanized pipe packed with copper shot or copper-magnesium oxide granules. A cooler and drier system similar to that employed for the hydrogen system was also used in the ethylene feed as illustrated in Figure 1.

Gas-Analysis System

The reactor operation was of the differential type; that is the conversion was limited to a few per cent. This reduces the problem of temperature and composition changes within the catalyst bed, but it requires precise analytical results to determine accurately the small conversions obtained. A thermal conductivity cell, operated at a current of 140.00 ± 0.05 ma., was used in this study. In order to increase the sensitivity of the apparatus for measuring the conversion the outlet gas from the reactor was compared with the inlet gas in a single cell. This is equivalent to using the inlet stream as the reference gas. Used in this way the unbalanced voltage of the bridge circuit of the cell was a direct measure of the increase in ethane concentration due to reaction. However it was necessary in using this method to calibrate the cell for each inlet-gas composition. The cell was calibrated by comparing a known sample mixture of hydrogen, ethylene, and ethane with a known reference mixture of hydrogen and ethylene. In the calibration procedure the ratio of hydrogen to ethylene was the same in the sample and reference gas mixtures. This does not correspond to the operation of the reactor, except when the ratio is unity. The error introduced because of this discrepancy is small because the thermal conductivities of ethane and ethylene are nearly the same, while that of hydrogen is almost seven times larger. Calculations, based upon the assumption that the conductivities are additive, indicate that the error introduced is less than 1.0% over the composition range 20 to 80 mole % hydrogen.

Analysis of the random or accidental errors in the calibration procedure indi-

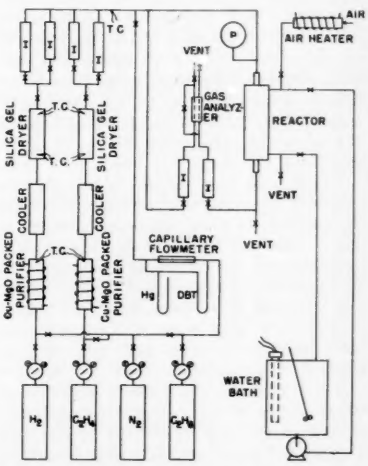

Fig. 1. Schematic diagram of apparatus.

Table 1. Summary of Experimental Investigations of the Catalytic Hydrogenation of Ethylene on Nickel

Catalyst	Temperature range, °C.	Total pressure, cm. Hg.	Gas agitation	Activation energy, kcal./mole	Rate relation*	Reference
Ni foil	73–200	12	No	1.8	$r = kp_A$ with B in excess $r = kp_B$ with A in excess	9
1% Ni on charcoal	—	—	—	3.6	$r = kp_A$	10
Ni ribbon	−10–130	0.003–0.02	—	0 (90°C.)	$r = kp_A$ ($T \leq 67$°C.) $r = kp_A(1 + Bp_A)$(120°C.)	18
Ni wire	20	4.2	No	—	$r = k$	4
Ni wire	0–17	0.34–1.3	No	0 (140°C.)	$r = k$	13
Ni mass	−78–0	20–56	No	6.1	$r = kp_A$ with P and p_B in excess r increases with decreasing p_B at constant P and p_A	11
Ni powder	99–165	20–60	No	—	$r = kp_A$ at constant P and p_B $r = \frac{kp_B}{1 + Bp_B}$ at constant P and p_A	12
Ni wire	60–207	3.7–7.2	No	14 (60°–100°C.) 0 (207°C.)	$r = kp_A$	15
Ni film	0	10–50	Yes	10.7 (−80° –150°C.)	$r = kp_A$	1 2
Ni film	20–180	4–15.4	Yes	10.2 (20°–145°C.) 0 (165°C.)	$r = kp_A$ (114°C.) $r = \frac{kp_Ap_B}{1 + Bp_B}$ (165°C.)	7

*A denotes hydrogen and B designates ethylene.

Table 2. Summary of Results at 50°C. and 1 Atm.

Run	Q_i, cc./min.	y_{ai}	y_{e0}	$(p_a)_{avg}$, atm.	$(p_b)_{avg}$, atm.	$r \times 10^5$, moles/(min.)(g.)	T_i, °C.	ΔT, °C.
3.5	2,010	0.730	0.101	0.716	0.234	122	50	5.5
3.7	2,010	0.730	0.0857	0.718	0.238	105	50	3.75
3.9	2,010	0.730	0.0700	0.721	0.244	87.0	50	2.5
3.12	2,010	0.730	0.0559	0.722	0.250	70.3	50	1.5
3.14	2,010	0.730	0.0489	0.723	0.252	62.0	50	1.0
4	2,010	0.730	0	0.730	0.270	0	50	0

cates a maximum error of about 2%. It is believed that the over-all errors in determining the mole-fraction ethane in the reactor effluent are less than ±5% under all the operating conditions.

CATALYST PREPARATION AND ACTIVATION

The carrier used for the catalyst consisted of 0.14-in. diameter spheres prepared by attrition from ⅜-in. alumina spheres. The internal area of the material was approximately 150 sq. m./g. An aqueous solution of nickel nitrate containing 10 g. of nickel/100 cc. of water was added to a flask containing the alumina carrier under a vacuum. The pellets were agitated for 1 hr. and the excess solution then poured off. After draining for 10 min. on cheesecloth the particles were dried in a laboratory oven at 220°F. for 2 hr. The nitrate was decomposed to nickel oxide by heating in a furnace at 400°C. for 10 hr. The nickel content at this stage was 2.94% by weight.

The reactor was packed with a 17-cm. length of plain alumina spheres preceding the catalyst to allow the entering gases to attain reaction temperature. Preliminary tests showed unimpregnated alumina had no catalytic activity at 110°C. The active bed consisted of a 39-cm. length of tubing packed with a mixture of three parts of plain alumina spheres and one part of catalyst (155 spheres with a mass of 6.27 g.). One thermocouple was placed at the entrance to the catalyst bed and the second 10 cm. prior to the exit of the bed. The reduction of nickel oxide to active nickel was carried out in place at 250°C. with hydrogen flow through the reactor for 24 hr.

SCOPE OF EXPERIMENTAL WORK

The feed-gas composition was varied from 40 to 90 mole % hydrogen and the total flow rate from 800 to 8,000 cc./min., measured at 1 atm. and 70°F. These rates correspond to a space-velocity interval of 66 to 660 reciprocal min. Runs were made at 70°C. over a pressure range from 14.7 to 70 lb./sq. in. abs. At atmospheric pressure data were obtained from 32° to 80°C., although most of the measurements were carried out at 50°, 70°, or 80°C.

RESULTS

With differential type of operation the rate of reaction can be computed directly from the measured ethane content of the product gas and the parameters of the feed. The expression for the rate, in terms of the moles of ethane produced per unit mass of catalyst per unit time, based upon the stoichiometry of the reaction, is

$$r = \frac{N_i}{(1 + y_e)^2}\frac{dy_e}{dW} \qquad (1)$$

Equation (1) applies to a truly differential reactor, that is one in which the change in mole-fraction ethane through the reactor and the mass of catalyst are both infinitesimal. For the actual reactor, approaching differential operation, this expression may be used to compute the rate corresponding to the arithmetic average composition in the reactor.

Equation (1) may be written in difference form:

$$r = \frac{N_i y_{e0}}{W}\left[\frac{1}{(1 + y_e)^2}\right] \cdots \qquad (2)$$

where the term in brackets represents the average value through the reactor.

The error, as a function of conversion or exit value of ethane mole fraction, introduced in the use of Equation (2) can be established from a rate equation. Since an expression of the form

$$r = \frac{kp_Ap_B}{1 + K_Bp_B} \qquad (3)$$

best fits the experimental data, Equation (3) was used with Equation (1) to obtain the correct rate at the average composition in the reactor. These correct

Table 3. Summary of Results at Varying Temperature and Constant Composition and Pressure

Run	Q_i, cc./min.	y_{ai}	y_{e0}	$(p_a)_{avg}$, atm.	$(p_b)_{avg}$, atm.	$r \times 10^5$, moles/(min.)(g.)	T_i, °C.	ΔT, °C.
8	814	0.730	0.0036	0.729	0.269	1.9	34.5	0
11	814	0.730	0.0069	0.729	0.268	3.7	43.2	0
14	814	0.730	0.0081	0.729	0.267	4.3	50.4	0
19	814	0.730	0.0183	0.727	0.264	9.7	61	0
21	814	0.730	0.0340	0.724	0.259	17.7	72.5	0
23	814	0.730	0.388	0.667	0.139	158	81	2.0

Table 4. Summary of Results at 80°C. and 1 Atm.

Run	Q_i, cc./min.	y_{ai}	y_{c0}	$(p_a)_{avg}$, atm.	$(p_b)_{avg}$, atm.	$r \times 10^5$, moles/(min.)(g.)	T_i, °C.	ΔT, °C.
42	912	0.909	0.0188	0.908	0.083	11.1	80	0
53	1,633	0.582	0.0210	0.578	0.411	22.2	80	0
54	1,034	0.579	0.319	0.512	0.329	172	81	4.2
57	1,812	0.904	0.0151	0.903	0.089	17.9	80	0.25
80	1,802	0.534	0.1288	0.504	0.432	137	81	2.2
84	1,047	0.912	0.0145	0.912	0.081	9.9	80.8	0.25
92	1,541	0.859	0.0246	0.857	0.131	24.5	80.2	0.5
100	1,944	0.630	0.1193	0.608	0.332	137.8	80	1.2

results, when compared with Equation (2), indicated that the error in the use of Equation (2) is less than 2% for feed gases containing 40 to 70 mole % hydrogen at values up to 20 mole % of ethane in the reactor effluents and that at 80 mole % hydrogen in the feed the error reaches 2% at 14.2% of ethane in the effluent.

In the experimental program the conversion was maintained well within these limits, so that the use of Equation (2) was justified. This analysis indicated that maintenance of small temperature gradients is more significant than small conversions, if precise rates of reaction are desired.

The temperature of the reactor was controlled by circulating water at the reaction temperature through the jacket around the catalyst tube. With this system and the diluted catalyst bed it was possible to reduce radial temperature changes to less than an estimated 2°C. Longitudinal temperature changes were a function of the extent of conversion and the pressure, and in a few instances these changes, at the highest pressures, reached values of 10° to 20°C. The rate computed from Equation (2) was given a temperature corresponding to the arithmetic average of the entrance and exit values. It was then corrected to the nominal run temperature by the use of an activation energy of 11,600 cal./g. mole. (This value was determined from experimental rate measurements at different temperatures.)

Tables 2 to 5* show the results of the rate measurements and include in successive columns the entrance flow rate (at 70°F. and 1 atm.); the inlet mole-fraction hydrogen; the exit mole-fraction ethane; the average partial pressures of hydrogen and ethylene, $(p_a)_{avg}$ and $(p_b)_{avg}$; the reaction rate; the inlet gas temperature; and the increase in gas temperature through the reactor, ΔT. Tables 2 and 4 depict a part of the preliminary data showing the effect of time and pretreatment upon the activity of the catalyst.

ANALYSIS OF THE DATA

Poisoning Reactions

Exposure of the catalyst to ethylene reduces its activity for the hydrogenation reaction. The data in Table 2 at a constant feed composition of 73 mole % hydrogen and a temperature of 50°C. illustrate this behavior. The decrease in rate and temperature rise is depicted for some of these runs in Figure 3.

These results fit the general model of ethylene poisoning of pure nickel films proposed by Jenkins and Rideal (7). It is postulated that ethylene is adsorbed and dissociates into an acetylenic residue plus two adsorbed hydrogen atoms. The hydrogen atoms are then available to react with ethylene, resulting in the so-called "self-hydrogenation reaction." The sites vacated by this reaction will adsorb more ethylene until all the groups of four sites capable of dissociatively adsorbing ethylene have been utilized. In Rideal's model the remaining sites are assumed to catalyze the hydrogenation of ethylene by adsorbing hydrogen, which then reacts with ethylene in the gas phase.

Pretreatment of the catalyst with ethylene at relatively high temperatures partially stabilizes the rates. Figure 4 has been drawn from the data in Table 3, which were obtained after passing ethylene through the reactor at 170°C. Although these rates were measured at 80°C., they are less than those shown in Figure 3 for the freshly activated catalyst. In terms of the Rideal model the high-temperature ethylene treatment results in breaking down the acetylenic complexes into hydrogen and carbide residues. Presumably the rate of reaction is stabilized because the rate of removal of the carbides by hydrogen in the feed gas is low at the normal reaction temperatures, that is 50° to 80°C.

The dependence of the rate on the partial pressures of hydrogen and ethylene is shown in Table 4 and Figure 5. These data are for a total pressure of 1 atm. and illustrate the combined effects of changes in both p_A and p_B. The circles show the results when the activated catalyst has been treated with ethylene at 170°C. for 12 hr. The squares represent the rates after the catalyst had been subsequently exposed to mixtures containing an excess of ethylene at 80°C. The decreased rate shown by comparing the squares and circles evidently results from the formation of additional acetylenic residues. The rates corresponding to the upright triangles were observed after the catalyst had been further exposed to hydrogen for 14 hr. at room temperature. From the results it is clear that the acetylenic residues are removed by hydrogen at relatively low temperatures. If the catalyst is exposed to ethylene for long periods of time, the acetylenic residues practically cover the surface as indicated by the results depicted by the inverted triangles. These low rates were measured after the catalyst had been treated for 48 hr. with ethylene at room temperature.

These preliminary data demonstrated that the catalyst surface was dependent upon its previous history and that a procedure for obtaining reproducible data

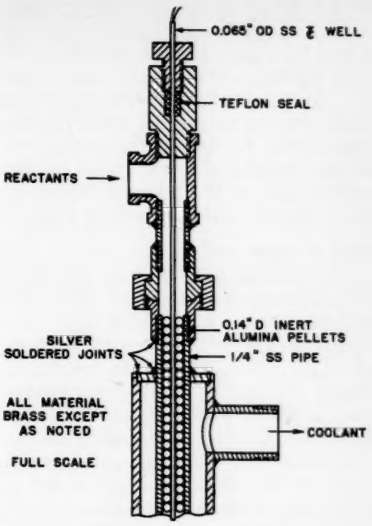

Fig. 2. Reactor detail.

Table 5. Summary of Results at 70°C. and Varying Pressure and Composition

Run	Q_i, cc./min.	y_{ai}	y_{c0}	$(p_a)_{avg}$, lb./sq. in. abs.	$(p_b)_{avg}$, lb./sq. in. abs.	$r \times 10^5$, moles/(min.)(g.)	$r_{70°} \times 10^5$	ΔT, °C.
212	4,048	0.50	0.0126	7.6	7.6	33.3	31.4	1.2
217	8,710	0.50	0.1600	31.0	31.0	805	280	22.6
218	3,370	0.40	0.00703	6.0	9.0	15.5	15.3	0.2
223	7,280	0.40	0.1534	24.0	38.6	645	257	19.5
224	1,404	0.80	0.0707	11.6	2.52	61.4	49.8	4.2
229	3,070	0.80	0.1789	53.2	8.71	312	173	12.2
235	3,970	0.90	0.0921	60.6	3.93	222	152	7.8
236	1,616	0.70	0.0536	10.2	4.13	54.2	44.0	4.2
241	3,580	0.70	0.1913	45.9	15.9	382	203	13.2

*Tabular material has been deposited as document 6050 with the American Documentation Institute, Photoduplication Service, Library of Congress, Washington 25, D. C., and may be obtained for $1.25 for photoprints or 35-mm. microfilm.

would have to be developed before kinetic studies were possible. It was found that pretreatment at 170°C. with feed mixtures of the same composition as those used for the following rate measurements results in a stable surface, presumably because the poisoning reactions reached a steady state. All the kinetic data at 70°C. were obtained by this procedure and are shown in Table 5.

Effect of Temperature

The data in Table 3 show the effect of temperature on the rate using the stabilized catalyst, that is after the surface has been treated with ethylene at 170°C. The plot of the results in Figure 6 indicate an apparent activation energy of 11,600 cal./g.-mole. The linear nature of the data strengthens the conclusion that diffusion of the reactants to the catalyst surface is not a significant resistance in the over-all process from reactants in the gas to product in the gas.

This activation energy was used to correct rate data for individual runs to the nominal temperature of the run series.

Rate Equation

The rate data of Table 5 were first used to determine the empirical dependence of the rate on the partial pressures. The method of least squares gave the following result:

$$r = 2.73 \times 10^{-5} p_A^{0.93} p_B^{0.33} \qquad (4)$$

The first-order dependence on hydrogen partial pressure confirms the results of earlier studies (*2, 9, 10, 11, 12, 15, 18*). The one-third power effect for ethylene suggests a Langmuir type of mechanism, in which the adsorption of ethylene on the surface is significant.

The derivation of rate equations based upon the Langmuir adsorption theory and the equilibrium postulate have been treated extensively in the literature (*5, 6, 17*). The equations are derived by the assumption of a mechanism for the reaction and then the supposition that the rate is determined by a single step in the process, the remaining steps occurring under equilibrium conditions. Within this framework the concept of the reaction which best fits the data is as follows.

If the adsorption on the active part of the surface for the reaction is ideal (that is Langmuir adsorption), and if the rates of all the steps except one in the over-all reaction are sufficiently fast that pseudo-equilibrium conditions are maintained, then the process is one in which ethylene is adsorbed on single sites, hydrogen and ethane are not adsorbed, and the controlling step is the reaction between adsorbed ethylene and gaseous hydrogen. The corresponding rate equation is

$$r = \frac{A p_A p_B}{1 + B p_B} \qquad (5)$$

and a least-squares fit of the data yields the numerical form

$$r = \frac{0.86 \times 10^{-5} p_A p_B}{1 + 0.079 p_B} \qquad (6)$$

Figure 7 shows both the experimental data and the line corresponding to Equation (6).

The catalyst-activity studies, Figures 3 to 5, and the work of Jenkins and Rideal (*7*) are not in agreement with the concept of a reaction between adsorbed ethylene and gaseous hydrogen. These studies suggest instead that ethylene dissociates when adsorbed, forming acetylenic or carbide residues. On this basis the hydrogenation reaction can occur only on those sites not occupied by the residues and only by reaction between adsorbed hydrogen and gaseous ethylene. The mechanism may be represented as follows:

$$H_2 + Ni_2 \underset{k_2}{\overset{k_1}{\rightleftharpoons}} H_2Ni_2 \qquad (7)$$

$$H_2Ni_2 + C_2H_4 \xrightarrow{k_3} C_2H_6 + Ni_2 \qquad (8)$$

Jenkins and Rideal used a steady state approach to derive a rate equation for this mechanism. In this method it is supposed that the concentrations do not vary with time once a steady state has been reached. It is not assumed that a single step is controlling, as in the development of Equation (5). In this sense the steady state method leads to more general equations, and indeed the single-step controlling equations can always be obtained from the steady state development by making additional assumptions.

If the fraction of the surface (available for the reaction) occupied by adsorbed hydrogen is θ, the steady state concept requires that $(d\theta/dt) = 0$. Hence from Equations (7) and (8)

$$\frac{d\theta}{dt} = 0 = k_1 p_A (1 - \theta) - k_2 \theta - k_3 \theta p_B \qquad (9)$$

In the formulation of this equation it is supposed that of the available surface part is occupied by hydrogen and part is bare. From Equation (9)

$$\theta = \frac{k_1 p_A}{k_2 + k_1 p_A + k_3 p_B} \qquad (10)$$

The rate of reaction is obtained from Equation (8):

$$r = k_3 \theta p_B = \frac{k_1 p_A p_B}{k_2 + k_1 p_A + k_3 p_B} \qquad (11)$$

Keii (*8*) found it necessary to postulate a very low surface concentration of adsorbed hydrogen in order to explain the rates of formation of the deutero-ethylenes and deutero-ethanes in the reaction between light ethylene and deuterium. Also the studies of the parahydrogen conversion on nickel (*4, 14, 15*), in which ethylene was found to inhibit the conversion, indicate that the concentration of adsorbed hydrogen must be very low. These separate studies suggest that the term $k_1 p_A$ in the denominator of Equation (11) is negligible, so that Jenkins and Rideal's final form of the rate equation

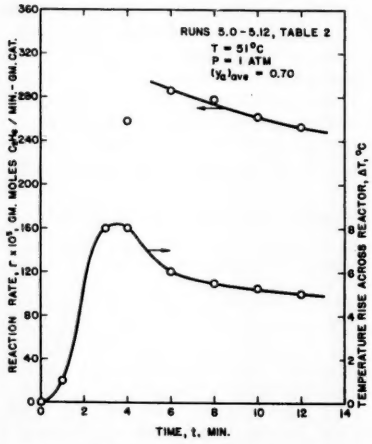

Fig. 3. Variation of catalyst activity with time.

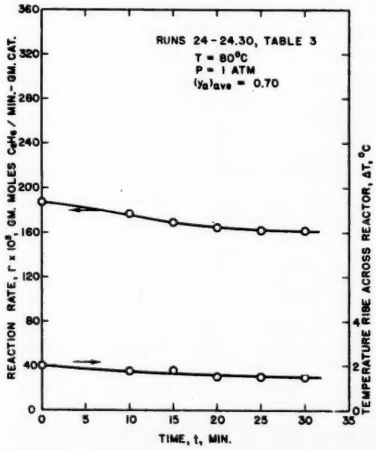

Fig. 4. Variation of catalyst activity with time.

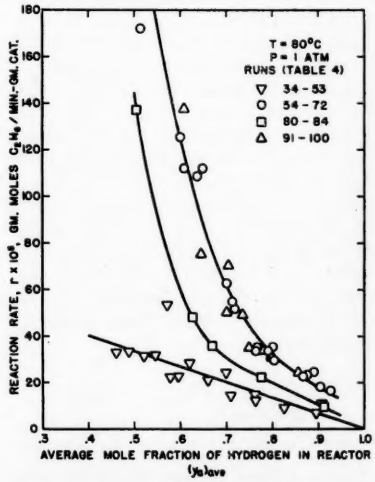

Fig. 5. Effect of catalyst treatment on reaction rate.

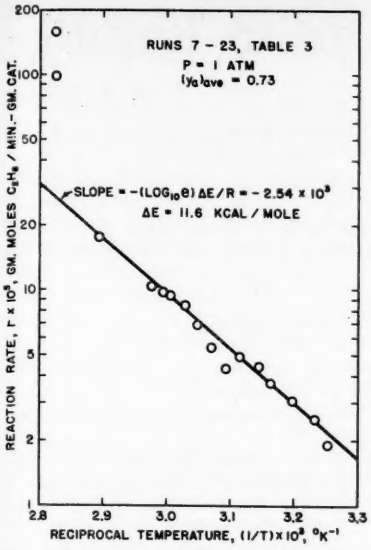

Fig. 6. Temperature dependence of reaction rate.

$$r = \frac{k_1 p_A p_B}{k_2 + k_3 p_B} \qquad (12)$$

is obtained.

Equation (12) is of the same form as Equation (6), which was found to fit best the experimental data. However the mechanisms upon which the two equations are based are different. In view of the catalyst activity studies and the considerable amount of kinetic data from other sources supporting the dissociation of ethylene on the catalyst the Jenkins and Rideal approach is favored.

Several other theories for the reaction have been proposed (*1, 3, 14*) and rate equations developed for them, either in the present investigation or by those suggesting the mechanism. None of these agree with the experimental rate data. Twigg's concept (*14*), which has enjoyed some popularity in the literature, requires that ethane be formed by the reaction between adsorbed ethyl radicals and adsorbed hydrogen atoms. Ethylene is adsorbed by the associative process, and hydrogen is adsorbed only through the interaction of a gaseous hydrogen molecule and an adsorbed ethylene complex. The data of this study do not fit such a picture. The arguments in favor of the Twigg concept are based not so much on the dependence of the rate on pressure and concentration as on the variation of first-order rate constants with temperature and on information for related reactions.

CONCLUSIONS

Studies of the rate of the reaction on an alumina-supported nickel catalyst from 14.7 to 70 lb./sq. in. abs. indicate complex kinetics. The commonly proposed simple rate equation, first order with respect to hydrogen and independent of ethylene partial pressure, is not valid.

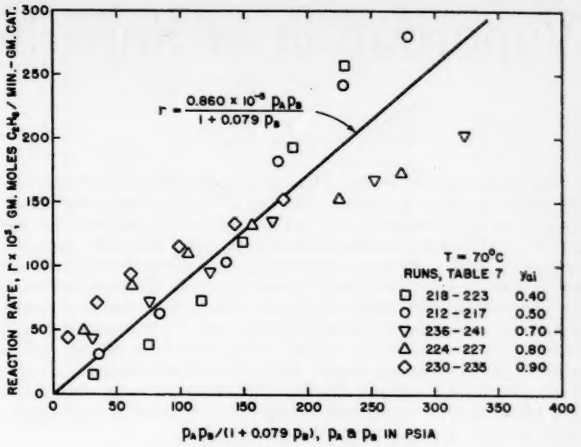

Fig. 7. Rate-data correlation.

Ethylene is a poison for the nickel-alumina catalyst, presumably owing to surface complexes of acetylene polymers formed when ethylene is adsorbed at low temperatures. These residues are only slowly removed by hydrogen at temperatures below 80°C. but are completely eliminated at high temperatures. Comparable rates of reaction, suitable for kinetic study, can be obtained by pretreating the catalyst at 170°C. with mixtures of hydrogen and ethylene. Rate data are then taken at lower temperatures with a feed of the same composition as used in the pretreatment.

The rate data alone are not sufficient to determine the mechanism of the reaction. The same satisfactory rate equation can be obtained from at least two concepts of how the reaction occurs. The previously available data for the nickel catalyzed reaction and the activity studies for the present catalyst suggest a reaction between adsorbed hydrogen and ethylene in the gas phase.

ACKNOWLEDGMENT

Financial support for this work was provided by the Engineering Experiment Station, Purdue University, and by the Pure Oil Company. J. M. Woods of Purdue University gave generously of his time for discussions of the project.

NOTATION

A = constant in Equation (5), dependent on temperature
B = constant in Equation (5), dependent upon temperature
ΔE = apparent activation energy
K = equilibrium constant
k = reaction-rate constant
N = molal flow rate, g.-moles/min.
p = partial pressure, atm.
Q = volumetric flow rate, cc./min. at 70°F. and 1 atm.
r = reaction rate, g.-moles/(min.)(g. of unreduced catalyst)
T = temperature
t = time, min.
W = mass of catalyst, g.
y = mole fraction
θ = fraction of catalyst surface covered by adsorbed hydrogen [Equation (10)]

Subscripts

A, a = hydrogen
B, b = ethylene
C, c = ethane
i = reactor inlet conditions
0 = reactor outlet conditions

LITERATURE CITED

1. Beeck, O., *Discussions Faraday Soc.*, **8**, 118 (1950).
2. ———, A. E. Smith, and A. Wheeler, *Proc. Roy. Soc. (London)*, **177**, 62 (1940).
3. Eley, D. D., in "Catalysis," vol. III, P. H. Emmet, Ed., p. 49, Reinhold, New York (1955).
4. Farkas, Adalbert, Ladislaus Farkas, and E. K. Rideal, *Proc. Roy. Soc. (London)*, **A146**, 630 (1934).
5. Herbo, C., *J. chim. phys.*, **47**, 454 (1950).
6. Hougen, O. A. and K. M. Watson, "Chemical Process Principles," vol. III, John Wiley, New York (1949).
7. Jenkins, G. I., and E. K. Rideal, *J. Chem. Soc. (London)*, 2490, 2496 (1955).
8. Keii, T., *J. Chem. Phys.*, **22**, 144 (1954).
9. Rideal, E. K., *J. Chem. Soc. (London)*, **121**, 309 (1922).
10. Schuster, C., *Trans. Faraday Soc.*, **28**, 406 (1932).
11. Toyama, O., *Rev. Phys. Chem. Japan*, **11**, 153 (1937).
12. *Ibid.*, **12**, 115 (1938).
13. Tucholski, T., and E. K. Rideal, *J. Chem. Soc. (London)*, 1701 (1935).
14. Twigg, G. H., *Discussions Faraday Soc.*, **8**, 152 (1950).
15. ———, and E. K. Rideal, *Proc. Roy. Soc. London*, **A171**, 55 (1939).
16. Wynkoop, Raymond, and R. H. Wilhelm, *Chem. Eng. Progr.*, **46**, 300 (1950).
17. Yang, K. H., and O. A. Hougen, *ibid.*, 146.
18. Zur Strassen, H., *Z. physik. Chem.*, **A169**, 81 (1934).

Manuscript received December 18, 1958; revision received March 30, 1959; paper accepted April 3, 1959. Paper presented at A.I.Ch.E. San Francisco meeting.

Vaporization of Superheated Drops in Liquids

G. R. MOORE

University of Wisconsin, Madison, Wisconsin

The work reported in this paper is an outgrowth of an exploratory investigation of the feasibility of spray drying of materials in solution by using direct-contact heat transfer from a hot liquid rather than a gas to vaporize the solvent from the drops. Unexpectedly, it was found that drops suspended in a hot liquid had to be superheated to a very extreme degree in order to initiate vaporization. This effect was of such interest that the investigation was modified to a fundamental study of the vaporization of drops containing no dissolved solids. The results are closely related to problems of bubble formation in boiling, cavitation, and in the evolution of gases from supersaturated solutions. The experimental technique developed in this study is believed to be unique and capable of giving quite accurate data on homogeneous nucleation in superheated drops. After a discussion of the theory of homogeneous nucleation in pure liquids, the theory is extended to the formation of bubbles in superheated drops. The theoretical predictions were found to be in close agreement with the experimental results.

Bubble formation in a superheated liquid is of current interest in chemical engineering because it is a fundamental process in heat transfer by boiling (*1*), cavitation in high-speed liquid flow (*2*), and ultrasonic cavitation in liquids (*3*). The term *superheated liquid* refers to a liquid at a pressure lower than the equilibrium vapor pressure corresponding to its temperature. In ordinary boiling and flow cavitation, bubble formation usually occurs at a solid surface in contact with the liquid and is influenced by gas bubbles on the solid surface. However because the physical conditions at the liquid-solid interface are not completely understood, no theory has been developed which accurately predicts the conditions for bubble formation at solid surfaces. Attention has turned, therefore, to bubble formation in the body of a superheated liquid, uninfluenced by solid surfaces or gas bubbles, as a distinct limiting case more susceptible to theoretical treatment. The theory of bubble formation under these conditions is one aspect of the theory of homogeneous nucleation. This theory should be directly applicable to ultrasonic cavitation in gas-free liquids and is expected to be of value as a starting point for a more general theory of nucleation applicable in the presence of solid surfaces, suspended gas bubbles, and dissolved gases.

The theory of homogeneous nucleation predicts the rate of bubble formation in a superheated liquid. Since pressures well below the equilibrium vapor pressure are required to produce bubble formation through homogeneous nucleation, the production of even one bubble in an isolated mass of superheated liquid is usually sufficient to raise the pressure to the vapor pressure or to permit all the liquid to vaporize. For this reason measurements of the rate of bubble formation are made by observing the length of time required for a single bubble to form at fixed conditions of liquid temperature and pressure or by gradually changing these conditions at a steady rate until the liquid mass is disrupted by the formation of a single bubble. The set of conditions of temperature, pressure, and composition at which the rate of bubble production becomes large enough for a vapor bubble of detectable size to form within the time of observation is called the *superheating limit*. Attempts to measure the superheating limit (*4, 5, 6, 7, 8*) have shown that liquids can be subjected to pressures as much as 100 atm. below the vapor pressure without the formation of vapor bubbles. A thorough check of theory against experiment has not been possible because previous experimental results have been capricious and nonreproducible, leaving doubt as to whether vaporization occurred through homogeneous nucleation, through the action of tiny gas bubbles trapped on vessel walls, or through some other external influence.

This paper presents the results of a reexamination and modification of the theory of homogeneous nucleation in superheated liquids as developed by Döring (*9*), Volmer (*10*), Frenkel (*11*), and Takagi (*12*) and the extension of the theory to bubble formation in superheated drops freely suspended in another liquid, together with the results of new experiments which are in close agreement with the modified theory (*13*). In these experiments the superheated liquid was dispersed into drops in another liquid, which minimized the effects of external influences and thereby made possible reproducible measurement of the superheating limit.

THEORETICAL DEVELOPMENT FOR A SINGLE-PHASE SYSTEM

The chemical potential of a superheated liquid is higher than that of the same substance in the bulk vapor state at the same temperature and pressure. Consequently if such a bulk vapor phase were permitted to contact the superheated liquid, and the temperature and pressure were maintained constant, the liquid would vaporize into it completely. However, in the absence of contact with such a bulk vapor phase and in the absence of other external influences the liquid in order to vaporize must itself generate the vapor phase. To do this, very small regions of vapor in the liquid, called *embryos* or *nuclei*, must first be formed. The unbalance of intermolecular forces accompanying the formation of these vapor nuclei surrounded by liquid causes the free energy of the liquid and vapor to be greater than that of an equal mass of liquid. Thus the thermodynamic reason for the existence of the metastable superheated state is that the formation of the first elements of the new phase requires a temporary increase in the free energy of the system.

The effects of intermolecular forces appear thermodynamically in the excess free energy of the surface and in the free energy of the vapor molecules in the bubble. The vapor molecules have high free energy per molecule relative to the liquid because they are under pressure higher than the equilibrium vapor pressure corresponding to the liquid pressure and temperature. The higher pressure results from the curvature of the bubble surface and the surface tension of the liquid. An embryo that is not too small, containing perhaps a few dozen molecules, can be expected to assume a spherical shape under the influence of the intermolecular forces. If such a bubble formed in a moderately superheated liquid, it would tend to collapse, accompanied by a decrease in the free energy of the system (the bubble and the surrounding liquid). However if, instead, the bubble should continually increase in size by adding molecules to the vapor phase, the pressure in the bubble would fall and the free energy of the system would increase until the bubble reached a certain radius, called the *critical radius*. At this bubble size the free energy of the system reaches a maximum, and the chemical potential of the vapor is equal to that of the liquid. On further increase in the radius and in the number of molecules, the pressure in the bubble would continue to fall, but the chemical potential of a molecule in the vapor would now be less than in the liquid, whereupon the bubble would tend to grow until all the liquid vaporized or the pressure in the liquid rose to the vapor pressure.

According to nucleation theory, the nuclei come into existence and grow through spontaneous statistical fluctuations in the density of the liquid, which arise from the thermal motion of the liquid molecules. In theory nuclei also

G.R. Moore is with Shell Development Company, Emeryville, California.

exist in nonsuperheated liquids, but the free energy of the system continually increases with bubble size because the molecular chemical potential in the vapor never becomes less than in the liquid. Consequently these bubbles do not grow to visible size. The following method of calculating the rate of production of visible bubbles through density fluctuations is based on the theory originally presented by Döring and later given a more extensive treatment by Volmer (*10*) in his book on the kinetics of phase transitions. The form of their presentation with certain modifications will be followed here.

BUBBLE FORMATION FREQUENCY

Döring and Volmer considered a vaporization process in a liquid at fixed temperature and pressure, with bubbles increasing and decreasing in size in a random fashion, due to local fluctuations in the energy of the molecules. In this process some bubbles vanish, others arise from homogeneous liquid, and some grow until they contain a number of molecules n_s, which is somewhat greater than the number n_k in a bubble of critical radius corresponding to the existing temperature and pressure in the liquid. The bubbles containing n_s molecules are considered removed from the liquid and an equivalent number of liquid molecules is added. The number of bubbles removed per unit time and volume is the nucleation frequency or bubble production rate. The bubbles which participate in these processes form a number distribution of bubbles of all sizes from those containing only a few molecules up to those containing n_s molecules. This distribution $Z(n)$ is the number of bubbles containing n molecules in unit volume of liquid.

The elementary microscopic process of growth is considered to be the transfer of a single molecule from liquid to vapor in a bubble containing n molecules to produce a bubble containing $n + 1$ molecules and the reverse for the process of collapse. The total area per unit volume available for the vaporization process is $Z(n)S(n)$ and for the condensation process $Z(n + 1)\ S(n)$. It is considered that at the moment the condensation process takes place, the effective area for condensation is equal to the area of the bubble after condensation because the finite size of the condensing molecule makes the effective radius smaller. The net flux of molecules between the two bubble sizes in unit volume of liquid in time dt is

$$J(n, t)\ dt = [Z(n, t)S(n)W_L(n) - Z(n + 1, t)S(n)W_V(n + 1)]\ dt$$

It is now assumed that the average value of $Z(n)$ does not change with time, under which condition J is not a function of time and is also not a function of n. The net rate of formation of visible bubbles is then equal to the difference between the rates of the two opposing processes for any size bubble, since every time a bubble grows to contain n_s molecules and is removed, there has been a net flow of one bubble through each size to produce it. With this assumption the above equation reduces to

$$J = Z(n)S(n)W_L(n) - Z(n + 1)S(n)W_V(n + 1). \quad (1)$$

One defines the quantity $\beta(n + 1) \equiv W_L(n)/W_V(n + 1)$ and introduces it into Equation (1) to obtain the first-order linear difference equation

$$\frac{Z_{n+1}}{\beta_{n+1}} - Z_n = -\frac{J}{W_{Ln}S_n} \quad (2)$$

which has the solution

$$Z_{n_0} - \frac{Z_{n_s}}{\prod_{i=n_0+1}^{n_s} \beta_i} = J\left[\sum_{n=n_0}^{n_s-1} \frac{1}{W_{Ln}S_n \prod_{i=n_0+1}^{n} \beta_i}\right] \quad (3)$$

The removal of bubbles containing n_s molecules makes

$$Z_{n_s} \Big/ \prod_{i=n_0+1}^{n_s} \beta_i$$

small compared to Z_{n_0}. Thus one obtains

$$J = Z_{n_0}\left[\sum_{n=n_0}^{n_s-1} \frac{1}{W_{Ln}S_n \prod_{i=n_0+1}^{n} \beta_i}\right]^{-1} \quad (4)$$

The quantity β_i is the ratio of the probability of the transfer of a molecule in a bubble containing i molecules from the vapor phase to the liquid to that of its return from the liquid to the vapor. This ratio may be evaluated by use of the following arguments. In accordance with classical statistical mechanics, the proportion of time a particle spends in each of two accessible regions of phase space is equal to the ratio of the total partition functions for the particle in the two regions. Further the probability of transition of a particle from one region to the other is inversely proportional to the mean residence time in that region, that is, the longer a particle stays in one region on the average the less likely it is to leave within a given time interval. This is expressed by the relation

$$\frac{W_{II}}{W_I} = \frac{t_{Im}}{t_{IIm}} = \frac{\text{total partition function per molecule for region I}}{\text{total partition function per molecule for region II}}$$

In addition, the chemical potential of a molecule in each region is given by

$$\frac{u_I}{kT} = \ln\left(\text{total partition function per molecule for region I}\right)$$

Thus

$$\frac{W_I}{W_{II}} = \beta_{II} = \exp\left(\frac{u_I - u_{II}}{kT}\right) \quad (5)$$

and

$$\prod_{i=n_0+1}^{n} \beta_{IIi} = \exp\left[\sum_{i=n_0+1}^{n} \frac{u_I - u_{IIi}}{kT}\right] \quad (6)$$

FREE ENERGY OF BUBBLE FORMATION

As pointed out by Takagi (*12*), the magnitude of the Helmholz free energy required to form a bubble containing n molecules from a bubble containing n_0 can be calculated by summing the difference in chemical potential as each molecule is brought in turn from the liquid into the vapor. Thus at constant system temperature and liquid pressure

$$\Delta A_n - \Delta A_{n_0} = \sum_{i=n_0+1}^{n} (u_i - u_L) \quad (7)$$

Now the thermodynamic development of the free energy of formation of the bubble containing n molecules from a bubble containing n_0 molecules actually need have no reference to bubbles as such but rather need refer only to the thermodynamic states of the molecules. Consequently the states need not be recognizable as bubbles for Equations (6) and (7) to apply; it is necessary only that the states be characterized by the number of molecules they contain and that there be some path available for transition between them. Therefore the liquid state can be thought of as being made up of bubbles containing one molecule and can serve as the reference state. For this state ΔA_{n_0} is zero, and Z_{n_0} equals the reciprocal of the volume per molecule in the liquid. Introducing Equations (6) and (7) into Equation (4) with these values for ΔA_{n_0} and Z_{n_0} one obtains

$$J = v_L^{-1}\left[\sum_{n=n_0}^{n_s-1} \frac{\exp\left(\frac{\Delta A_n}{kT}\right)}{W_{Ln}S_n}\right]^{-1} \quad (8)$$

The above interpretation is a departure from the presentation of Volmer and Döring, who concluded that the proper reference state should be a bubble containing no molecules, that is a hole the size of a molecule in the liquid. The present interpretation is that the smallest embryo is simply a molecule in the liquid state. The exact mechanism by which the transition from liquid to vapor takes place to form bubbles containing only a few molecules will not affect the calculation of the bubble-formation frequency as long as the contribution of such transitions to the sum in Equation (8) is small

compared with the contributions from transitions between larger bubbles. The author postulates that this is so.

To evaluate the sum in Equation (8) one uses the spherical bubble model. Volmer and Döring considered the vaporization probability per unit area W_L to be independent of bubble size. This follows from their assumption that the molecules in the liquid surface are in thermodynamic equilibrium with those in the main body of liquid, and so the chemical potential of the molecules at the surface is determined by the temperature and liquid pressure alone. This is probably not true for bubbles containing only a few molecules, but it is necessary only that it be approximately true for transitions which make large contributions to the sum in Equation (8). Since the vapor in the critical bubble is in equilibrium with the liquid, u_L is equal to the chemical potential of the vapor molecules in the critical bubble; thus from Equation (5) W_L equals W_{Vk}. W_{Vk} was calculated by Volmer and Döring as the mean collision frequency of vapor molecules on unit area of transfer surface, derived from the kinetic theory of gases to be

$$W_{Vk} = \left(\frac{kT}{2\pi m}\right)^{\frac{1}{2}} \cdot v_k^{-1} \qquad (9)$$

Volmer and Döring used the ideal-gas law throughout their development. This introduces some uncertainty in the results, and, since for many systems measurements at pressures above atmospheric can be made only at reduced temperatures above about nine tenths, it is desirable to examine the effects of vapor nonideality. First the following assumptions in the derivation of Equation (9) and in its application to the present problem may be examined:

1. The translational contributions to the partition functions are separable from all other contributions.
2. All contributions other than translational are the same in the transfer region as in the main body of vapor.
3. The particles are weakly interacting and have zero volume (ideal gas).
4. No potential-energy difference exists between the transfer region and main body of vapor at any time or in any region of the transfer surface.

The first two of these are good approximations for simple molecules with the same structure in the vapor as in the liquid. It is impossible to assess the effects of vapor nonideality on the partition functions without knowledge of the cause of any difference in potential in the transition region over that in the main vapor phase. If there is no such difference other than the existence of a uniform potential field that does not affect the intermolecular potential, the ratio of the number of particles in the transfer region to those in the main body of vapor reduces to that for an ideal gas, and so Equation (9) is valid for nonideal gases also. Ideal gas law deviations can then be handled by the use of

$$pV = znkT \qquad (10)$$

The restriction of no potential barriers means that there can be no steric hindrance repulsion effects or delays in transfer of excess translational energy to the liquid as the molecule passes from liquid to vapor and that the potential energy of a vapor molecule is always decreased on approaching the force field of the liquid surface. Potential barrier effects should be assessed for each individual vapor-liquid system, but the restriction should be satisfied for most nonpolar substances of simple structure. From these considerations

$$W_L = \frac{p_k}{z_k\sqrt{2\pi mkT}} \qquad (11)$$

is obtained.

The quantity ΔA_n has been evaluated in accordance with the spherical bubble model in terms of the radius of the bubble r_n and the pressure p_n within it for a vapor following the ideal gas law [Takagi (*12*)]

$$\Delta A_n = nkT \ln \frac{p_n}{p_k} + \frac{4}{3}\pi r_n^2\sigma \qquad (12)$$

For a vapor following the gas law, Equation (10), the equation for ΔA_n is different only in that the vapor pressures are replaced by fugacities. This equation is only valid for r_n and n sufficiently large for the spherical bubble model to be a reasonably close approximation to the actual state of the embyro. It is then independent of vapor nonideality for r equal to r_k, except insofar as nonideality affects r_k because the first term on the right-hand side vanishes and the second term depends only on the bubble radius and the surface tension. In adopting Equation (12) and later Equation (15) one must assume that the Gibbs theory of capillarity is adequate for this model and that in making numerical calculations one can use the macroscopic value of the surface tension without excessive error.

Now an examination of the terms of the sum in Equation (8) according to the model reveals that they reach a sharp maximum at $n = n_k$, and, for $n_k \gtrsim 50$, only terms for which $0.8 < r_n/r_k < 1.2$ are significant to the value of the sum. Consequently the failure of the model at small values of n is immaterial as long as n_k is reasonably large. Further, in these significant terms the ratio f_n/f_k will be nearly one, and, since the first term on the right hand side of Equation (12) is smaller than the second in this range, f_n/f_k can be replaced by p_n/p_k without noticeable error. For this reason nonideality of the vapor does not have a large effect on the work of formation even close to the critical point.

$$\sum_{n=n_0}^{n_s-1} \frac{\exp\left(\frac{\Delta A_n}{kT}\right)}{S_n} \doteq \frac{n_k}{S_k}\exp\left(\frac{\Delta A_k}{kT}\right)\int_{-\infty}^{\infty} \frac{3(1-b) + \frac{b}{r^*}\left\{2 + \left(\frac{\partial \ln z_n}{\partial \ln p_n}\right)_T\right\}}{z^*} \cdot \exp\left(-\frac{\Delta A_k}{kT}(3-b)x^2\right)\cdot dx \qquad (17)$$

Since the terms of the sum reach a sharp maximum at n equal to n_k, one may expand the logarithm about this point in powers of $x \equiv 1 - (r_n/r_k)$ and neglect powers of x higher than 2 to obtain

$$\frac{\Delta A_n}{kT} = \frac{\Delta A_k}{kT}[1 - (3-b)x^2] \qquad (13)$$

in which $b \equiv 1 - (p_L/p_k)$. For $n_k \gtrsim 100$, there are at least one hundred terms for which $0.8 < r_n/r_k < 1.2$ in the sum of Equation (8). Consequently the sum may be replaced by an integral, and because of the sharp maximum the limits may be extended from $-\infty$ to $+\infty$:

$$\sum_{n=n_0}^{n_s-1} \frac{\exp\left(\frac{\Delta A_n}{kT}\right)}{S_n} = \frac{1}{S_k} \cdot \int_{-\infty}^{\infty} \frac{\exp\frac{\Delta A_k}{kT}[1-(3-b)x^2]}{r^{*2}} \cdot \left(\frac{dn}{dr^*}\right) dr^* \qquad (14)$$

in which $r^* \equiv r_n/r_k$. Again using the gas law, Equation (10), and the condition of mechanical equilibrium

$$p_n - p_L = \frac{2\sigma}{r_n} \qquad (15)$$

one may evaluate the derivative

$$\frac{dn}{dr^*} = \frac{n_k}{z^*}\left[3(1-b)r^{*2} + br^*\left\{2 + \left(\frac{\partial \ln z_n}{\partial \ln p_n}\right)_T\right\}\right] \qquad (16)$$

in which $z^* = z_n/z_k$. On introducing Equation (16) into Equation (14) and noting that $dr^* = -dx$ one obtains

As previously noted, the entire significant contribution to the integral in Equation (17) occurs in the region of x close to zero. This is the justification for extending the limits of integration to infinity in

both directions and will further justify the substitutions $r^* = 1$ and $z^* = 1$, and the evaluation of $(\partial \ln z_n/\partial \ln p_n)_T$ at $p_n = p_k$ in the coefficient before the exponential. The asymptotic value of the integral for large n_k obtained by integrating with these approximations may be introduced into Equation (17) to give

$$\sum_{n=n_0}^{n_s-1} \frac{\exp\left(\frac{\Delta A_n}{kT}\right)}{S_n} \doteq \frac{\left[3 - b\left\{1 - \left(\frac{\partial \ln z}{\partial \ln p}\right)_T\Big|_{p_k}\right\}\right]}{S_k} \cdot \sqrt{\frac{2\pi n_k}{b(3-b)}} \cdot \exp\left(\frac{\Delta A_k}{kT}\right) \quad (18)$$

The quantity $(\partial \ln z/\partial \ln p)_T$ ap-

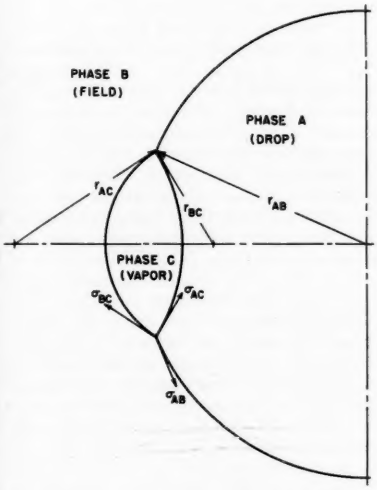

Fig. 1. Vapor lens at the surface of a drop.

proaches large negative values as the temperature approaches the critical temperatures; however it is only -0.6 at $T_r = 0.9$. The effect of this term is to make dn/dr^* smaller and thus to make the frequency of bubble formation given by Equation (18) smaller at a given value of P_L or b than would be obtained by omitting it. Equation (18) with this term omitted will then predict the nucleation pressure to be at a higher pressure than when it is included. However, because of the small value of b near the critical point, the inclusion of the derivative actually makes little difference in the nucleation frequency and far less in the nucleation pressure.

When Equations (10), (11), (15), (18), and $S_k = 4\pi r_k^2$ are substituted into Equation (8), one finds that

$$J = \frac{\sqrt{\frac{6\sigma(3-b)}{\pi m z_k}} \cdot \frac{1}{v_L} \cdot \exp\left(-\frac{\Delta A_k}{kT}\right)}{\left[3 - b\left\{1 - \frac{\partial \ln z}{\partial \ln p}\Big|_{p_k}\right\}\right]} \quad (19)$$

If z_k is set equal to one and $(\partial \ln z/\partial \ln p)$ is set equal to zero, this result reduces to that given by Volmer except that it contains no term involving the latent heat of vaporization of the liquid:

$$J = \sqrt{\frac{6\sigma}{\pi m(3-b)}} \cdot \frac{\exp\left(-\frac{\Delta A_k}{kT}\right)}{v_L} \quad (20)$$

The quantity ΔA_k is obtained by evaluating Equation (12) for the critical bubble:

$$\Delta A_k = \frac{4}{3}\pi r_k^2 \sigma \quad (21)$$

The critical radius is in turn evaluated by expressing the chemical potentials of vapor and liquid as functions of pressure and equating when the equilibrium difference in pressure is reached. The results, valid for n_k not too small, is

$$r_k = 2\sigma\left[\frac{\nu_\infty p_\infty}{\nu_k} \cdot \exp\left(\frac{v_{Lm}}{kT}(p_L - p_\infty)\right) - p_L\right]^{-1} \quad (22)$$

Equations (19), (21), and (22) permit any one of the quantities J, T, or P_L to be calculated from the other two for a pure substance, with the limitation that b must be somewhat less than 3. The mathematical approximations used to derive Equation (19) are not valid for b close to or greater than 3, and the upper limit $n_s - 1$ on the sum in Equation (3) must be evaluated somewhat differently (*12*).

It should be emphasized that the foregoing equations and development apply only to one-component systems. In order to establish the modifications required for comparison with the experimental results, the extension of the theory to the particular type of two-component system used is presented in the following paragraphs.

NUCLEATION OF BUBBLES IN DROPS

The application of the foregoing analysis to bubble formation in superheated drops is complicated by the presence of two components and of the liquid-liquid interface. It is possible for a vapor bubble to form either at the interface or in the interior of the drop, depending on the mechanical stability of a vapor mass at the interface. A bubble at the interface would be lens shaped (Figure 1), with spherical vapor-liquid surfaces which intersect at the surface of the drop. The stability of the lens is determined by the surface tensions at the lens edge, σ_{AB}, σ_{AC}, and σ_{BC}. The subscripts refer to the spherical surfaces between the phases; phase A is the drop, phase B is the surrounding liquid (field liquid), and phase C is the vapor lens. Now if $\sigma_{AC} > \sigma_{AB} + \sigma_{BC}$, the force related to σ_{AC} is able to overbalance both of the forces related to σ_{AB} and σ_{BC}, and the bubble would enter into the drop. If $\sigma_{BC} > \sigma_{AC} + \sigma_{AB}$, the bubble would be expelled into the surrounding liquid. If both $\sigma_{AC} \leq \sigma_{AB} + \sigma_{BC}$ and $\sigma_{BC} \leq \sigma_{AB} + \sigma_{AC}$, the lens would remain at the interface. The following analysis applies to the first-mentioned case, that is $\sigma_{AC} > \sigma_{AB} + \sigma_{BC}$. In this case the vaporization process should occur by formation of spherical bubbles in the interior of the drop.

The presence of two components will be treated by assuming the two liquids to be almost totally immiscible; that is, there is very little of the suspending liquid in the superheated drop but enough to make the total vapor pressure of the drop equal to the sum of the vapor

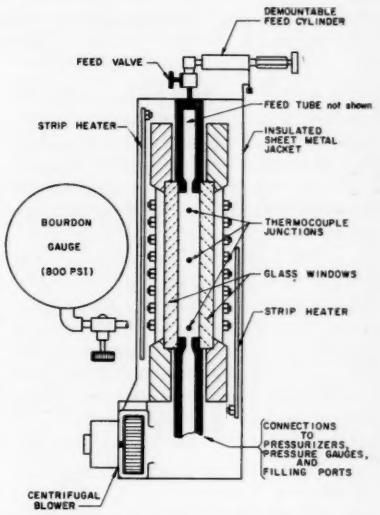

Fig. 2. Schematic sectional view of pressure cell.

pressures of the individual components. Further, the vapor solution will be assumed to be ideal, as expressed by the relations

$$f_a = y_a f_a^0 \qquad f_b = y_b f_b^0 \quad (23)$$

Since

$$f_{an}^0 = \nu_{an}^0 p_n \quad \text{and} \quad f_{bn}^0 = \nu_{bn}^0 p_n \quad (24)$$

the free-energy increase as each molecule vaporizes is given by the difference in chemical potential of its initial and final states in the form

$$\frac{u_n - u_L}{kT} = \ln\frac{f_n}{f_k} = \ln\frac{y_n \nu_n^0 p_n}{y_k \nu_k^0 p_k}. \quad (25)$$

for each component. From thermodynamic reasoning one may expect that the steps in the vaporization process will occur in the order of smallest free-energy increases; that is molecules of component

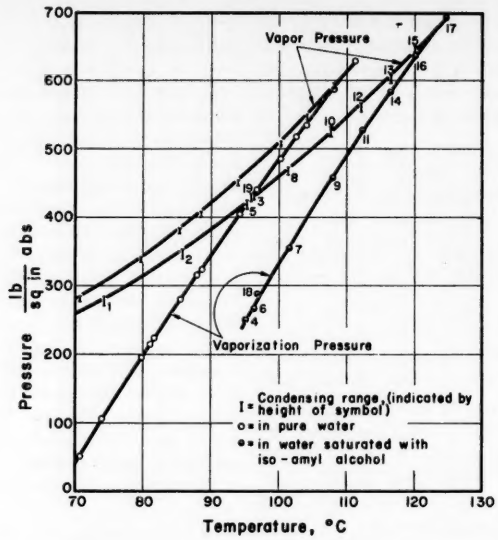

Fig. 3. Vaporization pressures for commercial-grade Freon-12 drops.

a will vaporize into a bubble until the free-energy increase resulting from the vaporization of a b molecule is less than that for another a molecule in the absence of the b molecule. The free-energy increase of the next a molecule to vaporize will be less than that for the same molecule if the b molecule had not vaporized because of the entropy increase accompanying the change in composition. Consequently it is reasonable to assume that for any size bubble the chemical potential differences for vaporization are the same for the two kinds of molecules and further that the composition of the vapor is the same as in the critical bubble. With these assumptions the work of formation of a bubble is given by Equation (12) as before. Further, although the individual transfer probabilities in an embryo are different for the two kinds of molecules, the ratio of transfer probabilities is the same for both kinds:

$$\beta_n = \exp(u_n - u_L)_a = \exp(u_n - u_L)_b$$

It may be noted that although the vapor was assumed to be an ideal solution and the mole fractions in the vapor to be constant in the redevelopment of Equation (12) for the two-component system, ΔA_k is given by Equation (21) irrespective of nonideality in the system, except insofar as nonideality affects r_k. This is due to the fact that once the critical radius of the bubble is fixed, mechanical considerations govern the bubble shape and the pressure within it and that the chemical potentials of the vapor molecules are the same as in their reference state, the liquid phase.

The critical radius may be obtained as before, with the assumption that the vapor pressures are additive. Thus

$$r_k = 2\sigma_{AC}\left\{\frac{\nu_{a\infty}p_{a\infty}}{\nu_{ak}^{0}} \cdot \exp\left[\frac{v_{am}}{kT}\left(p_B + \frac{2\sigma_{AB}}{r_{AB}} - p_{a\infty}\right)\right] + \frac{\nu_{b\infty}p_{b\infty}}{\nu_{bk}^{0}}\exp\left[\frac{v_{bm}}{kT}(p_B - p_{b\infty})\right] - p_B - \frac{2\sigma_{AB}}{r_{AB}}\right\}^{-1} \quad (26)$$

The rate equations for the net flow of bubbles may now be constructed as before, but the solution separates into two terms, one for each type of molecule:

$$J\left[\sum_{\substack{n=n_0 \\ \text{(only values of } n \\ \text{where an } a \text{ molecule} \\ \text{transfers)}}}^{n_s-1}\left[(W_I S_n)_a \prod_{i=n_0+1}^{n}\beta_i\right]^{-1} + \sum_{\substack{n=n_0 \\ \text{(only values of } n \\ \text{where a } b \text{ molecule} \\ \text{transfers)}}}^{n_s-1}\left[(W_I S_n)_b \prod_{i=n_0+1}^{n}\beta_i\right]^{-1}\right] = Z_0 - \frac{Z_s}{\prod_{i=n_0+1}^{n_s}\beta_i} \quad (27)$$

Under circumstances such that very few molecules of b vaporize along with the numerous a molecules in the formation of a bubble with n_s molecules, the quantity $(W_I S_n)_b$ can be assumed to equal $(W_I S_n)_a$ with small error, so that Equation (27) reduces to Equation (4) and the evaluation may be performed as before to produce Equation (19). Under these circumstances the net effect of introducing drops in another liquid has been to change the effective vapor pressure and thereby to change the critical radius, which is now given by Equation (26).

EXPERIMENTAL EQUIPMENT AND PROCEDURE

The superheating limit was measured experimentally by spraying drops of purified Freon-12 (dichlorodifluoromethane) into degassed distilled water in a pressure cell and, with temperature held constant, slowly releasing the pressure until several drops of a predetermined size vaporized simultaneously. The apparatus and techniques for the measurement of vaporization pressure and of physical properties necessary for comparison with the pressures predicted by theory are briefly described here.

The pressure cell (Figure 2) was a liquid-level gauge made of type-316 stainless steel, with Teflon-impregnated Fibreglas gaskets. Steel blocks were silver soldered to the ends of the chamber section and covers to increase the thermal capacity and minimize temperature gradients in the chamber section. Electrical strip heaters were attached to the edges of the chamber and covers. One-half-inch type-316 stainless steel pipe nipples passed through the end blocks and connected the chamber to fittings for the unheated parts. The cell was mounted in a U frame having sleeve bearings to permit inverting the cell for measurements with drops rising or falling.

Drops were produced by compressing liquid Freon-12 in feed cylinders with screw operated pistons, then releasing the pressure through a midget needle valve connected to a stainless steel feed capillary which entered the pressure cell through a Teflon-packed gland and delivered the Freon to a glass capillary. At the outlet of the glass capillary there was a small stage on which drops could be caught and observed microscopically for determination of vaporization and condensation pressures. Before the feed cylinders were filled, the Freon-12 was transferred from the supply cylinder through an evacuated manifold to a stainless steel reservoir and degassed by repetitive freezing in liquid air, evacuation, and boiling, until no pressure rise in the evacuated transfer manifold was observed on opening the reservoir valve over the frozen liquid. The degassed Freon-12 was heated and transferred under pressure to the evacuated feed cylinders, which were then removed from the manifold and attached to the feed capillary on the cell. The pressure cell was evacuated to 50μ, then filled by permitting distilled water degassed by boiling to flow into it.

Pressures up to 500 lb./sq. in. were applied with a lever-operated piston pressurizer and up to 1,500 lb./sq. in. with a screw-operated piston pressurizer similar to the feed cylinders, both Teflon-packed. Pressures were measured with a Bourdon gauge with a range up to 800 lb./sq. in. The gauge was calibrated and used in a vertical position. A very sensitive pressure balance was used to calibrate the gauge to the accuracy at which it could be read, namely 1 lb./sq. in. A 1,500 lb./sq. in.

Table 1. Purified Freon-12 Water System

Vapor pressure		Vaporization pressure	
Temperature, °C.	Condensation range, lb./sq. in. abs.	Temperature, °C.	Vaporization pressure, lb./sq. in. abs.
65.0	248–250	69.3	32
68.3	266–267	71.1	62
69.0	269–270	71.5	67
71.2	283–285	73.4	95
73.3	295–296	73.5	97
73.5	297–299	75.6	130
75.6	311–313	75.8	135
78.6	331–333	78.5	178
81.2	349–351	81.2	216
85.5	381–383	85.6	278
90.5	419–421	90.5	348
95.8	464–466	95.8	422
100.1	502–504	99.8	477
103.4	536–538	100.2	482
106.7	570–572	103.0	520
111.0	616–618	103.3	522
111.3	619–621	103.7	527
		106.7	566

Bourdon gauge was used for pressures above 800 lb./sq. in.

The temperature of the field liquid was measured at three places in the cell chamber by means of bare copper-constantan thermocouples which entered the cell through Teflon glands. One thermocouple was positioned near the observation stage, the second near the center of the cell chamber, and the third near the bottom, as shown in Figure 2. The thermocouples were calibrated to 0.1°C.

To achieve temperature uniformity, the cell and U frame were enclosed in a sheet-metal jacket, and air inside the jacket was circulated with a small blower. The jacket had a layer of asbestos paper on the outside to prevent burns and had plate-glass windows opposite the windows in the cell. The heaters on the cell were disconnected after heating to the desired temperature level, and four strip heaters inside the jacket connected to two variable-voltage circuits were used to regulate the cell temperature. Thermocouple traverses of the cell chamber showed that no hot spots were present when the thermocouple temperatures were within a few degrees of each other. For the experimental measurements the heater controls were adjusted until a variation of 0.1°C. or less between the center and end thermocouples was obtained.

To obtain vaporization pressures at temperatures where the drop density was greater or only a little less than the density of the field liquid (up to 100°C. for Freon-12 in water), the following technique was used. With the cell and feed cylinders at the same pressure above the vapor pressure at the cell temperature, a cloud of drops was produced by turning the hand-wheel on one of the cylinders about one-half turn with the feed valve shut, opening the valve quickly, and displacing the drops formed in the valve body and feed tube into the cell by a few turns of the hand-wheel. The excess Freon-12 was then drawn back through the valve by a few turns of the handwheel, and the valve closed. The cloud of drops so produced displayed a distribution of drop diameters from about 1 mm. down to those barely visible. The size distribution and total number of the drops could be controlled by the pressure applied to the liquid before the valve was opened and by the amount displaced into the cell. The largest drops moved relatively quickly, depending on the density difference at the existing temperature, and generally traveled down to the bottom of the cell. The intermediate sizes moved relatively slowly and the smallest hardly at all. Many of the smallest would disappear by dissolving as they were being observed. The valve to the lever pressure generator was opened and regulated so that the pressure in the system fell quickly at first and then slowly, at about 1 lb./sq. in./5 sec., as the pressure limit was approached. During the time the pressure was falling, the largest drops struck the metal at the bottom of the cell and vaporized. The resulting bubbles produced a moderate mixing action as they rose through the chamber. These large drops were all permitted to vaporize and leave the chamber before the pressure dropped the last few pounds to the vaporization limit. When the slowly moving drops, in the range 0.1 to 0.3 mm. in diameter, were observed to vaporize, as detected by the change in velocity and usually by a change in direction of motion, the valve to the pressure gauge was quickly closed the final one-half turn to hold the pressure reading on the gauge, and then the valve to the lever pressure generator was closed. Thermocouple voltages from the couples closest to the drops when they vaporized were measured, the Bourdon gauge was gently tapped to shake the movement to its equilibrium position, and the reading recorded. The cell was repressurized, and the measurements were repeated several times. The observed vaporization pressure generally varied at most by ±2 lb./sq. in. because of different rates of pressure fall, temperature variations of 0.1 to 0.2°, or differences in the drop sizes observed. Usually five to ten repetitions were made, depending on the size distribution and position of the cloud of drops produced. When a slow temperature drift was occurring, more repetitions were made.

The following observations give an indication of the sensitivity of this method. A temperature change of 0.1° made a noticeable change in the pressure readings obtained by this procedure. On occasion, while a temperature gradient to lower temperatures at the bottom of the cell existed, the drops were observed to vaporize progressively down the cell as the pressure was allowed to fall through a range of 5 lb./sq. in. Also when the drops were rising and higher temperatures existed at the top of the cell, it was possible to adjust the pressure to a constant value and observe the drops vaporize as they rose into the region alongside the upper thermocouple.

At temperatures where the drops were considerably less dense than the field liquid, the density change on vaporization was small enough to make the changes in velocity during vaporization difficult to observe. A single drop or a few drops were then captured on the face of the feed capillary alongside the outlet and observed with a 10-power microscope as the pressure was lowered with the screw pressurizer. The change in size on vaporization was easily observed. In fact, the variation of limiting pressure with drop size could be observed in a roughly quantitative way if a few drops of different sizes were observed at the same time. In regions where they could both be used conveniently, from 90 to 100°C. for Freon-12 in water, the methods of observing free-moving and captured drops gave the same results to within 1 lb./sq. in. The captured drops could be recondensed by pressurizing the cell and vaporization could be observed repeatedly and reproducibly; by permitting a temperature drift an essentially continuous curve could be obtained. The critical point for the system was observed by permitting a slowly-increasing-temperature drift and observing the interface as it progressed through the drop in both directions alternately. The temperature at which meniscus disappearance occurred could be detected to within 0.2°C. by this method.

At all temperatures the vapor pressure was measured by slowly increasing the pressure to cause condensation of a vapor bubble captured on the capillary face. The upper thermocouple was located about 5 mm. from this face.

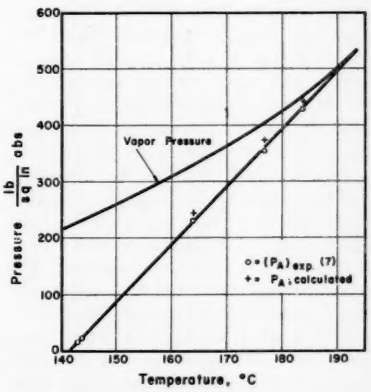

Fig. 4. Vaporization pressures for ethyl ether.

Table 2. Vaporization Pressure vs. Drop Diameter

Drop diameter, μ	Vaporization pressure, lb./sq. in.
52	62
65	64
130	66
195	67
910	73

Interfacial tension between the drop and field liquids was measured by the drop-volume technique. The glass feed tube in the pressure cell was replaced with a stalagmometer, and the feed cylinders were used to draw in and displace water from it.

RESULTS

The experimental vapor pressure and vaporization pressures for drops of purified Freon-12 in distilled water are presented in Table 1. The purified Freon-12 used was a 1-lb. sample described by the suppliers as having been taken from the stock used for measurement of accurate P-V-T properties, which was the center 50% of a careful distillation, dried over phosphorus pentoxide and deaerated. They found that the stock analyzed 0.01% of air by volume in the vapor phase and detected no impurities other than water by infrared absorption. In the present experimental work this material was found to have a 2 lb./sq. in. condensation range after it had been degassed. When the vapor pressure of the Freon-12–water system was calculated by adjusting the published vapor-pressure data (*14*) to the pressure in the cell and adding the vapor pressure of water, the result was within 1 lb./sq. in. of the limits of the experimental condensation range for the five points checked.

For an examination of the effects of a surface-active agent, vapor and vaporization pressures for degassed commercial-grade Freon-12 in distilled water and in water saturated with iso-amyl alcohol at about 85°C. were obtained. The results are shown in Figure 3. This sample of Freon had a 5 lb./sq. in. condensation range in distilled water. The effect of the iso-amyl alcohol was to decrease the vapor pressure and broaden the condensing range of the drops considerably and to decrease the vaporization pressure at a given temperature. It is not certain whether the pressure difference between the vaporization and vapor-pressure curves was decreased at a given reduced temperature as a result of the alcohol addition, because the critical point was difficult to observe and the composition of the system changed as more and more alcohol-free Freon was sprayed into the chamber. The data are numbered in the order in which they were taken so that the extent of the effects of the composition change can be seen.

Similar experiments with small amounts of Dreft and of the supernatant liquid from the Teflon suspensoid used in making up the pipe joints added to the water gave results no different from those obtained when the contaminants were not present. Subjecting the drops to mechanical shock by striking the cell with a metal hammer made no noticeable difference in the vaporization pressure. Vibration from the air-circulation blower had no effect, as checked by turning it off during a few measurements.

Motion pictures of droplet vaporization were made, and the details may be found in reference *13*.

The effect of drop diameter may be seen in the following results. At 71.4°C. the pressure was observed at which purified Freon-12 drops of various sizes vaporized on the glass stage as pressure was reduced fairly slowly. These data are given in Table 2. Diameters were estimated to the nearest one-tenth division of the ocular micrometer and thus are relatively inaccurate in the small sizes. As rate of pressure fall was not closely regulated, these data are not highly precise. However, as expected, larger drops clearly vaporized at higher pressures than smaller drops.

Some interesting phenomena were observed at temperatures between 100°C. and the critical point. With a drop of Freon-12 captured on the glass stage, the pressure was reduced rapidly with the screw pressurizer, while the drop was observed by transmitted light. At a definite pressure the drop momentarily became opaque because of the formation of hundreds of tiny bubbles in it; then it cleared as it became completely vaporized. With Freon-12 of condensing range 589 to 592 lb./sq. in. abs. at 108.2°C., when the pressure was held between 588 and 589 lb./sq. in. abs. dozens of bubbles were seen forming and rising through the drop to the vapor-liquid meniscus as it passed through the drop. Several seconds were required for the meniscus to pass through the drop. At 589 lb./sq. in. abs. the bubbles stopped forming, although the meniscus continued to move as vaporization from the surface took place. At 588 lb./sq. in. abs. the bubble-formation rate and the meniscus velocity were much greater and increased further at still lower pressures. Opalescence, believed to be of the type described by Maass, Mason, and coworkers (*15*), was observed in the neighborhood of the meniscus disappearance temperature, especially when sudden changes of about 5 lb./sq. in. or more in the pressure in the cell were made. The opalescence occurred in moving horizontal bands about one fifth as high as the bubble diameter. At 114.7°C. it was most pronounced at about 616 lb./sq. in., at 115.2°C. at 630 to 641 lb./sq. in., although present over the range 605 to 665 lb./sq. in. It was observed at temperatures from 110° to 116°C., with no indication that limits had been reached.

DISCUSSION

An estimate of n_k by use of Equation (10), the relation $V_n = (4/3)\pi r_n^3$, and the experimental vapor-pressure data indicated that there were from two-hundred to several thousand molecules in the critical bubble, the former figure for temperatures around 70°C. The mole fraction of water in the vapor is given approximately by the ratio of the vapor pressure of pure water to the vapor pressure of the mixture. At 70°C. the ratio is about 0.02, which indicates that about four molecules of water were present in the critical bubble. These numbers are small enough to permit neglecting the second sum of Equation (27) in analyzing the results of the experiments. The contribution of the second sum may be greater at higher temperatures, but it should be realized that an error of even a factor of two in the sum of the two terms represents only a change of at most 1 lb./sq. in. in the calculated vaporization pressure. Thus Equation (19) may be used for the calculation of the vaporization pressure. In this calculation, as a convenience to avoid repetitive trial and error, the experimental value of the vaporization pressure was used as a first approximation to determine the coefficient of the exponential in Equation (19), and the experimental conditions were used to determine the value of the bubble formation frequency. Equation (19) was then solved for $\Delta A_k/kT$. The value of r_k was obtained from Equation (21), and Equation (26) was solved for P_B, which was equal to P_A for the drop sizes observed. The resulting calculated value of P_A was always so close to the experimental that recalculation of the preexponential term was unnecessary. Since the interfacial tension was found in the experimental work to be about 25 dynes/cm., the term $2\sigma_{AB}/r_{AB}$ in Equation (26) is less than 0.1 lb./sq. in. for drops larger than 8 μ in diameter and thus can be neglected for such drops. For these larger drops the effect of drop size on nucleation pressure is limited to the change in bubble-formation frequency per drop resulting from the change in volume of the drop.

With regard to the surface tension of Freon-12 in the calculation, there was a small quantity of water dissolved in the Freon, which could be expected to raise its surface tension over that of pure Freon-12, the usual result for the solution of a nonsurface-active component in a liquid of lower surface tension. In the present case the effect should be slight because the solubility is very low. Consequently the recent data on the surface tension of dichlorodifluoromethane reported by Plank (*16*), at 0°C. 11.7

Table 3. Comparison of Calculated Vaporization Pressures for Freon-12 Drops in Water with Experimental Values

T, °C.	69.3	71.2	81.2	95.8	106.7
$(p_\infty)_{exp.}$, lb./sq. in. abs.	271–273	283–285	349–351	464–466	570–572
σ_{AC}, dynes/cm.	3.59	3.38	2.38	1.06	0.240
p_k, lb./sq. in. abs.	258	269	338	460	571
n_k,	206	237	531	3000	47,200
r_k, 10^{-7} cm.	4.52	4.67	5.64	8.58	18.2
$\frac{J_{P_A-1}}{J_{PA}}$	1.75	1.84	2.86	35.4	4×10^{14}
$P_A(+)_{calc.}$*, lb./sq. in. abs.	17	49	210	422	567
$(P_A)_{calc.}$*, lb./sq. in. abs.	28	59	216	424	567
$P_A(-)_{calc.}$*, lb./sq. in. abs.	38	68	221	426	567
$(P_A)_{exp.}$, lb./sq. in. abs.	32	63	216	422	566

*$(P_A)_{calc.}$, calculated for J = 1 bubble/(drop) (5 sec.).

dynes/cm., at 30°C. 8.1 dynes/cm., were used. These values were extrapolated into the region of interest by use of the relationship

$$\sigma = g(T_c - T)^j \qquad (28)$$

The exponent j was set equal to 11/9, the value found for a great number of organic compounds. The mean value $g = 0.0372$ derived from the two experimental values was used in the calculations.

Table 3 gives the summarized results of the calculations. In Table 3 P_A is the pressure at which a drop 0.2 mm. in diameter should vaporize within 5 sec. on the average, calculated from the theory by using values of surface tension from Equation (28). $P_A(-)$ and $P_A(+)$ are the pressures calculated when the surface tension from Equation (28) is decreased and increased by 3%. J_{P_A-1}/J_{P_A} is the approximate factor by which the bubble formation frequency increases with 1 lb./sq. in. decrease in P_A, as determined from the change in the work of formation. Table 3 also gives the number of molecules and radius of the critical bubble. Comparison of the theoretical vaporization pressures P_A with the experimental values $(P_A)_{exp}$ leads to the conclusion that within the experimental errors of ±0.1°C., ±1 lb./sq. in., drop diameters from 0.1 to 0.3 mm., and observation times from 1 to 5 sec. the theoretical curve is in agreement with the experimental data when reasonable latitude is allowed the value of the surface tension.

It is considered that the number and small size of the drops observed in this work precluded the possibility that the drops were caused to vaporize by the influence of cosmic rays or other background radiation or by the presence of solid particles and that the degassing of the liquids by boiling eliminated small gas bubbles so that they were not the cause of bubble formation. These certainly were not the origin of the copious bubble evolution seen in captured drops near the critical point. The decay rate of even recently formed organic matter resulting from the take-up of radioactive carbon-14 from the atmosphere is only about 12 disintegrations/min./g. of carbon. The particle produced is a weakly penetrating electron. Radiation from carbon-14 is not sufficient to influence the measurements because of the small quantity of carbon in a drop, the short time of exposure to low pressure, and the large number of drops observed. Since striking the cell with a hammer did not influence the results, the possible influence of vibrations in the building or from the air-circulation blower is improbable because the sharp shocks should have intensified any such effects and made them noticeable. There was never any indication that the motion of the drops had any effect on the nucleation pressure. Large free-falling drops vaporized at about the same pressure as drops trapped in the glass cage. In any event the small drops for which the comparison with theory was made moved slowly, and no effects of motion are to be expected.

The experimental vaporization pressures of Wismer (7) for ethyl ether were also compared with values predicted by the theory. The nucleation pressure for ethyl ether was calculated according to Equation (19) at a few temperatures, with vapor pressures and densities obtained from the data of Schnaible and Smith (17) and surface tensions from the data of Jeffries, Derrick, and Musgrave (18) extrapolated graphically by passing a line of slope 1.22 through a log-log plot of the data. The calculation technique followed was similar to the calculations for Freon-12 in water. J was assumed to be 1 bubble/cc./sec., which implies that the product of the experimental quantity of liquid and the observation time was 1 cc. sec. This product was not specifically stated in Wismer's work but should be of the correct order of magnitude. The summarized results of the calculations are given in Table 4. The agreement with Wismer's data, also given in Table 4, is satisfactory only at atmospheric pressure, since there only can the discrepancies observed be explained in terms of reasonable variations in the quantity of material and time of exposure to low pressure in the experiments. Curvature in the line through the experimental data (Figure 4), which should be evident over so large a temperature range regardless of the purity of the ether, is absent. It is to be especially noted that the experimental values not in agreement are lower than the theoretical, which indicates they could not be caused by external influences. The satisfactory agreement found for Freon-12 makes it unlikely that the discrepancies result from defects in the theory or from the assumptions made in the numerical calculations, except possibly that the surface tension of ether may not follow Equation (28) above 145°C., although there is no reason to suspect that it does not. It appears much more probable that a difference in the experimental conditions caused the high-pressure data to be erroneous, whereas the data at atmospheric pressure are valid. The most likely explanation appears to be that the Bourdon pressure gauge in the high-pressure apparatus of Wismer had an inaccurate calibration in addition to the large zero error mentioned in his description of the apparatus (7).

One should note that the exponential factor involving the latent heat of vaporization, which appeared in Döring's equation for the bubble formation rate and which has been rejected on theoretical grounds, would decrease the calculated vaporization pressure for Freon-12 in water by about 7 lb./sq. in. at 70°C. and about 4 lb./sq. in. at 80°C. The resulting values would still be reasonably close to the experimental values, considering the possible errors in surface tension among others, but the values calculated omitting the factor are in noticeably closer agreement. The same holds for the agreement with Wismer's data at atmospheric pressure.

SUMMARY AND CONCLUSIONS

This paper has presented the equations to be used for predicting the conditions required for homogeneous nucleation in liquids at atmospheric pressure and

Table 4. Vaporization Pressures for Ethyl Ether

T, °C.	143.0	143.8	163.8	176.8	183.8
$(p_\infty)_{exp}$, lb./sq. in. abs.	227	231	327	405	456
σ, dynes/cm.	3.70	3.63	1.94	0.97	0.51
p_k, lb./sq. in. abs.	214	218	319	401	455
P_A, lb./sq. in. abs.	12	22	244	375	445
$(P_A)^*_{exp}$, lb./sq. in. abs.	15	22	230	350	430

*Data of Wismer (7).

above; it has described the measurement of these conditions with an apparatus in which the effects of external influences are minimized or avoided, and it has shown the experimental and theoretical work to be in agreement.

Further applications of the principles and methods described should lead to further fundamental knowledge of the processes of bubble formation in boiling, flow cavitation, and evolution of gases from supersaturated solutions. Some of the most promising avenues should be the following:

1. Investigation of the effects of concentration of liquid solutions on bubble evolution.

2. Development of a flow apparatus with liquid interfaces used to eliminate the effects of solid surfaces, such as the annular flow of a superheated liquid within a nonsuperheated liquid through a constriction to produce a region of high velocity and low pressure. Such a condition might be approached with a swirl type of pressure nozzle in which the nonsuperheated and superheated liquid are contacted in the swirl-chamber orifice where an air core normally occurs.

3. Investigation of the effects of suspended particles, as for example very finely divided metals, degassed by boiling the liquid containing them.

4. Investigation of the effects of dissolved gases.

These and similar investigations may help to elucidate how an active center becomes active in boiling, how the nature of the solid surface affects boiling, and how the effects of composition of liquid mixtures on boiling heat transfer can be predicted.

ACKNOWLEDGMENT

The author wishes to express his deepest thanks to W. R. Marshall, Jr., for his guidance, encouragement, and support throughout the course of this work. Financial support was extended by the Procter and Gamble Company, the Wisconsin Alumni Research Foundation, and the Engineering Experiment Station. This support is gratefully acknowledged. The purified Freon-12 was generously supplied by du Pont.

NOTATION

A = Helmholtz free-energy or total-work function
b = $1 - (p_L/p_k)$
f = fugacity
g = constant in surface-tension correlation, Equation (28)
i = index for summation
j = constant in surface-tension correlation, Equation (28)
J = bubble production rate or nucleation frequency, no./(unit time) (unit volume)
J_{P_A} = bubble formation rate at pressure P_A
k = Boltzmann's constant
m = mass of a molecule
n = number of molecules in a bubble
n_k = number of molecules in a bubble of critical radius
n_s = number of molecules in a bubble large enough to be removed from the distribution
p = pressure
p_n = pressure in bubble with n molecules
p_k = pressure in bubble of critical size
P = vaporization pressure, pressure in liquid at which bubble formation rate is high enough to produce a visible bubble within the time of observation
r_n = radius of bubble with n molecules
r_k = radius of critical bubble
r^* = r_n/r_k
$S(n)$ = effective transfer area of a bubble containing n molecules
t = time
T = absolute temperature
T_c = critical temperature
u = chemical potential, energy/molecule
u_k = chemical potential of vapor molecules in critical bubble
v_k = volume per molecule in the vapor at the transfer surface of the critical bubble
v_L = volume per molecule in the liquid
v_{Lm} = mean value of specific volume of liquid between pressures p_L and p_∞, the vapor pressure over a plane surface ($r = \infty$)
V = volume
V_n = volume of bubble containing n molecules
$W_L(n)$ = probability of vaporization of a single molecule per unit area and time into a bubble containing n molecules
$W_V(n)$ = probability of condensation of a single molecule per unit area and time from a bubble containing n molecules
x = variable of integration, $x \equiv 1 - r^*$
y = mole fraction in vapor phase
z = compressibility factor = pV/nkT
$Z(n)$ = distribution function expressing the number of bubbles containing n molecules in a unit volume of liquid
$\beta(n)$ $\equiv W_L(n-1)/W_V(n)$
Δ = notation for difference or increment
ν = fugacity coefficient = f/p
σ = surface tension

Subscripts

a = molecular species a
A = liquid phase in drop
b = molecular species b
B = liquid phase in field
C = vapor phase in lens
L = liquid phase
k = critical bubble condition
n = number of molecules
0 = bubble containing minimum number of molecules
s = bubble of the size to be removed from the distribution
V = vapor phase
I, II = any two distinct accessible regions of phase space
∞ = condition of thermodynamic equilibrium between two phases separated by a plane interface ($r = \infty$)

Superscript

0 = standard state, the pure component at the temperature and pressure in the vapor

LITERATURE CITED

1. Westwater, J. W., "Advances in Chemical Engineering," Vol. I, p. 1, T. B. Drew and J. W. Hoopes, Jr., Editors, Academic Press, New York (1956).
2. Kermeen, R. W., J. T. McGraw, and B. R. Parkin, *Trans. Am. Soc. Mech. Engrs.*, **77**, 533 (1955).
3. Lindström, Olle, *J. Acoust. Soc. Am.*, **27**, 654 (1955).
4. Ackermann, C. B., Ph.D. thesis, Univ. Nebraska, Lincoln (1953), Publication 7914, University Microfilms, Ann Arbor, Michigan (1954).
5. Trevena, D. H., Ph.D. thesis, Univ. Wales (1950).
6. Kenrick, F. B., C. S. Gilbert, and K. L. Wismer, *J. Phys. Chem.*, **28**, 1297 (1924).
7. Wismer, K. L., *ibid.*, **26**, 301 (1922).
8. "Cavitation in Hydrodynamics," Proceedings of a Symposium (Sept. 14 to 17, 1955) London, H. M. Stationery Office (1956).
9. Döring, W., *Z. physik. Chem.*, **B36**, 371 (1937); **B38**, 292 (1938).
10. Volmer, M., "Kinetik der Phasenbildung," Theodor Steinkopff, Dresden and Leipzig, Germany (1939).
11. Frenkel, J., "Kinetic Theory of Liquids," p. 366, Oxford Univ. Press, London (1946).
12. Takagi, Shunsuke, *J. Appl. Phys.*, **24**, 1453 (1953).
13. Moore, G. R., Ph.D. thesis, Univ. Wisconsin, Madison (1956). Publication 17330, University Microfilms, Ann Arbor, Michigan.
14. "Pressure-Temperature Relationships of Refrigerants," Graph published by Kinetic Chemicals, Inc., Jackson Laboratory, Wilmington, Delaware (June, 1947).
15. Mason, S. G., and O. Maass, *Can. J. Res.*, **26B**, 592 (1948).
16. Plank, R., *Kältetechnik*, **6**, 58 (1954).
17. Schnaible, H. W., and J. M. Smith, *Chem. Eng. Progr. Symposium Ser. No. 7*, **49**, 159 (1953).
18. Jeffries, T. O., M. Derrick, and B. Musgrave, *J. Chem. Phys.* **23**, 1730 (1955).

Manuscript received October 3, 1958; revision received May 4, 1959; paper accepted May 8, 1959. Paper presented at A.I.Ch.E. Salt Lake City meeting.

Heat Transfer by Radiation through Porous Insulations

BERT K. LARKIN and STUART W. CHURCHILL

The University of Michigan, Ann Arbor, Michigan

Radiant transfer through fibrous and foamed insulating materials was investigated theoretically and experimentally. Transmission measurements were made under isothermal conditions with a black-body source varying from 200° to 800°F. Bulk density and fiber and pore size were also varied. These data were interpreted successfully in terms of a simple theoretical model. The results provide design information and define the contributions of the several mechanisms of transfer.

Because of savings in both space and weight, low-density insulating materials are being used increasingly in consumer appliances, clothing, homes, automobiles, aircraft, and industrial process equipment. The lightweight insulations possess a relatively large amount of void space; usually more than 95% of their volume is occupied by gas. Typical solid materials now being employed in these insulations are polystyrene, polyurethane, wood fibers, and glass. The insulations can be classified in two types from a geometrical point of view. In one type the solid is the continuous medium, the void space being dispersed bubbles; the other type consists of a matrix of solid fibers held together by a suitable bonding agent. Both types are considered in this investigation. {The particular insulations were chosen for experimental purposes, and direct comparison of their radiant properties is not appropriate.}

Heat transfer problems arising from the application of these materials have generally been solved by treating the heat transfer process as if it were wholly a conduction process. On the basis of a conduction mechanism the thermal conductivity should decrease continually with decreasing bulk density, finally approaching the conductivity of the gas filling the void space. The apparent conductivity is actually observed first to decrease and then to increase with decreasing bulk density. This suggests that the other heat transfer processes, such as radiation and free convection, must be contributing appreciably.

Bosworth (*2*) and Jakob (*10*) proposed on the basis of different analyses that radiation in porous materials be treated in terms of a radiant conductivity proportional to the cube of the absolute temperature. Topper (*17*) proposed the use of a radiant heat transfer coefficient with this same temperature dependence. Verschoor and Greebler (*18*) derived an expression for the heat transferred by fiber absorption and reradiation in the form of an infinite series which in the limit converges to essentially the same expression as that proposed by Jakob. Hamaker (*8*) presented an earlier and more extensive theoretical analysis of simultaneous radiation and conduction than any of the above. This investigation utilizes a similar mathematical treatment.

Experimental results are quite limited. From measurements of the total rate of heat transfer only, McIntire and Kennedy (*13*) estimated the radiant contribution to be 25% in pure Styrofoam. They also found from infrared transmission measurements and from heat transfer tests that the radiant contribution could be reduced by additives with higher reflectivities and absorptivities than polystyrene. Allcut (*1*) measured the apparent conductivity of glass wool faced first with paper and then with aluminum foil. From these data it can be inferred that radiation comprised from 1 to 10% of the heat transfer rate.

From infrared transmission measurements (not given) Verschoor and Greebler (*18*) determined the absorptivity of glass fibers. Radiation rates computed from these data were found to compare favorably with experimental rates of heat transfer in evacuated insulations.

Despite the work indicated above, the effects of the variables that influence radiation are almost wholly undefined, and so the objective of this investigation was to provide quantitative information on these variables. The problem is first formulated in terms of a simple model, in which the parameters are interpreted theoretically and evaluated experimentally. The significance of the experimental results is then discussed, and their application in the prediction of the performance of insulation is illustrated.

MATHEMATICAL REPRESENTATION OF RADIATION

Radiant transfer through a porous insulation occurs by direct transmission through the "holes," by scattering and by absorption and reradiation. Scattering occurs when electromagnetic waves encounter a discontinuity in refractive index. For fibrous materials this occurs at the surface of the fibers and for foamed materials at the surface of the bubbles. Absorption occurs primarily in transmission through the solid material.

Insofar as the insulation can be treated as an isotropic and continuous material, radiant transfer through porous or dispersed material can be described quite exactly in terms of an integrodifferential equation called the *transport equation* and a differential energy balance relating the rates of radiation, conduction, and convection. However the transport equation has been integrated only for highly restricted conditions (*4*) and is not directly applicable for prediction of radiant rates or for correlation of experimental data for thermal insulations. The idealization that the scattered and reradiated energy is propagated only in the forward and backward direction along the x axis, as suggested by Schuster (*15*), utilized by Hamaker (*8*), and extended by Chu and Churchill (*5*), is illustrated in Figure 1. This model yields the simpler and more tractable set of differential equations for the radiant flux density in the forward and backward directions:

$$\frac{dI_1(x)}{dx} = -n(BS_s + S_a)\cdot I_1(x) + n\cdot B\cdot S_s\cdot I_2(x) + nS_a\cdot\sigma\cdot T^4(x) \quad (1)$$

$$-\frac{dI_2(x)}{dx} = -n(BS_s + S_a)\cdot I_2(x) + nB\cdot S_s\cdot I_1(x) + nS_a\cdot\sigma\cdot T^4(x) \quad (2)$$

and

$$q = -k_e\frac{dT(x)}{dx} + I_1(x) - I_2(x) \quad (3)$$

Equation (1) states that in traversing the distance dx the radiant flux density in the forward direction is decreased in the amounts $n\cdot B\cdot S_s\cdot I_1\cdot dx$ owing to back scattering and $n\cdot S_A\cdot I_1\cdot dx$ owing to absorption; it is increased in the amounts $n\cdot B\cdot S_s\cdot I_2\cdot dx$ owing to back scattering of the backward radiant flux density and $n\cdot S_A\cdot\sigma\cdot T^4\cdot dx$ owing to reradiation. Equation (2) is the analogous balance for the backward radiant flux density. Equations (1) and (2) imply that the spectral distribution of the

Bert K. Larkin is with The Ohio Oil Co., Research Center, Littleton, Colorado.

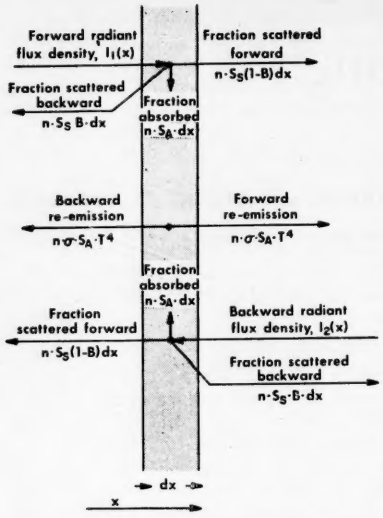

Fig. 1. Two-flux model for radiant transfer.

intercepted and reemitted radiation is the same, a reasonable assumption with the exception of extreme temperature gradients and optically thin slabs. Equation (3) states that the net heat-flux density in the x direction is equal to the rate of conduction plus convection, $-k_c\ dT/dx$, plus the net radiant flux, $I_1 - I_2$.

For convenience the following grouping of parameters will be defined:

$$M = n(BS_s + S_a) \tag{4}$$

$$N = nBS_s \tag{5}$$

$$P = M - N = nS_a \tag{6}$$

M, N, and P are the interception, backscattering, and absorption cross sections of a unit volume of insulation and will be assumed to be constant with respect to x. Obviously only two of these three parameters are independent, but all three are retained for convenience. Equations (1) and (2) then reduce to

$$\frac{dI_1}{dx} = -MI_1 + NI_2 + P\sigma T^4 \tag{7}$$

$$-\frac{dI_2}{dx} = -MI_2 + NI_1 + P\sigma T^4 \tag{8}$$

The boundary conditions for insulation faced with sheets of opaque material consist of the temperatures of the

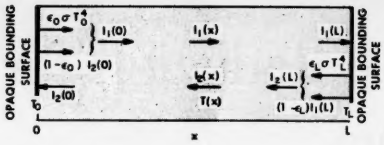

Fig. 2. Boundary conditions for two-flux model and opaque surfaces.

boundary, T_0 at $x = 0$ and T_L at $x = L$, and the radiant flux balances

$$I_1(0) = \sigma T_0^4 \epsilon_0 + (1 - \epsilon_0) I_2(0) \tag{9}$$

and

$$I_2(L) = \sigma T_L^4 \epsilon_L + (1 - \epsilon_{0L}) I_1(L) \tag{10}$$

which state that the radiant flux entering the insulation consists of the radiant emission from the boundary surface plus the fraction of the incident radiation reflected by the bounding surface (Figure 2). Alternative boundary conditions, such as for unfaced insulation, have been considered by Hamaker (*8*).

For nonabsorbing insulation [$P = 0$, $M = N$] and constant k_c, Equations (3), (7), and (8) can be readily solved with the preceding boundary conditions. The temperature varies linearly across the insulation, and the total heat flux is

$$q = \frac{k_c(T_0 - T_L)}{L} + \frac{\sigma[T_0^4 - T_L^4]}{\frac{1}{\epsilon_0} + \frac{1}{\epsilon_L} - 1 + NL} \tag{11}$$

The first term on the right is the rate of conduction and convection and the second term the rate of radiation. Both are constant across the insulation.

The equations are not readily solvable for absorbing materials [$P \neq 0$]. The three equations can be reduced to a pair of equations in any two of the three variables, but all such pairs are nonlinear. Although particular solutions of these pairs are obtainable from an analogue computer, greater accuracy and usefulness appeared possible with an approximate analytical solution.

If the net radiant heat-flux density is essentially constant or is a small fraction of the total heat transfer rate, and k_c is constant, it is apparent from Equation (3) that the temperature gradient will be nearly constant. The assumption of a constant temperature gradient and hence a linear variation in temperature across the insulation linearizes Equations (7) and (8). This linearized pair can be solved by ordinary methods to yield the radiant rate

$$q_1(x) = I_1(x) - I_2(x) = \frac{(2 - \epsilon_0)(M - N)W + AZ}{C} \cdot \sinh \sqrt{M^2 - N^2}x + \frac{\epsilon_0\sqrt{M^2 - N^2}W - G \cdot Z}{C} \cdot \cosh \sqrt{M^2 - N^2}x + 2X(x) \tag{12}$$

where

$$A = \epsilon_L\sqrt{M^2 - N^2} \cdot \sinh \sqrt{M^2 - N^2}L + (2 - \epsilon_L)(M - N) \cdot \cosh \sqrt{M^2 - N^2}L$$

$$W = \epsilon_L Y(L) - (2 - \epsilon_L)X(L)$$

$$Z = \epsilon_0 Y(0) + (2 - \epsilon_0)X(0)$$

$$G = (2 - \epsilon_L)(M - N) \cdot \sinh \sqrt{M^2 - N^2}L + \epsilon_L\sqrt{M^2 - N^2} \cdot \cosh \sqrt{M^2 - N^2}L$$

$$C = [(M - N)(2 - \epsilon_0 - \epsilon_L) + M\epsilon_0\epsilon_L] \sinh \sqrt{M^2 - N^2}L + \sqrt{M^2 - N^2}(\epsilon_0 + \epsilon_L - \epsilon_0\epsilon_L) \cdot \cosh \sqrt{M^2 - N^2}I$$

$$X(x) = \frac{4\sigma(T_0 - T_L)}{(M + N)L} \cdot \left[T^3(x) + \frac{6(T_0 - T_L)^2}{(M^2 - N^2)L^2}\ T(x)\right]$$

$$Y(x) = \frac{12\sigma(T_0 - T_L)^2}{(M^2 - N^2)L^2} \cdot \left[T^2(x) + \frac{2(T_0 - T_L)^2}{(M^2 - N^2)L}\right]$$

For $\sqrt{M^2 - N^2}L > 5$, which proved to be the case for an inch or more of all the commercial insulations studied

$$q_r(0) \cong \epsilon_0\left\{\frac{[(M + N)\epsilon_L + \sqrt{M^2 - N^2}(2 - \epsilon_L)]X(0) - [(2 - \epsilon_L)(M - N) + \epsilon_L\sqrt{M^2 - N^2}] \cdot Y(0)}{(M - N)(2 - \epsilon_0 - \epsilon_L) + M\epsilon_0\epsilon_L + \sqrt{M^2 - N^2}(\epsilon_0 + \epsilon_L - \epsilon_0\epsilon_L)}\right\} \tag{13}$$

If also

$$T_0 \gg \frac{3(T_0 - T_L)}{(M - N)L}$$

$$q_r(0) \cong \frac{4\sigma\epsilon_0(T_0 - T_L)}{(M + N)L}\left\{\frac{(M + N)\epsilon_L + \sqrt{M^2 - N^2}(2 - \epsilon_L)}{(M - N)(2 - \epsilon_0 - \epsilon_L) + M\epsilon_0\epsilon_L + \sqrt{M^2 - N^2}(\epsilon_0 + \epsilon_L - \epsilon_0\epsilon_L)}\right\}T_0^3 \tag{14}$$

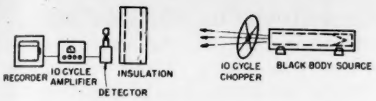

Fig. 3. Schematic diagram of equipment.

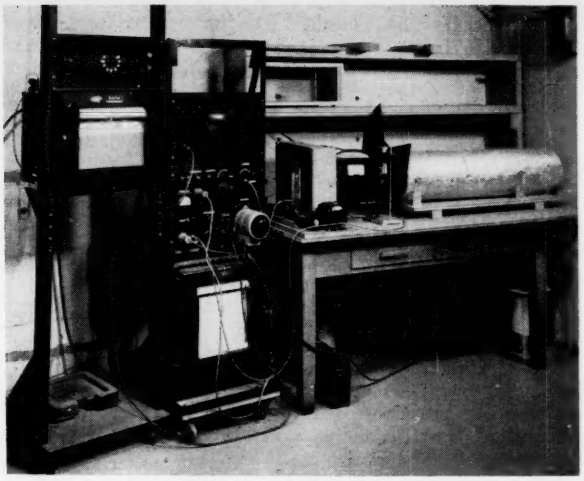

Fig. 4. Experimental apparatus.

THE EVALUATION OF RADIATION PARAMETERS FROM ELECTROMAGNETIC THEORY

Equations (11) and (12) yield the radiant contribution to heat transfer for nonabsorbing and absorbing insulation in terms of N and M and of N respectively. These parameters, which are functions of the physical properties of the insulations, can in principle be evaluated from electromagnetic theory.

Foamed Insulations

If the foamed insulation is assumed to contain a random dispersion of uniformly sized spheres of gas, the number of spheres per unit volume is found from a simple volume balance to be related to the sphere size and gas, solid and bulk densities as

$$n = \frac{3}{4\pi R^3} \cdot \frac{\rho_S - \rho}{\rho_S - \rho_G} \qquad (15)$$

The scattering cross section is usually expressed in terms of a scattering coefficient equal to the ratio of the scattering to the geometric cross section; that is

$$K_s = S_s/\pi R^2 \qquad (16)$$

Hence

$$N = \frac{3BK_s}{4R} \cdot \frac{\rho_S - \rho}{\rho_S \rho_G} \qquad (17)$$

The properties B and K_s can be computed from the Mie solutions of the Maxwell equations (*14, 6, 3*) if the relative index of refraction of the solid and gas is known. Unfortunately the required calculations are extensive, and the index of refraction of insulating materials is not known in the thermal range of wave lengths. However the effect of pore size can be inferred from limiting values of the Mie solution. For pores much larger than the wave length of the radiation, BK_s approaches a constant value, and hence N varies inversely with pore size; for pores much smaller than the wave length, BK_s is proportional to the fourth power of the pore radius, and hence N is proportional to the radius cubed. N is a measure of the ability of the insulation to scatter radiation backward, and the larger the value of N the smaller the rate of heat transfer by radiation. Since the large-pore approximation indicates that small pores are most effective and the small-pore approximation that large spheres are most effective, an optimum pore size is to be expected for a given porosity if scattering is controlling.

Theoretical evaluation of the absorption cross section is less certain. When one assumes that each pore is associated with a cube of solid which is large with respect to the wave length

$$S_a = n^{-\frac{2}{3}}(1 - e^{-\beta y}) \qquad (18)$$

$$y = R\left(\frac{\rho - \rho_G}{\rho_S - \rho_G}\right)\left(\frac{\rho_S - \rho_G}{\rho_S - \rho} \cdot \frac{4\pi}{3}\right)^{\frac{1}{3}} \qquad (19)$$

and hence

$$P = \frac{1}{R}\left(\frac{\rho_S - \rho_G}{\rho_S - \rho} \cdot \frac{4\pi}{3}\right)^{\frac{1}{3}}(1 - e^{-\beta y}) \qquad (20)$$

The necessary information on the absorptivity of insulating materials is currently unavailable. However, for small pores P would appear to be independent of pore size, and for large pores P would appear to be inversely proportional to pore size.

Fibrous Insulations

For a random matrix of uniformly sized cylinders with axes perpendicular

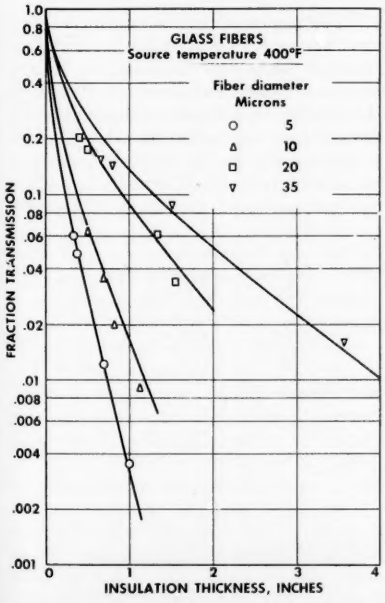

Fig. 5. Transmission of radiation through glass fibers.

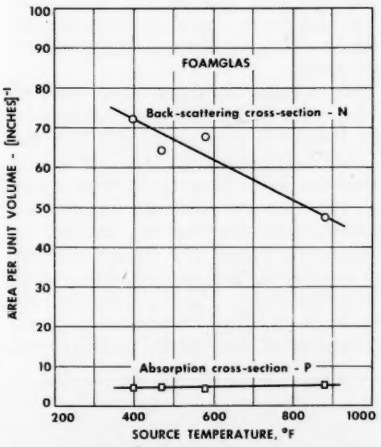

Fig. 6. Radiation parameters for Foamglas.

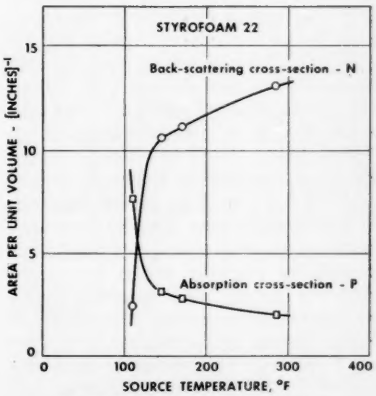

Fig. 7. Radiation parameters for Styrofoam-22.

to the direction of heat flow the following expressions are analogous to those for foamed insulations:

$$N = \frac{4BK_s}{\pi D_f} \cdot \frac{\rho - \rho_G}{\rho_S - \rho_G} \qquad (21)$$

and

$$P = \frac{4K_a}{\pi D_f} \cdot \frac{\rho - \rho_G}{\rho_S - \rho_G} \qquad (22)$$

BK_s and K_a can be computed from electromagnetic theory if the index of refraction and absorptivities are known. A summary of the theory and the results of illustrative calculations are presented in (*11*) and (*12*). Some of these values computed for specific indices of refraction are subsequently compared with the experimental data. The qualitative behavior of N and P for cylinders is similar to that for spheres. N and P vary inversely with fiber diameter for $D_f \gg \lambda$ and directly with fiber diameter squared for $D_f \ll \lambda$.

Limitations

The evaluation of the radiation parameters from electromagnetic theory is limited severely by current information on the index of refraction and absorptivity of the materials and even with these properties involves extensive calculations on a high-speed computer. The present contribution of theory is primarily in the qualitative prediction of effects.

EXPERIMENTAL EVALUATION OF RADIATION PARAMETERS

The radiation parameters N and M were evaluated experimentally for representative and specially selected insulations by transmission measurements with a black-body source at a series of temperatures. Reradiation and background radiation were minimized by modulating the source and using a sharply tuned 10 cycle/sec. amplifier. The insulation was maintained at room temperature to minimize conduction and further to minimize reradiation.

A schematic diagram of the equipment is shown in Figure 3 and a photograph of the equipment in Figure 4. The black-body source consisted of a 36-in.-long by 4-in.-diameter copper tube wrapped with heating wires and covered with insulation. One end of the tube was closed with a plug having an internal conical cavity. Temperatures along the inside of the pipe were maintained uniformly within ± 5°F. by control of the several segments of the heating wire. The chopper used to modulate the source consisted of a two-bladed propeller driven by a synchronous motor. The radiation falling on the insulation varied periodically as a 10 cycle/sec. square wave.

The detector was similar to those employed in infrared spectrometers and contained a blackened thermocouple. It was mounted to traverse a 3-in. path parallel to the surface of the insulation. Since the signal was often as low as a few hundredths of a microvolt, a high-gain amplifier was needed. A recorder was utilized to facilitate averaging the signal obtained with nonuniform insulations.

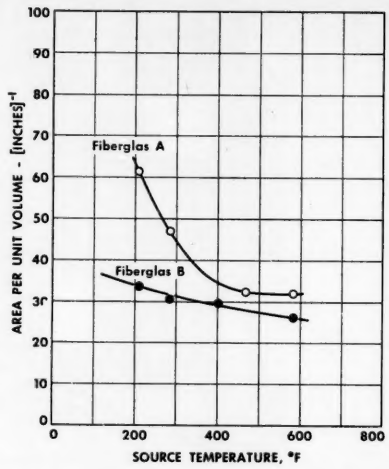

Fig. 8. Back-scattering cross-section N of Fiberglas *A* and *B*.

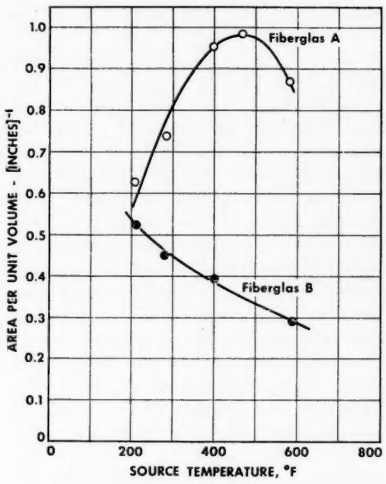

Fig. 9. Absorption cross-section P of Fiberglas *A* and *B*.

No change in signal was observed when part of the specimen was masked, an indication that an infinite slab was successfully simulated. The signal was observed to vary as the inverse square of the distance from an uncollimated source, indicating that the detector response was linear. The angular response of the detector was also tested and found to be acceptable. The detector signal was found to be closely proportional to the difference of the fourth power of the temperature of the source and receiver, indicating that both the source and receiver were nearly "black" or equally "gray." Additional details concerning the equipment are available *11*.

Several hours were required for the source to attain a steady state. The unattenuated radiation was first measured with the detector. From this trace and prior measurements of the variation of the flux with distance from the source the flux incident upon the insulation was computed. A traverse was then made with the specimen in place, and the amplifier gain increased as necessary. The average of this flux divided by the average flux incident upon the specimen was defined as the fractional transmission. If the electrical and thermal noise was appreciable, an additional traverse was made with the source shielded, and this signal was subtracted from both the unattenuated and attenuated readings. (The original data are tabulated in *11*.)

Table 1 gives the properties of the tested insulations. The specimens of commercial insulation were 11-in. squares and varied from $\frac{1}{8}$ to 1 in. in thickness. The specimens of unbonded glass fibers were cylinders 6 in. in diameter and less than $\frac{1}{2}$ in. in thickness. The mass, area, and thickness of the thickest specimens were measured and the bulk density computed. The thinner specimens were assumed to have the same bulk density, and their thickness was calculated from the mass and area. In all of the fibrous insulations the fibers were oriented perpendicular to the heat flux.

INTERPRETATION OF TRANSMISSION MEASUREMENTS

In terms of the components of the intensity previously defined, the flux incident upon the insulation is $I_1(0)$, and the transmitted flux is $I_1(L)$. Since the detector and insulation were at room temperature, and since the detector responded only to 10 cycle/sec. energy, reradiation from the fibers and surroundings was neglected. Equations (7) and (8) then reduce to

$$\frac{dI_1}{dx} = -MI_1 + NI_2 \qquad (23)$$

$$-\frac{dI_2}{dx} = -MI_2 + NI_1 \qquad (24)$$

and the boundary conditions can be written

$$I_1(0) = 1 \qquad (25)$$

and

$$I_2(L) = 0 \qquad (26)$$

The transmission is then

$$I_1(L) = \frac{1}{\cosh L\sqrt{M^2 - N^2} + \dfrac{M}{\sqrt{M^2 - N^2}} \cdot \sinh L\sqrt{M^2 - N^2}} \qquad (27)$$

Expanding Equation (27) in series one gets

$$I_1(L) = \frac{2\sqrt{M^2 - N^2}e^{-2L\sqrt{M^2-N^2}}}{M + \sqrt{M^2 - N^2}} \cdot \sum_{n=0}^{\infty} (-1)^{n+1} \cdot \left[\frac{M - \sqrt{M^2 - N^2}}{M + \sqrt{M^2 - N^2}}\right]^n \cdot e^{-2nL\sqrt{M^2-N^2}} \quad (28)$$

For $L\sqrt{M^2 - N^2} > 5$, the series in Equation (28) approaches unity. Under such conditions a semilog plot of transmission vs. thickness should yield a straight line. M and N could then be determined from the slope and intercept of the least square line through the data. A typical set of data is shown in Figure 5. It is evident that the logarithm of the transmission varies nearly linearly with large thickness in Figure 5 but must have curvature throughout to approach unity at zero thickness. Therefore the constants M and N were evaluated by successive approximation. First M and N were estimated from the straight-line region of the data. The series portion of Equation (28) was next evaluated by the use of the approximate values of M and N. The two groups of constants in the balance of Equation (28) were then evaluated by least squares, and M and N were calculated. This process was repeated as necessary. The curves shown in Figure 5 were obtained in this way.

Commercial Insulations

The experimentally determined values of the radiation parameters for four commercial insulations are plotted vs. source temperature in Figures 6 to 9. Since scattering and absorption depend primarily on the spectral distribution of the incident radiation rather than on the temperature of the material, these data are believed to be representative for insulations at these temperatures. As noted previously N and P are the cross sections per unit volume for back scattering and absorption respectively. The larger the values of N and P, the more effective is the insulation in reducing radiant transfer.

For the Foamglas N is much larger than P, an indication that scattering is predominant over absorption. The decrease in N with temperature is difficult to interpret without data on the index of refraction. P appears to be relatively independent of temperature, possibly owing to the absorptivity of the two major constituents, glass and carbon. Glass absorbs little in the visible range of wave lengths, moderately in the near infrared, and strongly in the far infrared. Carbon absorbs strongly in the visible but is relatively transparent in the infrared. As the temperature increases, the radiant energy shifts to shorter wave lengths, and the absorption may shift from glass to carbon.

For Styrofoam-22 N increases and P decreases with temperature. At 100°F. absorption is predominant, but above 150°F. back scattering predominates. Since the absorptivity of polystyrene is qualitatively similar to that of glass, the temperature dependence of P is understandable.

For the Fiberglas insulations absorption is negligible with respect to back scattering. The maximum in P for Fiberglas A is probably attributable to the bonding agent, which is 20 wt. % of the insulation, rather than to the glass.

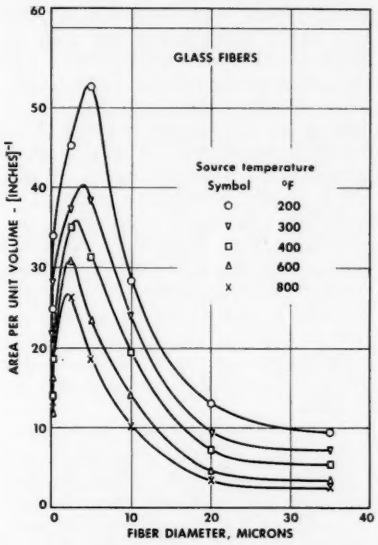

Fig. 10. Back-scattering cross-section N of glass fibers.

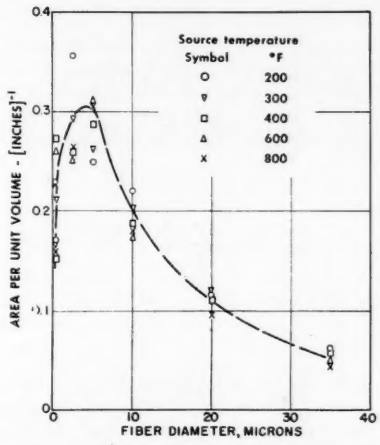

Fig. 11. Absorption cross-section P of glass fibers.

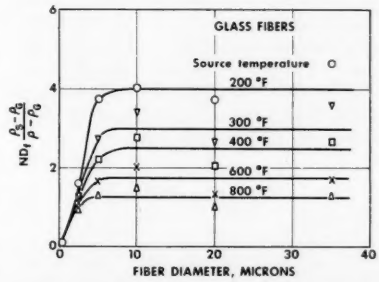

Fig. 12. Dimensionless scattering parameter for glass fibers.

Unbonded Glass Fibers

The values of N and P obtained with unbonded, uniformly sized glass fibers are shown in Figures 10 and 11. The fluence of fiber size on scattering is very great and demonstrates the maximum predicted by theory. The maximum shifts from about 5μ at 200°F. to about 2.5μ at 800°F.; P demonstrates similar behavior. The values of N and P are replotted in Figures 12 and 13 in the form which theory suggests should minimize dependence on fiber size for large fibers. The deviations due to experimental error are emphasized in this plot. Insufficient data were obtained to test the corresponding asymptotic relationships for small fibers.

Since the index of refraction and absorptivity of the glass fibers are not known as functions of wave length, the integration

$$BK_s(T, D_f, m) = \frac{\int_0^\infty B_\lambda K_{s\lambda} E_{\lambda T}\, d\lambda}{\sigma T^4} \quad (29)$$

was carried out with the use of theoretical values of $B_\lambda K_{s\lambda}$ (*11, 12*) for no absorption and fixed indices of 1.5, 2.0, and 2.5 (Figure 14). Qualitative agreement with the experimental data is demonstrated. This agreement is most significant, since it supports the theoretical basis for the correlation of the data and suggests that radiant transfer through insulations can be predicted quantitatively on the basis of the electromagnetic theory from measurements of the index of refraction and the absorptivity of the solid material only. However it should not be inferred from Figure 14 that the index of refraction of the fibers lies between 1.5 and 2.0, since the imaginary part of the index of refraction of glass is not zero, as assumed for the calculations.

COMPUTATION OF RADIANT TRANSFER

Equations (11) and (12) and the data in Figures 8 through 13 permit prediction of the rate of heat transfer by radiation through porous materials of the types tested for any fiber size, bulk density, temperatures, or boundary emissivities. These predictions will be illustrated

in terms of the radiant conductivity, defined as

$$k_r = \frac{I_1 - I_2}{\frac{-dT}{dx}} = \frac{q}{\frac{-dT}{dx}} \qquad (30)$$

$$- k_c = k - k_c$$

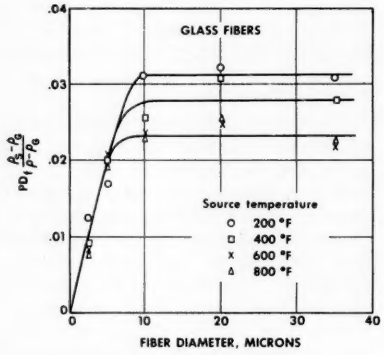

Fig. 13. Dimensionless absorption parameter for glass fibers.

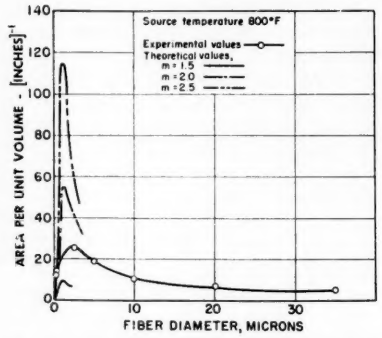

Fig. 14. Comparison of theoretically and experimentally evaluated parameters for glass fibers.

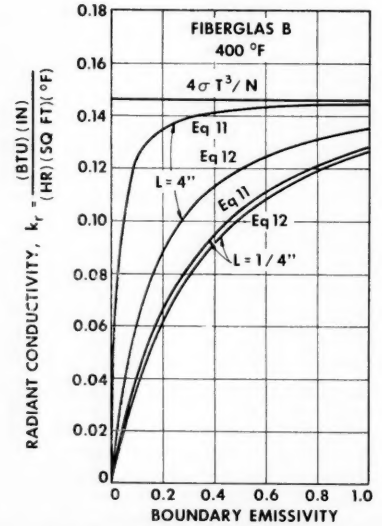

Fig. 15. Effect of boundary emissivity on radiant conductivity of Fiberglas *B*.

and in terms of the fraction of the heat transferred by radiation, k_r/k.

The absorption and scattering properties of materials are critically dependent upon the spectrum of the incident radiation but are essentially independent of the temperature of the material itself (*10*). Hence the data of this investigation, which were obtained with different source temperatures but with the material at room temperature, were correlated in terms of the source temperature. However these properties can be interpreted and applied in terms of the material temperature at any point in an insulation when the source of radiation is the surrounding material at essentially the same temperature. For simplicity the succeeding illustrative figures were prepared for a vanishingly small temperature difference and hence constant k_r and k_c. Similar plots taking into account the variation of k_c and k_r with temperature could readily be prepared for any specific temperature difference.

For all the materials investigated, except Styrofoam-22 below 150°F., absorption is sufficiently small so that Equation (11) is a fair approximation. It indicates that the effects of temperatures, boundary emissivities, fiber or pore size, and bulk density upon the radiant conductivity are dependent on the thickness of the insulation. However for thick slabs such that

$$L \gg \left(\frac{1}{\epsilon_0} + \frac{1}{\epsilon_L} - 1\right)/N$$

$$k_r = \frac{\sigma[T_0^2 + T_L^2][T_0 + T_L]L}{\frac{1}{\epsilon_0} + \frac{1}{\epsilon_L} - 1 + NL}$$

$$\rightarrow \frac{\sigma[T_0^2 + T_L^2][T_0 + T_L]}{N} \qquad (31)$$

$$\cong \frac{4\sigma T^3}{N}$$

Thus insofar as Equation (31) is a valid representation, the total heat transfer process in insulation can be treated as a conduction process with an effective conductivity that depends on temperature and the structure of the insulation but is independent of thickness and boundary conditions. If $[(1/\epsilon_0)+(1/\epsilon_L)-1] \gg NL$, the radiant conductivity of a nonabsorbing insulation depends critically upon the boundary emissivities and the thickness. If absorption is dominant ($M \gg N$), Equation (14) suggests that

$$k_r(0) \cong \frac{4\sigma\epsilon_0 T^3}{M} \qquad (32)$$

The dependence of the radiant conductivity of Fiberglas *B* (at the boundary) on thickness and boundary emissivity is indicated in Figure 15. The

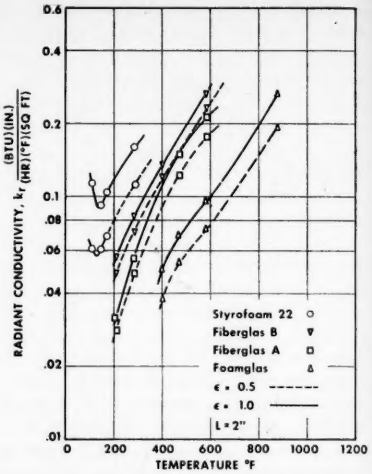

Fig. 16. Effect of temperature on radiant conductivity.

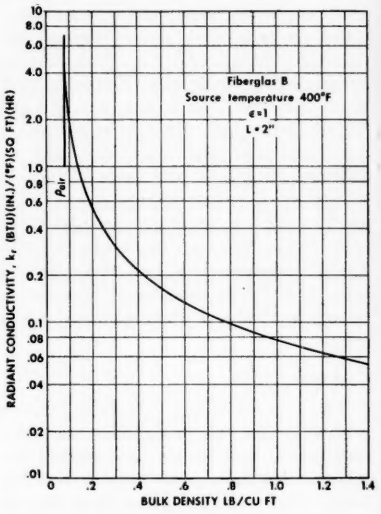

Fig. 17. Effect of bulk density on radiant conductivity of Fiberglas *B*.

limitations of the approximations represented by Equations (11) and (31) are also indicated.

Figure 16 illustrates the influence of temperature level on radiant transfer. Owing to the decrease in the radiation parameters with temperature, k_r is proportional to the second power or less of the absolute temperature rather than the third power predicted by earlier work. The importance of boundary emissivity is again apparent.

The effect of bulk density on radiant transfer through a fibrous insulation is illustrated in Figure 17. The curve terminates at a density of 0.07 lb./cu. ft., corresponding to no fibers, and a radiant conductivity corresponding to exchange between two infinite plates. The effect

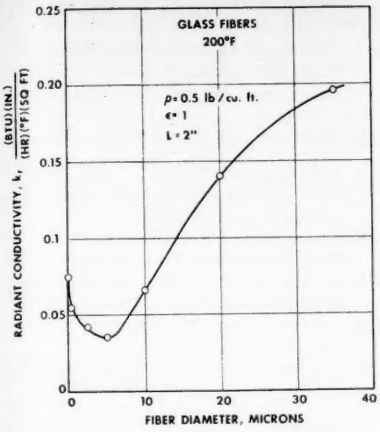

Fig. 18. Effect of fiber size on radiant conductivity of glass fibers.

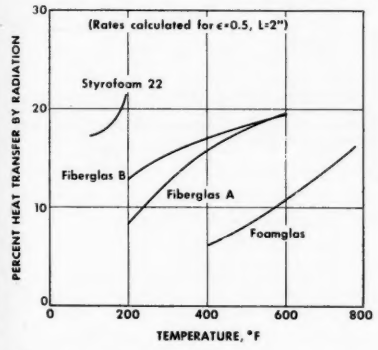

Fig. 19. Radiant contribution to heat transfer in insulations.

on foamed insulations is more complicated. If the bulk density is increased for a fixed bubble size, P increases and N decreases. The net effect depends upon the relative importance of scattering and absorption.

Figure 18 shows the variation of the radiant conductivity with fiber size. The optimum fiber size for the reduction of radiation is the same here as that which maximizes N, since absorption is negligible.

The fraction of the heat transfer due to radiation is plotted in Figure 19 for the commercial insulations. A boundary emissivity of 0.5 was arbitrarily assumed for these computations. A higher value of ϵ would lead to a greater radiant contribution. The total conductivities with which the radient conductivities are compared are given in Table 1. The computed rates of radiation are considerably less than those estimated by Verschoor and Greebler (*18*) from heat transfer data for evacuated fibrous insulations but are in relatively good agreement with the estimates of McIntire and Kennedy (*13*) for foamed insulations. Figure 19 should not be construed as a comparison of the merits of the three types of insulation. Other insulations of the same types could undoubtedly be chosen to reverse the relative magnitudes of the radiant conductivities.

SUMMARY AND CONCLUSIONS

A simple model has been developed for radiant transfer through porous insulating materials. The two parameters in this model can in principle be evaluated from electromagnetic wave theory, but the monochromatic index of refraction and absorptivity which is required is not currently available for the materials used in insulations. Illustrative calculations for arbitrary indices of refraction are in qualitative agreement with values obtained from black-body transmission measurements. The experimental values of the parameters permit calculation of radiant transfer for a wide range of conditions and materials.

Radiation contributes 5 to 20% of the heat transfer through typical insulations of Fiberglas, Foamglas, and Styrofoam. Scattering is the primary mechanism for the restriction of radiation in Fiberglas and Foamglas, but either scattering or absorption may be controlling in Styrofoam depending on the temperature. Consequently increasing the bulk density decreases the radiant transfer through Fiberglas and Foamglas but may increase or decrease the transfer through Styrofoam. In view of the small absorption by all the insulations tested, the addition of strongly absorbing materials should be effective.

The radiant conductivity is proportional to the second power or less of the absolute temperature for all the materials tested. Calculations indicate that the emissivity of the material bounding the insulation may be important under some circumstances. An optimum diameter in the range from 2 to 5μ exists for the restriction of radiation through glass fibers, and an optimum pore size is presumed to exist for foamed materials.

Table 1. Physical Properties of Insulations Studied

Insulation	Manufacturer	Reference	Mean fiber or pore size, μ	Bulk density, lb./cu. ft.	Temperature, °F.	k*, B.t.u./(hr.) (sq. ft.) (°F./in.)
Styrofoam-22	Dow Chemical	*16*	0.05 (in.)	1.8	50	0.26
					100	0.295
					150	0.335
Foamglas	Pittsburgh Corning	*7*	0.05 (in.)	9.0	100	0.43
					200	0.50
					300	0.55
					400	0.62
					500	0.62
Fiberglas *A*	Owens Corning Fiberglas	*9*	1.0	0.6	100	0.24
					200	0.32
					300	0.42
					400	0.58
Fiberglas *B*	Owens Corning Fiberglas	*9*	3.0	0.6	100	0.31
					200	0.43
					300	0.595
					400	0.83
Unbonded glass fibers	Owens Corning Fiberglas	*9*	0.17	0.50		
			0.20	0.50		
			2.5	0.50		
			5.0	0.50		
			10.0	0.50		
			20.0	0.50		
			35.0	0.50		

*These values were interpolated and extrapolated from data given in the references.

ACKNOWLEDGMENT

K. F. Gordon, R. L. Hess, C. W. Peters, and J. L. York of The University of Michigan and Marion Hollingsworth, Jr., of the Owens Corning Fiberglas Corporation provided invaluable advice. J. H. Chin, George C. Clark, and Phillip H. Scott assisted directly in the work. Insulations were provided by the Dow Chemical Company and the Pittsburgh Corning Corporation and special materials as well as insulations by the Owens Corning Fiberglas Corporation. Financial support was provided B. K. Larkin by the E. I. du Pont Fellowship in Chemical Engineering.

NOTATION

B = fraction of scattered radiation scattered into the background hemisphere.
D_f = fiber diameter
E_T = emission function
$I_1(x)$ = radiant flux density in the forward (positive x) direction
$I_2(x)$ = radiant flux density in the backward (negative x) direction
K_a = absorption coefficient of a fiber or pore; ratio of absorbed to geometrically obstructed radiation
K_s = scattering coefficient of a fiber

or pore; ratio of scattered to geometrically obstructed radiation

k = effective total conductivity
k_c = effective conductivity for gaseous conduction, solid conduction, and natural convection only
k_r = equivalent conductivity for radiation
L = thickness of insulation
M = interception cross section per unit volume of insulation
m = index of refraction
N = back scattering cross section per unit volume of insulation
n = number of scatters per unit volume
P = absorption cross section per unit volume of insulation
q = total heat-flux density (a constant across insulation)
$q_r(x)$ = net radiant heat-flux density
R = pore radius
S_a = absorption (and emission) cross section per scatter
S_s = scattering cross section per scatter
$T(x)$ = absolute temperature
x = distance through insulation
y = mean thickness of solid associated with a pore

Greek Letters

β = exponential absorption coefficient of solid material
ϵ = emissivity of boundary surface of insulation
λ = wave length
ρ = bulk density
ρ_G = gas density
ρ_S = solid density
σ = Stefan Boltzmann constant

Subscripts

0 — at $x = 0$ boundary
L — at $x = L$ boundary
λ — monochromatic

LITERATURE CITED

1. Allcut, E. A., Inst. Mech. Engrs. London, 232 (1951).
2. Bosworth, R. L. C., "Heat Transfer Phenomena," John Wiley, New York (1952).
3. Chu, C. M., G. C. Clark, and S. W. Churchill, "Angular Distribution Coefficients," Univ. Michigan Press, Ann Arbor, Michigan (1957).
4. Chu, C. M., and S. W. Churchill, *Trans. Inst. Radio Engrs.*, **AP-4**, 2, 142 (1956).
5. ———, *J. Phys. Chem.*, **59**, 855, (1955).
6. Clark, G. C., C. M. Chu, and S. W. Churchill, *J. Opt. Soc. Am.*, **47**, 81, (1957).
7. "Foamglas Insulation for Piping and Process Equipment," Pittsburgh Corning Corp., Pittsburgh, Pennsylvania (1951).
8. Hamaker, H. C., *Phillips Research Repts.*, **2**, 55, 103 (1947).
9. Hollingsworth, Marion, Jr., Owens Corning Fiberglas Corp., Newark, Ohio, private communication.
10. Jakob, Max, "Heat Transfer," Vol. I, John Wiley, New York (1949).
11. Larkin, B. K., Ph.D. thesis, Univ. Michigan, Ann Arbor, Michigan (1957).
12. ———, and S. W. Churchill, *J. Opt. Soc. Am.*, **49**, 188 (1959).
13. McIntire, O. R., and R. N. Kennedy, *Chem. Eng. Progr.*, **44**, 727 (1948).
14. Mie, Gustav, *Ann. Physik*, **25**, 377 (1908).
15. Schuster, Arthur, *Astrophys. J.*, **21**, 1 (1905).
16. "Styrofoam," The Dow Chemical Company, Midland, Michigan (1955).
17. Topper, Leonard, *Ind. Eng. Chem.*, **47**, 1377 (1955).
18. Verschoor, J. D., and Paul Greebler, *Trans., Am. Soc. Mech. Engrs.* **74**, 961 (1952).

Manuscript received May 21, 1958; revision received November 24, 1958; paper accepted November 28, 1958. Paper presented at A.I.Ch.E. Montreal meeting.

The Economic Design of Mixer-Settler Extractors

ROBERT E. TREYBAL

New York University, New York, New York

Relationships are developed for establishing the most economic values of the major variables of a liquid-extraction process, including the concentrations of solute in recycled solvent and rejected raffinate, the solvent-to-feed ratio, and for mixer-settlers certain of the design features. Consideration is given to costs of extraction and solvent recovery, as well as to the value of unextracted solute and lost solvent. For the design of mixer settlers scale-up relationships are developed to permit prediction of the stage efficiency of a large extractor from experimental data taken on a small scale. These are expressed in terms of a scale-up index relating the relative size of the mixer with the volumetric rates of liquid flow. It is shown that the cost of a multistage extractor increases with scale up in a different fashion from the stage efficiency, depending upon the scale-up index used. A detailed study of the costs for a typical case led to the development of economic scale-up indexes which, because they cover nearly a fivefold ratio of fixed to operating costs, are of fairly general utility. The common practice of scaling up with equal holding times on the large and small scale is shown to be amply safe from the point of view of stage efficiency to be realized on the large scale but usually uneconomic.

Simplification of the complete system of equations permits rapid estimation of the most economic circumstances for any type of countercurrent extractor of which the cost per stage is proportional to Q^a.

Despite the facts that mixer settlers are probably the oldest form of commercial liquid extractors and that new countercurrent tower devices are invented every year, mixer settlers have never been wholly superseded. In recent years there has even been an increased tendency to use them. The many reasons for this need not be dwelt upon here. It is sufficient to note that it is generally believed that small-scale experiments provide a reliable guide to the design of large-scale equipment.

Although there have been a number of new mixer-settler designs in the past few

years, the simplest arrangement consists of a combination of an agitated vessel (the mixer) through which the liquids to be contacted are passed and a settler in which the dispersion of liquids is settled by gravity. The two vessels constitute one stage, not necessarily ideal, and any number of stages may be joined to provide multistage, countercurrent effects. It is common procedure to determine the stage efficiency in a small-scale mixer and to scale up to a larger size by providing in the large scale equal agitator power per unit volume of liquids and a geometrically similar mixing vessel sized so as to provide equal holding time for both large and small scale. When the stage efficiency of the small vessel is essentially 1.0 (or 100%), this is said to give good results [Warner (*12*) for example]. It will be shown that these practices are almost certain to give good results but may be uneconomical.

What is really required is not merely a method of scale-up to produce a predictable performance but also a set of conditions for the large scale which results in the least cost of extraction. It is desirable not to be bound by the circumstances under which the small-scale experiment was run, since these may not necessarily be those which lead to the optimum large-scale plant. The scale-up procedure should therefore be adjustable so as to produce the optimum plant.

It is useful to consider the factors which enter into the cost of an extraction operation, the quantities which the designer may vary, and where the latter influence the costs. The total annual cost of extracting a solute from a feed solution may be considered to be the sum of six cost quantities, as outlined in Table 1. If a flow rate of feed solution, the concentration of contained solute, and the identity of the solvent to be used are stipulated, the quantities which may be set to produce an optimum arrangement are those listed in the lower part of Table 1, together with the cost items which each influences. A few of these have been studied in the recent literature (*6, 9*) without however full consideration of some important interrelationships which exist among them. It is the purpose here to present a more detailed and less restrictive study.

To minimize the total cost one must partially differentiate C_T with respect to each of the variable quantities while holding the others constant, set the resulting expressions equal to zero, and solve them simultaneously. The major assumptions made in the course of this development are listed in Table 2.

DESIGN OF EXTRACTOR STAGES

Item I, Table 1, is the only cost quantity which need be considered. The annual cost of a multistage, countercurrent extractor of n ideal stages and E_0 over-all stage efficiency may be described as

$$\mathrm{I} = nC_E/E_0 \qquad (1)$$

where

$$n = \frac{\log\left[\dfrac{(c_F - c_S/m)}{(c_R - c_S/m)}(1 - 1/mR) + 1/mR\right]}{\log mr} \qquad (2)$$

$$E_0 = \frac{\log\left[1 + E_M(mR - 1)\right]}{\log mR} \qquad (3)$$

$$C_E = C_V\left(\frac{p}{Y} + b\right) + (P_A + P_P)WH \qquad (4)$$

The number of ideal stages is quite independent of the stage design, whereas C_E and E_0 are affected, the latter through the stage efficiency of each stage E_M. Consequently

$$\frac{\partial \mathrm{I}}{\partial\,(\text{design})} = \frac{n\,\partial(C_E/E_0)}{\partial\,(\text{design})} \qquad (5)$$

and for optimum design

$$\frac{\partial(C_E/E_0)}{\partial\,(\text{design})} = 0 \qquad (6)$$

Stage Efficiency

The discussion here is limited to baffled mixing vessels in the form of vertically disposed circular cylinders of height equal to diameter, with centrally located flat-blade turbines as the agitating devices. For these it has been shown (*11*) that it is possible to estimate the stage efficiency. The relationships required lead to two dimensionless quantities, $X = mk_c d_p/2D_D'$ and $Z = 2mk_c\theta/d_p$, which together with the chart of Figure 1 permit estimation of the efficiency. Figure 1 is reproduced here in simplified form for purposes of demonstration later, and the earlier paper should be consulted for a working chart. Some of the relationships of that development are not well established, particularly several coefficients and the effective diffusivity. For this reason small-scale experiments are carried out. When the relationships are used only in ratio for scale up in the same chemical system and under conditions to be described, the uncertain quantities cancel out.

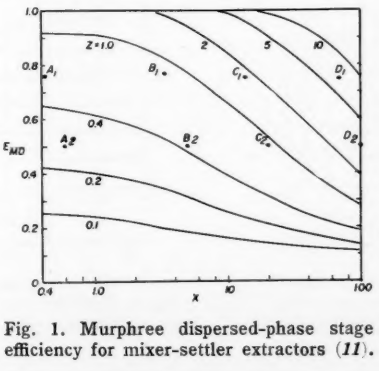

Fig. 1. Murphree dispersed-phase stage efficiency for mixer-settler extractors (*11*).

It is undoubtedly sound practice to scale up by using geometrically similar vessels (*4*). The use of equal power per unit volume of liquids, theoretically (*4*) and also according to the limited data available (*11*), will provide for equal degrees of dispersion of one of the liquids in the other. There remains the question of holding time. As indicated earlier equal holding time on small and large scale is common practice. Provision for equal mass velocities of the liquids might also be considered a logical scale up basis and this will mean an increase in holding time on the large scale. Equal holding times means a reduced mass velocity. The use of unequal holding times and mass velocities is certainly a possibility.

To investigate the effect of scale up of rate of flow on stage efficiency when all extraction conditions except total flow rate remain constant, a scale-up index is defined by Equation (7):

$$\frac{T_1}{T_2} = \left(\frac{Q_1}{Q_2}\right)^x \qquad (7)$$

Geometrically similar vessels and agitator turbines are specified so that

$$\frac{L_1}{L_2} = \frac{T_1}{T_2} \qquad (8)$$

In order that the fraction of the vessel contents devoted to dispersed phase be constant equal power per unit volume of flowing liquids will be applied (*11*):

$$\frac{P_1}{Q_1} = \frac{P_2}{Q_2} \qquad (9)$$

If the agitator Reynolds number is sufficiently large, the power number $Pg_c/\rho N^3 L^5$ remains constant. Under these circumstances it is possible to show* that the ratios of X and Z for scale up are

$$\frac{X_1}{X_2} = \left(\frac{Q_1}{Q_2}\right)^{0.322x+0.066} e^{0.70(T_2 - T_1)} \qquad (10)$$

$$\frac{Z_1}{Z_2} = \left(\frac{Q_1}{Q_2}\right)^{1.151x-0.592} e^{0.70(T_1 - T_2)} \qquad (11)$$

*Tabular material has been deposited as document 5968 with the American Documentation Institute, Photoduplication Service, Library of Congress, Washington 25, D. C., and may be obtained for $1.25 for photoprints or 35-mm. microfilm.

Table 1. Extraction Costs

C_T = I + II + III + IV + V + VI
C_T = annual total cost of extraction process
I = annual cost of multistage extractor
II = annual value of unextracted solute
III = annual cost of solvent recovery from the extract
IV = annual cost of solvent recovery from the raffinate
V = annual cost of lost solvent
VI = annual labor cost

Quantities to be optimized

Quantity	Cost term affected
1. Design of extractor stages	I
2. Concentration of solute in raffinate	I, II, III
3. Concentration of solute in recycled solvent	I, III
4. Solvent-to-feed ratio	I, III, V
5. Concentration of solvent left in product	III, V
6. Concentration of solvent in stripped raffinate	IV, V
7. Reflux ratio for solvent recovery from extract by distillation, or similar item if another operation is used	III
8. Reflux ratio for solvent recovery from raffinate by distillation	IV

Table 2. Major Assumptions

1. Constant annual labor cost.
2. Insolubility of solvent and feed.
3. Constant equilibrium distribution coefficient.
4. One solute extracted in a countercurrent multistage extractor.
5. On scale-up of mixer settlers,
   a. Geometrically similar, baffled mixers, height = diameter.
   b. Agitation with flat-blade turbine impellers.
   c. Equal agitator power to liquids per unit volume flow rate of liquids.
6. Constant Murphree stage efficiency of all stages in any one multistage cascade.
7. Constant relative volatility of solvent and extracted solute.
8. Loss of solvent in distilled product and stripped raffinite negligible.
9. Solvent loss proportional to number of extraction stages and solvent circulation rate.

For equal mass velocities in small and large scale $x = 0.5$; for equal holding times $x = 1/3$. Figures 2, 3, and 4 were prepared from these equations for these values of x and also for $x = 0.25$.

To demonstrate the method of developing the scale-up charts the case for $x = 0.5$, $T_2 = 1$, $E_{MD2} = 0.5$, and $Q_1/Q_2 = 4$ is considered. It follows that $T_1 = 2$ [Equation (7)], $X_1/X_2 = 0.68$ [Equation (10)], and $Z_1/Z_2 = 1.97$ [Equation (11)]. When one refers to Figure 1, it is clear that there are any number of combinations of X_2 and Z_2 corresponding to $E_{MD2} = 0.5$, but fortunately this does not have important influence on the final result. Thus when one starts with points A_2, B_2, C_2, and D_2 at $E_{MD2} = 0.5$, Figure 1, the scale-up relations provide the points A_1, B_1, C_1, and D_1, where the corresponding values of E_{MD1} are 0.76, 0.77, 0.75, and 0.74 respectively, averaging 0.754. The same averaging procedure was used throughout in establishing the scale-up charts, and nowhere were the variations in E_{MD1} any greater. On Figure 2 therefore point A corresponds to $E_{MD2} = 0.5$, $T_2 = 1$, and scale-up to $Q_1/Q_2 = 4$ provides B at $T_1 = 2$, relative volume rate = 4, $E_{MD1} = 0.754$.

The curves of Figures 2, 3, and 4 then become scale-up paths for the corresponding values of x. Thus it may be supposed that by experiment it is known that in passing 150 cu. ft./hr. of extracting liquids through a mixer 1.4 ft. in diam. a stage efficiency $E_{MD2} = 0.25$ is obtained. It is desired to estimate the stage efficiency for 1,500 cu. ft./hr. of liquids, scaled up according to the conditions established earlier with $x = 0.5$. The known conditions correspond to point C on Figure 2, where the relative volume rate of flow is 1.95. For a tenfold increase in flow rate the relative volume rate of flow is 19.5, the new conditions correspond to point D, and the new stage efficiency is $E_{MD1} = 0.94$. The corresponding tank diameter is 4.4 ft.

Figure 3 shows that scale up according to equal holding time from tanks 1-ft. diameter or larger always results in an appreciable improvement in stage efficiency. Constancy of stage efficiency on scale up is most nearly realized for $x = 0.25$ over the middle range of Figure 4. Truly constant stage efficiency would evidently require adjustment of the agitator power.

With the volume flow rate, the distribution coefficient, and the individual stage efficiency assumed the same for all stages, the over-all efficiency of the large extractor is given by Equation (3), with $E_M = E_{MD1}$. E_{01} thus depends, through E_{MD} and Figures 2 through 4, upon Q_1/Q_2 and x.

Extractor Costs

The vessel sizes and hence the costs per real stage at a given scale-up ratio Q_1/Q_2 are less at low values of x, but

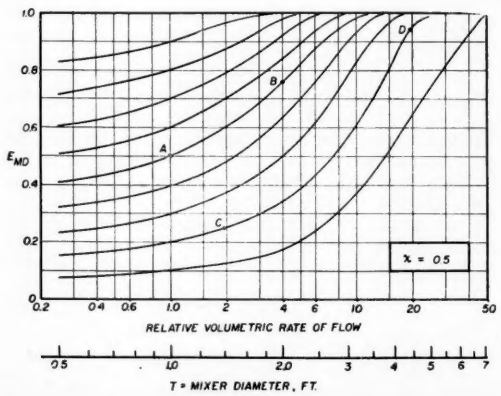

Fig. 2. Scale up at constant solvent/feed ratio, $x = 0.5$. Basis: geometrically similar vessels and equal power input per unit volumetric rate of flow.

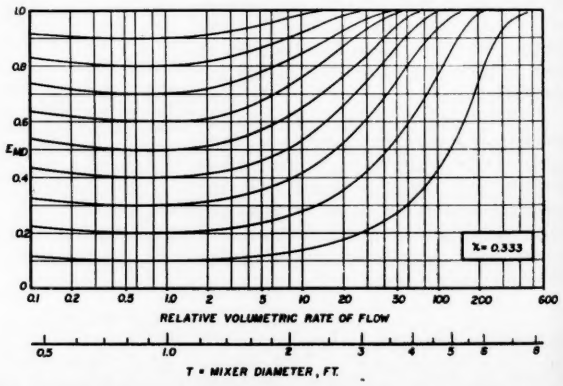

Fig. 3. Scale up at constant solvent/feed ratio, $x = 0.333$. Basis: geometrically similar vessels and equal power input per unit volumetric rate of flow.

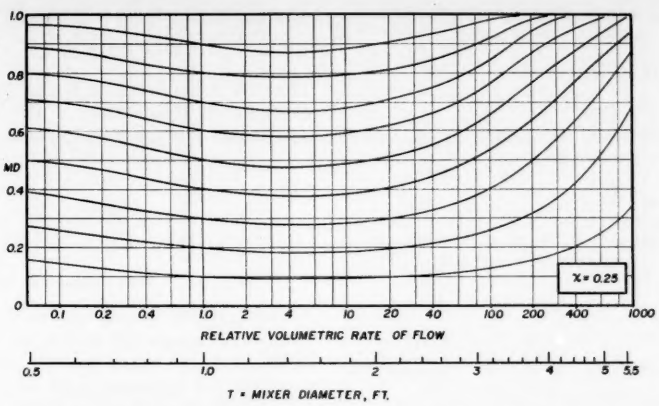

Fig. 4. Scale up at constant solvent/feed ratio, $x = 0.25$. Basis: geometrically similar vessels and equal power input per unit volumetric rate of flow.

since the stage efficiency is also less, more real stages are required. It follows that there should be a most economical x.

When one refers to Equation (4), the major equipment cost per stage is

$$C_V = C_M + C_A + C_S + C_P \qquad (12)$$

Data on costs of equipment and their variation with size were taken for the most part from the recent books by Aries and Newton (*1*) and Peters (*8*). For the empty mixer

$$C_{M1} = C_{M2}(V_1/V_2)^{0.55} = C_{M2}(Q_1/Q_2)^{1.65x} \qquad (13)$$

When one assumes that the settler increases in volume directly with that of the liquids to be handled

$$C_{S1} = C_{S2}(Q_1/Q_2)^{0.55} \qquad (14)$$

For the pumps

$$C_{P1} = C_{P2}(q_1/q_2)^{0.333} = C_{P2}(Q_1/Q_2)^{0.333} \qquad (15)$$

There may be either two pumps per stage if both liquids are pumped between stages, one if one of the liquids flows by gravity, or none if both flow by gravity. The agitating equipment covered by C_A includes the impeller shaft, stuffing box, explosion-proof motor, geared speed reducer, and mounting and support. It was found that the costs of these unfortunately must be established for specific cases. For example the shaft diameter and length depend on the vessel size, power, and speed. No simple generalization of the sort used for the other costs was possible.

When one assumes that the efficiency of the transmittal of power to the agitated liquids remains constant,

$$P_{A1} = P_{A2}(Q_1/Q_2) \qquad (16)$$

A few calculations for typical cases indicated that pump power for overcoming pipe friction was the only important consideration for this item. The power for pumping the dispersed liquid from stage to stage through piping is (*7*)

$$P_{P1} = K(q_D\rho_D)^{2.84}/d^{4.84}\rho_D^{2} \qquad (17)$$

and the economical pipe diameter is (*7*)

$$d = K'(q_D\rho_D)^{0.448}/\rho_D^{0.312} \qquad (18)$$

Combining Equations (17) and (18) and taking ratios at constant pump efficiency for the large and small scale, one gets

$$P_{P1} = P_{P2}(q_{D1}/q_{D2})^{0.67} = P_{P2}(Q_1/Q_2)^{0.67} \qquad (19)$$

A similar relation applies to a pump for the continuous phase.

It was indicated above that the cost of agitating equipment must be estimated for particular cases. To come to some conclusions about the scale-up index, a set of conditions were chosen which are believed to be representative of good practice, and the costs were determined. From the study of a fivefold variation in the payout time, thus covering a wide variation in the ratio of fixed to operating costs, it is thought that the conclusions become reasonably general. In any case the relative importance of many of the variables can be demonstrated. Table 3 lists the details of the chosen situation.

In the case of the agitating equipment the costs for recommended equipment with the customary allowances for power overload and discount were determined for several values of Q and the corresponding speed, power, and mixer size at each value of x studied (*5*). The resulting costs are shown in Figure 5. Figure 6 shows the uninstalled cost of major equipment, less pumps per stage. For values of Q_1 from 500 to 5,000 cu. ft./hr. these may be closely represented by

$$C_{M1} + C_{S1} + C_{A1} = 730(Q_1/100)^{0.520x+0.365} \qquad (20)$$

When one includes the single pump per stage, the costs are given closely by

$$C_{V1} = 1000(Q_1/100)^{0.468x+0.332} \qquad (21)$$

Annual costs were then computed for $Q_1/Q_2 = 5$ to 100; $Y = 1$, 2, and 5; extraction factor $mR = 0.05$ to 20; E_{MD2} in the small scale = 0.3 to 1.0;

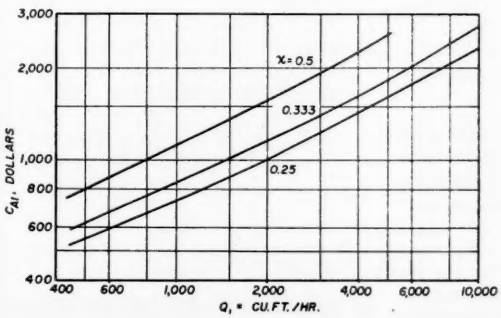

Fig. 5. Uninstalled cost of agitating equipment for one extraction stage. Basis: 12.5 gal./min. through a 1.5-ft.–diameter vessel, agitation intensity 1,000 (ft. lb./hr.)/(cu. ft./hr.).

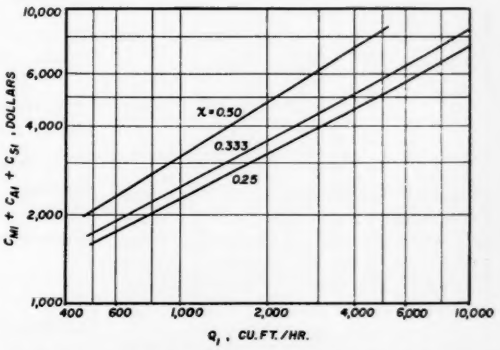

Fig. 6. Uninstalled cost of major equipment less pumps for one extraction stage. Basis: 12.5 gal./min. through a 1.5-ft.–diameter vessel, agitation intensity 1,000 (ft. lb./hr.)/(cu. ft./hr.).

Table 3. Conditions for Studying the Economic Scale-Up Index

Small-scale conditions

Total liquid flow, solvent + feed = 12.5 gal./min.; $Q_2 = 100$.
Mixing Vessel: diameter $T_2 = 1.5$ ft., $C_{M2} = \$123$.
Settling vessel: 10 min. holding time, 16.7 cu. ft.; $C_{S2} = \$338$.
Agitator: power to liquids = 0.05 horsepower = 1,000 (ft.-lb./hr.)/(cu. ft./hr.) $T/L = 3$, Efficiency of gear reducer and stuffing box = 0.90; of motor 0.85.
$P_{A2} = 0.05/(0.9)(0.85) = 0.066$ hp.
Pump: one per stage, pumping half the liquid (50 cu. ft./hr.).
$C_{P2} = \$235$; pump efficiency = 0.50; motor efficiency = 0.85.
Pipe: 1 in.; equivalent length including valves and fittings = 80 ft./stage; 2 enlargements 2 contractions/stage; change in elevation = 1 ft./stage. Pump power output = 0.051 hp., $P_{P2} = 0.051/0.50(0.85) = 0.12$ hp.

Large-scale conditions

Cost of agitator C_{A1}: see Figure 5.
Cost of power = \$0.015/kw.-hr. $W = \$0.0112$/(hp.)(hr.)
Annual time of operation $H = 7{,}200$ hr./yr.
Uninstalled cost of instruments = $0.15C_V$
Installation cost for vessels, agitators, pumps, instruments = $0.43\ (C_V + 0.15C_V)$
Installed cost of piping = $0.86C_V$
$p = 1 + 0.15 + 0.43(1 + 0.15) + 0.86 = 2.50$
Maintenance: $b = 0.06$

and $x = 0.25$ to 0.50. Values of x outside this range were not considered. At values of x below 0.25 the intensity of agitator-power input into relatively small vessels makes agitator selection difficult, and since computed droplet size decreases, there is increased likelihood of forming emulsions difficult to settle. Values of x above 0.5 are of use only for cases of unreasonably poor small-scale efficiency.

Economic Scale-Up Index

The most economical x, providing for minimum cost, is given by Equation (6). Since the charts of Figures 2 though 4, which cannot be conveniently expressed algebraically, are involved in the evaluation of E_{01}, a graphical procedure was used. Thus one may plot C_{E1}/E_{01} against x and observe the minimum at the economic x. Alternatively

$$\frac{\partial(C_{E1}/E_{01})}{\partial x} = (p/Y + b) \cdot \frac{\partial(C_{V1}/E_{01})}{\partial x} + (P_{A1} + P_{P1}) \cdot \frac{WH\ \partial(1/E_{01})}{\partial x} = 0 \qquad (22)$$

from which

$$\frac{\partial(C_{V1}/E_{01})/\partial x}{\partial(1/E_{01})/\partial x} = \frac{\partial(C_{V1}/E_{01})}{\partial(1/E_{01})} = \frac{-(P_{A1} + P_{P1})WH}{(p/Y) + b} \qquad (23)$$

One may therefore plot C_{V1}/E_{01} and $1/E_{01}$ against x and determine the value of x when the ratio of the slopes of the two curves equals the right-hand side of Equation (23); one may determine the value of x where the slope of a curve of C_{V1}/E_{01} vs. $1/E_{01}$ has this value

The results are summarized in Figure 7, and the economical x is independent of Y in the range studied. As the stage efficiency in the small scale becomes larger, the economical x becomes small. For $E_{MD2} = 1$ it will be 0.25 for all situations studied, since then $E_{01} = 1$, the costs per real stage and ideal stage are the same, and C_V is least for $x = 0.25$.

While these conclusions are necessarily dependent upon the circumstances chosen for study, it is believed that they may be generally useful as a guide to economical scale up for fairly wide variations in the quantity of liquid passed through the 1.5-ft.-diameter mixer, provided that the agitator power to the liquids in the 1.5-ft. tank is fixed at 0.05 hp. and that the abscissa of Figure 7 is considered as Q_1/Q_2 rather than $Q_1/100$.

It is fully recognized furthermore that these results represent only a limited consideration of the design features, those which are presently amenable to attack through the scaling up of small-scale experiments.

CONCENTRATION OF SOLUTE IN RAFFINATE AND RECOVERED SOLVENT

For the establishment of the most economic values of the concentration of solute in the raffinate from the extractor and in the recovered solvent the cost equations of Table 1 could be differentiated formally. For this purpose the cost of unextracted solute may be described as

$$\text{II} = Fq_Fc_RH \qquad (24)$$

The cost of distillation of the solvent was expressed in the manner of Happel (*3*) adapted to the present problem:

$$\text{III} = \frac{C_dn_d(p/Y + b)(O)(1 + r)}{E_dG_d} + \frac{C_h(p/Y + b)(O)(1 + r)}{G_h} + C_{hc}(O)(1 + r)H \qquad (25)$$

where

$$n_d = \gamma n_{d\min} \qquad (26)$$

The minimum number of ideal distillation trays can be obtained from the well-known Fenske equation. Where the solvent is the more volatile component of the extract

$$n_{d\min} = \frac{\log\left(\frac{\text{moles solvent/hr.}}{\text{moles solute/hr.}}\right)_{dist}}{\log \alpha} + \frac{\log\left(\frac{\text{moles solute/hr.}}{\text{moles solvent/hr.}}\right)_{botts}}{\log \alpha} - 1 \qquad (27)$$

where *dist* and *botts* refer respectively to distillate and still bottoms. If the solute is the more volatile, these subscripts are interchanged. For the case shown above the amount of solute in the botts, which is the product of the entire extraction process, is essentially that in the extractor feed and is independent of c_S. Product-purity specifications ordinarily require negligible solvent to be found in the botts, and the numerator of the first term on the right is essentially the entire flow rate of solvent. Therefore

$$\left(\frac{\text{moles solvent/hr.}}{\text{moles solute/hr.}}\right)_{dist} = \frac{q_FR\rho_S/M_S}{q_FRc_S/M_E} = \frac{\rho_SM_E}{M_Sc_S} \qquad (28)$$

The ultimate results, for either type of volatility, are*

$$\text{Econ.}\quad c_S = \frac{m\gamma C_d(p/Y + b)(O)(1 + r)}{E_dG_dFq_FH\ \ln \alpha} = \frac{m\gamma C_d(p/Y + b)B}{E_dG_dFq_FH\ \ln \alpha} \qquad (29)$$

where $B = O\ (1 + r)$, to be elaborated upon later.

$$\text{Econ.}\ (c_R - c_S/m) = (c_F - c_S/m) \cdot \frac{(1 - mR)}{2}\ (1 \pm \sqrt{J}) \qquad (30)$$

where

$$J = 1 + \frac{4C_E}{(c_F - c_S/m)Fq_FHE_0(mR - 1)\ \ln mR} \qquad (31)$$

In Equations (30) and (46) the negative square root is used if mR exceeds unity, the positive if mR is less than unity. In

*See footnote on page 475.

Equation (31) it is usually satisfactory to neglect c_S/m in comparison with c_F.

SOLVENT-TO-FEED RATIO

The solvent-to-feed ratio R affects cost items I, III, and V. Therefore

$$\frac{\partial C_T}{\partial R} = \frac{\partial \mathrm{I}}{\partial R} + \frac{\partial \mathrm{III}}{\partial R} + \frac{\partial \mathrm{V}}{\partial R} = 0 \qquad (32)$$

Effect on Extractor

The flow rate of feed to be extracted, that to be used on the large scale, remains constant, and it follows that the total volume of liquid through the extractor varies with the flow rate of solvent. The stage efficiency and consequently the extractor cost is therefore dependent upon the scale-up index used to establish the varying size of the stages while allowing R to vary. Since R also enters into Equation (2), then

$$\frac{\partial \mathrm{I}}{\partial R} = \frac{\partial (nC_E/E_0)}{\partial R} \qquad (33)$$

In studying the effect of R on C_E and E_0 it will be assumed that the cost of a large-scale extractor and its stage efficiency is known at some solvent/feed ratio R_1, and total liquid flow rate $Q_1 = q_F(R_1 + 1)$. These may be obtained, if necessary, from scale up of laboratory data in the manner described earlier. The variation of these with R on the large scale is then to be determined.

For geometrically similar mixers

$$\frac{T}{T_1} = \left(\frac{Q}{Q_1}\right)^x = \left(\frac{R+1}{R_1+1}\right)^x \qquad (34)$$

If sufficient agitator power, approximately 1,000 (ft. lb./hr.)/(cu. ft./hr.) or more (*11*), is used, the holding time for both continuous and dispersed phases within the vessel are equal. When one assumes equal power/volumetric rate of flow for the mixing, as before, the relationships used earlier (*11*) provide the equations of Table 4. The over-all efficiency may then be computed through Equation (3) Table 4 also shows the variation of costs with R, except for the agitating device which cannot be generalized in this manner. However if the basis for Figure 6 and Equations (20) and (21) is suitable, these may be used to compute C_V.

The number of ideal stages is given by Equation (2), which, together with Equation (30), provides

$$\text{Econ.} \quad n = \frac{\log\left[1 - 2/(1 \pm \sqrt{J})\right]}{\log mR} - 1 \qquad (46)$$

It is noteworthy that the varying values of c_S and c_R which enter into Equation (46) alter the usual n vs. R relationship obtained when these concentrations are held constant very considerably.

Table 4. Scale-Up for Constant Feed Rate, Varying Solvent/Feed Ratio, Geometrically Similar Vessels, and Equal Power/Volume Rate of Flow

Feed (raffinate) continuous, solvent (extract) dispersed

$q_F = q_C$ = constant, q_D varies, $R = q_D/q_C$

$$\frac{X}{X_1} = \left(\frac{R}{R_1}\right)^{0.43}\left(\frac{R+1}{R_1+1}\right)^{0.322x-0.299}\left(\frac{\rho_D R + \rho_C}{\rho_D R_1 + \rho_C}\right)^{0.645} \cdot \left[\frac{R_1\left(1 + \frac{1.5\mu_D}{\mu_C + \mu_D}\right) + 1}{R\left(1 + \frac{1.5\mu_D}{\mu_C + \mu_D}\right) + 1}\right]^{0.71} e^{0.70(T_1 - T)} \qquad (35)$$

$$\frac{Z}{Z_1} = \left(\frac{R_1}{R}\right)^{0.43}\left(\frac{R+1}{R_1+1}\right)^{1.151x+0.246}\left(\frac{\rho_D R + \rho_C}{\rho_D R_1 + \rho_C}\right)^{0.302} \cdot \left[\frac{R_1\left(1 + \frac{1.5\mu_D}{\mu_C + \mu_D}\right) + 1}{R\left(1 + \frac{1.5\mu_D}{\mu_C + \mu_D}\right) + 1}\right]^{0.71} e^{0.70(T - T_1)} \qquad (36)$$

Feed (raffinate) dispersed, solvent (extract) continuous

$q_F = q_D$ = constant, q_C varies, $R = q_C/q_D$

$$\frac{X}{X_1} = \left(\frac{R+1}{R_1+1}\right)^{0.322x-1.009}\left(\frac{\rho_D + \rho_C R}{\rho_D + \rho_C R_1}\right)^{0.645} \cdot \left[\frac{\frac{1}{R}\left(1 + \frac{1.5\mu_D}{\mu_C + \mu_D}\right) + 1}{\frac{1}{R_1}\left(1 + \frac{1.5\mu_D}{\mu_C + \mu_D}\right) + 1}\right]^{0.71} e^{0.70(T_1 - T)} \qquad (37)$$

$$\frac{Z}{Z_1} = \left(\frac{R+1}{R_1+1}\right)^{1.151x-0.464}\left(\frac{\rho_D + \rho_C R}{\rho_D + \rho_C R_1}\right)^{0.302} \cdot \left[\frac{\frac{1}{R}\left(1 + \frac{1.5\mu_D}{\mu_C + \mu_D}\right) + 1}{\frac{1}{R_1}\left(1 + \frac{1.5\mu_D}{\mu_C + \mu_D}\right) + 1}\right]^{0.71} e^{0.70(T - T_1)} \qquad (38)$$

Applicable to both cases:

$$C_M = C_{M1}\left(\frac{R+1}{R_1+1}\right)^{1.65x} \qquad (39)$$

$$C_S = C_{S1}\left(\frac{R+1}{R_1+1}\right)^{0.55x} \qquad (40)$$

$$C_P = C_{P1} \quad \text{for raffinate} \qquad (41)$$

$$C_P = C_{P1}(R/R_1)^{0.333} \quad \text{for extract} \qquad (42)$$

$$P_A = P_{A1}\left(\frac{R+1}{R_1+1}\right) \qquad (43)$$

$$P_P = P_{P1} \quad \text{for raffinate} \qquad (44)$$

$$P_P = P_{P1}(R/R_1)^{0.67} \quad \text{for extract} \qquad (45)$$

Solvent Recovery by Stripping

If the solvent is regenerated by extraction of the extract, the effect of R is given by Equation (33), with of course values of n, C_E, and E_0 appropriate to the stripping operation.

Solvent Recovery by Distillation

Equation (25) may be written

$$\mathrm{III} = A(O)(1 + r) = AB \qquad (47)$$

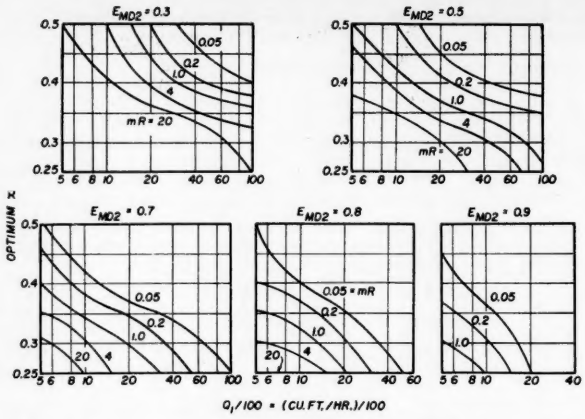

Fig. 7. Optimum x, constant solvent/feed ratio, for Y = 1 to 5 yr. For E_{MD} = extract efficiency, mR = (equilibrium c_E/c_R) (extract rate/raffinate rate). For E_{MD} = raffinate efficiency, mR = (equilibrium c_R/c_E) (raffinate rate/extract rate). Basis: 12.5 gal./min. through a 1.5-ft.-diameter vessel, agitation intensity 1,000 (ft. lb./hr.)/(cu. ft./hr.).

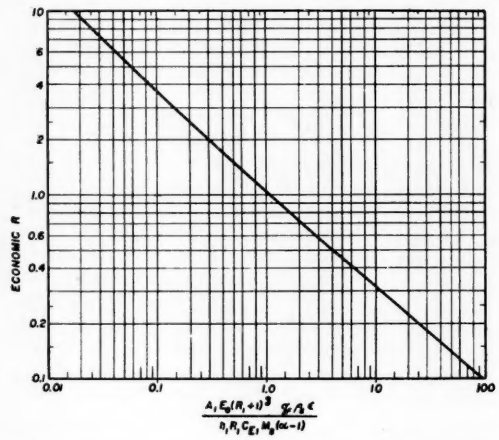

Fig. 8. Economic R for g = 0.45. Practically useful for g = 0.3 to 0.8.

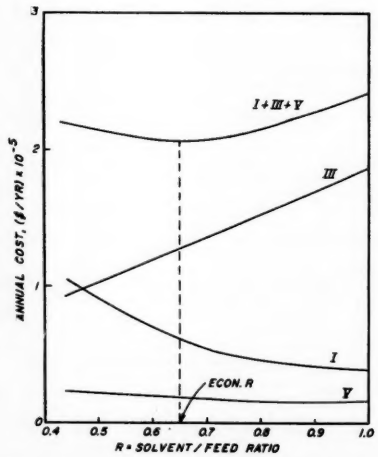

Fig. 9. Determination of optimum solvent/feed ratio.

where

$$A = \left(\frac{C_d \gamma m_{dmin}}{E_d G_d} + \frac{C_h}{G_h}\right)\left(\frac{p}{Y} + b\right) + C_{hc}H \quad (48)$$

It can be shown* that for cases where the solvent is more volatile than the extracted solute

$$B = O(1 + r) = \frac{Rq_F\rho_S}{M_S} \cdot \left(1 + \frac{\beta}{\alpha - 1}\right) + \frac{\beta U}{\alpha - 1} \quad (49)$$

and if the extracted solute is the more volatile

$$B = O(1 + r) = U\left(1 + \frac{\beta}{\alpha - 1}\right) + \frac{Rq_F\rho_S}{M_S(\alpha - 1)} \quad (50)$$

where

$$U = q_F(c_F - c_R)/M_E \quad (51)$$

*See footnote on page 475.

Cost of Lost Solvent

The losses contributing to item V may be considered as those occurring in the extractor stages, the solvent remaining in the stripped raffinate, and the solvent in the final product. The last two are considered negligible. The first of these is assumed to be proportional to the number of extractor stages and the solvent recirculation rate:

$$\mathrm{V} = \frac{nq_F RlSH}{E_0} \quad (52)$$

Economic R

The operation required by Equation (32), if attempted formally, is made difficult by the variation of E_0 with changing R. For a complete computation therefore the best procedure is to plot the sum (I + III + V) against R and locate the minimum in the curve. In the computation of these cost items the economic x, c_R, c_S, and n should be used. A sample calculation demonstrates the method.

Short-cut Method

If some reasonable approximations are made, Equation (32) can be made to yield the economic R fairly quickly. Equation (46) is such that the product nR is nearly constant over modest ranges of R, unlike the situation when c_S and c_R are held constant. Further E_0 is also nearly constant over quite wide ranges of R. If operating costs for the extraction stages are neglected in comparison with annual equipment costs, then

$$C_E = C_V(p/Y + b) = C_{E1}C_V/C_{V1} \quad (53)$$

For most situations Equation (21) is a special case of the more general relation

$$C_V = K''Q^g = K''[q_F(R + 1)]^g \quad (54)$$

The first differentiation of Equation (32) then becomes

$$\frac{\partial \mathrm{I}}{\partial R} = \frac{-n_1R_1C_{E1}}{E_0(R_1 + 1)^g} \cdot \left[\frac{1 + (1 - g)R}{(R + 1)^{1-g}R^2}\right] \quad (55)$$

It was also noted that n_{dmin} remains remarkably constant with fairly large

variations in R and so may be computed at any value R_1. Substituting Equations (28) and (29) in Equation (27) one gets

$$n_{d\min 1} = \frac{\log\left[\dfrac{2.3\rho_s M_E E_d G_d F q_F H k \log\alpha}{M_S m\gamma C_d(p/Y + b)B_1}\right]}{\log\alpha} - 1 \qquad (56)$$

where the subscript 1 indicates that B and n_{dmin} are evaluated at R_1. This value of n_{dmin} yields A_1 in Equation (48). Equations (48), (49), (50), and (47) then yield

$$\frac{\partial \mathrm{III}}{\partial R} = \frac{A_1 q_F \rho_S \epsilon}{M_S(\alpha - 1)} \qquad (57)$$

where $\epsilon = \alpha + \beta - 1$ for solvent more volatile, and $\epsilon = 1$ for solute more volatile.

If nR is considered constant, then $\partial V/\partial R = 0$. Equation (32) then provides the economic R:

$$\frac{1 + (1 - g)R}{R^2(R + 1)^{1-g}} = \frac{A_1 E_0 (R_1 + 1)^g q_F \rho_S \epsilon}{n_1 R_1 C_{E1} M_S(\alpha - 1)} \qquad (58)$$

Equation (58) should be reasonably useful for any countercurrent extractor, either tower or mixer settler, of which the cost per stage is proportional to Q^g. If Equation (21) is acceptable and $x = 0.25$, as it frequently will be, $g = 0.45$ and Figure 8 provides the solution to Equation (58). Actually the nature of Equation (58) is such that, for all practical purposes, Figure 8 may be used for any value of g from 0.3 to 0.8. In any case the economic c_S and c_R are taken into consideration.

The procedure to be followed in using Equation (58) or Figure 8 is

1. Choose any reasonable value for R_1.
2. Compute C_{V1} and $C_{E1} = C_{V1}(p/Y + b)$. C_{V1} is obtained through Equation (54) or in any convenient fashion, such as Equation (21).
3. Choose E_0. In most cases it can be taken as 0.90 or 0.95.
4. Compute B_1 [Equations (49) or (50)].
5. Compute J_1 [Equation (31)]. In most cases c_S/m may be neglected but is obtained through Equation (29) if desired.
6. Computer n_1 [Equation (46)].
7. Compute n_{dmin} [Equation (56)] and A_1 [Equation (48)].
8. Determine economic R by Equation (58) or Figure 8.
9. The economic values of n, c_R, and c_S may then be obtained by Equations (46), (30), and (29).

Some of the items of Table 1 have not been studied. The annual cost of solvent recovery from the raffinate, IV, is set in part by the solubility of the solvent in the raffinate, in turn dependent upon the chemical system used, and the concentration of solvent allowed to remain in the stripped raffinate. The complete economic design of this equipment may be attacked by the method of Sherwood and Pigford (*10*). Economic reflux ratios may be chosen through the correlations of Happel for this equipment (*3*).

The methods described here may also be extended to cases of countercurrent extraction with reflux to determine the best reflux ratio. It may be of interest in this connection to note that for systems of constant selectivity the relation among the number of extraction stages, the minimum number, the extraction reflux ratio, and the minimum reflux ratio has been found to follow quite well the familiar Gilliland chart prepared for distillation (*2*). The extractor computations may then be made reasonably quickly. They may also be extended to fractional extraction of two solutes with two solvents for determining the optimum solvent ratio and reflux ratios. In such processes the calculations predict different over-all stage efficiencies, if E_{MD} is not unity, for each of the solutes being extracted, although this apparently has not yet been reported from experiment.

SAMPLE COMPUTATION

A solute is to be extracted from a dilute aqueous solution in a countercurrent mixer-settler plant, the solute concentration in the feed being $c_F = 5$ lb./cu. ft. The aqueous volume will be $q_F = 1{,}000$ cu. ft./hr. The solvent, insoluble in the aqueous solution, provides a distribution coefficient $m = 2.0$ at the prevailing concentrations. In the mixers the solvent will be dispersed, the aqueous phase continuous. The various physical properties are as follows: mole wt. solute $= M_E = 60$; mole wt. solvent $= 100$; viscosity of solvent $= \mu_D = 0.6$ cp., of aqueous solutions $\mu_C = 1.0$ cp; density of solvent $= \rho_D = \rho_S = 50$, of aqueous $\rho_C = 62.4$ lb./cu. ft. The solvent will be recovered by distillation, where the solvent is the more volatile, and $\alpha = 2.5$. The finished product is to be 99.9 mole % extracted solute. A laboratory test in a 1.5-ft.–diameter mixer, with equal volume rates of feed and solvent, 100 cu. ft./hr. total flow, and agitator power 1,000 (ft. lb./hr.)/(cu. ft./hr.), showed a stage efficiency $E_{MD} = 0.7$.

The costs of Figure 6 will be assumed valid, and one pump per stage, for the aqueous, will be used. Solvent will flow by gravity between stages. Other items are as follows: $p = 2.5$, $b = 0.06$, $Y = 2$ yr., $H = 7{,}200$ hr./yr., $W = \$0.0112$/hp.-hr., $S = \$6$/cu. ft. (or 12¢/lb.) for the solvent, $F = \$0.50$/lb. for the solute, $l = 0.00005$ fractional solvent loss/stage. The following distillation values are suggested by Happel (*3*): $C_d = \$20$/sq. ft., $G_d = 15.0$, $G_h = 0.10$, $C_h = \$1.5$/sq. ft., $C_{hc} = \$0.0093$/lb. mole, $E_d = 0.90$, $\beta = 1.5$, $\gamma = 2.5$.

Complete solution

The computation will be made for $x = 0.25$, to be confirmed later. With a volumetric-rate-of-flow scale up of 20 from laboratory to plant at $R = 1$ Figure 4 shows the large scale conditions $R_1 = 1$, $Q_1 = 2{,}000$, $q_F = q_C = 1{,}000$, $q_{D1} = 1{,}000$, $T_1 = 3.17$, $E_{MD1} = 0.86$, with $P_{A1} = 1.32$ hp. [Equation (16)]. Computations for $R = 0.7$ follow.

Cost item I

Equation (34): $T = 3.17\ (1.7/2)^{0.25} = 3.04$ ft. Equation (35): $X/X_1 = 0.86$. Equation (36): $Z/Z_1 = 1.29$. Figure 1: $E_{MD} = E_M = 0.94$, the average of values varying from 0.93 to 0.95. Equation (3): $E_0 = 0.946$. $Q = q_F(R + 1) = 1{,}700$ cu. ft./hr. Figure 6: $C_M + C_S + C_A = \$2{,}960$. For 50 cu. ft./hr. of liquid the basic pump cost is (Table 3) \$235 and pump power 0.12 hp. Equation (15): for 1,000 cu. ft./hr. raffinate $C_P = \$640$. Equation (19): $P_P = 0.90$ hp. Equation (43): $P_A = 1.12$ hp. Equation (12): $C_V = \$3{,}600$. Equation (4): $C_E = \$4{,}873$/stage (yr.).

When one neglects c_R with respect to c_F, Equation (51): $U = 83.3$ lb.-moles/hr. Equation (49): $B = 783$. Equation (29): $c_S = 0.00231$ lb./cu. ft. Equation (31): $J = 1.0856$. Equation (46): $n = 10.5$ ideal stages. Equation (1): I = \$54,100/yr.

Cost item III

Equation (28): (moles solvent/hr.)/(moles solute/ hr.) in distillate $= 50(60)/100(0.00231) = 13{,}000$. (Moles solute/hr.)/(moles solvent/hr.) in botts. $= 99.9/0.1 = 999$. Equation (27): $n_{dmin} = 17.9$ ideal trays. Equation (26): $n_d = 44.7$ ideal trays. Equation (48): $A = 173.3$. Equation (47): III = \$135,800/yr.

Cost item V

Equation (52): $V = \$16{,}800$/yr.

Therefore I + III + V = \$206,700/yr. In similar fashion values of this sum were computed for other values of R and the results plotted in Figure 9. A minimum occurs at $R = 0.65$ cu. ft. solvent/cu. ft. feed. At this R, $E_{MD} = 0.95$, $T = 3.02$ ft. for 1,650 cu. ft./hr. total flow rate. When one refers to Figure 4 and scales down to the 1.5-ft. laboratory mixer, the latter would have provided a stage efficiency $E_{MD2} = 0.87$ at 100 cu. ft./hr., $R = 0.65$. Figure 7, at $mR = 2(0.65) = 1.3$, $Q_1/100 = 16.5$, confirms the use of $x = 0.25$.

The economical conditions are therefore $R = 0.65$, 12 ideal or 13 real extractor stages, $c_S = 0.00216$, $c_R = 0.00658$ lb./cu. ft., and a percentage recovery of extractable solute of 99.87%.

It is of interest to note that increasing the solvent loss to two and four times the amounts used above shifted the economic R to 0.67 and 0.70 respectively, indicating that R is relatively insensitive to this quantity.

Other computations made with different dollar values of the solute, which is a quantity of major importance, resulted in variations of the extractor cost which

were unexpected, at least to the author. Thus for a solute value of \$0.25/lb., half that used above, the economic R becomes 0.51 and the extractor cost is increased (14 stages), although of course the total cost is reduced, largely through changes in c_S and c_R and their effect on the cost of the solvent recovery system.

Approximate solution

Choose $R_1 = 1.0$, as in the laboratory test; hence $Q_1 = 2{,}000$. Choose $x = 0.25$. Equation (21): $C_{V1} = \$3{,}850$. $C_{E1} = C_{V1}(p/Y + b) = \$5{,}050$. Equation (31): $J_1 = 1.0171$. Equation (46): $n_1 = 6.87$. Equation (49): $B_1 = 1{,}083$. Equation (56): $n_{dmin} = 17.6$. Equation (48): $A_1 = 172.5$. Abscissa of Figure 8 = 2.15, and economic $R = 0.7$.

ACKNOWLEDGMENT

The author is very pleased to acknowledge the assistance of David MacLean, Turbo-Mixer Division of General American Transportation Corporation, who provided the cost data for the agitation equipment and advice in its selection, and the helpful suggestions of John Happel.

NOTATION

A = factor defined by Equation (48)
b = annual maintenance cost as a fraction of equipment cost
B = factor defined by Equations (49) and (50)
C_A = uninstalled cost of agitating equipment, \$/yr.
C_d = uninstalled cost of a distillation tray and accompanying shell, \$/sq. ft. tray
C_E = annual cost of a real extraction stage including equipment and operating cost, \$/yr.
C_h = uninstalled cost of heat transfer equipment, \$/sq. ft.
C_{hc} = cost of steam and coolant, \$/lb. mole distillate
C_M = uninstalled cost of empty mixing vessel, \$/stage
C_P = uninstalled cost of pump, \$/stage
C_S = uninstalled cost of settler, \$/stage
C_T = total annual cost of a complete extraction process, \$/yr.
C_V = uninstalled cost of major equipment of an extractor, \$/stage
c_F = concentration extractable solute in feed, lb./cu. ft.
c_R = concentration extractable solute in raffinate, lb./cu. ft.
c_S = concentration extractable solute in recycled solvent, lb./cu. ft.
D = molecular diffusivity, sq. ft./hr.
D' = effective molar diffusivity, sq. ft./hr.
d = pipe diameter, ft.
d_p = drop diameter, ft.
E_d = fractional over-all tray efficiency for distillation
E_M = fractional Murphree extract stage efficiency
E_{MD} = fractional Murphree dispersed-phase stage efficiency
E_0 = fractional over-all stage efficiency for extraction
e = 2.7183
F = value of extractable solute, \$/lb.
G_d = allowable mass velocity of vapor in distillation, lb.-moles/(hr.)(sq. ft.)
G_h = vapor handling capacity of heat transfer equipment, lb.-moles/(hr.)(sq. ft.)
g = constant, Equation (54).
g_c = conversion factor, (ft./hr.^{2}) (lb.-mass/lb.-force)
H = time of operation, hr./yr.
J = quantity defined by Equation (31)
K, K', K'' = constants
k = mole ratio, solute/solvent, in distilled product
k_C = mass transfer coefficient for continuous phase, ft./hr.
L = agitator turbine diameter, ft.
l = fraction of solvent flow lost/real stage
ln = natural logarithm
log = common logarithm
M_E = mole wt. extractable solute, lb./lb.-mole
M_S = mole wt. solvent, lb./lb.-mole
m = equilibrium distribution coefficient, (concentration in extract)/(concentration in raffinate), (lb./cu. ft.)/(lb./cu. ft.) Note: if raffinate is dispersed, m for Figure 7 only must be (concentration in raffinate)/(concentration in extract)
N = agitator speed, rev./hr.
n = number of ideal extraction stages
n_d = number of ideal distillation trays
n_{dmin} = minimum number of ideal distillation trays
O = rate of distillate flow, lb.-moles/hr.
P = agitator power applied to liquids, ft.-lb./hr. (stage)
P_A = agitator power, input to agitator drive, hp./stage
P_P = pump power, input to pump drive, hp./stage
p = (cost of instruments, piping, and installation as a fraction of major equipment cost) + 1
Q = volume rate of total liquid flow = $q_D + q_C$, cu. ft./hr.
q = volume rate of flow of a phase, cu. ft. /hr.
q_F = volume rate of feed flow to extractor, cu. ft./hr.
R = volumetric ratio of flow rates, extract/raffinate or solvent/feed. Note: if raffinate is dispersed, R for Figure 7 only must be raffinate rate/extract rate.
r = reflux ratio for distillation, lb.-mole/lb.-mole distillate
r_{min} = minimum reflux ratio for distillation
S = value of solvent, \$/cu. ft.
T = diameter and height of mixing vessel, ft.
U = rate of extraction, lb. mole solute extracted/hr.
V = volume of mixing vessel, cu. ft.
W = cost of power, \$/hp.
X = dimensionless parameter
x = scale-up index, defined by Equation (7)
Y = payout time, yr.
Z = dimensionless parameter
I, II, III, IV, V, VI = contributions to the cost of an extraction process, defined in Table 1, \$/yr.

Greek Letters

α = relative volatility
β = r/r_{min}
γ = n_d/n_{dmin}
$\Delta\rho$ = difference in densities, lb./cu. ft.
ϵ = $\alpha + \beta - 1$ if solvent is more volatile than solute
. = 1 if solute is more volatile than solvent
θ = holding time for dispersed phase in mixer, hr.
μ = viscosity, lb./ft. hr.
ρ = density, lb./cu. ft.
φ = volume fraction of a phase in the mixer

Subscripts

C = continuous phase
D = dispersed phase
S = solvent
1 = large-scale plant
2 = small-scale model

LITERATURE CITED

1. Aries, R. S., and R. D. Newton, "Chemical Engineering Cost Estimation," McGraw-Hill, New York (1955).
2. Gilliland, E. R., *Ind. Eng. Chem.*, **32**, 1220 (1940).
3. Happel, John, "Chemical Process Economics," pp. 203 to 209, Wiley, New York (1958).
4. Johnstone, R. E., and M. W. Thring, "Pilot Plants, Models, and Scale-Up Methods," p. 180, McGraw-Hill, New York (1957).
5. MacLean, David, personal communication.
6. Olson, R. S., *Chem. Eng.*, **65**, No. 20, 143 (1958).
7. Perry, J. H., ed., "The Chemical Engineers' Handbook," 3 ed. Section 5, McGraw-Hill, New York (1950).
8. Peters, M. S., "Plant Design and Economics for Chemical Engineers," McGraw-Hill, New York (1958).
9. Scheibel, E. G., *Chem. Eng.*, **64**, No. 11, 238 (1957).
10. Sherwood, T. K., and R. L. Pigford, "Absorption and Extraction," 2 ed., p. 451, McGraw-Hill, New York (1952).
11. Treybal, R. E., *A.I.Ch.E. Journal*, **4**, 202 (1958).
12. Warner, B. F., *Joint Symposium, The Scaling-Up of Chemical Plant and Processes*, Inst. Chem. Engrs., London (1957).

An Experimental Study of Diffusion-controlled Reactions in a Laminar Boundary Layer

MITCHELL LITT and S. K. FRIEDLANDER

Columbia University, New York, New York, and The Johns Hopkins University, Baltimore, Maryland

A brief review is presented of the theoretical solution obtained by the authors to the problem of a rapid second-order reaction in the incompressible laminar boundary layer on a flat plate. An experimental system is described for investigating reactions of this type, specifically the dissolution of plates and cylinders of benzoic and cinnamic acids in aqueous solutions of sodium and potassium hydroxide. Experimental data are reported in terms of a reaction factor, that is the ratio of the transfer rate with reaction to that in the absence of reaction. The reaction factor is independent of position. The theory closely predicts the reaction factor for cylinders as well as for flat plates. Data obtained by other investigators for packed beds can also be correlated although less successfully.

In a previous study (*1*) the authors obtained a theoretical solution to the problem of a rapid second-order reaction in the laminar boundary layer on a flat plate. Physically the problem treated was of the following nature: Substance A diffuses across a rigid interface into a fluid flowing over the surface. Substance B diffuses from the mainstream to a point (usually near the surface) where it meets A and the rapid, irreversible reaction

$$aA + bB \rightarrow \text{products} \qquad (1)$$

takes place. Components A and B and the products of reaction are convected downstream as the reaction proceeds. The reaction consumes A, steepens the concentration gradient at the interface, and increases the transfer rate. The principal contribution made in reference *1* was the development of a theoretical solution to the problem for an important convective system, namely the laminar boundary layer on a flat plate. This solution also gives a semiquantitative picture of transfer in the laminar boundary layers of other shapes such as spheres and cylinders.

In brief it was shown in the theoretical study that the mean Sherwood number for the entire plate up to any point L along the plate is given by

$$N_{Sh_M} = \left\{\frac{1}{1 - \theta_{1AR}}\right\} \cdot (0.664 N_{ScA}^{\frac{1}{3}} N_{ReL}^{\frac{1}{2}}) = F_R (0.664 N_{ScA}^{\frac{1}{3}} N_{ReL}^{\frac{1}{2}}) \qquad (2)$$

The relation between the mainstream concentration of B and the surface (saturation) concentration of A is

$$\frac{aC_{BM}}{bC_{AS}} = \left(\frac{N_{ScB}}{N_{ScA}}\right)^{\frac{1}{3}} \left(\frac{f_R''}{0.332}\right)^{N_{ScA} - N_{ScB}} \cdot \left\{\frac{\theta_{1BR}}{1 - \theta_{1AR}}\right\} \qquad (3)$$

where θ_1 is defined by

$$\theta_1(\eta, N_{Sc}) = \frac{\int_\eta^\infty (f'')^{N_{Sc}}\, d\eta}{\int_0^\infty (f'')^{N_{Sc}}\, d\eta} \qquad (4)$$

The function θ_1 is plotted by Schlichting (*4*). With these equations the rate of dissolution of any substance A as a function of mainstream concentration of B can be calculated if the Schmidt numbers are known.

The present paper deals with the application of these results to a specific experimental system, namely the dissolution of benzoic and cinnamic acids in dilute solutions of sodium and potassium hydroxide. These substances were chosen since they have been previously investigated and their physical properties are well known (*2, 3*).

EXPERIMENTAL

Experiments were carried out in the system shown in Figure 1. The solution of base was pumped from the holding tank to the head tank, and it then flowed through the Lucite test section. A well-faired entrance section was used to produce a uniform velocity profile across the duct. Screens inserted in the head tank to break up the large eddies in the water from the return line served also as a disengaging section for any air in the system, since fine bubbles tended to collect and grow on the wire and eventually make their way to the surface. During a run the temperature was constant to the nearest 0.5°C. However the energy imparted to the stream by the pump caused a slow rise in temperature, particularly at high bypass flows. Hence a cooling coil was installed in the holdup tank and the cooling water rate adjusted to keep the temperature constant over a series of runs. Most of the runs were made at a temperature of 25°C.

Figure 2 shows the details of the test section. Velocities up to 60 cm./sec. were attainable in the 9-sq.-cm. duct. The plate was placed in the center of the duct rather than in the wall so that the beginning of the velocity boundary layer would be known exactly. A correction to the theory was necessary because the velocity and concentration boundary layers began at different points, as can be seen from the drawing of the plate holder, Figure 3. The sampling section of the plate holder was approximately 5 cm. wide and 14 cm. long. Seven smaller plates, each 2 cm. long, were carefully fitted together in the

TABLE 1. SLOPES OF THE CURVES IN FIGURE 4

System	Observed $\frac{N_{Sh_M}}{N_{Re_L}^{1/2} N_{Sc}^{1/3}}$	Standard deviation, ±%	Calculated* $\frac{N_{Sh_M}}{N_{Re_L}^{1/2} N_{Sc}^{1/3}}$
Benzoic acid plates (A)	0.855	1.6	0.556
Cinnamic acid plates (F)	0.808	1.4	0.556
Benzoic acid cylinders (G)	0.741	1.6	

*By the von Kàrmàn approximate method.

Mitchell Litt is with Esso Research and Engineering Company, Linden, New Jersey.

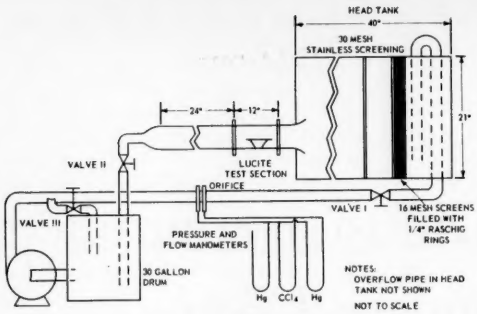

Fig. 1. Experimental apparatus.

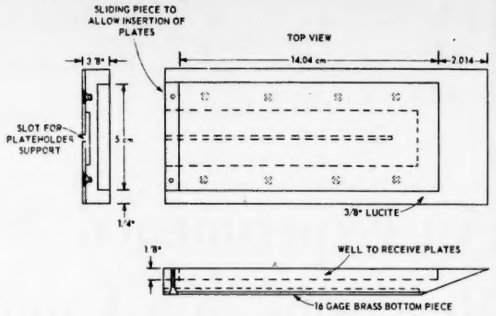

Fig. 3. Detail of plate holder.

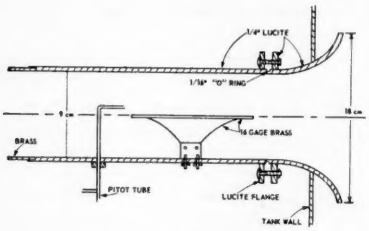

Fig. 2. Detail of test section with plate-holder support.

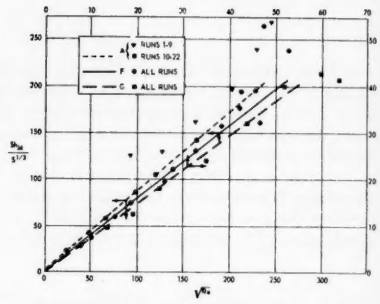

Fig. 4. Dissolution in water as a function of $N_{Re}^{\frac{1}{2}}$.

plate holder. The individual plates allowed determination of local mass transfer rates. Cylinders were used as well as plates to determine how sensitive the theoretical results were to geometry. The cylinders, which were 1 cm. in diameter and about 2 in. long, were held together by stainless steel pins and suspended in a holder.

The test pieces, both cylinders and plates, were pressed from reagent-grade benzoic and cinnanic acids. The powdered acid, as received, was first ground and then sieved to separate the fraction between 40 and 60 mesh. The weight of powder from this fraction necessary to give the desired thickness was poured into the mold and compressed in a laboratory press. No binder was required. The pieces were quite smooth to the touch and did not have the grainy crystal faces which resulted when efforts were made to cast pieces.

Dissolution rates were determined by weighing the test pieces before and after each run. Preliminary tests were run to determine variation of weight with immersion time and water absorption. The benzoic acid specimens were found to absorb a negligible amount of water upon immersion. They could be reweighed as soon as the surface liquid had evaporated, but it was necessary to do this soon after a run had been completed, since they lost weight by sublimation (about 0.5 mg./day). A standard procedure was developed in which the specimens were reweighed an hour after removal from the solution. The specimens were kept in an enclosed box containing Drierite to keep them clean and to promote drying.

The cinnamic acid plates absorbed a considerable amount of water upon immersion, approximately 5% of their original weight, depending upon immersion time. However it was found that after 3 hr. in the dry box the specimens all returned to their original weight. Further checks were made by inserting a complete plate, at zero flow, into the test section for a short time. After 3 hr. in the dry box the specimens had reached their original weight within the precision of the determination. This waiting time was included as part of the standard procedure in the cinnamic acid runs.

Runs were made in the following manner: setting the desired velocity and concentration, checking for constancy of temperature, and inserting the specimen through the entrance section. The time required for insertion and removal of the test pieces was only a small fraction of the total running time.

Because of the large volume of solution recirculated and the relative insolubility of the test materials, the increase of concentration of the dissolved acids was negligible. However to be on the safe side the liquid was changed after each series of runs. The water required aging for several days to remove dissolved air, which otherwise caused bubbles to form in the duct.

RESULTS AND DISCUSSION

Runs were made with water and solutions of sodium and potassium hydroxide. The results obtained with water are shown in Figure 4 and Table 1.* As theory predicted, the mean Sherwood number varied with the square root of the Reynolds number with little deviation from a least-squares line up to a Reynolds number of about 50,000. Above this value the dissolution rates rose sharply, probably owing to the onset of turbulence in the previously laminar boundary layer. The slopes of the lines, given in Table 1, were considerably higher than those predicted by the theory. [The theoretical constant was 0.556 and not 0.664, as in Equation (2), because the velocity and concentration boundary layers began at different points.] The factors contributing to this deviation were as follows.

1. *Mainstream turbulence*—This was reduced as much as possible in the design of the apparatus, but at the higher velocities the length of the calming tank was not sufficient to allow the turbulence to die out, as was shown by dye-stream studies.

2. *Surface roughness*—The test pieces were not hydrodynamically smooth as assumed in the theory; moreover, some disturbance was bound to be produced at the point where plates butted up to one another. For the high Schmidt numbers of this study the mass transfer was particularly sensitive to roughness near the surface which would tend to increase the mass transfer rate.

3. *Edge effects*—Since the plate was of finite width, transfer at the edges tended to increase the rate of solution above that predicted by the theory for the semi-infinite plate.

Other factors which may have tended to produce high results were vibration of the pump, stagnation at the front of the plate, and turbulence at the back end of the plate.

While the Sherwood number was higher than that predicted for dissolution in pure water, for the given experimental systems it was reproducible and hence was used to characterize the system in the absence of reaction. The effect of reaction was calculated in comparison to the effect without reaction; that is, the results with reaction are given in the form of a factor which is the ratio of the mean Sherwood number with reaction to that without reaction.

*The letters in this and the subsequent figures refer to the runs listed in tables of data deposited as document 6093 with the American Documentation Institute, Photoduplication Service, Library of Congress, Washington 25, D. C. It may be obtained for $2.50 for photoprints or $1.75 for 35-mm. microfilm.

The results are shown in Figures 5 and 6, where the reaction factors calculted from the mean and local Sherwood numbers, respectively, are plotted. (The values calculated from the local Sherwood numbers were obtained from the data for the first few plates.) The solid line is the reaction factor calculated from Equations (2) and (3), with 900 used as the Schmidt number of the acids and 300 as that of sodium hydroxide. It is seen that agreement between the observed and calculated results is good not only for the plate (which one might have excepted) but also for the cylinders. Also included are several points calculated from the data of Van Krevelen and Krekels (*5*) for sodium hydroxide flowing over a packed bed of benzioc acid pellets. One may conclude that the theory for the flat plate predicts the experimental reaction factor quite closely and is also relatively insensitive to geometry.

The values of the Schmidt numbers used in the calculation of the theoretical curve require some discussion. Schmidt numbers for molecular benzoic and cinnamic acids diffusing through water have been measured by a number of investigators, and some values are tabulated in reference *2*. The proper diffusivity for the sodium hydroxide is more difficult to determine. The reacting species is actually hydroxyl ion, but in the hydroxide boundary layer there are three ionic species: hydroxyl ion, sodium ion, and benzoate ion. The hydroxyl ion cannot diffuse independently of the sodium ion because of the requirements of electrical neutrality; however it is not retarded so much as it would be in pure water because the benzoate ion diffuses from the reaction zone. Data obtained by King and Brodie (*2*) do indeed show a dependence of sodium hydroxide diffusivity on benzoate-ion concentration, the diffusivity increasing with benzoate concentration. It is therefore to be expected that in such a system the actual diffusivity of the sodium hydroxide would lie somewhere between that of the free hydroxyl ion and sodium hydroxide in water. This was found to be the case.

The value of N_{ScB} which best correlated the experimental results was obtained in the following way. At high values of C_{BM}/C_{AS} Equation (3) reduces to

$$\frac{1}{1-\theta_{1AR}} = F_R \approx \left(\frac{N_{ScA}}{N_{ScB}}\right)^{\frac{1}{3}} \left(\frac{aC_{BM}}{bC_{AS}}\right) \qquad (5)$$

and a plot of reaction factor vs. C_{BM}/C_{AS} should be linear with a slope of $(N_{ScA}/N_{ScB})^{2/3}$. Such a plot for the benzoic acid–sodium hydroxide data is shown in Figure 7. A value for $N_{ScB} = 296$ calculated from the slope of the line was used to compute the full curve shown in Figures 5 and 6. It is interesting to note that Equation (5), derived for high values of C_{BM}/C_{AS}, actually holds fairly well for C_{BM}/C_{AS} as low as 1 or 2.

An independent estimate of the proper

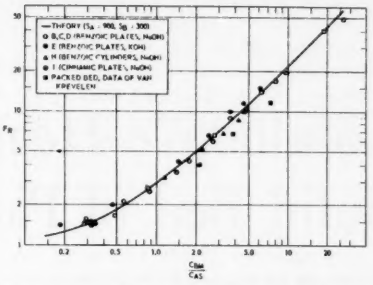

Fig. 5. Reaction factor vs. concentration ratio.

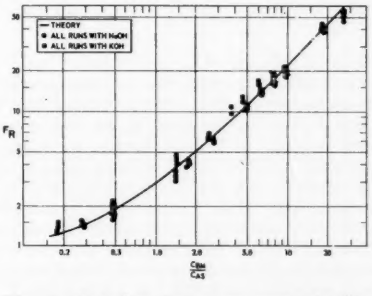

Fig. 6. Reaction factor vs. concentration ratio (calculated from local Sherwood numbers).

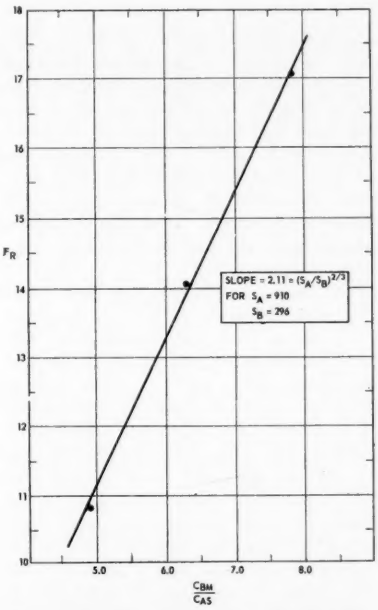

Fig. 7. Reaction factor vs. concentration ratio (series *D* for high C_{BM}/C_{AS}).

value of N_{ScB} can be obtained from the relations for ionic diffusion derived by Vinograd and McBain (*6*). From estimates of the concentrations and their gradients the diffusivity was calculated to be about half the value for the free ion, corresponding to a Schmidt number of 330. When one considers the roughness of the calculation, this compares fairly well with the value estimated from the experimental data.

ACKNOWLEDGMENT

The material presented in this paper was taken from the doctoral dissertation of Mitchell Litt, who wishes to acknowledge the support of a fellowship from the E. I. du Pont de Nemours Company, Inc. S. K. Friedlander wishes to acknowledge the assistance of National Science Foundation Grant 05079.

NOTATION

a, b	= stoichiometric coefficients of chemical reaction
C_{AS}	= surface concentration of A, moles/liter
C_{BM}	= mainstream concentration of B, moles/liter
f	= dimensionless Blasius stream function
F_R	= reaction factor, ratio of Sherwood number with reaction to Sherwood number in the absence of reaction
L	= distance from leading edge, cm.
N_{ReL}	= Reynolds number with L as the characteristic linear dimension
N_{Sc}	= Schmidt number
N_{ScA}, N_{ScB}	= Schmidt number for reactant A or reactant B
N_{ShM}	= mean Sherwood number
η	= dimensionless boundary-layer coordinate
θ_1	= dimensionless boundary-layer temperature
$\theta_{1AR}, \theta_{1BR}$	= dimensionless boundary-layer temperature based on N_{ScA} or N_{ScB} and evaluated at the reaction zone

LITERATURE CITED

1. Friedlander, S. K., and Mitchell Litt, *Chem. Eng. Sci.*, **7**, 229 (1958).
2. Hixson, A. W., and S. J. Baum, *Ind. Eng. Chem.*, **36**, 528 (1944); King, C. V., and S. S. Brodie, *J. Am. Chem. Soc.*, **59**, 1375 (1937).
3. Linton, W. H., Jr., and T. K. Sherwood, *Chem. Eng. Progr.*, **46**, 258 (1950).
4. Schlichting, Hermann, "Boundary Layer Theory," p. 265, McGraw-Hill, New York (1955).
5. Van Krevelen, D. W., and J. T. C. Krekels, *Rec. trav. chim.*, **67**, 512 (1948); **69**, 1519 (1950).
6. Vinograd, J. P., and J. W. McBain, *J. Am. Chem. Soc.*, **63**, 2008 (1941).

Manuscript received December 29, 1958; revision received April 7, 1959; paper accepted May 1, 1959.

Radiative and Conductive Heat Transfer in a Quiescent Gas-Solid Bed of Particles: Theory and Experiment

F. B. HILL and R. H. WILHELM

Princeton University, Princeton, New Jersey

This paper concerns a study of radiation as a contributing mechanism in the transfer of heat between discrete solid particles. A theory for transfer in such systems is generalized to include planar-, spherical-, and cylindrical-bed geometries; because of the particulate nature of the system the generalization is given in terms of finite-difference equations. Transfer experiments were performed in a quiescent cylindrical bed with an axial heat source and a cylindrical containing-wall sink. Heat fluxes and radial-temperature profiles were measured. As the experiments were arranged, only modest temperature gradients were established between source and sink, but the ambient sink temperature was taken in steps from 100° to 1,000°C. For a bed of 3.8-mm.-diameter alumina spheres the ratio of heat transferred by radiation to that transferred by conduction was estimated to increase with average bed temperature from the order of 0.1 at 100°C., to 1.2 at 1,000°C. The effects of temperature on bed reflectivity and transmissivity and on apparent boundary-temperature discontinuities are discussed.

Experimental indication of the relative importance of radiative and conductive heat transfer in quiescent gas-solid particle beds may be sought in measurements of the temperature dependence of the conductivity of such systems. On the assumption that the contribution of conduction is relatively temperature insensitive and that the radiation contribution depends strongly on temperature, an increase in conductivity with temperature will be largely an indication of an increase in the radiation contribution.

Few data at temperatures significant for radiation are available for interpretation. Many measurements have been made between room temperature and 100°C., where conductive heat transfer predominates. Since Waddams (*26*) summarized work in this temperature range prior to 1944, two additional sets of data (*19*, *27*) have appeared. Relatively fewer measurements have been made at temperatures above 100°C. Pirani and von Wangenheim (*17*) studied beds of various solids and particle sizes in air over a range of mean bed temperatures of from 460° to 800°C. Lucks, Linebrink, and Johnson (*12*) report conductivities of beds of foundry sands in air for three particle-size ranges from 260° to 1,230°C. Campbell and Huntington (*2*) have investigated evacuated beds of a number of industrially important particles and particle sizes at temperatures up to 360°C. The conductivities of beds of several solids and gases have been measured by Pollack (*18*) over a range of pressures (10 μ Hg to atmospheric pressure) and temperatures (room temperature to 340°C.). No evidence of convective heat transfer has been found for particles less than 0.5 cm. in diameter.

However with the exception of Pollack's work these measurements (as well as those below 100°C.) have been of over-all conductivities, which include wall effects and which are significantly smaller in value than local bed conductivities measured far from container walls, and the radiation contribution can best be found in practice from local conductivities. In addition, large temperature gradients, which tend to mask the effect of temperature level and to promote the interaction of radiation and conduction, were frequently employed in these measurements.

The interpretation of conductivity data usually involves the assumption that the conductivity of a bed of particles is the sum of the radiation and conduction contributions. Held (*7*) has shown this to be true for sufficiently small temperature gradients. Of the formulas proposed for the conduction contribution (*10*, *20*, *22*, *25*), the semitheoretical correlation of Schumann and Voss has been tested the most extensively. Wilhelm, Johnson, Wynkoop, and Collier (*28*) have derived a correction which enables prediction of 95% of a large body of data on over-all conductivities, obtained below 100°C., to within 8.5%. All expressions derived for the radiation contribution (*1*, *4*, *15*, *16*, *20*, *25*), expressed as a conductivity, have in common a dependence on cube of absolute temperature and on radiation-path length. None allows for the effects of all three processes, absorption, reflection, and transmission. All processes are considered by Hamaker (*6*) and by Held (*7*) in their treatments of the general problem of simultaneous radiative and conductive transfer. Also these authors have shown that near a container wall departure from the classical Fourier distribution exists and that the departure is due specifically to interaction of conduction and radiation.

In the present work Hamaker's theory, which was formulated for planar geometry in terms of continuous functions, is generalized to include cylindrical and spherical geometries. The generalization is given in terms of the calculus of finite differences, a form appropriate for systems composed of discrete particles. The

F. B. Hill is at Brookhaven National Laboratory, Upton, New York.

theory is compared with results of an experiment in which over-all and local conductivities were measured with small temperature gradients used at various levels between 100 and 1,000°C. Details beyond those presented here may be found in the study (*8*) upon which this paper is based.

THEORY

The radiation model presented here considers a bed of particles to be represented by a number of parallel surfaces with arbitrary spacing between successive surfaces, which, as interest may require, may be parallel planes of infinite extent, concentric cylinders of infinite length, or concentric spheres. Heat is assumed to flow in a direction perpendicular to the surfaces.

A set of such surfaces is considered, with index 1 through N. The medium contained between successive surfaces, representing the gas phase, is a perfect transmitter. Each surface is considered gray and is partially transparent, having a transmissivity τ, absorptivity α, and reflectivity ρ, with $\alpha + \rho + \tau = 1$. The fraction τ may be thought of as the effective fraction of open or free area through which radiant energy may be transmitted without absorption or reflection. The sum $\alpha + \rho$ may be thought of as representing the effective fraction of the area occupied by the packing. This fraction of the area is opaque to radiation. It emits, absorbs, and reflects radiant energy diffusely as a gray surface; that is, the absorptivity and reflectivity are constant and refer to total radiation.

The surfaces are bounded internally and externally by opaque isothermal surfaces, with indices zero and $N + 1$, and at the absolute temperatures T_0 and T_{N+1}, respectively, $T_0 > T_{N+1}$. The absorptivity and reflectivity of the inner bounding wall are α_0 and ρ_0, respectively, and those of the outer bounding wall are α_{N+1} and ρ_{N+1}, respectively. All surfaces, both opaque and partially transparent, are assumed to emit and reflect diffusely.

For this model the problem of interest is to calculate the temperature distribution in the partially transparent surfaces and the steady unidirectional heat transfer rate through the surfaces. From these results a quantity of interest in interpretation of data, the radiation conductivity of the model, may be derived. In the following paragraphs the mathematical formulation of the problem is presented, and the results of its solution are stated. Details of the solution are given in reference *8*.

The derivation is carried out in terms of concentric cylinders of infinite length or concentric spheres. Equations are derived by making energy balances based on a reference area of a given cylindrical or spherical surface. For concentric cylinders the areas referred to are areas per unit axial length; for spheres the areas are areas per sphere. Expressions appropriate for parallel planes of infinite extent may be obtained from the equations derived by assuming all the areas therein to be equal.

In the formulation of the problem, first all the surfaces are considered to be nonreflecting and, of the radiant energy which leaves a given convex or concave surface and which is diffusely distributed with respect to the given surface, the fraction which is incident on all other surfaces which the given surface can "see" is determined. The word *see* is used here in the sense that one surface includes another in its field of vision apart from the "dimming" of that vision by intervening partially transparent surfaces. The convex side of the ith surface is denoted by i^+ and the concave side by i^-.

The distribution of the radiant energy leaving a surface i^+, diffusely distributed with respect to i^+, over all surfaces which i^+ can see will be considered. In the absence of partially transparent surfaces between i and a surface m, $m > i$, all the energy must be incident on m^-, since i^+ cannot see itself and moreover can see only m^-, $m > i$. Thus in Figure 1 the field of vision of surface i^+, the convex side of surface i, includes only the concave side of surface m, that is m^-, where m has a radius greater than i, that is $m > i$. An observer located at the point P looking out from i^+ could see only those portions of m^- included between the lines PA and PB, as indicated by the arrows, and he could not see any portion of i^+. The effect of the presence of a partially transparent surface with transmissivity τ between i and m is to reduce the energy incident on m^- by the factor τ. Since there are $m - i - 1$ surfaces between i and m, the fraction of the energy incident on m^- is τ^{m-i-1}.

While a convex surface i^+ can see only one class of surfaces, a concave surface i^- can see three such classes. These classes are m^+, $m < i$; m^-, $m \leq i$; and m^-, $m > i$. Thus in Figure 2 the field of vision of the concave surface 3^- in the arbitrarily spaced concentric surfaces 0 to 7 is shown. Surface 0 is opaque, and all others are partially transparent. An observer located at the point P looking out from 3^- could see the three classes of surfaces referred to above and enumerated for this specific case as follows. Included in the class m^+, $m > i$ are 0^+, 1^+, and 2^+. The observer could see those portions of these surfaces which face the point P and which are included in the angles APA', BPB', and CPC', respectively. Included in the class m^-, $m \leq i$, are 1^-, 2^-, and 3^-. The observer could see those portions of 1^- included in the angles APB and $A'PB'$, those portions of 2^- included in the angles APC and $A'PC'$, and those portions of 3^- included in the angles APD and $A'PD'$. Finally included in the class m^-, $m > i$, are 4^-, 5^-, 6^-, and 7^-, of which the observer could see those portions included in the angles APD and $A'PD'$.

One may consider first the distribution of the radiant energy leaving i^-, diffusely distributed with respect to i^-, over the surfaces m^+, $m < i$. In the absence of partially transparent surfaces between i and m the fraction of the energy which is incident on m^+ has been shown to be S_m/S_i (*3*, *21*). Since there are $i - m - 1$ partially transparent surfaces between i and m, the fraction of the energy incident on m^+ is $\tau^{i-m-1}(S_m/S_i)$.

With reference to the class m^-, $m \leq i$, Figure 3 will be considered, in which the surfaces i^- and m^- are indicated. Following the arguments of the preceding paragraph the fraction $\tau^{i-m}(S_{m-1}/S_i)$ of the energy leaving i^- is incident on $(m - 1)^+$, and since the fraction $\tau^{i-m}(S_m/S_i)$ is transmitted through m, then the fraction incident on m^-, $m \leq i$, is $\tau^{i-m}[(S_m - S_{m-1})/S_i]$. This fraction reaches m^- through the angles APB and $A'PB'$. It is apparent from what has been said above and from the figure that the fraction $\tau^{i-m+2}[S_{m-1} - S_{m-2})/S_i]$ of the energy leaving i^- is incident on m^- through the angles BPC and $B'PC'$, and so on for the other angles indicated. Summing the contributions for all such paths one finds that the total fraction of the energy incident on m^-, $m \leq i$, is

$$\tau^{i-m}\left[\frac{S_m - S_{m-1}}{S_i} + \tau^2\,\frac{S_{m-1} - S_{m-2}}{S_i} + \cdots + \tau^{2(m-1)}\,\frac{S_1 - S_0}{S_i}\right] = \tau^{i-m}\sum_{k=1}^{m}\tau^{2(m-k)}\,\frac{S_k - S_{k-1}}{S_i}$$

From this expression it is evident that the fraction of the energy leaving i^-, diffusely distributed with respect to i^-, which is again incident on i^-, is $\sum_{k=1}^{i}\tau^{2(i-k)}[(S_k - S_{k-1})/S_i]$.

Of any radiant energy incident on a concave surface the fraction τ is transmitted through the surface, and the transmitted energy then leaves a convex surface. As was previously shown, the fraction τ^{m-i-1} of the radiation leaving i^+ is incident on the convex surface m^-, $m > i$. Hence any radiation incident on a surface, i^-, is diminished by the factor τ^{m-i} on reaching the surface m^-, $m > i$. Therefore for the third class of surfaces, m^-, $m > i$, since the fraction $\sum_{k=1}^{i}\tau^{2(i-k)}[(S_k - S_{k-1})/S_i]$ of the radiation leaving i^- has been shown to be again incident on i^-, the fraction $\tau^{m-i}\sum_{k=1}^{i}\tau^{2(i-k)}[(S_k - S_{k-1})/S_i]$ is incident on m^-, $m > i$.

The results of the foregoing discussion are summarized in Table 1.

The surfaces of the model may reflect as well as absorb and transmit. The effect of reflection is to increase the amount of radiation leaving a concave

TABLE 1. DISTRIBUTION OF RADIANT ENERGY IN NONREFLECTING PARTIALLY TRANSPARENT SURFACES

Radiant energy is diffusely distributed with respect to source. Geometry is that of arbitrarily spaced concentric cylinders or spheres. Innermost surface is opaque.

Fraction of source energy incident on receiver

Source	Receiver $m^+,\ m < i$	$m^-,\ m \le i$	$m^-,\ m > i$
i^+	0	0	τ^{m-i-1}
i^-	$\tau^{i-m-1}\dfrac{S_m}{S_i}$	$\tau^{i-m}\displaystyle\sum_{k=1}^{m}\tau^{2(m-k)}\dfrac{S_k - S_{k-1}}{S_i}$	$\tau^{m-i}\displaystyle\sum_{k=1}^{i}\tau^{2(i-k)}\dfrac{S_k - S_{k-1}}{S_i}$

surface above that leaving a nonreflecting concave surface. Since a concave surface can see itself, a certain fraction of the diffuse radiation leaving such a surface will again be incident on the surface. If the surface is nonreflecting, part of this fraction will be transmitted through the surface and the remainder will be absorbed by the surface. However for a reflecting surface with the same transmissivity some reflection (in effect reemission) will occur at the expense of absorption. Such a result is applicable only for concave surfaces, for, since convex surfaces cannot see themselves, "internal" reflections cannot occur at these surfaces.

It has been seen that, of the diffusely distributed radiant energy leaving i^-, in the absence of reflection the fraction $\tau^{i-m-1}(S_m/S_i)$ is incident on m^+, $m < i$, and the fraction

$$\sum_{k=1}^{i}\tau^{2(i-k)}\left[\frac{(S_k - S_{k-1})}{S_i}\right]$$

is incident on i^-. When, in the presence of reflection, this latter fraction of the energy is reflected by i^-, it becomes diffusely distributed with respect to i^-. In effect the fraction

$$\rho_i\sum_{k=1}^{i}\tau^{2(i-k)}\left[\frac{(S_k - S_{k-1})}{S_i}\right]$$

of the energy is reemitted by i^-, and consequently the additional fraction

$$\tau^{i-m-1}\frac{S_m}{S_i}\,\rho_i \cdot\sum_{k=1}^{i}\tau^{2(i-k)}\left[\frac{(S_k - S_{k-1})}{S_i}\right]$$

is incident on m^+, $m < i$, and

$$\sum_{k=1}^{i}\tau^{2(i-k)}\left[\frac{(S_k - S_{k-1})}{S_i}\right]\rho_i \cdot\sum_{k=1}^{i}\tau^{2(i-k)}\left[\frac{(S_k - S_{k-1})}{S_i}\right]$$

is again incident on i^-. This process is repeated ad infinitum with the result that the total fraction of the diffusely distributed energy leaving i^- which is incident on m^+, $m < i$, is

$$\tau^{i-m-1}\frac{S_m}{S_i}\cdot\left[1 + \rho_i\sum_{k=1}^{i}\tau^{2(i-k)}\frac{S_k - S_{k-1}}{S_i} + \left(\rho_i\sum_{k=1}^{i}\tau^{2(i-k)}\frac{S_k - S_{k-1}}{S_i}\right)^2 + \cdots\right] = \frac{\tau^{i-m-1}\dfrac{S_m}{S_i}}{1 - \rho_i\displaystyle\sum_{k=1}^{i}\tau^{2(i-k)}\dfrac{S_k - S_{k-1}}{S_i}}$$

Similar arguments applied to the other two classes of surfaces which i^- can see demonstrate that consideration of reflection leads to the same modification of all expressions in Table 1 related to a source i^-, namely multiplication of these expressions by the factor

$$\frac{1}{1 - \rho_i\displaystyle\sum_{k=1}^{i}\tau^{2(i-k)}\dfrac{S_k - S_{k-1}}{S_i}}$$

The results of the arguments regarding reflecting surfaces are summarized in Table 2.

For the reference area S_m of the surface m the sum of the emitted and reflected radiant energy per unit time of the surface m^+ may be defined as the radiance energy I_m, and the same quantity for the surface m^-, not including contributions from internal reflections at m^-, may be defined as the radiance energy J_m. By virtue of the specification of diffuse emission and reflection of the surfaces the radiance energies I_m and J_m are diffusely distributed with respect to m^+ and m^-,

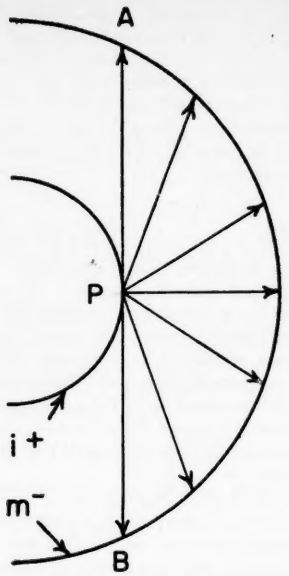

Fig. 1. Field of vision of a convex surface.

respectively. With the foregoing definitions and the aid of Table 2, the following expressions for I_m and J_m may be written:

$$I_m = \alpha_m W_m + \rho_m\sum_{i=m+1}^{N+1}\frac{\tau^{i-m-1}\dfrac{S_m}{S_i}}{1 - \rho_i\displaystyle\sum_{k=1}^{i}\tau^{2(i-k)}\dfrac{S_k - S_{k-1}}{S_i}}J_i, \qquad m = 0, 1, \cdots, N \qquad (1)$$

$$J_m = \alpha_m W_m + \rho_m\left[\sum_{i=0}^{m-1}\tau^{m-i-1}I_i + \sum_{i=1}^{m-1}\frac{\tau^{m-i}\displaystyle\sum_{k=1}^{i}\tau^{2(i-k)}\dfrac{S_k - S_{k-1}}{S_i}}{1 - \rho_i\displaystyle\sum_{k=1}^{i}\tau^{2(i-k)}\dfrac{S_k - S_{k-1}}{S_i}}J_i + \sum_{i=m+1}^{N+1}\frac{\tau^{i-m}\displaystyle\sum_{k=1}^{m}\tau^{2(m-k)}\dfrac{S_k - S_{k-1}}{S_i}}{1 - \rho_i\displaystyle\sum_{k=1}^{i}\tau^{2(i-k)}\dfrac{S_k - S_{k-1}}{S_i}}J_i\right], \quad m = 1, 2, \cdots, N+1 \qquad (2)$$

The first term on the right-hand side of each equation represents the radiant emission of the surface m given by the Stefan-Boltzmann law:

$$\alpha_m W_m = \alpha_m\sigma T_m^4 S_m$$

The remaining term or terms on the right-hand side of the equations represent the reflected radiation. Thus in Equation (1) from each of the surfaces i^-, $m < i \le N+1$, the radiance energy

$$\frac{\tau^{i-m-1}\dfrac{S_m}{S_i}}{1 - \rho_i\displaystyle\sum_{k=1}^{i}\tau^{2(i-k)}\dfrac{S_k - S_{k-1}}{S_i}}J_i$$

is incident on m^+. Hence the reflected energy contributing to I_m is

$$Q = \sum_{i=0}^{m} \tau^{m-i} I_i + \sum_{i=1}^{m} \frac{\tau^{m-i+1} \sum_{k=1}^{i} \tau^{2(i-k)} \frac{S_k - S_{k-1}}{S_i}}{1 - \rho_i \sum_{k=1}^{i} \tau^{2(i-k)} \frac{S_k - S_{k-1}}{S_i}} J_i$$

$$+ \sum_{i=m+1}^{N+1} \frac{\tau^{i-m+1} \sum_{k=1}^{m} \tau^{2(m-k)} \frac{S_k - S_{k-1}}{S_i}}{1 - \rho_i \sum_{k=1}^{i} \tau^{2(i-k)} \frac{S_k - S_{k-1}}{S_i}} J_i$$

$$- \sum_{i=m+1}^{N+1} \frac{\tau^{i-m-1} \frac{S_m}{S_i}}{1 - \rho_i \sum_{k=1}^{i} \tau^{2(i-k)} \frac{S_k - S_{k-1}}{S_i}} J_i, \qquad m = 0, 1, \cdots, N \tag{3}$$

$$\rho_m \sum_{i=m+1}^{N+1} \frac{\tau^{i-m-1} \frac{S_m}{S_i}}{1 - \rho_i \sum_{k=1}^{i} \tau^{2(i-k)} \frac{S_k - S_{k-1}}{S_i}} J_i$$

In Equation (2) the energy is reflected by the receiver m^-, for which the sources are for the terms in order, i^+, $m > i$; i^-, $m > i$; and i^-, $m < i$.

The second summation in Equation (2) is zero for $m = 1$, and the third summation is zero for $m = N + 1$. Also

$$\alpha_m = \alpha_0, \qquad \rho_m = \rho_0 \qquad \text{for} \quad m = 0$$

$$\alpha_m = \alpha, \qquad \rho_m = \rho \qquad \text{for} \quad m = 1, 2, \cdots, N$$

$$\alpha_m = \alpha_{N+1}, \qquad \rho_m = \rho_{N+1} \qquad \text{for} \quad m = N + 1$$

The steady radial rate of heat transfer per reference area is equal to the net radiance energy transfer in the direction of decreasing temperature; that is it is the radiance energy passing through the surface m^+ in the direction of increasing m minus the radiance energy incident on m^+ from the opposite direction. Again with the help of Table 2

$$I_{m'} = \sum_{i=0}^{m} \tau^{m-i} I_i \tag{4}$$

$$J_{m'} = \sum_{i=m}^{N+1} \frac{\tau^{i-m} \frac{S_{m-1}}{S_i}}{1 - \rho_i \sum_{k=1}^{i} \tau^{2(i-k)} \frac{S_k - S_{k-1}}{S_i}} J_i \tag{5}$$

Reference 8 gives the complete solution as well as a suggested method for numerical solution in the presence of conduction.

In the absence of conduction the temperature distribution, radial radiant heat transfer rate, and local radiation conductivity are found to be given by

$$\frac{T_0^4 - T_m^4}{T_0^4 - T_{N+1}^4} = \frac{\frac{1}{\alpha_0 S_0} + \frac{1 + \rho - \tau}{1 - \rho + \tau} \sum_{i=1}^{m} \frac{1}{S_i} - \frac{1}{1 - \rho + \tau} \frac{1}{S_m}}{\frac{1}{\alpha_0 S_0} + \frac{1 + \rho - \tau}{1 - \rho + \tau} \sum_{i=1}^{N} \frac{1}{S_i} + \frac{\rho_{N+1}}{\alpha_{N+1} S_{N+1}}} \tag{6}$$

$$Q = \frac{\sigma(T_0^4 - T_{N+1}^4)}{\frac{1}{\alpha_0 S_0} + \frac{1 + \rho - \tau}{1 - \rho + \tau} \sum_{i=1}^{N} \frac{1}{S_i} + \frac{\rho_{N+1}}{\alpha_{N+1} S_{N+1}}} \tag{7}$$

$$k_{r_m} = \frac{4\sigma \, \Delta r_m T_m^3}{\frac{1}{1 - \rho + \tau} \frac{S_m'}{S_m} + \frac{\rho - \tau}{1 - \rho + \tau} \frac{S_m'}{S_{m+1}}} \tag{8}$$

Equation (8) is valid for small temperature gradients.

The temperature dependent parts of the local radiation conductivity include not only the factor T_m^3 but also those terms containing the radiation constants α_0, ρ_0, ρ, τ, α_{N+1}, and ρ_{N+1}. These constants are assumed not to vary with temperature over small temperature ranges. However they may vary appreciably with large changes in temperature level, the reflectivity of nonmetals increasing with temperature and that of metals decreasing with increasing temperature. Ratios of areas in the bed are assumed not to vary

The positive terms on the right-hand side represent in order the sources i^+, $m > i$; i^-, $m \geq i$; and i^-, $m < i$. The receiver is m^-. Following incidence on m^-, the energy from these sources is transmitted through m and consequently in computing their contribution to Q the corresponding terms in Table 2 are each multiplied by τ. The last term in Equation (3) represents the contributions of the sources i^-, $m < i$, to the energy incident on the receiver m^+. If conduction and radiation are assumed to occur simultaneously, the term

$$\left[\frac{(k_{c_m} S_m')}{(r_{m+1} - r_m)}\right](T_{m+1} - T_m) - \left[\frac{(k_{c_{m-1}} S_{m-1}')}{(r_m - r_{m-1})}\right](T_m - T_{m-1})$$

is added to the right-hand side of Equation (3). The quantity S_m' is an appropriate average area for unidirectional conduction through the region bounded by the surfaces m amd $m + 1$.

Equations (1) to (3) constitute the mathematical formulation of the problem. The similarity of these equations to those of Hamaker (6) is discussed elsewhere (8).

In the absence of conduction the solution is straight forward after the following change of variables has been made:

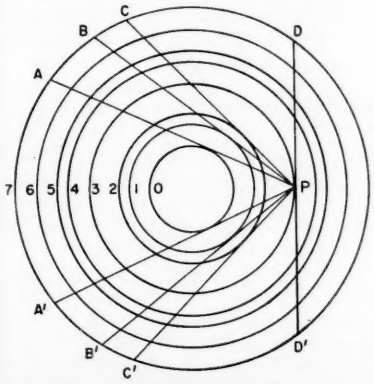

Fig. 2. Field of vision of a concave surface.

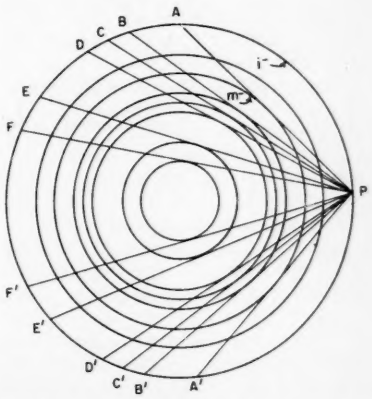

Fig. 3. Field of vision of i^- for m^-, $m \leq i$.

significantly with temperature. The local radiation conductivity is independent of wall properties but varies with position.

RELATION OF α, ρ, AND τ TO RADIATION CHARACTERISTICS OF PARTICLES OF BED

Some estimate of the relation of α, ρ, and τ, the effective radiation constants of the bed, to R, the reflectivity, and $A = 1 - R$, the absorptivity, of the surface of the particles of which the bed is composed, may be obtained by reference to Figure 4. In Figure 4 a small bundle of rays of radiant energy originating at particle 1 in a given layer is shown being distributed as a result of encountering particle 2 in another layer. Only a small bundle need be considered, since all such bundles, regardless of orientation with respect to their source layer, are assumed to suffer reflection and transmission to the same extent, characterized by the constants ρ and τ, upon being incident on a receiver layer. Some rays, A and B, are incident on particle 2; others, such as C, miss particle 2. These rays may be counted as being scattered forward. If the fraction of the energy leaving particle 1 which is not incident on particle 2 is T, then the fraction of this energy incident on particle 2 is $1 - T$. Of this fraction the fraction p is scattered backward and the fraction $1 - p$ is scattered forward. Then α may be taken to be

$$\alpha = (1 - T)(1 - R) \qquad (9)$$

and ρ is then

$$\rho = p(1 - T)R \qquad (10)$$

The quantity τ is used to represent forward scattered radiation. It must, on the basis of this discussion, include radiation actually reflected in the forward direction and radiation which misses a particle altogether. Thus

$$\tau = T + (1 - p)(1 - T)R \qquad (11)$$

A quantity of experimental interest is

$$\rho - \tau = (2p - 1)(1 - T)R - T \qquad (12)$$

The constants p and T are cosine-law view factors averaged over all possible relative positions of a particle and its nearest neighbors. Calculation of these constants is difficult if not impossible; probably they may be best determined experimentally.

EXPERIMENTAL

The thermal conductivity of a quiescent air-solid particle bed was measured as a function of temperature level and temperature gradient in an apparatus with cylindrical geometry (Figure 5). The bed was placed in a type-310 stainless steel container (4.75-in. I.D. by 24.1-in. inside length) having a tubular Calrod heater along its axis. For a given steady rate of radial heat flow through the bed, the steady state temperature distribution within the bed and at bounding surfaces was measured by thermocouples. The container was placed within a furnace which was used to produce a given temperature level within the bed upon which relatively small temperature gradients were imposed by means of the inner tubular heater.

The Calrod heater was 0.32 in. in diameter. Coil spacing over its effective heating length was found to be uniform by means of X-ray photographs. When installed in the apparatus, the effective heating length, which was greater than the length of the bed container, was centrally located with respect to the apparatus mid-plane.

Temperature was measured by means of thirteen chromel-alumel and two Pt-Pt 10% Rh thermocouples. The platinum thermocouples were calibrated at seventeen points between 0 and 1,500°C. by the National Bureau of Standards. The calibration had an uncertainty at the calibration points of 0.2°C. for temperatures less than 1,100°C. The chromel-alumel couples were calibrated in place by reference to the platinum couples. The measuring junctions of five thermocouples were placed within the bed at different radial positions at the bed mid-plane. The remainder were spot welded to the Calrod heater or were inserted in holes in the wall of the stainless steel container at the mid-plane and at points 9 in. above and below the mid-plane. A special tool inserted into the container during assembly was used to measure the radial position of measuring junctions within the bed. Thermocouple emf was measured with a potentiometer. Reference junctions were immersed in an ice bath.

An electromechanical voltage regulator supplied a voltage regulated to within 1% to two variable voltage autotransformers, one for the furnace and one for the Calrod heater.

The power supplied to the heater was measured with a wattmeter and a voltmeter.

The particles used in the experiments were alumina spheres. The particles were approximately spherical and nonporous. The mean particle diameter, based on the measurement of the diameters of 100 particles, was 3.81 ± 0.04 mm. Particle density as determined by duplicate pycnometer measurements was 3.49 g./cc.

Measured temperature distributions were corrected for the so-called "background temperature distribution." This distribution is the one obtained at any given temperature level with no power applied to the inner heater and is due to differences in thermocouple emf–temperature relations as well as to a nonisothermal temperature distribution. Ideally all temperatures throughout the bed should be the same under these conditions. In practice temperature differences of as much as 5°C. were found at the apparatus midplane, although the differences were usually not more than about 1°C. On the assumption that the steady state temperature distributions with and without power applied to the inner heater are describable by linear equations, the difference between these two distributions was taken to be the distribution corresponding to the radial heat flow.

Calculations were made which showed that the temperature distribution at the mid-plane of the bed of finite length was identical to that of an infinitely long bed

TABLE 2. DISTRIBUTION OF RADIANT ENERGY IN REFLECTING PARTIALLY TRANSPARENT SURFACES

Radiant energy is diffusely distributed with respect to source. Geometry is that of arbitrarily spaced concentric cylinders or spheres. Innermost surface is opaque.

Fraction of source energy incident on receiver

Source	Receiver m^+, $m < i$	Receiver m^-, $m \leq i$	Receiver m^-, $m > i$
i^+	0	0	τ^{m-i-1}
i^-	$\dfrac{\tau^{i-m-1}\dfrac{S_m}{S_i}}{1 - \rho_i \sum_{k=1}^{i} \tau^{2(i-k)} \dfrac{S_k - S_{k-1}}{S_i}}$	$\dfrac{\tau^{i-m} \sum_{k=1}^{m} \tau^{2(m-k)} \dfrac{S_k - S_{k-1}}{S_i}}{1 - \rho_i \sum_{k=1}^{i} \tau^{2(i-k)} \dfrac{S_k - S_{k-1}}{S_i}}$	$\dfrac{\tau^{m-i} \sum_{k=1}^{i} \tau^{2(i-k)} \dfrac{S_k - S_{k-1}}{S_i}}{1 - \rho_i \sum_{k=1}^{i} \tau^{2(i-k)} \dfrac{S_k - S_{k-1}}{S_i}}$

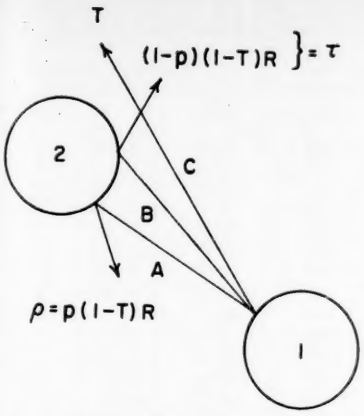

Fig. 4. Illustration of relation of ρ and τ to R and T.

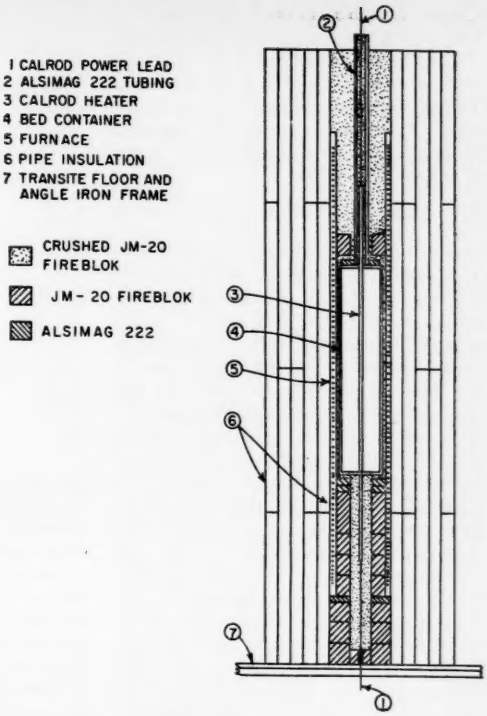

Fig. 5. Apparatus.

of the same diameter. Similar conclusions regarding this method were obtained by van Rinsum (*24*). Upon the application of a method presented by van Rinsum to the experimental data, it was found that, within the accuracy of the experiment, axial heat flow in the heater at the apparatus mid-plane was negiligible. Hence the heat-release rate and the temperature distribution at this position could be used in formulas appropriate for purely radial transfer. Experimental temperature distributions, corrected for background, were in good agreement with theoretical distributions, the agreement being better at high temperatures and small temperature gradients.

Course of Experiments

For a series of experiments at a given nominal temperature level (corresponding to a fixed furnace voltage) the furnace and its contents were first brought to temperature with no power on the Calrod heater. A period of about 4 to 5 days was required to establish temperature equilibrium. On each of the last 2 or 3 days of this period all thermocouple voltages were measured at 30-min. intervals for a period of $4\frac{1}{2}$ hr., and so ten sets of values of these variables were obtained. The variation of thermocouple voltages within the data for a given day and the variation of these voltages between data for successive days were used as the criteria for the establishment of steady state temperature distributions. The background temperature distribution was obtained in this way.

Then without a change in the furnace voltage, power was applied to the Calrod heater. As in the determination of the background distribution, time (3 to 4 days) was required for the establishment of steady temperatures. Measurement of the power consumed by the heater was made along with the same measurements of thermocouple voltages made in the background experiment.

A further experiment at the same nominal temperature level was carried out by changing the Calrod power to a new value and repeating the foregoing procedure.

The time variation of the individual temperature differences obtained from the resulting data (temperature in bed relative to container wall temperature, corrected for background) was of the order of 0.1 to 0.2°/hr., and conductivities computed from the averaged data for two successive days differed on the average by about 2% in an unsystematic way.

For several temperatures and especially at the highest temperatures investigated, the influence of heater and furnace voltages on thermocouple emf was determined by turning off power to these components momentarily and noting the resulting change in emf. No effect was found at low temperatures, and at the highest temperature level differences of as much as 8 μv. were found, for which correction was made.

RESULTS

Data, shown in Table 3, were obtained from a single packing of the container with the alumina particles described above used in air at atmospheric pressure. Temperature distributions were measured at four nominal temperature levels—100°, 400°, 700°, 1,000°C. and at several heat fluxes at each temperature level except at 1,000°C. The temperature levels are referred to as *nominal*, since for each heat flux at a given level the power applied to the furnace was kept constant and each increase in heat flux caused an increase in temperature level in the apparatus. Just one heat flux was used at 1,000°C. because during the equilibration period for a second flux the heater burned out and no further experiments were performed. Experiments are numbered in Table 3 in the order in which they were performed, generally in the order of increasing temperature level to avoid the effects of compression of the bed by the container on cooling.

Heat transfer rates in Table 3 were obtained from mean values of Calrod power corrected for the power consumed by the wattmeter and voltmeter and for the power consumed by the Calrod circuit apart from the central heating section. Also the elongation of the heater with temperature was taken into account. As stated earlier, no correction for axial heat flow was required. The temperature differences in Table 3 are indicated in Figure 6. It may be noted that in experiment 3, ΔT_c was negative. No reasonable explanation for this fact has been found.

Figure 6 shows a typical radial distribution at the apparatus mid-plane. Temperatures are corrected for background and are referred to container wall temperature. The abscissa is the finite differences function appropriate for purely radial transfer. These distributions exhibited the features predicted by Hamaker (*6*) and Held (*7*), namely a

Fourier distribution far from boundaries and departures from it near boundaries.

The distance coordinate in Figure 6 was calculated in the following way. The average particle spacing was evaluated by means of a relation proposed by Smith (*23*) for a rhombohedral array of spherical particles:

$$(\Delta r)^3 = 0.74\ D_p^3/(1 - f), \quad (13)$$

in which D_p was 0.38 cm. and f was 0.38. The particle spacing or radial distance between centers of successive particle layers, Δr, was then 0.40 cm. If f is 0.6 adjacent to the boundaries, the distance from a boundary to the center line of the adjacent layer is 0.47 cm. by the same formula. To accommodate radially an integral number of particle layers, namely 13, in the container, the average particle spacing in the bed proper was arbitrarily reduced to 0.39 cm. From these quantities the radius of each layer or surface was calculated. For the calculation of conductivities it was assumed that the average of two successive such radii was the appropriate radius upon which to base the area for heat transfer. Because the particle spacing was not uniform but was different at the walls from that in the bed, the function $\sum_{i=1}^{m} (\Delta r_i/S_i')$ was used as the distance coordinate for radial transfer rather than $\sum_{i=1}^{m} (1/S_i')$. Since the location of thermocouples within the bed did not coincide with the assumed location of particle layers, the value of the summation for a given couple was determined from a plot of $\sum_{i=1}^{m} (\Delta r_i/S_i')$ vs. r.

Local and over-all conductivities and boundary heat transfer coefficients derived from the data are given in Table 4 with corresponding average temperatures. These data are plotted in Figures 7 and 8. Conductivities were calculated from

$$k = \frac{[\text{radial heat transfer rate, cal./(sec)(cm)}]\left[\sum_{i=1}^{14} \frac{\Delta r_i}{S_i'}\right]}{\Delta T} \quad (14)$$

where ΔT_b was used for k_b and ΔT_{ov} for k_{ov}. The summation $\sum_{i=1}^{14} (\Delta r_i/S_i')$ had the value 0.351. The abscissa in Figure 7 is the temperature corresponding to the mid-point of the temperature drop associated with each conductivity. Both conductivities increased approximately linearly with temperature at low temperatures and increased more rapidly when the temperature exceeded 600°C. The local conductivity was greater than the over-all conductivity by about 40% at all temperatures.

Apparent boundary-temperature discontinuities (Figure 6) are shown in Table 4 and Figure 8 as apparent heat transfer coefficients with the units calories per second per square centimeter of bounding surface per degree centigrade temperature discontinuity. The abscissa in Figure 8 is the temperature corresponding to the mid-point of the temperature drop associated with each coefficient. The scatter exhibited by the coefficients was expected, for the temperature differences measured at the container wall were small, and at the Calrod heater the temperature differences involved the subtraction of data from base metal couples from that from platinum couples. There was nevertheless evident a trend of increasing coefficient with increasing temperature at both boundaries.

The accuracy of the conductivities is estimated to range from 5 to 25%, the smaller value applying for experiments involving the largest heat fluxes. The average accuracy of the boundary coefficients is about 50%.

The groups of points corresponding to each nominal temperature level are identified in Figures 7 and 8.

TABLE 3. DATA

Experiment no.	Nominal temperature level, °C.	Radial heat transfer rate, cal./(sec.)(cm. of heater length)	Wall temperature, °C.	Temperature difference, corrected for background, °C. ΔT_{ov}	ΔT_c	ΔT_b	ΔT_w
1	100	0.0362	105	15.0	2.5	12.1	0.4
2	100	0.0082	90	3.8	1.1	2.6	0.1
3	100	0.0797	127	25.8	−0.5	25.5	0.8
4	100	0.1477	154	71.0	22.2	46.8	2.0
5	100	0.0794	126	29.6	3.8	25.1	0.7
6	400	0.0390	402	12.5	3.8	8.4	0.3
7	400	0.0788	415	24.3	5.8	18.1	0.4
8	400	0.1602	441	46.8	11.6	34.0	1.2
9	400	0.339	497	90.1	20.5	68.0	1.6
10	700	0.0387	681	9.0	2.2	6.6	0.2
11	700	0.0776	690	17.6	4.5	12.7	0.4
12	700	0.1603	713	35.0	8.0	26.4	0.6
13	400	0.1227	430	34.2	8.1	25.5	0.6
14	1,000	0.0841	965	13.7	3.4	9.9	0.4

DISCUSSION

The relative importance of radiation as a contributing mechanism in the transfer of heat through the gas-solid bed may be obtained from the total local conductivity and an estimate of the local conduction conductivity. The local radiation conductivity is the difference between these quantities. The temperature dependence of the ratio of the radiation and conduction conductivities then shows the relative magnitude and rate of increase with temperature of the radiation contribution.

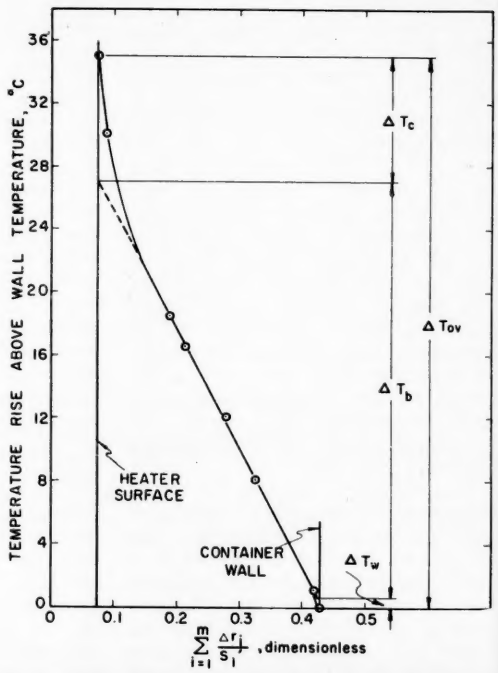

Fig. 6. Mid-plane radial temperature distribution, experiment 12.

Table 4. Conductivities and Boundary Heat Transfer Coefficients with Average Temperatures

Experiment no.	$10^5 k_{0v}$, cal./(sec.)(cm.)(°C.)	T, °C.	$10^5 k_b$, cal./(sec.)(cm.)(°C.)	T, °C.	$10^5 h_c$, cal./(sec.)(sq. cm.)(°C.)	T, °C.	$10^5 h_w$, cal./(sec.)(sq. cm.)(°C.)	T, °C.
1	85	113	105	111	560	119	240	105
2	76	92	111	91	290	93	220	90
3	108	140	110	141	...	...	260	127
4	73	190	111	179	260	214	200	155
5	94	141	111	139	810	154	300	126
6	109	408	163	406	400	412	340	402
7	114	427	153	424	530	436	520	415
8	120	464	166	459	530	482	350	442
9	132	542	175	533	640	577	560	498
10	151	685	206	684	680	689	510	681
11	155	699	214	697	670	706	510	690
12	161	731	213	727	780	744	710	713
13	126	447	163	443	590	460	540	430
14	216	972	298	970	960	977	560	965

Two types of comparison of theory and experiment may be made with the estimates of the radiation and conduction contributions. In one case values of the parameter, $\rho - \tau$, may be obtained from values of the local radiation conductivity used in conjunction with Equation (8). In the other, boundary heat transfer coefficients and the radiation and conduction conductivities may be used in an equation obtained from Hamaker's work to evaluate the parameter, $\rho + \tau$.

Each of the calculations indicated above assumes that the only heat transfer mechanisms present in the experiments were conduction and radiation; that is, convection was absent, and conduction and radiation did not interact. Therefore, the suitability of the data for such use will be considered before calculations are made.

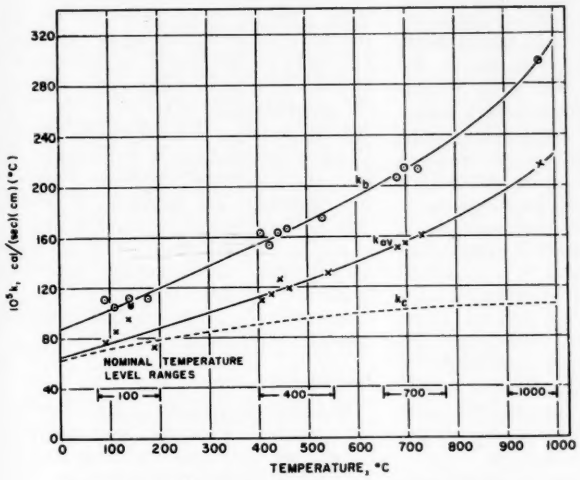

Fig. 7. Over-all and local bed thermal conductivities.

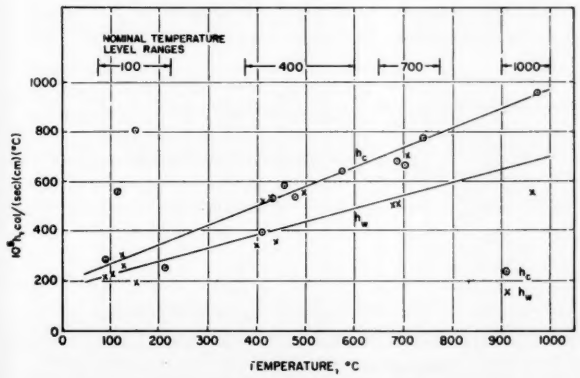

Fig. 8. Apparent boundary heat transfer coefficients.

Absence of Convection or Interaction of Radiation and Conduction

With reference to Figures 7 and 8, if one were to extrapolate the conductivities or heat transfer coefficients obtained as a function of temperature gradient at a given temperature level to zero gradient, and if this were done at a series of temperature levels, the extrapolated points would define the temperature dependence of the conductivity or heat transfer coefficient due to mechanisms other than convection, that is due to conduction and radiation alone. Further in the case of local conductivities the contributions of conduction and radiation would be additive, since Held (*7*) has shown that for sufficiently small temperature gradients the two processes take place in parallel without interaction. It was the intention in the present work to use these facts to determine whether convection or interaction of conduction and radiation was present in the experiments. Thus a departure from the zero-gradient curve would be an indication of the presence of these mechanisms. However the scatter of the data was such, particularly in the case of the boundary coefficients, that the solid curves in Figures 7 and 8, rather than being based on extrapolations to zero temperature gradient at the background temperature level, were drawn considering all of the data. Nevertheless in the case of the conductivities, temperature level, rather than temperature gradient, was the important variable. Thus effects of temperature gradient, such as convection and interaction of conduction and radiation, apparently were not present to an extent which was discernible by the method indicated, and in the ensuing calculations it was assumed that they were absent.

Ratio of Radiation to Conduction Heat Transfer

The conduction conductivity was estimated by means of the modified correlation of Schumann and Voss (*28*), which was assumed to predict k_c at any given temperature when the values of k_s and k_g corresponding to the given temperature were substituted in it. A value of 1.8 B.t.u./(hr.)(ft.)(°F.) for k_s at 1,000°C. was given by the manufacturer (*14*). It was then assumed that the temperature dependence of k_s was the same, on the basis of percentage, as that given for aluminum oxide by Jakob (*9*). The conductivity of air was taken from Glassmann and Bonilla (*5*). The results are plotted along with the experimental k_b and k_{ov} in Figure 7. It is seen that k_c is substantially lower than k_b even at low temperature but that it is in good agreement with k_{ov} at low temperature. Reasonable agreement might be expected,

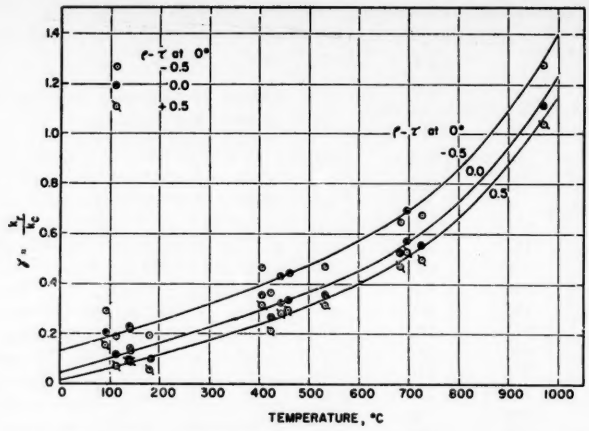

Fig. 9. Ratio of heat transfer by radiation to heat transfer by conduction.

since Schumann and Voss's correlation was based on room temperature experiments in which what has been identified here as k_{ov} was measured. Actually the agreement is better than expected and is partly fortuitous since the correlation was based on continuous distance coordinates.

In order to proceed further it was assumed that the predicted temperature dependence of k_c was valid and that, since k_b and k_{ov} exhibit similar temperature dependence, the values for k_c might be adjusted by the factor necessary to give good agreement with k_b at 0°C. In making the adjustment it was necessary to assume a value of $\rho - \tau$ at 0°C., for this quantity fixes k_r and hence k_c at 0°C. Three values of $\rho - \tau$ at 0° were assumed: -0.5, 0, $+0.5$. These values were assumed to cover the practical range of this difference. Then with $T = 273$°K. these values were inserted in Equation (8). The radius increment was assumed constant at 0.39 cm., and the average values of S_m'/S_m, 1.12, and S_m'/S_{m+1}, 0.90, in the vicinity of the linear portion of the bed radial-temperature distribution were used.

Having fixed k_c at 0°C. and adjusted k_c at all other temperatures accordingly, one obtained values of k_r by subtracting k_c from the smooth curve for k_b. The ratio, $\gamma = k_r/k_c$, is plotted in Figure 9 as a function of the average temperature of the temperature drop ΔT_b for all values of $\rho - \tau$ at 0°C. At room temperature the value of γ is about 0.1, and heat transfer by radiation is of the order of 10% of the total heat transfer. At high temperatures (1,000°C.) γ increases to about 1.2, and radiation heat transfer accounts for about 55% of the total.

Evaluation of $\rho - \tau$

From k_r and Equation (8) values of $\rho - \tau$ were obtained at all temperatures for each assumed value of $\rho - \tau$ at 0°. The results are shown in Figure 10 plotted against the average temperature of the temperature drop ΔT_b. It is seen that above 200° $\rho - \tau$ increases with temperature. This behavior would be expected at all temperatures, since for refractory materials the reflectivity increases with temperature and it would seem reasonable that the transmissivity of a packed bed would be relatively insensitive to temperature. The initial decrease of $\rho - \tau$ with temperature in two of the curves is unreasonable on this basis and may be due to the shape of the correlation used to predict k_c in the low temperature range. The curve used for k_b is concave upward, while those for k_c are concave downward. This fact is emphasized at low temperatures and large values of $\rho - \tau$ at 0° where the difference, k_r, is smallest. No significance is attached to the slight decrease in $\rho - \tau$ at 1,000° since whether the curves increase monotonically or exhibit maxima at about 900° depends on how one draws the relation between k_b and temperature in Figure 7 in the vicinity of 800 to 1,000° where there is but one experimental point. A sharper maximum is obtained if the curve for k_b rises more sharply.

It may be noted that all curves converge approximately to a value of 0.4 at 1,000°. Convergence might be expected, since γ is greatest here and slight changes in the assumed value of k_c have little effect on the resulting value of k_r and the value of $\rho - \tau$ calculated from k_r.

Even though the necessary assumptions make these calculations only approximate, it is interesting to see what values of p and T are consistent with them. Extrapolating values of R for aluminum oxide taken from Jakob (*9*) one finds that $R = 0.82$ at 1,000°C. When one uses this value and $\rho - \tau = 0.4$ at 1,000°, it is found on substituting in Equation (12) that this equation can be satisfied only by $0.7 < p < 1.0$ and $0 < T < 0.2$. The values for T are somewhat lower than estimates which one might be tempted to use. Thus one might improperly identify T with an estimate of the geometrical fraction free area, $f^{2/3}$, which in the case of these experiments would make $T = 0.52$.

More accurate and more direct estimation of radiation constants may be obtained by measurements either of the reflectivity of an exterior surface of an isothermal bed as a function of bed thickness and temperature or of transmission through such a bed. Measurements of the latter type have been made on porous and fibrous insulation by Verschoor and Greebler (*25*) and Larkin and Churchill (*11*). Equations useful for these purposes have been derived by Hamaker (*6*) for the flat-plate geometry. For other geometries the equations may be derived by solving Equations (1) and (2) simultaneously with $W_m = W_0$, the radiant emission corresponding to the constant temperature T_0 throughout the bed. Once accurate estimates of radiation constants are obtained, it would then be possible in heat transfer experiments to obtain values of k_c at high temperatures. This constant has been measured at low temperatures only where virtually all of the heat is transferred by conduction.

Evaluation of $\rho + \tau$

Hamaker (*6*) solved the equations for simultaneous conduction and radiation for the flat-plate geometry expressed in continuous distance coordinates. The corresponding solution from the present theory has not been found. The relation obtained by Hamaker for the apparent boundary temperature discontinuity is

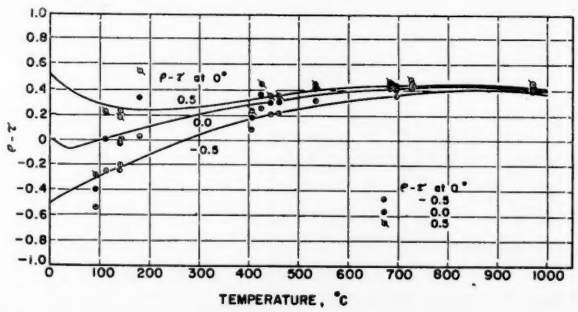

Fig. 10. Values of $\rho - \tau$ derived from data.

presented here rearranged and expressed as a heat transfer coefficient. Hamaker's absorption coefficient a has been replaced by $a = \alpha/\Delta r$:

$$h_w = \frac{8\sigma T^3}{S_w}\left(\frac{1+\gamma}{\gamma}\right)^2 \cdot \left[\sqrt{\frac{\alpha k_c}{8\sigma T^3\,\Delta r}\left(\frac{\gamma}{1+\gamma}\right)} + \frac{1-\rho_w}{1+\rho_w}\right] \tag{15}$$

All quantities in this relation may be obtained from experiments of the type described in this paper except the bed absorptivity, the conduction conductivity, and the reflectivity of the bounding surface. If estimates of k_c and ρ_w are available, then $\alpha = 1 - (\rho + \tau)$, and in turn $\rho + \tau$ may be calculated. It must be assumed that the equation applies when the boundary temperature discontinuities and hence the boundary heat transfer coefficients are obtained from plots of temperature vs. $\sum_{i=1}^{m} (\Delta r_i/S_i')$. Such calculations were made for both bounding surfaces with experimental values for h_w, S_w, T and Δr, values of k_c and γ derived from the data, and values for ρ_w taken from McAdams (*13*). For all values of $\rho - \tau$ at 0° (which determined k_c and γ) $\rho + \tau$ was found to decrease with temperature, whereas it should increase with temperature. Moreover agreement of values obtained at the two surfaces was poor, and values at the container surface were in some cases negative. These results indicate that the phenomena causing boundary temperature discontinuities may not primarily involve interaction of radiation and conduction. A further calculation indicated that conduction alone may cause the discontinuities.

The boundary coefficients increased by a factor of 3 to 4 over the temperature range of 100° to 975°. The conductivity of air increases by a factor of 2.5 over the same temperature range, and if one sets

$$h_w = \frac{k_{air}}{\Delta r_{air}} \tag{16}$$

it is found that effectively an air film existed of 0.2- to 0.3-mm. thickness at the heater and 0.3- to 0.4-mm. thickness at the container surface. No significance is necessarily attached to the difference in thicknesses at the two boundaries. Thus it is suggested that the boundary heat transfer mechanism primarily involved conduction across an air film. A similar conclusion was drawn by Pollack (*18*).

CONCLUSIONS

1. The theory of Hamaker was generalized to permit consideration of spherical and cylindrical as well as planar geometries. The generalization was expressed in terms of finite differences, a form appropriate for particulate systems. The conductivity of the radiation model was derived.

2. Unidirectional heat transfer rates and the corresponding temperature distributions were measured in a fixed bed of ceramic particles and air at atmospheric pressure over the temperature range 100° to 1,000°C. Conductivities and boundary heat transfer coefficients increased with temperature level. No effect of temperature gradient was discernible.

3. With the use of the theoretical expression for the radiation conductivity and independent estimates of the conduction conductivity, values of γ, the ratio of radiation to conduction heat transfer rates in the bed, and $\rho - \tau$, the difference between the reflectivity and the transmissivity of a layer of particles one average particle spacing thick, were derived from the data. Values of γ increased from about 0.1 at 100°C. to 1.2 at 1,000°C. The value of $\rho - \tau$ at 1,000°C. was 0.4.

4. Boundary temperature discontinuities could better be ascribed to imperfect thermal contact and not to interaction of conduction and radiation. Local conductivities in the bed proper exceeded over-all conductivities by 40% at all temperatures.

5. It was suggested that the estimates of $\rho - \tau$ deducted here from heat transfer experiments should be refined by means of optical measurement of the effective radiation characteristics of isothermal beds and that then it would be possible in subsequent heat transfer experiments to characterize conduction at high temperatures.

ACKNOWLEDGMENT

This work was supported by generous financial aid in the form of a fellowship grant from the Pittsburgh Consolidation Coal Company. The authors are indebted to W. L. Dennison of the Princeton University Infirmary for X-ray pictures of Calrod heaters, to the Radio Corporation of America for thermocouple fabrication, and to the Johns-Manville Corporation for the supply of insulation.

NOTATION

Dimensional Units

L = length
M = mass
H = quantity of heat
θ = time
T = temperature

Letter Symbols

a = absorption coefficient (L^{-1})
A = absorptivity of surface of gray ceramic particle (dimensionless)
D_p = particle diameter (L)
f = fraction void (dimensionless)
h_c = heat transfer coefficient at Calrod heater surface ($H/L^2\theta T$)
h_w = heat transfer coefficient at the container wall, or at any boundary ($H/L^2\theta T$)
i = surface i
i^+ = convex side of surface i
i^- = concave side of surface i
I_m = radiance energy of reference area, S_m, of convex side of surface m($H/\theta L$ for cylinders, H/θ for spheres)
I'_m = quantity defined by Equation (4) (units same as for I_m)
J_m = radiance energy of reference area, S_m, of concave surface of surface m (units same as for I_m)
J'_m = quantity defined by Equation (5) (units same as for I_m)
k_{air} = thermal conductivity of air ($H/L\theta T$)
k_b = total local thermal conductivity of particle bed far from bounding surfaces ($H/\theta LT$)
k_c = average local thermal conductivity due to conduction in particle bed ($H/\theta LT$)
k_{c_m} = thermal conductivity due to conduction at position m in particle bed ($H/\theta LT$)
k_g = thermal conductivity of gas phase ($H/\theta LT$)
k_{ov} = total thermal conductivity of particle bed including effect of bounding surfaces ($H/\theta LT$)
k_r = average local thermal conductivity due to radiation in a particle bed ($H/\theta LT$)
k_{r_m} = k_r at position m ($H/\theta LT$)
k_s = thermal conductivity of solid phase ($H/\theta LT$): see m, m^+, m^-; i, i^+, i^-
N = number of concentric surfaces representing particle bed(dimensionless)
p = fraction of radiation incident on a particle which is scattered backward (dimensionless)
Q = heat transfer rate through reference area in a direction normal to S_m (units same as for I_m)
r_m = radial position of $m-th$ surface (L)
Δr = average particle spacing (L)
Δr_{air} = effective thickness of air film (L)
Δr_m = Δr at position m(L)
R = reflectivity of surface of gray ceramic particle (dimensionless)
S_m = reference area of surface m: area per unit axial length for concentric cylinders (L), area per sphere for spheres (L^2)
S_m' = area appropriate for conduction heat transfer normal to and through the region bounded by S_m and S_{m+1} (units same as for S_m)
S_w = reference area of a bounding surface (units same as for S_m)
T = absolute temperature (T); fraction of energy of rays incident on a layer of particles which is transmitted through layer apart from reflection (dimensionless)

T_m = absolute temperature of surface m (T)
ΔT_b = temperature drop across bed based on linear portion of distribution in bed (T)
ΔT_c = temperature discontinuity at heater surface (T)
ΔT_{ov} = over-all temperature drop across bed (T)
ΔT_w = temperature discontinuity at container wall (T)
W_m = radiant energy emitted by reference area S_m per unit time (units same as for I_m)

Greek Letters

α = average effective absorptivity of gray surface of layer of particles one average particle spacing thick (dimensionless)
α_m = effective absorptivity of gray surface m (dimensionless)
γ = ratio of heat transfer by radiation to heat transfer by conduction (dimensionless)
ρ = average effective reflectivity of gray surface of layer of particles one average particle spacing thick (dimensionless)
ρ_m = effective reflectivity of gray surface m (dimensionless)
ρ_w = reflectivity of an opaque bounding surface (dimensionless)
σ = Stefan-Boltzmann constant, 1.378×10^{-12} cal./(sec.)(sq. cm.)(°K.)^4
τ = average effective transmissivity of layer of particles one average particle spacing thick (dimensionless)

LITERATURE CITED

1. Bosworth, R. C. L., "Heat Transfer Phenomena," John Wiley, New York (1952).
2. Campbell, J. M., and R. L. Huntington, *Petrol. Refiner*, **31**, 123 (1952).
3. Christiansen, C., *Ann. Physik. Chem.*, **19**, 267 (1883).
4. Damköhler, G., "Der Chemie-Ingenieur," Eucken-Jakob, Vol. III, Part 1, p. 445, Akademische Verlagsgesellschaft M.B.H., Leipzig, Germany (1937).
5. Glassmann, Irvin, and C. F. Bonilla, *Chem. Eng. Progr. Symposium Ser., No. 5*, **49**, 153 (1953).
6. Hamaker, H. C., *Philips Research Repts.*, **2**, 55, 103, 112, 420 (1947).
7. Held, E. F. M. van der, *Appl. Sci. Res.*, **A3**, 237 (1953); **A4**, 77 (1954).
8. Hill, F. B., Ph.D. thesis, Princeton Univ., Princeton, New Jersey (1958).
9. Jakob, Max, "Heat Transfer," John Wiley, New York (1949).
10. Kistler, S. S., *J. Phys. Chem.*, **39**, 79 (1935).
11. Larkin, B. K., and S. W. Churchill, *A.I.Ch.E. Journal*, **5**, No. 4, 467 (1959).
12. Lucks, C. F., O. L. Linebrink, and K. L. Johnson, *Trans. Am. Foundrymen's Assoc.*, **55**, 62 (1947); **56**, 363 (1948).
13. McAdams, W. H., "Heat Transmission," 3 ed., McGraw-Hill, New York (1954).
14. Norton Co., personal communication.
15. Norton, F. H., and W. D. Kingery, "The Measurement of Thermal Conductivity of Refractory Materials," Quarterly Progress Report for the Period Ending April 1, 1955, NYO-6449, Mass. Inst. Technol., Cambridge.
16. Nusselt, W., *Z. bayer. Revisions.-ver.*, **17**, No. 13 and 14 (1913).
17. Pirani, M., and von Wangenheim, *Z. tech. Physik.*, **10**, 413 (1929).
18. Pollack, J. A., Sc.D. thesis, Mass. Inst. Technol., Cambridge (1948).
19. Prins, J. A., J. Schenk, and A. J. G. L. Schram, *Physica*, **16**, 379 (1950).
20. Russell, H. W., *J. Am. Ceram. Soc.*, **18**, 1 (1935).
21. Saunders, O. A., *Proc. Phys. Soc. (London)*, **41**, 569 (1929).
22. Schumann, T. E. W., and V. Voss, *Fuel*, **13**, 249 (1934).
23. Smith, W. O., *Physics*, **1**, 18 (1931).
24. Van Rinsum, W., *Beilage zu Forsch. Gebiete Ingenieurw.*, **228** (1920).
25. Verschoor, J. D., and P. Greebler, *Trans. Am. Soc. Mech. Engrs.*, **74**, 961 (1952).
26. Waddams, A. L., *Chem. & Ind. (London)*, p. 206 (1944).
27. Weininger, J. L., and W. G. Schneider, *Ind. Eng. Chem.*, **43**, 1229 (1951).
28. Wilhelm, R. H., W. L. Johnson, R. Wynkoop, and D. W. Collier, *Chem. Eng. Progr.*, **44**, 105 (1948).

Manuscript received November 5, 1958; revision received April 29, 1959; paper accepted May 5, 1959. Paper presented at A.I.Ch.E.-A.S.M.E. 1958 Heat Transfer Conference.

The Vapor-phase Catalytic Hydration of Ethylene Oxide to Glycols

A. B. METZNER and J. E. EHRREICH

University of Delaware, Newark, Delaware

The vapor-phase reaction between ethylene oxide and water to form glycols has been carried out under a wide range of conditions with particles of polystyrene-sulfonic acid ion exchange resins used as catalysts. The rates observed appeared to be directly proportional to the product of the partial pressure of ethylene oxide and the amount of water sorbed by the resin. By use of the Brunauer, Emmett, and Teller equation to describe the amount of water sorbed by the resin, the experimental data were correlated over a sixty-fold range of reaction rates with a mean deviation of 15%.

To obtain data of value in elucidating reaction mechanisms, the reactor was usually run under "differential" conditions, that is low conversions. However in a few runs conversions of as high as 54% were obtained for a contact time of 0.02 sec. The ratio of ethylene glycol to higher glycols (selectivity) obtained varied between 73 and 99% but was usually above 80% under conditions of high conversion. However it could also be reduced forcibly to produce higher glycols as the major product, if desired.

The growing demand for ethylene-glycol has stimulated a great deal of research. Until recently all the ethylene oxide hydration studies were concentrated on understanding the homogeneous reaction, primarily the sulfuric-acid catalyzed reaction (*2, 5, 11, 12, 14*) between water and dissolved ethylene oxide. Of the heterogeneous solid catalyzed reactions, the more interesting ones appear to be those involving a strong hydrogen ion exchange resin as the catalyst. Othmer and Thakar (*12*) studied the use of batch and fluidized beds for the liquid-solid heterogeneous system. Reed, Wenzel, and O'Hara (*15*) published data on a continuous packed-bed reactor for the vapor-solid and vapor-

J. E. Ehrreich is with the Dewey and Almy Chemicals Company, Cambridge, Massachusetts.

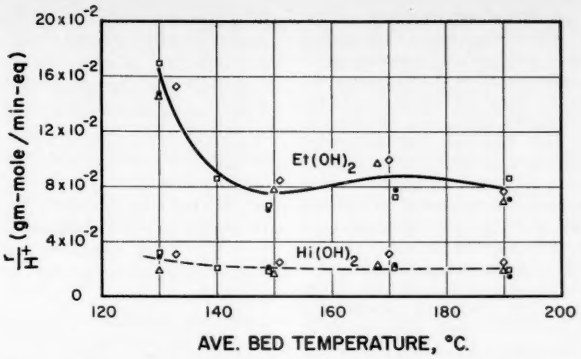

Fig. 1. Effects of Reynolds number and temperature on reaction rates.

Symbol	Molal ratio, water: EtO	Reynolds number
◇	10:1	200.
●	15:1	100.
△	10:1	150.
○	10:1	250.
□	10:1	50.

Pressure: 35.7 lb./sq. in abs.
Particle diameter: 0.78 mm. (air dried).

liquid-solid heterogeneous systems. The data obtained from the continuous fluidized and packed-bed reactors were of limited value in the understanding of the kinetics of the reactions, owing to the narrow ranges of conditions studied and to the fact that the reactors were of the integral type. At approximately the same time that Reed was carrying out studies on an integral reactor Hamilton and Metzner (*9*) were studying the vapor-solid reaction using a differential packed bed. These latter studies showed a pronounced effect of Reynolds number on reaction rates. The object of this work was to extend the ranges of these data to higher Reynolds numbers and to study pressure effects.

EXPERIMENTAL EQUIPMENT AND PROCEDURE

Details of equipment and procedure are described elsewhere (*6*). In general, the reactor as well as the operational and analytical procedures were all similar to those used by Hamilton (*9*) but with the following important improvements:

1. More accurate metering of both steam and ethylene oxide was achieved by replacing the gas-phase metering apparatus used previously. In this work the necessary steam was produced by pumping distilled water into a vaporizer with a metering pump, and flow rates of liquid ethylene oxide were measured with rotameters.

2. The ethylene oxide was vaporized in a steam-heated chamber packed with ball bearings just before it entered the reactor. This vaporizer served as an effective knock-out trap for polymers of ethylene oxide, thereby ensuring a clean vapor feed to the catalyst.

3. Physical analytical procedures (such as distillation or refractive-index measurements) used frequently by previous workers do not provide the degree of accuracy desired; therefore, chemical methods were used exclusively. For determination of ethylene glycol and of unreacted ethylene oxide in the product samples periodic acid oxidation and the Lubatti (magnesium chloride–hydrochloric acid) method respectively were used as before (*9*). For determination of the presence of higher glycols, Hamilton and Metzner used a dichromate oxidation which effectively determined all higher glycols as well as any ethylene oxide polymers. Conclusively to avoid errors due to the presence of the latter in this work the higher glycols were determined by colorimetric analysis, with colored complexes which may be formed between the hydroxyl groups on the glycols and ammonium hexanitratocerate (*4*). For this purpose a Beckman colorimeter, operated at a wave length of 542 mμ., was used.

All analytical procedures were thoroughly tested with mixtures of known composition as well as with pure samples. In all cases the maximum error due to analysis was less than 5%.

Preliminary runs, by means of imperfected operational procedures, indicated that about 2 hr. was required for attainment of steady state conditions. This period was progressively shortened, but usually several samples were taken (at half-hour intervals) to ensure the absence of any deviations from steady state conditions when data were being collected. These data indicated a mean reproducibility of all results, when analytical errors were included, of about ± 10%.

RESULTS

Conditions Studied

Table 1 compares the ranges of variables covered in this work with those used previously. In general, conditions which were studied extensively previously were not covered in detail in this work, and vice versa. Both resins used in this work were of the strong acid (polystyrene sulfonic) type, as the weaker IRC-50 carboxylic acid was shown previously to have little catalytic activity. In the production of Duolite resins additional steps are taken to provide a high degree of porosity (*1*), so that the final product may more nearly represent a usual catalyst rather than one having the continuous gel structure of other ion exchange resins.

Experimental Observations and Their Interpretation

The first series of runs was to determine whether the Reynolds numbers in the present work were sufficiently high to get entirely out of the region in which external, or gas-phase, mass transfer rates influence the results. At the same time it was desired to check the peculiar temperature effects observed earlier (*9*),

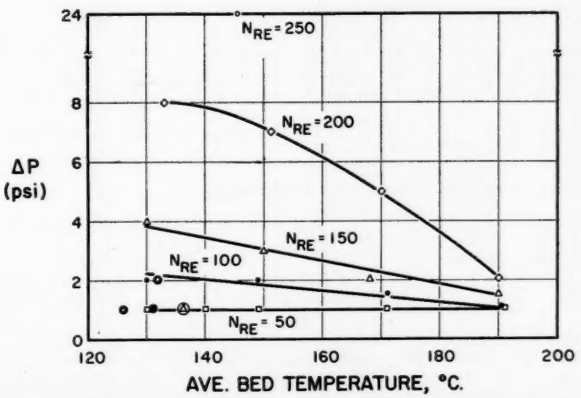

Fig. 2. Pressure drop across catalyst bed (symbols as in Figure 1).

where the rates were found to decrease with increasing temperature in the range up to about 150°C. As Figure 1 shows, the rates in the present study confirm the earlier effects of temperature observed in this region. More important there is clearly no consistent effect of Reynolds number, showing that complications due to external mass transfer effects are clearly absent. In the region above 150°C., temperature is seen to have little effect on the reaction rates. Clarification of this point will be possible in the light of other data later in the paper.

Figure 2 defines the peculiar pressure-drop effects observed in this system. At the higher flow rates the pressure drop through the bed becomes strongly dependent on temperature as well as on the Reynolds number. Normally only the small variations due to gas-density changes with temperature are expected (*10, 13*), and these are in the opposite direction from the trends shown in Figure 2. Furthermore the pressure losses shown in Figure 2 become increasingly sensitive to flow rate as the flow rate increases. During the start-up, when superheated steam alone was passed through the catalyst bed, the pressure drops were always much less than those obtained when both steam and ethylene oxide were added to the catalyst bed. Further the pressure drops were extremely high; the bed depth corresponding to the data of Figure 2 was only about 2 in.*

To define clearly the reasons for the peculiar pressure-drop effects and thereby to develop a lucid picture of the catalyst structure under reaction conditions, several runs were made in a glass-walled reactor. These runs also served to obtain an estimate of the catalyst particle size during a run. The glass-walled reactor used to carry out the runs in which the particle size and structure under operating conditions were to be observed was a Jerguson gauge with a sight glass calibrated to determine the resin volume. The same start-up procedure was used as during the runs in the stainless steel reactor. After 25 ml. of wet resin was added to the Jerguson gauge, superheated steam was passed through the reactor. At an average bed pressure of 19 lb./sq. in. gauge and 141 °C. the resin volume shrank from 25 to 13.5 ml. (as compared to a volume of 17.2 ml. for air-dried resin and 13.0 ml. for oven-dried particles). When ethylene oxide (water/ethylene oxide mole ratio of 10) was added with the steam to the reactor at an average bed pressure of 13 lb./sq. in. gauge and 144°C., the resin volume increased to 14.8 ml. Not only did the volume of the resin change, but the appearance changed from a dry brown color when the superheated steam was passed through the bed to a moist (brown-sugary) appearance after the addition of ethylene oxide. Therefore the visual observations clearly indicated that the resin was sorbing large quantities of the components of the gas stream and as a result undoubtedly softening. As the temperature increases at constant total pressure, the quantities sorbed would decrease, hardening the resin and thereby decreasing the pressure drop. As a result of the softening at the lower temperatures, the pressure drop would serve to compact the bed and have a cumulative effect; the pressure drop, while low during start-up, compacts the bed slightly. This in turn further increases the pressure drop, resulting in further compaction, and so on, until finally at steady state the very high-pressure losses and great effect of flow rate shown in Figure 2 were obtained.

The most interesting series of runs were those that showed the effect of total pressure on reaction rates. An enormous dependence of the rates on total pressure was always observed, those of Figure 3 being typical. This dependence ranged from one of the second power of total pressure at the lower pressures to a fourth-power dependence as saturation pressures were approached at the other extreme. To determine whether these extraordinary pressure effects were due to changes in the partial pressure of ethylene oxide or that of the water, complete data were obtained at one temperature. Summarized by the solid lines of Figure 4, these data show approximately a first-power dependence of reaction rates on the ethylene oxide partial pressure. Therefore the enormously greater effects of total pressure must be due to changes in the partial pressure of water and therefore to its sorption by the resin. As conditions close to saturation are approached, the quantities of water sorbed should increase rapidly, thereby leading to the great effect of pressure shown in Figures 3 and 4. An alternate method of approaching saturation is that of decreasing the temperature at constant total pressure; if water sorption were the primary variable affecting reaction rates, then the lower the temperature the higher the reaction rate would become. This importance of water sorption is clearly confirmed by the data at 130° to 150°C. in Figure 1.

All rate data have been expressed in terms of the equivalents of acid catalyst. These rates may be converted to rates per mass or volume of catalyst by means of the following conversions: there are 4.14 equivalents per 1,000 g. (air dried) resin and 1.87 equivalents per 1,000 ml. of wet resin.

Development of a Quantitative Correlation

Correlation of the reaction-rate data must consider quantitatively the effects of water sorption described above. Quantitative water-adsorption data on ion exchange resins, at least at lower temperatures, have been reported by Sundheim, Waxman, and Gregor (*16*), and more completely by Glueckauf and Kitt (*8*). On the basis of these results the

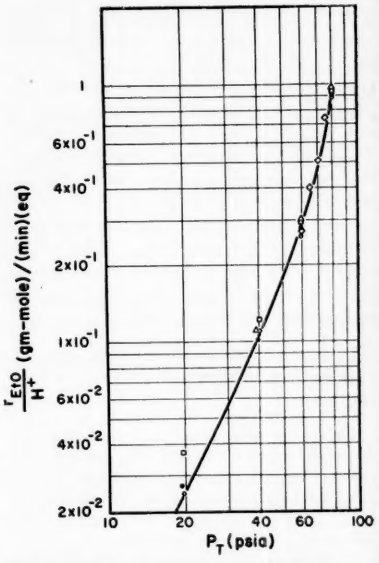

Fig. 3. Effect of pressure on ethylene oxide reaction rate: temperature, 160°C.; resin diameter, 0.78 mm.; water: EtO ratio, 15:1. Typical run conditions:

Symbol	N_{Re}	Selectivity
□	100	77.5–81.4
◇	200	78.8–84.2
▽	100	75.0–85.5
○	101	79.8–81.9
●	202	77.0–82.2

Selectivity expressed as the molal percentage of ethylene glycol in the product mixture of glycols.

*The very high values of the pressure drop and the comparatively low values of the Reynolds numbers used are perhaps not quite so surprising when one considers the gas velocities used. In the present study gas velocities of up to 200 ft/sec. were employed. The Reynolds numbers are low in spite of these high velocities, since the diameter term is very small.

Table 1. Levels of Experimental Variables

	This work	Hamilton and Metzner (*9*)
Modified Reynolds numbers	50 to 250	10 to 60
Total pressure	15 to 80 lb./sq. in. abs.	18 lb./sq. in. abs.
Catalyst types	Amberlite IR-120 and Duolite C-25	IR-120 and IRC-50
Catalyst particle diameters	0.088, 0.46 and 0.78 mm.	0.35 and 0.71 mm.
Temperature	130° to 190°C.	110° to 200°C.
Molar ratio of steam to ethylene oxide	5.08 to 20	7.5 to 32

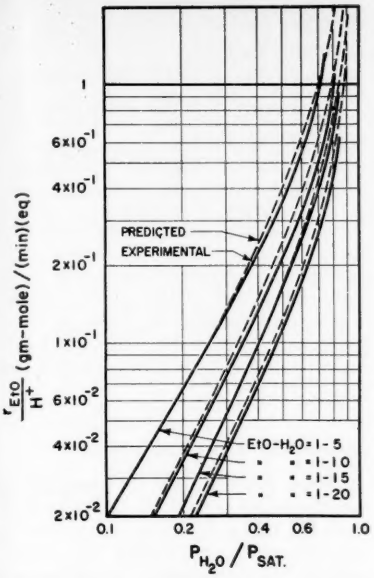

Fig. 4. Effect of pressure on reaction rates (summary).

B.E.T. (3) equation was chosen to represent the water-sorption isotherm:

$$v_{BET} = \frac{b(p_{H_2O}/p_{sat})}{[1 + a(p_{H_2O}/p_{sat})][1 - p_{H_2O}/p_{sat}]} \qquad (1)$$

The over-all rates must also be proportional to the total amount of catalyst used, or more specifically, to the equivalents of acidity which serve to catalyze the reaction. The final equation for reaction rates derived from these considerations may be written (at constant temperature) as

$$r_{EtO} = k'''(p_{EtO})(v_{BET})(H^+) \qquad (2)$$

Experimentally the variation of the rate constant with temperature could be described by an activation energy of 9.0 kcal./g. mole. Since this is identical to the latent heat of vaporization of water, an alternate statement of the same fact is that k''' varies with temperature in the same way as does the vapor pressure of water. Therefore

$$k''' = k''(p_{sat}) \qquad (3)$$

A combination of Equations (1) to (3) gives

$$r_{EtO} = \frac{k(p_{H_2O})(p_{EtO})(H^+)}{[1 + a(p_{H_2O}/p_{sat})][1 - p_{H_2O}/p_{sat}]} \qquad (4)$$

Figure 4 compares the rates predicted by means of Equation (4) with experimental results obtained at 160°C. The data cover a fourfold range of pressures and over a sixtyfold range of reaction rates. In view of the wide range of rates and the simple development of Equation (4), the fact that the results and predictions always agreed within about 20% (and usually better) is truly remarkable.

All the experimental data obtained, at all temperatures (130 to 190°C.), with the larger size particles are compared with Equation (4) on Figure 5 with coordinates suggested by the form of the B.E.T. equation used. The reciprocal of the rate constant is given by the intercept at a reduced pressure of zero; the slope of the line is equal to (a/k). Even from visual inspection alone it is evident that the only points which deviate by 15 to 20% or more are those runs for which the experimental scatter is greatest. The accuracy of the correlation is therefore more strongly limited by random errors in the data than by the form of the correlating equation. The mean deviation of points from the equation is 15%.

It is particularly noteworthy to consider that this correlation which uses a single set of values for a and k correlated the data over the entire 60°C. temperature range. This is equivalent to stating that not only is the rate constant correctly portrayed by Equation (3) but the sorption constants of Equation (1) are independent of temperature. A direct and independent check of this conclusion is available in the adsorption data of Glueckauf and Kitt (8) at somewhat lower temperatures; over a 25°C. range of temperatures the volumes of water adsorbed on a similar ion exchange resin changed only by between 6.5 and 0.7%, depending on the pressure used.

THEORETICAL INTERPRETATIONS

Of the usual steps which may influence the over-all reaction rates (chemical kinetics, sorption rates, internal and external mass transfer), only external mass transfer has been conclusively eliminated thus far. The correlating equations further show the extreme importance of water-sorptional effects, but exactly how these effects determine the over-all rates has not yet been established. For example, the sorption of water could possibly determine the rate of internal diffusion through the particle through its effect on particle size. Alternately, chemical kinetics could be rate controlling with the water sorption determining the activity of the protons which are responsible for catalysis of the reactions. The purpose of this section is to examine these questions and to consider the structure of the catalyst particle under reaction conditions in further detail.

Internal Diffusion and Conditions Within the Particle

To determine the importance, if any, of internal mass transfer rates (that is, diffusion within the particle) two additional types of experiments were carried out. In the first place runs with Duloite and Amberlite catalyst were made under identical conditions. The ethylene oxide reaction rates found were identical. Therefore one can conclude that either the Duolite was not porous under reaction conditions or that the porosity was not useful; that is the diffusion rates through the resin were as high as in the pores, or possibly diffusion rates were not limiting in any case. To check these findings the particle size of the Amberlite resin was changed from 0.78 to 0.46 and to 0.088 mm. The results given in Table 2 show that decreases in diameter indeed increased the rates, very nearly in direct proportion to the changes in surface area. The fact that the ratios of reaction rates are consistently slightly smaller than the measured ratios of diameters is felt to be due to the fact that the diameter ratios were measured prior to reaction; during startup a slight attrition always took place. This was more serious for the larger particles; hence the true diameter ratios under reaction conditions are somewhat smaller than the values of 1.68 and 8.8 reported. It is therefore concluded that the reaction zone was undoubtedly confined to a very thin region near the surface of the catalyst particles.

These conditions of surface reaction could have been caused by a low rate of diffusion of any one or more of the reactants or products through the catalyst particles. However the correlating equations clearly show no dependence of rate upon the partial pressure of ethylene glycol and of higher glycols in the gas phase around the particle. The rates of formation of the higher glycols were usually not great, but as the temperature, pressure, and Reynolds number were varied, the concentration of ethylene glycol in the gases leaving the reactor was varied all the way from saturation down to only a few percent of its saturation value. The absence of any effect of this variation upon the conversion rates clearly eliminates the possibility that diffusion of glycol through the particle may have been rate controlling. The same conclusion may be reached by noting that the formation rates of higher glycols were always low, and catalytic activity remained high. If much glycol had remained within the particle for an appreciable length of time, it would have the opportunity to react further with ethylene oxide to produce pro-

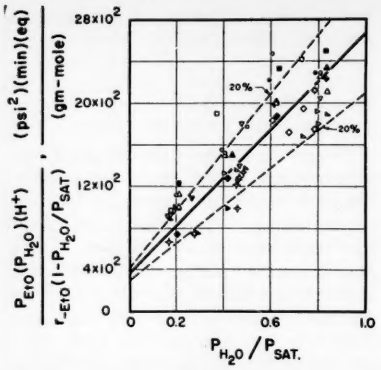

Fig. 5. Correlation of all data on 0.78 mm. catalyst particles.

Symbol	Reynolds number	Water: EtO molal ratio	Temperature °C.	Pressure lb./sq. in. abs.
○	210	10.4:1	150	35
⊡	190 220	10.3:1	130-190	35
◪	193-224	10.3:1	133-190	35
◭	89-103	15 4:1	130-191	35
▽	143-167	10.3:1	130-190	35
▼	48-56	10.3:1	130-191	35
▷	100	10.0:1	135	20-40
▶	200	10.0:1	135	21-40
●	100	10.0:1	160	19.7-80
○	203	10 0:1	160	19.7-80
△	100	15.0:1	160	19.5-80
▲	200	15.0:1	160	19.7-80
□	101	5.08:1	160	19.7-80
■	199	20.0:1	160	19.7-80
◇	101	15.2:1	160	59.8-74.8
◆	202	15.2:1	160	19.6-80

gressively higher glycols, eventually producing polyethylene oxide polymers which would completely plug or inactivate the catalyst. The fact that this did not occur is a further clear indication that both ethylene glycol and the higher glycols could diffuse from the scene of reaction rapidly in comparison to their rates of formation. Finally the rates should not have depended strongly on the ethylene oxide partial pressure if the diffusion of products was the rate-controlling step.* Further since water is probably the major adsorbed component in the gel (*9*) and its sorptional variations have been expressed through an equilibrium relationship, its diffusion rate may also be ruled out.

These arguments lead to the following conclusions:

1. The concentrations of water, glycol, and the higher glycols throughout the catalyst particle are essentially in equilibrium with the gas phase.

2. Internal diffusion of ethylene oxide may be at least partially rate controlling.

In the limiting case in which internal-diffusional resistances are very high, permitting only a very limited penetration of reactants into the resin, the rate expression is given by equations of the form (*7, 17*):

rate per catalyst particle

$$= A(p_{EtO})\sqrt{kD_e} \qquad (5)$$

Therefore if ethylene oxide diffusion were entirely rate controlling, the large effect of partial pressure of water given by Equation (4) would be due to its influence on the square root term in Equation (5). It should be noted that Equation (5) predicts that the observed activation energy would be about half as great under diffusion-controlled conditions as that of the kinetically controlled reaction itself. The value found in the present work (the latent heat of vaporization of water or approximately 9 kcal./g.-mole) is exactly half the value reported for the liquid-phase acid-catalysed reaction (*12*).

Sorption Rates

Detailed arguments similar to those in the above section show (*6*) that if sorption rates were controlling, they could have been only the rates of ethylene oxide sorption. In this case the large effect of partial pressure of water could be explained by the assumption that ethylene oxide adsorption occurs primarily on wetted sites and therefore is a strong function of the number of such sites. Insufficient general information on the factors controlling these rates in systems of catalytic gels is available to confirm or to rule out such a rate-controlling mechanism.

Chemical Kinetics

In situations in which the chemical kinetics are slower than the other rate steps the reaction usually takes place rather uniformly throughout the entire particle. Since this is obviously not the case here, it is probable that this step was not rate controlling.

The single exception to complete particle utilization under kinetically controlled situations occurs when the reaction is confined entirely to the external surface of the particle, as in the case of a solid in which all diffusivities are essentially zero. If this were the case here, the rates should follow conventional kinetic relationships, including the usual large effects of temperature. Since the activation energies found in this work were only half as great as those of the liquid phase, acid-catalyzed reaction may quite probably be ruled out.

*This statement rests on the fact that ethylene oxide is the component adsorbed in the smallest quantities (*9*). If it were adsorbed in as large quantities as water, it could possibly influence product diffusion rates through its effect on particle swelling, hence the diffusivity of all components.

Table 2. Effect of Particle Size on Reaction Rates

Runs	Temperature, °C.	Pressure, lb./sq. in. abs.	Ratio of diameters	Ratio of rates
47a and 68a	160	19.5	$D_{47}/D_{68} = 1.68$	$r_{68}/_{47} = 1.16$
47b and 67b	160	39.8	1.68	1.40
47a and 71a	160	19.5	$D_{47}/D_{71} = 8.8$	$r_{71}/r_{47} = 7.9$
47b and 71b	160	39.8	8.8	6.6

In summary all possible rate-controlling steps except ethylene oxide sorption and internal-diffusion rates have been ruled out with a considerable degree of certainty. As both of these mechanisms will fit the observed experimental data, no distinction between them is possible.

COMPARISON WITH PRIOR STUDIES

Choice of the B.E.T. equation to describe water adsorption in the present work has one unfortunate aspect due to the inherent limitations of the B.E.T. equation. As saturation conditions are approached, the equation breaks down, predicting infinite rates of reaction. As a result no extrapolation of the present data to liquid-phase conditions is possible, and the present data cannot be compared with those of Othmer and Thaker (*12*).

The differential rates obtained in the present study were several times as high as those obtained on Reed's (*15*) integral reactor, while the product-distribution range was approximately the same. The large effect of the amount of water in the resin on the reaction rates was observed but not fully recognized by Reed. The temperature variation throughout their integral reactor, as well as the absence of knowledge of their average particle sizes, prevents any more detailed comparison.

Duplication of several of the runs reported by Hamilton and Metzner (*9*) gave ethylene glycol rates that agreed within the small analytical error, while the diethylene glycol rates were very much lower in this work than in Hamilton's. The analytical procedure which was used previously for measuring the total glycol rates (dichromate-acid oxidation) was susceptible to errors due to polymer impurities in the feed, and since low conversions were obtained, these errors magnified the rates for the higher glycols. There appeared in Hamilton's studies to have been no appreciable effect of the partial pressure of ethylene oxide and temperatures above 150°C. on reaction rates. The small temperature effect on reaction rates for catalyst conditions far from saturation was confirmed by the present data, but the small effect of the partial pressure of ethylene oxide was not. A possible reason for the Reynolds number effect on the reaction rates found by Hamilton (and the small effect of the ethylene oxide) was that polymer in the feed was

carried over and coated the resin, with the result that the rate-determining step became diffusion of ethylene glycol through the coated film. Further and conclusive evidence of resin coating in the previous study lies in the weight gain of Hamilton's catalyst particles during reaction and in the low activity of the used catalyst. In the present work, in which polymer entrainment into the reactor was eliminated, both the activity and appearance of the used and fresh particles were nearly the same, except for the highest temperature runs, in which some thermal degradation started to take place. Thus the earlier data (*9*) on ethylene glycol formation rates are confirmed herein, but resin activity (life) and the selectivity of glycol formation are both much higher than reported earlier.

PRACTICAL ASPECTS

This section presents preliminary information on factors of primary importance insofar as the commercial aspects of the reaction are concerned, as well as further scientific data.

Catalyst Life and Activity

The production of glycols was varied from 0.5 to 50 lb. of glycol produced/lb. of catalyst. The data (*6*) showed no trend in catalyst activity with time after the initial start-up. The resin activity rapidly decreased to about 85 to 90% of its initial activity and then remained at this level indefinitely.

Product Distribution

Detailed data (*6*) on selectivity of the catalyst toward formation of ethylene glycol (that is minimization of the formation of higher glycols) show that there is no trend with temperature, pressure, or Reynolds number. The variation with molal ratio of water to ethylene oxide is unusually slight, particularly when compared with the results reported by the prior art on sulfuric acid catalysts.

Effect of Conversion Level

The highest ethylene-oxide conversion studied was 54%, due to limitations of the equipment. (At higher conversion levels the temperature control was inadequate to cope with the high rates of heat release as the 54% conversion took place in a contact time of only 0.02 sec.) The products obtained under conditions of high conversion depend on the pressure and molal ratio of ethylene oxide to water in the feed stream. When both are low, conversion level does not appear to influence the product composition; that is 75 to 90% of the glycol mixture consists of ethylene glycol, just as at lower conversion levels. However the production of ethylene glycol may be nearly completely suppressed by running at pressures and molal ratios such that the reaction gases become supersaturated with respect to ethylene glycol. This suppression of ethylene glycol formation is not due to a loss of catalytic selectivity under such conditions but rather depends on the fact that the ethylene glycol formed has no place to go. Since it cannot leave the reactor so rapidly as it is being formed, it is converted into a mixture of higher molecular-weight glycols. Thus it is seen that the excellent selectivity of the present catalyst may either be exploited or masked completely by proper choice of the reaction conditions.

CONCLUSIONS

A mechanistic study of ethylene oxide hydration in the vapor phase over acidic cation exchange resins in a differential reactor showed that the rate-controlling step was either the diffusion rate of ethylene oxide into the catalyst particle or its rate of sorption onto the surface of the particle. The rate-controlling step is strongly influenced by the amounts of water sorbed by the catalyst. As a result the usual B.E.T. adsorption equation was used as a basis for quantitative correlation of the rate data.

No particular attempt was made to define all the factors which might conceivably affect the commercial aspects of this catalyst. However data obtained incidental to the above study showed excellent catalyst life and unusual selectivity over the entire range of variables studied.

ACKNOWLEDGMENT

The Research Corporation kindly extended financial assistance which made this research possible. Professor Harold Kwart, Department of Chemistry, University of Delaware, was frequently consulted and contributed materially to the success of the work. Both contributions are gratefully acknowledged.

NOTATION

a = constant in B.E.T. adsorption equation
A = surface area
b = constant in B.E.T. equation
B.E.T. = Brunauer, Emmett, and Teller
D or D_p = particle diameter; numerical subscripts refer to run numbers
$Et(OH)_2$ = ethylene glycol
G = mass velocity based on empty cross-sectional area of reactor
$Hi(OH)_2$ = higher molecular-weight glycols (diglycol and up)
H^+ = equivalents of hydrogen ion (proportional to mass of catalyst used)
k''' = reaction-rate constant
k, k'' = proportionality constants in Equations (4) and (3) respectively (temperature-independent reaction-rate constants)
N_{Re} = modified Reynolds number for use in packed-bed calculations (*10, 13*), $N_{Re} = (D_pG/\mu)$
P, p = pressure, p_{EtO}, p_{H_2O}, p_{sat}, p_T refer to the partial pressures of ethylene oxide, water, the saturation (vapor) pressure of water, and the total pressure, respectively
r = reaction rate, r_{EtO}, reaction rate of ethylene oxide, moles per unit time; numerical subscripts refer to run numbers
v_{BET} = specific quantity of adsorbed water, as given by the B.E.T. equation
μ = viscosity of gas mixture passing through bed.

LITERATURE CITED

1. Abrams, I. M., *Ind. Eng. Chem.*, **48**, 1469 (1956).
2. Bronsted, J. N., Mary Kilpatrick, and Martin Kilpatrick, *J. Am. Chem. Soc.*, **51**, 428 (1929).
3. Brunauer, Stephen, P. H. Emmett, and Edward Teller, *ibid.*, **60**, 309 (1938).
4. Curme, G. O. Jr., and Franklin Johnson, "Glycols," p. 343, Reinhold, New York (1953).
5. Davis, P. C., C. S. von Waaden, and Fred Kurata, *Chem. Eng. Progr. Symposium Ser. No. 4*, **48**, 91 (1952).
6. Ehrreich, J. E., thesis, Univ. Delaware, Newark, Delaware (1958).
7. Frank-Kamenetskii, D. A., "Diffusion and Heat Exchange in Chemical Kinetics," Trans. by N. Thon, Princeton Univ. Press, Princeton, N. J. (1955).
8. Glueckauf, E., and G. P. Kitt, *Proc. Royal Soc. (London)*, **A228**, 322 (1955).
9. Hamilton, G. E., and A. B. Metzner, *Ind. Eng. Chem.*, **49**, 838 (1956).
10. Hougen, O. A., and K. M. Watson, "Kinetics and Catalysis," p. 975, John Wiley, New York (1947).
11. Matignon, Camille, Henri Moureu, and Maurice Dode, *Bull. Soc. chim.*, **1**, 1308 (1934).
12. Othmer, D. F., and M. S. Thakar, *Ind. Eng. Chem.*, **50**, 1235 (1958).
13. Perry, J. H., ed., "Chemical Engineers' Handbook," 3 ed., p. 546, McGraw-Hill, New York (1950).
14. Pritchard, J. G., and F. A. Long, *J. Am. Chem. Soc.*, **78**, 2663 (1956).
15. Reed, L. M., L. A. Wenzel, and J. B. O'Hara, *Ind. Eng. Chem.*, **48**, 205 (1956).
16. Sundheim, B. R., M. H. Waxman, and A. P. Gregor, *J. Phys. Chem.*, **57**, 974 (1953).
17. Unpublished notes on reaction kinetics, Univ. of Delaware, Newark, Delaware (1956).

Manuscript received August 25, 1958; revision received January 9, 1959; paper accepted January 21, 1959.

Transfer Resistance and Fluid Mechanics

ROBERT J. McCARTER and LEROY F. STUTZMAN

Remington Rand Univac, St. Paul, Minnesota

Pure liquids were evaporated in a wetted-wall column into flowing streams of air to investigate the thickness and transfer resistance of gas films.

It was found necessary to express Reynolds number relative to the liquid surface to correlate transfer with gas flow.

Laminar and buffer layers in the gas phase were calculated from fluid-flow principles and compared to the effective film thickness calculated from mass transfer and molecular diffusivity. Good agreement was obtained, indicating applicability of fluid mechanics to mass transfer problems.

Eddy diffusivity was indicated to have a negligible effect upon the total resistance to transfer. Consequently it might be concluded that in packed towers where distances in the turbulent phase are shorter transfer between phases depends almost entirely upon molecular diffusivity.

Particularly fundamental to gas absorption theory has been the two-film concept first proposed by Whitman (*29*). This concept assumes that the principal resistances to interphase transfer are contained in stable fluid films on each side of the liquid-gas interface through through which material flows by molecular diffusion.

The object of this investigation was to evaluate the additional resistance that may be presented by eddy-diffusion transfer and to compare the film concept with the physical approximations of fluid mechanics. Summaries of fluid-flow knowledge as it pertains to this study are available in works by Bakhmeteff (*2*), McAdams (*18*), and Rouse (*23*).

EXPERIMENTAL APPARATUS

The wetted-wall column offers simplifying advantages for mass transfer studies. By evaporating pure liquids, liquid film resistances are eliminated as no concentration gradients exist in the liquid. The partial pressure of the diffusing material at the liquid-gas interface is the vapor pressure of the pure material. Compositions in the gas phase may be determined by simple measurement of material loss from the liquid system. The fluid-flow characteristics of the gas phase, as contained in a cylindrical duct, are the most standard and the best understood.

The apparatus was in principle similar to that used in previous studies but with the diameter of the wetted-wall section proportionately enlarged to intensify any possible resistance effects of eddy diffusivity. Thus the ratio of the volume in eddy-diffusion transfer to the area of molecular-diffusion flow was arranged as high as conveniently possible and exceeds that of previous work.

Figure 1 shows a schematic drawing of the apparatus. The column was constructed so that different sections of wetted height could be installed. A collar of 40-mesh screen assisted distribution of liquid at the entry slot. Another slot approximately 20 deg. from the vertical allowed exit of the liquid at the bottom of the wetted wall. Vapor seals in the inlet and outlet chambers were maintained by proper liquid levels. A planetary type of gear pump with valved bypass and ¼-in. copper tubing lines formed the liquid recirculation system. A liquid reservoir was formed by a section of ⅔-in. I.D. glass tubing placed vertically below the outlet line from the column. The level in this tube was sensitive to liquid losses from the system. Make-up liquid was added here from a burette at measured rates to maintain a constant level. Liquid circulation rates were obtained at the conclusion of runs by diverting the liquid flow into a volumetric container and timing with a stop watch. Liquid temperatures were measured by fine wire copper-constantan thermocouples and a precision potentiometer.

A ⅛ horsepower blower supplied air through a standard 2-in. steel pipe to the column. A valved line and side bleed allowed adjustment of rate. Measurement of air flow was made by standard orifice technique. Sufficient length was provided in the unwetted bottom section of the column to standardize the gas flow. Air temperatures were measured by thermometers. Inlet air humidity was determined by a standard ether-cooled dew point instrument.

Liquids for study were selected to give the widest practical variation in volatility and chemical nature with the limitation that sufficient physical properties be known for the necessary calculations. The availability of vapor-pressure and molecular-diffusivity data was of particular pertinence and eliminated many materials of interest. Benzyl chloride and *n*-amyl alcohol were selected as low volatility compounds; acetone and ethyl acetate as high volatility compounds; and water, toluene, and *n*-butanol as intermediates.

The fundamental equation of diffusion

$$Na = -D_v \frac{dc}{dL} \qquad (1)$$

is modified (24) for application to wetted-wall columns to

$$Na = \frac{D_v p}{RTx} \frac{\Delta p}{p_{bm}} \qquad (2)$$

where the effective film thickness is the desired result and represents the thickness of a purely stagnant gas film that would offer the same resistance as that encountered by the measured transfer.

EXPERIMENTAL PROCEDURE

The liquid system flow was adjusted to a rate sufficient to insure complete liquid coverage of the column wall without ripples upon the surface. Because of surface-tension effects this adjustment required care and close observation of the liquid surface. Generally the satisfactory range of flow was quite narrow. The view afforded through the glass wall of the column as well as that down the bore of the column were necessary to certify complete liquid coverage entirely in smooth laminar flow. Unwetted areas and particularly ripples are suspected as defects of some reported data. As wetting agents were not used, their possible influence on vapor pressure was not a factor. The air flow was adjusted to the desired rate by the line and bleed valves. The apparatus was run until temperature and rate equilibriums were obtained, and the previously enumerated measurements were then recorded. Measurements were continued until check results were obtained and large enough volumes of liquid had been evaporated to ensure volumetric accuracy. Successive air rates were varied as widely as possible within the turbulent range.

EXPERIMENTAL RESULTS

Table I exemplifies the experimental data (columns 1 to 6) and the transfer

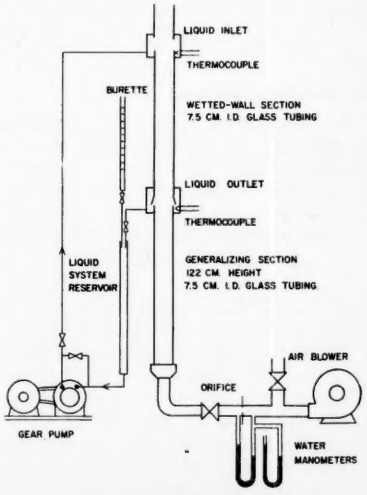

Fig. 1. Equipment.

Robert J. McCarter is now with California Research Corporation, Richmond, California, and Leroy F. Stutzman with the State Department Educational Mission to the University of Valparaiso, Valparaiso, Chile.

calculations (columns 7 to 11).* The gas-transfer coefficient was calculated and included for convenience to related studies.

To correlate film thickness with turbulence, it was necessary to relate the gas flow to the moving-liquid surface rather than the stationary column wall. Since the liquid surface was in direct contact with the gas film, its velocity would contribute to the shear forces determining the thickness of the laminar layer. Without inclusion of the effects of liquid motion, log-log plots of the column diameter to film thickness parameter vs. the Reynolds number of the gas flow yielded slopes varying from 0.56 to 0.80. This variation was unrelated to any apparent physical variable of the gas stream. However when the Reynolds number of the gas stream was calculated to relate to the liquid surface on the wetted wall (that is liquid surface velocity added to air flow velocity to obtain total flow velocity V), the plots of Figures 2 and 3 were obtained. All compounds correlated within the limits of experimental error with an 0.8 line slope, yielding an exponent common to transfer relations.

Surface velocities were estimated by the equation (*6, 28*)

$$u_s = 1/2\left(\frac{9g\rho q^2}{\mu}\right)^{1/3} \qquad (4)$$

The viscosity of the air stream was calculated to be sufficiently low so that its effect on the liquid surface might be neglected.

Table 2 summarizes the calculations of layer thicknesses as predicted by fluid mechanics.* The data of Nikuradse (*21*) were used as reported by McAdams (*18*) and Rouse (*23*). Plots of Nikuradse's data consist of generalized velocity-distribution diagrams in which the parameter,

$$u^+ = u \Big/ \sqrt{\frac{\tau_0 g}{\rho}},$$

is plotted as a function of the parameter,

$$y^+ = \frac{y\rho}{\mu}\sqrt{\frac{\tau_0 g}{\rho}}.$$

This distribution, derived from water data, has proved applicable to compressible fluids at moderate velocities. As reported by McAdams (*18*), the data permit the evaluation of the laminar layer (y^+ from 0 — 5), the buffer layer (y^+ from 5 — 30), and the turbulent core ($y^+ > 30$). However, Rouse (*23*) divides the intermediate or transition layer and reports only two zones, an effective laminar layer (y^+ from 0 to 11.6) and a turbulent core ($y^+ > 11.6$).

It was necessary to consider the variable concentration of the diffusing material as it affected the physical properties of the various layers. The average concentration in the laminar layer was estimated upon the assumption that the transfer proceeded solely by molecular diffusion. Calculated densities and viscosities were correspondingly adjusted. A cut-and-try calculation was employed to obtain agreement between laminar-layer thickness (column 7) and average composition.

The distance from the liquid to the core edge of the buffer layer was similarly calculated. This distance less the laminar-layer thickness then represented the buffer-layer thickness (column 8). The average composition in the layer was estimated from the average of the partial pressures in the core and at the boundary of the laminar layer.

The McAdams laminar layer was multiplied by the ratio of $y^+ = 11.6$ to $y^+ = 5$ to obtain the Rouse laminar layer (column 9). This ignores the variation in average composition between the layers, but this difference was shown to have negligible effect.

Values of eddy diffusivity (column 6) were calculated from the Sherwood and Woertz (*26*) equation:

$$\delta_E = 0.08\bar{u}r\sqrt{f} \qquad (5)$$

A previous investigation by the authors (*19*) verified the reliability of Equation (5) when applied to gases flowing in cylindrical ducts.

*Tabular material has been deposited as document 6053 with the American Documentation Institute, Photoduplication Service, Library of Congress, Washington 25, D. C., and may be obtained for $1.25 for photoprints or 35-mm. microfilm.

*See footnote in column 1.

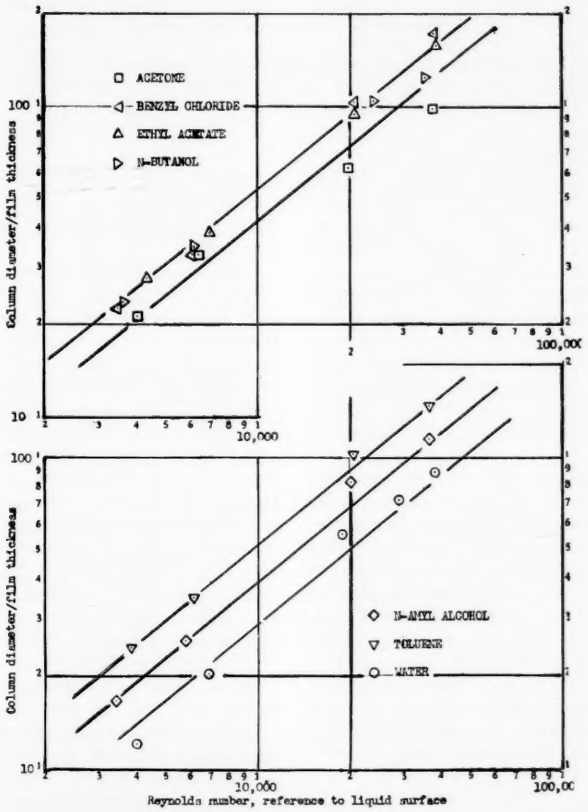

Fig. 2. Column-diameter–to–film-thickness parameter vs. Reynolds number. Evaporation of pure liquids into air in a 3-in.–diameter wetted-wall column, 40-in. wetted height.

Discussion of Results

The 0.8 exponent obtained in Figures 2 and 3 is a further point of consistency with fluid mechanics.

An attempt to adjust these lines to a single correlation on the properties of the laminar gas layer resulted in the equation

$$D/x = 0.024(N_{Re})^{0.8}(N_{Sc})^{0.4} \qquad (6)$$

where the Reynolds number of the gas flow is calculated relative to the liquid surface.

This equation correlated the lines with an average deviation of 12%. The range of the Schmidt number was not sufficient to lend precision to its exponent [derived by log-log plot of $D/x(N_{Re})^{0.8}$ vs. N_{Sc}]. The equation resembles prior results (*10*), but a quite different relationship is expressed at lower gas velocities due to a difference in definition of Reynolds number.

It may be noted that the correlation lines for acetone in Figures 2 and 3 are weighted to the data points at lower Reynolds numbers. After experiments were concluded, heat balances disclosed that evaporation was no longer adiabatic at the highest flow rates for acetone. Thus at the most severe conditions heat transfer of effect had occurred through the column wall. Hence the liquid surface temperature in this case was less than that indicated by measurement, and in turn the partial pressure driving force was less, the effective film thickness less, and the diameter to thickness parameter greater. Appropriate wall insulation would have eliminated this effect.

No appreciable difference in results occurred with the different heights of wetted section. Thus eddy diffusivity was indicated to add little additional transfer resistance in the taller wetted wall.

The simplest correlation of the Table 2 data is the agreement between Rouse laminar-layer thickness (column 9) and effective film thickness (column 10). Apparently the Rouse arbitrary boundary limit results in a division of zones that gives a reasonable physical representation in terms of resistance to mass transfer. However the transfer data would favor a slightly thicker laminar layer, as indicated by the effective film thickness exceeding the Rouse laminar layer in nearly all cases. A division of zones at about $y^+ = 13.5$ would be inferred from the transfer data, as displayed by Figure 4 (estimate of y^+ derived by linear plot of

$$x\rho/\mu \text{ vs. } \sqrt{\frac{\rho}{\tau_0 g}}, \text{ where } \sqrt{\frac{\tau_0 g}{\rho}} = u^*$$

the friction velocity).

If this relationship to fluid dynamics might be firmly defined by further work, it is suggested that the wetted-wall column could then become a relatively simple means to experimentally determine values of molecular diffusivity. The complications of other apparatus are testified to by the scarcity and variance of molecular diffusivity data in the literature. A considerable service would be performed by such determinations, as evidenced by numerous pleas for such data originating from several fields of inquiry.

Evaluation of most aspects of the results is obstructed by the uncertainty attached to molecular diffusivity values. Additionally at the conditions of this study the very low concentration of diffusing material (for example about 0.02 mole fraction water or 0.0015 mole fraction of benzyl chloride) in the gas layer of interest raises the question of how molecular diffusivity may vary with concentration. The literature contains theory (*7, 9, 11, 12, 15, 20*) about the amount of such variation, but a conclusive answer is not available. No adjustment of values was made in this study. Water, the only strongly polar compound used, would be a prime suspect in this respect. Looser confidence limits would be attached to the molecular diffusivity values for acetone as derived from an empirical formula. The largest discrepancies from the mean of the correlations were obtained with water and with acetone, producing a temptation to improve the derived correlations by deleting the data for these two materials.

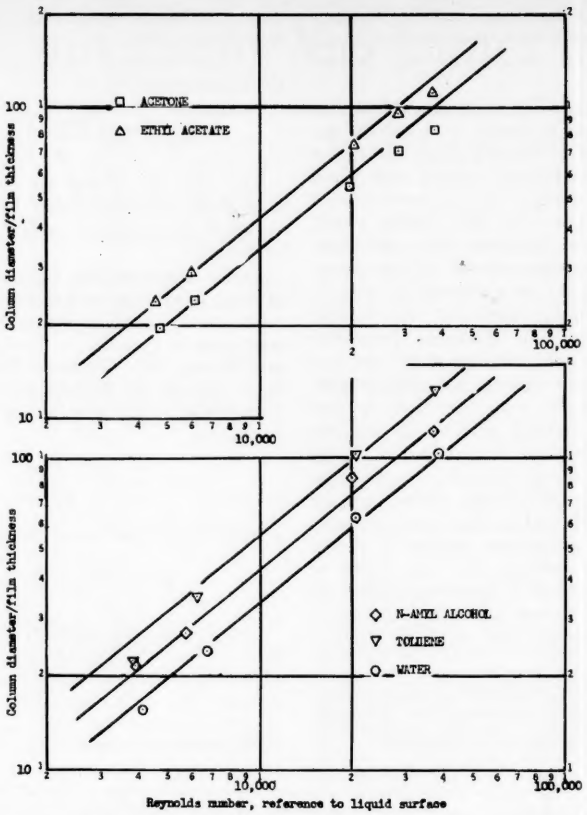

Fig. 3. Column-diameter–to–film-thickness parameter vs. Reynolds number. Evaporation of pure liquids into air in a 3-in.–diameter wetted-wall column, 14-in. wetted height.

Inspection of the relative extension of effective film thickness into the buffer layer revealed only a linear correlation and indicated no dependence upon eddy diffusivity. Further calculations upon the influence of eddy diffusivity were pursued in which it was assumed that the magnitude of eddy diffusivity was proportional to the gas velocity from the center of the core to the edge of the buffer layer. These calculations indicated a very minor contribution to resistance by eddy diffusivity in the turbulent core.

CONCLUSIONS

The velocity of the liquid surface influenced the transfer resistance encountered, and inclusion of this effect allowed correlation of the film data with the 0.8 exponent common to transfer relations.

Reasonable agreement was obtained between laminar gas layers calculated from fluid-flow theory and effective film thicknesses derived experimentally, in view of the uncertainties in the accuracy of molecular diffusivity values. The division of fluid characteristics into two zones of laminar and turbulent flow as advocated by Rouse (*23*) represented a reasonable approximation to the physical transfer resistances measured in the wetted-wall column, although a slightly thicker laminar layer would be estimated from the transfer data. If this relationship were proven and refined, the wetted-wall column might then usefully serve to determine diffusivity values.

No correlative effect of eddy diffusivity could be found upon transfer through the buffer zone as defined by fluid-flow theory. No appreciable difference in results was obtained by a threefold change in wetted-wall height. This, combined with the calculated relative values of eddy diffusivity, indicated a negligible contribution by eddy diffusivity to the total transfer resistance with the dimen-

sions of transfer as employed. The dimensions of most gas absorption in comparison are such that eddy diffusivity is indicated to be an unimportant factor.

ACKNOWLEDGMENT

The United States Navy, Office of Naval Research, sponsored this study performed at Northwestern Technological Institute, Evanston, Illinois. Appreciation is expressed to Howard A. Koch, Jr., Harold A. Blum, Thomas A. Peake, Paul G. Reis, and Wayne S. Dodds for valuable help.

NOTATION

c = concentration, g. mole/cc.
D = column diameter, cm.
D_v = molecular diffusivity, sq. cm./sec.*
f = Fanning friction factor, dimensionless
g = acceleration of gravity, cm./sec.^{2}
kg = gas-transfer coefficient
L = distance, cm.
Na = rate of diffusion, g. mole/sq. cm. sec.**
N_{Re} = Reynolds number, $DV\rho/\mu$, dimensionless
N_{Sc} = Schmidt number, $\mu/\rho D_v$, dimensionless
p = total pressure, mm.Hg***
Δp = average partial pressure driving force effecting transfer, mm.Hg†
p_{bm} = average partial pressure of inerts, mm.Hg††
q = volumetric flow per width of film, cc./cm. sec.
r = distance from wall to center of duct, cm.
R = gas law constant, mm.Hg cc./g. mole °K.
T = absolute temperature, °K.†††
u = local gas velocity, cm./sec.
$\bar{u}$ = average gas velocity, cm./sec.
u^* = friction velocity, cm./sec.
u_s = liquid surface velocity, cm./sec.
V = flow velocity, cm./sec. (herein equal to the sum of air flow and liquid surface velocities)
x = effective film thickness, cm.
y = distance from wall, cm.
ρ = density, g./cc.
μ = absolute viscosity, g./cm. sec.
τ_0 = shearing force at wall, g./sq. cm.
δ_E = eddy diffusivity, sq. cm./sec.

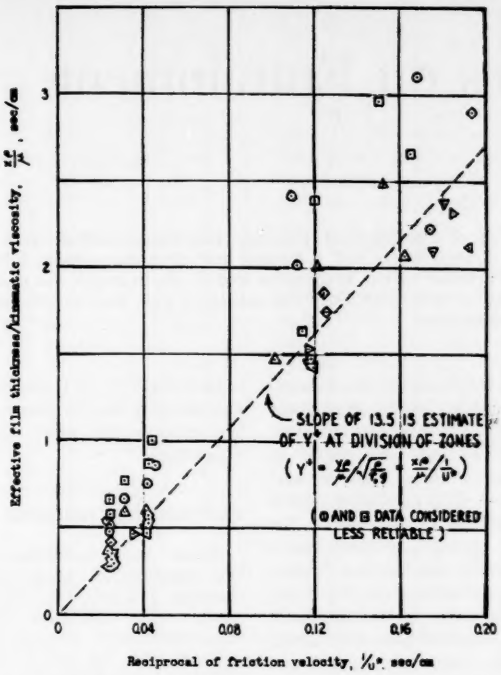

Fig. 4. Estimate of zone division from transfer data.

LITERATURE CITED

1. Arnold, J. H., *Physics*, **4**, 225 (1933).
2. Bakhmeteff, B. A., "The Mechanics of Turbulent Flow," Princeton Univ. Press, Princeton, New Jersey (1941).
3. Chapman, S., and T. G. Cowling, "The Mathematical Theory of Non-Uniform Gases," Cambridge Univ. Press, Cambridge, England (1939).
4. Chilton, T. H., and A. P. Colburn, *Ind. Eng. Chem.*, **26**, 1183 (1934).
5. Colburn, A. P., *ibid.*, **22**, 967 (1930).
6. ———, and O. A. Hougen, *Bull. Univ. Wisconsin Eng. Exp. Sta.*, Series No. 70 (October, 1930).
7. Corcoran, W. H., B. Roudebush, and B. H. Sage, *Chem. Eng. Progr.*, **43**, 135 (1947).
8. Drew, T. B., *Trans. Am. Inst. Chem. Engrs.*, **26**, 26 (1931).
9. Furry, W. H., *Amer. J. Phys.*, **16**, 70 (1948).
10. Gilliland, E. R., and T. K. Sherwood, *Ind. Eng. Chem.*, **26**, 516 (1934).
11. Hirschfelder, J. O., C. F. Curtiss, and R. B. Bird, "Molecular Theory of Gases and Liquids," John Wiley, New York (1954).
12. Jeans, J. H., "Dynamical Theory of Gases," 2d., Cambridge Univ. Press, Cambridge, England (1904).
13. Johnstone, H. F., and A. D. Singh, *Ind. Eng. Chem.*, **29**, 286 (1937).
14. Kalinske, A. A., and C. L. Pien, *ibid.*, **36**, 220 (1934).
15. King, C. V., and P. L. Howard, *ibid.*, **29**, 75 (1937).
16. Lamb, H., "Hydrodynamics," Cambridge Univ. Press, Cambridge, England (1916).
17. Lonius, *Ann. Physik*, **29**, 664 (1929).
18. McAdams, W. H., "Heat Transmission," McGraw-Hill, New York (1942).
19. McCarter, R. J., L. F. Stutzman, and H. Koch, *Ind. Eng. Chem.*, **41**, 1290 (1949).
20. Meyer, O. E., "Kinetic Theory of Gases," Longmans, Green, and Co., New York (1899).
21. Nikuradse, J., *Forschungsheft*, **361**, 1 (1933).
22. Prandtl, L. A., *Z. angew. Math. u. Mech.*, **5**, 136 (1925).
23. Rouse, Hunter, "Fluid Mechanics for Hydraulic Engineers," McGraw-Hill, New York (1938).
24. Sherwood, T. K., "Absorption and Extraction," McGraw-Hill, New York (1937).
25. ———, and E. W. Comings, *Trans. Amer. Inst. Chem. Engrs.*, **28**, 88 (1932).
26. ———, and B. B. Woertz, *ibid.*, **35**, 517 (1939).
27. Stull, D. R., *Ind. Eng. Chem.*, **39**, 517 (1947).
28. Thomas, W. J., and S. Portalski, *ibid.*, **50**, 1081 (1958).
29. Whitman, W. G., *Chem. & Met. Eng.*, **29**, 146 (1923).

Manuscript received December 1, 1958; revision received March 11, 1959; paper accepted March 27, 1959.

*Calculated from experimental values presented in the International Critical Tables, with the exception that an empirical formula (11) was used for acetone.

**Calculated from measurement of the rate of material volume loss from the liquid circulation system, the density and molecular weight of the evaporating material, and the wetted area of the column.

***Measured by barometer.

†Calculated as the log mean difference between the liquid vapor pressures and the partial pressures of the diffusing material in the air stream at the top and bottom of the wetted-wall section. The liquid vapor pressures (or interface partial pressures) were calculated from the determined inlet and outlet liquid temperatures and vapor-pressure data compiled by Stull (*27*). The partial pressure of the diffusing material in the inlet air was zero, with the exception of the water case where the inlet humidity was determined by dew point. The partial pressure in the outlet air was calculated from a material balance of the liquid evaporation rate and air flow rate. The discrepancy between this average partial pressure and the exact partial pressure at the limit of the gas film at the outlet was calculated to be small, since a majority of the transfer resistance was indicated to be contained in the laminar and buffer layers and the outlet partial pressures were generally small in comparison to liquid vapor pressures.

††Calculated as the total pressure minus the arithmetic average of the interface and air stream partial pressures of the diffusing material at inlet and outlet of the wetted-wall section.

†††Calculated for the gas film as the arithmetic average of the inlet and outlet liquid temperatures and inlet and outlet gas temperatures.

Studies on Entrainment

SHUICHI AIBA and TOYOKAZU YAMADA

University of Tokyo, Tokyo, Japan

After application of a biochemical technique, size distribution of liquid drops from air bubbles blown through water and a butanol and glycerine solution filled to a certain depth in a glass cylinder 9.6 cm. in diameter and 47 cm. in length was measured.

The initial vertical velocity of drops was estimated from the experimental results, with reference to its trajectory.

Entrainment is frequently encountered in such equipment as distillation columns and evaporators. The phenomenon generally causes low plate efficiencies in distillation and reduced purity and yield of products. The published papers on entrainment have advocated the provision of an appropriate space above the liquid surface or the use of a reasonable gas or vapor velocity in the space (*1, 2, 5*). These studies have been made under specific experimental conditions. For instance, in the study of entrainment in evaporators a small amount of sodium chloride solution is added to the boiling liquid and the chloride ion content of the condensate is determined in order to evaluate the over-all degree of entrainment (*2*).

Recently Newitt *et al.* (*6*) took high-speed photographs of air bubbles bursting at a water-air interface. Garner *et al.* (*3*) also measured the size and number of drops thus generated. Such studies were undertaken to clarify the mechanism of drop formation, an intrinsic feature of entrainment.

Since the phenomenon is very complicated, many facts remain to be disclosed experimentally and theoretically before entrainment can be prevented, therefore this experimental study on entrainment was made.

EQUIPMENT AND PROCEDURE

Figure 1*a* is a schematic diagram of the experimental apparatus. The inner diameter and height of the glass cylinder used in this experiment are 9.6 and 47 cm., respectively. Adjacent to its bottom, a brass pipe 1.0 cm. in diameter, with closed end, was inserted horizontally along a radius of the cylinder. Along the top line of the pipe nine orifices each 0.103 cm. in diameter were bored at 1.0-cm. intervals, and air from a compressor was blown through them. The rate of air flow was measured with an orifice flow meter.

Water, butanol, and glycerine solutions were used in this series of experiments. The glass cylinder was filled with each liquid to a certain depth above the pipe. Air bubbling was continued for several minutes; then liquid drops entrained in the space above the liquid were sampled, and the size distribution was determined by the following procedure.

First, a glass plate (7.7 by 2.6 by 0.1 cm.), after being cleansed with cleaning solution, distilled water, and alcohol, was placed at a certain height above the liquid surface, perpendicular to the air flow to catch the liquid drops.

Second, a cascade impactor, made of a tin plate, was used to trap droplets which are small enough to bypass the glass plate. The linear velocity of air at the entrance of the impactor was adjusted so as to be identical with the nominal linear velocity of air in the glass cylinder. The principal dimension of the impactor is also shown in Figure 1*a*.

A species of bacteria, *Serratia marcescens*, was suspended in each liquid (10^7 cells/cc. of the liquid). Impinged drops which contain the bacterial cells left on the glass ring-shaped stains formed by the cells aligned along their circumferences. The stains were then colored with methylene blue solution, and the size was easily determined with a microscope, as shown in Figure 1*b*.

It was ascertained that such a concentration of the bacterial suspension exerted little influence on the physical properties of the liquid, in particular on the density, viscosity, and surface tension.

It is possible that small droplets impinged on the glass plate will be vaporized immediately after the glass is taken outside for inspection and thus missed; however this possibility is minimized by the procedure outlined above.

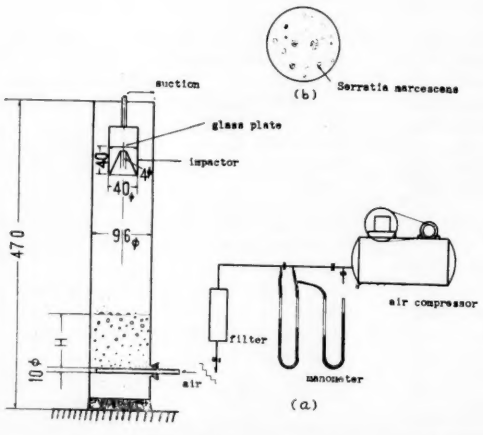

Fig. 1. Schematic diagram of experimental apparatus.

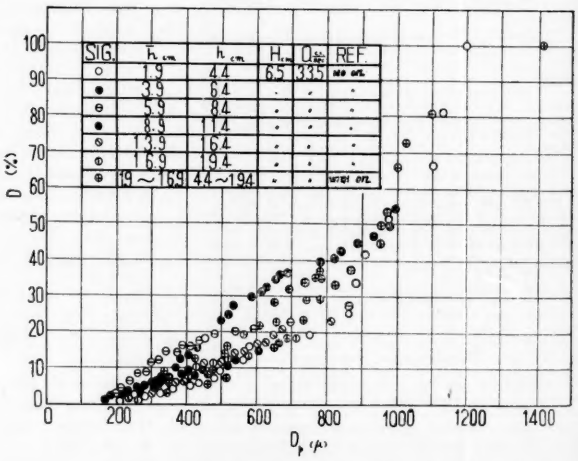

Fig. 2. Comparison between cumulative volume curves obtained by the use of glass plates with and without oil; $v' = 0.46$ cm./sec.

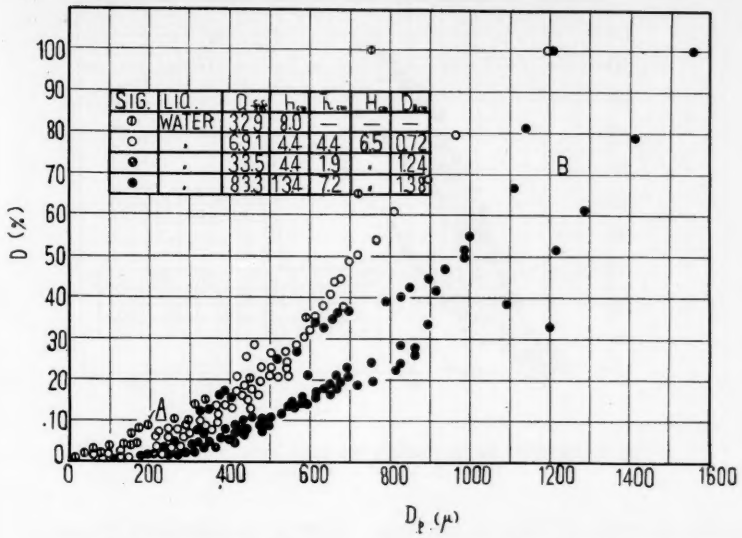

Fig. 3. Effect of air flow rate on cumulative volume curves of liquid drops. *A* refers to the data (*1*). $v' = 0.86$ to 10.37 cm./sec. ($Q = 6.91$ to 83.3 cc./sec.).

Under each experimental condition, which will be referred to later, the height of sampling was changed, and the diameters of the stains were then determined, except when the drops were apparently split owing to impingement.

The diameters thus determined are thought to be very different from those of drops just before they impinge, because of the contact angle between the liquid and the glass plate. Therefore the diameters of drops before the impingement were estimated by the following calibration.

Liquid drops from a glass capillary were dropped onto a glass plate and the volumetric mean diameter was calculated on the basis of the measurement of the total number and the mass of these drops. On the other hand, the diameters of the stains were determined as explained previously and the volumetric mean was calculated. Thus the correction factor, defined by the ratio of the former diameter to the latter, was found to be 0.5 ± 0.1 in the range of $D_p' = 3{,}000$ to 500μ. It was assumed that such a calibration also holds true for the case of D_p' less than 500μ.

Furthermore, to ascertain the reliability of the calibration, a glass plate coated with a mixture of grease and gas oil was suspended inside the cylinder to catch the entrained drops.

Effects of air flow rate, liquid surface tension, liquid viscosity, and liquid depth on the size distribution of the entrained drops were studied. Concomitantly photographs of air bubbles at the liquid surface were taken, and the volumetric mean diameters (on the assumption that they were spherical) were computed. Since it was seen that the air bubbles at the liquid surface were rather uniformly distributed, the apprehension of nonuniformity of generation of air bubbles through the nine orifices seems unbounded.

This series of experiments was conducted at room temperature (20° to 25°C.), the surface tension and viscosity of the liquid being determined by the use of the platinum-wire method and the Ostwald viscometer, respectively.

EXPERIMENTAL RESULTS*

It was found that the cascade impactor was effective only when the sampling location was far from the bubbling surface. Conversely, near the surface the existence of larger drops made the determination of small droplets difficult.

When it was noted that the vaporization of liquid drops seemed unlikely in the space inside the glass cylinder, the cumulative volume curves relating to each sampling location were superimposed on the curve that was obtained at the lowest sampling height, as shown in Figure 2. It is also noted from Figure 2, which represents an average of the size distribution of drops collected at $h = 4.4$ cm., that the aforementioned calibration of diameters of liquid drops is reasonable, because the data thus calibrated agree well with those which are considered to be free from the deformation of drops.

In the same manner the experimental results relating to other conditions are summarized in Figures 3 to 6 Most of these cumulative curves have a sampling location of $h = 4.4$ cm. In these figures the volumetric mean diameter of bubbles at the liquid surface is also shown.

Though the height of sampling is not always the same in these figures, these curves indicate the size distribution of drops near the bubbling liquid surface. It is seen that the cumulative volume of small droplets less than about $100\ \mu$ is negligible. It is also seen that the physical properties of the liquid and the operating conditions exert a rather marked influence on each curve of the size distribution.

DISCUSSION OF EXPERIMENTAL RESULTS

Since these drops are collected predominantly by inertia, it is necessary to estimate the collection efficiency. The

*Tabular material has been deposited as document 6049 with the American Documentation Institute, Photoduplication Service, Library of Congress, Washington 25, D. C., and may be obtained for $1.25 for photoprints or 35-mm. microfilm.

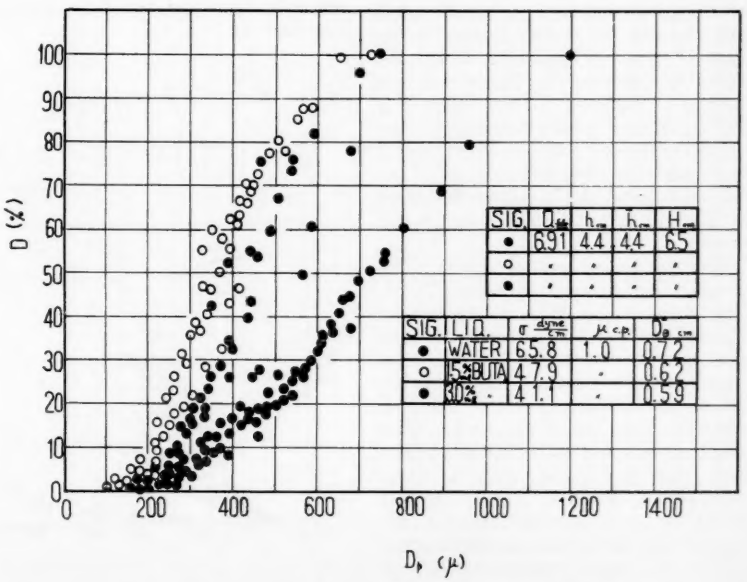

Fig. 4. Effect of liquid surface tension on cumulative volume curves of liquid drops; $v' = 0.86$ cm./sec.

result of this estimation with the equation presented by Ranz *et al.* (*8*) used showed that η for the droplet, for example of 10 μ collected by the cascade impactor, was about 100%. The estimation of η for larger drops collected without the impactor is difficult because the velocity of impingement of these drops is unknown. However with an assumption that the velocity is of the order of the nominal linear velocity of air above the liquid, η for the drop of 100 μ was estimated to be of the order of 50% in the experimental range of air flow rates. Therefore as far as the distribution expressed by the cumulative volume percentage is concerned, the effect of η on the distribution curve seems to be negligible.

In Figure 3, with the increase of Q, rather large drops are likely to become predominant, though each curve does not correspond to the same height of sampling because of foaming. This tendency agrees qualitatively with the experimental results of Akselyrod (*1*) and Garner (*3*), an exact comparison between them is difficult.

The volumetric mean diameter of bubbles in Figure 3 is plotted against Q in Figure 7 (*a*). The relationship is approximately expressed by

$$\bar{D}_B \propto Q^{1/3} \qquad (1)$$

Equation (1) is similar to an empirical correlation presented by Leibson *et al.* (*4*). It is seen from Figure 4 that the decrease in σ tends to decrease the number of large drops. $\bar{D}_B$ in Figure 4 is plotted against σ in Figure 7 (*b*). The correlation is approximately expressed by

$$\bar{D}_B \propto \sigma^{1/3} \qquad (2)$$

As is shown in Figure 5 it is difficult to change the viscosity exclusively without affecting the surface tension in the case of glycerine solution. When one refers to Equation (2), $\bar{D}_B\sigma^{-1/3}$ vs. μ is plotted in Figure 7 (*c*). The effect of μ on $\bar{D}_B$ is not clear. Accordingly the change of the size distribution in Figure 5 is caused primarily by the change of the surface tension, and therefore the effect of viscosity μ on the drop size is not evident.

The experimental relationship between H and $\bar{D}_B$ is shown in Figure 7 (*d*). The effect of H on $\bar{D}_B$ is not very clear. Most of the curves in Figure 6 also indicate that the increase of $\bar{D}_B$ is accompanied by the predominance of larger drops. In the case of $H = 0.6$ cm., specially large drops are seen; direct splashing of liquid by the air flow might have been the cause, since in most cases effect of these various factors might be equivalent to that of the bubble diameter on the size distribution.

Next the initial vertical velocity of drops will be considered. In this consideration small droplets, the terminal

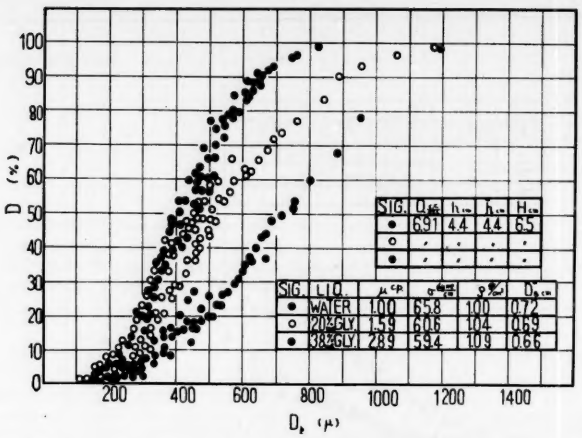

Fig. 5. Effect of liquid viscosity on cumulative volume curves of liquid drops; v' = 0.86 cm./sec.

settling velocity of which is less than each nominal linear velocity of air in the space above the liquid, were excluded.

First the volumetric mean diameter of the drops collected at the highest sampling location $h = h_1$ made in each experiment was calculated. Second $\bar{D}_{p2}$ of the drops at $h = h_2$, excluding those less than $\bar{D}_{p1}$, was determined. In the same manner $\bar{D}_{p3}$, $\bar{D}_{p4}$, and so on, corresponding to $h = h_3$, h_4, respectively, was thus determined ($h_1 > h_2 > h_3 > h_4$). It was postulated that the distance the drop of $\bar{D}_{p2}$ could reach was within the range from h_2 to h_1, while that of $\bar{D}_{p3}$ was from h_3 to h_2. In this calculation the surface of the foaming layer, if any, was chosen as the datum of the distance.

On the other hand the equation of motion of a spherical drop which is assumed, for simplicity, to be ejected vertically from the liquid-air interface is as follows:

$$\frac{dv}{d\theta} = -g\left(\frac{\rho - \rho'}{\rho}\right) \mp \left(\frac{3\rho'}{4\rho D_p}\right)\cdot C\cdot(v - v')^2 \qquad (3)$$

where $\mp$ corresponds to the case $v \geqq v'$ and $v \leqq v'$, respectively. When

$$g\left(\frac{\rho - \rho'}{\rho}\right) = a,$$

$$\frac{dv}{d\theta} = \frac{dv}{ds}\cdot\frac{ds}{d\theta} = \frac{dv}{ds}\cdot v$$

$$\frac{3\rho'}{4\rho D_p} = b$$

Equation (3) is simplified as follows:

$$v\,dv/ds = -a \mp b\cdot C\cdot(v - v')^2$$

Then the distance S the drop reaches is expressed by Equation (4):

$$S = \int_{v_0}^{v'} \frac{v\,dv}{-a - b\cdot C\cdot(v - v')^2} + \int_{v'}^{0} \frac{v\,dv}{-a + b\cdot C\cdot(v - v')^2} = \int_{N_{Re_0}}^{0} \frac{(kN_{Re} + v')k}{-a - b\cdot C\cdot k^2\cdot N_{Re}^2}\,dN_{Re} + \int_{0}^{N_{Re}'} \frac{(kN_{Re} + v')k}{-a + b\cdot C\cdot k^2\cdot N_{Re}^2}\,dN_{Re} \qquad (4)$$

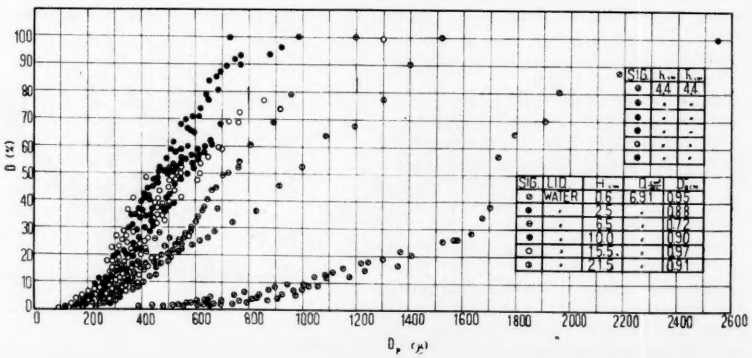

Fig. 6. Effect of orifice submergence on cumulative volume curves of liquid drops; v' = 0.86 cm./sec.

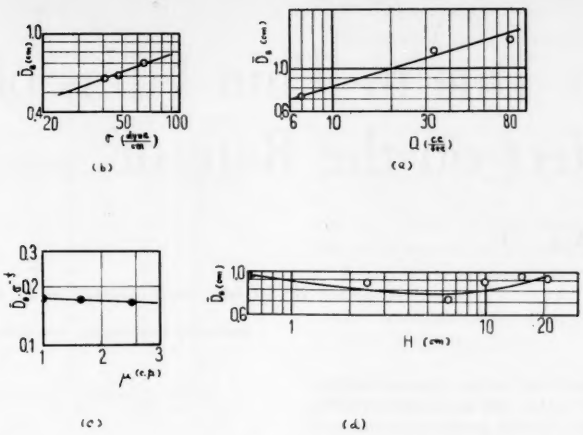

Fig. 7. Relations between bubble diameters and various factors.

where

$$N_{Re} = \frac{D_p(v - v')\rho'}{\mu'} = \frac{v - v'}{k};$$

$$k = \frac{\mu'}{D_p\rho'}; \qquad v_0 - v' = kN_{Re0}$$

$$- v' = kN_{Re'}$$

Relating to each nominal velocity of air above the interface, one could calculate in advance the trajectories of the drop under various initial velocities. In these calculations the drag coefficient was taken from the published data (*7*). When one referred to these diagrams of trajectories and the data of distance the drop could reach, the initial vertical velocity was estimated.

Figure 8 summarizes the result of the same procedure of estimation. It is noted from Figure 8 that v_0 seems to depend on $\bar{D}_p$, and the effect of the aforediscussed factors on v_0 is not evident.

Although the probable error accompanying such estimations is of the order of 10%, the trajectories of drops, in practice, are considered to be far from those which are calculated from the simple assumptions described above. Therefore only the order of magnitude of v_0 is to be noted from Figure 8. The published data of v_0 (*1*), the procedure of estimation being about the same as in this paper, agree well with those of this series of experiments.

CONCLUSIONS

1. After the application of a biochemical technique, the effects of the physical properties of liquid, including those of some operating conditions on the size distribution of drops, were experimentally studied. Rather marked effects of these factors on the drop size were noted.

2. In most cases the drop-size distribution seem to be closely related to the bubble diameter bursting at the interface.

3. The initial vertical velocity of drops was estimated. As far as larger drops are concerned, such information will furnish a clue to determining the height of space above the foaming layer necessary to minimize entrainment.

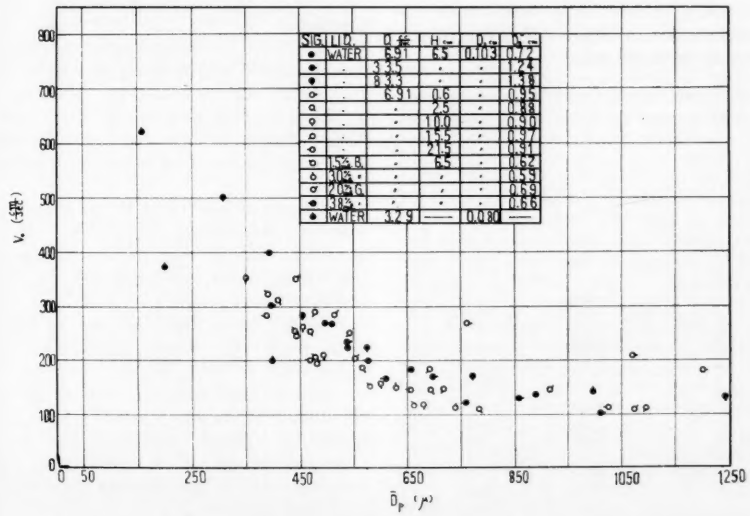

Fig. 8. Initial vertical velocity of liquid drops. Data of $D_0 = 0.080$ (cm.) are concerned with reference *1*.

NOTATION

C = drag coefficient
D = cumulative volume, %
D_0 = orifice diameter, cm.
$\bar{D}_B$ = volumetric mean diameter of bubbles, cm.
D_p = diameter of liquid drop, cm., μ
$\bar{D}_p$ = volumetric mean diameter of liquid drops, μ
D'_p = diameter of a stain of liquid drop collected on a glass plate, μ
g = accerelation due to gravity, cm./sec.^{2}
h = height of sampling above the liquid surface at standstill, cm.
$\bar{h}$ = height of sampling above the surface of the foaming layer, cm.
H = liquid depth (orifice submergence), cm.
N_{Re} = Reynolds number of liquid drop, $[D_p(v - v')\rho'/\mu']$
Q = flow rate of air through an orifice (total flow rate divided by the number of orifices), cc./sec.
s = distance
S = distance a drop can reach, cm.
v = vertical velocity of liquid drop, cm./sec.
v' = vertical velocity of air flow, cm./sec.
v_0 = initial vertical velocity of liquid drop, cm./sec.

Greek Letters

η = collection efficiency
θ = time
ρ, ρ' = densities of liquid and air, respectively, g./cc.
μ, μ' = viscosities of liquid and air, respectively, g./cm.-sec.
σ = surface tension of liquid, dyne/cm.

LITERATURE CITED

1. Akselyrod, L. S., *et al.*, *Zhur. Priklad. Khim.*, **30**, 697 (1957).
2. Carpenter, C. L., *et al.*, *A.I.Ch.E. Journal*, **1**, 549 (1955).
3. Garner, F. H., *et al.*, *Trans. Inst. Chem. Engrs. (London)*, **32**, 222 (1954).
4. Leibson, Irving, *et al.*, *A.I.Ch.E. Journal*, **2**, 296 (1956).
5. Manowitz, B., *et al.*, *Chem. Eng. Progr.*, **51**, 313 (1955).
6. Newitt, D. M., *et al.*, *Trans. Inst. Chem. Engrs. (London)*, **32**, 244 (1954).
7. Perry, J. H., "Chemical Engineers' Handbook," 3d., p. 1018, McGraw-Hill, New York (1952).
8. Ranz, W. E., *et al.*, *Ind. Eng. Chem.*, **44**, 1317 (1952).

Manuscript received August 29, 1958; revision received April 13, 1959; paper accepted April 20, 1959.

Interfacial Resistance Due to Thin Films of Alcohols and Its Effect on the Rate of Evaporation of Water

LALIT H. UDANI and KENNETH F. GORDON

University of Michigan, Ann Arbor, Michigan

Measurements were obtained of the interfacial resistance due to thin films of straight-chain higher alcohols and their effect on the evaporation of water. This was done by passing preheated dry air at a constant rate over water in a beaker. Unlike previous studies both phases were stirred. Four alcohols, dodecyl, myristyl, cetyl, and stearyl, were studied. A large reduction in evaporation was observed when 0.00025 gm. of cetyl alcohol was added to 1 liter of water with gas-liquid interfacial area of 0.2015 sq. ft. A much higher amount of stearyl alcohol, 0.0006 g., was needed for commensurate effect. Resistance due to films of dodecyl and myristyl alcohols was neglibible. For the most part cetyl alcohol is the most effective of those tested. Plots are given of the pseudo mass transfer coefficients and interfacial resistances as a function of the amount of the various alcohols.

When placed on a water surface an insoluble substance will spread on the surface if the energy of adhesion between the molecules of the substance and water is greater than that between the molecules of the substance itself. Long-chain fatty acids and alcohols fulfill this condition and form a layer on water surface. This layer can be regarded as the solution in water of the hydrophilic end group of the molecule, with the hydrophobic end tending towards the gas phase. Such a film is known to retard the evaporation of a liquid into both stagnant and flowing air streams. A brief review of the past work falls naturally into three sections, each with a quiet unstirred water phase.

QUIET AIR PHASE AT REDUCED PRESSURE

Rideal (*23*) used an evacuated inverted *U* tube with one leg containing water at either 25° or 35°C. and the other at 0°C. Considerable reduction in evaporation was observed with films of stearic, lauric, and oleic acids. Sebba and Sutin (*27*) measured the rate of evaporation of water into an evacuated chamber as a function of the surface pressure of the film of stearic acid achieving up to 80% reduction but found no effect for cholesterol.

QUIET AIR PHASE AT ATMOSPHERIC PRESSURE

Powell (*21*) has studied the effect of oil films up to 2.5 cm. thickness. Langmuir and Schaefer (*14*), Archer and La Mer (*2*), and Rosano and La Mer (*24*) have also reported reductions in evaporation. The latter used nine substances, alcohols, acids, and esters all spread as monomolecular layers. Arachidic acid gave the highest resistance, twice that of cetyl alcohol. They examined surface pressure-area isotherms, surface viscosity, and the surface pressure-evaporation resistance relationship and concluded that incompressible films gave the highest resistance. Mansfield (*22*) found that the resistance of cetyl alcohol changed little with time, while that of both myristyl alcohol and cholesterol dropped to one quarter of their initial values in 300 min. The resistance of cetyl alcohol was a strong function of temperature, remaining constant from 20° to 30°C., declining to one third of the 30°C. values at 40°C., and to one quarter of the 30°C. value at 50°C. Field results are included. McArthur and Durham (*17*) give values of the film resistance of various combinations of alcohols.

FLOWING AIR AT ATMOSPHERIC PRESSURE INCLUDING RESERVOIRS

Although Hedestrand (*12*) has reported no effect due to films of palmitic and oleic acid in the evaporation of water in a dish, others have found a definite decrease. Langmuir and Langmuir (*13*) observed appreciable reductions only with films of cetyl alcohol and confirmed Hedestrand; however they did observe a reduction in rate of evaporation of ether from an aqueous ether solution with different films. Docking and coworkers (*4*) using paraffin oil films 1 to 2 μ thick observed a reduction of up to 60% in evaporation from open Petri dishes and up to 99% with neutral oil of retort tar. Sebba and Briscoe (*25*) found large reductions due to unimolecular films of various alcohols and acids. Powell (*21*) working with Petri dishes in a wind tunnel reports large reductions in evaporation of water due to thin multimolecular oil films. Recently Mysels (*20*) published a short note on the resistance of cetyl alcohol to evaporation from a dish. McArthur and Durham (*17*) have obtained up to 67% less evaporation using cetyl alcohol in various combinations with other alcohols in tests employing Petri dishes. Baranaev and his associates (*3, 28, 29, 30*) studying systems with air or hydrogen bubbling through liquid and with air flowing over the liquid surface observed reductions in the rate of evaporation of water and other compounds from aqueous solutions with cetyl alcohol and other substances as films.

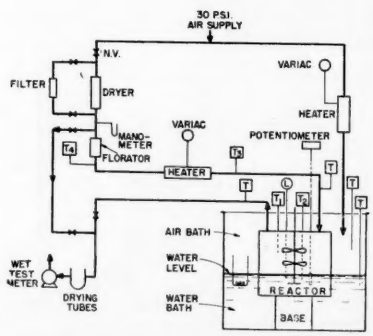

Fig. 1. Flow sheet, L = level indicator, T = thermometer, N.V. = needle valve.

Applications are found in the retardation of evaporation from lakes and reservoirs such as reported by Moulton (*19*), Grundy (*10*), and Mansfield (*15, 16, 22*) who found about 75% reduction in evaporation with cetyl alcohol in field tests. Groth (*9*) briefly mentions the suppression of evaporation from snow by alcohol films obtaining up to 50% reduction. Economics have been discussed by Dressler and Johanson (*5*). The proceedings of a conference on reservoir evaporation control has been published (*22*).

A review of Russian work should include that of Glazov (*7, 8*) who reports

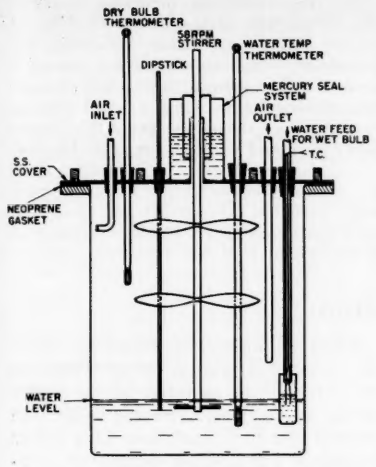

Fig. 2. Vessel.

on various alcohols which are more effective than acids or amines in reducing evaporation. Where possible, representative data of various authors have been converted to resistances in the same units as used in the present work and are given in Table 1. The conversions are obtained with the assumption that the gas-liquid interface is at the same temperature as the bulk of water. Because the mixing in the water is unknown interfacial conditions cannot be accurately estimated. The partial-pressure driving force at the interface is taken to be that corresponding to the assumed interfacial temperature. It may be noted that the magnitude of the coefficients and resistances varies considerably for different authors. This is due to the great differences in the equipment and procedures used. The error introduced by the assumption that the interfacial temperature is the same as the bulk water temperature may be appreciable. If the interfacial temperature is taken to be the same as the wet-bulb temperature corresponding to the temperature of the entering dry air, the driving force is reduced by a factor of about 2½ which in turn would increase K_{oG} and reduce the resistance correspondingly. Even for the case of no surfactant the interfacial conditions cannot be accurately estimated for the runs reported in the literature. There the bulk water and interfacial temperatures are different. Thus some assumption must be made to obtain an estimate of the magnitude of K_{oG} and hence of the resistance. However these estimates of mass transfer coefficients and resistances will be useful for comparison with our experimental results. It will be seen that in the present work the mass transfer coefficient for pure water without surfactant is accurately known, for the bulk water and wet-bulb temperatures are the same.

OBJECTIVE

The present work was undertaken to obtain laboratory measurements of interfacial film resistance due to alcohol films in an apparatus resembling commercial chemical equipment in that both phases are agitated. The reduction of the rate of evaporation of water in the presence of various amounts of straight-chain higher alcohols was measured. The alcohols used were dodecyl alcohol, myristyl alcohol, cetyl alcohol, and stearyl alcohol. It was desired to determine the amount needed to obtain a significant reduction in the rate of evaporation.

APPARATUS

The flow sheet of the process is presented in Figure 1. Air at 0.74 cu. ft./min. from a 30 lb./sq. in. line was dried by passing through Drierite, then through a tubular furnace, and on to the vessel containing the evaporating water. The constant air flow was measured by a Florator with a mercury manometer to give the air pressure. The unbaffled vessel, shown in Figure 2, was a 3½ liter stainless steel beaker fitted with an air tight stainless steel cover with a neoprene gasket. A motor and reducing gear gave a constant stirrer speed of 58 rev./min. One liter of distilled water was initially put in the beaker with a few cubic centimeters makeup periodically added to maintain the level with negligible variation. The surface area of the water was 0.2015 sq. ft., as determined by the cross section of the vessel. A system consisting of a glass water reservoir and copper constantan thermocouple, with a wick which was well exposed to the flowing air, was used to measure the wet-bulb temperature of the air. The air left the vessel through a tube placed where it would give the maximum concentration of water in the air, namely 2 in. above the surface. Other positions apparently gave greater bypassing.

The stirrer consisted of a mercury sealed ¼-in. shaft extending to within ¾ in. of the beaker floor with a single ⅛-in. diameter rod of total length 2¼ in. centered at right angles through the vertical shaft and approximately ¾ in. below the water surface which was 2 1/16 in. above the beaker floor. In the gas phase were two 3-in. diameter four blade propellers, one 1¼ in. and the other 4¾ in. above the water surface, as well as a 3-in. diameter two blade propeller 3¾ in. above the interface. Like the beaker and cover the stirrer was wholly of stainless steel. During runs both phases were turbulent; yet the interface was relatively smooth with surface ripples but no waves.

A glass tube reaching into the water phase was used to indicate the pressure in the vessel by the height of water in the tube. Water in the vessel was maintained at 25°C. by immersing the vessel in a water bath up to the level of water inside the vessel. The water-bath temperature was controlled by a system of a cooling coil and a thermostat controlled knife heater, while the rest of the vessel was surrounded by an air bath which was maintained at the same temperature as the air leaving the vessel. The air fed to the air bath was preheated in a Variac controlled tubular heater as was the air to the vessel. To reduce the heat transfer between the air and water baths a partition of a thin copper plate and a dry plywood sheet separated them. Increments of measured amounts of alcohol were added to give a cumulative effect. When the steady state had been achieved, a 0.50 cu. ft. sample of the exit air from the vessel was drawn through a series of drying tubes and then to a wet test meter. In order to avoid a build-up of pressure in the vessel during sampling a bypass was used to let most of the air to the atmosphere. To maintain constant pressure in the vessel during a run air was continuously bled through a dummy sample train. During actual sampling the air was switched from the dummy to the real sample train. This precaution eliminated fluctuations in the observed wet-bulb temperature during tests before the runs. The humidity of the dried inlet air was determined by drawing a 1 cu. ft. sample through a series of drying tubes.

With pure water a bulk gas temperature of 49.3°C. and a bulk liquid temperature of 25°C. allowed a wet bulb of 25 ± 0.2°C. to be maintained, showing that control of bulk temperatures gave reproducable operating conditions. This obviated difficulties with wet-bulb readings on alcohol contaminated systems. Since the wet-bulb system was not used during a run, no correction was required for evaporation from the wick.

Once added, alcohols adhered to equipment parts so tenaciously that unless extra precautions to clean the equipment were taken, the subsequent results would be vitiated. Since fatty alcohols are soluble in ether, the equipment was first thoroughly cleaned with ether. The reactor was then filled with 2% sodium hydroxide solution and heated to boiling for 15 min. After the alkali had been washed away with water, the vessel was filled with water and heated to boiling. Each time the cover was placed in position the stirrer, etc. were given this treatment. To obtain consistent readings it was also found necessary to let the equipment run for 3 to 4 hr. after every addition of alcohol before making measurements. After this initial period

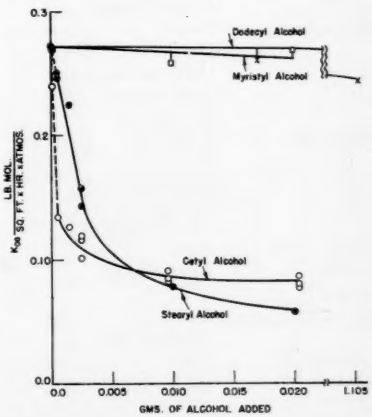

Fig. 3. Effect of alchol on mass transfer coefficient.

Table 1. Summary of Literature Data on Interfacial Resistance—Water Unstirred

Source	Surfactant	Surface pressure, dynes/cm.	(Pseudo)K_{OG} lb. mole / (hr.)(sq. ft.)(atm.)	R_i (hr.)(sq. ft.)(atm.) / lb. mole
	None	(0)		(0)
Archer and	C_{19}-acid in benzene	3		0.60
La Mer (*2*)		12		0.80
Air velocity		16		1.66
0 ft./sec.		23		3.65
		26		5.15
Both phases		29.5		6.64
25°C.	C_{19}-acid in	8		7.98
	Petro ether	13		9.26
		18		10.62
		25		11.95
		29		13.28
Rosano and	Ethyl palmitate	22		0
La Mer (*24*)	Ethyl linoleate	25		0
Air velocity	Ethyl elaidate	18		0
0 ft./sec.	Ethyl stearate	31		13.6
	Arachidic acid	4–32		17.3
	Stearic acid	13–24		6.0
	1-Octadecanal	42		11.0
	Cetyl alcohol	44		8.6
	1, 1, 13-Trihydroperfluorotridecyl alcohol	19–37		5.6
	Curves of data from the above points to the origin are given (*24*)			
Mansfield (*22*)	Cetyl alcohol			11.
Air velocity	Cholesterol			5.
0 ft./sec.	Tetradecanol			9.
Bulk air 25°C.	Values as a function of temperature for cetyl alcohol and as a function of time for all three are given (22)			
McArthur and	Cetyl and other			2.7–8.2
Durham (*17*)	alcohols			
0 ft./sec.				
Rideal (*23*)	None		16.9	0
	None		12.2	0
Air velocity	Lauric acid		9.76	0.0043
0 ft./sec.			8.23	0.0039
Water	Oleic acid		8.23	0.0039
Alternately 25°, 35°C.			6.05	0.0083
Vacuum				
	Stearic acid		12.2	0.0023
	"		9.65	0.0022
Langmuir and	None		0.0298	0
Langmuir (*13*)	Oleic acid		0.00338	262
Ethyl ether				
from water	Stearic acid		0.00515	160
Air velocity	Cetyl palmitate		0.00465	182
0 ft./sec.				
	Cetyl alcohol		0.0032	278
	Myricyl alcohol		0.00438	194
2.0 ft./sec.	None		0.071	0
	Oleic acid		0.00375	253
	Cetyl palmitate		0.00450	208
	Stearic acid		0.00455	206
	Cetyl acid		0.00342	278
5.0 ft./sec.	None		0.0808	0
	Oleic acid		0.00375	255
	Cetyl palmitate		0.00495	190
	Stearic acid		0.00561	166
	Cetyl alcohol		0.00425	228
Water from	None		0.0309	0
water	Cetyl alcohol		0.0255	6.8
v = 0 ft./sec.				
v = 5.8 ft./sec.	None		0.197	0
	Cetyl alchol		0.104	4.55
Mysels (*20*)	None		0.825	0
Air velocity	Cetyl alcohol			6.44
8.8 ft./sec.				
26.4 ft./sec.	None		1.482	0
	Cetyl alcohol			7.08

where the resistance increased, possibly due to solution of the added alcohol, no further change was observed during the experiment which sometimes was extended over a 24-hr. period. Sebba and Briscoe (*26*) observed that aging reduced the resistance of a *n*-docosanol film, while Mansfield (*22*) found no effect for cetyl alcohol.

The surface pressure was obtained from the difference of the surface tension of pure water and that measured in the apparatus by a ring tensiometer. It varied from 0 to 51 dynes/cm.

RESULTS

When an alcohol is added to water the actual saturation temperature at the interface is expected to be higher owing to decreased cooling with the lowered rate of evaporation. This higher interfacial temperature cannot be satisfactorily measured by the usual techniques. As the decrease of evaporation rates with alcohols was the main interest, the results are presented to show the reduction. This was done by plotting the pseudo mass transfer coefficient for the runs with alcohols. The pseudo coefficient was calculated from the measured rate of evaporation with the difference between the vapor pressure of pure water at 25°C. and the measured partial pressure of water in the exit stream which was taken to be that of the bulk gas used as the driving force. It is to be noted that when no alcohol is present the pseudo coefficient becomes the usual coefficient.

Figure 3 is a plot of the pseudo mass transfer coefficient against the amount of alcohol added. Figure 4 shows the apparent interfacial resistance for various alcohols against the amount of alcohols added. The interfacial resistance was determined from

$$R_i = \frac{1}{k_f} = \frac{1}{K_{OG}} - \frac{1}{k_g} \qquad (1)$$

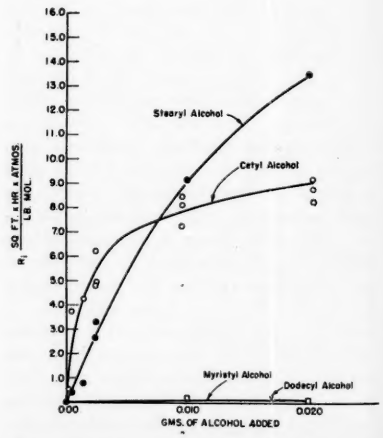

Fig. 4. Apparent interfacial resistance as a function of alcohol added.

From Figure 4 it is clear that the interfacial film resistance of cetyl alcohol increases rapidly on a slight addition of the compound as compared with stearyl alcohol. In the case of stearyl alcohol resistance increases gradually but is greater than that of cetyl alcohol when a larger amount of alcohol is added. The resistance due to dodecyl alcohol and myristyl alcohol appears to be negligible.

When one assumes that the effective cross section of an alcohol molecule is 20.5 sq Å. (*1*), the amounts of fatty alcohols required to form a monomolecular layer on the air-water surface available in the vessel, 0.2015 sq. ft., are for cetyl alcohol, 0.000037 g., and for stearyl alcohol, 0.000041 g. From Figure 3 it is seen that in the present work a much larger amount of alcohol than that required for a monomolecular layer is necessary to cause a significant reduction in the rate of evaporation. It was considered that since water wetted the stainless steel beaker wall, the surfactant would creep along the walls of the container. Milbauer (*18*) has observed the effect of various treatments, like coating, etching, and tinning the surface of the vessel, on the rate of evaporation of water in the presence of films. Such treatment affected the wettability of walls with water and hence the film formation. Hence it is believed that the formation of film was affected by the condition of the wall. In a study bearing on wall films Fowkes and Harkins (*6*, *11*) determined values of surface pressure at solid—liquid interfaces presenting data for a number of aqueous systems observing that the films are gaseous at low pressure. It is believed that adsorption at the liquid-metal interface and possible creep of the alcohol molecules up the wall due to wetting of the wall by water resulted in more alcohol than was necessary to form monolayers at the gas-liquid interface. When one neglects any water creeping up the beaker walls, the total apparent water-interfacial area is 2.95 times the water-air interface. The amount of alcohol and water creeping up the walls of the beaker may well depend on the concentration and nature of the alcohol. The wall appeared to be dry.

In the case of cetyl alcohol a noticeable reduction in evaporation rate is achieved with the lowest amount added in this study, 0.00025 g. With stearyl alcohol a much higher amount is required, 0.0006 g., for a commensurate effect. With 0.0005 g. cetyl alcohol a large and possible useful retardation is obtained. At low concentrations, 0.001 g. in our apparatus, cetyl alcohol is the most effective of the alcohols considered, while stearyl alcohol is more effective at 0.020 g. By contrast 1.1 g. dodecyl alcohol has the same effect as 0.00025 g. of cetyl alcohol.

This investigation shows that resistance values of R_i of the order of 10 sq. ft. hr. atm. (lb. mole)$^{-1}$ are obtained for effective retardants which are of the same order found by Mysels; by Langmuir and Langmuir for water into flowing air; and by Mansfield; by Rosano and La Mer; and by Archer and La Mer as well as McArthur and Durham for the evaporation of water into still air. This leads one to suspect that this is the maximum to be achieved with monomolecular films in both engineering and laboratory operations with water at atmospheric pressures.

Values twentyfold higher are obtained by Langmuir and Langmuir for the evaporation of ethyl ether from water through various films with both stagnant and flowing air. The higher resistance may well be due to the film giving a higher diffusion resistance to the larger ethyl ether molecule.

In the vacuum work of Rideal where the rates are so much higher, 200 to 3,300 times the authors', the resistance required to reduce the evaporation to one half, as observed, will be 1/200 to 1/3,300 that of the authors'. It is difficult to see why the presence of the vacuum or high rates should alter the film resistance unless the interface is agitated by a phemomenon related to boiling.

CONCLUSIONS

The magnitude of gas-liquid interfacial resistances under controlled conditions has been measured over wide concentration ranges with four alcohols yielding quite different results. From the partial data available in the literature interfacial resistances in the work of others have been estimated and compared with those of the present study. This should allow a prediction of the order of magnitude of such effects in a number of practical situations.

ACKNOWLEDGMENT

The assistance of the Faculty Research Fund of the Horace H. Rackham School of Graduate Studies of The University of Michigan with a grant which was used in part for the equipment and preliminary work of this study is acknowledged with appreciation.

NOTATION

K_{OG} = pseudo mass transfer coefficient, lb. mole/(hr.)(sq. ft.)(atm.)

$k_f = 1/R_i$ = film mass transfer coefficient, lb. mole/(hr.)(sq. ft.)(atm.)

k_G = gas-phase mass transfer coefficient (determined with no alcohol present), lb. mole/(hr.)(sq. ft.)(atm.)

$R_i = 1/k_f$ = interfacial film resistance, (hr.)(sq. ft.)(atm.)/lb. mole

LITERATURE CITED

1. Adam, J., "Physics and Chemistry of Surfaces," 3 ed., p. 25, Oxford Univ. Press, Oxford, England (1941).
2. Archer, R. J., and V. K. La Mer, *J. Am. Chem. Soc.*, **59**, 200 (1955).
3. Baranaev, M., *J. Phys. Chem. (U.S.S.R.)*, **9**, 69 (1937), as reported in *Chem. Abstr.*, **31**, 4190 (1937).
4. Docking, A. R., E. Heymann, L. F. Kerley, and K. N. Mortensen, *Nature*, **146**, 265 (1940).
5. Dressler, R. G., and A. G. Johanson, *Chem. Eng. Progr.*, **54**, 66 (1958).
6. Fowkes, F. M., and W. D. Harkins, *J. Am. Chem. Soc.*, **62**, 3377 (1940).
7. Glazov, N. I., *J. Phys. Chem. (U.S.S.R.)*, **13**, 840 (1939), as reported in *Chem. Abstr.*, **34**, 7697 (1940).
8. *Ibid.*, 1642 (1939), as reported in *Chem. Abstr.*, **35**, 17 (1941).
9. Groth, K., "Second International Congress of Surface Activity," Vol. I, p. 275, Butterworths, London (1957).
10. Grundy, F., *ibid.*, p. 270.
11. Harkins, W. D., and F. M. Fowkes, *J. Am. Chem. Soc.*, **60**, 1511 (1938).
12. Hedestrand, Gunnar, *J. Phys. Chem.*, **28**, 1245 (1924).
13. Langmuir, Irving, and D. B. Langmuir, *ibid.*, **31**, 1719 (1927).
14. Langmuir, Irving, and V. J. Schaefer, *J. Franklin Inst.*, **235**, 119 (1943).
15. Mansfield, W. W., *Nature*, **172**, 1101 (1953).
16. *Ibid.*, **175**, 247 (1955).
17. McArthur, I. K. H., and K. Durham, "Second International Congress of Surface Activity," vol. I, p. 262, Butterworths, London (1957).
18. Milbauer, Zdenek, *Listy Cukrovar*, **56**, 421 (1938), as reported in *Chem. Abstr.*, **32**, 8816 (1938).
19. Moulton, K. B., *Weather*, **12**, 223 (July 1957).
20. Mysels, K. J., *Science*, **129**, 38 (1959).
21. Powell, R. W., *Trans. Faraday Soc.*, **39**, 311 (1943).
22. Proceedings of the First International Conference on Reservoir Evaporation Control, Southwest Research Institute, San Antonio, Texas (1956).
23. Rideal, E. K., *J. Phys. Chem.*, **29**, 1585 (1925).
24. Rosano, H. L., and V. K. La Mer, *J. Am. Chem. Soc.*, **60**, 348 (1950).
25. Sebba, F., and H. V. A. Briscoe, *J. Chem. Soc.*, 106 (1940).
26. *Ibid.*, 128 (1940).
27. Sebba, F., and N. Sutin, *ibid.*, 2513 (1952).
28. Sklyarenko, S. I., and M. K. Baranaev, *J. Phys. Chem. (U.S.S.R.)*, **12**, 271 (1938), as reported in *Chem. Abstr.*, **33** 4846 (1939).
29. *Ibid.*, **14**, 839 (1940), as reported in *Chem. Abstr.*, **36**, 4002 (1942).
30. ———, and K. I. Mezhueva, *ibid.*, **18**, 447 (1944), as reported in *Chem. Abstr.*, **39**, 2919 (1945).
31. Sternling, C. V., and L. E. Scriven, *A.I.Ch.E. Journal*, **5**, No. 4, 514 (1959).

Manuscript received August 9, 1958; revision received March 30, 1959; paper accepted April 3, 1959 Paper presented at A.I.Ch.E. Atlantic City meeting

Interfacial Turbulence: Hydrodynamic Instability and the Marangoni Effect

C. V. STERNLING and L. E. SCRIVEN

Shell Development Company, Emeryville, California

The origin of interfacial turbulence, spontaneous agitation of the interface between two unequilibrated liquids, has been explained in terms of classical flow, diffusion, and surface processes. The essence of the explanation is the long-known though much neglected Marangoni effect, wherein movement in an interface is caused by longitudinal variations of interfacial tension. It is proposed that interfacial turbulence is a manifestation of hydrodynamic instability, which is touched off by ever present, small, random fluctuations about the interface.

A simplified mathematical model has been analyzed in order to detail the mechanism of the "interfacial engine" which supplies the mechanical energy of interfacial turbulence. In its present form the analysis incorporates several drastic simplifications, though ways of removing some of these have been suggested. The groundwork has been laid for the more elaborate analyses that are needed for a decisive test of the theory.

The analysis shows how some systems may be stable with solute transfer in one direction yet unstable with transfer in the opposite direction, a striking result. It also suggests that interfacial turbulence is usually promoted by (1) solute transfer out of the phase of higher viscosity, (2) solute transfer out of the phase in which its diffusivity is lower, (3) large differences in kinematic viscosity and solute diffusivity between the two phases, (4) steep concentration gradients near the interface, (5) interfacial tension highly sensitive to solute concentration, (6) low viscosities and diffusivities in both phases, (7) absence of surface-active agents, and (8) interfaces of large extent.

That some of these effects have been observed in the laboratory lends credence to the theory.

Strange are the effects when unequilibrated liquids are brought into contact. If a solution of 10% methanol in toluene is placed quietly upon water, the water remains clear, but in the organic phase a turbid emulsion of water droplets appears. With a solution of 40% methanol in toluene the organic phase remains clear, while an emulsion appears in the water (*19*). Yet if pure toluene is placed upon water containing methanol, no spontaneous emulsification occurs. If pure toluene is placed upon an aqueous solution of butyric or valeric acid, there arises intense though localized stirring on the toluene side of the interface; but if under the same conditions the solute transferred is acetic or propionic acid, there is no stirring action at all (*26*). If diglycol laurate is placed upon water, streamers of the organic material very slowly extend downward into the water, bend round when they near the bottom of the container, and then slowly grow upward (*19*).

An extensive qualitative investigation by Wei (*27*) points up the widespread occurrence of these and similar effects. Having noticed localized stirring at the interface in certain liquid extraction experiments which gave unexpectedly high mass transfer coefficients, Wei went on to test systematically for spontaneous interfacial activity between many different liquids, some pure and others containing a solute. No activity is seen when neither phase contains a solute. Sometimes there is activity when a single solute is extracted without chemical reaction. There is pronounced activity in almost every instance where the two phases contain reacting solutes. Wei distinguishes several general types of disturbance, which at times occur together: localized stirring with rippling and twitching of the interface; slow moving transparent streams leaving the interface, evidently differing slightly in composition or temperature from the bulk through which they move; slower moving opaque streams from the tips of which tiny droplets disengage, often forming an emulsion; and mistlike emulsions slowly forming about the interface. The intensity of the activity varies markedly from system to system. It is usually greater for solute transfer from organic to aqueous phase than for transfer in the opposite direction. It is also influenced by solute concentration and the presence of surface-active agents. The greatest intensity is observed when there is rapid and highly exothermic reaction between two solutes near the interface, especially in systems with low interfacial tension (*23, 27*).

In some cases the behavior is even more bizarre; for example, when a layer of wet isobutanol containing hydrochloric acid is gently placed upon water saturated with isobutanol and containing ammonia, not only is there rippling and twitching of the interface but also, after 30 sec. or so, a water drop forms in the alcohol phase, grows, sags down into the interface, and then bursts through, acquiring in the process a thin covering film of isobutanol. The double drop is propelled several centimeters into the aqueous phase, whereupon it disintegrates, leaving a much smaller droplet of isobutanol that descends another 10 to 30 cm., reverses direction, rises to the interface, and finally merges with the upper phase. Meanwhile a new drop forms above the interface, and the sequence is repeated.

Although the experiments so far described all involve nearly flat interfaces, disturbances of the same sort occur at rounded interfaces. When a drop of liquid is formed at a capillary tip immersed in a second immiscible liquid and a solute is initially present in one or the other phase, the interface is, in many cases, disturbed by rippling, while the adjoining liquid is turbulently agitated (*11, 14, 24*). At times there are localized eruptions at the interface (*24*). If it is pendent, the entire drop often pulsates violently and erratically (*5, 7, 11*); unattached drops behave in the same way (*11, 23, 24*). As in Wei's experiments the occurrence and intensity of these effects depend on the solvents and solute employed, upon solute concentration, and sometimes upon the direction of solute transfer. Surface-active agents tend to reduce the violence of the upsets, sometimes suppressing them completely.

Convection develops spontaneously at gas-liquid interfaces too. The clean surface of an ether-water solution twitches continuously during evaporation of the ether. However, the Langmuirs (*10*) observed that certain insoluble surface films can arrest the motion, thereby greatly reducing the rate of evaporation.

All these phenomena, with the possible exception of some cases of spontaneous emulsification (*4*), involve gross fluid motions and therefore demand the concepts of hydrodynamics for their explanation. The situation is unusual, however, in that the source of energy for driving the flows surely is the difference in chemical potential between the two phases. In a closed system such a potential difference diminishes as thermodynamic equilibrium is approached; accordingly, it is found experimentally that as time passes after the phases are first brought together, the disturbances

L. E. Scriven is with the University of Minnesota, Minneapolis, Minnesota.

ultimately subside. Furthermore no disturbances are observed on contact of phases already nearly in equilibrium. It is as though an engine were actuated by concentration and temperature gradients, more precisely by a gradient of chemical potential in the neighborhood of the interface. Many investigators have suggested that the engine is the interface itself (*7, 10, 14, 18, 19, 24*), but no detailed theory of its action has been advanced, except one of limited scope recently proposed by Haydon (*8*). It is well known that longitudinal variations of surface tension not only cause movement in a liquid surface but also bring forces to bear on the underlying liquid, setting it in motion. This has been called the *Marangoni effect* (*1*), although it was first explained by James Thomson (*25*). There are several very familiar examples of surface-tension-driven flows: tears of strong wine (*16, 25*), camphor dance, and crystal climbing (*1*). It is therefore to be expected that a synthesis of the dynamics of an interface, hydrodynamics, and diffusional transport will be required for a quantitative understanding of the interfacial engine.

What is the practical significance of the various kinds of spontaneous interfacial agitation, which collectively have come to be called *interfacial turbulence*?* Rates of mass transfer tend to be abnormally high in those extraction systems in which interfacial turbulence occurs; this is evident from Lewis's continuing research with a variety of systems (*12, 13*). Transfer rates may be several times as great as predicted from measured single-phase rate coefficients and current theories which assume a stagnant interface, as Sherwood and Wei found with certain extraction systems involving simultaneous chemical reaction (*27*). Although reports of these effects have thus far come only from laboratory experiments under well-controlled conditions, interfacial turbulence must also occur in industrial practice, but when and to what extent are unsettled. Thus laboratory and pilot plant extraction studies cannot be interpreted and are of limited use in scale up unless the state of the interface is known or can be predicted.

INTERFACIAL TURBULENCE AND HYDRODYNAMIC STABILITY

What is the mechanism of interfacial turbulence? How can one recognize beforehand the situations in which it will arise? How can one predict its form and magnitude from first principles? Only when these queries have been answered will it be possible to attack the problem of great practical importance, quantitative prediction of the effect of interfacial turbulence on the rate of mass transfer between phases.

The key to understanding interfacial turbulence is the answer to the question when is a given system unstable relative to small perturbations in the vicinity of the interface? This may be posed as a problem of hydrodynamic stability with diffusion and interfacial movement playing indispensable parts. The methods of conventional linearized stability theory (*15, 22d*) may then be applied to determine the conditions for the onset of instability and the nature of the dominant disturbance. Unless simplifications are made, the mathematical exposition becomes so overgrown that its connection with physical reality is obscured. To lay bare the path, attention is focused on a highly pruned model that is not strictly realizable. But if it displays the salient behavior of actual systems—and it does—the fruitfulness of the approach is established. Moreover the resultant simplified theory then provides the needed groundwork for handling more complete models.

The authors' approach parallels the analysis of the stability of thermally stratified layers of fluid, begun by Rayleigh, which has been successfully applied to the prediction of onset of convection in fluids heated from below (*15b, 21*).

Description of the Model

The configuration to be studied is two semi-infinite, quiescent fluid phases in contact along a plane interface. The phases are in thermal but not in chemical equilibrium. A single solute, present in such low concentration that fluid properties may be taken as constant, is transferring between the phases. In at least two other nonequilibrium situations interfacial turbulence may arise. These are transfer of heat between phases in chemical equilibrium and transfer of materials which can react chemically to release heat or surface-active products near the interface. The first of these is virtually the same as the case selected because of the formal similarities of mass and heat transport and of the composition and temperature dependencies of interfacial tension; the second is but a combination of the mass and heat transfer cases, with, to be sure, added complications.

In the undisturbed state of the authors' model there is steady transfer of solute. This requires that the concentration gradient be linear throughout each phase. Although such a state is not entirely realistic, states closely resembling it in the neighborhood of the interface do obtain after two unequilibrated phases are brought together and diffusion is allowed to proceed.

The stability of this system is studied relative to two-dimensional infinitesmal disturbances. It suffices to consider a single Fourier component corresponding to the roll cells shown in Figure 1, for any arbitrary infinitesmal disturbance can be represented by superposition of such components.

The relevant set of linear, homogeneous, partial differential equations contains time only through derivatives with respect to time. Hence the solutions contain an exponential time factor; that is, the disturbances either amplify or decay exponentially. Thus one is led to a characteristic-value problem with the growth-rate constant as the parameter, the solution of which gives the initial growth rate of a disturbance of given cell size (wave length). If the real part of the growth constant, the amplification factor, is negative for all values of cell size, the system is stable; if it is positive for some values of cell size, the system is unstable. The unstable disturbances do not continue indefinitely to grow exponentially in time, of course; they eventually reach some fully developed form of finite amplitude. The rigorous deduction of the resultant finite flow is such a formidable problem that approximate methods are in order. Of these the most promising is the method applied by Malkus and Veronis to the Rayleigh problem (*17*). They have shown how to relate the macroscopic flow to the solution of the corresponding linearized stability problem. In any case one may reasonably expect that the nature of the fully developed flow is closely connected with the properties of that infinitesmal disturbance which is dominant, that is for which the amplification factor has the greatest positive value.

One point deserves special emphasis. In this model interfacial turbulence may arise spontaneously from ever-present small fluctuations about the interface. Neither the large-scale convection currents postulated by Haydon (*8*) nor any other gross upset originating at a distance from the interface need necessarily be present in the system.

Qualitative Behavior of the Disturbed System

If solute is diffusing from phase A to phase B, the roll cell conveys liquid rich in solute from phase A and liquid lean in solute from phase B toward the interface at point 1 (Figure 1). In the case of a developing disturbance the rates of convection differ in the two phases, being higher in the phase of greater kinematic viscosity.* Consequently the net change in solute concentration at point 1 depends, in part, on the ratio of kinematic viscosities of the two phases. The net change also depends on the ratio of solute diffusivities in the two phases, because molecular diffusion alters the composition of each parcel of liquid as it is conveyed toward the interface, tending to restore the original linear concentration gradients but acting more strongly in the phase of higher diffusivity.

If viscosity is higher in phase A, for example, the convection current is stronger there. If in addition the diffusivity is lower in phase A, the flow-induced concentration upset there is less affected by diffusion than in phase B; hence the

*Both highly irregular and more or less ordered flows originating in the interface are included under the name.

*For an account of the effect of viscosity in accelerating flows, see Schlichting (*22c*).

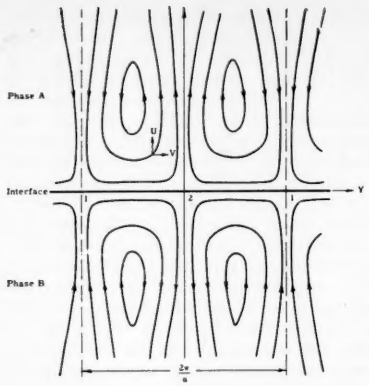

Fig. 1. Schematic diagram of flow disturbance showing circulation pattern of two-dimensional roll cells in cross section.

effect of the disturbance is greater on the side of phase A and the interfacial solute concentration is increased at 1. Because of symmetry and the necessary conservation of solute, the change in solute concentration is in the opposite direction at 2. Thus variations in concentration, hence also in interfacial tension, are induced along the interface. The interface is no longer in mechanical equilibrium and seeks a state of lower free energy through expansion of regions of low interfacial tension at the expense of adjacent regions of higher tension (the Marangoni effect). And because there can be no discontinuity in velocity at the interface, motion in it induces flows in the adjoining fluids.

Thus if interfacial tension increases with increasing solute concentration, the interface contracts at 1 and stretches at 2, and this motion opposes the original disturbance, causing it to be damped. If, on the other hand, interfacial tension decreases with increasing solute concentration, the motion of the interface is from 1 toward 2, which reinforces the original disturbance and causes it to be amplified.

Clearly if viscosity is lower and diffusivity is higher in phase A, or if the direction of solute transfer is reversed, the flow in the surface between 1 and 2 is reversed, producing just the converse of the effect described above. If the viscosity and diffusivity are both higher in the same phase, however, the direction of motion in the interface cannot be inferred except from the more detailed analysis which follows, for in this case convection and diffusion evidently are competing effects.

From these intuitive arguments one may anticipate that the stability of the disturbed system depends on the viscosity ratio, the diffusivity ratio, the direction of solute transfer, and the sign of the rate of change of interfacial tension with concentration. One sees that instability, when it occurs, is driven by variations of surface tension; hence the phenomenon might be called *Marangoni instability*.

Synopsis of the Analysis

In dealing with an interface undergoing deformation, one should recognize that the interfacial tension under dynamic conditions differs from that exhibited under static conditions. In the following section the stability problem is formulated mathematically and its solution found. Because the coupling of flow and diffusion processes appears only in the interfacial shear-stress boundary condition on the flow and in the convective transport terms of the diffusion equation, it is possible to solve the hydrodynamic equations first. The diffusion equation describing the concentration disturbance is then solved, and finally the two solutions are combined by means of the interfacial shear-stress boundary condition to give the characteristic equation for the system.

Succeeding sections are devoted to the interpretation of the characteristic equation, which is complicated by the implicit nature of the equation and the necessity of handling both stationary and oscillatory instabilities, and to a discussion of the theoretical results. In this final section the consequences of the simplifying assumptions are reviewed, a program for generalizing the analysis is outlined, and some practical implications of the theory for the planning, reporting, and correlation of mass transfer experiments are given.

DYNAMIC INTERFACIAL TENSION

Long ago Plateau discovered experimentally, Marangoni explained qualitatively, and Gibbs deduced rigorously, that in multicomponent systems extension of an interface produces an increase and contraction a decrease from the static interfacial tension, effects which resemble the action of a dilational viscosity operating in the surface (*6*). The magnitude of the change increases with rate of deformation and decreases with the rate at which equilibrium between the interface and the substrate phases is reestablished by transport of heat and material to or from the interface. This phenomenon is vital to this analysis because deformation of the interface results when an initial flow disturbance causes local variations in interfacial tension. This effect might be included in the analysis by computing the rates of change of temperature and concentration in and about a postulated separate surface phase. However, the required physical properties of the surface phase are unknown, and the computation is forbiddingly complex. Instead another approach, to be explained shortly, is used.

Another aspect of interfacial deformation must be considered. When an interface is subjected to shear wholly in the plane of the interface, the surface molecules must be reoriented even when there is no change in area. The energy dissipated increases with the rate of shearing and is distinct from but analogous to the dissipation by ordinary viscosity in three-dimensional fluids. In many systems containing surface-active agents this surface shear viscosity is large and easily measured (*9*).

In classical fluid mechanics the substrate phases are treated as continuous media, and the phase interface is regarded as a mathematical surface subjected to a membrane tension. This approach is fruitful in physical problems where system dimensions and characteristic times are large compared with molecular dimensions and relaxation times, respectively. When these conditions obtain, the viscouslike interfacial effects described above are most conveniently incorporated into a hydrodynamic formulation by introducing two coefficients of surface viscosity. The stress, composition, and temperature of the substrate phases are assumed to follow the classical equations of motion and diffusion right up to a mathematical surface located in the phase interface. The two phases are assumed to be in thermal and chemical equilibrium at the interface. All departures of interfacial stress (tension) from that existing in a static system are attributed to surface viscosity regardless of their ultimate causes. The mathematical statement of this idealization of the interface is due to Boussinesq (*3*). By a procedure analogous to that used in deriving the Navier-Stokes equation it can be shown that any arbitrary surface deformation can be resolved into an isotropic dilation superimposed on a pure shear; likewise the stress in a surface can be resolved into an isotropic tension and a pure stress.* The dilational surface viscosity κ and the surface shear viscosity ϵ are defined as the ratios of the stress components to the corresponding components of the rate of deformation. These viscosities depend upon the temperature and composition of the substrate fluids and generally on the past history of

*Actually, surface deformation and stress are best represented as two-dimensional symmetric tensors.

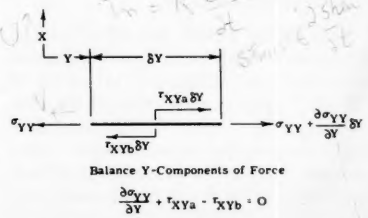

Fig. 2. Shear-stress boundary condition at the interface.

surface deformation. One can, however, consider only the simple case in which κ and ϵ are independent of the history of deformation. The corresponding idealization for three-dimensional fluids, which is actually the definition of a Newtonian fluid, proves to be entirely satisfactory for gases and many liquids. Nevertheless it is recognized that interfaces may exhibit any or all of the non-Newtonian effects that have been encountered in bulk fluids.

Thus in the first approximation the tension in the interface exceeds the static (equilibrium) interfacial tension by an amount κ times the rate of dilation (rate of area increase per unit original area per unit time), and the surface shear stress is ϵ times the rate of shearing in the interface.

MATHEMATICAL FORMULATION

Equations of Motion

For two-dimensional flow of an incompressible Newtonian fluid in the absence of body forces the Navier-Stokes equations reduce to (*22b*)

$$\frac{\partial U}{\partial t} + U\frac{\partial U}{\partial X} + V\frac{\partial U}{\partial Y} = -\frac{1}{\rho}\frac{\partial P}{\partial X} + \nu\left(\frac{\partial^2 U}{\partial X^2} + \frac{\partial^2 U}{\partial Y^2}\right) \quad (1)$$

$$\frac{\partial V}{\partial t} + U\frac{\partial V}{\partial X} + V\frac{\partial V}{\partial Y} = -\frac{1}{\rho}\frac{\partial P}{\partial Y} + \nu\left(\frac{\partial^2 V}{\partial X^2} + \frac{\partial^2 V}{\partial Y^2}\right) \quad (2)$$

The continuity equation is

$$\frac{\partial U}{\partial X} + \frac{\partial V}{\partial Y} = 0 \quad (3)$$

The development of flows of infinitesimal magnitude in an initially quiescent system is being investigated–that is, creeping flows; consequently the nonlinear terms of Equations (1) and and (2) are of the second order of smallness and may be neglected in comparison with first-order terms. The pressure may be eliminated by cross differentiation and subtraction of Equation (1) from Equation (2):

$$\frac{\partial^2 V}{\partial t\,\partial X} - \frac{\partial^2 U}{\partial t\,\partial Y} = \nu\left(\frac{\partial^3 V}{\partial X^3} + \frac{\partial^3 V}{\partial X\,\partial Y^2} - \frac{\partial^3 U}{\partial X^2\,\partial Y} - \frac{\partial^3 U}{\partial Y^3}\right) \quad (4)$$

It is convenient to introduce the stream function so that the continuity equation may be identically satisfied:

$$U = -\frac{\partial \psi}{\partial Y}, \qquad V = \frac{\partial \psi}{\partial X}$$

A solution is sought for ψ of the form $\psi = \varphi(X)e^{i\alpha Y}e^{\beta t}$. With this form for ψ one obtains from Equation (4) the Orr-Sommerfeld equation for a two-dimensional flow disturbance in an initially quiescent system:

$$\varphi'''' - 2\varphi'' + \varphi = \frac{\beta}{\alpha^2\nu}(\varphi'' - \varphi) \quad (5)$$

The solution of this equation when $\beta \neq 0$ is

$$\varphi = \mathfrak{A}_1 e^{x} + \mathfrak{A}_2 e^{-x} + \mathfrak{A}_3 e^{px} + \mathfrak{A}_4 e^{-px} \quad (6)$$

where

$$p = \sqrt{1 + \frac{\beta}{\alpha^2\nu}}.$$

When $\beta = 0$, the solution is

$$\varphi = \mathfrak{A}_5 e^{x} + \mathfrak{A}_6 e^{-x} + \mathfrak{A}_7 x e^{x} + \mathfrak{A}_8 x e^{-x} \quad (6n)^*$$

where the arbitrary constants $\mathfrak{A}_1$ through $\mathfrak{A}_8$ are yet to be evaluated from the boundary conditions.

For simplicity it is supposed that the interfacial tension is sufficiently great so that the interface remains substantially planar. The eight boundary conditions required to specify φ (and thereby the velocities) in both phases are (i) to (iv) the disturbance remains finite at large distances from the interface; i.e. U_a and V_a are finite as $X \to \infty$ and likewise U_b and V_b as $X \to -\infty$; (v), (vi) the interface, which is the plane $X = 0$, is a streamline; that is $U_a(0, Y, t) = U_b(0, T, t) = 0$; (vii) there is no slip at the interface; that is $V_a(0, Y, t) = V_b(0, Y, t)$; (viii) there is continuity of tangential stress at the interface. The essence of the analysis lies in (viii), which requires that

$$\tau_{XYb} - \tau_{XYa} = \frac{\partial \sigma_{YY}}{\partial Y} \quad \text{at} \quad X = 0 \quad (7)$$

(Figure 2), where the shear stress on the upper side of the interface is given by (*22a*)

$$\tau_{XYa} = \mu_a\left(\frac{\partial U_a}{\partial Y} + \frac{\partial V_a}{\partial X}\right) \quad (8)$$

and similarly for the lower side. The interfacial tension in Equation (7) is the dynamic interfacial tension. In accordance with the formulation of Boussinesq (*3*), this tension depends upon the rate of deformation of the surface:

$$\sigma_{YY} = \sigma_0 + \kappa\left(\frac{\partial V}{\partial Y} + \frac{\partial W}{\partial Z}\right) + \epsilon\left(\frac{\partial V}{\partial Y} - \frac{\partial W}{\partial Z}\right) \quad \text{at} \quad X = 0) \quad (9)$$

It is assumed that the two phases are in thermodynamic equilibrium at all points of contact; hence σ_0 may be expressed in terms of the composition at $X = 0$ of either phase A or ph... By hypothesis the concentration va... tions along the interface are small; hence with sufficient accuracy one can set

$$\frac{\partial \sigma_{YY}}{\partial Y} = \left(\frac{d\sigma_0}{dC_a}\right)\left(\frac{\partial C_a}{\partial Y}\right) + \mu_s\left(\frac{\partial^2 V}{\partial Y^2}\right) \quad \text{at} \quad X = 0 \quad (10)$$

where $\mu_s = \kappa + \epsilon$ and the derivative $\partial W/\partial Z$ vanishes for the two-dimensional formulation.

Boundary conditions (i) to (vii) require that $\varphi_a(\infty) = \varphi_b(-\infty) = \varphi_a(0) = \varphi_b(0) = 0$ and $\varphi'_a(0) = \varphi'_b(0)$, whence

$$\varphi_a = \mathfrak{A}_2(e^{-x} - e^{-p_a x}), \qquad x \geq 0 \quad (11)$$

$$\varphi_b = -\mathfrak{A}_2\left(\frac{1 - p_a}{1 - p_b}\right)(e^{x} - e^{p_b x}), \qquad x \leq 0 \quad (12)$$

or, in the case $\beta = 0$

$$\varphi_a = \mathfrak{A}_8 x e^{-x}, \qquad x \geq 0 \quad (11n)$$

$$\varphi_b = \mathfrak{A}_8 x e^{x}, \qquad x \leq 0 \quad (12n)$$

At this point one has solved the equations of motion for a roll-cell disturbance of wave length $\lambda = 2\pi/\alpha$ and small but unspecified (as reflected in the single remaining arbitrary constant) initial strength. The behavior with time of such disturbances is examined next, and to this end one considers the interfacial shear-stress boundary condition (viii), which with Equations (7 to 12) becomes

$$\zeta_a\left(\frac{\partial C_a}{\partial Y}\right)_{X=0} = \mathfrak{A}_2\mu_a\alpha^2 e^{i\alpha Y}e^{\beta t}(p_a - 1) \cdot\left[(1 + p_a) + \frac{\mu_b}{\mu_a}(1 + p_b) + \frac{\alpha\mu_s}{\mu_a}\right], \qquad \beta \neq 0 \quad (13)$$

$$\zeta_a\left(\frac{\partial C_a}{\partial Y}\right)_{X=0} = 2\mathfrak{A}_8\mu_a\alpha_n^2 e^{i\alpha Y} \cdot\left(1 + \frac{\mu_b}{\mu_a} + \frac{\alpha_n\mu_s}{2\mu_a}\right), \quad \beta = 0 \quad (13n)$$

where $\zeta_a = d\sigma_0/dC_a$. These equations enable one to calculate the growth constant β for any given wave number α and assignment of system properties. First however one must determine the surface concentration gradient $(\partial C_a/\partial Y)_{X=0}$.

Diffusion Equations

For simplicity of illustration it is assumed that constant fluxes of solute have been established in the undisturbed system, at least within that region about the interface within which interfacial turbulence may arise. The undisturbed concentrations are taken as

$$C_a^{\,0} = \mathfrak{J}_a + \mathfrak{L}_a X, \qquad X \geq 0 \quad (14)$$

*The letter n is used to identify formulas applying to the special case of $\beta = 0$ (neutrally stable stationary disturbance).

$$\mathcal{J}_b + \mathcal{L}_b X \qquad X \leq 0 \qquad (15)$$

These concentration distributions are perturbed by the flow disturbances already treated. The concentration disturbance is governed by the equation for diffusion in a constant-mass-density, binary, two-dimensional system

$$\frac{\partial C}{\partial t} + U\frac{\partial C}{\partial X} + V\frac{\partial C}{\partial Y} = \mathfrak{D}\left(\frac{\partial^2 C}{\partial X^2} + \frac{\partial^2 C}{\partial Y^2}\right) \qquad (16)$$

where now

$$U = -i\alpha\varphi(X)e^{i\alpha Y}e^{\beta t} \qquad (17)$$

$$V = \frac{d\varphi(X)}{dX}e^{i\alpha Y}e^{\beta t} \qquad (18)$$

In the initial stages of growth of the disturbances the concentration perturbation is of the same order of smallness as the velocities. Therefore one sets

$$C = C^0(X) + G(X, Y, t) \qquad (19)$$

inserts this expression in Equation (16), and neglects terms of the second order of smallness, thereby obtaining

$$\frac{\partial G}{\partial t} - \mathfrak{D}\left(\frac{\partial^2 G}{\partial X^2} + \frac{\partial^2 G}{\partial Y^2}\right) = -U\frac{dC^0}{dX} \qquad (20)$$

A solution is sought for the concentration perturbation of the form $G = H(X)e^{i\alpha Y}e^{\beta t}$. With this form for G it follows from Equations (14), (15), (17), and (20) that $H(X)$ must satisfy

$$H'' - \left(1 + \frac{\beta}{\alpha^2\mathfrak{D}}\right)H = -\frac{i\mathcal{L}}{\alpha\mathfrak{D}}\varphi \qquad (21)$$

The solution of this equation is

$$H = \mathfrak{a}_9 e^{qx} + \mathfrak{a}_{10}e^{-qx} - lI \qquad (22)$$

where

$$q = \sqrt{1 + \frac{\beta}{\alpha^2\mathfrak{D}}}$$

$$l = i\mathcal{L}/\alpha\mathfrak{D}$$

$$I = e^{qx}\int e^{-2qx}\int e^{qx}\varphi\,(dx)^2$$

Table 1 gives the particular integral I for the stream functions of Equations (11) and (12). The arbitrary constants $\mathfrak{a}_9$ and $\mathfrak{a}_{10}$ (and $\mathfrak{B}_9$ and $\mathfrak{B}_{10}$ for the second phase) are yet to be evaluated from the boundary conditions.

The boundary conditions required to specify H (and thereby the concentration) in both phases are

ix, x. The concentration disturbance vanishes at large distances from the interface; that is $C_a \to C_a^0$ as $X \to \infty$ and $C_b \to C_b^0$ as $X \to -\infty$

xi. The two phases are in thermodynamic equilibrium at the interface; that is $m_{ab}C_a(0, Y, t) = C_b(0, Y, t)$

xii. There is conservation of solute at the interface; that is, $\mathfrak{D}_a(\partial C_a/\partial X) = \mathfrak{D}_b(\partial C_b\partial X)$ at $(0, Y, t)$. These conditions lead to the relations

$$m_{ab}\mathcal{J}_a = \mathcal{J}_b \qquad (23)$$

$$r^2\mathcal{L}_a = \mathcal{L}_b, \qquad r^2 = \mathfrak{D}_a/\mathfrak{D}_b \qquad (24)$$

for the undisturbed concentration distributions and

$$m_{ab}[\mathfrak{a}_{10} - l_a I_a(0)] = \mathfrak{B}_9 - l_b I_b(0) \qquad (25)$$

$$r^2[\mathfrak{a}_{10}q_a + l_a I_a'(0)] = -\mathfrak{B}_9 q_b + l_b I_b'(0) \qquad (26)$$

for the constants of the perturbed concentration distributions. From these expressions one finally obtains

$$H_a(0) = \frac{l_b[I_b'(0) - q_b I_b(0)] - r^2 l_a[I_a'(0) + q_a I_a(0)]}{m_{ab}q_b + r^2 q_a} \qquad (27)$$

from which the desired surface gradient follows immediately, since

$$\left(\frac{\partial C_a}{\partial Y}\right)_{X=0} = \left(\frac{\partial G_a}{\partial Y}\right)_{X=0} = H_a(0)i\alpha e^{i\alpha Y}e^{\beta t} \qquad (28)$$

Characteristic Equation

Substituting Equations (27) and (28) in (13) gives

$$B = \frac{\left(\frac{q_b - 1}{q_b + p_b} - \frac{q_a - 1}{q_a + p_a}\right)}{\left(\frac{m_{ab}}{r^2}q_b + q_a\right)\left[\frac{\mu_b}{\mu_a}(1 + p_b) + (1 + p_a) + \frac{\alpha\mu_s}{\mu_a}\right]} \qquad (29)$$

or

$$A = \frac{\left[\frac{r^2}{(q_b + 1)(q_b + p_b)} - \frac{1}{(q_a + 1)(q_a + p_a)}\right]}{d^2\left(\frac{m_{ab}}{r^2}q_b + q_a\right)\left[\frac{\mu_b}{\mu_a}(1 + p_b) + (1 + p_a) + \frac{\alpha\mu_s}{\mu_a}\right]} \qquad (30)$$

and

$$A_{NS} = \frac{(r^2 - 1)}{8\,d^2\left(\frac{m_{ab}}{r^2} + 1\right)\left(\frac{\mu_b}{\mu_a} + 1 + \frac{\alpha_n\mu_s}{2\mu_a}\right)}, \qquad \beta = 0 \qquad (30n)$$

where

$$B = \left(\frac{\mu_a}{\zeta_a\mathcal{L}_a}\right)\beta \text{ and } A = \left(\frac{\nu_a\mu_a}{\zeta_a\mathcal{L}_a}\right)\alpha^2$$

are dimensionless forms of the growth constant and wave number, respectively. It is convenient to introduce additional dimensionless quantities:

$$\xi = \beta/\alpha^2\mathfrak{D}_a = B/d^2A$$

$$d = \sqrt{\mathfrak{D}_a/\nu_a}$$

$$e = \sqrt{\nu_a/\nu_b}$$

Then in Equations (29) and (30)

$$q_a = \sqrt{1 + \xi}, \qquad q_b = \sqrt{1 + r^2\xi}$$

$$p_a = \sqrt{1 + d^2\xi}, \quad p_b = \sqrt{1 + d^2e^2\xi}$$

For a given system all the properties, d, e, r, m_{ab}, μ_b, μ_a, μ_s, ζ_a, $\mathcal{L}_a$, and $\mathfrak{D}_a$, are assigned, and so Equation (29) determines the complex growth constant β (in B) for each wave number α (in A) of the disturbance. Unhappily this characteristic equation is implicit in the dependent variable B and besides contains four vexatious radicals.

INTERPRETATION OF THE CHARACTERISTIC EQUATION

The wave number of a disturbance is real and positive. The growth constant in $e^{\beta t}$ is complex:

$$\beta = \hat{\beta} \pm i\tilde{\beta}$$

Disturbances for which $\hat{\beta} < 0$ are damped; those for which $\hat{\beta} > 0$ are amplified and instability sets in.

Regimes of Instability

There exist two kinds of instability. The first is an oscillatory regime (sometimes named *overstability*), wherein the growing disturbance displays temporal periodicity with period $2\pi/\tilde{\beta}$ and a translatory motion with speed of propagation $\tilde{\beta}/\alpha$. The second is a stationary regime (often called *convective instability*) corresponding to $\tilde{\beta} = 0$, in which the disturbance grows in place without oscillation or translation. For each regime there may exist certain wave numbers for which $\hat{\beta} = 0$, an indication of marginal or neutral stability; that is the disturbance neither grows nor decays in time. Thus zeros of the function $\hat{\beta}(\alpha)$

are of particular interest, since they demarcate stable and unstable wave numbers.

In some problems of hydrodynamic stability, for example the Rayleigh problem (*15b, 21*), it has been possible to prove the so-called "principle of exchange of stabilities," which states that $\hat{\beta} < 0$ for all $\tilde{\beta} \neq 0$, whence all oscillatory disturbances decay and only the stationary regime of instability need be considered. However this principle does not apply to this model, as is shown below. The interpretation of Equation (29) is complicated by the existence of both regimes of instability; indeed in some cases they may set in simultaneously with one or the other dominating in time.

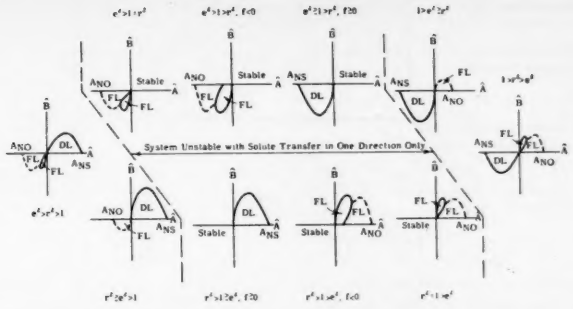

Fig. 4. Amplification factor vs. wave number (in dimensionless form). Solid curves denote stationary regimes; broken curves, oscillatory regimes. $e^2 \equiv v_a/v_b$; $r^2 \equiv \mathfrak{D}_a/\mathfrak{D}_b$; f given by Equation (34); $B \equiv (\mu_a/\zeta_a\mathfrak{L}_a)\hat{\beta}$; $\hat{A} \equiv (\nu_a\mu_a/\zeta_a\mathfrak{L}_a)a^2$

Functional Behavior

It is instructive to regard ξ temporarily as the independent variable in Equations (29) and (30) and to let μ_s be zero, since the equations are explicit from this point of view. The equations define two complex functions, $A = \hat{A} + i\tilde{A}$ and $B = \hat{B} + i\tilde{B}$, of the complex variable $\xi = \hat{\xi} + i\tilde{\xi}$. In seeking conditions for instability one may restrict $\hat{\xi}$ and $\tilde{\xi}$ to nonnegative values; for if $\hat{\xi} < 0$, then either $\hat{\beta} < 0$ and the disturbance is damped or else $\alpha^2 < 0$, which is physically meaningless, and on physical grounds $\hat{B}$ and $\hat{A}$ are both even functions of $\tilde{\xi}$. The functions $A(\xi)$ and $B(\xi)$ are analytic on the quadrant $\hat{\xi} \geq 0$, $\tilde{\xi} \geq 0$.

Because wave number must be real, only real values of A have physical meaning. Therefore one looks for parametric curves of $\hat{A} = 0$ in the quadrant of interest. One such curve is the real axis, inasmuch as $\tilde{A}(\hat{\xi}, 0)$ is identically zero. This curve corresponds to a stationary regime of instability, since $\tilde{B}(\hat{\xi}, 0)$ is also identically zero.

Information about the stationary regime (and oscillatory regimes too) may be gained by an examination of the limiting behavior of $A(\xi)$ and $B(\xi)$.

Making use of the appropriate expansions in Equation (29), one finds, after some manipulation,

$$\lim_{\xi\to 0} B = \frac{(r^2-1)}{8\left(\frac{m_{ab}}{r^2}+1\right)\left(\frac{\mu_b}{\mu_a}+1+\frac{\alpha\mu_s}{2\mu_a}\right)}\xi + 0(\xi^2) \qquad (31)$$

$$\lim_{\xi\to\infty} B = \frac{(r^2-e^2)}{(r+e)(r+de)(d+1)\left(\frac{m_{ab}}{r}+1\right)\left(\frac{\mu_b}{\mu_a}e+1\right)}\xi^{-1} + 0(\xi^{-3/2}) \qquad (32)$$

also, from Equation (30),

$$\lim_{\xi\to 0} A = \frac{(r^2-1)}{8\,d^2\left(\frac{m_{ab}}{r^2}+1\right)\left(\frac{\mu_b}{\mu_a}+1+\frac{\alpha\mu_s}{2\mu_a}\right)}\cdot(1-\xi f) + 0(\xi^2) = A_{NS}(1-\xi f) + 0(\xi^2) \qquad (33)$$

where

$$f = \frac{r^2+1}{2} + \frac{m_{ab}+1}{2\left(\frac{m_{ab}}{r^2}+1\right)} + \frac{d^2\left(\frac{\mu_b}{\mu_a}e^2+1\right)}{4\left(\frac{\mu_b}{\mu_a}+1+\frac{\alpha_{NS}\mu_s}{2\mu_a}\right)} + \frac{d^2(r^2e^2-1)}{4(r^2-1)} \qquad (34)$$

and

$$\lim_{\xi\to\infty} A = \frac{(r^2-e^2)}{d^2(r+e)(r+de)(d+1)\left(\frac{m_{ab}}{r}+1\right)\left(\frac{\mu_b}{\mu_a}e+1\right)}\xi^{-2} + \frac{(e^2-1)\left[\frac{\mu_b}{\mu_a}(r+de)+d+1\right]}{d^3(e+1)(r+de)(d+1)\left(\frac{m_{ab}}{r}+1\right)\left(\frac{\mu_b}{\mu_a}e+1\right)^2}\xi^{-5/2} + 0(\xi^{-3}) \qquad (35)$$

Thus two zeros of the characteristic function $B(A)$ are

$$B = 0 \quad \text{for} \quad A = A_{NS} \quad [\xi = 0;\ \text{cf. Equation (30}n\text{)}]$$

$$B = 0 \quad \text{for} \quad A = 0 \quad (\xi \to \infty)$$

and these represent neutrally stable stationary disturbances of wave numbers $\alpha = \alpha_{NS}$ and $\alpha = 0$, respectively.

There may exist a third distinct zero of $B(\xi)$ by virtue of a zero of the numerator of Equation (29) for real ξ. It can be proved that there exists exactly one such additional zero, at $\xi = \hat{\xi}_0$ where $0 < \hat{\xi}_0 < \infty$, if, and only if, the quantities (r^2-1) and (r^2-e^2) are of opposite signs.* If $B(\hat{\xi}_0) = 0$, then $A(\hat{\xi}_0) = 0$, and the point

$$B = 0 \quad \text{for} \quad A = 0 \quad (\xi = \hat{\xi}_0)$$

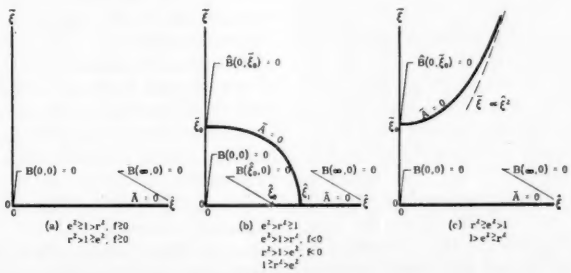

Fig. 3. The function $\tilde{A}$ on the ξ plane.

*See Appendix, which has been deposited as document No. 6048 with the American Documentation Institute, Photoduplication Service, Library of Congress, Washington 25, D. C., and may be obtained for $1.25 for photoprints or 35-mm. microfilm.

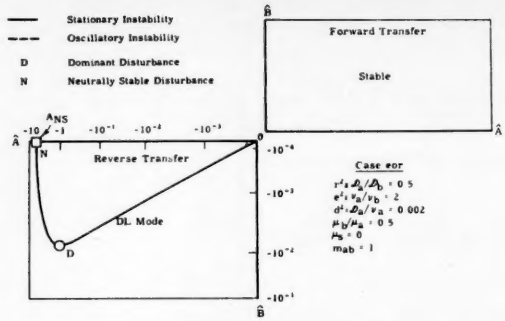

Fig. 5. Results of computation.

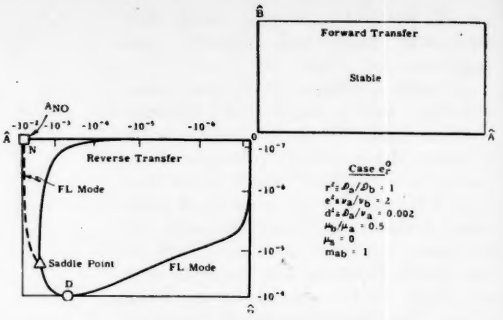

Fig. 6. Results of computation.

represents another neutrally stable stationary disturbance of wave number $\alpha = 0$. Whenever this is the case, the function $B(A)$ is evidently double valued on some interval of A which contains $A = 0$.

To establish the existence of oscillatory regimes, one looks for zeros of $\tilde{A}(0, \xi)$, which must lie on parametric curves of $\tilde{A} = 0$. Moreover these zeros are also zeros of $\hat{B}(0, \xi)$ and therefore represent neutrally stable oscillatory disturbances (provided $\xi \neq 0$). The argument hinges on the limiting behavior of $\tilde{A}$, which is easily inferred from Equations (33) and (35) and is given in Table 2. There it is seen that in the limit $\hat{\xi} = 0$, $\xi \to 0$, $\tilde{A}$ has the same sign as $-(r^2 - 1)f$; in the limit $\hat{\xi} = 0$, $\xi \to \infty$, it has the same sign as $(e^2 - 1)$. It follows immediately that if $(r^2 - 1)f$ and $(e^2 - 1)$ have the same sign, there exists an odd number of zeros of $\tilde{A}(0, \xi)$, and there is at least one wave number α_{NO} for which the system is neutrally stable relative to an oscillatory disturbance. On the other hand, if $(r^2 - 1)f$ and $(e^2 - 1)$ are of opposite signs an even number of zeros of $\tilde{A}(0, \xi)$ exist, and so it is at least possible that the system is stable relative to oscillatory disturbances.

The oscillatory and stationary regimes are connected if $\partial\tilde{A}/\partial\hat{\xi} = \partial A/\partial\xi = 0$ at some point $(\hat{\xi}, 0)$, that is if there is a saddle point on the real axis. At such a saddle point A has a local extremum, and the curve of $\tilde{A} = 0$ lying on the real axis and representing stationary instability is intersected perpendicularly by a second curve of $\tilde{A} = 0$ representing oscillatory instability. It can be shown that there is a saddle point on the real axis if $(r^2 - 1)$ and $(r^2 - e^2)$ are of opposite signs [note that this is the same criterion as applies to the existence of a third zero of $B(\xi)$] or if f is negative and $(r^2 - 1)$ and $(r^2 - e^2)$ have the same sign.*

Not every curve of oscillatory instability, however, intersects the real axis. For if $(e^2 - 1)$ and $(r^2 - e^2)$ have the same sign, there may be no saddle point on the real axis, but there is a curve of $\tilde{A} = 0$ which approaches asymptotically a parabola, ξ proportional to $\hat{\xi}^2$, and terminates at the branch point, $\xi = \infty$. Furthermore, if $(e^2 - 1)$ and $(r^2 - e^2)$ are of opposite signs, there is no branch of $\tilde{A} = 0$ in the far reaches of the quadrant.*

It may be concluded from all this information that three possible pictures of $\tilde{A}(\hat{\xi}, \xi) = 0$, contingent on the relative magnitudes of r^2, e^2, and unity and on the sign of f, are as shown schematically in Figure 3. In these three pictures, which encompass all possible combinations of the parameters, the heavy lines are loci of unstable disturbances. Although the possibility of additional curves of $\tilde{A} = 0$ intruding across the imaginary axis has not been ruled out entirely,* such curves would require the existence of more than one neutrally stable oscillatory disturbance, which seems unlikely on physical grounds. Furthermore, none have been found in the course of extensive numerical solutions of the characteristic equation.

Criteria for Instability

The physical behavior of the system for any given set of parameters may be inferred from the dependence, implicit in Figure 3, of amplification factor on real wave number. This dependence is clear in Figure 4, where the dimensionless amplification factor $\hat{B} = \hat{\beta}(\mu_a/\zeta_a\mathcal{L}_a)$ is plotted as a function of the dimensionless wave number $\hat{A} = \alpha^2(\nu_a\mu_a/\zeta_a\mathcal{L}_a)$ for all of the loci of instability in Figure 3. Both $\hat{B}$ and $\hat{A}$ can be either positive or negative depending on the signs of $\mathcal{L}_a$ (which defines the direction of transfer) and ζ_a (which gives the change of interfacial tension with concentration). Now for instability both $\hat{\beta}$ and α^2 are positive, and therefore $\hat{B}$ and $\hat{A}$ have the same sign; in other words, only the first and third quadrants of the plots in Figure 4 can contain instability curves. From the figure it may be seen that the location of such curves, in one or the other or both quadrants, depends on the viscosity and diffusivity ratios and the related parameter f. It is further seen that regardless of the parameter values there is at least one instability curve in every case. Once physical properties have been assigned, the sign of $\hat{A}$ depends solely on the direction of solute transfer (sign of $\mathcal{L}_a$). Thus one is led to a remarkable conclusion: the system studied here is always unstable relative to roll-cell disturbances—if not with solute transfer from phase A to phase B, then with transfer in the opposite direction. Moreover if kinematic viscosity and solute diffusivity are both lower in one phase (that is, $e^2 > 1$ and $r^2 > 1$ or $e^2 < 1$ and $r^2 < 1$ in Figure 4) the system is unstable with transfer in either direction. This result decides the point left unsettled in the preliminary description of the behavior of the disturbed system: how does the system behave when convection and diffusion are competing effects? Although these effects appear to be in competition, the system responds to the one promoting instability in a given situation. It should be remarked here that systems in which viscosity and diffusivity are both lower in the same phase are not often encountered.

Interfacial tension commonly decreases with increasing solute concentration in a two-phase system; that is, the concentration coefficient of interfacial tension ζ_a is usually negative. When this is the case, instability arises whenever solute is being transferred out of the phase in which kinematic viscosity is higher or out of the phase in which solute diffusivity is lower.

If the kinematic viscosities are equal $(e^2 = 1)$, the onset of instability clearly is controlled by the restorative action of molecular diffusion. Conversely, if the diffusivities are equal $(r^2 = 1)$, the flow effects are paramount. It is on this basis that the distinction is drawn in Figure 4 between diffusion-limited and flow-limited modes, labeled DL and FL, respectively.

It is evident from Figure 4 and the preceding investigation of functional behavior that even when instability occurs the system remains stable relative to all disturbances with wave number

*See footnote p. 519.

*See footnote p. 519.

TABLE 1. QUANTITIES APPEARING IN EQUATIONS (22) TO (28)

	$\phi(x)/\mathcal{L}_a$	$I(x)/\mathcal{L}_a$	$I(0)/\mathcal{L}_a$	$I'(0)/\mathcal{L}_a$	$H_a(0)/\mathcal{L}_a$
$\beta \neq 0$					
Phase a $x \geq 0$	$e^{-x}-e^{-p_a x}$	$-\left(\frac{e^{-x}}{q_a^2-1}-\frac{e^{-p_a x}}{q_a^2-p_a^2}\right)$	$\frac{(p_a^2-1)}{(q_a^2-1)(q_a^2-p_a^2)}$	$\frac{(1-p_a)(q_a^2+p_a)}{(q_a^2-1)(q_a^2-p_a^2)}$	$\frac{\mathcal{L}_a 10(p_a-1)}{\beta(\frac{\mathcal{D}_a}{\mathcal{D}_b}q_b+q_a)}\left(\frac{q_a-1}{q_a+p_a}-\frac{q_b-1}{q_b+p_b}\right)$
Phase b $x \leq 0$	$-\left(\frac{1-p_a}{1-p_b}\right)(e^x-e^{p_b x})$	$\left(\frac{1-p_a}{1-p_b}\right)\left(\frac{e^x}{q_b-1}-\frac{e^{p_b x}}{q_b^2-p_b^2}\right)-\left(\frac{1-p_a}{1-p_b}\right)\frac{(p_b^2-1)}{(q_b^2-1)(q_b^2-p_b^2)}$	$\frac{(1-p_a)(q_b^2+p_b)}{(q_b^2-1)(q_b^2-p_b^2)}$		
$\beta = 0$					
Phase a $x \geq 0$	xe^{-x}	$-\frac{x(x+1)}{4}e^{-x}$	0	$-1/4$	$\frac{\mathcal{L}_a 1(1-r^2)}{4\alpha\mathcal{D}_a(\frac{r}{m^{1/2}}r^2+1)}$
Phase b $x \leq 0$	xe^{-x}	$\frac{x(x-1)}{4}e^{x}$	0	$-1/4$	

TABLE 2. LIMITING BEHAVIOR OF EQUATIONS (29) AND (30), INHERENTLY POSITIVE CONSTANTS ARE OMITTED

$\hat{\xi}$	$\tilde{\xi}$	$\hat{A}$	$\tilde{A}$	$\hat{B}$
$\to 0$	$= 0$	(r^2-1)	0	$(r^2-1)\hat{\xi}$
$= 0$	$\to 0$	(r^2-1)	$-(r^2-1)\Gamma\tilde{\xi}$	$(r^2-1)\Gamma\tilde{\xi}^2$
$= 0$	$\to \infty$	$-(r^2-e^2)\tilde{\xi}^{-2}$	$(e^2-1)\tilde{\xi}^{-3/2}$	$-(e^2-1)\tilde{\xi}^{-3/2}$
$\to \infty$	$= 0$	$(r^2-e^2)\hat{\xi}^{-2}$	0	$(r^2-e^2)\hat{\xi}^{-1}$
$\hat{\xi} = \tilde{\xi} \to \infty$		$-(e^2-1)\hat{\xi}^{-5/2}$	$-(r^2-e^2)\hat{\xi}^{-2}$	$-(r^2-e^2)\hat{\xi}^{-1}$

greater than some finite value, $\alpha_N(\alpha_{NS}$ or $\alpha_{NO})$. Furthermore, the unstable disturbances with very small wave numbers are amplified least rapidly; hence there is one wave number α_D, where $0 < \alpha_D < \alpha_N$, which is amplified most rapidly and ultimately dominates the system. Now wave length or cell size is inversely proportional to wave number; that is, $\lambda = 2\pi/\alpha$. Thus in small cells the motive force in the interface is more than offset by the viscous shear forces opposing motion, and the initial motion is damped. The contrary is true when cell size is larger than $\lambda_N = 2\pi/\alpha_N$, and the motion is amplified; the rate of amplification is vanishingly small in extremely large cells because of the inertia of the greater volume of fluid per cell.

Whereas the onset of instability is governed by the signs of the quantities $\nu_a - \nu_b$, $\mathcal{D}_a - \mathcal{D}_b$, ζ_a, and $\mathcal{L}_a$, the cell size and the rate of amplification of the dominant disturbance are also influenced by the magnitudes of these quantities and of the ordinary viscosities μ_a and μ_b, the surface viscosity μ_s, the Schmidt number d^{-2}, and the solute distribution coefficient m_{ab} as well. The qualitative effects may be summarized as follows: stronger variation of interfacial tension with concentration and steeper concentration gradients promote smaller cells and more rapid amplification, and so also do greater disparities of viscosity and diffusivity between phases. Higher diffusivities and viscosities in both phases lead to larger cells and slower amplification, and this tendency is more pronounced in the range of small cell sizes. The qualitative effects of d^2 and m_{ab} are not directly evident and hence must be found by calculation.

Results of Computation

That the authors' simplified model is subject to Marangoni instability is now established. Yet it may be that the wave lengths are so great, or the amplification rates so slow that the instability cannot manifest itself within the space and time available in the laboratory. Accordingly, values of α and β have been computed for four typical cases, selected to include all the regimes and modes of instability which are described above. The parameters which do not strongly affect the kind of instability, d, m_{ab}, μ_b/μ_a, and μ_s, were assigned the same values in all four cases. So also was the ratio of kinematic viscosities, at $e^2 = 2$. The cases were distinguished by four different values of the diffusivity ratio, $r^2 = 0.5, 1, 1.5$, and 4.

The results of the computations are shown in dimensionless form in Figures 5 through 8, where an unusual coordinate scale is employed for clarity of presentation.* Of greatest consequence are the points corresponding to neutrally stable and dominant disturbances; these are labeled N and D, respectively, in Figures 5 through 8 and are also given in Table 3.* Note that the dominant disturbance is of much smaller wave length (greater wave number) and is amplified far more rapidly in the diffusion-limited modes than in the flow-limited modes. Note also the curious contrast between the cases in Figures 6 and 7. In both whenever the direction of transfer is such as to make A negative (reverse direction of transfer), stationary and oscillatory disturbances set in simultaneously. A stationary disturbance prevails if the solute diffusivities are equal (Figure 6), whereas an oscillatory disturbance predominates if the diffusivity ratio is 1.5 (Figure 7).

To convert the calculated dimensionless quantities to the desired wave lengths and amplification factors, it is necessary to assign magnitudes to certain physical properties. Let $\mu_a = 10^{-2}$ g./(cm.)(sec.) and $\rho_a = 1$ g./cc. Then $\nu_a = 10^{-2}$ sq. cm./sec. and, because the Schmidt number $d^{-2} = 5 \times 10^2$, it follows that $\mathcal{D}_a = 2 \times 10^{-5}$ sq. cm./sec. Let the concentration coefficient of interfacial tension $\zeta_a = -10^2$ (g./sec.^{2})/(g./cc.), a value typical of such systems as toluene-water with acetic acid as the consolute (*28*). Let the undisturbed concentration gradient $\mathcal{L}_a = 1$(g./cc.)/cm., a value that obtains at the interface 0.4 sec. after a phase A containing 1% of solute is contacted with a phase B initially devoid of solute, if $m_{ab} = 1$ and $\mathcal{D}_b = 2 \times 10^{-5}$ sq. cm./sec. The magnitudes of λ and β are then as given in Table 4. It should be emphasized that Table 4 contains the results of sample calculations. By choosing other values for the physical properties, it is possible to obtain values of λ and β which differ from those shown by severalfold or even, in extreme cases, by a few orders of magnitude.

Neither the tabulated wave lengths nor amplification factors are so large as to refute the explanation of interfacial turbulence in terms of Marangoni instability. The flow-limited modes are characterized by dominant disturbances which have cells a few millimeters in breadth and which double in intensity every second or so. In marked contrast are the dominant disturbances of the diffusion-limited modes, which are of much smaller cell size and are amplified far more rapidly. The microscopic scale of the latter type of disturbance and the rapidity with which it develops suggest a possible explanation for the lack of visible convective motion in some instances of spontaneous emulsification (*4, 19*).

DISCUSSION

The conception of Marangoni instability has led to a credible explanation of interfacial turbulence. The analysis shows clearly how it is possible for some systems to be unstable with solute transfer in one direction yet stable with transfer in the opposite direction, and others to be unstable with either direction of transfer. The analysis also shows that instability may be contingent upon other parameters heretofore unsuspected. These are the direction in which interfacial tension changes with solute concentration and the signs of differences between the solute diffusivities and kinematic viscosities of the two phases. The theoretical results suggest several variables whose influence may account for observed contrasts in intensity of interfacial

*The computations themselves are tabulated in the Appendix. See footnote on p. 519.

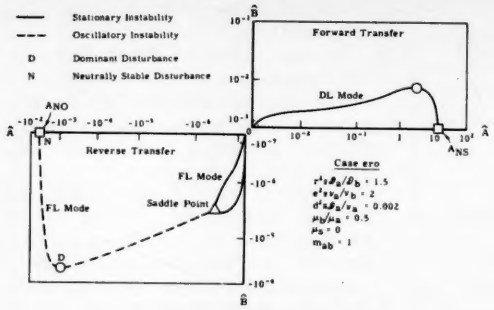

Fig. 7. Results of computation.

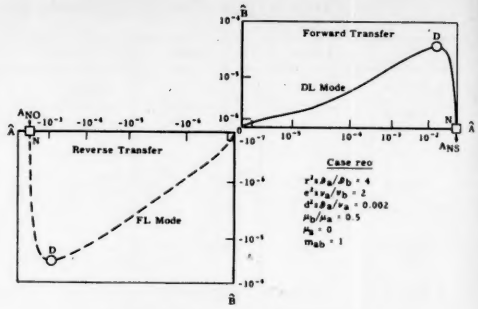

Fig. 8. Results of computation.

turbulence from one system to the next. The importance of two of these is already confirmed by experiment; they are the steepness of the concentration profile near the interface, which is related to the initial difference of solute concentrations, and the magnitude of the surface viscosity, which reflects the presence of highly surface-active agents.

The explanation is not completely convincing however. At present the analysis is based on a model too simplified to be reproduced in the laboratory; therefore direct, quantitative comparisons with experiment are impossible. Although many new experiments come to mind, the additional evidence that they will provide cannot be used for a decisive test of the theory until several of its deficiencies have been removed.

First one may ask to what extent temperature variations along the interface contribute to the Marangoni effect. Some investigators have speculated that interfacial agitation is caused by variations of interfacial tension occurring as a result of uneven release of heat of solution when solute passes through the interface (3, 14). This effect is easily incorporated in the authors' simplified treatment. The interfacial flux boundary condition on the diffusion equation is altered to include a heat-source term, and an appropriate undisturbed temperature profile is assumed. The interfacial shear-stress boundary condition on the flow equation is recast to account for the dependence of interfacial tension on temperature as well as on concentration. The resulting characteristic equation for $B(A)$ includes a term that represents the solution heat effect, a term involving the heat of transfer, the relative rates of change of interfacial tension with temperature and concentration, and the ratio of mass to thermal diffusivities. By inserting in this term the properties of one typical system, benzene-acetone-water, one finds the interfacial forces generated by temperature variations to be roughly a thousandfold less than those simultaneously generated by concentration variations. This comparison, though by no means settling the matter, suggests that it will be most profitable to concentrate on consequences of solute transfer in isothermal systems.

Other troublesome complications which are not included in the simplified theory but which are of importance in experiments are

1. The disturbances are not two dimensional.
2. The interface does not remain fixed in position; rather, it is free to twitch.
3. The system does not consist of two semi-infinite slabs; very often one phase is in the form of nearly spherical drops.
4. Solute transfer is not steady in the undisturbed state.
5. Not only is there transfer of solute, but the solvents themselves interdiffuse.
6. The diffusivities, rather than being constants, usually depend strongly on concentration.

Analyses that take the first four items into account are in progress and will be reported in detail later, but some remarks about them are apt here. A pattern of cylindrical convection cells oriented normal to the interface, which simulates square or hexagonal cell patterns, leads to the same characteristic equation as given above for the two-dimensional, roll-cell pattern. The present proscription on motion of the interface normal to itself, which amounts to a tacit assumption of great interfacial tension, is easily removed by allowing the interface to be deformed by the normal fluid stresses. When this is done, an additional parameter that involves the magnitude of interfacial tension appears in the characteristic equation. It will probably be possible in this way to explain the more intense interfacial turbulence in systems of lower interfacial tension. The formulation of the stability problem for a spherical drop suspended in a second phase is straightforward. Solutions of stability problems in which the undisturbed system is not at steady state are hard to find. However, if the undisturbed diffusion changes the system much less rapidly than the nascent disturbances do, one can use the artifice of freezing

TABLE 4. TYPICAL MAGNITUDES

$\zeta_a = -100 \frac{\text{dynes/cm}}{\text{gm/cm}^3}$, $\mu_a = .01 \frac{\text{gm}}{(\text{cm})(\text{sec})}$, $\mathcal{D}_a = 2 \times 10^{-5} \frac{\text{cm}^2}{\text{sec}}$, $m_{ab} = 1$, $\frac{\mu_b}{\mu_a} = 2$, $\mu_s = 0$

Case	eor	e_r^o	ero	reo
ν_a/ν_b	2	2	2	2
$\mathcal{D}_a/\mathcal{D}_b$	0.5	1	1.5	4
Transfer from Phase B to Phase A, $\alpha_a = -1.0$ (gm/cm^3)/cm				
Mode	Stable	Stable	DL	DL
Neutrally stable wave length, λ_N, cm	-	-	.0018	.00063
Temporal period, $2\pi/\hat{\beta}_N$, sec	-	-	∞	∞
Speed of propagation, $\hat{\beta}_N/\alpha_N$, cm/sec	-	-	0	0
Dominant wave length, λ_D, cm	-	-	.0039	.0014
Amplification factor, $\hat{\beta}_D$, sec^{-1}	-	-	64	350
Temporal period, $2\pi/\hat{\beta}_D$, sec	-	-	∞	∞
Speed of propagation, $\hat{\beta}_D/\alpha_D$, cm/sec	-	-	0	0
Transfer from Phase A to Phase B, $\alpha_a = +1.0$ (gm/cm^3)/cm				
Mode	DL	FL	FL	FL
Neutrally stable wave length, λ_N, cm	.0024	.070	.082	.086
Temporal period, $2\pi/\hat{\beta}_N$, sec		19	.77	.45
Speed of propagation, $\hat{\beta}_N/\alpha_N$, cm/sec	0	.0037	.11	.19
Dominant wave length, λ_D, cm	.0053	.27	.25	.20
Amplification factor, $\hat{\beta}_D$, sec^{-1}	71	.99	.43	.32
Temporal period, $2\pi/\hat{\beta}_D$, sec	∞	∞	2.4	1.0
Speed of propagation, $\hat{\beta}_D/\alpha_D$, cm/sec	0	0	.10	.20

the concentration profile in its shape at any arbitrary instant and examining the stability of the system in that state. This scheme was recently applied to the Rayleigh problem by Morton (*20*).

The above list is ordered roughly in increasing mathematical difficulty. The ordering is also nearly that of increasing physical importance, the matter of variable diffusivities being greatest consequence for linking experiment with theory. But the fruitfulness of the simplified treatment justifies more elaborate analyses, for which the ground work is now laid.

Recommendations

Although the goal of a full understanding of interphase mass transfer is still a long way off, the following recommendations may hasten its attainment. Since interfacial turbulence unquestionably enhances the rate of mass transfer, experimenters studying extraction should, whenever possible, report direct observations of the phase interface with their extraction data. In any case the direction of transfer, concentration levels, and presence or absence of surface-active contamination should be noted. Viscosities, diffusivities, and the variation of interfacial tension with composition should be estimated or, preferably, measured. This information will be needed not only for the proper interpretation of simple laboratory experiments, but also for the rational scale up of bench and pilot plant extraction equipment.

Good empirical correlations of mass transfer rates in liquid-liquid extraction are lacking, partly because interfacial effects have been overlooked. (The same is true of flooding-point and capacity correlations.) More trustworthy correlations can be made by the conservative expedient of simply rejecting data known or suspected to be affected by interfacial turbulence. But sooner or later, in order to exploit fully the effect when it does occur, a correlation should be developed which accounts for those parameters that influence the onset and intensity of interfacial turbulence.

ACKNOWLEDGMENT

The authors are indebted to C. H. Barkelew for many helpful suggestions and discussions.

NOTATION

A = $(\nu_a\mu_a/\zeta_a\mathfrak{L}_a)\alpha^2$, dimensionless wave number
$\mathfrak{A}$ = constant of integration
B = $(\mu_a/\zeta_a\mathfrak{L}_a)\beta$, dimensionless growth constant
$\mathfrak{B}$ = constant of integration
C = solute concentration $[ML^{-3}]$
d = $\sqrt{\mathfrak{D}_a/\nu_a}$, dimensionless
$\mathfrak{D}$ = solute diffusivity $[L^2\theta^{-1}]$
e = $\sqrt{\nu_a/\nu_b}$, dimensionless
f = function defined by Equation (34), dimensionless
G = concentration perturbation $[ML^{-3}]$
H = X part of the concentration perturbation $[ML^{-3}]$
i = $\sqrt{-1}$
I = particular integral in Equation (22)
$\mathfrak{J}$ = undisturbed interfacial concentration $[ML^{-3}]$
l = $(i/\alpha\mathfrak{D})\mathfrak{L}$ $[ML^{-5}\theta]$
$\mathfrak{L}$ = undisturbed concentration gradient $[ML^{-4}]$
m_{ab} = C_b/C_a at equilibrium, distribution coefficient, dimensionless
p = $\sqrt{1 + (\beta/\alpha^2\nu)}$, dimensionless
P = pressure $[ML^{-1}\theta^{-2}]$
q = $\sqrt{1 + (\beta/\alpha^2\mathfrak{D})}$ dimensionless
r = $\sqrt{\mathfrak{D}_a/\mathfrak{D}_b}$, dimensionless
t = time coordinate $[\theta]$
U, V, W = X, Y, and Z components of velocity $[L\theta^{-1}]$
X, Y, Z = spatial coordinates $[L]$

Greek Letters

α = wave number $[L^{-1}]$
β = growth constant $[\theta^{-1}]$
$\bar{\beta}$ = circular frequency
$\hat{\beta}$ = amplification factor for the disturbance
ϵ = surface-shear viscosity $[M\theta^{-1}]$
ζ = concentration coefficient of interfacial tension $[L^3\theta^{-2}]$
κ = dilational surface viscosity $[M\theta^{-1}]$
λ = wave length $[L]$
μ = ordinary viscosity $[ML^{-1}\theta^{-1}]$
μ_s = $\epsilon + \kappa$, composite surface viscosity $[M\theta^{-1}]$
ν = kinematic viscosity $[L^2\theta^{-1}]$
ξ = $\beta/\alpha^2\mathfrak{D}_a$, dimensionless
ρ = density $[ML^{-3}]$
σ_0 = equilibrium interfacial tension $[M\theta^{-2}]$
σ_{YY} = Y component of the longitudinal surface stress $[M\theta^{-2}]$
τ_{XY} = Y component of the fluid shear stress $[ML^{-1}\theta^{-2}]$
φ = X part of the stream function $[L^2\theta^{-1}]$
ψ = stream function $[L^2\theta^{-1}]$

Subscripts

a = phase $A (X > 0)$
b = phase $B (X < 0)$
D = dominant unstable disturbance
N = neutrally stable disturbance
O = oscillatory disturbance
S = stationary disturbance

Superscripts

0 = value in the undisturbed state
$\hat{}$ = real part in a complex variable
$\tilde{}$ = imaginary part of a complex variable
primes = differentiation with respect to dimensionless quantity
x = αX

LITERATURE CITED

1. Bikerman, J. J., "Surface Chemistry," 2ed., Academic Press, New York (1958).
2. Blokker, P. C., in "Proc. Second Intern. Congr. Surface Activity," vol. I, Academic Press, New York (1957).
3. Boussinesq, J., *Ann. chim. et phys.*, **29**, 349 (1913).
4. Davies, J. T., and D. A. Haydon in "Proc. Second Intern. Congr. Surface Activity," vol. I, Adademic Press, New York (1957).
5. Garner, F. H., C. W. Nutt, and M. F. Mohtadi, *Nature*, **175**, 603 (1955).
6. Gibbs, J. W., "Collected Works," vol. I, pp. 272–274, Longmans, Green, New York (1931).
7. Haydon, D. A., *Nature*, **176**, 839 (1955).
8. ———, *Proc. Roy. Soc.* (*London*), **A243**, 483 (1958).
9. Joly, M., *J. Colloid Sci.*, **11**, 519 (1956).
10. Langmuir, Irving, and D. B. Langmuir, *J. Phys. Chem.*, **31**, 1719 (1927).
11. Lewis, J. B., *Trans. Inst. Chem. Engrs.* (*London*), **31**, 323, 325 (1953).
12. ———, *Chem. Eng. Sci.*, **3**, 248, 260 (1954).
13. *Ibid.*, **8**, 295 (1958).
14. ———, and H. R. C. Pratt, *Nature*, **171**, 1155 (1953).
15. Lin, C. C., "The Theory of Hydrodynamic Stability," Cambridge Univ. Press, Cambridge, England (1955); (a) Chap. 1, (b) Chap. 7.
16. Loewenthal, M., *Phil. Mag.*, **12**, 462 (1931).
17. Malkus, W. V. R., and G. Veronis, *J. Fluid Mech.*, **4**, 225 (1958).
18. Mansfield, W. W., *Australian J. Sci. Research*, **5A**, 331 (1952).
19. McBain, J. W., and T. Woo, *Proc. Roy. Soc.* (*London*), **A163**, 182 (1937).
20. Morton, B. R., *Quart. J. Mech. Appl. Math.*, **10**, 433 (1957).
21. Ostrach, S., *Trans. Am. Soc. Mech. Engrs.*, **79**, 299 (1957).
22. Schlichting, Hermann, "Boundary Layer Theory," McGraw-Hill, New York (1955); (*a*) p. 46, (*b*) p. 54, (*c*) p. 64, (*d*) p. 314.
23. Sherwood, T. K., and J. C. Wei, *Ind. Eng. Chem.*, **49**, 1030 (1957).
24. Sigwart, K., and H. Nassenstein, *Ver. deut. Ingenieurw. Zeit.*, **98**, 453 (1956).
25. Thomson, James, *Phil. Mag.* [4], **10**, 330 (1855); see also Maxwell, J. C., "Capillary Action," in *Encyclopedia Britannica*, vol. V, 9 ed., Samuel L. Hall, New York (1878).
26. Ward, A. F. H., and L. H. Brooks, *Trans. Faraday Soc.*, **48**, 1124 (1952).
27. Wei, J. C., thesis, Mass. Inst. Technol., Cambridge (1955).
28. Woodman, R. M., *J. Phys. Chem.*, **31**, 1742 (1927).

Manuscript received December 12, 1958; revision received May 4, 1959; paper accepted May 8, 1959. Paper presented at A.I.Ch.E. Atlantic City meeting.

Automatic Control of Fluid Flow

N. H. CEAGLSKE

University of Minnesota, Minneapolis, Minnesota

This paper illustrates the use of analytical methods for the design of a flow-control system. Linearized equations are derived and a complete analysis is made of the control of the system. The effect of controller modes and process time constants is investigated. The calculations show that there is an optimum value of the process time constant for optimum response.

DERIVATION OF EQUATIONS

In the chemical industries the automatic control of fluid flow is encountered perhaps more often than the control of any other single variable. The successful control of fluid flow is not simple, primarily because of the small time constants involved in the flow process. This paper will analyze flow control in detail and will point out some of the factors where difficulty may be encountered.

The System

The most commonly used method of controlling flow is to insert a flow meter and control valve into the flow line. The signal from the flow meter actuates a controller, which in turn operates the control valve.

The analysis of the system requires the derivation of the dynamic equations for each part of the system. The equations which truly represent the flow process are nonlinear. Owing to the difficulty of solving nonlinear equations without a computer, only linearized equations will be used in this paper. This procedure is justified because the analysis is simplified and the methods of analysis for linear equations can be applied. Furthermore much valuable information can be obtained from linear equations, and in many instances the responses calculated will check the experimental results if the disturbance is not too large.

An important feature of the analytical procedure to be presented is that an over-all view of the system operation is obtained, allowing the determination of the effect of each of the system parameters upon both the transient and frequency responses.

The Process

The process under consideration is the pipeline and control valve. For any given system two variables, the pressure drop and the valve opening, determine the rate of flow of the fluid. The exact equation describing the flow is rather complicated. Many system properties such as pipe length and volume, compressor or pump characteristics, and flow characteristics and fluid inertia have a part in fixing the time constants of the process. The time constants of the process and the other parts of the system determine the types of responses the system will have. The limiting case occurs when the response to change in pressure drop or valve opening is instantaneous. The process time constant is then 0. In the first part of this paper the system will be considered to have a zero time constant, and then the effect of a finite process time constant will be investigated.

A linear process with a 0 time constant will have a transfer function

$$G_p = K_p \tag{1}$$

The same process with a simple resistance and capacitance will have a transfer function

$$G_p = \frac{K_p}{T_p s + 1} \tag{2}$$

The Controller

Usually in the design of a control system all parts of the system are fixed except for the controller modes and the controller parameters. The equations for the ideal controller modes are easily written. There is another important characteristic of controllers which must be considered and that is the time lag in the controller mechanism. In most control systems time lags other than the process time lag may be neglected. However in flow control, with small process time lags, the lags in the other parts of the system become significant. Unfortunately there is little published information on the dynamic characteristics of industrial controllers. Information of this type would be very helpful to control engineers. A time constant of 1 sec. will be assumed. The controller transfer functions then are proportional control

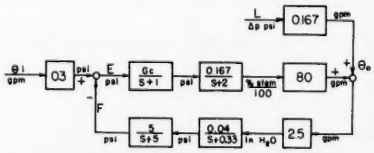

Fig. 1. Block diagram showing specific transfer functions.

$$G_c' = \frac{K_c}{s + 1} \tag{3}$$

proportional plus integral control

$$G_c' = \frac{K_c[1 + 1/(T_i s)]}{s + 1} = \frac{K_c(s + 1/T_i)}{s(s + 1)} = \frac{K_c(s + z)}{s(s + 1)} \tag{4}$$

and proportional plus integral plus rate control (three mode)

$$G_c' = \frac{K_c[1 + 1/(T_i s) + T_r s]}{s + 1} = \frac{K_c(T_r T_i s^2 + T_i s + 1)}{T_i s(s + 1)} = \frac{K_c T_r (s + z_1)(s + z_2)}{s(s + 1)} \tag{5}$$

The Transmitter

The transmitter is the mechanism which converts the differential pressure of the flowmeter to a pneumatic pressure in the range of 3 to 15 lb./sq. in. There is again little published information on the dynamic response of transmitters. The author has seen some information that suggests that a reasonable time constant is 3 sec. The transfer function of the transmitter then is

$$G_{tr} = \frac{K_{tr}}{3s + 1} \tag{6}$$

The Pneumatic Tubing

In any pneumatic control system, tubing is used to transmit signals from the measuring means to the controller and to the control valve. A study of the several papers published on the dynamic response of pneumatic tubing (*1, 2, 3*) indicates that the response can be accurately represented only by rather complex equations. Furthermore, under some conditions the frequency-response curves are somewhat cyclic. The action of a control system with tubing under these conditions would be very peculiar. In order to simplify the analysis, it will be assumed that the tubing is of such diameter and length that the response is similar to that of a first-order system over the range of frequencies to be used and that the time constant is 0.2 sec.

The transfer function then is

$$G_{tu} = \frac{K_{tu}}{0.2s + 1} = \frac{5K_{tu}}{s + 5} \qquad (7)$$

The Control Valve

Most control valves have a dynamic action that can be represented by a second order equation; however the second time constant is small and can usually be neglected. A time constant of 0.5 sec. will be assumed; then

$$G_v = \frac{K_v}{0.5s + 1} \qquad (8)$$

Operating Conditions

The following numerical values have been selected for the flow system to be discussed:

CONTROL POINT: 40 gal./min.

FLOWMETER: at a flow of 40 g./min. $\Delta h_m = 50$ in. of water. The flow–pressure-drop relationship is parabolic.

PROCESS: time constant of 0. At control point the pressure drop across the valve is 120 lb./sq. in.

CONTROL VALVE: at the control point the valve is 50% open, and the valve top pressure is 9 lb./sq. in. The flow-valve stem relationship is linear. The time constant is 0.5 sec.

TRANSMITTER: at the control point the output is 9 lb./sq. in. The time constant is 3 sec.

TUBING: the time constant is 0.2 sec.

CONTROLLER: in addition to the normal controller functions, the controller has a time constant of 1 sec.

System Transfer Functions

Controller

If G_c is the controller mode, then

$$G_c' = \frac{G_c}{s + 1} \frac{\text{lb./sq. in.}}{\text{lb./sq. in.}} \qquad (9)$$

Valve

Since the valve is 50% open when the valve top pressure is 9 lb./sq. in. and the valve is a linear valve,

$$K_v = 0.5/6 = 0.0833 \frac{\%\text{ stem position}/100}{\text{lb./sq. in.}}$$

and

$$G_v = \frac{0.0833}{0.5s + 1} = \frac{0.167}{s + 2} \cdot \frac{\%\text{ stem position}/100}{\text{lb./sq. in.}} \qquad (10)$$

Transmitter

The output of the transmitter is 9 lb./sq. in. when the input is 50 in. of water. Then

$$K_{tr} = 6/50 = 0.12 \frac{\text{lb./sq. in.}}{\text{in. water}}$$

and

$$G_{tr} = \frac{0.12}{3s + 1} = \frac{0.04}{s + 0.333} \cdot \frac{\text{lb./sq. in.}}{\text{in. water}} \qquad (11)$$

Tubing

The time constant is 0.2 sec., and there is no change of units; therefore

$$G_{tu} = \frac{1}{0.2s + 1} = \frac{5}{s + 5} \cdot \frac{\text{lb./sq. in.}}{\text{lb./sq. in.}} \qquad (12)$$

Process, valve stem position

The flow of 40 gal./min. occurs when the valve is 50% open and the valve is linear; then

$$K_p = 40/0.5 = 80 \cdot \frac{\text{gal./min.}}{\%\text{ stem position}/100} \qquad (13)$$

Process, pressure drop

The flow–pressure-drop relationship is parabolic; therefore K_p' is the slope of the flow curve at 40 gal./min., where $Q = c\sqrt{\Delta_p}$ and $c = 40/\sqrt{120} = 3.66$; then

$$G_L = K_p' = \frac{dQ}{d\Delta p} = 0.167 \frac{\text{gal./min.}}{\Delta p} \qquad (14)$$

Another conversion factor needed is one to change units from flow in gallons per minute to differential in inches of water. The relationship is parabloic so that $c = 5.66$ when $Q = 40$ and $\Delta h_m = 50$. Then

$$\frac{dQ}{d\,\Delta h_m} = 0.4 \frac{\text{gal./min.}}{\text{in. water}} \qquad (15)$$

Likewise the control-point index indicates gallons per minute, but the signal to the controller is pounds per square inch; therefore the conversion factor at the control point is

$$K = 0.12 \times 2.5 = 0.3 \frac{\text{lb./sq. in.}}{\text{gal./min.}} \qquad (16)$$

The block diagram for the system with all the transfer functions inserted in the blocks is shown in Figure 1.

The System Equations

The open-loop equations for this system are

$$\frac{\theta_0}{E} = \frac{0.167 \times 80G_c}{(s + 1)(s + 2)} = \frac{13.333G_c}{(s + 1)(s + 2)} \qquad (17)$$

$$\frac{F}{\theta_0} = \frac{2.5 \times 0.04 \times 5}{(s + 0.333)(s + 5)} = \frac{0.5}{(s + 0.333)(s + 5)} \qquad (18)$$

The closed-loop equations are

$$\frac{\theta_0}{\theta_i} = \frac{0.3\theta_0/E}{1 + (\theta_0/E)(F/\theta_0)} = \frac{4G_c(s + 0.333)(s + 5)}{(s + 0.333)(s + 1)(s + 2)(s + 5) + 6.67G_c} \cdot \frac{\text{gal./min.}}{\text{gal./min.}} \qquad (19)$$

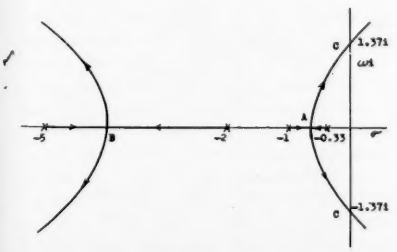

Fig. 2. Root-locus diagram with proportional control.

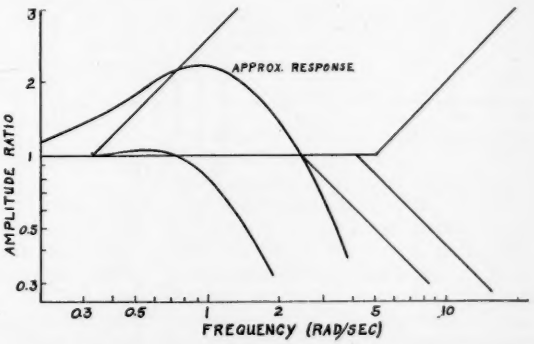

Fig. 3. Approximate frequency response with porportional control.

$$\frac{\theta_0}{L} = \frac{G_L}{1 + (\theta_0/E)(F/\theta_0)} = \frac{0.167(s + 0.333)(s + 1)(s + 2)(s + 5)}{(s + 0.333)(s + 1)(s + 2)(s + 5) + 6.67G_c} \cdot \frac{\text{gal./min}}{\Delta p} \quad (20)$$

Equations (19) and (20) are the linear equations representing the dynamic action of the flow control system. If nonlinear effects are to be investigated, the proper equations must be derived and the solutions obtained by an electronic computer.

The procedure for the selection of the modes of control and the controller parameters will be found in the following sections.

The modes of control and the specific controller parameters selected will determine the responses of the system to any input. The simplest type of controller is the proportional controller; therefore it should be studied to determine its effectiveness in controlling the given flow process. The transfer function for the proportional controller is given by Equation (3). Equations (19) and (20) then become

$$\frac{\theta_0}{\theta_i} = \frac{4K_c(s + 0.333)(s + 5)}{(s + 0.333)(s + 1)(s + 2)(s + 5) + 6.67K_c} \quad (21)$$

$$\frac{\theta_0}{L} = \frac{(s + 0.333)(s + 1)(s + 2)(s + 5)}{(s + 0.333)(s + 1)(s + 2)(s + 5) + 6.67K_c} \quad (22)$$

PROPORTIONAL CONTROL

The root-loci method (*5*, *6*) will be used to analyze the system. A method estimating the effect of each of the system parameters upon the responses (*4*) is very helpful in the analysis. It will be shown that a great deal of information can be obtained about the system with very little calculation.

In the previous section the dynamic equations for the flow system were derived. Equation (20) can be written without the constant in the numerator, making the ratio θ_0/L dimensionless. Inspection of the derivation shows that a change in flow of 1 gal./min. is caused by a change in Δp of 6 lb./sq. in. The equation will be used in this form.

The root-locus diagram is a plot of the roots (closed-loop poles) of the denominators of Equations (21) and (22) as a function of K_c. Figure 2 shows the root-locus diagram for this system with proportional control. The points marked x are the poles of the product $\theta_0/E \times F/\theta_0$. The arrows indicate the direction of increasing K_c as K_c goes from 0 to ∞. The approximate curves can be drawn without any calculation. (Rules for the construction of root-loci diagrams are given in references *5* and *6*.) The curves show that the system is overdamped; that is the closed-loop poles are real and negative as K_c goes from 0 to some value at which point A or B is reached. As K_c increases, the roots become complex and the system is then underdamped. As the closed-loop poles on the right branch pass the point C, the system becomes unstable. The exact location of the curves can be calculated, but that is not necessary at this time. The one value of interest is the value of K_c at the point C, which is found to be 4.52.

The final or steady state values of θ_0/θ_i and θ_0/L after a step change are found from the final value theorem and are

$$\left(\frac{\theta_0}{\theta_i}\right)_{ss} = \frac{4 \times 5 \times 0.333K_c}{1 \times 2 \times 5 \times 0.333 + 6.67K_c} = \frac{2K_c}{1 + 2K_c} \quad (23)$$

$$\left(\frac{\theta_0}{L}\right)_{ss} = \frac{1 \times 2 \times 5 \times 0.333}{1 \times 2 \times 5 \times 0.333 + 6.67K_c} = \frac{1}{1 + 2K_c} \quad (24)$$

When $K_c = 4.52$

$$\left(\frac{\theta_0}{\theta_i}\right)_{ss} = \frac{2 \times 4.52}{1 + 2 \times 4.52} = 0.869 \quad (25)$$

$$\left(\frac{\theta_0}{L}\right)_{ss} = \frac{1}{1 + 2 \times 4.52} = 0.096 \quad (26)$$

These values indicate that if the control point is changed, the steady state value reached will be only 86.9% of the change, or the error will be 13.1%. Likewise if a change in L is made, the steady state error will be 9.6% of the change. Actually the system would not be operated with $K_c = 4.52$, since it would be at the point of instability. A smaller value of K_c such as 2 would cause the steady state errors to be even greater.

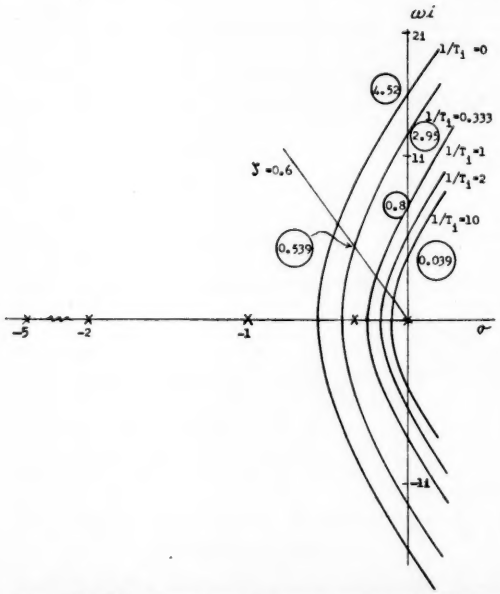

Fig. 4. Effect of zeros at $-1/T_i$ on the root-loci curves.

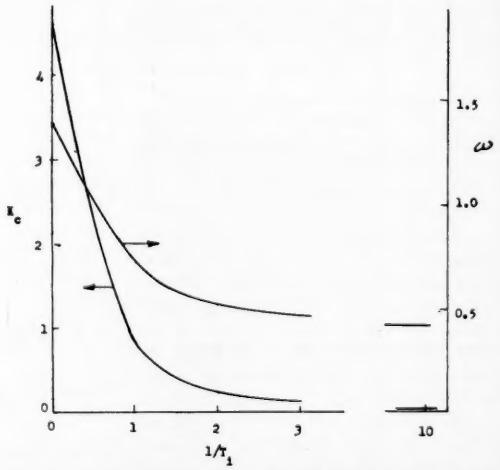

Fig. 5. Effect of zeros at $-1/T_i$ on K_c and ω at the point of intersection with the imaginary axis.

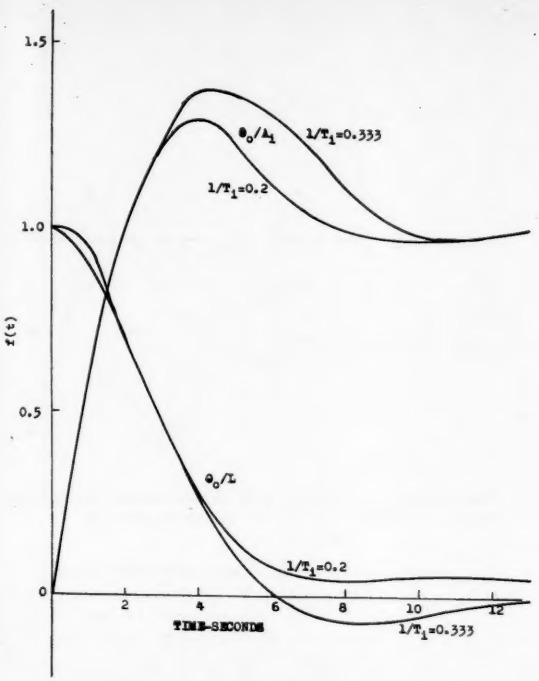

Fig. 6. Transient responses after step inputs.

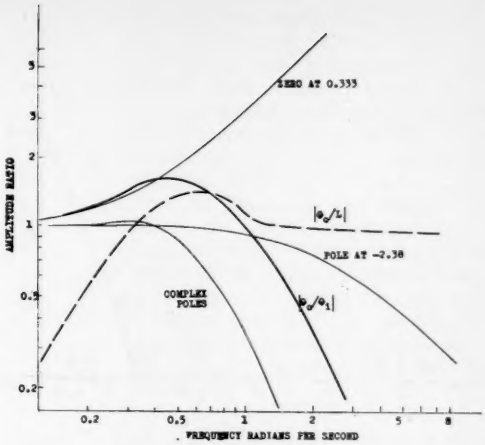

Fig. 7. Frequency responses.

Whether or not these steady state errors are too large depends upon the process requirements. If one assumes that the errors are too large, it is obvious that proportional control is not satisfactory and consequently other modes of control must be used.

The value of the root-loci diagram can be illustrated at this point. Figure 2 shows the individual time constants of the system and their effect upon the poles of the closed-loop functions. Any closed-loop poles far to the left will have little effect upon responses. These poles produce terms of the form Ae^{-pt} in the transient response, where if p is large the term becomes 0 in a very short time. It is the poles close to the origin that control the response. The poles close to the origin in this system are present because of the time constants of the controller and transmitter. In other words, the control action is limited not by the process lag but by the slow action of the transmitter and controller.

It is customary to choose the conjugate complex poles which control the response so that the damping coefficient is in the neighborhood of 0.6 to 0.7. This selection then fixes the values of the closed-loop poles. The exact values of these poles can be easily calculated when necessary. The transient response following a step input of θ_0/θ_i is determined almost entirely by the complex poles and the zero at −0.333 [Equation (21)]. The response will be that of a normal second-order system modified by the zero, which will tend to make the response much more cyclic.

The frequency response is easily approximated as shown in Figure 3. The natural frequency can be obtained by direct measurement from Figure 2. Only the asymptotic lines are shown for the first-order terms, since only an approximation is desired. For the second-order term the peak occurs at $\omega_s = 0.53$ and has a value of 1.04; the curves pass through the ordinate 0.707 when $\omega_s = 1.15$. Up to a frequency of about 0.4 radian/sec. the response is close to 1. As the frequency increases to about 0.8 radian/sec., the amplitude ratio increases to over 2, an undesirably high value.

A similar analysis may be made of Equation (22) for the ratio θ_0/L. Equations (21) and (22) have the same poles, but Equation (22) has two more zeros. The zeros and poles far to the left have little effect upon the transient response. The zeros at −1 and −0.333 will cause a very cyclic response. The frequency response can be approximated graphically as shown above. Owing to the zeros at −1 and −0.333 the frequency response will be high over a wide range. The ratio $|\theta_0/L|$ should approach 0 quickly in a well-controlled system.

From the approximate analysis made, it is quite positive that proportional control will not produce satisfactory results for this system. Therefore the use of other modes of control must be investigated.

PROPORTIONAL PLUS INTEGRAL CONTROL

Since proportional control proved to be unsatisfactory, the next step is to investigate the effect of the combination proportional plus integral control. It is known that the addition of integral control will cause the steady state error to be 0, and it also may have some other beneficial effects.

The controller transfer function is given be Equation (4). The product of the forward and feedback transfer functions from Equations (17) and (18) is

$$\frac{\theta_0}{E} \times \frac{F}{\theta_0} = \frac{6.67K_c(s + 1/T_i)}{s(s + 0.333)(s + 1)(s + 2)(s + 5)} \tag{27}$$

The closed-loop equations then are

$$\frac{\theta_0}{\theta_i} = \frac{4K_c(s + 0.333)(s + 5)(s + 1/T_i)}{s(s + 0.333)(s + 1)(s + 2)(s + 5) + 6.67K_c(s + 1/T_i)} \tag{28}$$

$$\frac{\theta_0}{L} = \frac{s(s + 0.333)(s + 1)(s + 2)(s + 5)}{s(s + 0.333)(s + 1)(s + 2)(s + 5) + 6.67K_c(s + 1/T_i)} \tag{29}$$

The integral mode of control has added the terms which contain the term $1/T_i$. The quantity $1/T_i$ may theoretically have any value from 0 to ∞ but is actually limited by range built into the controller. With $1/T_i = 0$ the control is proportional only, and with $1/T_i = \infty$ the integral action is so fast that the controller acts in the same manner as a two-position controller. Therefore as the zero at $-1/T_i$ moves away from the origin, the speed of the integral action is increasing.

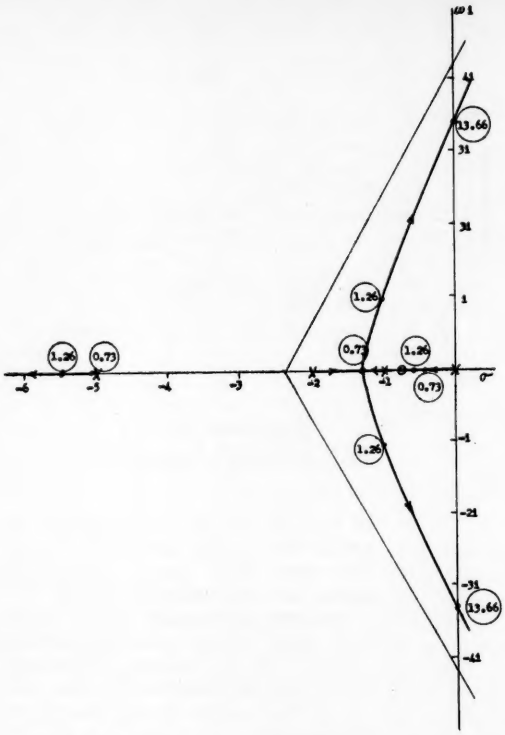

Fig. 8. Root-locus diagram with three-mode control; $z_1 = 0.333$, $z_2 = 0.8$.

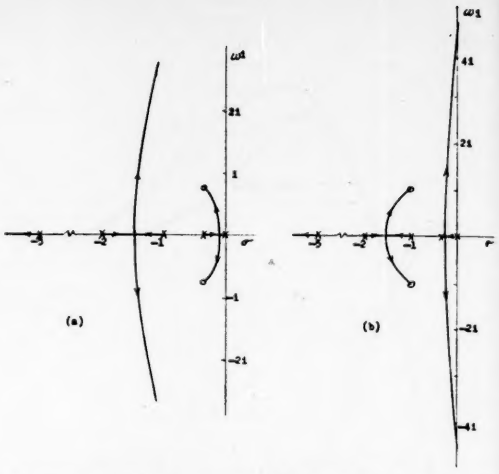

Fig. 9. Root-loci diagrams with complex zeros; (*a*) complex zeros at -0.375 ± 0.75, (*b*) complex zeros at $-1 \pm i$.

The approximate root-loci diagrams for several values of $1/T_i$ are shown in Figure 4 (the zeros at $-1/T_i$ are not shown). The numbers within the circles are the values of K_c at the point. Very few calculations are needed to sketch the curves in the form shown (*6*). The effect of changing the values of $1/T_i$ upon the closed-loop poles is at once obvious. When these approximate values are substituted into Equations (28) and (29), one can make a reasonable estimate of the responses.

Specifically as $1/T_i$ increases, it is seen that the branched part of the curve contracts and the value of K_c, when the loci curve intersects the imaginary axis, decreases. This change indicates that the system is becoming less stable and becomes unstable at smaller values of K_c. Figure 5 shows the effects more clearly where K_c and ω drop rapidly as $1/T_i$ increases. Actually the control system should not be operated at the point of intersection of the loci curve and the imaginary axis. Often a suitable operating point is that which gives a damping coefficient of about 0.6. The line representing $\zeta = 0.6$ is shown in Figure 4, and it is seen that K_c at this point is much less than at the point of intersection of the loci curve and the imaginary axis. From a practical standpoint there is a limit to how small K_c can become, since most industrial controllers have a maximum proportional band of 150 to 200%. This means that K_c must be greater than 0.5. Therefore the present system could not be operated with $1/T_i$ greater than about 0.333, for under these conditions with $\zeta = 0.6$, $K_c = 0.539$ (proportional band 186%).

It so happens that when $1/T_i = 0.333$, one of the poles in Equations (27) is canceled, simplified the equations. Therefore this a convenient selection of $1/T_i$ for which the transient and frequency response of the system will be determined. Then for a step change in θ_i the ratio θ_0/θ_i is

$$\frac{\theta_0}{\theta_i} = \frac{4K_c(s + 0.333)(s + 5)}{s(s + p_3)(s + p_4)(s + \sigma + \omega i)(s + \sigma - \omega i)} \tag{30}$$

The poles p_3 and p_4 will have values between -2 and -5; the other two terms represent the conjugate complex poles, the values of which depend upon the value of the damping coefficient selected. The position of the poles p_3 and p_4 will not be greatly changed by any change made in the damping coefficient. The position of the poles can be calculated by any one of several methods (*6*).

When $1/T_i = 0.333$ and $\zeta = 0.6$, then $p_3 = 2.38$, $p_4 = 4.96$, $\sigma = 0.333$, $\omega = 0.44$, $\omega_n = 0.56$, and $K_c = 0.539$. Equation (30) then becomes for a step change in θ_i

$$\frac{\theta_0}{A_i} = \frac{4 \times 0.539(s + 0.333)(s + 5)}{s(s + 4.96)(s + 2.38)(s + 0.333 + 0.44i)(s + 0.333 - 0.44i)} \tag{31}$$

The terms $s + 5$ and $s + 4.96$ are so nearly equal that they will be canceled.

The transient response is shown in Figure 6. The response is relatively fast, but the maximum overshoot of 38% is perhaps too large. If a smaller overshoot is desired, the only change that can be made is to move the zero at $-1/T_i$ nearer to the origin. For example if $1/T_i = 0.2$, the rate of rise is not changed but the overshoot is now about 30%. From the root-loci diagram it can be seen that moving the zero at $-1/T_i$ nearer to the origin produces a closed-loop zero at $-1/T_i$ and pole between the origin and $-1/T_i$. The pole being nearest the origin will exert the greater effect upon the response; however the combination of a pole and zero close together will not have an appreciable effect.

The ratio θ_0/L with $1/T_i = 0.333$ and $\zeta = 0.6$ is investigated. Then for a step change in the pressure drop Equation (29) becomes

$$\frac{\theta_0}{A_L} = \frac{s(s + 1)(s + 2)(s + 5)}{s(s + 4.96)(s + 2.38)(s + 0.333 + 0.44i)(s + 0.333 - 0.44i)} \tag{32}$$

Again the terms $s + 5$ and $s + 4.96$ are canceled. The curves have an initial value of 1 when $t = 0+$ because the

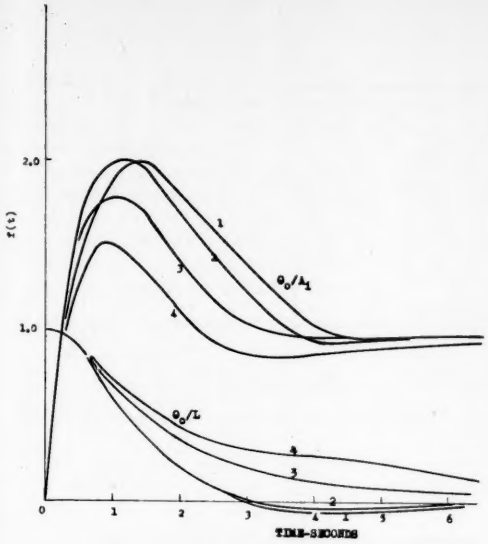

Fig. 10. Transient responses after a step input.

Curve	z_1	z_2
1	0.333	1.0
2	0.333	0.8
3	0.333	0.6
4	0.333	0.333

number of zeros and poles are equal in Equation (32). Moving $1/T_i$ nearer to the origin will not change the curve at the initially high start. This can be accomplished only by the addition of a pole in the closed-loop equation so that there will be an excess of poles over the zeros. As the move toward the origin takes place, a pole near the origin is introduced, resulting in a slow response. The curve for $1/T_i = 0.2$ is shown in Figure 6, where it is seen that the curve is less cyclic but that an error tends to persist for a longer time. This effect becomes more pronoumced as $1/T_i$ approaches the origin.

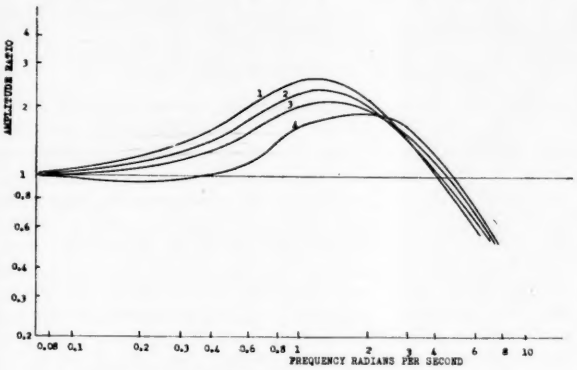

Fig. 11. Frequency response-control point change.

Curve	z_1	z_2
1	0.333	1.0
2	0.333	0.8
3	0.333	0.6
4	0.333	0.333

The frequency response is obtained from the following equation:

$$\frac{\theta_0}{\theta_i} = \frac{4 \times 0.539(s + 0.333)}{(s + 2.38)(s + 0.333 + 0.44i)(s + 0.333 - 0.44i)} \quad (33)$$

Figure 7 shows the individual terms of Equation (33) and the response curve with the details of construction not indicated. The term $s + 0.333$ is fixed by the system and cannot be changed unless the transmitter time constant is changed. The term $1/(s + 2.38)$ has little effect upon the response; consequently small changes in its location due to changing controller parameters will not change the response curve. The second-order curve can be changed in shape by changing the damping coefficient. As the damping coefficient decreases, the curve develops a higher peak, and when it is 0.707 there is no peak at all. As ω_n at constant ζ increases, the curve moves toward the right with no change in shape. It is possible then to modify the frequency-response curve somewhat by varying the controller parameters.

The frequency-response specifications will depend upon the process requirements. In general θ_0/θ_i should not have a high maximum because then any extraneous signals (noise) in the controller may cause a large error on the controlled variable.

The frequency response with the pressure-drop sinusoidal is obtained from the equation

$$\frac{\theta_0}{L} = \frac{s(s + 1)(s + 2)}{(s + 2.38)(s + 0.333 + 0.44i)(s + 0.333 - 0.44i)} \quad (34)$$

The response curve is high and remains high for all frequencies, which of course is very undesirable.

A study of the figures shows that the responses are not entirely satisfactory. With proportional and integral control there is little that can be done to improve the responses. If $1/T_i$ is made much smaller, a sluggish response is obtained. As previously discussed, the damping coefficient cannot be changed sufficiently to cause much change in the responses. The addition of the integral mode of control has eliminated the steady state error but otherwise has not greatly affected or improved the response.

THREE-MODE CONTROL

The previous sections have shown that for the flow system being discussed proportional or proportional plus integral control has not proved to be satisfactory. The addition of the rate mode provides another possibility of improving the responses to both step and sinusoidal inputs.

The controller transfer function for the three-mode control is given by Equation (5). The zeros at $-z_1$ and $-z_2$ are

$$z_1, z_2 = \frac{1}{2T_r}\left(1 \pm \sqrt{1 - 4T_r/T_i}\right) \quad (35)$$

The zeros are real if $4T_r/T_i < 1$ and complex if $4T_r/T_i > 1$ and are equal when $4T_r/T_i = 1$. The values which T_r and T_i may assume are limited only by values available on the controller being used. The effect of the choice of T_r and T_i will now be investigated.

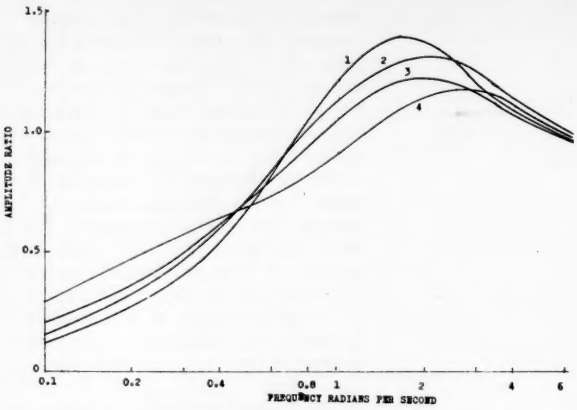

Fig. 12. Frequency response-pressure drop change.

Curve	z_1	z_2
1	0.333	1.0
2	0.333	0.8
3	0.333	0.6
4	0.333	0.333

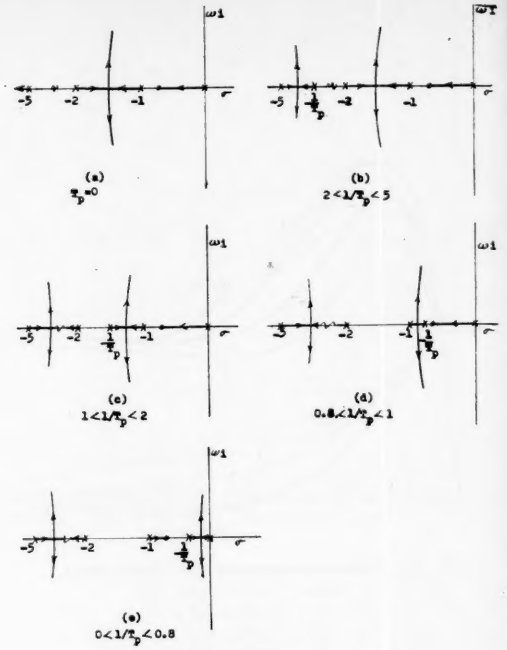

Fig. 13. Root-loci diagrams with a process lag.

TABLE 1. SUMMARY OF CALCULATIONS

z_1	0.333	0.333	0.333	0.333
z_2	1.0	0.8	0.6	0.333
T_r	0.75	0.882	1.07	1.5
T_i	4.0	4.24	4.66	6.06
For the closed-loop with $\zeta = 0.707$				
$\sigma = \omega$	0.81	0.962	1.08	1.16
p_3	—	0.583	0.38	0.19
p_4	5.38	5.49	5.46	5.49
K_c	1.41	1.26	1.08	0.84
K_cT_r	1.06	1.12	1.16	1.26
ω_n	1.145	1.356	1.53	1.643

From Equations (17) and (18) the product

$$\frac{\theta_0}{E} \times \frac{F}{\theta_0}$$

$$= \frac{6.67K_cT_r(s + z_1)(s + z_2)}{s(s + 0.333)(s + 1)(s + 2)(s + 5)} \tag{36}$$

A comparison of Equation (36) with Equation (27) shows that the addition of the rate mode has added another zero and the term T_r in the numerator. The additional zero can be used to counteract the effect of another of the poles just as the single zero was used with two-mode control. The addition of T_r has the effect of changing the effective gain of the open-loop function. The total gain is K_cT_r, which may be greater of less than K_c.

The closed-loop equations now become

$$\frac{\theta_0}{\theta_i} = \frac{4K_cT_r(s + 0.333)(s + 5)(s + z_1)(s + z_2)}{s(s + 0.333)(s + 1)(s + 2)(s + 5) + 6.67K_cT_r(s + z_1)(s + z_2)} \tag{37}$$

$$\frac{\theta_0}{L} = \frac{s(s + 0.333)(s + 1)(s + 2)(s + 5)}{s(s + 0.333)(s + 1)(s + 2)(s + 5) + 6.67K_cT_r(s + z_1)(s + z_2)} \tag{38}$$

There are now two arbitrary parameters z_1 and z_2 which may be selected. The values selected determine the zeros in Equation (36), which in turn fix the location of the root-loci curves. A typical root-locus curve is shown in Figure 8 for $z_1 = 0.333$ and $z_2 = 0.8$. It was shown in the last section that as the zero moves away from the origin the system becomes less stable. This is again illustrated by the fact that as the zeros move away from the origin the branched part of the curve moves toward the origin. At the same time when one of the zeros is near the origin, a closed-loop pole is introduced near the origin. This pole produces a term in the time response that does not come to 0 very rapidly. Therefore although the response may not be cyclic, it will be slow, and excessive time will be required for the system to come to a steady state.

A study of the approximate root-loci diagrams allows one to make reasonable selections of a few sets of controller parameters for more complete calculations. A tabulation of values which have been calculated for several sets of the controller parameters is given in Table 1.

Some choices of T_r and T_i will cause z_1 and z_2 to be conjugate complex numbers thereby producing complex zeros in Equation (36). In some systems the use of complex zeros may prove beneficial. Root-loci diagrams are shown in Figure 9 for two choices of complex zeros. When the zeros are placed at

$$-1 \pm i\ (T_r = T_i = 0.5)$$

the left-branched curves no longer go to infinity but end at the zeros. For this system this change has little significance. The right-branched curves change their location so as to intersect the imaginary axis at a high value of ω with a corresponding increase in K_c. The system then will not become unstable so easily, but the closed-loop poles are too near the origin to produce a satisfactory response. The loci curves with the zeros placed at $-0.375 \pm 0.75i (T_r = 1.33,\ T_i = 1.07)$ show that the right-branched curves now end at the zeros. Since the right-branched curves do not cross the imaginary axis, the system will be stable at very high values of K_c. However the closed-loop poles near the origin are again disadvantageous.

The responses to step changes in the control point are shown in Figure 10 for a selection of controller parameters. As might be expected, the overshoot decreases as the zeros move toward the origin, and at the same time the settling time increases.

The responses to step changes in the pressure drop across the control valve are also shown in Figure 10. The maximum deviation is high for all the curves, and the time to reach steady state increases as the zeros move toward the origin. The maximum error cannot be decreased as

long as the number of closed-loop poles and zeros are equal. An increase in K_c (decreasing ζ) will cause a somewhat faster recovery but will also increase the overshoot of θ_0/θ_i, which is already beyond the desirable limit.

The frequency response with the control point being varied in a sinusoidal manner is shown in Figure 11. The maximum in the curves decreases as the zeros approach the origin, with the lowest maximum being about 1.8. This is somewhat above the recommended level of 1.2 to 1.5.

A sinusoidal variation of the pressure drop across the valve produces the responses shown in Figure 12. Again the lowest maximum is obtained with the zeros nearest the origin, although there is not a significant difference between all of the curves. Curve 4 has a high value even at low frequencies, an indication that slowly changing pressure drops will cause relatively large errors in the flow rate.

PROCESS TIME CONSTANT

The previous sections have shown that the control of fluid flow when the flow system has a 0 time constant is difficult. The common industrial controllers will not give so close control as desired or necessary. One method of improving the control that immediately comes to mind is the addition of a process time constant. This could be accomplished by the addition of a capacitance and resistance with $T_p = RC$. The open-loop equation with three-mode control is

$$\frac{\theta_0}{E} = \frac{13.33K_cT_r(s + z_1)(s + z_2)}{T_p(s + 1)(s + 2)(s + 1/T_p)} \quad (39)$$

The ratio

$$\frac{\theta_0}{E} \times \frac{E}{\theta_0} = \frac{6.67K_cT_r(s + z_1)(s + z_2)}{T_ps(s + 0.333)(s + 1)(s + 2)(s + 5)(s + 1/T_p)} \quad (40)$$

The closed-loop equations become

$$\frac{\theta_0}{\theta_i} = \frac{4K_c(T_r/T_p)(s+0.333)(s+5)(s+z_1)(s+z_2)}{s(s+0.333)(s+1)(s+2)(s+5)(s+1/T_p)+6.67K_c(T_r/T_p)(s+z_1)(s+z_2)} \quad (41)$$

$$\frac{\theta_0}{L} = \frac{(1/T_p)s(s+0.333)(s+1)(s+2)(s+5)}{s(s+0.333)(s+1)(s+2)(s+5)(s+1/T_p)+6.67K_c(T_r/T_p)(s+z_1)(s+z_2)} \quad (42)$$

The addition of a process time constant produces two significant changes in the equations. The term $1/T_p$ occurs in the numerator of both θ_0/θ_i and θ_0/L. Then if T_p is greater than 1, both ratios will be decreased. With large values of T_p the ratio θ_0/θ_i will be very small, which is undesirable because the system then would not respond to control-point changes. On the other hand, a large value of T_p will cause θ_0/L to be small, which is desirable. Obviously, some compromise must be made that will produce reasonably satisfactory responses of both ratios.

The second change in the equations is that an additional pole has been added to both ratios. This is significant for the ratio θ_0/L, since now the equation has an excess of one pole and the transient response curves will begin at 0 rather than 1 when $t = 0+$. Furthermore that pole at $-1/T_p$ if properly placed will produce a closed-loop pole which will partially cancel the effect of the zero at -0.333.

In a few minutes it is possible to sketch root-loci diagrams for many combinations of $1/T_p$, z_1, and z_2. Such a study will soon give one a good idea of approximate locations of these parameters for satisfactory responses. Space does not permit a complete discussion, but a brief summary follows. One zero is placed at -0.333 to cancel the pole at this point. The other zero is placed at approximately -0.8 so that the closed-loop pole will be in the neighborhood of -0.5, thereby partially canceling the effect of the zero at -0.333. Figure 13 shows the effect of the position of the pole at $-1/T_p$ upon the root-loci curves. When $1/T_p$ is larger than 2, the effect is very small as is seen by comparing Figures 13*a* and *b*. From Figures 13*b*, *c* and *d* it is seen that as $1/T_p$ becomes smaller, the branched curve approaches the origin. The branched curve should not be too near the origin; therefore there is a limit to the amount that the process time constant can be increased. It appears that letting $1/T_p$ have a value in the neighborhood of 2 will produce the best results. The responses to step inputs for several combinations of the parameters are shown in Figures 14 and 16. The differences are obvious. If one is interested, more calculations can easily be made. The corresponding frequency responses are shown in Figures 15 and 17.

All the curves show that the choice of $1/T_p = 1.8$ is approximately the best. Slight variations may improve the responses slightly. As seen from the curves, when $1/T_p$ becomes very small the responses are sluggish, requiring a long time for the system to reach the new steady state.

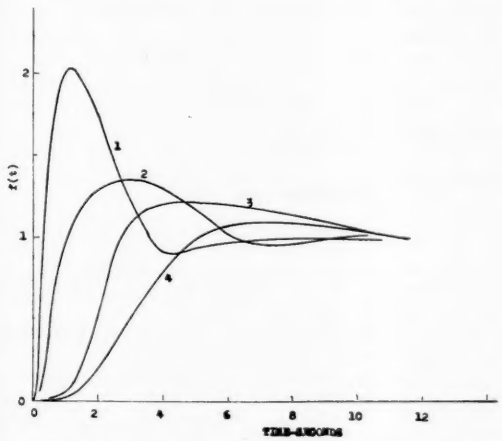

Fig. 14. Transient response after a step change in the control point.

Curve	z_1	z_2	$1/T_p$
1	0.333	0.8	∞
2	0.333	0.8	1.8
3	0.333	0.8	0.8
4	0.333	0.1	0.1

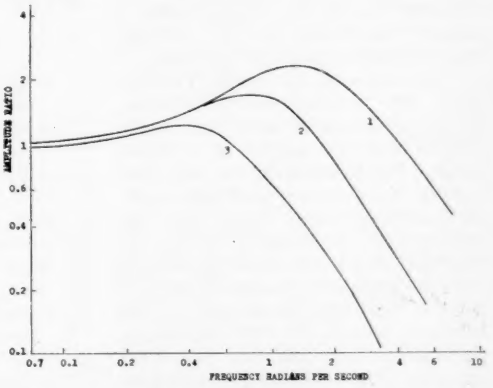

Fig. 15. Frequency response-control point change.

Curve	z_1	z_2	$1/T_p$
1	0.333	0.8	∞
2	0.333	0.8	1.8
3	0.333	0.1	0.1

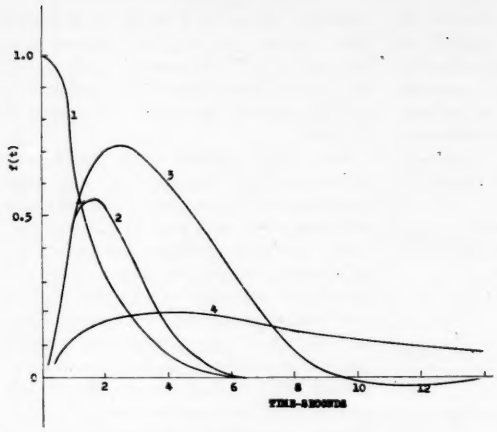

Fig. 16. Transient response after a step change in the pressure drop.

Curve	z_1	z_2	$1/T_p$
1	0.333	0.8	∞
2	0.333	0.8	1.8
3	0.333	0.8	0.8
4	0.333	0.1	0.1

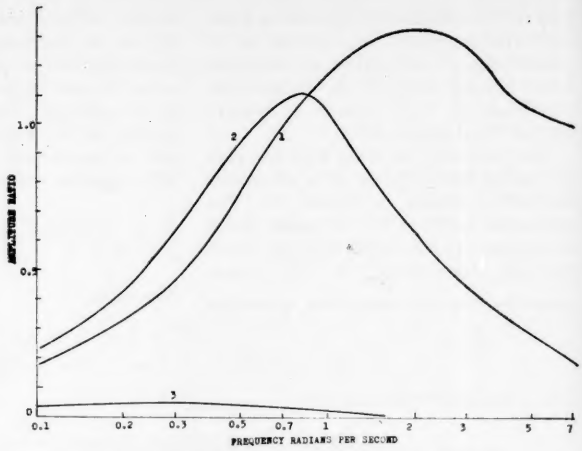

Fig. 17. Frequency response-pressure drop change.

Curve	z_1	z_2	$1/T_p$
1	0.333	0.8	∞
2	0.333	0.8	1.8
3	0.333	0.1	0.1

OTHER MODIFICATIONS OF THE SYSTEM

There are several other modifications which would improve the responses if it is found necessary to do so. As complete discussion is beyond the scope of this paper, the methods will be listed only: (a) addition of a pressure controller in the flow line (7) either as a separate controller or in cascade, (b) the design of a controller with other than the standard three modes of control, and (c) the use of an additional controller in the feedback loop or as a feed forward controller.

CONCLUSIONS

A relatively complete analysis has been made of the control of fluid flow with a flowmeter as the measuring with a flowmeter as the measuring instrument, a controller, and a control valve. The analysis is more complete than is ordinarily necessary. Anyone with a working knowledge of the methods could eliminate some of the steps or at least some of the detail. This example was carried out to illustrate the methods and to show how easily one can make an analysis of a control system. The methods of control-system analysis given have several advantages, the most important being that the engineer has a complete picture of the effect of all the system parameters upon the responses. A second important point is that much of the analysis can be made with very little calculation, particularly after one has had some experience. Obviously all this could have been done with a computer, with however the great disadvantage that one has lost completely the over-all view of the effect of the system parameters. The author believes that the procedure given is quite satisfactory for most purposes and is an excellent preliminary analysis if it is desired to investigate the nonlinear system with a computer.

Conclusions with respect to the specific control system are

1. Linearized equations for the system have been derived.
2. Proportional control is not satisfactory if the system is likely to be subjected to changing pressure drops of any great magnitude.
3. Proportional plus integral control removed the steady state error but otherwise had little effect upon the responses.
4. Three-mode control improved the responses but still not enough if very close control was wanted.
5. The addition of a process time constant of the proper value greatly improved the responses.

NOTATION

A_i = step change in reference input or control point
A_L = step change in the pressure drop across the control valve
C = capacitance
E = error signal
f = frequency cycles/sec. = (radians/sec.)/2π
F = signal
G = transfer function
h_m = pressure differential
K = constant
K_c = controller gain, (reciprocal of the proportional band/100)
L = load function, pressure drop across the valve
Δp = pressure drop across the valve
Q = flow rate
R = flow resistance
s = independent variable in transformed equations
T = time constant
z = zeros, functions of the controllers parameters

Greek Letters

ζ = damping coefficient
θ_i = reference input signal (control point)
θ_0 = controlled variable, flow rate
σ = real coordinate of the conjugate complex poles
ω = imaginary coordinate of the conjugate complex poles
ω_n = natural frequency, radians/sec.
ω_o = frequency of sinusoidal input, radians/sec.

Subscripts

c = controller
i = integral mode of control
p = process
r = rate mode of control
ss = steady state
tr = transmitter
tu = tubing
v = valve

LITERATURE CITED

1. Moise, J. C., *ISA Journal*, **1**, 35 (1954).
2. Rohman, G. P., and E. C. Grogan, presented at the Semiannual meeting of the Am. Soc. Mech. Engrs., Cleveland, Ohio (June 1956).
3. Sandell, R. P., and N. H. Ceaglske, *ISA Journal*, **3**, 482 (1956).
4. Ceaglske, N. H., unpublished paper.
5. Evans, W. R., "Control System Dynamics," McGraw-Hill, New York (1954).
6. Truxal, John C., "Control System Synthesis," McGraw-Hill, New York (1955).
7. Leland, Roger, M.S. thesis, Univ. Minnesota, Minneapolis (1957).

Manuscript received July 7, 1958; revision received April 27, 1959; paper accepted May 4, 1959.

The Mechanics of Vertical Moving Liquid-Liquid Fluidized Systems: I. Interphase Contacting of Droplets Passing Through a Second Quiescent Fluid

ROBERT E. C. WEAVER, LEON LAPIDUS, and J. C. ELGIN

Princeton University, Princeton, New Jersey

Previous publications have shown that for solid spheres fluidized in water a unique relationship exists between the slip velocity and the system holdup. With this work as a model a method is now presented for estimating the behavior of the liquid-in-liquid spray column in which droplets of one phase move through a second quiescent phase.

Combining the solids fluidization results with information on the single droplet terminal velocity one can obtain a design estimate of the holdup or interphase contact area for the liquid-liquid spray column. This design estimate includes the particular nature of the liquid droplet of being susceptible to internal circulation, oscillation, and distortion.

The effective contact area between two phases directly affects the over-all rate of any process occurring across the phase boundary. In most transfer operations, where one fluid is dispersed through the other, this area can at present be estimated or the system holdup determined only by a difficult direct measurement. Consequently most earlier studies of transfer processes have combined the contact area with the intrinsic rate characteristics of the system.

In a previous publication from this laboratory (*12*) a detailed theoretical analysis was presented for predicting the behavior of all types of vertical moving fluidized systems. The basic postulate of this development was the proposal that a single unique relationship exists between the slip velocity and the holdup for a system comprising one particle size. For such a system the holdup is related directly to the interfacial area. Subsequent publications (*14, 15, 17*) have tested this theory with rigid glass spheres fluidized by water. Under all vertical-flow arrangements the agreement between theory and experiment was excellent thereby substantiating the single unique relationship mentioned above.

The fluidized systems thus studied may be characterized as ideal in the sense that they involve uniform dispersed particles which are rigid and impermeable. Particulate fluidization always occurs under these operating conditions. Of paramount importance is the extension of the concepts developed for ideal systems to the area of nonideal systems. This paper reports on the behavior of the liquid-in-liquid spray column in which droplets of one phase move through a second quiescent continuous phase. In contrast to the previous ideal systems with solid spheres, the liquid droplets are subject to internal circulation, oscillation, and distortion as they pass through the second fluid.

The present experimental results demonstrate that the holdup may be related directly to a slip-velocity ratio, for example a ratio of the normal slip velocity between the two phases in the column to the terminal velocity of a representative single droplet. This relationship is a generalization of the previously defined unique slip velocity-holdup function for solid particles.

Holdup data are presented for the systems methyl isobutyl ketone-water, isobutanol-water, toluene-water, and isoamyl alcohol-water operating in a 1-⅞-in. Elgin type of spray tower. In each case the organic solvent is the dispersed phase. The holdup was measured directly in the tower as a function of the system parameters by sealing off a part of the tower proper. The system parameters included the dispersed phase flow rate, the droplet size in the column, and the physical properties of the organic solvents. Detailed data are also presented to show that the droplet size distribution in the tower is normal in the Gaussian sense.

BACKGROUND INFORMATION

Since the present liquid-in-liquid system compares with the familiar batch fluidization of solids, an extensive survey was made of the present status of this latter type of operation. In addition to the normal experimental and empirical approach a number of models have been proposed in which the fluidized state is treated as an ideal gas (*20*), as a liquid (*3*), or in terms of statistical interactions (*16*). To the present day however the voluminous experimental information has defied a simple analytical description.

Direct resort to the data itself, codified in various dimensionless number presentations, appears the most reliable method of obtaining an indication of the holdup of solid particles under different flow conditions. The compilation of Zenz (*21*), illustrated in Figure 1, is based on a good cross section of the published studies; this convenient description in three parameters, representing the particle size, velocity, and holdup, has been the source of the fluidization information used in the present study.

The fact that liquid droplets passing through a second continuous fluid are subject to various degrees of nonideality, that is induced internal circulation, distortion, and oscillation of the drop-

Robert E. C. Weaver is with the Ethyl Corporation, Baton Rouge, Louisiana.

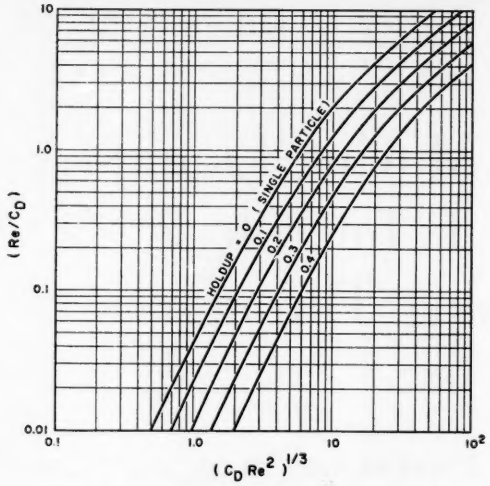

Fig. 1. Zenz correlation for fluidized solids.

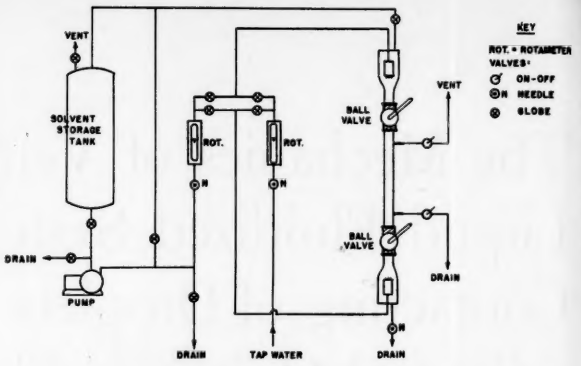

Fig. 2. Schematic diagram of experimental apparatus.

lets, has been described by a number of authors (*1, 4, 5, 7, 8, 11, 13, 18*). Specific consideration of these phenomena by Calderbank and Korchinski (*2*) has given an indication that the pertinent dimensionless criteria are the Reynolds and Weber numbers along with the conventional drag coefficient. Klee and Treybal (*10*) confirmed this in their investigation; they were able to obtain a general correlation in these terms. The fall velocity of the liquid droplets reported by these authors as a function of the drop diameter shows two clear regimes. These can be described analytically in terms of the above mentioned groups, but the hump or maximum found to exist in the transition zone between the two regimes has not been amenable to an analytical description. When presented in terms of the drag coefficient vs. the Reynolds number the Klee-Treybal data result in a family of curves which are functions of the surface tension. These curves indicate that the effects of internal circulation, droplet oscillation, and distortion (significant particularly for the larger drop sizes and high Reynolds numbers) are more pronounced the lower is the interfacial tension of the system. As a result the experimental drag coefficient curves cross each other.

EXPERIMENTAL

Apparatus

The equipment for the present study was designed to permit precise measurements of the holdup in the operating liquid-liquid spray tower. Other variables defining the process and requiring measurement included the flow rates of both phases, fluid system properties, operating temperature, and the droplet size in the tower. The particular liquid-liquid systems consisted in each case of water with one of several organic solvents; these included methyl isobutyl ketone, isobutanol, toluene, and isoamyl alcohol. The solvents were chosen to provide a representative range of the pertinent physical properties: density, viscosity, and interfacial tension.

Figure 2 shows a schematic view of the over-all apparatus and Figure 3 a diagram of the tower proper. The end sections of the glass extraction tower were constructed in the accepted Elgin design with 16-deg. conical frustra leading to the expanded ends. These sections were connected to

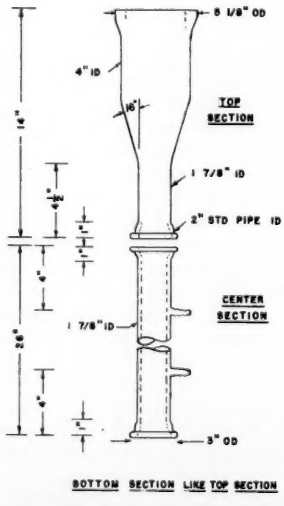

Fig. 3. Schematic diagram of glass column.

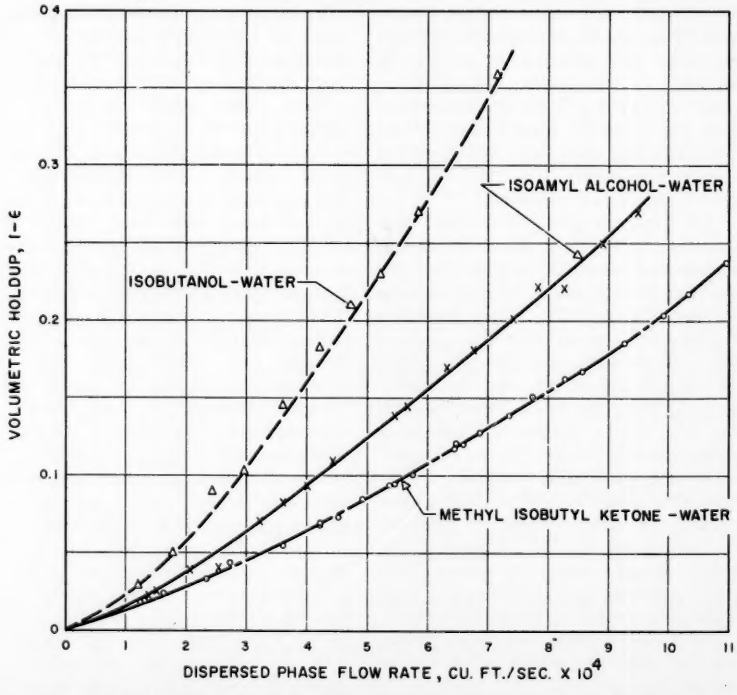

Fig. 4. Experimental holdups vs. dispersed-phase flow rate, 1/8-in. nozzles.

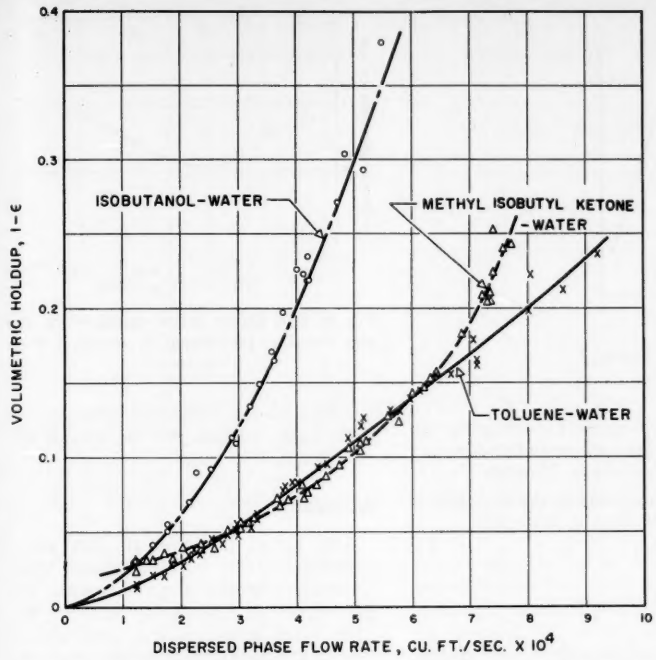

Fig. 5. Experimental holdups vs. dispersed-phase flow rate, 1/16-in. nozzles.

the center section through two quick opening ball valves. When open the valves offered an unobstructed uniform cross-section path through the entire tower. Holdup in the central section could be directly measured upon simultaneously closing these two valves and allowing the two phases to separate. Two condenser taps along the length of the center section were used in venting and provided sample taps during column operation.

Both phases were supplied to the column through the standard type of nozzle heads. In all cases the organic solvent was the dispersed phase. Each head was packed with ¼-in. glass rings to circumvent channeling and allow a uniform delivery through all the nozzles. The nozzles themselves, ⅛ and 1/16 in. diameter, were of a sharp edged variety and were machined from a single diameter brass rod so as to be interchangeable in number and size.

Drop sizes and shapes were recorded photographically for representative runs during the operation of the tower. Correction was made for the distorting effect of refraction through the curved column wall. The correction was significant for droplets larger than 3 mm. diameter. The physical properties and the operating-tower temperature were measured in the samples tapped from the tower during the course of the experimental run. The properties used to describe the particular systems were density, viscosity, and surface tension. These were measured by the pycnometer, the Ostwald viscosimeter, and Harkins drop-weight method (*6*), respectively. These measurements were reproducible with no change evident during the course of the experiments. In all cases the liquids used were mutually saturated. Table 1 summarizes the experimentally determined results.

PROCEDURE AND OBSERVATIONS

The experimental procedure used to establish the relationship between the slip velocity and the holdup in the liquid-liquid spray tower included the following:

Table 1. Tabulation of Physical Properties

Key:
Visc. = viscosity at 25°C. in centipoises
Dens. = density at 25°C. in g./cc.
I. T. = interfacial tension with water at 25°C., dynes/cm.

Liquid	Visc.	Dens.	I. T.
Methyl isobutyl ketone	0.8252	0.7995	8.82
Isobutanol	4.2789	0.8185	2.08
Toluene	0.7158	0.8595	30.3
Isoamyl alcohol	4.8812	0.8220	4.58

1. After steady state was reached in each run, the flow rate of the organic phase was measured by a rotameter. Throughout the present work a static continuous phase was used.
2. For a representative number of runs photographs were taken to be used subsequently in determining the droplet sizes.
3. Samples were tapped to obtain an indication of the temperature in the operating tower and to be used for physical property measurements.
4. The ball valves were then quickly closed, isolating the central section of the tower; after settling the volume of the dispersed phase (that is the holdup) was measured.

The following general observations were made during the experiments:

1. The data were all taken between 22° and 26°C., and no meaningful temperature effect could be detected in this narrow range.
2. The character of the droplet distribution did not change noticeably along the

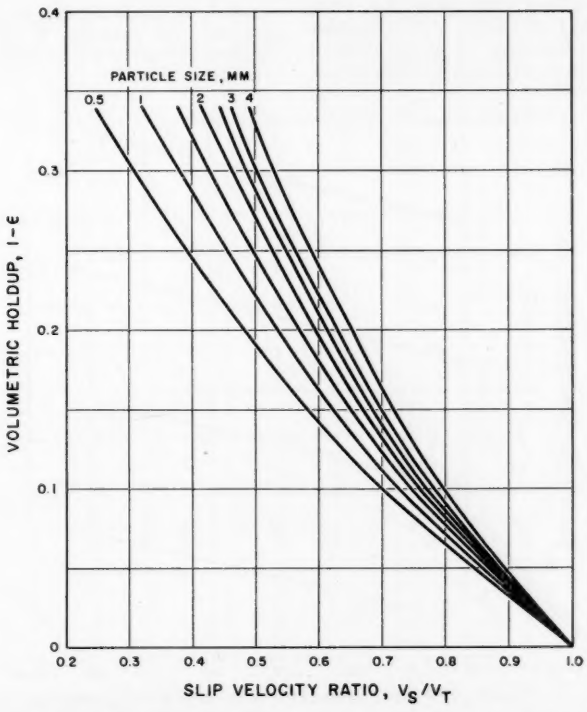

Fig. 6. Batch expansion curve for a system of rigid spheres of density equal to isobutanol as predicted by the Zenz correlation.

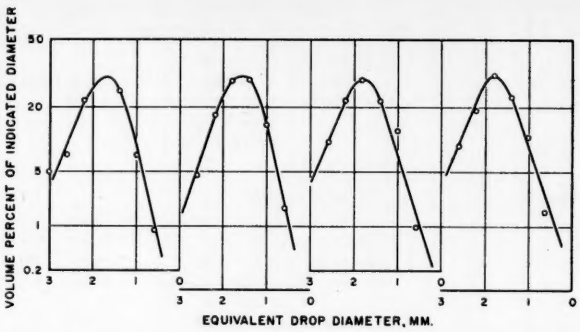

Fig. 7. Drop-size distributions for isobutanol in water, 1/8-in. nozzles.

length of the center section of the tower. No droplet coalescense in the tower proper was observed, although some foaming was observed at the terminals in several of the high-holdup runs of the methyl isobutyl ketone-water systems.

3. The droplets were somewhat distorted from the spherical into oblate ellipsoids while moving through the tower. However, as earlier workers have successfully treated their data in terms of the Sauter mean diameter, the measured droplet dimensions here have also been converted into this form. The Sauter mean is simply the diameter of a sphere of the same volume as the distorted droplet.

EXPERIMENTAL RESULTS

Figures 4 and 5 present (in the form of disperse-phase holdup vs. the disperse-phase flow rate) the experimental data collected in the present investigation. Figure 4 shows data using the $\frac{1}{8}$-in. nozzles and Figure 5 the 1/16-in. nozzles. The reproducibility of these data is excellent. In the discussion which follows

Table 2. Drop-Size Measurements and Distortion for System of Isobutanol-Water—$\frac{1}{8}$-in. Nozzles

Run no.	1	2	3	4
Volume percentages in the size range indicated by its midpoint				
Mean size of droplets (mm.)				
0.6	1.0	1.8	1.6	0.9
1.0	13.1	14.9	11.7	7.9
1.4	22.5	30.8	23.2	26.0
1.8	30.2	30.3	35.2	30.1
2.2	23.1	17.5	18.7	22.3
2.6	10.1	4.7	9.6	7.9
3.0				5.0
Distortion $(a/b)_m$	0.805	0.849	0.824	0.856

Mean size of droplets given in terms of Sauter-mean diameters of individual droplets.

a and b are characterizing dimensions of droplets. The distortion is the volume-weighted average of the individual droplets a/b values.

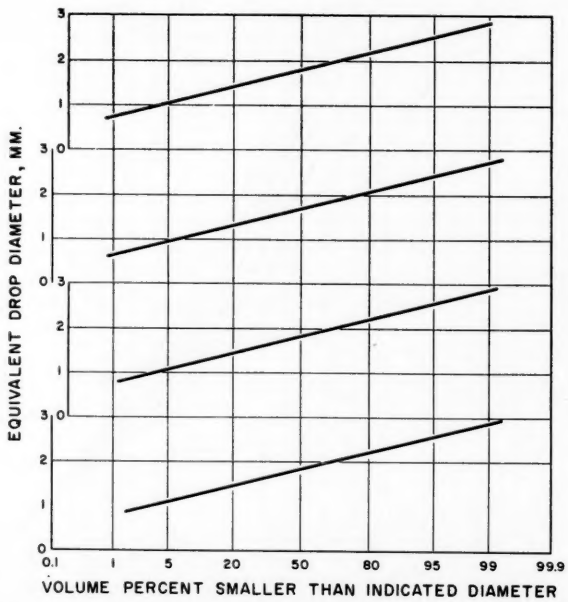

Fig. 8. Cumulative drop-size distribution for isobutanol in water, 1/8-in. nozzles.

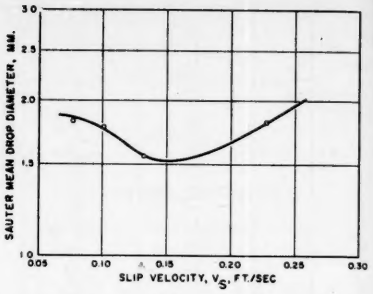

Fig. 9. The Sauter mean diameter vs. the slip velocity. Isobutanol in water, 1/8-in. nozzles.

the data for the isobutanol-water system with $\frac{1}{8}$-in. nozzles will be specifically considered.

DISCUSSION

The model proposed in this paper assumes that, for both liquid and solids dispersed systems, a given holdup will define a unique slip-velocity ratio, V_S/V_T. This ratio measures the approach of the slip velocity in the tower to the terminal velocity for the single droplet or particle. The unique ratio proposed is an extension of the previous relationship for ideal systems but one which now takes into account the nonideal flow behavior of liquid-liquid fluidized systems. In order to confirm or to disprove this model the present liquid-liquid data will be compared with the data for an analogous system of batch fluidized solid particles.

BEHAVIOR OF SOLID PARTICLES ANALOGOUS TO LIQUID DROPS

The Zenz correlation may be used to provide an estimate of the holdup-slip velocity ratio relationship for a solid particles fluidized system. When one assumes that solid spheres of density equal to that of isobutanol are fluidized by water, this correlation yields the data represented graphically in Figure 6.

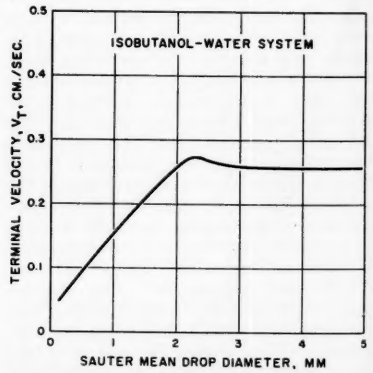

Fig. 10. Terminal velocity of isobutanol droplets in water as predicted by the Klee and Treybal correlation.

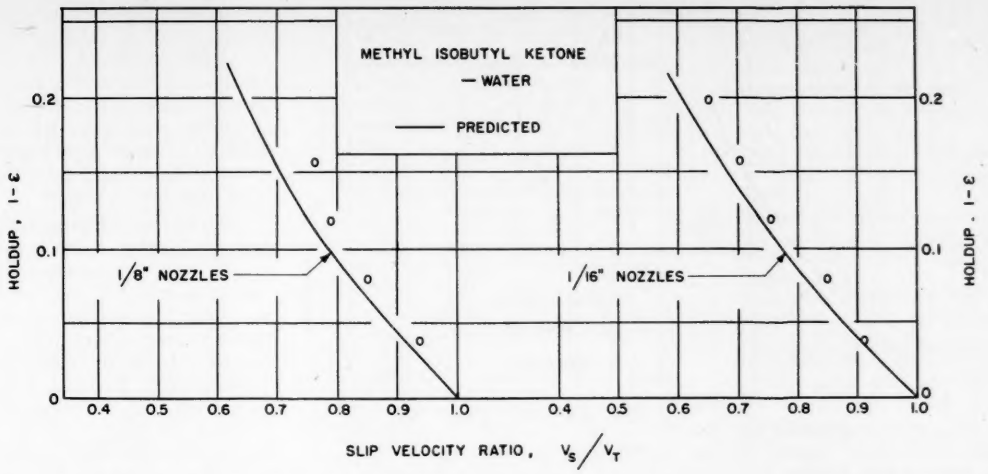

Fig. 11. Observed vs. predicted slip velocity-holdup curves for methyl isobutyl ketone water, 1/16-and 1/8-in. nozzles.

In this chart the holdup is plotted vs. the slip-velocity ratio for a range of spherical particle diameters. These curves correspond to the behavior of hypothetical rigid isobutanol spheres fluidized by water.

DROPLET SIZE DISTRIBUTION IN TOWER

Visual observations of the droplets passing through the tower suggests that a distribution of droplet sizes exists at any given tower cross section. Since the theoretical fluidization analysis previously referred to considers in each case all particles present in the system to be of the same fixed particle size, it is necessary to obtain a mean diameter for the spectrum of droplet sizes which occurs with the liquid in liquid systems studied here. A large number of photographs were taken of the tower as the disperse droplets passed through the second continuous fluid. Detailed measurements of the droplets in these photographs were then used to obtain droplet size distributions. Figure 7 shows the result of such measurements for the isobutanol-water system with 1/8-in. nozzles and is typical of all of the systems studied. The data are shown for four representative experimental runs with different flow rates used and the Sauter mean diameter of the droplets plotted vs. the volume fraction corresponding to the diameter indicated. The Sauter mean diameter is the diameter of a sphere of the same volume as the distorted droplet. Table 2 presents the data used in Figure 7 plus the actual distortion measurements of the droplets. From these curves the Sauter drop diameters were then plotted vs. the cumulative distributions in Figure 8 with probability paper used. It is notable that straight lines which are characteristic of a normal or Gaussian distribution describe the data. Furthermore uniform slopes are obtained indicating a constant variance of the distributions. This makes it possible to describe the effect of velocity on the droplet size in a given system by means of a single size parameter and the uniform slope. When one takes the 50% mean diameter of the cumulative distribution as the appropriate size parameter, the slip velocity of the system can be calculated as a function of the drop size. The data thus calculated are shown in Figure 9. Figure 9 is typical but represents only a small portion of the data available for this system and for the other liquid-liquid

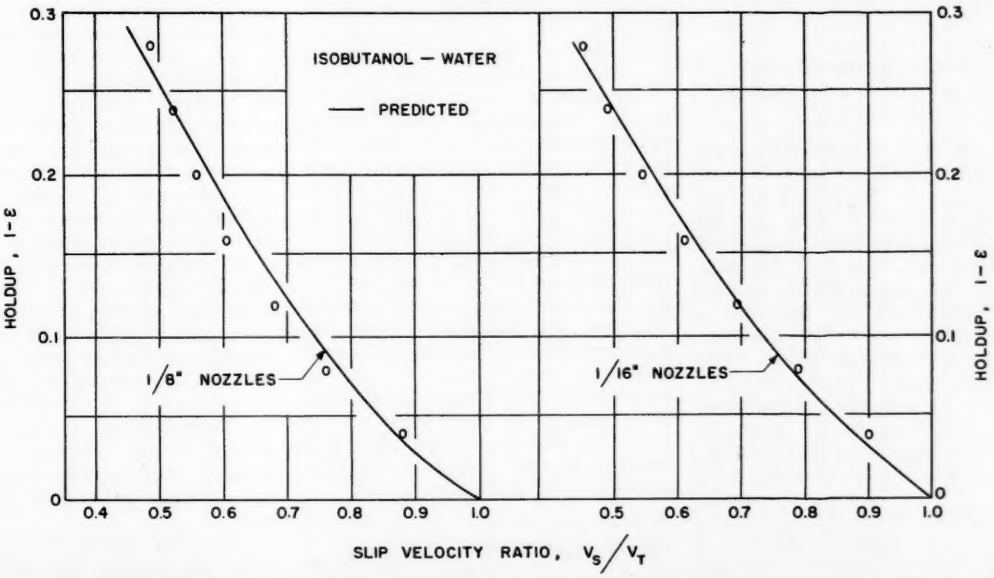

Fig. 12. Observed vs. predicted slip velocity-holdup curves for isobutanol water, 1/16-and 1/8-in. nozzles.

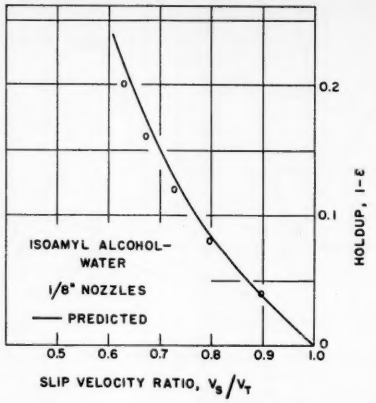

Fig. 13. Observed vs. predicted slip velocity-holdup curves for isoamyl alcohol water, 1/8-in. nozzles.

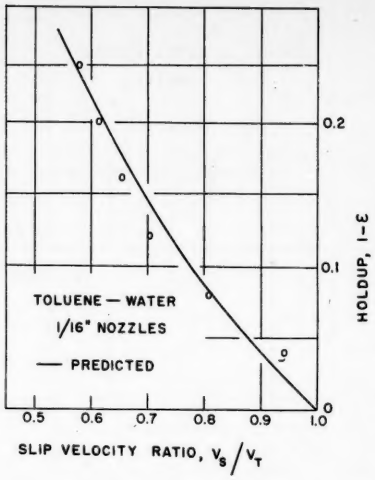

Fig. 14. Observed vs. predicted slip velocity-holdup curves for toluene water, 1/16-in. nozzles.

systems investigated in this study (*19*). In all cases the results are comparable.

MEAN DROPLET TERMINAL VELOCITIES

From the data of Keith and Hixson (*9*) and from the correlation of Klee and Treybal the terminal velocity of single droplets of isobutanol in water can be calculated as a function of the Sauter drop diameter. Figure 10 shows a plot of some of these data. Since the present data, with a mass of droplets passing through the column, exhibit droplet size distribution, there is no one single terminal velocity for all droplets in the system. A mean droplet terminal velocity can however be calculated with the volume weighted mean sizes used. Specifically the 10–30–50–70–90% points of the size distributions can be selected and the corresponding terminal velocities averaged to yield a mean terminal velocity for the mass of isobutanol droplets.

COMPARISON OF LIQUID-DROPLET AND SOLID-PARTICLE HOLDUPS AS A FUNCTION OF THE SLIP-VELOCITY RATIO

There are now sufficient data and information available to allow a direct comparison to be made between the actual liquid-droplet holdups and the hypothetical holdups which would exist in a solid-particle system of the same density as a function of the slip-velocity ratio. To illustrate the technique a holdup of $(1 - \epsilon) = 0.200$ has been experimentally measured for the isobutanol-water system. From Figure 4 this holdup corresponds to a flow rate of 4.66×10^{-4} cu. ft./sec. Since the tower cross section is 1.92×10^{-2} sq. ft., the slip velocity can be calculated to be

$$V_s = \frac{(4.66 \times 10^{-4})(0.200)}{1.92 \times 10^{-2}} = 0.121 \text{ ft./sec.}$$

From Figure 9 the Sauter mean droplet diameter under these conditions is 0.162 cm. Using this as the 50% point of the drop distribution and constructing a line parallel to those in Figure 8, one can obtain an estimate of the distribution in terms of the 10–30–50–70–90% drop dimensions. The appropriate terminal velocities for each of these can be found from Figure 8. An averaging of the results yields the mean terminal velocity of 0.217 ft./sec. The slip-velocity ratio based upon experiment is then

$$V_s/V_T = 0.121/0.217 = 0.558$$

From Figure 6 it can be seen that a slip-velocity ratio of 0.558 produces a fractional holdup of 0.215 for the solid-particle fluidized system. In this example the difference between the experimentally measured holdup of 0.200 and that predicted for the system from the fluidization data for solid particles is 7.5%.

The result of similar calculations for the six experimental systems studied are shown graphically in Figures 11 to 14. The results predicted on the basis of the solid-particle model agree with the experimental liquid-liquid results with an over-all average deviation of 11%. In view of the fact that the parent information on the solids behavior and for the single liquid droplet terminal velocities are themselves subject to departures of about this order of magnitude, these results may be taken as confirmation of the basic model. Thus it is possible to predict the holdup (and from this the contact area) in a liquid-liquid spray tower on the basis of solid-particle fluidization results.

POSSIBLE DISCREPANCIES IN THE MODEL

Two possible sources of departures of the experimental data from the predicted behavior of the rigid-particle analogue are most prominent: the shortcomings of the model for treating the methyl isobutyl ketone systems and the tendency in all the systems for the liquid-droplet holdups to curve more rapidly with increasing slip-velocity ratio than do their solid particle counterparts.

Difficulty would be expected in treating the methyl isobutyl ketone-water system for two reasons. The terminal velocities reported for this system by the several investigators cited were in distinct disagreement where they overlapped. Further the nozzles used in the present study produced droplets which partly fell into the region of Treybal's "critical diameter," where the correlation could not reliably supplement the lack of experimental data. Although no change in the interfacial tension of the system could be detected, foam was also observed to develop for this particular system at the higher holdups. No coalescense occurred in the main section of the column, but the foam did appear to promote its occurrence along the walls of the entrance region. Any influence which these factors might have had could explain departures in the directions noted.

The main weakness of the present model is the apparent tendency of all the experimental data to curve somewhat more than the predicted behavior would indicate should be the case. It is difficult to judge the significance of this tendency, but a drift toward higher slip velocities at the higher holdups seems persistent. Among the phenomena which could be responsible for the presumably faster slip of the droplets here would be their involvement in gross circulation patterns (since liquid densities are actually less than those of any solid particles studied). Such circulation was observed; however without evidence as to its occurrence in the corresponding solids systems upon which the predicted behavior was based, one cannot judge the extent of the net effect. The low-density liquid droplets are also more subject to the virtual mass effect than are the systems upon which the fluidization correlations are based. The virtual mass concept one recalls is involved with accelerated (or decelerated) motion when the mass of the displaced fluid relative to that of the moving body is significant. Qualitatively virtual mass considerations would lead one to expect relatively higher slip velocities at the higher holdups in the spray column. No effect would be expected in the more uniform motion obtained at very low holdups. At the present time one is not in a position to be more specific than this.

Future publications from this laboratory will consider the effect of the continuous-phase flow on the present

results as well as an extension into the area of the gas-in-liquid spray tower.

ACKNOWLEDGMENT

The financial support of the Monsanto Chemical Company in the form of a fellowship to R. E. C. Weaver during a part of the period covered by this investigation and of the California Research Corporation for a grant-in-aid is gratefully acknowledged. The present work was made possible through this support.

NOTATION

$1 - \epsilon$ = volumetric holdup
V_s = slip velocity, ft./sec. = vectorial difference between the average discontinuous fluid velocity and the average continuous velocity.
V_T = droplet terminal velocity, ft./sec.
Re = Reynolds number
C_D = drag coefficient

LITERATURE CITED

1. Bond, W. N., and D. A. Newton, *Phil. Mag.* (7), **5**, 794 (1928).
2. Calderbank, P. H., and I. J. O. Korchinski, *Chem. Eng. Sci.*, **6**, 65 (1956).
3. Furukawa, Junji, and Tsutomu Ohmae, *Ind. Eng. Chem.*, **50**, 821 (1958).
4. Garner, F. H., and A. H. P. Skelland, *Chem. Eng. Sci.*, **4**, 149 (1955).
5. Hadamard, J. C. R., *Compt. rend.*, **152**, 1735 (1911).
6. Harkins, W. D., "Techniques of Organic Chemistry," Vol. I, Chap. 9, p. 353ff., Interscience Publishers, New York, (1949).
7. Hayworth, C. B., and R. E. Treybal, *Ind. Eng. Chem.*, **42**, 1174 (1950).
8. Hinze, J. O., *A.I.Ch.E. Journal*, **1**, 289 (1955).
9. Keith, F. W., and A. N. Hixson, *Ind. Eng. Chem.*, **47**, 258 (1955).
10. Klee, A. J., and R. E. Treybal, *A.I.Ch.E. Journal*, **2**, 445 (1956).
11. Kronig, R., and J. C. Brink, *Appl. Sci. Res.*, **A2**, 142 (1950).
12. Lapidus, Leon, and J. C. Elgin, *A.I.Ch.E. Journal*, **3**, 63 (1957).
13. Licht, William, and G. S. R. Narasimhamurty, *ibid.*, **1**, 366 (1955).
14. Price, B. G., Leon Lapidus, and J. C. Elgin, *ibid.*, **5**, 93 (1959).
15. Quinn, John, Ph.D. dissertation, Princeton Univ., Princeton, New Jersey (1958).
16. Soo, S. L., *Chem. Eng. Sci.*, **5**, 57 (1956).
17. Struve, Don, Leon Lapidus, and J. C. Elgin, *Can. J. Chem. Eng.*, **36**, 141 (August, 1958).
18. Taylor, G. I., *Proc. Roy. Soc.* (*London*), **A146**, 501 (1934).
19. Weaver, R. E. C., Ph.D. dissertation, Princeton Univ., Princeton, New Jersey (1958).
20. Wilhelm, R. H., Proceedings, Second Midwestern Conference on Fluid Mechanics, p. 379, Columbus, Ohio State Univ., (1952).
21. Zenz, F. A., *Petrol. Refiner*, **36**, No. 8, 147 (1957).

Manuscript received January 19, 1959; revision received May 7, 1959; paper accepted May 11, 1959

Reaction Rates in the Synthesis of Ammonia

A. K. MILLS and C. O. BENNETT

Purdue University, West Lafayette, Indiana

A study has been made of the reaction rates of mixtures of hydrogen and nitrogen to form ammonia over a doubly promoted iron catalyst at 400° and 450°C. and at pressures up to 1,000 atm. In this work particular care has been taken to obtain data representing the true kinetics of the reaction. The reactor used was essentially isothermal, and the effects of diffusion have been reduced to a minimum. The results have been correlated by the use of the mechanism proposed by Temkin and Pyschev (*19*) with moderate success.

The kinetics of the ammonia synthesis reaction have been the subject of many investigations, and results have been published by Adams and Comings (*1*), Uchida and Kuraishi (*21*), Bokhoven and van Raayen (*3*), Siderov and Livshits (*17, 18*), Nielsen (*14*), Emmett and Kummer (*6*), Almquist and Crittenden (*2*), and Larson and Tour (*13*). Of these investigations only three (*1, 17, 18*) make a claim to an essentially isothermal catalyst bed; the others report temperature variations in the bed, running as high as 15° in one case (*14*). Siderov and Livshits (*18*) report the highest pressure (500 atm.), and in no case has the entire diffusion problem been analyzed, although Bokhoven and his associates (*3, 8*) have done valuable work on the question of diffusion within the catalyst pores, and Adams and Comings (*1*) report a calculation for the effect of diffusion between the bulk of the gas and the surface of the catalyst.

A. K. Mills is with Dow Chemical Company, Midland, Michigan. C. O. Bennett is with the Lummus Company, New York, NewYork.

APPARATUS

Figure 1 shows the general flow diagram for the process. The mixture of hydrogen and nitrogen was compressed over mercury in the *U*-tube made from two 3-liter vessels, *E*. The pump, *B*, pumped oil into one leg of the *U*-tube and could develop a pressure of 20,000 lb./sq. in. The compressed synthesis gas was stored in the two 3.5-liter vessels, *H*; these vessels could store enough gas for about a week of continuous running at about 400 atm. pressure in the reactor.

During a run the gases passed from the storage vessels, *H*, through the clean-up train (*14, 13, 8, 12, 11*) to the reactor, *R*. This train consisted of a 1-liter vessel filled with sodium hydroxide pellets and activated carbon; here carbon dioxide and possibly oil mist were removed. Next came a 300 cc. vessel containing finely divided copper maintained at 300°C.; the copper was made from the reduction of copper hydroxide in a stream of hydrogen or synthesis gas. This vessel was intended to remove oxygen. Any water formed was removed in the condenser and separator (*8, 12*) followed by the vessels, *M*, containing silica gel.

After passing through the reactor the gases were expanded to atmospheric pressure in the heated valve, *S*; the ammonia was absorbed in the sulfuric acid bubblers, *T*, and the rate of flow of the residual hydrogen-nitrogen was obtained by the wet test meter, *U*.

The reactor itself (Figure 2) was made from a 14-in. length of standard 9/16 × 3/16 in. tubing. 1.625 g. of unreduced catalyst were contained in a 5-cm. length of this tube, and three thermocouples were placed in the bed. In no case was the variation in temperature among these thermocouples more than 3°C., and in most cases it was less than 1°C. The catalyst occupied a space of 0.602 cc., not counting the thermocouple wires (30-gauge iron constantan); the void fraction was 0.46. The particles in the bed were roughly 2 mm. in diameter (9–10 mesh). The catalyst was activated by the standard procedure (*14*). Several external heaters were installed to control the longitudinal temperature variation within the bed.

The design of the reactor described above was determined by the following factors. (1) The large length-to-diameter ratio insured the highest possible linear velocity past the pellets, thus reducing the effect of longitudinal diffusion and diffusion to the catalyst surface to a minimum. (2) The small pellet size reduced the effect of diffusion within the catalyst pores to a minimum. (3) The whole arrangement, with several separately controlled heaters, resulted in very good control of temperature in the bed. (4) The small diameter held the radial temperature differences to minimum values. Usually a bed diameter to pellet diameter of at least ten is used to reduce

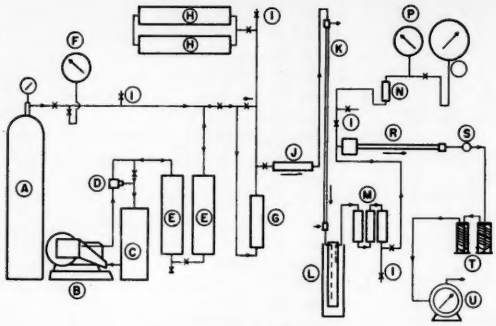

Fig. 1. Flow diagram.

radial gradients of temperature, velocity, and composition; however even a rather large temperature gradient over the 2.38-mm. radius of the present reactor does not give a large temperature difference.

RESULTS

The data were obtained directly as a precentage ammonia in the gas leaving the reactor as a function of space velocity, pressure, temperature, and composition of the feed. Figure 3 illustrates the data obtained for the 3 : 1 hydrogen-nitrogen feed mixture. Wherever possible the curves have been extrapolated to the equilibrium composition (*12, 11*) at a zero space velocity.

The usual method of obtaining the rate of reaction from information on the composition of the gas leaving the reactor is based on the equation

$$r = \frac{dx}{d\left(\frac{1}{S_0}\right)} \qquad (1)$$

derived from the basic definitions (*9*)

$$r\,dV = F\,dx \qquad (2)$$

and

$$S_0 = \frac{F}{V} \qquad (3)$$

The space-time yield is related to the degree of conversion by

$$x = \frac{\sigma}{S_0} \qquad (4)$$

for the reaction being considered. Thus the rate can be calculated from data on the space-time yield by the equation

$$r = \sigma - S_0 \frac{d\sigma}{dS_0} \qquad (5)$$

Curves of the space-time yield as a function of space velocity are given in Figure 4. These curves are easily plotted from the original experimental data, and they have the advantage of permitting a more reliable curve to be drawn in the region of low S_0 than could be done by the use of x vs. $1/S_0$ [refer to Equation (1)]. All the curves must pass through the origin, and in addition

$$\left(\frac{d\sigma}{dS_0}\right)_{S_0=0} = \left(\frac{Z_{NH_3}}{1 + Z_{NH_3}}\right)_{equilibrium} \qquad (6)$$

The precision of the points obtained at high S_0 is considerably higher than that for the points at low S_0, so it is very helpful to know how the curves begin.

The determination of r from the experimental data as described above is based on the assumption of plug flow through the reactor with no longitudinal diffusion. It will be shown below that longitudinal diffusion is not significant, and the shape of the reactor makes the assumption of plug flow at least more plausible than the assumption would be for a short, fat reactor. Incidentally, for a reactor with complete internal mixing Equation (5) should be replaced by $r = \sigma$.

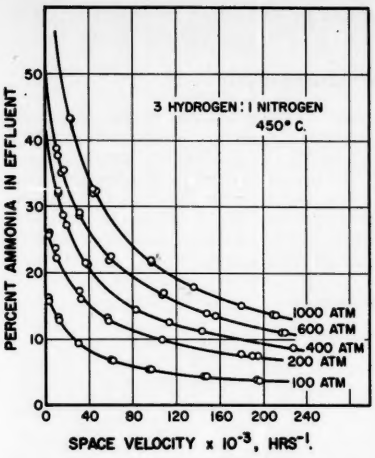

Fig. 3. The effect of space velocity on the ammonia concentration in the product.

Equation (5) can be used with the data of Figure 4 to obtain the reaction rates as a function of pressure, temperature, initial composition, and mole-fraction ammonia. The rates for all the conditions investigated are given in Figures 5 to 8; the procedure used involved the finding of an empirical, analytical expression for σ as a function of S_0. An advantage of reporting the rate in this form is that it is independent of any assumed mechanism of reaction; it can be directly used for the design of a reactor.

INTERPRETATION OF THE DATA BY THE TEMKIN MECHANISM

The most plausible explanation of the kinetics of the ammonia synthesis reaction is usually accepted as that of Temkin

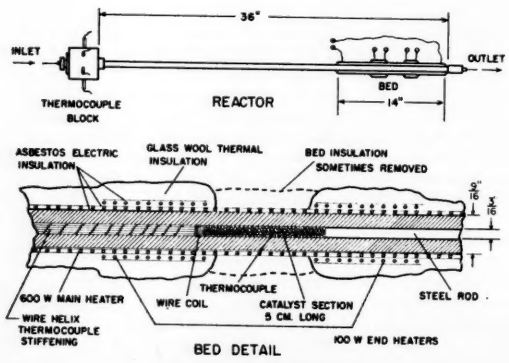

Fig. 2. Reactor details.

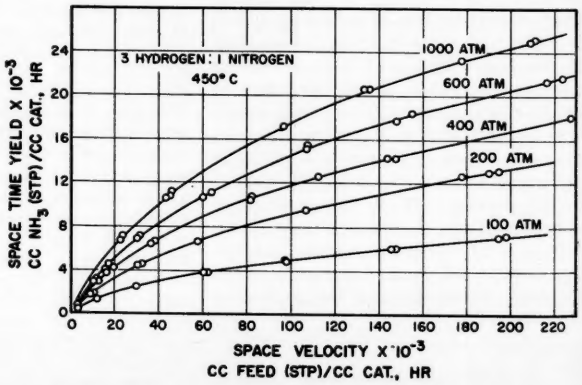

Fig. 4. The effect of space velocity on space-time yield.

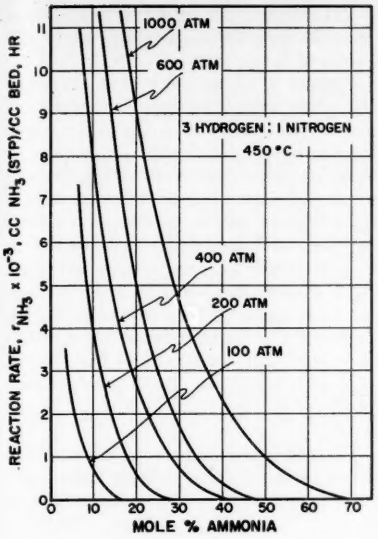

Fig. 5. Reaction rates for the 3:1 mixture at 450°C.

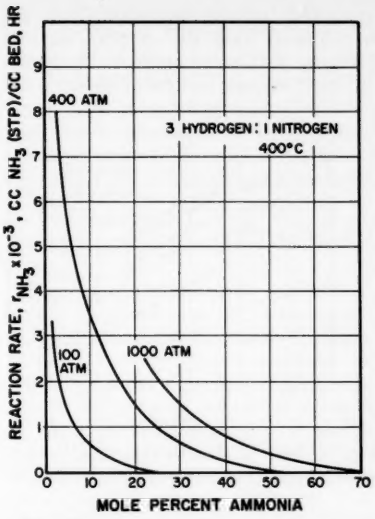

Fig. 6. Reaction rates for the 3:1 mixture at 400°C.

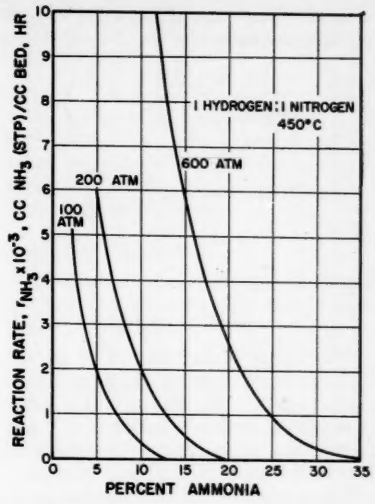

Fig. 7. Reaction rates for the 1:1 mixture at 450°C.

and Pyzhev (*20*). Among the assumptions involved in this mechanism are:

1. The rate of adsorption of nitrogen on the surface of the catalyst is the rate-controlling step. From this it follows that the adsorbed nitrogen is in equilibrium with the hydrogen and ammonia in the gas phase.

2. The adsorption of nitrogen is described by the Temkin isotherm, which is based on a linear variation of activation energy of adsorption and heat of adsorption with the fraction of available surface covered.

3. The nitrogen adsorption phenomena are not affected by the presence of varying amounts of hydrogen and ammonia.

The above factors have been extensively discussed in the literature, and much experimental evidence exists in support of these ideas. As an example of such a discussion the recent work edited by Emmett may be cited (*5*).

The rate equation was originally proposed (*20*) with partial pressures used as a measure of concentration, but more recently the equation has been revised for use at high pressures by the introduction of fugacities and an additional correction term (*19*). This latter equation is

$$r = \left(k_1 f_{N_2}\left[\frac{f_{H_2}^{\,3}}{f_{NH_3}^{\,2}}\right]^{\alpha} - k_2\left[\frac{f_{NH_3}^{\,2}}{f_{H_2}^{\,3}}\right]^{1-\alpha}\right) \cdot \exp\frac{(\alpha\bar{V}_S - \bar{V}_a)P}{RT} \quad (7)$$

where k_1 and k_2 are related by

$$k_1 = k_2 K_e \quad (8)$$

Let us define

$$\psi = \exp\frac{(\alpha\bar{V}_S - \bar{V}_a)P}{RT} \quad (9)$$

and rearrange Equation (7) to give

$$r = k_2\left(\left[Ke\,\frac{f_{N_2} f_{H_2}^{\,3}}{f_{NH_3}^{\,2}} - 1\right] \cdot \left[\frac{f_{NH_3}^{\,2}}{f_{H_2}^{\,3}}\right]^{1-\alpha}\right)\psi \quad (10)$$

According to the theory on which Equation (10) is based, k_2 should be a function of temperature only, and ψ should be a function of temperature and pressure only. From experimental data the best values of $k_2\psi$ and α can be found. The quantity ψ can be calculated, although there is difficulty in estimating the values of $\bar{V}_S$ and $\bar{V}_a$. Temkin (*19*) suggests using the molar value of solid nitrogen, 27 cc./g. mole, for both $\bar{V}_S$ and $\bar{V}_a$.

The value of $k_2\psi$, or k_2, if the above values of $\bar{V}_a$ and $\bar{V}_S$ are used, as well as the value of α can be found from the data on reaction rate vs. composition at various constant pressures and temperature. It will be seen that α is fairly independent of pressure and temperature but that k_2 is not independent of pressure, as required by the ideas leading to Equation (*10*). The constants are con-

Table 1. Experimental Values of the Temkin Rate Constant

Temperature and initial composition	Pressure, atm.	ψ	$k_2 \times 10^{-4}$, cc. S.T.P. NH_3/hr. cc. atm.$^{-1/2}$
	100	0.978	1.82
	200	0.956	2.19
450°C.	400	0.913	1.10
$3H_2$:$1N_2$	600	0.874	0.830
	1000	0.798	0.396
	100	0.976	0.282
400°C.	400	0.906	0.110
$3H_2$:$1N_2$	1000	0.783	0.025
	100	0.978	1.41
450°C.	200	0.956	1.23
$1H_2$:$1N_2$	600	0.874	0.690
450°C.	100	0.978	1.78
$2H_2$:$1N_2$	200	0.956	1.58
	600	0.874	0.95

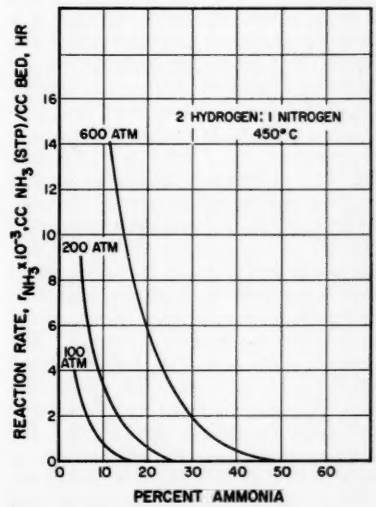

Fig. 8. Reaction rates for the 2:1 mixture at 450°C.

veniently evaluated if Equation (10) is put into the form

$$\log\left[\frac{r}{K_e\dfrac{f_{N_2}f_{H_2}^{3}}{f_{NH_3}^{2}}}\right] = \log k_2\psi + (1-\alpha)\log\left(\frac{f_{NH_3}^{2}}{f_{H_2}^{3}}\right) \qquad (11)$$

or

$$\log Y = \log k_2\psi + (1-\alpha)\log X \qquad (12)$$

The values of $k_2\psi$ and $(1-\alpha)$ can be found from a plot of log Y vs. log X, (Figures 9 to 12). However the choice of a method for the calculation of Y and X from the composition of the gas from the reactor presents a difficult problem.

Three methods for the calculations of the fugacities were considered: ideal solutions, Joffe's method (*10*), and the method of Redlich, *et al.* (*15*). The last method listed had to be abandoned as impractical when it was found impossible to fit the Redlich and Kwong (*16*) equation of state to data on pure ammonia with a reasonable precision. In order to test the other two methods values of the fugacity ratio at equilibrium were calculated at a series of pressures and compared to the experimental results obtained from the data of Larson and Dodge (*12*) and the equations

$$K_e = K_\nu K_z p^{-2} \qquad (13)$$

$$\Delta G^0 = -RT \ln K_e \qquad (14)$$

$$K_z = \frac{Z_{NH_3}^{2}}{Z_{N_2}Z_{H_2}^{3}} \qquad (15)$$

The results are shown in Figure 13. In all cases the generalized charts of Hougen and Watson (*9*) were used, and Kay's rule was used with Joffe's method. Although Method 4 is the best, Method 2 works suprisingly well, and since it is so much simpler to use, this method was chosen for succeeding calculations. In addition Figure 14 points out another reason for being content with the ideal-solution method. At a given pressure and temperature the ν ratio is a constant for ideal solutions. The value of this ratio is the experimental one obtained from Equation (13) and does not involve the use of the generalized charts. Now for a nonideal solution the changing of the composition at constant temperature and pressure results in a change in the ν ratio; it no longer equals K_ν. The extreme sensitiveness of Joffe's method to the way in which the generalized charts are used is illustrated. In view of this behavior it was decided that the ideal-solution method was about as reliable as that of Joffe. If it turned out that the kinetic data were accurate and faithfully represented by Equation (10), at least at constant temperature, pressure, and initial composition, it would be required that the ν ratio vary as given by the dotted curve in Figure 14. It would be very interesting to know the P-V-T relations of suitable mixtures in order to be able to calculate the actual values of the ν-ratio.

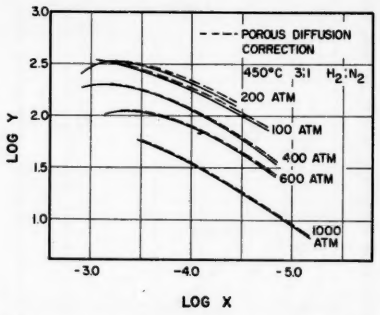

Fig. 9. Test of the Temkin and Pyshev equation for the 3:1 mixture at 450°C.

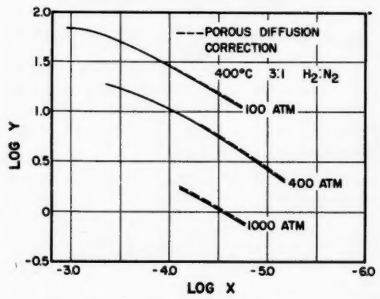

Fig. 10. Test of the Temkin and Pyshev equation for the 3:1 mixture at 400°C.

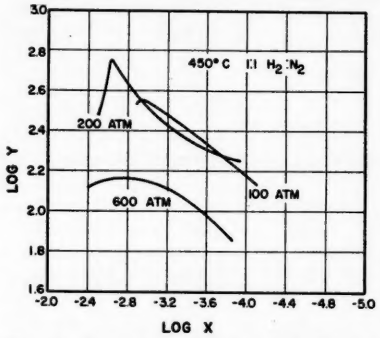

Fig. 11. Test of the Temkin and Pyshev equation for the 1:1 mixture at 450°C.

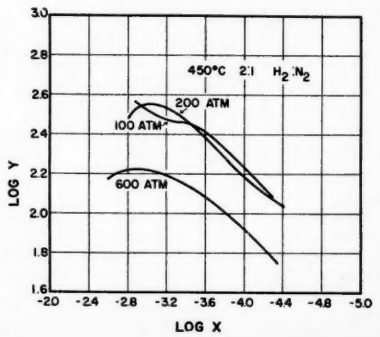

Fig. 12. Test of the Temkin and Pyshev equation for the 2:1 mixture at 450°C.

Figures 9 to 12 show that Equation (10) gives a fairly reasonable representation of the data at a given pressure, temperature, and initial composition. Most of these figures do not include a small correction due to diffusion within the catalyst pores to be discussed below. By the statement that the ψ correction is not included, it is emphasized that log Y rather than log Y/ψ is plotted vs. log X. Supposedly all the lines in Figure 13 should be bought into one if log (Y/ψ) were used, but actual use of the ψ term does not bring the lines much closer together; the variation in ψ is much too small.

The value of α was estimated from the slopes of the lines over their right-hand portions, where they approximate straight lines. Rather than obtain a separate α value for each curve a mean value of 0.5 is proposed for all curves. It is of interest to observe that this value of α, and in fact the whole Temkin-Pyzhev expression, can be obtained by the simplified treatment proposed by Weller (*22*) and by Boudart (*3a*). The straight line defined by the value of α is then considered to coincide with the experimental curve at a point about in the middle of the fairly straight portion of the curves. In this way the values of k_2 given in Table 1 were obtained.

From the values of k_2 given for 400° and 450°C. there can be calculated the following energies of activation:

Pressure	Energy of activation
100	36,000 cal./g. mole
400	44,000 cal./g. mole
1000	53,000 cal./g. mole

Since these values are based on only two temperatures, they are not very precise; indeed the value at 100 atm. is substantially lower than that found by Emmett and Kummer (*6*).

Diffusion Effects

The accuracy of the preceding treatment depends on the absence of diffusion effects of any kind. It will now be shown that under the experimental conditions of this investigation these effects were indeed small.

Diffusion into the Catalyst Pores

The methods of Bokhoven and van Raayen (*3*) will be followed, and the calculations will be based on the rate of transfer of ammonia from the interior of a spherical catalyst pellet to the surface. The rate of reaction will be expressed in terms of a pseudo first-order rate constant defined by the expression

$$\text{Reaction rate, g.mole } NH_3/\text{cc. catalyst sec.} = k'\rho_M(Z_e - Z)_{NH_3} \qquad (16)$$

In terms of the value of r reported in Figures 5 to 8

$$k' = \frac{r}{(22{,}400)(3600)} \cdot \frac{\rho_c}{\rho_B \rho_M (Z_e - Z)_{NH_3}} \quad (17)$$

$$k' = 2.29 \times 10^{-8} r/\rho_M \phi \quad (18)$$

where

$$\phi = (Z_e - Z)_{NH_3} \quad (19)$$

Now the rate of diffusion will be defined by

Diffusion rate, g.moles NH_3/sq. cm. sec. $= -D_{eff}\rho_M (dZ_{NH_3}/dr_c)$ (20)

If a mass balance is made over a spherical shell of thickness dr, there is obtained

$$\frac{d^2\phi}{dy^2} + \frac{2}{y}\frac{d\phi}{dy} = h^2\phi \quad (21)$$

where

$$r_c = yR \quad (22)$$

and

$$h^2 = \frac{k'R^2}{D_{eff}} \quad (23)$$

Integration of Equation (21) gives

$$\phi = \frac{\phi_s \sinh hy}{y \sinh h} \quad (24)$$

$$\phi_s = \phi \quad \text{at} \quad y = 1.0$$

If an effectiveness factor is defined as the ratio of the reaction rate per pellet to that which would be obtained if the diffusion from the interior were very fast, one gets

$$E = \frac{4\pi\rho_M k' R^3 \int_0^1 \phi y^2\, dy}{\frac{4}{3}\pi R^3 \rho_M k' \phi_s} \quad (25)$$

and

$$E = \frac{3}{h}\left[\coth h - \frac{1}{h}\right] \quad (26)$$

Values for k' were calculated from the data of Figures 9 to 12 by the use of Equation (18) with ϕ equal to ϕ_s. This result is of course very approximate, for the data do not actually follow Equation (18). Values for D_{eff} were calculated by the assumption, for the purpose of estimating the diffusivity, that ammonia was an ideal gas and by the use of the data of Bokhoven and van Raayen (*3*) for diffusion rates through porous catalyst pellets.

The effect of porous diffusion is shown graphically by the dashed lines of Figures 9 and 10. At 400°C. the lowest value of E is 0.90, and at 450°C. the lowest values of E is 0.88; both are for the lowest pressure, 100 atm. As is to be expected the value of E is smaller when the reaction rate is larger, that is away from equilibrium, at the right-hand extremities of the curves of Figures 9 and 10. There appears to be no way to tell from these data whether surface migration of the ammonia or other adsorbed fragments adds to the rate of transfer within the catalyst pellets at the highest pressures.

Diffusion to the Catalyst Surface

In order to evaluate the effect of diffusion between the bulk of the gas and the surface of the catalyst pellets the partial pressure drop for nitrogen necessary to give the observed reaction rate was calculated. The basic equation is

$$r = 2\rho_B (22{,}400) k_g a_m \Delta P_{N_2} \quad (27)$$

For these rough estimates ideal gases are assumed. The factor of two appears in Equation (27), since r refers to the rate of reaction of ammonia. The coefficient k_g was found from the j_D factors published by Gamson, Thodos, and Hougen (*7*). The Schmidt number used was 1.08, based on diffusion in the system hydrogen-nitrogen. After one uses the equation given by these authors for j_D and suitable values for the constants, Equation (27) becomes

$$\Delta P_{N_2} = 0.0190 r/S_0^{0.40} \quad (28)$$

Calculations with Equation (28) show that even at the lowest space velocities and conversions the value of ΔP_{N_2} is a small fraction of the total nitrogen partial pressure.

Longitudinal Diffusion

A material balance on the hydrogen entering and leaving a differential length of the reactor gives

$$r = -\tfrac{2}{3}(22{,}400)(3600)\frac{d(Z_{H_2}G_M)}{dl} + \tfrac{2}{3}(22{,}400)(3600) D_e \rho_M \frac{d^2 Z_{H_2}}{dl^2} \quad (29)$$

where

$$G_M = \frac{S_0 L}{(22{,}400)(3600)}\left(\frac{1}{1 + Z_{NH_3}}\right) \quad (30)$$

In the above equation S_0 is a constant corresponding to a certain feed rate. If the second term in Equation (29) is omitted, the first term becomes simply r as defined by Equation (2). The value of $d^2Z_{H_2}/dl^2$ and thus the second term of Equation (29) can be approximated from the rate data already obtained by neglecting the second term. If this term is only a small fraction of the first, that is of the value of r, it may be concluded that longitudinal diffusion is not important. If the second terms is an appreciable fraction of the first, the simple procedure for the calculation of $d^2Z_{H_2}/dl^2$ to be given below becomes invalid.

In the absence of mass transfer effects the reaction rate at any point in the reactor will be a function of Z only at a given pressure, temperature, space velocity, and initial composition. The de-

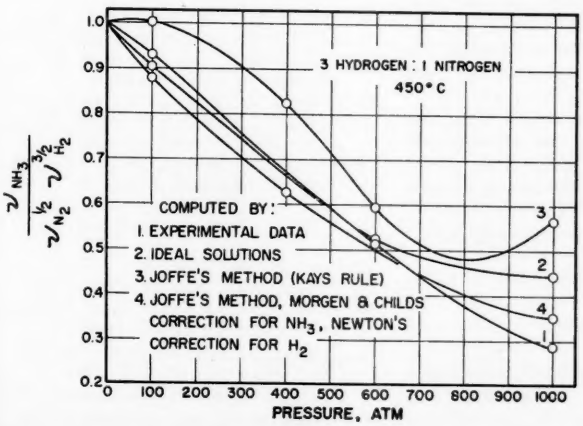

Fig. 13. Test of alternate methods of calculating fugacities at equilibrium.

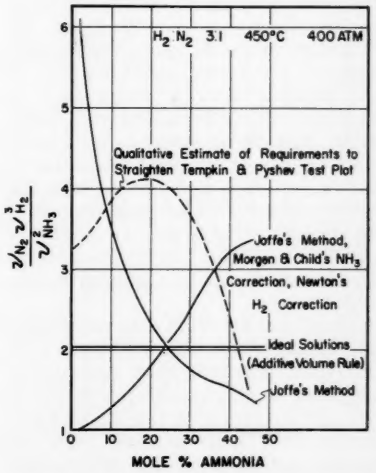

Fig. 14. Variation of fugacity-coefficient ratio with conversion.

gree of conversion will depend only on the time of contact, so that the composition at a point one tenth of the way through the reactor at an S_0 of 10,000 will correspond to the composition at the exit of the reactor at an S_0 of 100,000. In this way a curve is obtained of Z_{H_2} as a function of l, and thus $d\,Z_{H_2}/dl^2$ can be obtained. The value of D_e is difficult to estimate. The work of Deisler and Wilhelm (*4*) and of McHenry and Wilhelm (*13a*) indicate that D_e is two or three times the ordinary molecular diffusivity at much higher Reynolds numbers than those used in this work. In view of this uncertainty a value of D_e equal to three times the molecular diffusivity has been used here.

The longitudinal diffusion term in Equation (21) has been calculated at several positions in the bed and for several space velocities. Even at the lowest space velocity and at points very near the entrance to the bed longitudinal diffusion is not important.

CONCLUSIONS

As a result of the tests of the Temkin mechanism it can be stated that the method correlates data at any one temperature, pressure, and initial composition fairly well at degrees of conversion not too close to equilibrium. It may be remarked that most of the erratic behavior of the curves of log Y vs. log X, particularly noticeable in Figures 11 and 12, can probably be explained by the fact that, as equilibrium is approached, both the numerator and the denominator in the expression for Y [Equation (11)] are approaching zero. An error of only a few per cent in the reaction rate is multiplied as much as one hundred fold in the value of Y at conversions near equilibrium.

Although the effect of space velocity may be considered as fairly well accounted for by the Temkin mechanism, the effect of pressure is not predicted so well. In order to account for the separation of the curves in Figure 9 for instance, the partial molar volumes of the adsorbed nitrogen would need to be in the order of 200 to 500 cc./g. mole, rather that 20 to 50 cc./g. mole as is more probably the case. As a matter of fact the effect of ψ when one uses the latter values is so small that the curves for 100 and 200 atm. may be considered roughly in accord with the theory; similar remarks apply to Figures 11 and 12.

The available P-V-T- data on mixtures of hydrogen, nitrogen, and ammonia have been used recently to show qualitatively the effect on the reaction rates of using the correct fugacities instead of those predicted by ideal solutions (*2a*). Although the range of the P-V-T data does not permit a quantitative comparison with the data of the present work, the results of reference (*2a*) indicate that the curves of Figures 9 to 12 would not be straightened by the use of the correct, real-solution fugacities.

ACKNOWLEDGMENT

The authors express their appreciation to the Proctor and Gamble Company and to the Purdue University Engineering Experiment Station for financial support of this research.

NOTATION

D_e = longitudinal eddy diffusivity, sq. cm./sec.

D_{eff} = effective diffusivity through porous catalyst, sq. cm./sec.

E = effectiveness factor

F = feed rate, cc. at standard temperature and pressure/hr.

G_M = gas mass velocity at a point in the reactor, g. mole/sec. sq. cm.

L = length of reactor, 5.0 cm.

K_e = equilibrium constant, $f_{NH_3}{}^2/f_{H_2}{}^3 f_{N_2}$

K_Z = ratio of mole fraction at equilibrium $Z_{NH_3}{}^2/Z_{H_2}{}^3 Z_{N_2}$

K_ν = ratio of fugacity coefficients at equilibrium, $\nu_{NH_3}{}^2/\nu_{N_2}\nu_{H_2}{}^3$

R = radius of spherical catalyst pellet. cm.

S_0 = space velocity, cc. S.T.P. feed/(hr.)(cc. bed)

V = volume of bed, cc.

X = $f_{NH_3}{}^2/f_{H_2}{}^3$

$$Y = r \Big/ \left[K_e \frac{f_{N_2} f_{H_2}{}^3}{f_{NH_3}{}^2} - 1 \right]$$

Z_i = mole fraction

a_m = surface of catalyst per unit mass, 8.3 sq. cm./g.

f_i = fugacity, atm.

$$h = \sqrt{\frac{k'R^2}{D_{eff}}}$$

j_D = Chilton and Colburn mass transfer factor

k_1 = forward reaction rate constant, cc. S.T.P. NH_3/hr. cc. bed $(atm.)^{3/2}$

k_2 = reverse reaction rate constant, cc. S.T.P. NH_3/hr. cc. bed $(atm.)^{-1/2}$

k' = pseudo first-order reaction rate constant, cc. gas mixture/sec. cc. catalyst

k_g = mass transfer coefficient, g. mole N_2/hr. sq. cm. atm.

l = distance from reactor inlet, cm.

p = pressure, atm.

r = reaction rate, cc. S.T.P. NH_3/hr. cc. bed

r_c = distance from center of catalyst pellet, cm.

$\bar{V}_a$ = partial molal volume of nitrogen activated complex adsorbed, cc./g. mole

$\bar{V}_s$ = partial molal volume of nitrogen adsorbed, cc./g. mole

x = degree of conversion, cc. S.T.P. NH_3 formed/cc. S.T.P. feed

y = r_c/R

Greek Letters

α = constant, 0.5

ϵ = void fraction bed, 0.40

ν_i = fugacity coefficient, f_i/p

ϕ = $(Z_e - Z)_{\vec{NH_3}}$

ψ = $\exp(\alpha\bar{V}_s - \bar{V}_a)p/RT$

ρ_M = molar density of gas, g. mole/cc.

ρ_B = density of bed, 2.7 g. catalyst/cc. bed

ρ_c = density of catalyst, 5.0 g. catalyst/cc. catalyst

σ = space-time yield, cc. S.T.P. NH_3/hr. cc. bed

LITERATURE CITED

1. Adams, R. M., and E. W. Comings, *Chem. Eng. Progr.*, **49**, 359 (1953).
2. Almquist, J. A., and E. D. Crittenden, *Ind. Eng. Chem.*, **18**, 1307 (1926).

2a. Bennett, C. O., *J. Chim. Phys.*, **55**, 570 (1958).

3. Bokhoven, C., and W. van Raayen, *J. Phys. Chem.*, **58**, 471 (1954).

3a. Boudart, Michel, *A.I.Ch.E. Journal*, **2**, 62 (1956).

4. Deisler, P. F., and R. H. Wilhelm, *Ind. Eng. Chem.*, **45**, 1219 (1953).
5. Emmett, P. H., "Catalysis," Vol. III, Chap. 6 and 7, Reinhold, New York (1955).
6. ———, and J. T. Kummer, *Ind. Eng. Chem.*, **35**, 677 (1943).
7. Gamson, B. W., George Thodos, and O. A. Hougen, *Trans. Am. Inst. Chem. Engrs.*, **39**, 1 (1943).
8. Hoogschagen, Jan, *Ind. Eng. Chem.*, **47**, 906 (1955).
9. Hougen, O. A., and K. M. Watson, "Chemical Process Principles," John Wiley, New York (1947).
10. Joffe, Joseph, *Ind. Eng. Chem.*, **40**, 1738 (1948).
11. Larson, A. T., *J. Am. Chem. Soc.*, **46**, 367 (1924).
12. Larson, A. T., and R. L. Dodge, *J. Am. Chem. Soc.*, **45**, 2918 (1923).
13. Larson, A. T., and R. S. Tour, *Chem. & Met. Eng.*, **26**, 647 (1922).

13a. McHenry, K. W. Jr., and R. H. Wilhelm, *A.I.Ch.E. Journal*, **3**, 83 (1957).

14. Nielsen, A., "An Investigation on Promoted Iron Catalysts for the Synthesis of Ammonia," Jul. Gjellerups Forlag, Copenhagen, Denmark (1950).
15. Redlich, O., A. T. Kister, and C. E. Turnquist, *Chem. Eng. Progr. Symposium Ser. No. 2*, **48**, 49 (1952).
16. Redlich, O., and J. N. S. Kwong, *Chem. Rev.*, **44**, 233 (1949).
17. Siderov, I. P., and V. D. Livshits, *J. Phys. Chem. (U.S.S.R.)*, **21**, 1171 (1947).
18. *Ibid.*, **26**, 538 (1952).
19. Temkin, M. I., *ibid.*, **24**, 1312 (1950).
20. ———, and V. Pyzhev, *Acta Physicochim. (U.S.S.R.)*, **12**, 327 (1940).
21. Uchida, A., and M. Kuraishi, *Bull. Chem. Soc. Japan*, **28**, 106 (1955).
22. Weller, Sol, *A.I.Ch.E. Journal*, **2**, 59 (1956).

Manuscript received November 14, 1958; revision received April 3, 1959; paper accepted April 7, 1959.

Heterogeneous Phase Equilibria of the Hydrogen Sulfide–Carbon Dioxide System

D. P. SOBOCINSKI and FRED KURATA

University of Kansas, Lawrence, Kansas

An experimental study on the system hydrogen sulfide-carbon dioxide was performed from the critical region to the solid-liquid-vapor region. For seven mixtures individual phase diagrams were determined by the establishment of dew, volume percentage liquid, bubble, critical, and triple points. A splendid study of this system had been reported earlier by Bierlein and Kay (*1*) for temperatures above 32°F. However from a temperature point of view this earlier work represents about one half of the phase diagram from the critical locus to the locus of triple points. Hence in this study particular attention was devoted to the lower temperature regions.

Equilibrium constants were determined from 100 to 1,200 lb./sq. in. abs. Vapor and liquid equilibrium compositions from this investigation were compared with those obtained by Bierlein and Kay (*1*) at 20, 40, 60, and 80 atm.

Solid-liquid-vapor loci were found to meet at a minimum temperature, lower than either of the individual pure component triple points, due to the formation of a eutectic mixture consisting of 12.5 mole % carbon dioxide. Vapor and liquid compositions in equilibrium with solid were established along the vapor-liquid-solid carbon dioxide and vapor-liquid-solid hydrogen sulfide loci.

Hydrogen sulfide and carbon dioxide are two acidic components frequently found with the hydrocarbons of petroleum reservoirs.

After crude oil is refined, these constituents, the hydrogen sulfide and carbon dioxide, tend to concentrate in the light fractions, and physical separation schemes require knowledge of the phase behavior of such systems.

Moreover the behavior of hydrogen sulfide and carbon dioxide is becoming increasingly important in connection with the removal of these components from natural gases. Various concentrations of these gases can be effectively removed by different scrubbing and sorption schemes. However for the large-scale removal of these impurities considerable interest has centered on low temperature processes, where these components can be removed by distillation, as immiscible liquids, or as solids.

The phase behavior, vapor-liquid equilibrium compositions, triple-point loci, and triple point liquid compositions were reported for the methane–carbon dioxide system by Donnelly and Katz (*2*). Their data extended from the critical point of carbon dioxide to −110°F; triple-point studies for this system were extended to −260°F. by Kohn and Kurata (*3*).

Reamer, Sage, and Lacey (*4*) have studied the phase and volumetric behavior of the methane-hydrogen sulfide system from 40° to 340°F. and at pressures from 200 to 10,000 lb./sq. in. abs. Kohn and Kurata (*5*) verified much of the work of Reamer *et al.* and extended the study of this system to −160°F., encountering a locus of "type *K*—singular points" (*6*), where one of two phases is in critical identity with a third phase. These phases were shown to consist of a methane rich vapor phase, a methane rich liquid phase, and a hydrogen sulfide rich liquid phase.

The hydrogen sulfide-carbon dioxide binary has been studied by Bierlein and Kay (*1*) from 0°C. to the critical temperature of hydrogen sulfide. Earlier Steckel (*7*) had reported isothermal dew and bubble-point pressures for this system at 0°, −26.8°, and −52°C. His results at 0°C., though qualitatively similar, differed somewhat quantitatively from those of Bierlein and Kay.

The only known published work concerning the methane–carbon dioxide-hydrogen sulfide ternary is that of Robinson and Bailey (*18*). These investigators reported equilibrium constants for each component as a function of pressure and the ratio of other components at 100°F. and 600, 1,200 and 1,800 lb./sq. in. abs.

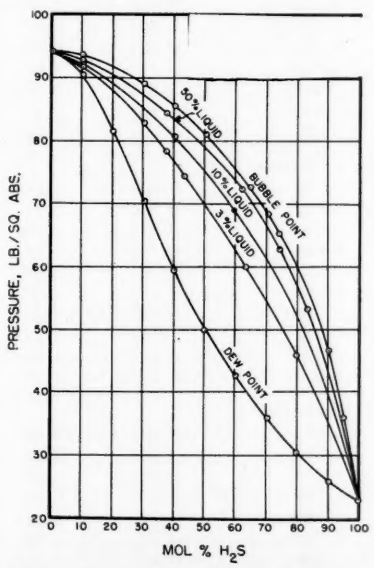

Fig. 1. Pressure-composition diagram at −60°F. for hydrogen sulfide–carbon dioxide system.

APPARATUS

Equipment for this study was built and reported by Kohn and Kurata (*8*) and was a modification of earlier equipment used by Davis (*9*).

Basically this equipment consists of two major units. One unit serves as a reservoir which maintains the gas to be studied at a constant temperature above its cricondentherm temperature.

A second unit houses a calibrated glass equilibrium cell, heating unit, liquid nitrogen cooling coil and expansion section, a means for agitation, and a resistance thermometer. All these are immersed in a bath of appropriate fluid maintained at constant temperature or varied by proper use of the cooling system or heating element.

When the temperature and pressure conditions of the gas mixture confined in the equilibrium cell are controlled, the various phase changes may be visually observed. Where necessary a special sampling device permits various phases in the cell to be obtained for analytical purposes. Volumetric data can also be obtained concurrently by metering the gas to be studied into the equilibrium cell.

PROCEDURE

The experimental method involved obtaining dew- and bubble-point pressures

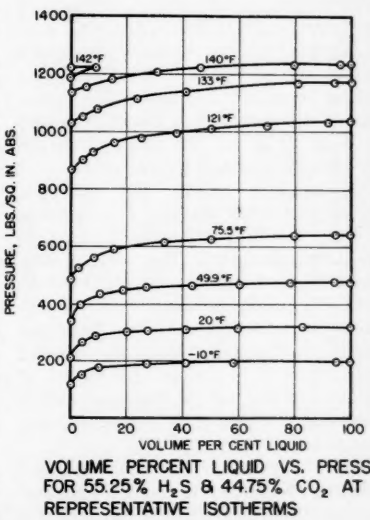

VOLUME PERCENT LIQUID VS. PRESSURE FOR 55.25% H_2S & 44.75% CO_2 AT REPRESENTATIVE ISOTHERMS

Fig. 2. Volume percentage liquid vs. pressure for 55.25% hydrogen sulfide and 44.75% carbon dioxide at representative isotherms.

at various isotherms for a number of gas mixtures. Volume percentage liquid at intermediate pressures for each mixture at each isotherm was also obtained in proceeding from dew to bubble points by reading the calibrations on the equilibrium cell.

The procedure used to determine the critical values for the mixtures involved taking finite decrements in temperature (starting above the cricondentherm) along with discrete increases in pressure to obtain the upper dew points. The point where the locus of dew points became the locus of bubble points (or vice versa depending upon critical location) was the critical point.

The locus of the solid-liquid-vapor boundary and crystal points were obtained by noticing where the formation of solids occurred at the terminal ends of the dew and bubble points.

With binary systems no samples need to be taken in the divariant vapor-liquid region to establish equilibrium compositions. This generally is not true for the vapor-liquid-solid region. However for a binary on a triple-point locus the system remains univariant. Thus by maintaining constant temperature one can sample any phase without upsetting equilibrium; however sampling must be accomplished slowly to prevent pressure or temperature disturbances in the system.

MATERIALS

Hydrogen Sulfide

Hydrogen sulfide used in this investigation was stated to be 99.9 mole % pure. However the change in pressure from the dew to bubble point at 45°F. was found to be in excess of 40 lb./sq. in. The pressure slope (pressure vs. volume percentage liquid) indicated that some heavy ends were present but that light ends were predominant. A number of packed adsorption schemes were devised with activated alumina, activated charcoals, and molecular sieves and were used at different temperatures to remove many of the heavy ends. It was hoped that slow weathering of the cylinder hydrogen sulfide would remove the light ends (felt to be mainly hydrogen). Re-evaluation of the conditioned gas still showed a 10 to 12 lb./sq. in. pressure change between the dew and bubble points.

To improve purity the hydrogen sulfide was batch distilled 6 to 8 times at from −50° to 0°F. The upper 5 to 10% was discarded. The middle 80% was condensed with dry ice and bottoms were discarded. A dew- and bubble-point pressure check of the hydrogen sulfide so purified frequently showed less than a 2 lb./sq. in. differential at 45°F., with 90% of the hydrogen sulfide condensing within a 1 lb./sq. in. differential.

When the batch distilled hydrogen sulfide was lowered to dry-ice temperature and below, and 1% of the system was withdrawn as vapor and discarded, a recheck of the dew- and bubble-point differential at 45°F. showed that it was

Table 1. Equilibrium Vaporization Constants for the Hydrogen Sulfide—Carbon Dioxide System

Temperature, °F.	Mole fraction H_2S, vapor phase	Mole fraction H_2S, liquid phase	Equilibrium constants, H_2S	Equilibrium constants, CO_2
	Pressure = 100 lb./sq. in. abs.			
0	0.840	0.984	0.854	10.00
−10	0.700	0.956	0.732	6.82
−20	0.572	0.915	0.625	5.04
−30	0.450	0.850	0.529	3.67
−40	0.329	0.714	0.461	2.35
−50	0.204	0.501	0.407	1.60
−55	0.102	0.282	0.362	1.25
	Pressure = 200 lb./sq. in. abs.			
45	0.922	0.983	0.938	4.59
40	0.855	0.967	0.884	4.39
30	0.723	0.931	0.777	4.01
20	0.590	0.887	0.665	3.63
10	0.475	0.822	0.578	2.95
0	0.369	0.720	0.513	2.25
−10	0.259	0.547	0.473	1.64
−20	0.120	0.235	0.511	1.15
−22	0.075	0.141	0.531	1.08
	Pressure = 300 lb./sq. in. abs.			
70	0.894	0.978	0.914	4.82
60	0.770	0.948	0.812	4.42
50	0.651	0.907	0.718	3.75
40	0.540	0.850	0.635	3.07
30	0.436	0.752	0.580	2.27
20	0.340	0.630	0.540	1.78
10	0.241	0.449	0.537	1.38
5	0.175	0.301	0.581	1.18
2	0.119	0.195	0.610	1.09
	Pressure = 400 lb./sq. in. abs.			
90	0.871	0.971	0.897	4.45
80	0.750	0.933	0.804	3.73
70	0.637	0.884	0.721	3.13
60	0.540	0.815	0.663	2.49
50	0.449	0.725	0.619	2.00
40	0.355	0.605	0.587	1.63
30	0.251	0.430	0.584	1.31
25	0.185	0.317	0.583	1.19
20	0.095	0.164	0.579	1.08
	Pressure = 500 lb./sq. in. abs.			
110	0.899	0.975	0.922	4.04
100	0.784	0.935	0.839	3.32
90	0.680	0.885	0.768	2.78
80	0.583	0.826	0.706	2.40
70	0.489	0.750	0.652	2.04
60	0.395	0.640	0.617	1.68
50	0.303	0.497	0.610	1.39
40	0.185	0.290	0.638	1.15
35	0.100	0.154	0.649	1.06
	Pressure = 600 lb./sq. in. abs.			
130	0.957	0.989	0.968	3.91
120	0.835	0.947	0.881	3.11
110	0.731	0.901	0.811	2.72
100	0.638	0.848	0.752	2.38
90	0.548	0.780	0.703	2.05
80	0.460	0.700	0.657	1.80
70	0.369	0.577	0.640	1.49
60	0.272	0.419	0.649	1.25
50	0.140	0.209	0.670	1.09
47	0.088	0.130	0.677	1.05
	Pressure = 800 lb./sq. in. abs.			
150	0.891	0.959	0.929	2.66
140	0.790	0.914	0.864	2.44
130	0.695	0.860	0.808	2.17
120	0.604	0.800	0.755	1.98
110	0.522	0.720	0.725	1.71
100	0.440	0.626	0.703	1.50
90	0.352	0.505	0.697	1.31
80	0.245	0.356	0.688	1.17
70	0.112	0.150	0.747	1.04
68	0.075	0.100	0.750	1.03

TABLE 1. (Continued)

Temperature, °F.	Mole fraction H_2S, vapor phase	Mole fraction H_2S, liquid phase	Equilibrium constants, H_2S	Equilibrium constants, CO_2
	Pressure = 1,000 lb./sq. in. abs.			
175	0.937	0.966	0.970	1.85
170	0.894	0.941	0.950	1.80
160	0.805	0.891	0.903	1.79
150	0.715	0.840	0.851	1.78
140	0.630	0.781	0.807	1.70
130	0.540	0.701	0.770	1.54
120	0.451	0.599	0.753	1.37
110	0.364	0.487	0.747	1.24
100	0.270	0.360	0.750	1.14
90	0.155	0.195	0.795	1.05
85	0.072	0.090	0.800	1.02
	Pressure = 1,200 lb./sq. in. abs.			
195	0.939	0.962	0.976	1.61
190	0.901	0.938	0.961	1.60
180	0.830	0.888	0.935	1.52
170	0.760	0.835	0.910	1.45
160	0.684	0.774	0.884	1.40
150	0.610	0.696	0.876	1.28
140	0.545	0.595	0.916	1.12
135	0.515	0.535	0.963	1.04
132.2	0.500	0.500	1.000	1.000

less than 1 lb./sq. in., with 90% condensing within ½ lb./sq. in. Calculations based on the worst of probable impurities, (methyl mercaptan, methylene chloride, and carbon disulfide) indicated that the hydrogen sulfide was at least 99.94 mole % pure. Material of the above purity was used in this study.

Carbon Dioxide

When carbon dioxide was passed through silica gel, a 2 to 2½ lb./sq. in. differential existed between dew and bubble points at 66°F., with 90% condensing within 1 lb./sq. in. Experimental vapor pressures agreed well with those reported in the literature (*10*). This carbon dioxide was estimated to have a minimum purity of 99.5 mole %, a probable purity of 99.9 mole %.

TRIPLE POINTS OF THE PURE CONSTITUENTS

Hydrogen Sulfide

The triple point of the hydrogen sulfide used in this work was consistently found to be −120.8° ± 0.1°F. This temperature does not agree with the triple-point temperature as commonly reported in the various data sources. The triple point for hydrogen sulfide appears to be based, among others, on the work of Maass and McIntosh (*11*) and Cardoso and Arni (*12*) whose triple-point temperatures appear to have been obtained incidentally in connection with their determinations of the vapor pressure of hydrogen sulfide. Although earlier workers found even lower values, the accepted value is reported to be −117.2°F. The freezing point of hydrogen sulfide under atmospheric pressure has been determined more recently by several investigators and is reported as

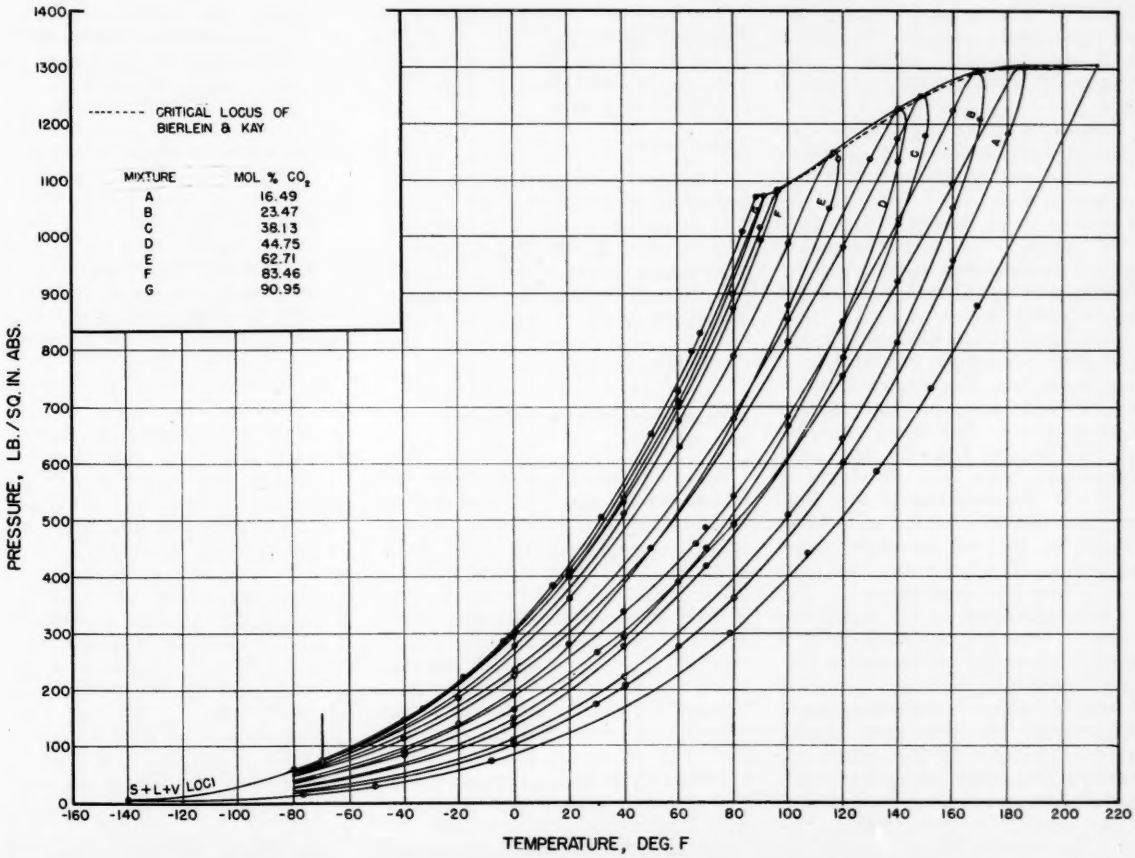

Fig. 3. Pressure-temperature diagram for the hydrogen sulfide-carbon dioxide system.

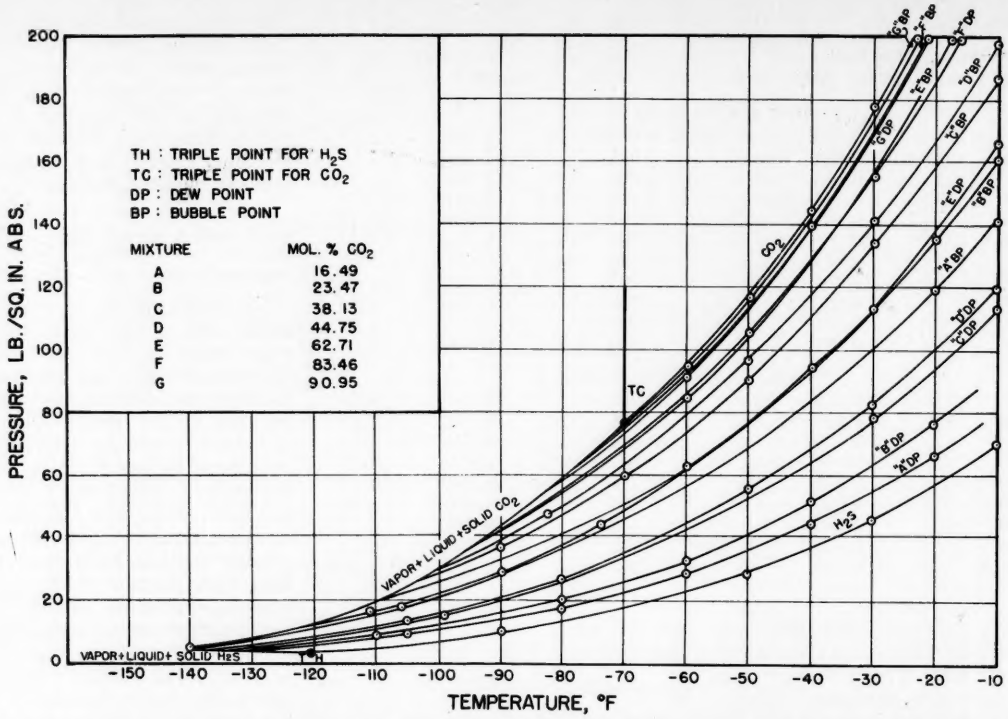

Fig. 4. Low temperature-pressure diagram for the hydrogen sulfide–carbon dioxide system describing $S + L + V$ loci.

−121.9°F. The freezing point of the hydrogen sulfide used by he authors under local barometric pressure (about 735 mm Hg) was found to be −121.7°± 0.1°F.

Regardless of the purification upon the hydrogen sulfide the literature triple-point temperature could not be confirmed. Even by differentially removing as vapor 80% of the hydrogen sulfide confined in an equilibrium cell as liquid at incipient freezing, no perceptible change could be effected in the value for the triple point.

The triple point was redetermined with hydrogen sulfide generated in a Kipp apparatus. This hydrogen sulfide was purified in a manner similar to that reported above, that is by repeated batch distillations. Again the triple-point temperature value was found to be −120.8°F. Concentration of the Kipp generated hydrogen sulfide at incipient freezing to 20% of the initial liquid made no significant change in the value for the triple-point temperature.

The temperature in the triple-point determinations was measured with a platinum resistance thermometer calibrated against a National Bureau of Standards calibrated platinum resistance thermometer. The thermometer–Mueller bridge circuit used by the authors was compared to another independently calibrated platinum resistance thermometer-bridge circuit. Deviation between the two thermometer-bridge circuits at −120°F. was approximately 0.2°F.

The measured triple-point pressure of hydrogen sulfide was found to be 3.5 lb./sq. in. abs. ± 0.2 lb./sq. in. The value in the *International Critical Tables* is 3.33 lb./sq. in. abs.

Carbon Dioxide

Equipment used in hydrogen sulfide triple-point determinations was similarly used for carbon dioxide. The triple point of the carbon dioxide used in the work was found to exist at −69.9°F. ± 0.05°F. and 76.9 lb./sq. in. abs. Triple-point values commonly reported for carbon dioxide (*10*) are −69.9°F. and 5.2 atm. (76.5 lb./sq. in. abs.).

EXPERIMENTAL COMPOSITIONS AND ANALYSIS

Seven mixtures of hydrogen sulfide and carbon dioxide that were prepared for study contained the following amounts of carbon dioxide: 16.49, 23.47, 38.13, 44.75, 62.71, 83.46, and 90.95 mole %. These mixtures were prepared by condensing with dry ice hydrogen sulfide which was admitted under its own vapor pressure into an evacuated stainless steel cylinder in the reservoir unit. Subsequently the hydrogen sulfide was diluted with carbon dioxide. Initial and final weights of the hydrogen sulfide cylinder plus the known volumetric addition of carbon dioxide allowed approximate compositions to be calculated.

Gas analyses were made with density determinations obtained by direct weighings. This method required accurate compressibility factors for the pure components at atmospheric pressure and room temperatures. Low-pressure compressibility factors, determined under identical conditions for the purified hydrogen sulfide, were found to be greater than those reported by Reamer, Sage, and Lacey (*13*) by slightly more than 0.1% and had an average deviation of 0.055%. Unlike those interpolated from West (*14*) atmospheric pressure compressibility factors derivable from the work of Moles (*15*) agreed moderately well with those of Reamer, Sage, and Lacey (*13*).

Atmospheric pressure compressibility factors for carbon dioxide determined for analytical purposes in this work agreed to about 0.1% with those values reported by Bottomley *et al.* (*16*). These had an average deviation of 0.061%.

Since no correction was made for gas adsorption within the density bulbs, and since the analytical procedure may have possessed intrinsically a 0.1% deviation in the absolute values for compressibility factors (or molecular weights), the constants for the pure components, as determined in this work, were used in analytical calculations. In this way possible inaccuracies were cancelled in the relative molecular weight determinations. The mean average deviation of the samples for all mixtures analyzed in this manner was 0.14%.

Spot checks indicated a linear relationship for compressibility factors of

mixtures. Hence a trial and error method with interpolation determined compressibility factors for mixtures.

RESULTS

Most of the data for a mixture was obtained in the form of volume percentage liquid vs. pressure, with parameters of temperature. In addition to describing the system more extensively this method sometimes provided a further verification on dew- and bubble-point pressures by extrapolation of the volume percentage data to 0 and 100% liquid conditions. In this system, particularly at lower temperatures, there was a large pressure differential for a mixture at its dew point and that of the mixture containing only several percent liquid. Figure 1 presents a typical isotherm for the hydrogen sulfide–carbon dioxide system at −60°F., where generally about 50% of the pressure change between dew and bubble points occurs with less than 3% liquid in the system. With increasing temperatures isotherms show a lower slope in volume percentage liquid-pressure plots. Complete volume percentage-pressure data for the mixtures in this study can be found in the work of Sobocinski (*17*). Typical volume percentage liquid vs. pressure data at several isotherms are presented in Figure 2 for a 55.25% hydrogen sulfide and 44.75% carbon dioxide mixture.

Pressure-Temperature Diagram

A generalized pressure-temperature plot for the hydrogen sulfide-carbon dioxide system appears as Figure 3. Dew- and bubble-point pressures for each of the seven mixtures are presented along with vapor-pressure curves for hydrogen sulfide and carbon dioxide. This plot is similar to that presented by Bierlein and Kay (*1*) but represents the results of a single study on the system in question from the critical locus to the solid-liquid-vapor region. The dashed line on Figure 3 represents the critical locus as found by Bierlein and Kay.

Equilibrium Compositions

Large scale pressure-temperature diagrams were cross plotted to furnish isobaric compositions for the system as a function of temperature. Such isobars were prepared for 100, 200, 300, 400, 500, 600, 800, 1,000, and 1,200 lb./sq. in. abs. In Table 1 equilibrium vaporization constants determined from these graphs are presented along with the vapor and liquid equilibrium compositions for each of the isobars. It is difficult to assign some degree of error to the compositions obtained in this manner. However it is felt that the data presented are accurate to the second decimal place. Possibly greater error exists with the higher pressure data and with the data for carbon dioxide rich mixtures. A comparison of equilibrium compositions obtained from this study with those of Bierlein and Kay (*1*) was made at 20, 40, 60, and 80 atm. Table 2 shows an average composition deviation of 3.2% for vapor and 2.2% for liquid.*

Solid Liquid-Vapor Loci

Figures 4, 5, 6, and 7 furnish information concerning the low-temperature regions of the system and describe behavior along solid-liquid-vapor loci.

Figure 4 is an extension of Figure 3 to low pressures and temperatures. Bubble-point and dew-point curves for each of the mixtures are shown to meet the solid region at triple points containing vapor, liquid, and either solid carbon dioxide or solid hydrogen sulfide.

The two triple-point loci found extend from the triple points of the pure components and meet at the eutectic temperature of −140.1°F. and 5 lb./sq. in. abs. This pressure and all pressures on the vapor-liquid-solid carbon dioxide representation are considered accurate to 1 lb./sq. in. Binary triple points with solid hydrogen sulfide are considered accurate to less than 1 lb./sq. in.

Compositions of the liquid and vapor in equilibrium with solid along the triple-point loci are presented on Figure 5 as a function of temperature. Liquid and vapor compositions become identical at the triple points for the pure components but pass through a maximum composition deviation at the eutectic temperature.

Thiel and Schulte (*19*) obtained vapor and liquid compositions for hydrogen sulfide and carbon dioxide in equilibrium with solid carbon dioxide at 14.5 lb./sq. in. abs. and −115.8°F. Their vapor composition was found to be 24.7% hydrogen sulfide and 75.3% carbon dioxide; liquid composition was found to be 74.6% hydrogen sulfide and 25.4% carbon dioxide. Composition results from this study at similar conditions indicated a vapor composition of 26.5% hydrogen sulfide and 73.5% carbon dioxide, and the liquid 78.0% hydrogen sulfide and 22.0% carbon dioxide.

Two methods were used to obtain the compositions along the three-phase loci. One method involved obtaining liquid and vapor samples at various known points along the curve at superatmospheric pressures. These were subsequently analyzed by gas-density measurements. Also for many of the seven mixtures, temperatures and pressures at which dew and bubble points first encountered solid were measured. The observed point of simultaneous incipient liquid and solid formation provided the composition of the vapor at this temperature-pressure point. This composition was the known mixture composition. Similarly the liquid in equilibrium with solid and vapor had a composition identical with that of the known mixture when, at its bubble point, solid was first encountered.

Not only were the previously mentioned mixtures used to determine triple-point compositions but several carbon dioxide lean mixtures were prepared to describe the composition, particularly of the liquid, along vapor, liquid, and solid (hydrogen sulfide or carbon dioxide) points.

The composition curves presented on Figure 5 represent the best plot for the differently obtained composition points. The liquid curve is in worst deviation from determined points by about 1.0 mole % composition. A composition deviation of 5 to 10 mole % might easily exist for the vapor composition plot and represents the most unrealiable portion of this work. The dashed portion of the vapor-composition plot estimates compositions where no dependable determinations were obtained.

On Figure 6 are plotted low-temperature isotherms for the hydrogen sulfide-carbon dioxide system as functions of pressure and composition. As indicated, dashed lines represent vapor and liquid compositions along triple-point loci. The

*Tabular material has been deposited as document No. 6054 with the American Documentation Institute, Photoduplication Service, Library of Congress, Washington 25, D. C., and may be obtained for $1.25 for photoprints or 35-mm. microfilm.

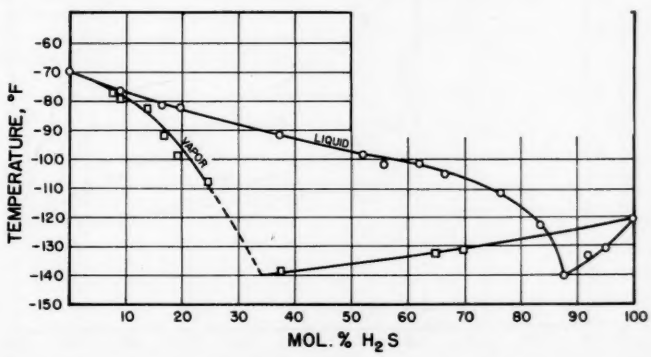

Fig. 5. Vapor and liquid composition along $V + L^+$ hydrogen sulfide solid and $V + L^+$ carbon dioxide solid loci for the hydrogen sulfide–carbon dioxide system.

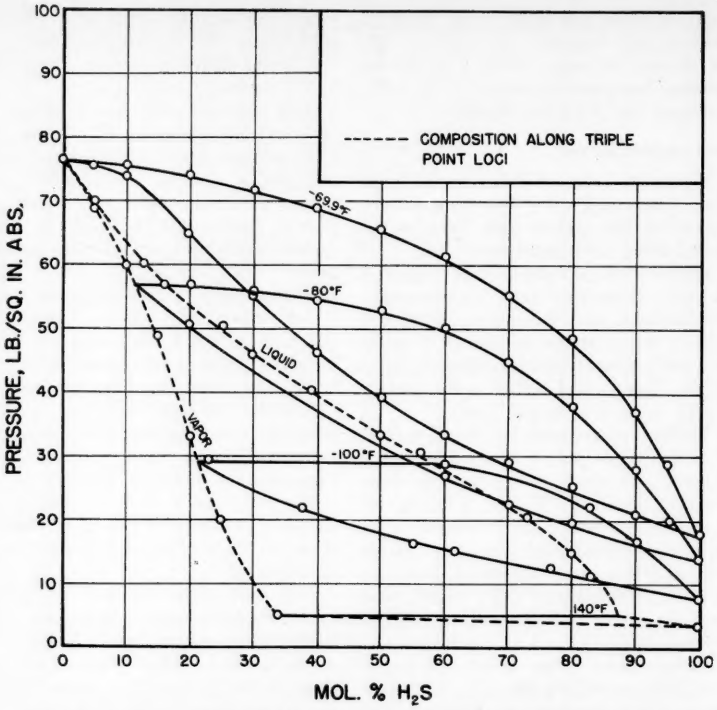

Fig. 6. Pressure–composition diagram for isotherms along the triple-point loci ($S + L + V$) for the system hydrogen sulfide–carbon dioxide.

line representing the −140.1°F. isotherm corresponds to the eutectic temperature.

Figure 7 is an extension of Figure 6 to an enlarged low-pressure scale. Both graphs were obtained by cross plotting information contained on Figures 4 and 5.

Errors

Subatmospheric pressures and some pressures to 2 atm. were measured with a mercury manometer. All other pressures were read on a calibrated Heise bourdon tube gauge. Dew-point pressures are estimated to be accurate to 1 lb./sq. in. at pressures below 500 lb./sq. in. and to 2 lb./sq. in. at pressures above 500 lb./sq. in. All bubble-point pressures are considered to be accurate to within less than 1 lb./sq. in.

Critical points are estimated as accurate to 1°F. and 5 lb./sq. in. for mixtures containing 60% and higher mole % hydrogen sulfide. Critical points for considered to be accurate to within 0.5°F. and 2 lb./sq. in.

All temperature measurements above −100°F. are considered to be accurate to 0.1°F.; below −100°F. to 0.2°F.

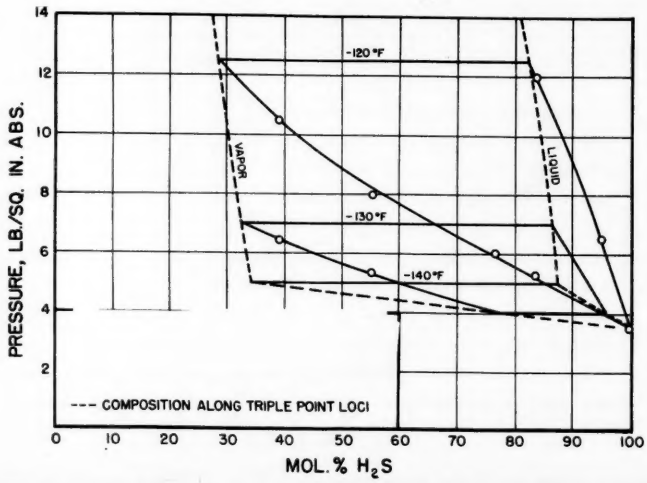

Fig. 7. Pressure-composition diagram for isotherms near eutectic temperature for the system hydrogen sulfide–carbon dioxide.

DISCUSSION

For the most part the phase diagram for the hydrogen sulfide–carbon dioxide system exhibits no particularly unusual behavior. The critical locus exhibits neither a maximum nor a minimum but does approach the pure component critical points with a slope of almost zero. The tendency toward azeotropism at the carbon dioxide rich end is clearly suggested for any isotherm on Figure 3 by the flat profile of the bubble and dew points for mixtures containing 90.95 and 83.46 mole % carbon dioxide. This tendency increases with decreasing temperature (−69.9°F. isotherm on Figure 6), but as Steckel (7) had found to −52°C. the incipient minimum boiling mixture never quite forms, even below the triple point for carbon dioxide.

Two vapor-liquid-solid loci were specially interesting. Vapor, liquid and solid hydrogen sulfide and vapor, liquid and solid carbon dioxide ruled surfaces meet at −140.1°F. and 5 lb./sq. in. abs. At these conditions two other ruled surfaces representing S-S-L and S-S-V equilibria meet, thus establishing the quadruple point. Joint analyses of Figures 4 to 7 describe the behavior of mixtures in this region.

As an example it is assumed that a mixture containing 10 mole % carbon dioxide and 90 mole % hydrogen sulfide is maintained at its dew point by decreasing the pressure as the temperature is lowered. Reference to Figure 5 shows that this mixture will first encounter hydrogen sulfide solid on the vapor-liquid-solid hydrogen sulfide locus at −124°F. If the pressure of the system is now raised, solid hydrogen sulfide in equilibrium with liquid and vapor will be found to extend as low as −137.5°F. The pressures corresponding to these temperatures can be read from Figure 4 but can be found more accurately by referring to either Figure 6 or 7. From Figure 7 the range of triple-point pressures for the 90 mole % hydrogen sulfide mixture extends from 3.8 to 4.6 lb./sq. in abs. Figure 7 also furnishes corresponding dew- and bubble-point pressures for the mixture at −130 and −120°F.

As another example a system containing 60% hydrogen sulfide and 40% carbon dioxide is considered. Reference to Figures 5 to 7 shows that if the mixture is compressed isothermally from the vapor phase at some temperature above −133°F., for example −130°F., a dew point exists at 5 lb./sq. in. abs. (Fig. 7). Continued conpression increases the amount of liquid until at 7 lb./sq. in. abs. (Figure 7) vapor and liquid are in equilimixtures with less hydrogen sulfide are brium with incipient solid carbon dioxide. Corresponding vapor and liquid compositions at −130°F. and 7 lb./sq. in. abs. are 32% hydrogen sulfide, 68% carbon dioxide and 85.5% hydrogen

sulfide, 14.5% carbon dioxide respectively (Figure 5 or 7).

Isothermal compression of the 60% hydrogen sulfide mixture from the vapor phase at −133°F. shows that at 4.4 lb./sq. in. abs. the vapor is in equilibrium with incipient solid hydrogen sulfide and liquid. Continued compression causes the system to enter the vapor-liquid region until at 6.5 lb./sq. in. abs. solid carbon dioxide forms. At the latter condition vapor and liquid in equilibrium with solid carbon dioxide have compositions of 32.5% hydrogen sulfide, 67.5% carbon dioxide and 86% hydrogen sulfide, 14% carbon dioxide respectively.

If compression from the vapor phase for the 60% hydrogen sulfide mixture now occurs at −137°F., solid hydrogen sulfide forms. Upon further compression liquid forms at a vapor-liquid-solid hydrogen sulfide triple point at −137°F. and 4.7 lb./sq. in. abs. Vapor and liquid compositions at this point are 45% hydrogen sulfide, 55% carbon dioxide and 91% hydrogen sulfide, 9% carbon dioxide respectively. Vapor and liquid exist at pressures between 4.7 and 5.5 lb./sq. in. abs. at −137°F. At 5.5 lb./sq. in. abs. and −137°F. vapor, liquid, and solid carbon dioxide coexist where vapor composition is 33% hydrogen sulfide and liquid composition is 87% hydrogen sulfide.

Similar analyses can describe the behavior of any mixture in the low-temperature region. As directly indicated on Figures 5 to 7 systems containing between 12.5 and 66 mole % carbon dioxide have triple points at which vapor, liquid, and either solid hydrogen sulfide or solid carbon dioxide are in mutual equilibrium. Those mixtures with more than 66 mole % carbon dioxide can have vapor and liquid in equilibrium only with solid carbon dioxide; those with less than 12.5 mole % carbon dioxide have triple-point equilibria with solid hydrogen sulfide.

In view of the availability of the phase data at temperatures down to the solid-liquid-vapor loci of the three binary systems which comprise the methane-hydrogen sulfide–carbon dioxide ternary system, it is interesting to speculate about the behavior of the ternary.

It would be particularly interesting to know what influence carbon dioxide has upon the heterogeneous liquid-liquid-vapor behavior reported for the methane-hydrogen sulfide system (*5*).

ACKNOWLEDGMENT

The authors wish to thank the Ethyl Corporation for their generous support of this work through their sponsoring of fellowships. Thanks are also due to Mr. Jerome Brewer for his considerable assistance in the laboratory program.

Phillips Petroleum Company donated the hydrocarbons used in the low-temperature bath.

LITERATURE CITED

1. Bierlein, J. A., and W. B. Kay, *Ind. Eng. Chem.*, **45**, No. 3, 618 (1953).
2. Donnelly, H. G., and D. L. Katz, *ibid.*, **46**, 511 (1954).
3. Kohn, J. P., and Fred Kurata, Univ. Kansas, Lawrence (1955).
4. Reamer, H. H., B. H. Sage, and W. N. Lacey, *Ind. Eng. Chem.*, **43**, 976 (1951).
5. Kohn, J. P., Ph.D. thesis, Univ. Kansas, Lawrence (1956).
6. Ricci, J. E., "The Phase Rule and Heterogeneous Equilibrium," D. Van Nostrand, New York (1951).
7. Steckel, F., *Svensk Kem. Tidskr.*, **57**, 209 (1945); see (*1*).
8. Kohn, J. P., and Fred Kurata, *Pet. Proc.*, **11**, No. 12, 57 (1956).
9. Davis, P. C., Ph.D. thesis, Univ. Kansas, Lawrence (1951).
10. Lange, N. A., "Handbook of Chemistry," Handbook Publishers, Sandusky, Ohio (1956).
11. Maass, O., and D. McIntosh, *Trans. Roy. Soc. Can.*, **3**, No. 8, 65 (1914).
12. Cardoso, E., and E. Armi, *J. Chem. Phys.*, **10**, 504 (1913).
13. Reamer, H. H., B. H. Sage, and W. N. Lacey, *Ind. Eng. Chem.*, **42**, 140 (1950).
14. West, J. R., *Chem. Eng. Progr.*, **44**, No. 4, 287 (1948).
15. Moles, E., *Bull. soc. chim. France*, p. 1006 (Nov.-Dec. 1950).
16. Bottomley, G. A., D. S. Massie, and R. Whythlow-Gray, *Proc. Roy. Soc. (London)*, **A200**, 201 (1950).
17. Sobocinski, D. P., Ph.D. thesis, Univ. Kansas, Lawrence (in preparation).
18. Robinson, D. B., and J. A. Bailey, *Can. J. Chem. Eng.*, **35**, No. 4, 151 (December, 1957).
19. Thiel, A., and E. Schulte, *Z. physik. Chem.*, **96**, 328 (1920).

Manuscript received December 8, 1958; revision received April 27, 1959; paper accepted April 27, 1959. Paper presented at A.I.Ch.E. Cincinnati meeting.

The Enthalpy of Water in the Liquid State

ROBERT BYRNE and GEORGE THODOS

Northwestern University, Evanston, Illinois

The enthalpy of water in the liquid state has been calculated from 32°F. to temperatures approaching the critical and pressures ranging from saturated conditions to 160,000 lb./sq. in. abs. (approximately 11,000 atm). The results of this study are presented graphically and show that the influence of pressure on enthalpy is significant, particularly in the lower temperature region. At these conditions pressure is found to increase the enthalpy of liquid water by as much as 360 B.t.u./lb. above the corresponding enthalpy of the saturated liquid state.

A comprehensive literature search disclosed PVT data for water that permitted the construction of a density correlation. This correlation expressed in reduced coordinates extends from the normal freezing point of water to temperatures of 1,870°F. (T_R = 2.0) and pressures ranging up to 10,915 atm. (P_R = 50). The recent extensive PVT data of Kennedy reported in 1950 supplemented with the earlier data of Amagat and Bridgman allowed the calculation of enthalpies at these elevated temperatures and pressures. For these calculations basic thermodynamic relationships were adapted which utilized this reduced density correlation. This approach has made possible the extension of the thermodynamic properties of liquid water above the highest pressure reported by Keenan and Keys. Below this pressure of 6,000 lb./sq. in abs. good agreement was found to exist between the enthalpy values presented by Keenan and Keyes and those reported in this investigation.

Considerable information is presented in the literature on the thermodynamic properties of nonpolar compounds. These substances are composed of electrically symmetrical molecules which tend to behave as perfect gases or ideal solutions. The hydrocarbons are characteristic of this class of compounds for which thermodynamic properties can be readily pre-

dicted from generalized thermodynamic correlations. The prediction of these thermodynamic properties for nonpolar substances depends upon the critical temperature and pressure and, as recently proposed by Meissner and Seferian (*24*), also upon the critical compressibility factor.

For nonpolar substances such as argon, nitrogen, and methane the critical compressibility factors extend up to a value of 0.291. Values of the critical compressibility factors for helium, hydrogen, and neon are yet higher ($z_c = 0.307$); however these substances fail to follow the theorem of corresponding states, as expected from their identical critical compressibility factors. This abnormal behavior is attributed to quantum effects which are significant for these three substances. Conversely polar substances have characteristically lower z_c values; for example, water and methyl alcohol have z_c values of 0.231 and 0.222, respectively. The lowest z_c value is reported by Lydersen, Greenkorn, and Hougen (*23*) as 0.197 for hydrogen cyanide. Other substances reported in the literature have critical compressibility factors ranging from 0.231 to 0.291.

The direct association of polarity and the critical compressibility factor of substances is apparent, thus leading to the qualitative generalization that substances having high dipole moments are always associated with low critical compressibility factors. Since water is characteristic of substances having high dipole moments ($\mu = 1.87$ debye units) (*38*), its thermodynamic properties cannot be accurately developed from existing generalized correlations (*9, 12*). Therefore water has been selected as typical of those compounds which must be treated individually for an evaluation of their thermodynamic properties. This investigation is concerned with the calculation of enthalpy for water in the liquid state at elevated temperatures and pressures. The results of this study permit the extension of the enthalpies reported by Keenan and Keyes (*16*) from pressures of 6,000 to 160,000 lb./sq. in. abs. and temperatures up to 650°F.

REDUCED-STATE DENSITY CORRELATION

A comprehensive literature search for density data of water has resulted in a compilation showing the dependence of density on both temperature and pressure. Experimental densities for the liquid and gaseous states including values in the critical region have been considered in this study. The critical constants for water reported by Kobe and Lynn (*22*) were used to calculate reduced temperatures, pressures, and densities. These critical constants are $T_c = 647.4$°K., $P_c = 218.3$ atm., and $\rho_c = 0.32$ g./cc.

Since the majority of density data could not be conveniently expressed as a function of reduced pressure, it became necessary to cross-plot the original density data in order to obtain reduced densities at the appropriate reduced pressures. Figure 1 presents the final correlation of reduced density for water. In this compilation the saturated density data of Batelli (*2, 3*), Mendelejeff (*25*), Perot (*29*), Waterston (*37*), and Wüllner and Grotrian (*39*) obtained before the turn of the century were found to be in good agreement with the data of a number of investigators (*8, 10, 15, 18, 35*) who later reported density data for the saturated envelope. The experimental high-pressure data of Amagat (*1*) and Bridgman (*5, 6*) for liquid water cover the temperature range of −20° to 198°C. and account for densities up to pressures of 160,000 lb./sq. in. abs. Of particular interest are the data reported in 1950 by Kennedy (*17*) which permit the extension of the reduced density correlation into temperature and pressure regions where no data were previously available. Consequently densities now can be defined in the temperature region of $0.6 \leq T_R \leq 1.35$ to pressures as high as $P_R = 10$ (2,183 atm.) and for the higher temperature region of $1.35 \leq T_R \leq 2.00$ up to pressures of $P_R = 6.0$ (1,310 atm.).

In Figure 1 the density correlation has been presented on rectilinear coordinates to accentuate the regions of interest for water in the liquid state. Reduced-state correlations of this type, as well as those expressed on logarithmic coordinates, are receiving considerable attention in attempts to generalize the PVT behavior of substances. In addition to the correlating parameters of reduced temperature and pressure, Lydersen, Greenkorn, and Hougen (*23*) have utilized the critical compressibility factor as the third correlating parameter in their studies involving the thermodynamic properties of substances.

THERMODYNAMIC TREATMENT

The enthalpy change of a system as a function of temperature and pressure can be expressed in differential form as

$$dH = \left(\frac{\partial H}{\partial T}\right)_P dT + \left(\frac{\partial H}{\partial P}\right)_T dP \qquad (1)$$

Equation (1) is equivalent to the thermodynamic relationship

$$dH = C_p\, dT + \left[V - T\left(\frac{\partial V}{\partial T}\right)_P\right] dP \qquad (2)$$

where

$$\left(\frac{\partial H}{\partial T}\right)_P = C_p$$

and

$$\left(\frac{\partial H}{\partial P}\right)_T = V - T\left(\frac{\partial V}{\partial T}\right)_P$$

Table 1. Enthalpy Differences for Compressed Liquid Water (Low-Pressure Region)

$h - h_s$, Enthalpy difference, B.t.u./lb.

Pressure, lb./sq. in. abs.	32°F.	50°F.	100°F.	150°F.	200°F.	250°F.	300°F.	350°F.	400°F.	450°F.	500°F.	550°F.	600°F.	650°F.
1,000	2.9	2.8	2.6	2.4	2.1	2.0	1.9	1.3	1.0	0.3	−0.1			
2,000	5.5	5.3	5.1	4.8	4.5	4.0	3.6	2.9	2.0	0.9	−0.6	−1.6	−1.8	
3,000	8.1	8.0	7.7	7.1	6.8	6.1	5.6	4.4	3.2	1.5	−0.6	−2.9	−5.3	−7.4
4,000	10.9	10.8	10.1	9.7	9.0	8.2	7.5	6.0	4.4	2.1	−0.3	−3.9	−8.3	−14.6
5,000	13.6	13.5	12.9	12.1	11.3	10.3	9.3	7.7	5.7	3.0	−0.1	−4.7	−10.7	−20.1
6,000	16.2	16.1	15.4	14.7	13.7	12.7	11.2	9.3	7.0	4.1	0.2	−5.2	−12.2	−24.2
8,000	21.8	21.6	20.6	19.6	18.3	17.0	15.2	12.9	9.9	6.2	1.3	−5.3	−14.5	−30.1
10,000	27.1	26.9	25.7	24.4	22.9	21.2	19.1	16.5	13.0	8.9	3.1	−5.6	−15.2	−33.7
12,500	34.0	33.6	32.1	30.5	28.7	26.6	24.1	21.1	17.1	12.2	5.8	−2.9	−15.2	−35.6
15,000	40.6	40.1	38.3	36.6	34.4	32.1	29.1	26.0	21.4	16.1	8.9	−0.6	−14.3	−35.8
17,500	47.1	46.7	44.7	42.7	40.2	37.5	34.2	30.9	25.9	19.9	12.2	2.0	−12.7	−35.3
20,000	53.7	53.0	51.0	48.9	46.2	43.1	39.4	35.7	30.3	24.0	16.0	4.9	−10.2	−34.1
25,000	66.4	65.7	63.1	60.7	57.6	54.0	49.9	45.6	39.6	32.9	23.6	11.2	−4.9	−30.5
30,000	78.9	77.9	75.1	72.3	69.0	65.1	60.7	55.6	49.0	41.9	31.7	18.2	1.2	−25.2
35,000	90.9	89.9	87.1	84.0	80.2	76.2	71.7	65.7	58.8	50.5	39.9	25.9	7.9	−18.5

Reference state: h_s = enthalpy of water at saturated-state conditions

In order to utilize the density information presented in Figure 1, the following substitutions for pressure, temperature, and density were used:

$$P = P_c P_R, \qquad T = T_c T_R$$

and

$$V = \frac{M}{\rho_c \rho_R}$$

to produce Equation (3), which relates the effect of pressure on enthalpy above a reference state that has been selected as the enthalpy of liquid water at its corresponding vapor pressure:

$$\int_{h_s}^{h} dH = \frac{MP_c}{\rho_c} \cdot \int_{(P_R)_{s,p}}^{P_R} \left[\frac{1}{\rho_R} + \frac{T_R}{\rho_R^2} \left(\frac{\partial \rho_R}{\partial T_R} \right)_{P_R} \right] dP_R \qquad (3)$$

Equation (3) permits the calculation of enthalpy changes due to pressure at isothermal conditions. Integration of Equation (3) requires the evaluation of the function

$$f(\rho_R, T_R) = (1/\rho_R) + (T_R/\rho_R^2)(\partial \rho_R/\partial T_R)_{P_R}.$$

Graphical differentiation utilizing the chord-area method has been employed to produce the slopes $(\partial \rho_R/\partial T_R)_{P_R}$ from Figure 1 as functions of reduced temperature for constant parameters of reduced pressure. The pressures considered ranged from the saturated state to $P_R = 50$ in the temperature interval $0.422 \leq T_R \leq 0.6$ and to $P_R = 10$ in the temperature interval $0.6 \leq T_R \leq 1.20$. Utilizing this information, one could directly obtain the dimensionless quantity

$$(1/\rho_R) + (T_R/\rho_R^2)(\partial \rho_R/\partial T_R)_{P_R}$$

for the temperature interval $0.422 \leq T_R \leq 0.95$. The function $f(\rho_R, T_R)$ did not become negative until the reduced temperature became $T_R = 0.85$. These negative values can be explained from the fact that the negative contribution of the quantity $(T_R/\rho_R^2)(\partial \rho_R/\partial T_R)_{P_R}$ becomes larger than the quantity $(1/\rho_R)$ for $T_R \geq 0.85$. With this information Equation (3) was graphically integrated for a number of constant temperatures between the limits of the reduced vapor pressure and reduced pressure. The results of this procedure produced enthalpy changes due to pressure above the reference saturation pressure. For these calculations the vapor pressures compiled by Keenan and Keyes (*16*) have been used.

The results of this study are presented in Table 1 and also graphically in Figure 2 for pressures up to 35,000 lb./sq. in. abs. and for temperatures up to 650°F. Keenan and Keyes (*16*) present enthalpy differences for liquid water at pressures up to 6,000 lb./sq. in. abs. Values reported by Keenan and Keyes and those resulting from this study are found to be in agreement. Enthalpy differences for pressures above 35,000 lb./sq. in. abs. are presented in Table 2 for temperatures ranging from 32° to 250°F. and for pressures as high as 160,000 lb./sq. in. abs.

ENTHALPY OF SATURATED LIQUID WATER

The majority of heat-capacity data available are restricted to low temperatures. Rossini (*28*) points out that at present the data of Osborne, Stimson, and Ginnings (*27*) are the most reliable for the heat capacity of water up to

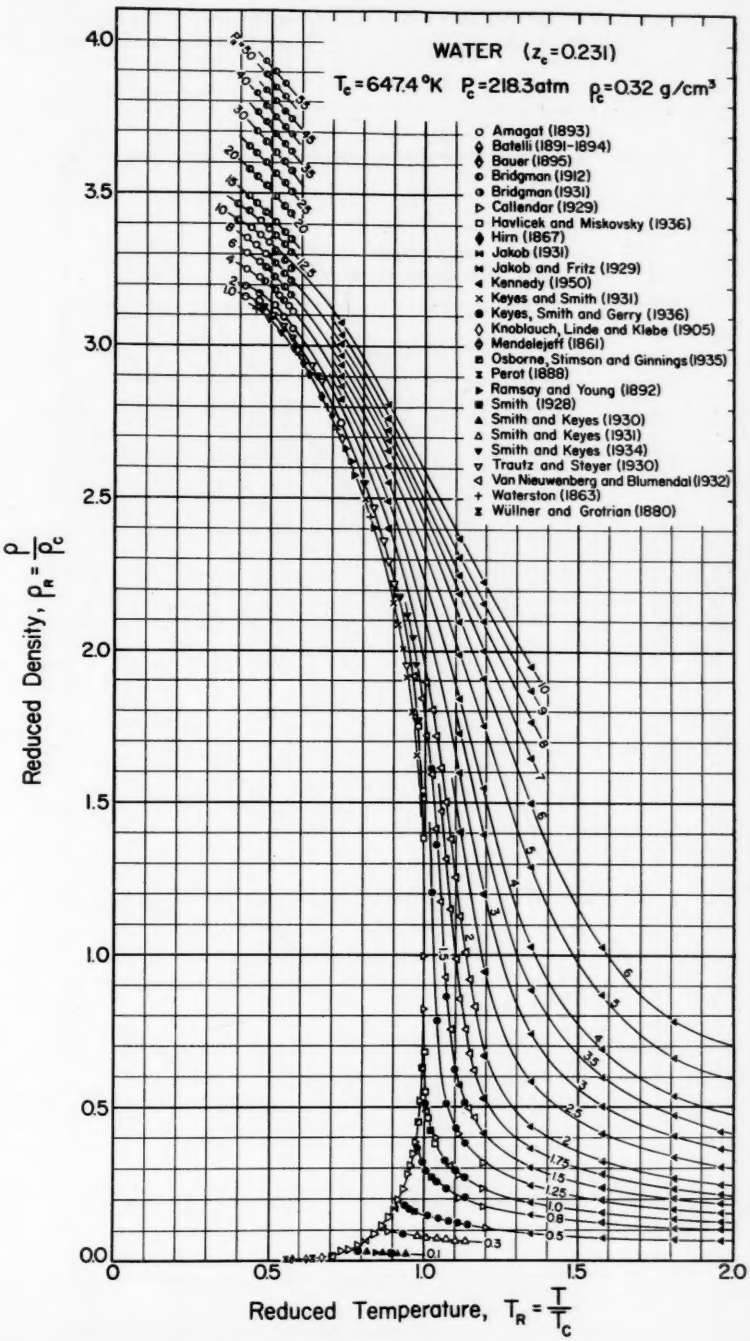

Fig. 1. Reduced-density correlation for water (rectilinear coordinates).

212°F. Since temperatures up to 650°F. have been considered in this study, their data were of restricted value. Because of the temperature limitation of their data, the constant-pressure heat-capacity data of Koch (*20*) were utilized to establish the enthalpy of water in the saturated liquid state up to 650°F.

For this analysis the heat-capacity data of Koch at 150 and 300 atm. were graphically integrated to produce the respective enthalpies above a reference state of 32°F. Enthalpy changes, $h - h_s$, for pressure effects, as obtained from Figure 2, made possible the calculation of enthalpies for the corresponding saturated liquid state. The following representative values are summarized:

		Koch (*20*)	
°F.	Keenan and Keyes (*16*)	150 atm.	300 atm.
200	168.0	167.6	167.2
400	375.0	374.7	373.5
600	617.0	615.3	613.8

The results produced from Koch's data at 150 atm. are in closer agreement with the values reported by Keenan and Keyes (*16*). This comparison appears acceptable, particularly since the saturated enthalpy values for the liquid state have been obtained by an approach different from that employed by Keenan and Keyes (*16*). The calculation of enthalpies for the saturated liquid state with the data of Koch used has been carried out in order to establish these values directly from data for the liquid state. The agreement of these values and those reported by Keenan and Keyes appears reasonable. Therefore the values reported by Keenan and Keyes have been accepted to produce the saturated enthalpy values presented in Figure 3.

The enthalpy differences for compressed liquid water presented in Tables 1 and 2 have been consolidated with the saturated enthalpy of liquid water to produce Figure 3. The isobars of 10,000, 20,000, and 30,000 lb./sq. in. abs. extend to 650°F., while those of higher pressures were limited to temperatures of 250°F. Restrictions have been imposed on the low-temperature range to account for the polymorphic behavior of water (*13*) in the formation of the different types of ices.

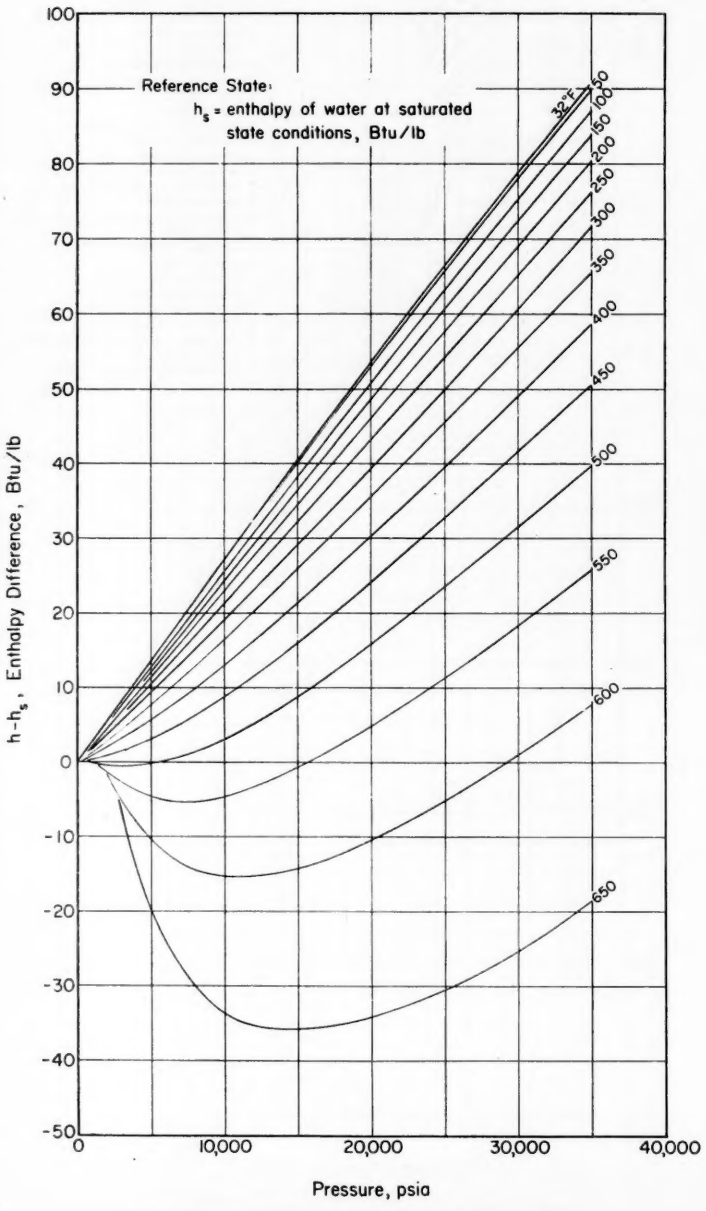

Fig. 2. Effect of pressure on enthalpy of liquid water.

NOTATION

C_p = molar heat capacity at constant pressure, cal./(g.-mole) (°K.)
h = enthalpy for liquid state, B.t.u./lb.
h_s = enthalpy for saturated liquid state, B.t.u./lb.
H = enthalpy
M = molecular weight, g./g.-mole
P = pressure, atm.
P_c = critical pressure, atm.
P_R = reduced pressure, P/P_c
$(P_R)_{v.p.}$ = reduced vapor pressure
R = gas constant
T = temperature, °K.
T_c = critical temperature, °K.
T_R = reduced temperature, T/T_c
V = volume, cc./g.-mole
V_c = critical volume, cc./g.-mole
z_c = critical compressibility factor, P_cV_c/RT_c
μ = dipole moment, debye units
ρ = density, g./cc.
ρ_c = critical density, g./cc.
ρ_R = reduced density, ρ/ρ_c

LITERATURE CITED

1. Amagat, E. H., *Ann. chim. et phys.* (*6*), **29**, 505 (1893).
2. Batelli, Angelo, *Acad. Mem. Torino* (*2*), **41**, 55 (1891).
3. ———, *Ann. chim. et phys.* (*7*), **3**, 408 (1894).
4. Bauer, Gustav, *Ann. Phys. Chem.*, **55**, 184 (1895).
5. Bridgman, P. W., *Proc. Am. Acad. Arts Sci.*, **47**, 439 (1912).
6. *Ibid.*, **66**, 185 (1931).
7. Callendar, H. L., *Phil. Trans. Roy. Soc.* (*London*), **A212**, 1 (1912).

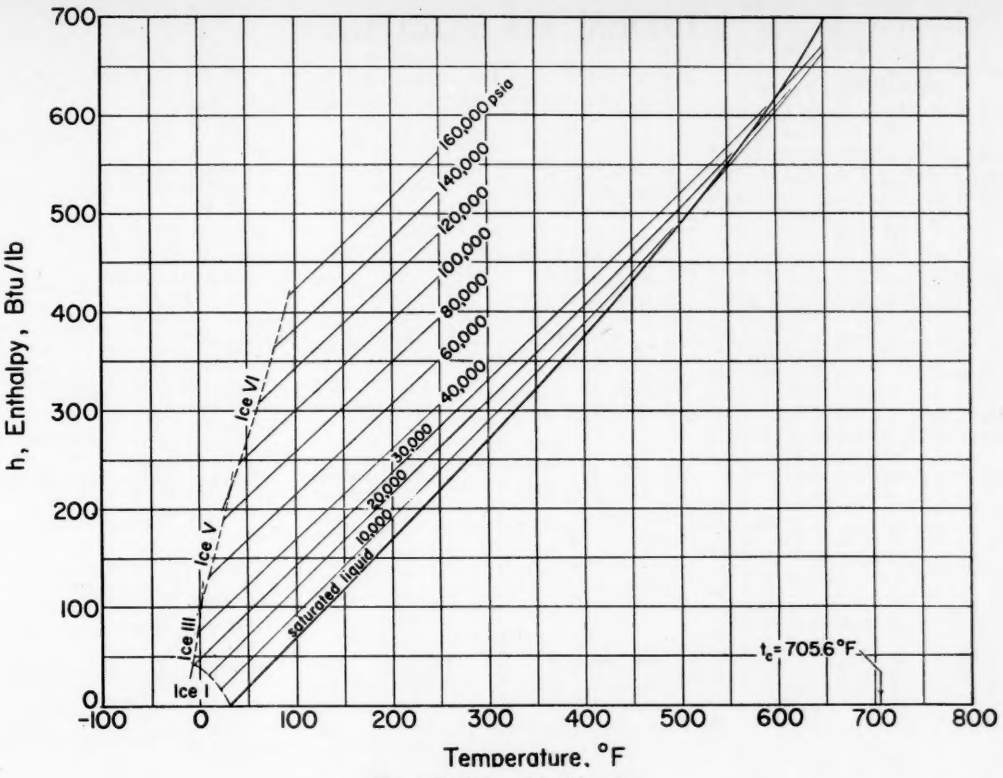

Fig. 3. Enthalpy of liquid water.

8. ———, *Proc. Inst. Mech. Engrs.* (*London*), **116**, 507 (1929).
9. Edmister, W. C., *Ind. Eng. Chem.*, **30**, 352 (1938).
10. Havlicek, Jaroslav, and Ladislav Miskovsky, *Helv. Phys. Acta*, **9**, 161 (1936).
11. Hirn, G. A., *Ann. chim. et phys.*, **10**, 32 (1867).
12. Hougen, O. A., and K. M. Watson, "Chemical Process Principles," p. 479, John Wiley, New York (1947).
13. International Critical Tables, **4**, p. 11, McGraw-Hill, New Yrok (1928).
14. Jakob, Max, *Engineering*, **132**, 684 (1931).
15. ———, and W. Fritz, *Z. Ver. deut. Ing.*, **73**, 629 (1929).
16. Keenan, J. H., and F. G. Keyes, "Thermodynamic Properties of Steam," John Wiley, New York (1936).
17. Kennedy, G. C., *Am. J. Sci.*, **248**, 540 (1950).
18. Keyes, F. G., and L. B. Smith, *Mech. Eng.*, **53**, 132 (1931).
19. ———, and H. T. Gerry, *Proc. Am. Acad. Arts Sci.*, **70**, 319 (1936).
20. Koch, W., *Forsch. Gebiete Ingenieurw.*, **5**, 138 (1934).
21. Knoblauch, Oscar, R. Linde, and H. Klebe, *Z. Ver. deut. Ing.* **49**, 1697 (1905).
22. Kobe, K. A., and R. E. Lynn, Jr., *Chem. Revs.*, **52**, 117 (1953).
23. Lydersen, A. L., R. A. Greenkorn, and O. A. Hougen, *Rept. 4*, Eng. Exp. Sta., Univ. Wisconsin, Madison (1955).
24. Meissner, H. P., and Ralph Seferian, *Chem. Eng. Progr.*, **47**, 579 (1951).
25. Mendelejeff, D. I., *Liebig Annal.*, **119**, 1 (1861).
26. Osborne, N. S., H. F. Stimson, and D. C. Ginnings, *Mech. Eng.*, **57**, 162 (1935).
27. ———, *J. Research Natl. Bur. Standards*, **23**, 197 (1939).
28. Rossini, F. D., "Chemical Thermodynamics," p. 31, John Wiley, New York (1950).
29. Perot, Alfred, *Ann. chim. et phys.* (*6*), **13**, 145 (1888).
30. Ramsay, William, and Sydney Young, *Phil. Trans. Roy. Soc.* (*London*), **A183**, 108 (1892).
31. Smith, L. B., *Mech. Eng.*, **50**, 153 (1928).
32. ———, and F. G. Keyes, *ibid.*, **52**, 123 (1930).
33. *Ibid.*, **53**, 135 (1931).
34. ———, *Proc. Am. Acad. Arts Sci.*, **69**, 285 (1934).
35. Trautz, Max, and Hans Steyer, *Forsch. Gebiete Ingenieurw.*, **2**, 45 (1930).
36. Van Nieuwenburg, C. J., and H. B. Blumendal, *Rec. trav. chim.*, **51**, 707 (1932).
37. Waterston, J. J., *Phil. Mag.* (*4*), **26**, 116 (1863).
38. Wesson, L. G., "Tables of Electric Dipole Moments," The Technology Press, Mass. Inst. Technol., Cambridge (1948).
39. Wüllner, F. H. A. A., and Otto Grotrian, *Annal. Phys. Chem.*, **11**, 545 (1880).

TABLE 2. ENTHALPY DIFFERENCES FOR COMPRESSED LIQUID WATER (HIGH-PRESSURE REGION)

$h - h_s$, Enthalpy difference, B.t.u./lb.

t, °F.	40,000 lb./sq. in. abs.	60,000 lb./sq. in. abs.	80,000 lb./sq. in. abs.	100,000 lb./sq. in. abs.	120,000 lb./sq. in. abs.	140,000 lb./sq. in. abs.	160,000 lb./sq. in. abs.
32	102.7	149.9	194.6	238.0	279.9	320.8	360.2
50	101.8	148.8	193.3	236.6	278.3	319.2	359.2
100	99.0	145.5	189.6	232.1	274.0	314.9	355.8
150	95.9	141.7	185.2	227.2	269.3	310.3	352.0
200	92.1	136.6	179.9	222.3	264.5	305.9	347.6
250	87.8	131.2	174.1	216.7	259.1	301.1	342.8

Manuscript received September 18, 1958; revision received March 30, 1959; paper accepted April 2, 1959.

INDEX TO VOLUME 5

Authors

Subject Index

CHEMICAL ENGINEERING PROGRESS SYMPOSIUM SERIES ABSTRACTS

The Chemical Engineering Progress Symposium Series is composed of papers on specific subjects conveniently bound in individual books, which are published at intervals. The books are 8½ by 11 inches, paper covered, and cost as follows: "Computer Techniques in Chemical Engineering," $3.00 to members, $4.00 to nonmembers; "Nuclear Engineering Part V," $3.50 to members, $4.50 to nonmembers; "Adsorption, Dialysis, and Ion Exchange," $3.50 to members, $4.50 to nonmembers. They may be ordered from the Secretary's Office, the American Institute of Chemical Engineers, 25 West 45 Street, New York 36, New York.

The *A.I.Ch.E. Journal* will publish, from time to time, abstracts of the articles appearing in the Symposium Series volumes, beginning with volume 55.

COMPUTER TECHNIQUES IN CHEMICAL ENGINEERING, Vol. 55, No. 21, 1959

Machine Computations of K-Values, Edward Gordon, M. J. Goodwill, and J. W. Paylor. For computations involving equilibrium between vapor and liquid phases, the oil and natural gas industries find it necessary to obtain much of their phase-equilibrium data from graphical K-value correlations. One such accurate correlation has been converted into relatively compact equations suitable for use with digital computers. **Solution of a Multicomponent-Distillation Problem With Two Feeds or a Side Stream,** R. J. Hengstebeck. Multicomponent distillation problems involving two feed streams or a side stream can be solved by a graphical method developed for simpler towers. The section between the feeds of a two-feed tower and the trays near the feeds require special treatment. A tower with a side stream becomes two simpler towers. The splits of the light components can be approximated. **Evaluation of Benedict-Webb-Rubin Equation for Prediction of Phase Equilibrium of Light Hydrocarbon Mixtures at Low Temperatures,** A. Roy Price, T. W. Leland, and Riki Kobayashi. An analysis of the Benedict-Webb-Rubin equation of state for light hydrocarbons at low temperatures and high pressures has been made with a medium-speed digital computer on the basis of original data for the methane-ethane-propane system. Pairs of plots employing molal average boiling point as composition parameters represent smoothed experimental data for each component. The correlational properties of these plots are confirmed by checks of the K values of methane, ethane, and propane with those from other experimental sources. **Present and Prospective Use of Computers in Management Control,** Robert H. Gregory. Data-processing systems attempt to meet managerial requirements concerning past history and future prospects by developing both data—the mass of facts concerning a business—and information—the small number of facts that are useful for decision making. **Development and Application of a General-Purpose Analogue Computer Circuit to Steady State Multicomponent-Distillation Calculations,** N. G. O'Brien and R. G. E. Franks. The problem studied was separation of acetylene from ethylene by extractive distillation. The numerical values computed for one set of operating conditions by manual, analogue, and digital computation are compared. Electrical analogue circuits capable of handling plate-to-plate calculations where the vapor composition is known are given. The liquid composition on a plate containing a large amount of nonvolatile solvent is computed. **The Use of a Computing System in a Large Chemical Company,** F. A. Landee. The preparation by hand and in the original machine language of programs for an electrical digital computer is a long, expensive, and error-prone process. This paper describes a rather complete system devised at The Dow Chemical Company for use with an intermediate-sized computer to reduce the difficulty of the programming problem. **Optimum Design of Ejectors Using Digital Computers,** L. A. DeFrate and A. E. Hoerl. An earlier one-dimensional analysis of single-stage jet ejectors is extended by accounting for the effects of dissimilarities in molecular weights between the motive and suction gases. The numerical solution of the resulting nonlinear simultaneous equations on digital computers is discussed, and a dimensionless design chart for jet ejectors in chemical processes is presented. **Prerequisite for Computer Applications,** H. A. Hashbarger and N. L. Sample. Monsanto's experience with the IBM 702-EDPM is described, and its utilization in management control is presented, together with advantages and benefits which have been achieved, difficulties that have been encountered, and prerequisites for successful utilization. Translating existing company control techniques into programs that can be handled by the computer is discussed. **Fractionater Design with Automatic Computing Equipment, Part I,** Robert L. McIntire. A step-by-step method of fractionator design directed specifically toward application to

automatic digital computing equipment is presented. The procedure is used to predict the number of ideal equilibrium steps required to make a given separation of a multicomponent feed. Examples of machine solutions are given to demonstrate this method of solving process-design and operating problems. **Fractionater Design, Part II,** R. O. SHELTON AND R. L. MCINTIRE. A step-by-step fractionator-design method developed for application to automatic computers is presented. This system of equations is used to calculate the separation of a multicomponent feed which is obtained with fixed operating conditions in a given fractionator. Heat, material, and equilibrium balances are used throughout. The convergence equations given require no manual intervention once the process is started on a computer. **Automatic Computer Procedure for Calculating Plates Required for Nonideal Ternary Continuous Distillation,** ARTHUR ROSE, RICHARD E. STILLMAN, THEODORE J. WILLIAMS, AND HARRISON C. CARLSON. This paper describes an automatic-computer trial-and-error procedure for calculating reflux ratio, total plates, and feed-plate location required for meeting specification requirements in continuous distillation of a ternary mixture with activity coefficients fitted by three-suffix equations in volume fractions. It is the general approach for a nonideal situation that is the basis for the discussion in this paper. **An Integrated System for the Automatic Solution of Distillation Problems,** J. S. BONNER. An automatic computation system for the solution of any problem must meet several basic requirements, such as precision, speed, generality, and simplicity of application. This paper describes a system which meets all these requirements.

NUCLEAR ENGINEERING—PART V,

Vol. 55, No. 22, 1959

Engineering Hot-Channel Factors, B. W. LETOURNEAU AND R. E. GRIMBLE. Engineering hot-channel factors have been established to account for small dimensional deviations from the nominal design of reactor fuel elements. Common deviations are described, together with methods of estimating the effect on channel enthalpy rise, film temperature difference, and maximum heat flux.

Examples are given for parallel-plate type of fuel elements separated by rectangular coolant channels. **An In-Pile Study of Organics as Nuclear Reactor Coolants,** MALCOLM MCEWEN AND EDWARD W. WIEDERHOLD. In a study of the feasibility of using organic chemicals as nuclear reactor coolant-moderators, a test loop was operated in conjunction with the reactor at Brookhaven to determine for these organics the specific radiolytic-decomposition rate, gas-generation rate, induced-radioactivity levels, and effect of decomposition products on the operating characteristics of the system and on the engineering properties of each material. **The Inside-Out Reactor,** MILAN OSREDKAR AND RICHARD STEPHENSON. A reactor design is described which offers the possibility of obtaining a given thermal flux at a power less than that of a conventional reactor such as the MTR. **Use Of a Nuclear Reactor as a Process Heat Source,** R. W. RITZMANN. Possible methods of using a nuclear reactor as the endothermic-chemical-reaction heat source in a coal-gasification plant are discussed. The economics are discussed, and charts showing the effects of steam temperature and heat recovery on the threshold economics are presented. The cost of heat produced by a nuclear reactor is compared with the cost of heat supplied by the conventional method of burning coal with oxygen. **Continuous Dissolution of Uranium-Aluminum Fuels in a Trickle-Type Column Dissolver,** J. C. BRESEE, D. L. FOSTER, AND E. O. NURMI. A continuous column dissolver may be operated with critically safe dimensions; hence this type of dissolver may have an unlimited charge of metal per unit with no theoretical upper limit to the capacity. With the advantage that a continuous dissolver may better serve a continuous solvent-extraction process than a batch dissolver, the continuous column dissolver is potentially the most satisfactory type for short fuel elements or sections of elements. **Design of Plutonium Processing Plants,** B. F. JUDSON. This paper presents a design philosophy for plutonium processing plants based upon the experience gained in the operation of a semiworks facility at Hanford Atomic Products Operation. Prime concepts include the use of contamination barriers made of sealed hoods and directionalized air flow, partial separation of operating and maintenance functions in the physical layout, inclusion of multicomponent processing systems in single large hoods, and the considerations necessary for critical mass control. **Radioactivity Levels and Temperature Variations of the Columbia River,** ROYAL E. ROSTENBACH. The Columbia River was a prime factor in the selection of the Hanford site for the AEC's water-cooled nuclear reactors. Besides cooling the reactors, the river also serves to dispose of radioactive waste. River water passes through the reactors and large retention basins and is then discharged to the river as a warm radioactive effluent under carefully controlled conditions. This report considers temperature and radioactivity levels of the river. **Studies On X Rays and Bremsstrahlen,** L. E. BROWNELL AND E. W. COLEMAN. Although secondary radiations may be predicted accurately for very simple situations, such methods are of little value in real situations. The complexity of the problem is apparent if one considers that the production and absorption of electrons and of photons are interdependent processes. This paper discusses briefly some of the factors considered in developing bremsstrahlen sources for medical radiography. **Application of the Packed Column to the Redox Process,** E. R. IRISH. A brief description is presented of the Redox process for plutonium and uranium separation and decontamination from fission products contained in irradiated uranium fuel elements. Performance characteristics determined for packed solvent-extraction columns during development work are discussed. Instrumentation for control and observation of performance is described briefly. **Electrolytic Recycle Method for the Treatment of Radioactive Nitric Acid Waste,** H. W. ALTER, D. L. BARNEY, A. C. SCHAFER, AND F. J. WITT. The bulk of high-level, radioactive waste will consist of solvent extraction raffinate. Most of this will be nitric acid containing over 95% of the fission products from the separation process and small amounts of nitrate salts. The first objective in waste treatment is volume reduction of the waste to yield the mixed fission products in a small, high-specific activity package without the simultaneous production of large volumes of low-level waste. **Industry's Role in University Programs of Nuclear Engineering,** D. W. MCLENEGAN. In training tomorrow's engineers, today's specific problem becomes secondary to the fields of knowledge and the processes of analysis which this problem and others are likely to demand.

This concept tells how industry can best cooperate with the colleges to their advantage and its own, particularly in the long range sense. **The Subcritical Assembly in Engineering Teaching,** W. F. FAGEN AND JOSEPH WEIL. The advent of the subcritical assembly has provided university instructors with a versatile laboratory tool which can be used for studying the basic factors involved in reactor design and operation without the hazards produced by criticality. At the same time measurements can be made within the lattice, and the behavior of the neutrons in environments associated with reactors can be analyzed. In addition, neutrons can readily be detected and measured. Design predictions also can be compared with actual practical measurements. **Radiation Source Fabrication and Handling,** EUGENE LAMB. Radiation sources containing greater quantities of separated fission products than are now available will be produced in the Fission Products Pilot Plant at Oak Ridge.

It is expected that much of the plant output will be used in gamma irradiators of intermediate or pilot plant size. Therefore, integrated planning will be necessary from the design of the source unit to its installation in the irradiator. Certain limitations are placed on the source unit by the fabricator's plant, the intended use of the source, the characteristics of the fission products in the source, and the method of shipment. **Design and Construction Criteria for In-Pile Experimental Chemical Reactors,** D. J. DANIELS, M. C. SCHROEDAR, D. D. FOLEY, AND R. B. FILBERT, JR. Use of nuclear radiation in carrying out chemical reactions is now being extensively explored by chemists and chemical engineers. Of the various radiation sources the nuclear reactor is by far the most powerful in terms of intensity of penetrating radiation available and may be the most likely source of nuclear radiations for chemical processing.

A number of the specific problems encountered in the design and construction of chemical processing loops were not evident at the outset, and one of the purposes of this discussion is, therefore, to alert others venturing into the area. **Report on Process Steam Reactors,** E. L. HELLER AND D. O. HUBBARD. The chemical industries

require an uninterrupted, reliable, and constant source of heat for their continuously operating processes. In many plants, load factors of 90 to 95% of demand are the rule rather than the exception. Those conditions are ideal for nuclear reactors.

On the basis of recent experience, it is safe to assume that the potential market is 50 to 100 process steam-generator units a year. **Nuclear Considerations in Design of High-Temperature-Process Heat Reactors,** J. T. ROBERTS. Designers of high-temperature-process heat reactors must be careful not to rely uncritically on nuclear generalizations based on low-temperature thermal reactors. Differences are reflected in differences in critical size and mass and in control problems associated with temperature coefficient of reactivity and degree of fuel burn-up attainable before processing. **Design of a Plant for Recovery of Uranium by Liquid Ion Exchange (Solvent Extraction),** KATHLEEN BLACK AND JOSEPH KOSLOV. A process description for the recovery of uranium from sulfuric acid leach solutions by solvent extraction, designed to process 600 tons of ore daily, is presented. **Indirect Cycle Nuclear Reactor System to Furnish Process Heat,** R. CARSON DALZELL AND JAMES P. MCGEE. Use of nuclear fission for chemical process heat offers the special advantage of high temperature, limited only by materials of construction. The process heat may be supplied economically at elevated pressures, since no compression of combustion air is required. The major problems are the design of high-temperature fuel elements, construction of an exchanger to transfer heat to process streams in the range of 2,500°F., and development of compressors capable of recycling helium at 1,000°F. and above. **Direct Utilization of Fission Energy for Radiation Processing,** WARD S. DIETHORN, PAUL SCHALL, JR., AND G. D. CALKINS. Radiation-induced degradation, polymerization, and synthesis of both organic and inorganic compounds have been reported. High chemical yields in some of these systems suggest the possibility of utilizing radiation sources for the commercial production of chemicals.

If fission recoils could be utilized in a reactor, it would be a highly efficient radiation processing source. The purpose of this paper is to discuss a reactor application of this type. **Experimental Determination of Dose Distribution in the Proposed Fir Gamma Irradiator,** B. MANOWITZ, D. M. RICHMAN, L. GALANTER, AND O. A. KUHL. This paper presents an experimental program to determine the depth-dose distribution in food packages for several gamma irradiator geometries and to examine the nature of aqueous, indium-salt solutions. The experimental results of the irradiator experiments were compared to theoretical calculations of depth-dose distributions and reactor power required for one particular irradiator geometry. **Engineering Continuous Filtration to the Uranium Ore-Processing Flow Sheet,** C. F. CORNELL, R. C. EMMETT, AND D. A. DAHLSTROM. Rapid development of uranium-ore milling has required the solution of several difficult and critical liquid-solids separations. Filtration has been given a large place in the flow sheet in finding these solutions. Filtration theory, test procedures, methods of correlation, and filter construction had to be developed. **High-Operating-Temperature Reactor Design,** JOSEPH DEFELICE. The design presented affords a method of immediate entry into the field of high-temperature nuclear reactors for chemical processing. The reactor described is, in essence, a test reactor for the development of high-temperature fuel elements. **Process Applications and Construction Materials for a High-Temperature Nuclear Reactor for Chemical Processing,** LEON DAVIDSON AND ALFRED A. STRASSER. A preliminary study to explore the design and application of a high-temperature process heat reactor.

With known technology a relatively small demonstration reactor could be built in which an insulated central fuel region, running at high temperature, could be used to develop and demonstrate high-temperature components. **The Effects of Gamma Radiation on Several Polysulfone Reactions,** BRUCE G. BRAY, JOSEPH J. MARTIN, AND LEIGH C. ANDERSON. The advent of the atomic energy program stimulated many research activities to discover uses for the high-energy radiation made available in the fission products of the nuclear reactors. The use of this radiation as a catalyst in chemical reactions has been shown to be very effective in certain cases and may prove to be advantageous on an industrial scale.

ADSORPTION, DIALYSIS, AND ION EXCHANGE, Vol. 55, No. 24, 1959

Similarities in Adsorption, Dialysis, and Ion Exchange, G. P. MONET. If adsorption, dialysis, and ion exchange are grouped together, there are many obvious similarities of a physicochemical and chemical engineering nature. Classification of the three fields into one is expected to facilitate chemical engineering instruction, to stimulate further research, and lead to increased commercial application. **Adsorption Equilibria,** DONALD GRAHAM. The nature and energies of adsorption are reviewed with particular reference to its use in clarification or fractionation. Experimental techniques for obtaining adsorption equilibrium data and analytical methods for their interpretation are reviewed. Factors which should be considered in the selection of an adsorbent for a specific purpose are discussed, and methods for handling solid adsorbents in fluid media are outlined. **Kinetics of Batch Adsorption of Dichlorophenol on Activated Carbon,** S. B. SMITH, A. X. HILTGEN, AND A. J. JUHOLA. The rate of adsorption of 2, 4-dichlorophenol from aqueous solution by granular activated carbons of various sizes and types was followed for 3-hr. periods. The effects of adsorbent structure, particle size, initial adsorbate concentration, temperature, and adsorbent-solution ratio were studied and mathematical treatments tested. A proposed semiempirical treatment permits determination of relative diffusivities within the particles. **Deactivation and Reactivation Phenomena During Charcoal Adsorption of Hydrocarbon Gases,** R. F. BADDOUR AND R. L. GEDDES. The effect of hydrocarbon pyrolysis gas on the adsorptive capacity of activated petroleum coke was explored in bench-scale experiments with fixed char beds. Deactivation and reactivation phenomena were studied at varying conditions in an effort to gain information useful in commercial design work. **Molecular Sieves,** G. J. GRIESMER, R. A. JONES, AND HARRY LAUTENSACK. Since molecular-sieve adsorbents were introduced, they have been applied by the process industries to the drying and purification of a large variety of gas and liquid streams. This paper deals with the properties and uses of molecular sieves. **Application of Ion Exchange Equilibrium Relationships to Process Design,** NORMAN W. FRISCH AND FRANCIS X. MCGARVEY. Kinetic relationships which describe ion exchange processes have been developed, each relationship depending upon a mass balance, a rate equation, an equilibrium relationship (isotherm), and a set of boundary conditions. In many design applications, expressions based on equilibrium concepts yield important process information. **Kinetic Relationships for Ion Exchange Processes,** THEODORE VERMEULEN AND NEVIN K. HIESTER. Efforts to place ion exchange and related adsorption operations on a sound theoretical basis are reviewed. Graphs and tables are cited which present the results of complex mathematical analysis in readily usable form. Finally, resin utilization and regenerant efficiency important in the economic design of processes for cyclic operation are discussed. **Ion Exchange Kinetics,** R. L. MOISON AND H. A. O'HERN, JR. New data were obtained on ion exchange in deep, fixed-bed equipment. The data for favorable equilibria were correlated by a variation of the "exchange zone" concept of Michaels, and the results revealed that liquid-phase diffusion is controlling with feed concentrations of 0.01 to 0.10 *N*. Heights of transfer units were found to be proportional to the 0.4 power of Reynolds number and the 0.3 power of the ratio of bed depth to particle diameter. **Semicontinuous Countercurrent Apparatus for Contacting Granular Solids and Solution,** C. W. HANCHER AND S. H. JURY. Progress is reported in the field of semicontinuous countercurrent ion exchange at Oak Ridge National Laboratory. Additional operating data are given on a 12-in. diameter pilot-scale slurry contactor operating on low-grade Western uranium ore. Hydraulic data from a 36-in. contactor with new types of pulsing mechanisms are presented to show the decreased effect of wall resistance in the larger contactors.

(*Continued from p. 412*)

Professor Peters has written a readable book which emphasizes the dual economic and technical basis for plant design. It will be of use to chemical engineering students and practicing engineers not directly concerned with cost estimation.

J. FRIEDLANDER

COMMUNICATIONS TO THE EDITOR

Liquid Mixing on Bubble Trays — A Correction

Dear Editor:

The paper by Oliver and Watson in your March, 1956, issue has been misinterpreted by Foss, Gerster, and Pigford in the June, 1958, issue.

In preparing a paper, one is faced with the necessity of being as brief as possible consistent with understandability. In view of the misunderstanding, our brevity was excessive in this instance. I, therefore, request publication of the analysis which follows:

We are stated by Foss, *et al.*, to "have assumed that a certain fraction of the liquid at the exit weir is recircuited to the inlet weir, where it is mixed with the incoming liquid. This mechanism is not explicitly stated by Oliver and Watson. . . ." This is incorrect. The statement in our paper "the assumption that the rate of mixing is uniform across the plate makes possible a solution. . ." was meant to indicate the derivation. The assumption is continuous, constant, back mixing across the plate.

NEW ASSUMPTIONS OF OLIVER AND WATSON

1. A constant fraction of the liquid flow is transferred bodily from downstream to upstream of a differential slab without mass transfer. Thus, the total liquid flow through the slab is $(1 + C)L$ in the direction of flow.

2. Volatile component concentration in liquid rises from x_n at the exit to x_e just downstream of inlet weir; x_{n-1} is higher than x_e (or equal if $C = 0$).

ASSUMPTIONS OF LEWIS CASE I (1)

3. Vapor enters a differential slab (which is transverse to liquid flow) with concentration y_{n+1} and leaves with concentration y'.

4. y_{n+1} is constant.

5. Total liquid and gas flows are constant.

6. The true point efficiency is constant on the tray.

7. Liquid concentration is vertically invariant.

By material balance the amount of volatile component entering the vapor equals that leaving the liquid:

$$(y' - y_{n+1})\, dG = (1 + C)L\, dx \qquad (1)$$

The assumptions are illustrated in Figure 1. By definition

$$E_{OGT} = \frac{y' - y_{n+1}}{y^* - y_{n+1}} \qquad (2)$$

Substituting in Equation (1) one gets

$$E_{OGT}(y^* - y_{n+1})\, dG = (1 + C)L\, dx \qquad (3)$$

Integrating and rearranging yields

$$E_{OGT} = \frac{(1 + C)L}{G} \int_{x_n}^{x_e} \frac{dx}{y^* - y_{n+1}} \qquad (4)$$

Now the liquid concentration change due to contacting vapor for a flow of $(1 + C)\, L$ is $1/(1 + C)$ times what it would be with flow of L. The total change without liquid mixing would be $(x_{n-1} - x_n)$. Thus

$$\int_{x_n}^{x_e} (1 + C)\, dx = x_{n-1} - x_n \qquad (5)$$

Integrating and rearranging, one obtains

$$1 + C = \frac{x_{n-1} - x_n}{x_e - x_n} \qquad (6)$$

By definition

$$F = \frac{x_{n-1} - x_e}{x_{n-1} - x_n} \qquad (7)$$

$$1 - F = \frac{x_e - x_n}{x_{n-1} - x_n} \qquad (8)$$

$$\frac{1}{1 - F} = \frac{x_{n-1} - x_n}{x_e - x_n} = 1 + C$$

and the substitution of (8) in (4) yields

$$E_{OGT} = \frac{L}{G(1 - F)} \int_{x_n}^{x_e} \frac{dx}{y^* - y_{n+1}} \qquad (9)$$

This is Equation (13) of our paper, from which the others readily follow.

The equations of our paper are thus not dependent on a patently false assumption about mixing which would cast doubt on their validity. While not demonstrably true, the assumption actually made is not unreasonable as an approximation.

It is clear that the relations are the same whether the mixing takes place continuously or in finite steps, provided the total flow subjected to mass transfer is constant, since recycling of liquid from exit to entrance gives the same result as localized mixing through a differential slab.

The mechanism postulated makes the rate of mixing independent of the concentration gradient, which is not uniform.

It is to be hoped and expected that the modern statistical methods employed by Foss, Gerster, and Pigford, coupled with concerted efforts at amassing data, will be more powerful than past approaches in investigating efficiency phenomena. Until efficiencies can be reliably correlated in terms of system properties, flow rates, and geometry for bubble cap as well as the more elementary sieve trays, the simple equations resulting from the fractional mixing concept may find use when the effect of liquid mixing can be adequately described by a constant. The accuracy may conceivably be as good as the application of the two-film theory to distillation, which depends on vertical constancy of liquid composition in order for the relation between point efficiency and transfer units to be valid.

NOTATION

- C = fraction of liquid locally recirculated
- dG = vapor entering differential slab.
- E_{OGT} = true local efficiency
- F = fractional mixing, defined as concentration drop across inlet weir divided by total concentration drop across plate
- G = mass velocity of vapor
- L = mass velocity of liquid
- x = mole fraction of low boiler in liquid
- y = mole fraction of low boiler in vapor
- y' = mole fraction of low boiler in vapor leaving differential slab
- y^* = mole fraction of low boiler in vapor in equilibrium with liquid of concentration x

Subscripts

- e = entering tray, just downstream of inlet weir
- n = tray number, down from top

LITERATURE CITED

1. Lewis, W. K., Jr., *Ind. Eng. Chem.*, **28**, 399 (1936).

Very truly yours,
Earl D. Oliver
Shell Development Company,
Emeryville, California

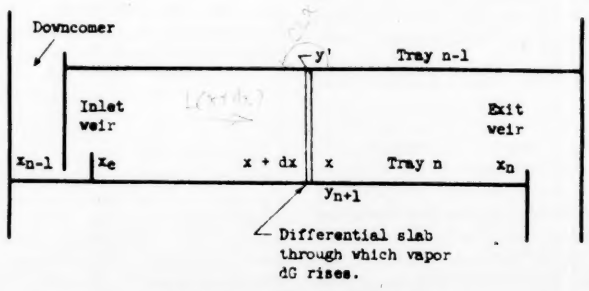

Fig. 1. Illustration of assumptions.

Unsteady Pseudoplastic Flow Near a Moving Wall

R. BYRON BIRD

University of Wisconsin, Madison, Wisconsin

There are available in the literature (*1, 2, 3*) analytical solutions for the power-law (Ostwald-de Waele) model for pseudoplastic non-Newtonian fluids for a number of different geometries. These solutions are however all for steady flow. Here the solution to an unsteady flow problem is given.

A semi-infinite body of pseudoplastic fluid extends from $y = 0$ to $y = \infty$ and is bounded on one side by a solid surface imbedded in the xz plane. Initially the fluid is at rest, but for time $t \geq 0$ the solid surface moves in the x direction with a constant velocity. It is desired to know the x component of the velocity v_x as a function of the distance from the solid surface and the time for a pseudoplastic fluid which obeys the following relation for the components of the momentum flux:

$$\tau_{ij} = -m\left(\tfrac{1}{2}\sum_k\sum_l \Delta_{kl}^2\right)^{(n-1)/2}\Delta_{ij} \tag{1}$$

In this expression $\Delta_{ij} = (\partial v_i/\partial x_j + \partial v_j/\partial x_i)$ is the ij component of the rate-of-strain tensor.* For the problem stated above this relationship gives

$$\tau_{xy} = -m\,|\partial v_x/\partial y|^{n-1}\,(\partial v_x/\partial y) \tag{2}$$

for the xy component of the momentum flux.

The equation of motion for the system is

$$\rho(\partial v_x/\partial t) = -(\partial \tau_{xy}/\partial y) \tag{3}$$

Substituting Equation (2) into Equation (3), taking into account the fact that $\partial v_x/\partial y$ is everywhere negative, one obtains the partial differential equation for the velocity distribution:

$$\rho(\partial v_x/\partial t) = -m\frac{\partial}{\partial y}(-\partial v_x/\partial y)^n \tag{4}$$

This is to be solved with the boundary conditions $v_x = V$ at $y = 0$, $v_x = 0$ at $y = \infty$, and the initial condition that $v_x = 0$ for $t < 0$. According to the method of combination of variables y and t are combined into a new dimensionless variable:

$$r = (n+1)^{-1}y(\rho/mtV^{n-1})^{1/(n+1)} \tag{5}$$

Now one anticipates that the dimensionless velocity $\phi_n = v_x/V$ will be a function of r alone. This allows Equation (4) to be transformed into the following ordinary differential equation:

$$\phi_n''(-\phi_n')^{n-1} + (n+1)^n n^{-1} r\phi_n' = 0 \tag{6}$$

with boundary conditions such that $\phi_n = 1$ at $r = 0$, and $\phi_n = 0$ at $r = \infty$; primes denote differentiation with respect to r. For $n = 1$ (Newtonian flow) Equation (6) becomes $\phi_1'' + 2r\phi_1' = 0$, for which the solution (*6*) is $\phi_1 = \text{erfc}\, r$; here $r = y/\sqrt{4\mu t/\rho}$.

For $n < 1$ (pseudoplastic flow) Equation (6) may be integrated twice to give

$$\phi_n = \beta_n^{-1/(1-n)}\cdot\int_r^\infty (B_n + r^2)^{-1/(1-n)}\,dr \tag{7}$$

in which $\beta_n = (1+n)^n(1-n)/2n$. The constant of integration B_n is determined from the boundary condition at $r = 0$, which may be written as

$$1 = \beta_n^{-1/(1-n)}\cdot\int_0^\infty (B_n + r^2)^{-1/(1-n)}\,dr \tag{8}$$

If now a new variable defined by

$$s^2 = r^2/(B_n + r^2) \tag{9}$$

is introduced, then integrals of the following form appear in Equations (7) and (8):

$$I_n(s) = \int_s^1 (1-u^2)^{(3n-1)/2(1-n)}\,du \tag{10}$$

In terms of these quantities the integration constant and the dimensionless velocity distribution assume the final form

$$B_n = \beta_n^{-2/(1+n)}[I_n(0)]^{2(1-n)/(1+n)} \tag{11}$$

$$\phi_n = I_n(s)/I_n(0) \tag{12}$$

(*Continued on page 6D*)

TABLE 1. NUMERICAL VALUES FOR CALCULATING VELOCITY PROFILES

n	$I_n(0)$	B_n	r_1
1/3	1	0.8660	6.57
1/2	$\pi/4$	1.6370	4.30
2/3	$3\pi/16$	2.8383	3.05
5/6	$63\pi/512$	5.9782	2.29
1	...	...	1.83

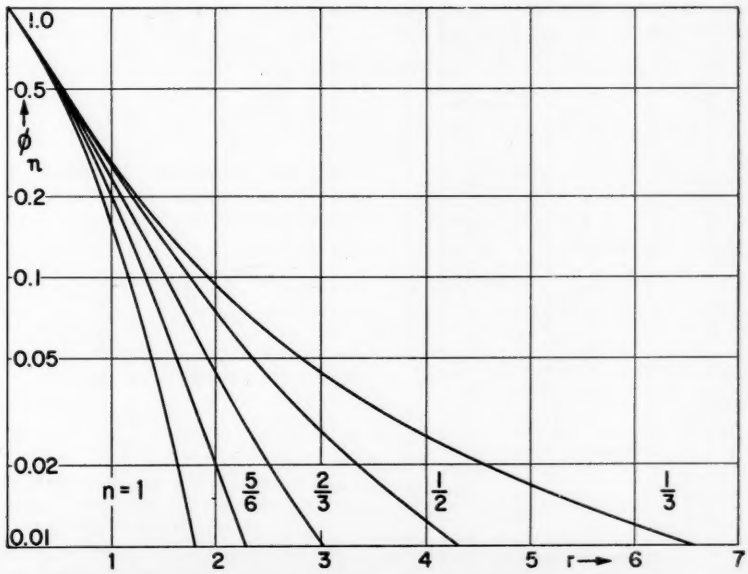

Fig. 1. Dimensionless velocity profiles for flow of a pseudoplastic fluid near a flat surface suddenly set in motion with a constant velocity.

*The writing of the power law in the form given in Equation (1) insures proper behavior under coordinate transformation (*4*). Equation (3) in a previous paper (*5*) should have been written in this way; clearly the unspecified form used there was adequate for dimensional considerations.

Center-Line Value of the Eddy Viscosity

SCOTT LYNN

The Dow Chemical Company, Pittsburg, California

The article by R. R. Rothfus and co-workers (*5*) is a valuable correlation of the best data on turbulent flow in pipes. In their discussion however the authors conclude that both the eddy viscosity and the mixing-length parameter tend toward zero near the center of a tube or channel. The work of some investigators in the field has indicated that this is not so (*1, 2, 4*), and the writer feels that a discussion of the two points of view is of some interest because of the differences in the nature of turbulent flow which are implied.

Using the authors' nomenclature, this writer defines the eddy viscosity as

$$\epsilon = -\frac{\tau g_0}{\frac{du}{dr}} - \mu \qquad (1)$$

It is easily shown that for steady, uniform flow the shearing stress varies linearly with the distance from the wall of the tube irrespective of the nature of the flow. Thus

$$\tau = \tau_0 \frac{r}{r_0} \qquad (2)$$

where r_0 is the radius of the tube.

It is apparent from a consideration of Equations (1) and (2) that the value of the eddy viscosity as defined by Equation (1) is indeterminate at the center of the tube, that is when $r = 0$. However it has been shown (*2*) that a simple mathematical operation greatly increases the ease of interpreting the experimental data in the central region of a tube or channel. By considering the variable of radial position to be the square of the distance from the center, one can handle the equations as follows: let

$$\xi = \left(\frac{r}{r_0}\right)^2 \qquad (3)$$

Then

$$d\xi = 2\frac{r}{r_0}\, d\left(\frac{r}{r_0}\right) = 2\frac{r}{r_0^2}\, dr \qquad (4)$$

When one substitutes Equations (2) and (4) in Equation (1), the definition of eddy viscosity becomes

$$\epsilon = -\frac{r_0 \tau_0 g_0}{2\frac{du}{d\xi}} - \mu \qquad (5)$$

The mixing-length parameter l is defined by the authors in the equation

$$\epsilon = -\rho l^2 \frac{du}{dr} \qquad (6)$$

If ϵ is not zero at the center of the tube, l will tend toward infinity there because du/dr must be zero at the center line.

In discussing the value of ϵ at the center of the tube, an additional relationship should be noted. From Equations (3) and (4) it is seen that

$$\frac{du}{dr} = \frac{2r}{r_0^2}\frac{du}{d\xi} \qquad (7)$$

and

$$\frac{d^2u}{dr^2} = \frac{2}{r_0^2}\frac{du}{d\xi} + \frac{2r}{r_0}\frac{d}{dr}\frac{du}{d\xi} \qquad (8)$$

Thus

$$\lim_{r\to 0} \frac{d^2u}{dr^2} = \frac{2}{r_0^2}\frac{du}{d\xi} \qquad (9)$$

Equation (9) is true as long as $du/d\xi$ does not tend toward infinity as r approaches zero.

Since the viscosity term in Equation (5) is usually relatively small, the value of $du/d\xi$ would have to be quite large at the center of the tube in order for ϵ to be zero. From Equation (9) it is seen that a large value of $du/d\xi$ indicates a pointed velocity profile. If $du/d\xi$ tended toward zero at the center of the tube, ϵ would of course tend toward infinity.

The reason for the controversy over the value of the eddy viscosity at the center of the channel can be understood by reference to a typical velocity profile from the work of Nikuradse (*3*). In Figure 1 u is plotted against r/r_0. A twenty-fivefold enlargement of the velocity scale in the central region is shown, and the extraordinarily low scatter of the data can be appreciated. The dashed line in the enlarged plot is the best fit (by eye) to the experimental points and forms a distinctly pointed profile. The solid curve in the enlarged plot is the best fit (again by eye) to the experimental points with the additional requirement of zero slope at the center line. The two curves are indistinguishable in the plot of the entire profile.

Figure 2 shows the same data plotted vs. the parameter ξ. The expanded view of the central region corresponds to the expanded region in Figure 1, and the dashed and solid curves also correspond in the two figures. By this method of plotting the difference in the way the

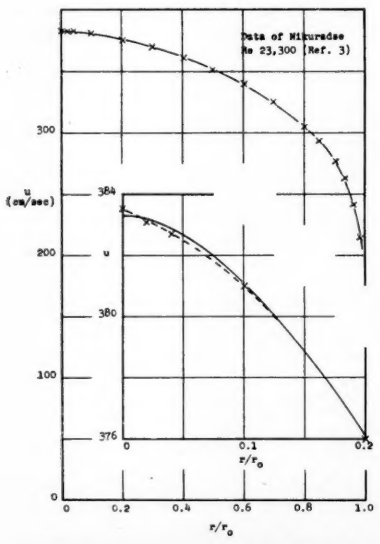

Fig. 1. Velocity vs. radial position.

two curves approach the center line (and hence the difference which will be obtained in the eddy viscosities) is readily seen. The two profiles differ at most by only 0.05%. Yet the center-line value of the eddy viscosity determined for the dashed curve, which comes in almost tangent to the center line, is approximately zero, whereas the center-line value for the solid curves is about 50% of the maximum value of the eddy viscosity for this profile.

The data of Nikuradse have been used here to illustrate the effect of a pointed velocity profile on the determination of the center-line value of the eddy viscosity. The data of other investigators could also have been used. In the work of Sage *et al.* (*1, 2, 4*) no tendency of the eddy viscosity to go to zero at the center line was reported. Values of the eddy viscosity were not given in the paper by Senecal and Rothfus (*7*), in which the region below *Re* 4,000 was studied. However Professor Rothfus (*5*) has informed the writer that low values of the eddy viscosity at the center line were obtained with Senecal's data used.

It was shown above that the low value of the eddy viscosity at the center line reported by Nikuradse on the basis of his data at 23,300 was obtained because the velocity profile was drawn without regard to its slope at the center line. The central core of a fluid flowing in a tube or channel is a zone of relatively uniform, nearly isotropic turbulence. A velocity profile drawn through a set of experimental points in this region should show no sharp changes in the first or second derivatives unless the data demand it, and on the basis of symmetry the first derivative at the center line must be zero. In other words a velocity profile should be no sharper than the scatter of the data requires. The method of plotting illustrated in Figure 2 is a convenience in meeting these requirements.

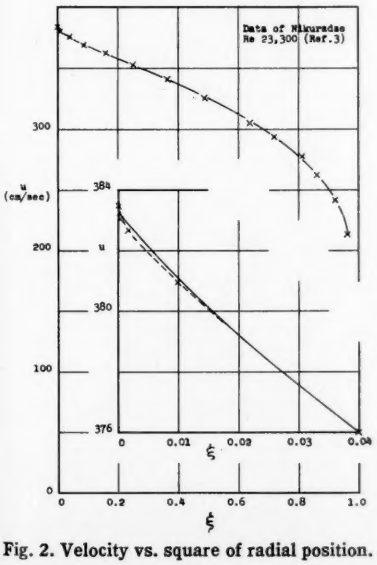

Fig. 2. Velocity vs. square of radial position.

The authors depended primarily on three sources for their eddy viscosities (*1, 3, 7*). Using the above criteria in plotting the writer has found that the data of Nikuradse (*3*) and Sage *et al.* (*1*) show a center-line value of the eddy viscosity which is generally 50% of the maximum value in the channel or greater. The same thing can probably be said of the data of Senecal and Rothfus. Such a relatively high value of the eddy viscosity is in accord with the work on eddy conductivity by Sage *et al.* (*4*) and is supported by the general picture of turbulent transport.

LITERATURE CITED

1. Corcoran, W. H., Franklin Page, Jr., W. G. Schlinger, and B. H. Sage, *Ind. Eng. Chem.*, **44**, 410 (1952).
2. Lynn, Scott, W. H. Corcoran, and B. H. Sage, *A.I.Ch.E. Journal*, **3**, 11 (1957).
3. Nikuradse, J., *V.D.I. Forschungsheft*, **356**, 1 (1932).
4. Page, Franklin, Jr., W. H. Corcoran, W. G. Schlinger, and B. H. Sage, *Ind. Eng. Chem.*, **44**, 424 (1952).
5. Rothfus, R. R., personal communication to the writer (July 7, 1958).
6. Rothfus, R. R., D. H. Archer, and K. G. Sikchi, *A.I.Ch.E. Journal*, **4**, 27 (1958).
7. Senecal, V. E., and R. R. Rothfus, *Chem. Eng. Progr.*, **49**, 533 (1953).

Reply

R. R. ROTHFUS and D. H. ARCHER

Carnegie Institute of Technology, Pittsburgh, Pennsylvania

It is surely possible that the eddy-viscosity pattern close to the center of a tube may be quite different from that shown in the authors' original paper. There are certain difficulties with the experimental velocity data, particularly with the center-line values. On the other hand it is hard to say whether these data should be set aside in favor of results on other modes of transfer or extrapolations based on certain models of the transport process. The central region is very complicated because small gradients of transferable properties may be important there, even though they are insignificant elsewhere in the stream. In addition the degree of correlation among the components of the velocity fluctuations changes rapidly with position in the vicinity of the center, making it hard to predict what may happen in the limit as the center is approached. All in all it seems that the eddy-viscosity profile near the center is largely uncertain and that the nature of the turbulent transport in this region remains the thing to be determined by further work.

(Continued from page 565.)

In the accompanying table numerical values needed for calculating several velocity profiles are given; the equations for the profiles are

$$\phi_{1/3} = 1 - s \tag{13}$$

$$\phi_{1/2} = 1 - (2/\pi)(cs + \arcsin s) \tag{14}$$

$$\phi_{2/3} = 1 - (2/\pi)(\tfrac{2}{3}c^3 s + cs + \arcsin s) \tag{15}$$

$$\phi_{5/6} = 1 - (2/\pi)\left(\frac{128}{315}c^9 s + \frac{16}{35}c^7 s + \frac{8}{15}c^5 s + \tfrac{2}{3}c^3 s + cs + \arcsin s\right) \tag{16}$$

wherein $c = (1 - s^2)^{1/2}$. These curves are presented in the accompanying figure. From the curves one can obtain the values of the reduced variable r for which the fluid velocity has fallen off to 1% of the velocity of the moving wall; this value r_1 given in the table is a measure of the extent of momentum penetration.

ACKNOWLEDGMENT

This work was begun while the author was the holder of a Guggenheim research grant at the Technische Hogeschool in Delft (Holland). The author wishes to thank Professor Hans Kramers and his staff for the hospitality accorded him at the Laboratorium voor Physische Technologie.

NOTATION

B_n = constant of integration
m, n = parameters characterizing a pseudoplastic fluid
r = reduced variable
s = variable defined in Equation (9)
t = time after wall begins to move
V = constant velocity of moving wall
y = distance from moving wall
μ = Newtonian viscosity
ρ = fluid density
ϕ_n = dimensionless velocity distribution

LITERATURE CITED

1. Reiner, Marcus, "Rhéologie Théorique," Dunod, Paris (1955).
2. Philippoff, Wladimir, "Viskosität der Kolloïde," Steinkopff, Germany (1942).
3. Fredrickson, A. G., and R. B. Bird, *Ind. Eng. Chem.*, **50**, 347 (1958).
4. Oldroyd, J. G., in "Rheology," ed. by F. R. Eirich, chap. 16, Academic Press, New York (1956).
5. Bird R. B., *A.I.Ch.E. Journal*, **2**, 428, 8S (1956).
6. Schlichting, Hermann, "Grenzschicht-Theorie," p. 63, Braun, Karlsruhe, Germany (1951).

nerical
several
ations

(13)

(14)

(15)

(16)

curves
nying
obtain
r for
off to
wall;
is a
entum

author
search
ool in
nes to
nd his
im at
Tech-

pseu-

on (9)
ove
g wall

stribu-

ique,"
it der
1942).
d, *Ind.*

ed. by
Press,

, 428,

chicht-
lsruhe,

1959